MULTI-PROXY PALAEOCLIMATE RECONSTRUCTION OF THE PERMIAN–TRIASSIC MASS EXTINCTION EVENT

by

TIMOTHY KEARSEY

A thesis submitted to the University of Plymouth
in partial fulfilment for the degree of

DOCTOR OF PHILOSOPHY

School of Earth, Ocean & Environmental Sciences
Faculty of Science

February 2009

MULTI-PROXY PALAEOCLIMATE RECONSTRUCTION OF THE PERMIAN–TRIASSIC MASS EXTINCTION EVENT

TIMOTHY KEARSEY

The Permian/Triassic (P/Tr) boundary is widely assumed to have been a time of extreme environmental upheaval and change. In the terrestrial realm, a negative anomaly in $\delta^{13}C$ isotope values has been reported from organic carbon in Antarctica, Australia, India and Madagascar, and from marine carbonate in the Karoo Basin. However, these sections are all from southern palaeolatitudes.

Analysis from the Permian–Triassic terrestrial sedimentary record of the South Urals, in Russia, comprising of many Aridisol and Vertisol horizons has revealed that, like the Southern Hemisphere, there is a dramatic change in paleosol morphology across the P/Tr boundary linked to a shift from meandering rivers to conglomeratic alluvial fans. Most of the paleosols include pedogenic carbonates at different stages of development, both above and below the P/Tr boundary. By the Triassic there is evidence of depressed water tables and increased seasonality. Analyses of the $\delta^{13}C_{carb}$ and $\delta^{18}O_{carb}$ signatures of these pedogenic carbonates have revealed a number of negative excursions in $\delta^{13}C_{carb}$ and $\delta^{18}O_{carb}$ in the Late Permian, including a negative excursion in the mid-Changhsingian, the first time such an event has been recorded in a terrestrial environment. Associated with this excursion are indicators of increasing extremes of climate, including pedogenic dolomite, which suggest a dramatic change in climate up to the P/Tr boundary. Equally, there is an increase in the range of precipitation, suggesting that what caused this mid-Changhsingian event also had a profound effect on the atmosphere.

There is also evidence, in the form of the $\delta^{18}O_{carb}$ excursion, of a rise in temperature just prior to the onset of the conglomeratic alluvial fan deposits, which mark the P/Tr boundary in Russia. Although in the Russian paleosols this excursion could be explained by a rise in the effect of seasonal rain or atmospheric temperature, estimates from unaltered brachiopods from the Italian Dolomites confirm that there is a rise in temperature and suggests that this is in the region of 7-8°C. These paleosols also record a dramatic rise in pCO_2 in the Earliest Triassic similar to what has been recorded in stomatal records across this period suggesting a dramatic input of CO_2 in to the atmosphere.

Contents

Abstract		**i**
Contents		**ii**
List of Figures		**vii**
List of Tables		**xiii**
List of Equations		**xv**
Acknowledgements		**xvii**
Author's declaration		**xviii**
Chapter 1	**Introduction**	**1**
1.1	**Rationale**	**1**
1.2	**Environmental and sedimentological variation**	**3**
1.2.1	***Sedimentological evidence***	**3**
1.2.2	***Isotope evidence***	**4**
1.3	**Temperature and pCO_2 changes**	**8**
1.4	**Aims**	**10**
1.4.1	***Objectives***	**10**
Chapter 2	**Methodology**	**13**
2.1	**Introduction**	**13**
2.2	**Field methods**	**13**
2.2.1	***Paleosol field methodology***	**13**
2.2.2	***Paleosol classification***	**16**
2.2.3	***Marine rocks field methodology***	**19**
2.3	**Laboratory methods**	**19**
2.3.1	***Stable isotope analysis methods***	**20**
2.3.2	***Carbonate bulk rock preparation***	**21**
2.3.3	***Pedogenic carbonate nodule preparation***	**22**
2.3.4	***Fossil preparation***	**22**
2.3.5	***$\delta^{13}C$ Organic carbon analysis***	**23**
2.3.6	***X-Ray diffractometer methods***	**24**

2.3.7 ICP OES methods 25

2.3.8 Cathodoluminescence methods 25

2.3.9 SEM microprobe methods 26

2.4 Petrographic slide preparation 27

2.5 Mathematical methods 29

2.5.1 Temperature equations 29

2.5.2 Solving cubic equations 30

2.5.3 Applications 32

2.5.4 Mathematical problems with estimates 35

2.5.5 Statistical methods 36

Chapter 3 Paleosols of the South Urals, Russia 39

3.1 Introduction 39

3.2 Geological background 39

3.2.1 Stratigraphic position 41

3.2.2 Studied sections 44

3.3 Field results: Palaeopedology 46

3.3.1 Boyevaya Gora 46

3.3.2 Sambullak 56

3.3.3 Tuyembetka 62

3.3.4 Vozdvizhenka 67

3.3.5 Krasnogor 70

3.3.6 Petropavlovka 71

3.3.7 Mescheryakovka 75

3.4 Discussion 78

3.4.1 Classification 78

3.4.2 Palaeoenvironmental interpretation 83

3.4.3 Changes across the P/Tr boundary 86

3.5 Summary 88

Chapter 4 Isotopic and mineralogical variation in paleosols from the Southern Urals 90

4.1 Introduction 90

4.2 Isotope results 91

4.3 Diagenesis and alteration of the isotope signal 95
4.3.1 Stages of calcrete development 96
4.3.2 Macromorphology 98
4.3.3 Micromorphology 99
4.3.4 Isotopic composition of spar and micrite 104
4.3.5 Variation with depth in paleosol 106
4.3.6 X-Ray diffraction results 109
4.3.7 Scanning electron microscopy 112
4.4 Quantifying the effects of alternation on the isotope signature 117
4.4.1 Statistical analysis 132
4.5 Discussion 134
4.5.1 Dolomite in the Russian sections 134
4.5.2 Stable isotope results 141
4.6 Summary 147

Chapter 5 Palaeoclimate analysis of the Southern Urals of Russia 149
5.1 Introduction 149
5.1.1 Pedological and mineralogical indicators of changes in climate 149
5.2 Palaeoprecipitation 154
5.2.1 Palaeoprecipitation estimates for the Southern Urals 158
5.3 Palaeotemperature and $\delta^{18}O$ composition of pedogenic carbonate 164
5.3.1 Different Methods 165
5.3.2 Monsoonal effects on oxygen isotopes 185
5.4 Discussion 187
5.5 Summary 193

Chapter 6 Isotopic variation in the Italian Dolomites 195
6.1 Introduction 195
6.2 Geological setting and stratigraphic position 196

6.3 Results – bulk rock stable isotopes 200
6.4 Results – brachiopods stable isotopes 203
6.4.1 Alteration of brachiopod shells 205
6.5 Discussion 208
6.5.1 Disparity between bulk rock and brachiopod values 212
6.5.2 Palaeotemperature estimates 215
6.5.3 $\delta^{13}C$ of the Permian atmosphere 218
6.6 Summary 219

Chapter 7 Atmospheric carbon dioxide and the $\delta^{13}C$ composition of pedogenic carbonate 221
7.1 The model 221
7.1.1 Generating the variables 222
$S_{(z)}$ – Soil respiration 222
$\delta^{13}C_a$ – isotopic composition of the atmosphere 222
$\delta^{13}C_\Phi$ – isotopic composition of soil organic matter 224
$\delta^{13}C_s$ – isotopic composition of soil water 225
7.2 Application and results from Russia 228
7.2.1 Results 230
7.3 Discussion 234
7.3.1 Comparison previous pCO_2 estimates 235
7.3.2 Modelling pCO_2 over the negative $\delta^{13}C_{carb}$ excursions 238
7.4 Summary 244

Chapter 8 Global comparisons 247
8.1 Introduction 247
8.2 P/Tr Global correlations and stratigraphy 250
8.3 Terrestrial isotopic comparison 256
8.3.1 Karoo Basin, South Africa 256
8.3.2 Antarctica 261
8.3.3 Other terrestrial section 264

8.4 Marine $\delta^{13}C$ comparisons 266
8.4.1 Chemostratigraphic correlations 269
8.5 $\delta^{18}O$ and temperature 270
8.6 Paleosol climate records 272
8.7 Siberian Traps correlation 275
8.8 Discussion 277
8.8.1 Palaeotemperature and palaeoenvironmental change 279
8.9 Summary 280

Chapter 9 Conclusions 283

References 289

Appendix 1 Paleosol feature descriptions and field data 323
A1.1 Pedological features of paleosols from Boyevaya Gora 324
A1.2 Pedological features of paleosols from Sambullak 327
A1.3 Pedological features of paleosols from Tuyembetka 328
A1.4 Pedological features of paleosols from Vozdvizhenka 332
A1.5 Pedological features of paleosols from Krasnogor 333
A1.6 Pedological features of paleosols from Petropavlovka 334
A1.7 Pedological features of paleosols from Mescheryakovka 335

Appendix 2 Paleosol isotope data, XRD data and statistical data 337
A2.1 Table of all isotope analysis from the Southern Urals of Russia 338
A2.2 Variation in stable isotope results for individual paleosols 354
A2.3 Detailed investigations into the presence of dolomite in pedogenic nodules 370
A2.4 X-ray diffraction results 373
A2.5 Statistical treatment paleosols 381
A2.6 Calibrated values for NBS 19 384

Appendix 3 Palaeoprecipitation, Palaeotemperature, and pCO_2calculations 389
A3.1 Palaeoprecipitation calculations 390
A3.2 Mean annual range of precipitation estimates 392
A3.3 Palaeotemperature calculations 395
A3.4 Atmospheric carbon dioxide calculations 398

Appendix 4 Italian dolomite brachiopods and bulk rock isotope Isotope results and palaeotemperature estimates 405
A4.1 Isotope results and palaeotemperature estimates for brachiopods 406
A4.2 Isotope results and palaeotemperature estimates for brachiopods 409
A4.3 Cross plots and isotopic variation across the shell for all the brachiopods 411
A4.4 Isotope drill sites on brachiopods 413

Appendix 5 A study of the effects of diagenetic dolomitisation on the isotopic composition of paleosols from the Italian Dolomites 415

List of Figures

Chapter 1

Figure 1.1 Terrestrial isotope sections P/Tr sections. 7

Chapter 2

Figure 2.1 Soil classification key. 18
Figure 2.2 A theoretical cubic function. 29
Figure 2.3 A cubic solution when $D \geq 0$. 34
Figure 2.4 Palaeotemperature estimates for equation (5.8c) using $\delta^{18}O_{carb}$ values from 0‰ to -12‰ VPDB. 36

Figure 2.5 Graphical statistical summary for the $\delta^{18}O$ values from paleosol KOR 22 at Boyevaya Gora. **37**

Chapter 3

Figure 3.1 Stratigraphy of the Cis-Ural Trough. **42**

Figure 3.2 Field area in Southern Urals. **44**

Figure 3.3 The stratigraphic position of all the sections studied in Russia. **45**

Figure 3.4 The studied section at Boyevaya Gora. **47**

Figure 3.5 Root traces in Russia. **49**

Figure 3.6 Bk horizon development stages in Russia. **50**

Figure 3.7 Ostracod in KOR17 suggesting a lacustrine environment. **51**

Figure 3.8 Paleosol developed channels and pedogenic slickensides. **52**

Figure 3.9 The Stage V at Boyevaya Gora. **53**

Figure 3.10 Variations of gley and mottles. **54**

Figure 3.11 Root traces in Triassic paleosols at Boyevaya Gora. **56**

Figure 3.12 The studied section at Sambullak. **58**

Figure 3.13 Palustrine associated paleosol (SAM2). **59**

Figure 3.14 A poorly developed paleosol (SAM 6). **60**

Figure 3.15 A stage IV carbonate horizon at Sambullak (SAM18). **61**

Figure 3.16 The studied section at Tuyembetka. **63**

Figure 3.17 Deep root traces at Tuyembetka (TUY46). **64**

Figure 3.18 'Knobbly' surface texture seen in surface calcite skins in many of the paleosols at Tuyembetka. **65**

Figure 3.19 Large cracks (A) and voids (B) unfilled with sparry calcite seen at Tuyembetka. **67**

Figure 3.20 The studied section at Vozdvizhenka. **68**

Figure 3.21 Paleosol VOZ9 with large blocky (9cm) nodules. **69**

Figure 3.22 Paleosol VOZ14 at Vozdvizhenka. **69**

Figure 3.23 The studied section at Krasnogor. **70**

Figure 3.24 The section at Petropavlovka. **72**

Figure 3.25 (5cm) mottles areas in the paleosols at Petropavlovka. Scale is 1metre in length. **73**

Figure 3.26 The studied section at Mescheryakovka. **74**

Figure 3.27 'Speckled' gley in the A horizon of MES8. 75
Figure 3.28 Tubular rhizoconcretion from Mescheryakovka. 76
Figure 3.29 Pseudo-gleyed paleosol at the top of Mescheryakovka. 77
Figure 3.30 A typical Stage II paleosol from the Permian and Triassic of Boyevaya Gora. 87

Chapter 4

Figure 4.1 Micritic carbonate values from the Late Permian and earliest Triassic sections from the Southern Urals of Russia. 92
Figure 4.2 Micritic carbonate values from Mescheryakovka in the Olenekian. 95
Figure 4.3 Cross plot of those micritic carbonate values from palustrine and mature micrite compared against micritic pedogenic values from stage II and I calcretes. 97
Figure 4.4 Internal macromorphology of pedogenic nodules. 98
Figure 4.5 Groundwater carbonate nodules from Petropavlovka. 99
Figure 4.6 Photomicrographs of typical textures seen in the carbonate nodules. 101
Figure 4.7 Digenetic textures. 102
Figure 4.8 Cross plot of those micritic carbonate values from microcrystalline calcite nodules. 104
Figure 4.9 Two isotopic depth plots of micritic and spar components. 105
Figure 4.10 Isotopic depth plots of micritic and spar components within individual paleosol horizons. 107
Figure 4.11 The relative peak heights between the dolomite response and the calcite response for different grain sizes of a disarticulated nodule. 111
Figure 4.12 Effects of the dolomite, and calcite specific stains. 112
Figure 4.13 SEM analysis of a nodule (KOR 2.4) which produced a dolomitic response on XRD. 113
Figure 4.14 Elemental mapping of a calcitic nodule (KOR 22.6). 114
Figure 4.15 Paleosol at Boyevaya Gora which contained both dolomitic and calcitic nodules. 115
Figure 4.16 $\delta^{13}C$ and $\delta^{18}O$ cross plots for Boyevaya Gora and Sambullak. 116

Figure 4.17 The isotope results from Boyevaya Gora screened using the criteria in Table 4.1. **126**

Figure 4.18 The isotope results from Sambullak screened using the criteria in Table 4.1. **128**

Figure 4.19 The isotope results from Tuyembetka screened using the criteria in Table 4.1. **129**

Figure 4.20 The isotope results from Krasnogor screened using the criteria in Table 4.1. **130**

Figure 4.21 The isotope results from Mescheryakovka screened using the criteria in Table 4.1. **131**

Figure 4.22 Dolomitic nodule from Russia (KORR2.4) and a dolomite nodule from the Dolomites of Italy. **134**

Figure 4.23 The ranges and medians (median represented by tick) of Type A and Type B dolomite from this study compared to isotope results from other studies. **136**

Figure 4.24 A typical paleosol containing Type B dolomite. **138**

Figure 4.25 The distribution of Type A and B dolomite in Russia. **140**

Figure 4.26 The ranges of different micritic carbonate components found in Russia. **142**

Figure 4.27 Screened and unscreened data from Boyevaya Gora and Sambullak correlated. **146**

Chapter 5

Figure 5.1 Summary of the pedological and isotopic features seen at Boyevaya Gora. **150**

Figure 5.2 Summary of the pedological and isotopic features seen at Sambullak. **152**

Figure 5.3 Summary of the pedological and isotopic features seen at Tuyembetka. **152**

Figure 5.4 Summary of the pedological and isotopic features seen at Mescheryakovka. **154**

Figure 5.5 Illustration how the depth to Bk horizon can be overprinted in stacked paleosols sequences. **156**

Figure 5.6 MAP estimates using equations at Boyevaya Gora. **160**

Figure 5.7 MAP estimates using equations at Sambullak. **160**

Figure 5.8 MAP estimates using equations at Tuyembetka. **161**

Figure 5.9 MAP estimates using equations at Mescheryakovka. **163**

Figure 5.10 Palaeotemperatures produced by equations (5.6) min, max and Mean modern values for $\delta^{18}O_p$ from 30–35°N. **167**

Figure 5.11 Palaeotemperatures produced by equations (5.6) Mean modern values for $\delta^{18}O_p$ from 30–35°N. **169**

Figure 5.12 The modern day relationships between $\delta^{18}O_p$ and temperature. **170**

Figure 5.13 The Summer/winter comparison from the same data used to produce equation (5.7c). **172**

Figure 5.14 Palaeotemperature estimates using equation (5.8a) for Boyevaya Gora, Sambullak and Mescheryakovka. **175**

Figure 5.15 Palaeotemperature estimates using equation (5.9) for Boyevaya Gora, Sambullak and Mescheryakovka. **178**

Figure 5.16 Weighted mean annual precipitation for 6 years plotted against mean annual temperature for Saratov station. **180**

Figure 5.17 The plots of the monthly data collected at Saratov. **181**

Figure 5.18 Weighted mean annual precipitation plotted against mean annual temperature. **182**

Figure 5.19 Palaeotemperature estimates using equation (5.10) for Boyevaya Gora, Sambullak and Mescheryakovka. **184**

Figure 5.20 Variation in $\delta^{18}O_{carb}$ of pedogenic carbonate plotted next to mean annual range of precipitation at Boyevaya Gora and Sambullak. **186**

Figure 5.21 The factors that can affect the $\delta^{18}O$ of soil carbonate. **190**

Chapter 6

Figure 6.1 Map of the South Tyrol region of Northern Italy with the study locality (Val Brutta and Tesero) marked. **197**

Figure 6.2 Detail of the beds around the Bellerophon Formation, Tesero Member boundary. **198**

Figure 6.3 Stable isotope results for both the brachiopods and bulk rock through the section at Val Brutta plotted against lithology. **201**

Figure 6.4 The photomicrographs represent the different lithologies. **204**

Figure 6.5 Stable isotope results for both the brachiopods and bulk rock through the section at Tesero plotted against lithology. **205**

Figure 6.6 Petrographic and cathodoluminescent images of the brachiopod shells. **206**

Figure 6.7 Petrographic and Cathodoluminescence image of TS1. **206**

Figure 6.8 Variation in $\delta^{18}O$ ratios across the fibrous and prismatic layers within brachiopod fossils. **208**

Figure 6.9 Carbonate isotope variations across the Permian – Triassic boundary in Italy and the Southern Alps. **209**

Figure 6.10 Recrystallisation textures in the Tesero. **210**

Figure 6.11 Brachiopod isotopic composition compared to bulk rock values from the Italian Dolomites. **213**

Figure 6.12 Comparison of the isotopic composition of micritic mud from within an articulated brachiopod. **214**

Chapter 7

Figure 7.1 pCO_2 estimates for the screened data from Boyevaya Gora. **231**

Figure 7.2 pCO_2 estimates for the screened data from Sambullak. **232**

Figure 7.3 pCO_2 estimates for the screened data from Mescheryakovka. **233**

Figure 7.4 The $pCO2$ estimates from this study compared to previously published data. **237**

Figure 7.5 Results from the scenario described in Table 7.7. **240**

Figure 7.6 The dominance of the two component mixing model described by Cerling (1991) and Ekart *et al.* (1999). **241**

Figure 7.7 Comparison of modelled $\delta^{13}C_{carb}$ values using the parameters in Table 7.7 with recorded $\delta^{13}C_{carb}$ values from Boyevaya Gora and Sambullak. **242**

Chapter 8

Figure 8.1 Magnetostatigraphic correlations used in this study. **255**

Figure 8.2 The ranges of other pedogenic carbonate studies across the Permian-Triassic boundary from the Karoo basin. **256**

Figure 8.3 Pedogenic carbonate nodules from Russia (this Study) and the Karoo basin (South Africa) correlated using magnetostratigraphic data. **257**

Figure 8.4 Pedogenic nodules from Bethulie section from the Karoo Basin and Sambullak from the Southern Urals. **259**

Figure 8.5 Therapsid tusks from Karoo compared to Boyevaya Gora section. **260**

Figure 8.6 Organic carbon values from Graphite peak in Antarctica Fishburn Australia compared to Boyevaya Gora in Russia. **263**

Figure 8.7 Russian section at Boyevaya Gora correlated with marine sections at Meishan and India. **267**

Figure 8.8 Bulk rock marine isotope records from the Italian Dolomites compared to Sambullak in Russia. **268**

Figure 8.9 Temperature estimates from the Italian Brachiopods with the estimates for Boyevaya Gora and Sambullak. **271**

Figure 8.9 The extent of the Siberian large igneous province (LIP) in both surface outcrop and subcrop and the field area of this study. **275**

List of Tables

Chapter 1

Table 1.1 A summary of the carbon and oxygen isotopic excursion across the Permian Triassic boundary in marine section. **5**

Table 1.2 A summary of the carbon and oxygen isotopic excursion across the Permian Triassic boundary in terrestrial section. **6**

Chapter 2

Table 2.1 Locality codes for Russian samples collected for isotope analysis. **14**

Table 2.2 Bk horizon classification used in the field. **15**

Table 2.3 Dixon's staining technique. **28**

Table 2.4 The calculated intermediate definitions for the equation (3a) with inputs of $\delta^{18}O_{carb}$ VSMOW = 30.39‰. **33**

Table 2.5 Values for the three different *x* intercepts in both °K and °C. **33**

Table 2.6 Values for the three different *x* intercepts in both °K and °C. **34**

Table 2.7	Values for x_1 intercepts in both °K and °C.	**35**

Chapter 3

Table 3.1	Classification used by Cleveland *et al.* (2008).	**80**
Table 3.2	Paleosol classification used in this study and the equivalent classifications based on the Retallack (1993).	**82**
Table 3.3	Summary of the level of Bk development in the South Urals, Russia.	**84**

Chapter 4

Table 4.1	Summary of multiple drill site XRD test.	**110**
Table 4.2	Summary of the screening results for all isotope results from Russia.	**125**
Table 4.3	Summary of statistical tests using the Mann-Whitney test.	**133**
Table 4.4	Ranges from micritic pedogenic calcite values from other paleosol studies across the P/Tr boundary.	**144**

Chapter 5

Table 5.1	The average MAP from the four longest Russian sections for the four different MAP equations.	**159**
Table 5.2	The mean annual air temperatures (in °K and °C) for equations (5.8b) and (5.8c).	**176**
Table 5.3	Values from the three palaeotemperature equations.	**188**
Table 5.4	The change in $\delta^{18}O_p$ to generate excursion P3 at Boyevaya Gora and Sambullak if temperature is held constant.	**192**

Chapter 6

Table 6.1	Trace elemental analysis and cathodoluminescence results for the brachiopod fossils and bulk rock.	**207**
Table 6.2	Palaeotemperature estimates from unaltered brachiopods at different salinity and thus $\delta^{18}O$ seawater compositions.	**217**

Chapter 7

Table 7.1 The maximum range of brachiopod values from before and after the P/Tr boundary from published data and field data. **223**

Table 7.2 Values for organic carbon recovered from Sambullak. **224**

Table 7.3 Calculated values of $\delta^{13}C$ calcite if only formed from CO_2 produced from organic carbon present in the soil. **227**

Table 7.4 The variables used in the three different methods used for generating the pCO_2 estimates. **229**

Table 7.5 Published pCO_2 estimates using both Calcic paleosols and stomatal indexes across the Permian –Triassic period. **230**

Table 7.6 Summary of average atmospheric carbon dioxide calculations. **235**

Table 7.7 Input parameters for the model using equation 7.1 solved for $\delta^{13}C_s$ **239**

Chapter 8

Table 8.1 Paleosol and palaeoclimate changes across the P/Tr boundary in Terrestrial environments. **273**

List of Equations

Chapter 2

Equation 2.1 Derivation of the delta values. **20**

Equation 2.2 Conversion from VPDB to VSMOW. **20**

Equation 2.3 Standard solution for the roots of a cubic equation. **30**

Equation 2.4a Definition of intermediate function p. **30**

Equation 2.4b Definition of intermediate function q. **30**

Equation 2.4c Definition of intermediate function D. **30**

Equation 2.5a Definition of intermediate function u. **30**

Equation 2.5b Definition of intermediate function v. **31**

Equation 2.5c Definition of intermediate function y_1 $D \geq 0$. **31**

Equation 2.5d Definition of intermediate function $y_{2,3}$ $D \geq 0$. **31**

Equation 2.6a Definition of intermediate function φ. **31**

Equation 2.6b Definition of intermediate function y_1 $D < 0$. **31**

Equation 2.6c Definition of intermediate function $y_{2,3}$ $D < 0$. **32**

Equation 2.7 Definition of intermediate function x_n. **32**

Chapter 5

Equation 5.1 Decompression algorithm. **156**

Equation 5.2 Palaeoprecipitation equation proposed by Retallack (2005). **157**

Equation 5.3a Palaeoprecipitation equation for Vertisols (microlows). **157**

Equation 5.3b Palaeoprecipitation equation for Vertisols (microhighs). **157**

Equation 5.4 Palaeoprecipitation equation for Aridisols. **157**

Equation 5.5 Annual range of precipitation equation. **158**

Equation 5.6 Meteoric precipitation and temperature on the $\delta^{18}O$ of the pedogenic carbonate. **165**

Equation 5.7a Modern global relation between changes in MAT and $\delta^{18}O_p$. **171**

Equation 5.7b The modern summer and winter $\delta^{18}O_p$ MAT relationship from a station in Waco Texas. **171**

Equation 5.7c The modern summer and winter $\delta^{18}O_p$ MAT relationship from a station in Saratov Russia. **172**

Equation 5.8a Third-order cubic polynomial for both the spatial relationship. **173**

Equation 5.8b Third-order cubic polynomial for both the temporal relationship (Waco Texas). **173**

Equation 5.8c Third-order cubic polynomial for both the temporal relationship (Saratov). **173**

Equation 5.9 MAT and modern pedogenic carbonates, from the IAE/WMO database. **177**

Equation 5.10 Third-order cubic polynomial for both the temporal relationship (Saratov weighed Annual means). **183**

Chapter 6

Equation 6.1 Relationship between shell $\delta^{18}O$ calcite precipitation temperature (Auclair *et al.* 2003). **215**

Equation 6.2 Relationship between shell $\delta^{18}O$ calcite precipitation temperature (Parkinson *et al.* 2005). **215**

Chapter 7

Equation 7.1 Modelling pCO_2 using pedogenic carbonate. **221**

Equation 7.2 Relationship between $\delta^{13}C_a$ and $\delta^{13}C_\Phi$. **224**

Equation 7.3 Temperature-dependent fractionation factor described by Romanek *et al.* (1992). **226**

Acknowledgements

Firstly I would like to thank my supervisors Dr Richard Twitchett, Dr Stephen Grimes and Dr Gregory Price for their help, supervision, advice, criticisms and discussions over the past three years.

My thanks also go to the Russia 2006 Field team and especially Prof Michael Benton, Dr Misha Surkov, Dr Valentin Tverdokhlebov, Dr Andy Newell, Dr Richard Twitchett and Dr Graeme Taylor. Also I would especially like to thank Dr Andrew Newell and Dr Richard Twitchett for their access to their unpublished field data and Dr Graeme Taylor for access and advice to his magnetostatigraphic data and for numerous discussions on that and many other aspects of the project.

For all his help advice and assistance running the IRMS I would especially like to thank Dr Paul Sutton and also for allowing me to run it late into the night and at weekends. My thanks also go to Dr Roy Moate and the Scanning Election Microscopy Centre; Dr Andrew Fisher for his help with the ICP OES analysis; Mr Peter Frost and Camborne School of Mines for allowing me to use their Cathodoluminescence Microscope and Dr Neil Ogle of Queens University, Belfast for running the organic carbon samples. Also I my gratitude goes to Dr Rana Moyeed and Dr Stephen Kearsey for their help and advice on the mathematical and statistical methods used in this thesis and to Dr Nathan Sheldon for discussions and advice on many of the isotopic and temperature modelling aspects of this thesis. To Mrs. Susan Kearsey for proof reading many drafts of this thesis, sometimes at very short notice. I would also like to thank Mr Jonathon Dyson and Miss Elizabeth Pascoe for acting as my field assistants on the 2007 Italian Dolomites field season.

I would also like to thank the University of Plymouth for funding my PhD and both the Palaeontological Association and the Geological Society for funding the Italian Fieldwork.

Finally I would like to thank my parents for their support and interest throughout this project and all my friends who made me take time out to go into the mountains when I needed to regain perspective.

Author's Declaration

At no time during the registration for the degree of Doctor of Philosophy has the author been registration for any other University award without prior agreement of the Graduate Committee.

This study was financed with the aid of a studentship from the University of Plymouth. The Russian analysis and fieldwork was funded by National Geographic (746903) (2004) and NERC (NE/C518973/1) (2006) Awarded to Prof M.J. Benton and Dr R.J. Twitchett. The Italy analysis and fieldwork was funded by the Sylvester Bradley Award from the Palaeontological Association (2005) and the Timothy Jefferson Field Fund Research from Geological Society (2006) awarded to T. Kearsey.

Relevant scientific seminars and conferences were regularly attended at which work was often presented; external institutions were visited for consultation purpose and several papers prepared for publication.

Publications:

Kearsey, T. 2007, High resolution isotopic curves and palaeotemperature through the Permian/Triassic extinction, *The Palaeontological Association Newsletter*, **65**. 99-102

Kearsey, T. Twitchett. R.J., Newell, A.J. The origin and significance of pedogenic dolomite from the Upper Permian of the South Urals of Russia, *Geology. (in review)*

Kearsey, T., Twitchett R.J., Price, G.D., Grimes S.T. Isotope excursions and palaeotemperature estimates from the Permian/Triassic Boundary in the Italian Dolomites. *Palaeogeography, Palaeoclimatology, Palaeoecology (in review)*

Taylor, G.K., Tucker, C.W., Twitchett, R.T., Kearsey, T., Benton, M.J., Newell, A.J., Surkov, M.V., Magnetostratigraphy of Permian/Triassic boundary sequences in the Cis-Urals, Russia: No evidence for a major temporal hiatus. *Earth and Planetary Science Letters (in review)*

Presentation and Conferences Attended:

International Congress – Palaeozoic Climates. Lille, France (Aug 2008)

Annual Meeting of the Palaeontological Association, Uppsala, Sweden (Dec 2007)

Geological Society of America Annual meeting, Denver, USA (Aug 2007)

International Field Workshop on 'The Triassic of eastern France', Strasbourg, France (Oct 2006)

British Sedimentary Research Group Annual Meeting, Aberdeen, UK (Dec 2006)

Annual Meeting of the Palaeontological Association, Oxford, UK (Dec 2005)

Word count of main body of thesis: 63998 words

Signed.....Tim Kearsey.....

Date..24th April 2009.....

Chapter 1. Introduction

1.1 Rationale

The end-Permian mass extinction event is recognised as being the greatest mass extinction of the whole Phanerozoic (Hallam and Wignall 1997; Benton and Twitchett 2003; Erwin 2006). Estimates of the extinction suggest 80-96% marine species became extinct, and a similar or greater loss in the terrestrial realm (Benton 1995; Hallam and Wignall 1997). Studies have suggested that the extinction was in the order of 10^{4-5} years (Rampino *et al.* 2000; Twitchett *et al.* 2001) and that the $\delta^{13}C$ excursions, which are linked to the mass extinctions, also only lasted for <10,000years (Retallack and Jahren 2008).

The causes of the mass extinction are still strongly debated and no one mechanism has yet been shown to explain all the evidence. There has been some proposed evidence for an impact event at the Permian/Triassic (P/Tr) boundary based on both chemical data, such as extraterrestrial helium trapped in fullerenes, and a possible impact structure in Bedout in north western Australia (Becker *et al.* 2001; Becker *et al.* 2004). However, both these lines of evidence have been highly criticised (Koeberl *et al.* 2004; Renne *et al.* 2004; Wignall *et al.* 2004; Farley *et al.* 2005; Müller *et al.* 2005). A kill mechanism which has long been proposed as causing the end Permian mass extinction is the Siberian Traps. These are continental flood basalts (Bryan and Ernst 2008) which cover an area of over 2,300,000km^3, although this estimate does not take into account erosion since their emplacement (Reichnow *et al.* 2002). They represent the biggest continental flood basalt event in the Phanerozoic (Hallam and Wignall 1997) and have been linked to a vast input of carbon dioxide into the atmosphere which caused dramatic global warming (e.g. Wignall 2001; Kidder and Worsley 2004; Twitchett 2007).

Krull and Retallack (2001) have observed extremely negative $\delta^{13}C$ values of –46.2‰ from paleosol-derived organic carbon from Graphite Peak in Antarctica, just before the P/Tr boundary (as defined by Collinson *et al.* 2006). They interpret this as being caused by methanotrophic bacteria, which are supposed to be present in high abundance due to the presence of high atmospheric methane levels. This methane was thought to have been generated from the destabilisation of methane clathrates (Erwin 1993; Krull and Retallack 2001). However, clathrates as the source of this methane has been recently questioned (Berner 2002; Payne and Kump 2007; Retallack and Jahren 2008). Instead it is proposed that the methane was produced by the Siberian Traps intruding into the extensive carbon-rich sediment found in the Siberian basin metamorphosing the coal and producing methane (Erwin 2006; Krull and Retallack 2006; Retallack and Jahren 2008).

It has also been suggested that there may have been multiple causes of the extinction (Erwin, 1993; 2006, so-called 'Murder on the Orient Express' hypothesis). This envisages many, or all, of the above mechanisms causing, or having an impact upon, the extinction event (e.g. Kidder and Worsley 2004) which were either triggered by the Siberian Traps (Wignall 2007; Twitchett 2007) or methane production related to some other factor, such as a mantle plume, which caused both the events (e.g. Heydari *et al.* 2008). To resolve the lack of consensus, it is important to assess the different environmental, sedimentological and geochemical evidence for climate change across the P/Tr boundary to see if there are any gaps in our understanding that might lead to a resolution of this debate.

1.2 Environmental and sedimentological variation

1.2.1 Sedimentological evidence

There was a significant change in environment across the P/Tr boundary. The evidence for dramatic climate change across the P/Tr boundary in terrestrial sequences is especially marked. The most striking is the sudden change in facies from quiescent meandering river systems to braided river and conglomeratic fans (Newell *et al.* 1999; Ward *et al.* 2000). This shift to coarser-grained facies concurrent with the P/Tr boundary has been observed in the Karoo Basin of South Africa (Ward *et al.* 2000), Antarctica (Retallack and Krull 1999, Retallack 2005a), Australia (Retallack 1999; Michaelsen 2002) India (Sarkar *et al.* 2003), the Iberian ranges of Spain (Arche *et al.* 2005; Benito *et al.* 2005) and the South Urals of Russia (Newell *et al.* 1999; Benton *et al.* 2004). This global distribution is taken to suggest that the cause is not the result of localised changes in uplift and deposition rates, rather it is thought to be caused by a major die-off of rooted plant life causing destabilisation of the surface and resulting in dramatic erosion in highland source areas (Ward *et al.* 2000; Retallack 2005a).

It has also been observed that in all sections that span the P/Tr boundary that there is no coal in the earliest Triassic (Retallack *et al.* 1996; Michaelsen 2002; Retallack *et al.* 2005) and this is thought to be due to an extinction of coal floras (Retallack *et al.* 1996). An increase in global aridity is inferred through the Permian (Ziegler *et al.* 1997; Roscher and Schneider 2006).

In both Antarctica and the Karoo Basin it has been inferred that there is a significant increase in mean annual precipitation (Retallack and Krull 1999; Retallack *et al* 2003). This is not, however, a globally consistent picture as in Australia it has been observed that there was a drop in precipitation from the latest Permian and earliest Triassic to the Early Triassic

(Retallack 1999). Rises in precipitation are linked to an abrupt increase in chemical weathering observed at Graphite Peak in Antarctica, suggested by increased leaching of the soil recorded in geochemical ratios (Sheldon.2006). This is similar to physical leaching observed in the boundary breccias found in Australia (Retallack 1999). Also the identification of berthierine in the earliest Triassic Antarctica paleosols suggests a reducing environment in the paleosols, possibly caused by methane oxidation in the atmosphere (Sheldon and Retallack 2002; Retallack *et al.* 2006).

It is important to identify global similarities and differences in the evidence, in order to show which factors were acting regionally and which require a global explanation. This is important in understanding the global significance of any particular factor in explaining the cause of the P/Tr mass extinction.

1.2.2 Isotopic evidence

It has been observed globally that the Permian mass extinction is coincident, or just before or after a marked negative excursion in $\delta^{13}C$ isotope values in both marine and terrestrial sections (e.g. Erwin 1993; Kidder and Worsley 2006; Erwin 2006, Krull and Retallack 2006; Gorjan *et al.* 2008; Retallack and Jahren 2008). Variation in $\delta^{13}C$ has been linked to many of the environmental effects of the extinction as well as changes in atmospheric carbon dioxide (pCO_2). It has also been linked to changes in the input of terrestrial carbon into marine sections and upwelling of anoxic bottom waters, in marine sections (Foster *et al.*1997; Ekart *et al.* 1999; Kidder and Woresley; Algeo *et al.* 2007) and the presence of methane in the atmosphere (Krull and Retallack 2001).

Location	Material	Excursion (‰, VPDB)			Source
		$\delta^{13}C_{carb}$	$\delta^{18}O_{carb}$	$\delta^{13}C_{org}$	
British Columbia	Kerogen	-		-3.0	Wang *et al.* 1994
Gartnerkofel-1, Austria	Carbonate and Kerogen	-3.4	-3.0	-15.9	Magaritz *et al.* 1991; Magaritz *et al.* 1992
Japan	Carbonate and Kerogen	-2.0		-1.4	Musashi *et al.* 2001
Meshian, China	Carbonate	-8.0			Yin *et al.* 2001
Abadaeh, Iran	Carbonate and Kerogen	-5.1		-3.2	Heydari *et al.* 2000
Emarat, Iran	Carbonate	-4.9			Baud *et al.* 1989
Nammal Gorge, Pakistan	Carbonate	-4.4			Baud *et al.* 1996
Soverashan, Armenian	Carbonate	-3.5			Baud *et al.* 1989
Wadi Wasit, Oman	Carbonate	-3.5			Krystyn *et al.* 2003
Jameson Land, East Greenland	Carbonate and Kerogen	-8.5		-10.5	Twitchett *et al.* 2001
Heping, China	Carbonate	-6			Krull *et al.* 2004
Dolomites, Italy	Carbonate	Between -1 to -3			Korte and Kozur 2005
Gerennavar, Hungary	Carbonate	-2.6			Korte and Kozur 2005
Slovenia	Carbonate and Kerogen	-12.5	-5.3	-6.5	Dolenec *et al.* 1999, 2001
Nhi Tao, Vietnam	Carbonate	-3			Algeo *et al.* 2007
Tesero, Italy	Carbonate	-2	-3		Magaritz *et al.* 1988
Northern India	Carbonate	-4	-6.0		Baud *et al.* 1996
Dicksonland, Spitsbergen	Kerogen			-8.5	Wignall *et al.* 1998
Sverdrup Basin, Arctic Canada	Kerogen			-6.5 to -3.5	Grasby and Beachamp 2008

Table 1.1 A summary of the carbon and oxygen isotopic excursion across the Permian/Triassic boundary in marine sections.

The $\delta^{13}C_{carb}$ carbonate anomaly is recorded globally (Table 1.1) both in equatorial localities such as the Italian Dolomites to high latitudes such as Spitzbergen (Table 1.1; Retallack and Krull 2006). Equally it has been observed both in organic carbon in deep waters settings (cf. Wang *et al.* 1994) and shallow marine settings (cf. Magaritz *et al.* 1992). There is a variation in the relative sizes of the excursion globally (Table 1.1). Grasby and Beauchamp (2008) suggest that some of this may simply reflect local basin-scale processes. In their study in the Sverdrup Basin, Arctic Canada, they observe that $\delta^{13}C_{org}$ organic values decrease progressively from –6.5‰ on the basin margin to –3.5‰ in the basin centre. However, others

have argued that the global variation is more to do with the relative impact of the extinction event than localised variation (Retallack and Krull 2006; Retallack and Jahren 2008).

		Excursion (‰, VPDB)			
Location	**Material**	**$\delta^{13}C_{org}$**	**$\delta^{13}C_{carb}$**	**$\delta^{18}O_{carb}$**	**Source**
Commando Drift Dam, Karoo	Nodular carbonate, Organic carbon	no trend	-2		Coney *et al.* 2007
Eddystone, Australia	Organic carbon	-3.2			Morante 1996
Xinjiang Province, China	Organic carbon	many excursions			Metcalfe *et al.* 2008
Raniganj Coalfield, India	Organic carbon	-13.8			de Wit *et al.* 2002
Talcher Coalfield, India	Organic carbon	-8.8			de Wit *et al.* 2003
Morondava, Madagascar	Organic carbon	-7.9			de Wit *et al.* 2004
Graphite Peak, Antarctica	Organic carbon	-22.2			Krull and Retallack 2000
Portal Mountain, Antarctica	Organic carbon	-3			Retallack *et al.* 2006
Raniganj Coalfield, India	Organic carbon	-9			Sarkar *et al.* 2003
Bethulie, Karoo	Nodular carbonate		-10	-1	MacLoed *et al.* 2000
Bethulie, Karoo	Vertebrate teeth and tusks		-1.9	-0.53	MacLoed *et al.* 2000
Karoo Composite	Nodular carbonate	-2	-12		Ward *et al.* 2005

Table 1.2 The carbon and oxygen isotopic excursion across the Permian / Triassic boundary in terrestrial sections.

There are far fewer terrestrial isotope studies (Table 1.2) than marine, however, their significance is in many ways more important as they represent a direct interaction with climate and the atmosphere rather than being buffered by ocean chemistry (Krull and Retallack 2001; de Wit *et al.* 2002). Thus, they will be directly influenced by the proposed extinction mechanism such as the input of volcanogenic carbon dioxide or methane (de Wit *et al.* 2002). Terrestrial isotope excursions have been recorded in other locations globally (Table 1.2, Figure 1.1) including in South Africa, Australia, India and China.

Three types of material have been used as proxies to record $\delta^{13}C$ in terrestrial sequences: organic matter, vertebrate teeth and carbonate nodules. The $\delta^{13}C$ values of these all record subtly different things. Soil organic carbon records the composition of organic matter

preserved in a soil, which chart atmospheric $\delta^{13}C$ that is assimilated into and fractionated by plants (Arens *et al.* 2000) recording variation over a matter of years (Retallack and Jahren 2008). Vertebrate teeth record the isotopic composition of the animal's diet when it the organism is growing teeth (Thackeray *et al.* 1990; MacLeod *et al.* 2000) On the other hand, paleosol carbonate in nodules can take thousands of years to form and thus represents a time-averaged signal (Liu *et al.* 1996; Retallack 2001a; Alonso-Zarza 2003). The values from the Karoo Basin, from organic matter, carbonate nodule (Ward *et al.* 2000; Coney *et al.* 2007) and vertebrate tusks (MacLeod *et al.* 2000), show excursions in both $\delta^{13}C$ and $\delta^{18}O$ at the P/Tr boundary. However, it has been argued that at least the pedogenic carbonate values may represent local soil conditions rather than atmospheric variation because some of these soils show strong evidence of being waterlogged (Tabor *et al.* 2007).

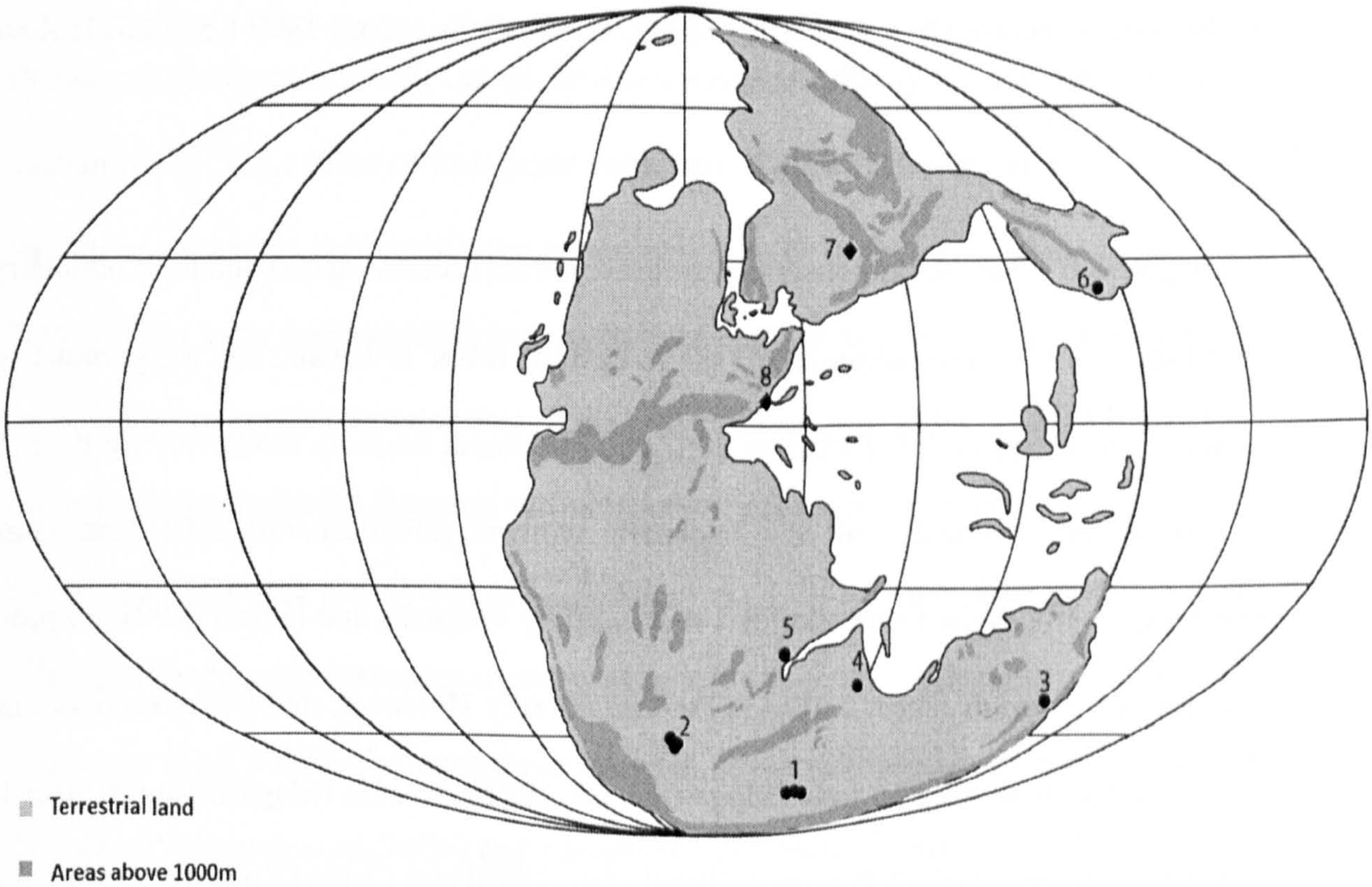

Figure 1.1 Terrestrial P/Tr isotope sections 1. Antarctica (e.g. Krull and Retallack 2001), 2. Karoo basin, South Africa (MacLeod *et al.* 2000; Ward *et al.* 2005), 3. Australia (e.g. Morante 1996), 4. India (e.g. deWit *et al.* 2002), 5. Madagascar (e.g. deWit *et al.* 2002), 6. North China (Metcalfe *et al.* 2008). Field areas investigated in this study 7. South Urals of Russia and 8. Marine sections from the Italian Dolomites. (base map adapted from Rowley 2008, Changhsingian 252Ma).

The $\delta^{13}C$ and $\delta^{18}O$ excursions have been observed to be greater at high latitudes in the southern hemisphere (Table 1.2). Studies in North China have failed to show any organic carbon anomaly (Metcalfe *et al.* 2008) and as yet there have been no studies into terrestrial pedogenic carbonate from the northern hemisphere or studies that investigate as far into the late Permian as has been studied in Antarctica and Australia (cf. Morante 1996; Krull and Retallack 2001; Metcalfe *et al.* 2008).

1.3 Temperature and pCO_2 changes

One of the main indicators of a rise in temperature across the Permian/Triassic boundary comes from the terrestrial realm. It has been observed that there was a migration of thermophilic plants and a change in paleosols in the high latitudes of both the northern and southern hemispheres (Retallack 1999, 2002, Retallack and Krull 1999 Looy 2001; Retallack and Krull 2006).

The negative $\delta^{18}O$ excursion observed in some marine sections across the P/Tr boundary is linked to a 5-6°C rise in temperature (Magaritz and Holser 1991) and this temperature is often quoted in the literature (cf. Twitchett 2007 and references therein). However, the P/Tr $\delta^{18}O$ excursions may also be a result of a diagenetic overprint (Heydari *et al.* 2001; Hass *et al.* 2006), especially as the Gartnerkofel-1 core used by Magaritz and Holser (1991) to produce this estimate is heavily recrystallised (Twitchett 2007). However, this $\delta^{18}O$ excursion has also been recorded in sections in Italy (Magaritz *et al.* 1988), Austria (Magaritz and Holser 1991), Slovenia (Dolenec *et al.* 1999), India (Baud *et al.* 1996) and China (Xu *et al.* 1986) which may also suggest that it is a global event rather than a localised diagenetic overprint. In the analysis of their data Magaritz and Holser (1991) conclude that a similar negative $\delta^{18}O$ shift could also be caused by a decrease in salinity.

The study of the isotopic composition of fossil carbonate shells such as brachiopods has the potential to avoid some of these issues because they form in equilibrium with seawater and so represent a direct interaction with the water chemistry (Auclair *et al.* 2003). Fossil brachiopods, due to their low-Mg calcite composition, which is a diagenetically more stable polymorph of calcite, have the potential to preserve a primary isotopic signal (Auclair *et al.* 2003). Korte *et al.* (2005a,b) carried out studies into brachiopod variation through the Permian and Triassic to investigate coeval isotopic variation of seawater and palaeotemperature. However, crucially, they found no unaltered brachiopods from the earliest Triassic (Korte *et al.* 2005b) and do not compare the brachiopod records and bulk rock values from the same locality.

Pedogenic carbonate nodules can be used to investigate changes in palaeotemperature though variation in $\delta^{18}O_{carb}$ value of pedogenic carbonate. This is based on the principle that $\delta^{18}O$ in terrestrial sediments is derived from meteoric water (Dworkin *et al.* 2005; Prochnow *et al.* 2006). It has been demonstrated that the oxygen isotopic composition of unaltered soil carbonates is directly related to that of the ambient meteoric water, and the $\delta^{18}O$ of the meteoric water is itself a function of fractionation during precipitation and atmospheric temperature (Cerling and Quade 1993; Mack *et al.*, 1991). It may therefore be possible to use $\delta^{18}O_{carb}$ of pedogenic carbonate to estimate palaeotemperature (Dworkin *et al.* 2005; Prochnow *et al.* 2006). This technique has been effectively used in paleosols from the late Triassic (Prochnow *et al.* 2006) and across the Cretaceous/Tertiary boundary (Dworkin *et al.* 2005) but has not yet been applied to the Permian/Triassic boundary.

The $\delta^{13}C$ composition of pedogenic carbonate from paleosols can also be used to calculate atmospheric pCO_2 although this depends on the paleosol not being formed in non-

waterlogged conditions (Cerling 1984; Cerling 1991; Ekart *et al.* 1999). This technique has been applied to paleosols from the early Guadalupian and Middle Triassic in India and a ~500ppmV rise in pCO_2 across this interval has been inferred (Ghosh *et al.* 2001).

1.4 Aims

The aims of this project are to investigate changes in climate, precipitation, stable isotopes, temperature and carbon dioxide variation through the Late Permian and Early Triassic recorded in sections in the northern hemisphere. It will focus on paleosols from terrestrial sections in the South Urals of Russia and compare them to previously published studies from Southern Hemisphere to ascertain whether the recorded changes are global.

1.4.1 Objectives

- To investigate paleosols from the South Urals of Russia and to determine the environment of their formation and how they vary both laterally and vertically in stratigraphic section across the South Urals basin.
- To study the stable isotope composition of pedogenic carbonate from the paleosols, determine the effects of diagenesis and other influences on the carbonate, and assess whether recorded changes are the result of changes in atmospheric conditions or localised soil waters.
- To use the information gained from the paleosols and the isotope results to investigate changes in precipitation and temperature through the P/Tr boundary.
- To study the stable isotope composition of brachiopods from the Italian Dolomites across the P/Tr boundary to produce estimates for atmospheric $\delta^{13}C$ compositions and accurate palaeotemperature estimates which can be compared with the results from the South Urals to test the validity of the paleosol estimates.

- To use the isotopic information from both the Italian brachiopods and Russian pedogenic carbonate to investigate variations in pCO_2.
- To compare these results with those recovered from other terrestrial and marine studies across the P/Tr boundary.

Chapter 2. Methodology

2.1 Introduction

The data and samples used in this study were collected during four field seasons; two investigating the terrestrial sequence of the South Urals of Russia in 2004 and 2006, and two in the Italian Dolomites investigating terrestrial and marine sections in 2006 and 2007. The field localities are described in the relevant results chapters (Chapters 3 and 6). The Russian field seasons were as part of the Bristol–Plymouth–Saratov Expedition, headed by Prof Mike Benton, Dr Richard Twitchett, Misha Surkov and Dr Valentin Tverdokhlebov. The author was not present on the 2004 Russian field season and thus the samples collected from that year (labelled 04.--. --) were not sampled by the method described below.

This chapter describes the methods used both in the field and laboratory analysis for further discussion of the techniques used see Chapters 4 and 6. This chapter also discusses the mathematical and statistical techniques used in Chapters 4 and 5. For discussion of the palaeotemperature equations and how they were generated see Chapter 5.

2.2 Field methods

2.2.1 Paleosol field methodology

All paleosols identified in this study were logged using a standardised field methodology, base on methods suggested by Retallack (1997, 2001). Paleosols were initially identified on 1) their presence within terrestrial sequences; 2) the presence of root traces or evident mud cracking which would suggest subaerial exposure; 3) the presence of mottling and/or carbonate nodules. The paleosols were named using a three-letter locality code (i.e.

Sambullak = SAM) and a number referring to that paleosol horizon (Table 2.1). Where subsequent analysis has revealed that a paleosol is actually part of a stacked sequence of paleosols, or for time reasons in the field they were grouped as one unit, the names are subdivided using alphabetic symbols (i.e. KOR1a, KOR1b). The paleosols from the Boyevaya Gora section are labelled KOR as the field name for this locality was Korolki (the Korolki ravine is only part of the Boyevaya Gora exposure).

Locality	Locality code
Boyevaya Gora	KOR
Sambullak	SAM
Tuyembetka	TUY
Krasnogor	KRA
Vozdvizhenka	VOZ
Petropavlovka	PET
Mescheryakovka	MES

Table 2.1 Locality codes for Russian samples collected for isotope analysis.

In the field, once a paleosol had been located, the top of the horizon was identified and the paleosol profile was logged from there down at centimetre scale. Grain size changes through these profiles were identified and noted, along with other features such as: the presence and shape of nodules and their composition (i.e. carbonate, siderite or other); the nature, depth of penetration, and preservation of root traces; the shape and nature of the ped; evidence of desiccation and pedogenic slickensides (identified on the basis of being restricted to horizons within a paleosol); and other pedogenic features such as relict bedding.

All of these features were graphically represented on the field logs with emphasis on accurate scaled representation, especially with reference to depth within the horizon, rather than stylisation. Colour changes and mottling were recorded with reference to a Munsell colour chart (Rock Color Chart 1991) and noted next to relevant part of the field log. 10% hydrochloric acid was used to identify the presence of carbonate in a paleosol and to track its

changes with depth. Each horizon was photographed with a Kodak Z740 digital camera and any relevant, remarkable or unidentifiable features within the profile were also photographed and notes were made on the logs of the position of the photographs.

The majority of the paleosols identified in the field areas contain pedogenic carbonate nodules. As the carbonate nodules were to be used for stable isotope analysis particular attention was given to them. Each paleosol carbonate (Bk) horizon was classified on the level of carbonate development (after Machette 1985; Retallack 2001a, Alonso-Zarza 2003) (Table 2.2). Each carbonate horizon was logged in detail with the exact location and pattern of the carbonate within the horizon described on the log. Notes were also made of the presence of root traces, mottling and other features in the carbonate horizon and how they interacted with the carbonate present.

Stage	Soil development in gravel	Soil development in sand, silt or clay
I	Thin discontinuous coatings on and under clasts	Dispersed powdery and filamentous carbonate
II	Continuous, coating around and between clasts; more discontinuous carbonate beyond main horizon	Few to common carbonate nodules and powdery carbonate between the nodules
III	Carbonate a continuous layer enveloping clasts; less pervasive carbonate beyond main horizon	Carbonate a continuous layer of coalescing nodule, some nodules and powdery carbonate beyond horizon
IV	Upper part of solid carbonate layers with a weakly developed platy or lamellar structure capping less pervasively calcareous parts of the profile	
V	Platy or lamellar cap to the carbonate layer strongly expressed in places, brecciated and pisoliths of carbonate	
VI	Brecciation and recementation as well as pisoliths common in association with the lamellar upper layer	

Table 2.2 Bk horizon classification used in the field based on that of Retallack (2001).

Within nodular carbonate horizons a minimum of four nodules was collected. The precise height and location of each nodule within the paleosol was recorded. Within nodule horizons >10cm thick, nodules were taken from equal spacing through the nodular horizon. Where possible, samples were taken laterally within a horizon to quantify the lateral isotopic

variation. Sections made of continuous carbonate (Stage III – VI, see Table 2.2) were sampled from equal spacing though the carbonate horizon. Samples of the material from around the nodules and other prominent non-carbonate horizons in the paleosol were also collected for thin sectioning and bulk rock analysis. Each sample had its orientation recorded and was placed in a separate labelled sample bag to avoid cross-contamination in transport.

Each paleosol was plotted on a stratigraphic section which was logged using standard sedimentary methods (in Russia this was undertaken by Dr Andy Newell and Dr Richard Twitchett). The local sedimentary facies and structures were described to give context to the paleosols. At each section, the strike and dip of the beds were recorded.

2.2.2 Paleosol classification

Classification of paleosols is crucial for comparison of different sections, both across and within basins, and to interpret the palaeoclimatic and palaeoenvironmental variation (Kraus 1999). It has been suggested that soil classification is best undertaken in the field (Retallack 1997). However, classification of paleosols has been much debated in the literature, and there are many different proposed classification schemes.

The disputes arise primarily because there is an already established system for classification of modern soils (Soil Survey Staff 1999 and the Food and Agriculture Organisations schemes; see Retallack 2001a and reference there in). Using a paleosol classification system based on this makes it easier to draw comparisons with modern soils (Kraus 1999). Problems arise, however, as many features used to classify modern soils are destroyed or altered by diagenesis and so this detailed classification can prove problematic when applied to paleosols (Mack *et al* 1993; Retallack 2001a; Krasinikov and Calderón 2006). Equally it has been debated

whether it is appropriate to apply modern names and terms to ancient soils as confusions may arise (Daham and Holliday 1998; Nettleton *et al.* 1998; Nettleton *et al.* 2000).

Some authors use the system proposed by Mack *et al.* (1993) (refined by Mack and James 1994) which is based purely on field observations. This has been proposed to provide a systematic approach to paleosol classification which can be uniformly applied to paleosols of all ages (Mack *et al.* 1993). However, many authors feel that this is over simplistic and makes it hard to compare with modern analogues, thus diminishing the environmental information that can be gained from them (Kraus 1999; Retallack 2001a).

Other authors prefer the system proposed by Retallack (1993, 1994, 1997, 2001a) which advocates a simplified use of the United States Department of Agriculture (USDA) soil classification scheme (Soil Survey Staff 1999). This is based on 19 diagnostic sub-surface horizons (Retallack 2001a) which can be broken down into 11 principal soil orders (Retallack 1993). Other authors have also proposed an altered version of USDA classification; either altering the Soil Survey Staff (1999) scheme to make it relevant to paleosols (Nettleton *et al.* 1998; Nettleton *et al.* 2000) or using a different modern classification (i.e. the World Reference Base for Soil Resources as proposed by Krasinikov and Calderón 2006).

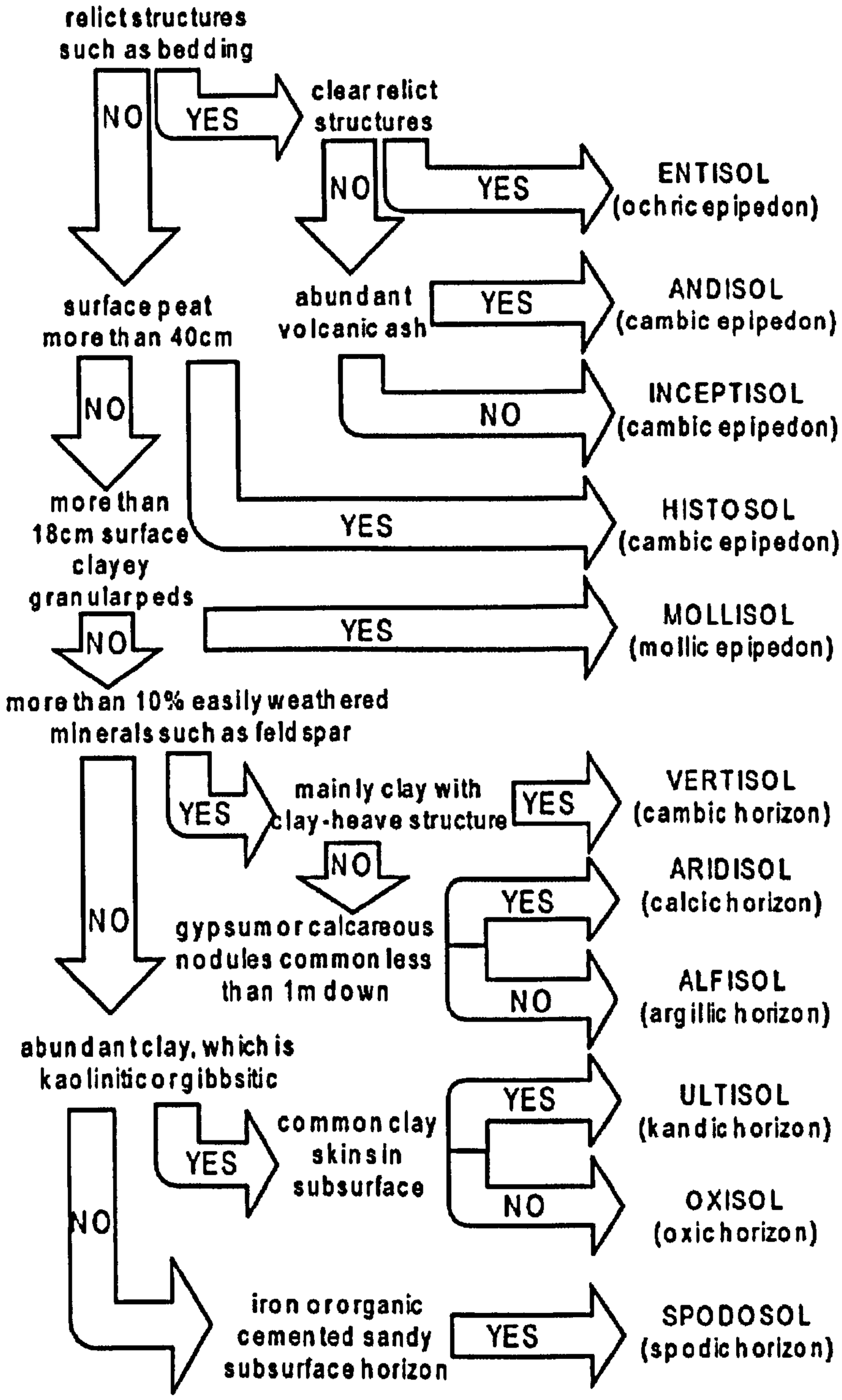

Figure 2.1Soil classification key proposed by Retallack (1993) used for field classification.

In the field the simplified classification key proposed by Retallack (1993) was used (Figure 2.1). There was an emphasis on observed field structure (such as carbonate nodules, pedogenic slickensides etc.) to avoid the pitfalls inherent in misclassifying horizons which may have been altered by diagenesis and burial (cf. Daham and Holliday 1998).

2.2.3 Marine rocks field methodology

The marine limestones identified in the Italian Dolomites (see Chapter 6 for field localities) were sampled for bulk stable isotope analysis. Also any brachiopod fossil- rich beds were identified and brachiopod samples were collected for stable isotope analysis. Limestone sections were logged at a scale of 1:10 (at Tesero and the section around the Bellerophon/Werfen Formations contact at Val Brutta) and the longer sections (the whole of the Bellerophon Formation exposed at Val Brutta) at 1:50. Sections were logged using the methods described by Tucker (2003) and Tucker and Wright (1990). Limestones were classified in the field using Dunham's classification scheme (Dunham 1962; Tucker and Wright 1990). Clastic rocks were classified using the standard sedimentary grain size classification devised by Udden and Wentworth (Tucker 2001). Any sedimentary features (cross beds, ripples, stylolites etc.) were marked on the log using standardised symbols (after Tucker 2003) and any other detail was recorded in notes next to the logs. Those sections logged at 1:10 were sampled every 10cm and those logged at 1:50 were sampled for isotopic analysis every 100cm, or where exposure allowed. At all field localities bulk rock samples of between 10 and 100g were taken (depending on lithology and exposure) and care was taken to take samples big enough to avoid areas of weathering or surface alteration.

Beds containing brachiopod fossils were sampled and the exact positions of the fossils within each bed were recorded.

2.3 Laboratory methods

The laboratory work for this project was primarily carried out by the author, from preparation to running of the analysis, at the University of Plymouth. The only exceptions to this were the cathodoluminescence microscopy, which was carried out by the author and Miss Nikita

Jacobsen, at Camborne School of Mines in Falmouth, and the isotopic composition of organic carbon isotope analysis which were performed by Dr Neil Ogle at Queen's University, Belfast.

2.3.1 Stable isotope analysis methods

The fractionation of stable isotopes is due to thermodynamic properties of the atoms based on the relative atomic masses of which they are composed (Faure 1986). Thus, factors such as changes in temperature, atmospheric carbon dioxide, the introduction of gas in the biosphere and metabolic effects will be recorded in biogenic and non-biogenic isotopic changes in $\delta^{13}C$ and $\delta^{18}O$ carbonate material (Brownlow 1996). For this study, interest was focused on the effects of changes in atmospheric and oceanic conditions (such as temperature and carbon dioxide) on carbonate in brachiopod fossils and in pedogenic carbonate from paleosols.

All results in this study were described as an isotopic ratio between the two stable isotopes ($^{13}C/^{12}C$ and $^{18}O/^{16}O$) and as a deviation from a standard by delta values (δ) in per mil (‰) (Brownlow 1996):

$$\delta\,‰ = \left(\frac{isotopic\ ratio\ for\ sample}{isotopic\ ratio\ for\ standard} - 1\right) 1000 \qquad (2.1)$$

Isotope results were measured relative to Vienna Pee Dee Belemnite (VPDB). To convert values to Vienna Standard Mean Ocean Water (VSMOW) the equation of Coplen *et al.* (1983).

$$\delta^{18}O_{VSMOW} = (1.03039\ \delta^{18}O_{VPDB}) + 30.39 \qquad (2.2)$$

All stable carbon and oxygen carbonate analyses were carried out on a GV Instruments Isoprime mass spectrometer with a Gilson Multiflow carbonate auto-sampler at the University of Plymouth. The carbonate powders were reacted with 100% phosphoric acid at 90°C for 1 hour. The evolved CO_2 was then sampled, passed through a Thermal Conductivity Detector (TCD) and then into an Isotope Ratio Mass Spectrometer (IRMS). Any results below 1.2 nA were removed from the dataset and rerun. The results were calibrated against VPDB using the international standard NBS-19 (National Bureau of Standards 19 published values; $\delta^{13}C$ = 1.95‰ $\delta^{18}O$= –2.20‰), IAEA -CO-8 (International Atomic Energy Agency -CO-8 published values; $\delta^{13}C$ = –5.75‰ $\delta^{18}O$= –22.67‰), and IAEA-CO-9 (International Atomic Energy Agency -CO-9 published values; $\delta^{13}C$ = –45.12‰ $\delta^{18}O$= –15.28‰). To correct for daily drift within individual isotope runs NBS-19 and an internal lab standard which were placed after every ten unknown samples. These standards were used to correct for any drift that occurred within a run by comparing analysed standard values with the published values and using this difference to correct the daily offset for the unknown samples. The average measured values for NBS19 $\delta^{13}C$ = 2.00‰ (±0.45‰ 1σ std) $\delta^{18}O$ = -2.50‰ (±0.49‰ 1σ std) for all analyses carried out over a 3 year period (for full list of all standards run see appendix A2.6).

In this study three types of carbonate material were analysed in the mass spectrometer: marine and terrestrial carbonate bulk rock samples, pedogenic carbonate and brachiopod fossils. These materials were prepared using the following methods.

2.3.2 Carbonate bulk rock preparation

The marine bulk samples from the Italian Dolomites and terrestrial carbonate samples from the South Urals of Russia for stable isotope analysis were prepared as follows. 1) Each bulk sample or nodule was cut in half and one side was retained for petrographic analysis. 2) The other half was cleaned in an ultrasonic bath for 5 minutes to remove any weathered surface

material. 3) The cut face was then sampled with a microdrill (0.75mm diameter) taking samples of between 300-500μg from the fine fraction carbonate areas avoiding any fossil material and sparry calcite. For the carbonate nodules, material drilled from the most homogeneous area of micrite from the centre of the nodule. 4) The resulting powders were placed in a sealed sample vial and weighed. They were then run on the IRMS using the method described in Section 2.3.1.

2.3.3 Pedogenic carbonate nodules

Robinson *et al.* (2002) noted considerable isotopic variation between the micritic and sparry parts of pedogenic nodules, thought to be related to changes in the source of the calcite-forming water (Robinson *et al.* 2002; Quast *et al.* 2006). However, it has been suggested that the spar-forming waters can overprint the micritic values without altering the texture of the micrite (Quast *et al.* 2006). Therefore, for every nodule that contained both spar and micritic material, both were sampled separately to compare the values and to test for overprinting. They were prepared and analysed using the method described above. When determining the experimental error between the micritic and sparry component of a carbonate nodule (see Chapter 4) the isotopic standards from the precise run containing both spar and micrite analysis was used to calculate the experimental error to account for long term drifts in the analysis. These daily offsets values can be found in Appendix A2.6.

2.3.4 Fossil preparation

Seven articulate brachiopods, including representatives of *Janiceps, Comelicania,* and *Orbicoelia,* were analysed from Val Brutta and one from Tesero in the Italian Dolomites (see Chapter 6). The brachiopods were cleaned and sectioned longitudinally across the shell. All samples were photographed under both a petrographic and cathodoluminescence (CL)

microscope. This latter technique was used to provide an estimate of the degree of diagenetic alteration. The areas of the shell were divided into four categories depending on the amount of luminescence displayed under cathodoluminescence (following the method of Mii *et al.* 1997). These categories were: (a) NL: Non-Luminescent, and showing clear internal structure; (b) NL+SL: Non-Luminescent with Slightly Luminescent areas, showing clear internal structure, and >50% non-luminescence by area, but with some luminescence in places; (c) L+SNL: Luminescent and Slightly Non- Luminescent shells, with <50% Non Luminescence by area; and (d) L: those areas that were completely luminescent. A microdrill (0.75mm diameter) and a binocular optical microscope were used to drill samples from individual layers identified by the CL and petrographic microscopy in transects both across and along the length of each shell (see Appendix A4.4). The carbonate powders were analysed for $\delta^{13}C$ and $\delta^{18}O$ using the same method as that used for the bulk rock analysis.

Some brachiopods were encased in silt sediment. To remove this sediment the samples were treated with white spirit (following the method of Brasier 1980). This involves removing as much sediment around the fossil as possible mechanically, drying in an oven for 24 hours at 40°C, then removing the sample from the oven and placing it in a beaker with just enough white spirit to cover the sample and leaving it for 30 minutes to 8 hours. The white spirit is then removed and replaced with hot distilled deionised water and left to break down the sample. Finally, the fossil was placed in an ultrasonic bath of distilled deionised water until all remaining sediment was removed.

2.3.5 $\delta^{13}C$ Organic carbon analysis

The organic carbon component of the rock was liberated by dissolving 4-5g of sample in 5ml of 10% hydrochloric acid (HCl) which was left for at least 24 hours or until any reaction had

ceased. The sample was then washed in ultra-pure deionised water and filtered through a non-organic filter. The filtrate was then dried in a petri dish for 5hrs at 30°C before any organic matter was picked out and placed in a sterile sample vial and sealed prior to being sent away for analysis. All organic carbon was analysed at the Stable Isotope Facility, Environmental Engineering Research Centre, Queen's University, and Belfast on a SerCon ABCA Isotope Ratio Mass Spectrometer with ANCA Combustion/Reduction interface by Dr Neil Ogle. Unfortunately only three samples contained enough organic carbon to generate accurate analyses. All of these were from the Sambullak section (Chapter 4, 6).

2.3.6 X-Ray diffractometer methods

X-ray diffraction (XRD) analysis was used to investigate the mineral composition of carbonate from both Italy and Russia. The powder XRD analyses were conducted on a Phillips PW 1729 X-ray generator at the University of Plymouth, using an X'Pert Quantify computer interface. A Cu anode source was used with generator settings of 30kV and 40mA. Computer-based mineral identification of the traces was achieved using X'Pert High Score identification software. Manual identification was completed with reference to the Joint Committee on Powder Diffraction Standards (1971) index. Samples of crystalline calcite and dolomite from the Plymouth University's mineral collection were also run to verify the results of both the computer and manual identification results. The identification of crystalline calcite and dolomite was verified using calcite and dolomite specific stains (see below).

Samples to be analysed on the XRD were drilled from the same stub as the stable isotope analysis. 1-2g of material was drilled using a 1mm drill bit. In all cases, the sample for analysis was taken from as close as possible to the isotope analysis sample. All samples were placed in their own glass vials to avoid cross-contamination between samples. The powder

was compacted on a silica slide and placed in the machine for analysis. In cases where counts were recorded for the 100% 2°0 peak were ≤ 100counts the sample was rearranged on the slide and re-run.

2.3.7 ICP OES methods

Inductively Coupled Plasma Optical Emission Spectrometry (ICP OES) was used to determine the trace elemental composition of the brachiopod fossils used in this study. All analyses were conducted at the University of Plymouth on a Varian 725-ES ICP OES. The elements Al, Fe, Mg, Mn, Na, S and Sr were investigated as these have been successfully used to determine the level of alteration in brachiopod shells (Mii *et al.* 1997; Brand *et al.* 2003; Korte *et al.* 2005; van Gelden *et al.* 2006). 20-50mg of the shell and bulk rock material from each sample was reacted with 20% nitric acid in 10ml dilutions. The resulting solution was analysed for the proportions of major elements present by calibrating against standard solutions. The run was calibrated for the elements to be investigated by using dilutions of standard solutions for Al, Fe, Mg, Mn, Na, S and Sr.

2.3.8 Cathodoluminescence methods

Cathodoluminescence (CL) has been shown to be an indicator of diagenetic alteration in fossil brachiopod shell (Veizer 1983; Mii *et al.*1997; Korte *et al.* 2005a, b, Tomašových and Farkaš 2005). This is because the activation of cathodoluminescence is primarily by Mn^{2+} which is associated with altered carbonate, and inhibited by Fe^{2+} associated with unaltered carbonate (Veizer 1983). It has been suggested that cathodoluminescence may be used to assess alteration of paleosol carbonate (Budd *et al.* 2002, Williams and Krause 1998). However, the rapidly changing redox potentials in soils during pedogenesis (Dworkin *et al.* 2005) and the

large amounts of free iron oxides in the rock obscure the cathodoluminescence of carbonate paleosols (Dr Gregory Price, *pers. comm.*).

The brachiopods were cleaned and sectioned longitudinally across the shell. These sections were mounted on glass slides using optical resin and the slides were then surfaced polished on a Petropol Buehler using 0.3μm aluminium oxide.

CL photography was carried out at Camborne School of Mines in Falmouth using a CITL CL MK3A Luminscope. The samples were placed in a vacuum chamber under an electron gun emitting a cathode-ray which was set at ~450μA and ~10kv. The sections were photographed through a petrographic microscope. All analyses were carried out by the author apart from brachiopod TS1 which was photographed by Miss Nikita Jacobsen.

2.3.9 SEM microprobe methods

A Scanning Electron Microscope (SEM) was used to investigate the crystal shape and elemental composition of the dolomitic and calcitic carbonate nodules. The scanning electron microscope images were analysed on a Jeol Jsm-6100 SEM at the University of Plymouth, using an Oxford Inca X-Ray analysis system to identify the elemental components of different crystals. This method of element identification is energy-dispersive X-ray spectroscopy (EDS) and was used to identify the relative levels of O, Mg, Ca and Si.

Samples were prepared by taking the thin section side of a carbonate nodule (the opposite of that used for the IRMS and XRD analysis) and mounting it on a glass slide. The slide was then polished with 0.3μm aluminium oxide on a Petropol Buehler, until the sample was 1mm

thick. These slides were then coated with a layer of carbon before being introduced into the SEM.

2.4 Petrographic slide preparation

Petrographic thin sections were made of both the Italian and Russian material. In the case of the Russian material many of the samples were so poorly lithified that they had to be injected with paraloid or encased in resin to stabilise them for thin sectioning. The non-calcareous samples taken in Russia were so poorly consolidated it was impossible to produce thin sections of them. All sections that were taken were mounted on glass slides using optical resin and ground down using a Precision Lapping and Polishing Machine to a thickness of 30μm with 25μm silicon carbide powder. The slide was then protected by a cover-slip.

Stains – Dickson's stain

Dickson's stain method was used to identify the presence of calcite in the thin sections (Dickson 1966). The method used is that proposed by Allman and Lawrence (1972), as listed below (Table 2.3). The etch solution is 1000ml of 1.5% hydrochloric acid solution. Staining solution 1 is produced in two parts; part A is 0.2g alizarin red S and 100ml 1.5% HCl solution; part B is 2g potassium ferricyanide and 100ml 1.5% HCl solution. Staining solution 2 is 0.2g alizarin red S dissolved in 1.5% HCl solution 100ml.

Procedure		Time	Carbonate	Result
Stage 1	Etch solution	10-15sec	Calcite ferroan calcite	Considerable etch
			Dolomite ferroan dolomite	Negligible etch
Stage 2	Staining solution 1 3 part A and 2 parts B	30-45 sec Medium stain 40 sec Light stain 30 sec	Calcite	Very pale pink to red depending on optical orientation
			Ferroan calcite	Very pale pink to red, pale blue to dark blue; the two superimposed give mauve–purple–royal blue
			dolomite	no colour
			Ferroan dolomite	Pale to deep turquoise depending on ferrous content
Stage 3	Staining solution 2	10-15 sec Medium stain 15 sec Light stain 10 sec	calcite	Very pale pink–red
			Ferroan calcite	Mauve–purple–royal blue
			dolomite	No colour
			Ferroan dolomite	Pale to deep turquoise

Table 2.3 Dickson's staining technique (after Allman and Lawrence 1972).

Stains – Alkaline alizarin red S

Alkaline alizarin red S is a dolomite-specific stain which stains dolomite purple and leaves calcite unstained. It was used in both the carbonate nodules from Russia and the Italian samples to identify the presence of dolomite in thin section.

The method is based on that proposed by Miller (1988). The staining reagent is produced by: (a) dissolving 0.2g of alizarin red S in 25ml methanol in a small beaker over a hot water bath; (b) carefully dissolving 30g sodium hydroxide pellets in 70ml water.

The staining procedure is: (a) add 15ml of the 30% NaOH solution to the alizarin red solution and bring to the boil; (b) immerse the thin section in boiling reagent for at least five minutes; (c) add a few drops of methanol to compensate for evaporation; (c) rinse in distilled water.

2.5 Mathematical methods

Both mathematical and statistical techniques were used in this project. The mathematical techniques were used in modelling the palaeotemperature equations, while statistical techniques were applied to the Russian data to determine the significance of the isotope excursions seen between the isotope results from nodules from different paleosol horizons.

2.5.1 Temperature equations

Dworkin *et al.* (2005) and Prochnow *et al.* (2006) created a palaeotemperature equation combining the relationship between mean annual ambient temperature (MAT) and the $\delta^{18}O$ composition of calcite in soil (Friedman and O'Neil 1977), and the relationship between $\delta^{18}O_p$ and MAT in modern terrestrial environments (Fricke and O'Neil 1999; Dworkin *et al.* 2005) to produce a cubic function. When these equations have been solved for zero (Dworkin *et al.* 2005; Prochnow *et al.* 2006) the palaeotemperature estimate is the value at which the curve of the equations cuts the x axis. However, cubic functions can have three possible solutions for x (see Figure 2.2), so there can be up to three temperatures that satisfy these equations, though not all of these may be physically possible in the real world.

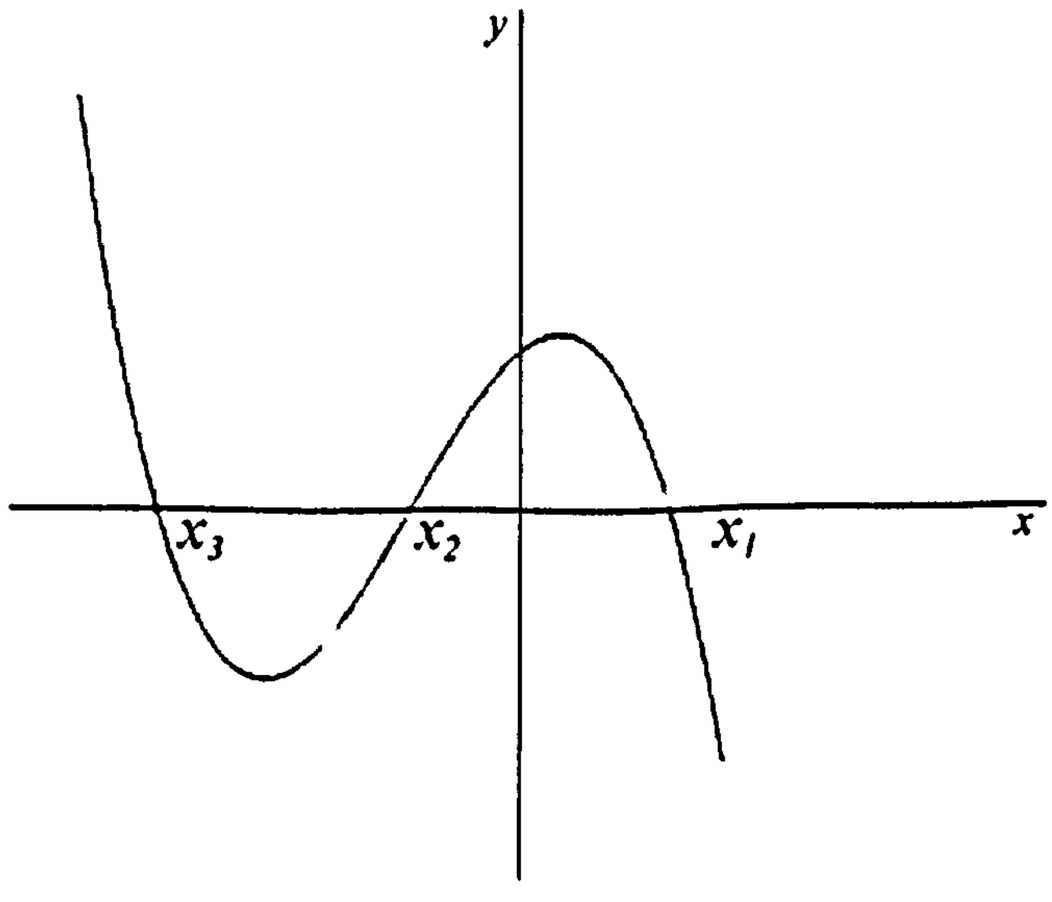

Figure 2.2 A theoretical cubic function showing the three points at which it cuts the x axis.

2.5.2 Solving cubic equations

The method used in this study to solve cubic equations is as follows. Assuming the cubic equation is as follows (after Woan 2000):

$$ax^3+bx^2+cx+d=0 \ (a\neq 0) \tag{2.3}$$

Where x is variable and a, b, c, d are real constants. To solve this equation for x the following intermediate definitions p, q and D must first be calculated

$$p=\frac{1}{3}\left(\frac{3c}{a}-\frac{b^2}{a^2}\right) \tag{2.4a}$$

$$q=\frac{1}{27}\left(\frac{2b^3}{a^3}-\frac{9bc}{a^2}+\frac{27d}{a}\right) \tag{2.4b}$$

$$D=\left(\frac{p}{3}\right)^3+\left(\frac{q}{2}\right)^2 \tag{2.4c}$$

If $D\geq 0$ then the following intermediate definitions must also be calculated

$$u=\left(\frac{-q}{2}+D^{1/2}\right)^{1/3} \tag{2.5a}$$

$$v = \left(\frac{-q}{2} \cdot D^{1/2}\right)^{1/3} \tag{2.5b}$$

$$y_1 = u + v \tag{2.5c}$$

$$y_{2,3} = \frac{-(u+v)}{2} \pm i\,\frac{u-v}{2}\,3^{1/2} \tag{2.5d}$$

If $D<0$ then the following intermediate definitions must also be calculated

$$\varphi = \arccos\left[\frac{-q}{2}\left(\frac{abs(p)}{3}\right)^{-3/2}\right] \tag{2.6a}$$

$$y_1 = 2\left(\frac{abs(p)}{3}\right)^{1/2}\cos\frac{\varphi}{3} \tag{2.6b}$$

$$y_{2,3}=-2\left(\frac{abs(p)}{3}\right)^{1/2}\cos\frac{\varphi\pm\pi}{3} \tag{2.6c}$$

Then the roots of equation (A) are as follows:

$$x_n=y_n-\frac{b}{3a} \tag{2.7}$$

2.5.3 Application

Solution for where D<0

Using the spatial relationship described by Dworkin *et al.* (2005) (equation 5.8a, see Chapter 5) as an example:

$$-0.50T^3+(\delta^{18}O_{carb}+152.04)T^2-2.78\times10^6=0 \tag{5.8a}$$

the values for *a, b, c, and d* and *x* are as follows:

a = -0.50

b =($\delta^{18}O_{cc}$+ 152.04)

c = 0

d = –2.78×10^6

x = T

Then using the value for $\delta^{18}O_{carb}$ = 30.39‰ (‰, VSMOW) (which is equal to 0‰, VPDB) the first the intermediate definitions *p*, *q* and *D* must first be calculated.

a	*b*	*c*	*d*	*p*	*q*	*D*
-0.5	182.43	0	-2.78E+06	-44374.2732	1.96E+06	-2.27E+12

Table 2.4 The calculated intermediate definitions for the equation (3a) with inputs of δ18OcarbVSMOW = 30.39‰.

Table 2.4 shows the input values and the intermediate definitions created by equations (2.4a), (2.4c), and (2.4d). As $D<0$ equation (5.8a) was used to calculate φ and equation (2.6b) and (2.6c) was used to produce y_1, y_2 and y_3. From these results equation (2.7) was used to calculate x_1, x_2 and x_3 (MAT in °K). These was converted to °C using the conversion °C = °K – 273.15 (Bureau International des Poidset Mesures 2008) (Table 2.4).

	φ	y	x (°K)	x (°C)
1	2.147615	183.53	305.15	32.15
2	2.147615	110.24	231.86	-41.14
3	2.147615	-242.90	-121.28	-394.28

Table 2.5 Values for the three different *x* intercepts in both °K and °C.

Three possible temperatures are produced: x_1 = 32.25°C; x_2 = –41.14°C and x_3 = –394.28°C (Table 2.5). The value for x_3 can be easily discounted as, being below 0°K, it is physically impossible. Equally the value for x_2 is also very cold and there is no evidence of ice wedging in any of the sections so this can be discounted. Thus, the value for x_1 can be taken as the palaeotemperature estimate.

Solution for where D≥0

When $D \geq 0$ there is only one real root (x_1) as the other two are (x_2, x_3) are complex roots (Figure 2.3) and do not have real solutions (Woan 2000). Thus, in these circumstances only one temperature estimate can be generated. The temporal relationship described by Dworkin *et al.* (2005) (equation 5.8b) is an example of an equation where $D \geq 0$.

$$-0.22\,T^3 + (\delta^{18}O_{carb} + 61.99)\,T^2 - 2.78\times10^6 = 0 \qquad (5.8b)$$

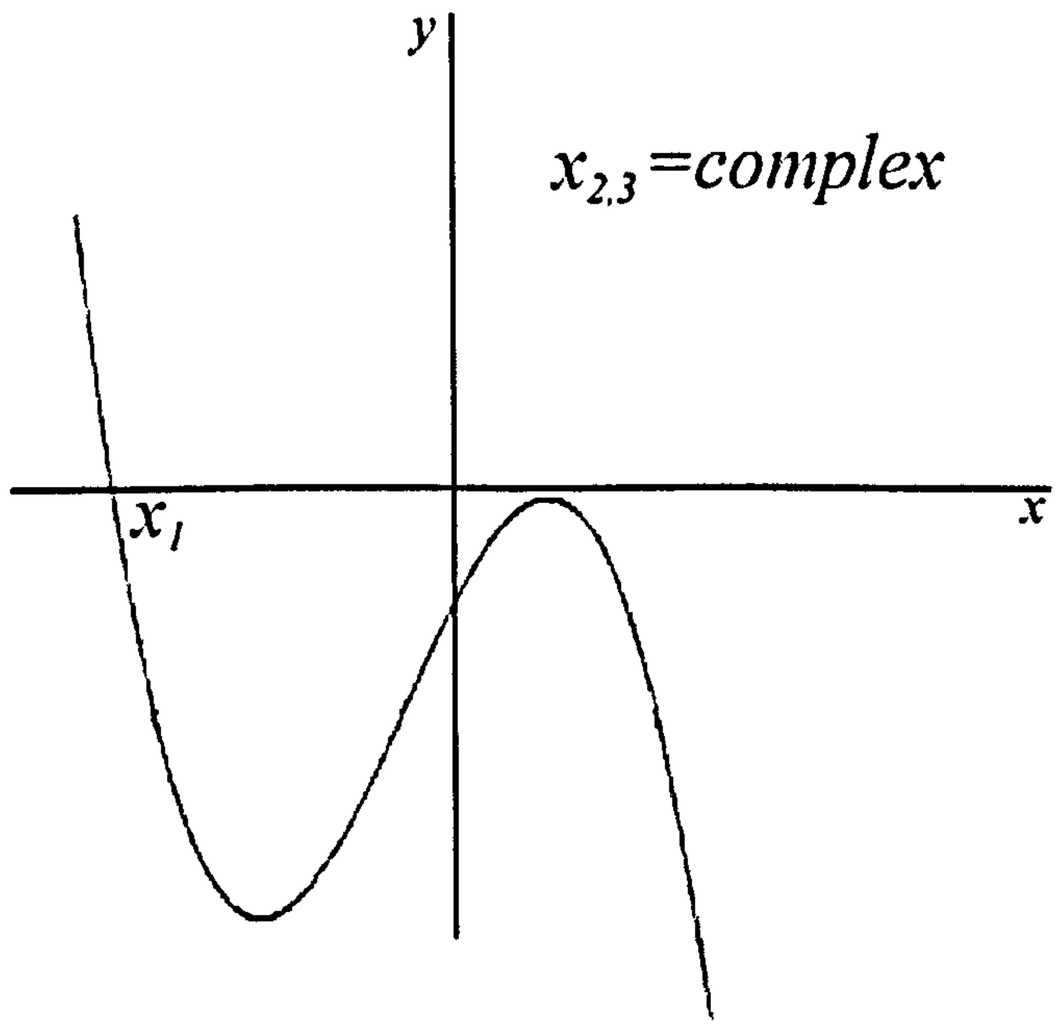

Figure 2.3 A cubic solution when $D \geq 0$, there is only one real root, the other two are complex roots.

Again using the value for $\delta^{18}O_{carb}$ VSMOW = 30.39‰ (which is equal to 0‰ $\delta^{18}O_{carb}$ VPDB) first the intermediate definitions *p*, *q* and *D* must first be calculated (Table 2.6).

a	*b*	*c*	*d*	*p*	*q*	*D*
-0.22	92.85	0	-2.78E+06	-59374.1219	7.07E+06	4.74E+12

Table 2.6 The calculated intermediate definitions for the equation (5.8b) with inputs of $\delta^{18}O_{cc}$ VSMOW = 30.39‰

In this case as $D \geq 0$ rather than using equations (2.6a, 2.6b, 2.6b) the equations (2.4a), (2.4b) and (2.4c) are needed to solve the intermediate definitions u, v, and y_1 respectively. Equation (2.6) was uses to calculate x_1 (temperatures in °K). This was converted into °C using the conversion °C = °K – 273.15 (Bureau International des Poidset Mesures 2008).

	u	v	y	x (°K)	x (°C)
1	-110.72	-178.73	-289.466	-148.78	-421.78

Table 2.7 Values for x_1 intercepts in both °K and °C.

To solve for y_2 and y_3 the equation (2.2e) has the value i which is an imaginary number and thus the roots are not real solutions (Woan 2000; Dr S. Kearsey *pers. comm.*). Thus, these values can be discounted in this study.

As all palaeotemperature solutions were produced using Microsoft Excel 2007 it was a useful check to ensure that substituting the derived temperature solutions back into the cubic function produced zero values.

2.5.4 Mathematical problems with estimates

Problems occur with the palaeotemperature equations if the D value changes from <0 to ≥ 0 within the experimentally measured values for $\delta^{18}O_{carb}$. This occurs with the summer/winter rainfall equation produced from the data from the Saratov weather station (IAEA/WMO, 2008) (Equation 5.8c)

$$-0.28\,T^3 + (\delta^{18}O_{carb} + 92.24)\,T^2 - 2.78\times10^6 = 0 \qquad (5.8c)$$

(see Chapter 5 for how this equation was created)

This equation changes from $D<0$ to $D\geq0$ at $\delta^{18}O_{cc}$ values of -10‰ (VPDB) and below, as a result the predicted temperature jumps from 6°C to -409°C (Figure 2.4). This is because the cubic function changes from having three points where it cuts the x axes (Figure 2.2) to having only one (Figure 2.3). As –409°C is obviously an unrealistic value it can be said that for $\delta^{18}O_{carb}$ values of –10‰ (VPDB) and below, the initial equations cannot be a valid model of the processes at that locality.

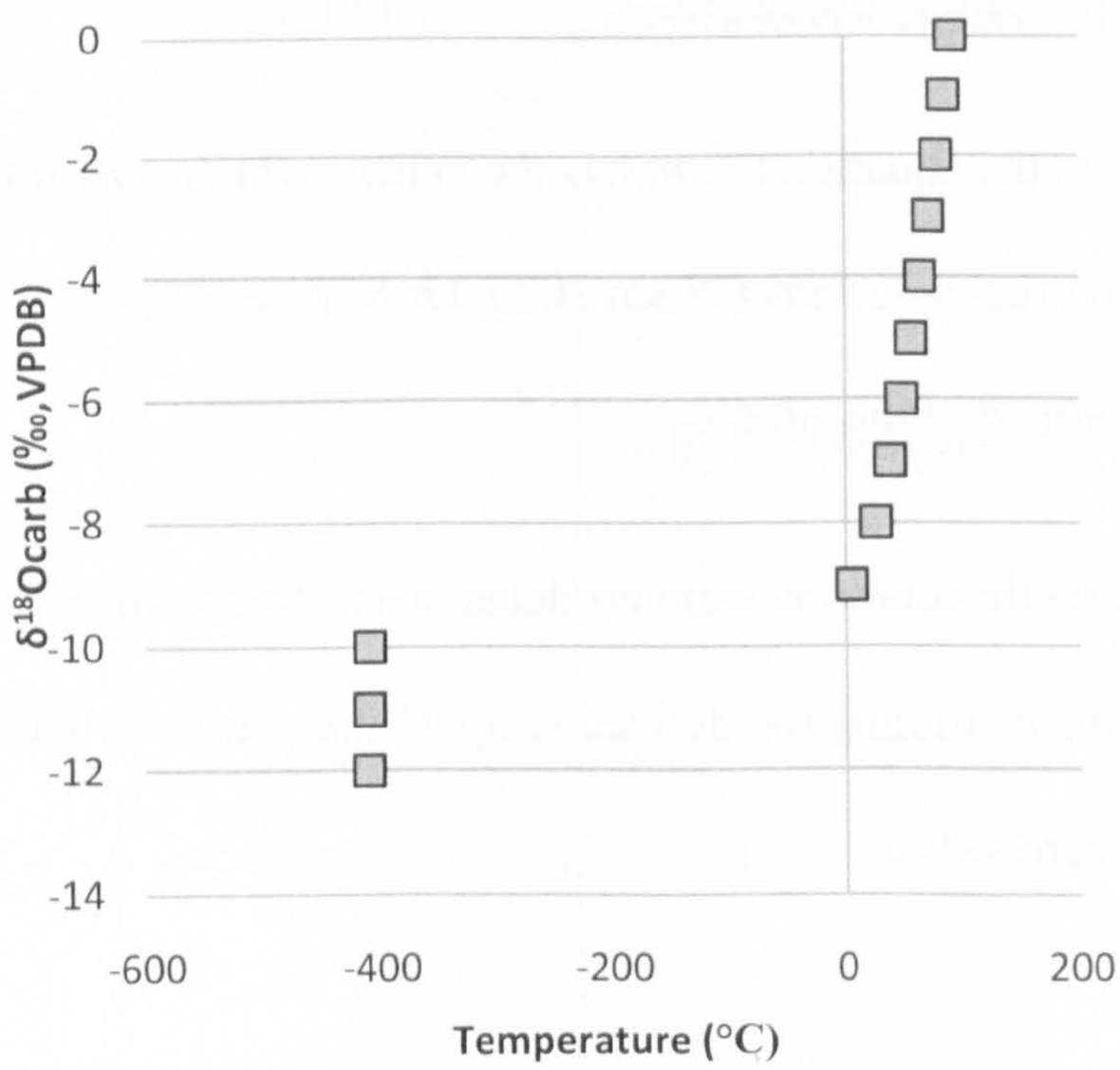

Figure 2.4 Palaeotemperature estimates for equation (5.8c) using $\delta^{18}O_{cc}$ values from 0‰ to -12‰ VPDB. Note the sudden negative jump in the palaeotemperature estimates resulting from $D<0$ to $D\geq0$.

2.5.5 Statistical methods

It is observed that there was a lot of variation in the isotopic composition of different nodules in certain paleosols (Chapter 4). It is important to determine if these variations in the isotopic signal through time represent true excursions, or are just an increase in the range of values from the mean. This assumes that results from different nodules within a paleosol represent an average of the isotopic composition of the soil water for the entire time that soil was active.

This assumption may become problematic if there is significant environmental change for the period that a soil is active creating a large spread of isotopic values in one paleosol. The isotopic variation of nodules within a paleosol does not always show a normal distribution (Figure 2.5) and thus parametric statistics such as Student's t-test cannot be used (Rana Moyeed *pers. comm.*)

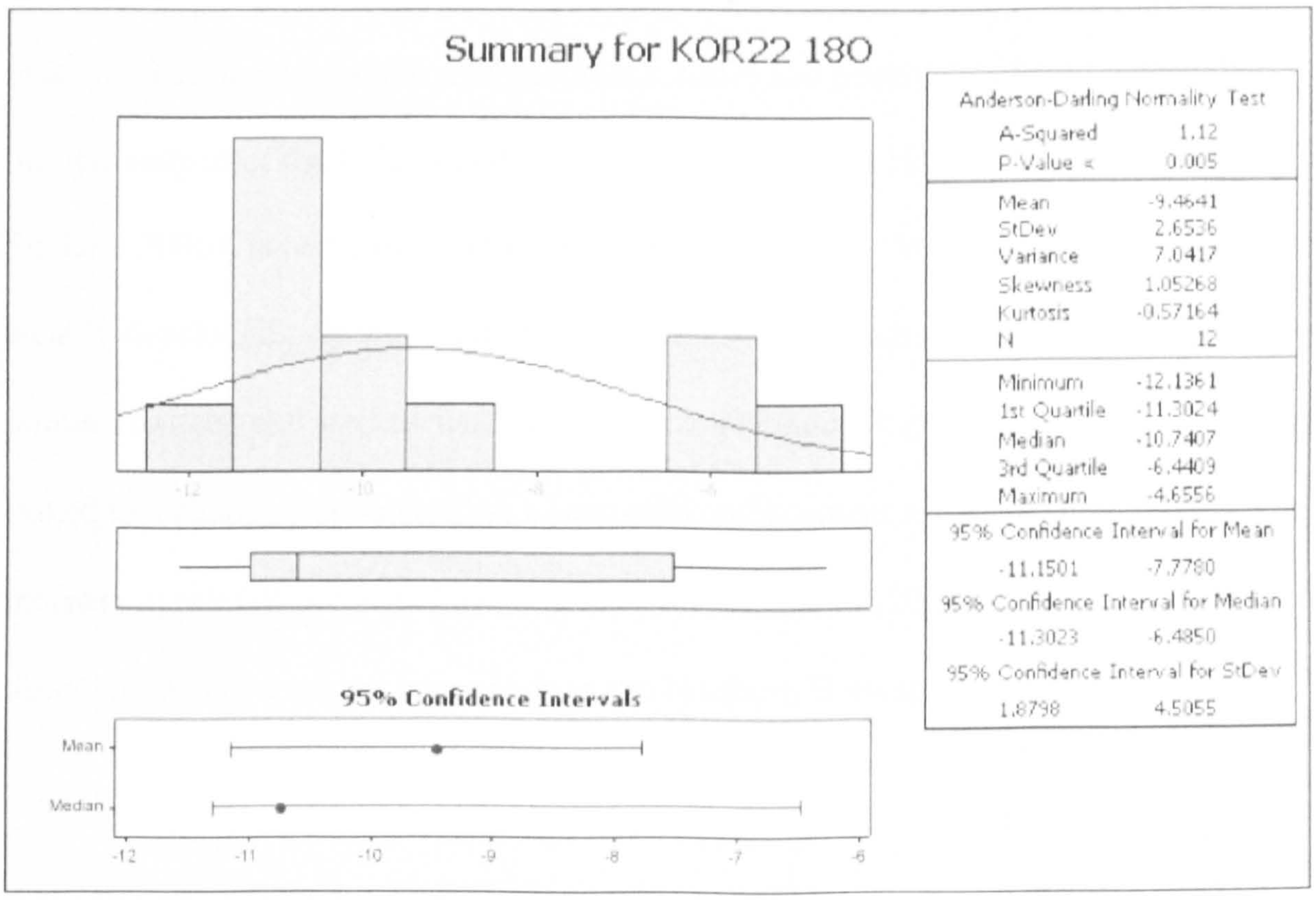

Figure 2.5 Graphical statistical summary for the $\delta^{18}O$ values from paleosol KOR 22 at Boyevaya Gora showing a non-normal distribution.

To investigate the significance of an isotope excursion between paleosols the Mann-Whitney test was used. This is a non-parametric test which has a null hypothesis that the two data sets are from the same population. The underlying assumptions in the Mann-Whitney Test are that: 1) both samples are random samples from their respective populations; 2) there is mutual independence between the two samples; 3) that the results are continuous measurements (Conover 1980).

All statistical analyses were conducted using the statistical program Minitab 15.1.0.0. Below a $p \leq 0.1$ it is statistically likely that the null hypothesis is invalid (to a 90% confidence interval) and the two datasets are from separate populations (Dr R. Moyeed *pers. comm.*; Conover 1980).

Chapter 3. Paleosols of the South Urals, Russia

3.1 Introduction

Paleosols are a direct product of environmental influences and thus are extremely useful in investigating changes in climate (Retallack 1994; 1997; 2001). Previous studies into paleosols in Antarctica at the P/Tr boundary have identified a dramatic ecosystem reorganisation relating to changes in root traces (Retallack 2007) and poorly developed paleosols immediately after the P/Tr boundary (Retallack and Krull 1999; Krull and Retallack 2000; Sheldon 2006). Investigations into paleosols in the Karoo Basin, South Africa have recorded weakly developed paleosols just after the boundary and a change from shallow calcareous nodules to deep and well focused calcic horizon (Retallack *et al.* 2007). This is thought to be linked to a change from an arid to a semi-arid environment across the boundary and an increase in rainfall in the earliest Triassic (Retallack *et al.* 2007). However, similar detailed observations have not yet been made in the Northern Hemisphere.

3.2 Geological background

The Upper Permian to Lower Triassic strata of the South Urals consist of 1000 metres of terrestrial fluvial siliciclastic rocks. The exposure is largely restricted to streams cut in low relief, grass-covered terrain and small escarpments (Newell *et al.* 1999; Surkov *et al.* 2007; Dr A. Newell and Dr R. Twitchett, unpublished field data, T.K. personal observations). The overall palaeogeography of the area is a foreland basin to the Ural mountain range which was active through the Permian-Triassic periods. As such it is part of a major north–south linear depocentre that extends for some 2500km across mainland Russia from the Arctic to the Aral Sea (Newell *et al.* 1999; Tverdokhlebov *et al.* 2002).

The depocentre was formed by flexure of the European craton, as a result of the Ural orogenic event to the east (Zonenshian *et al.* 1984). The basin was active from the Mid-Carboniferous through to the Early Triassic. The earliest Carboniferous rocks consist of marine turbidites which sit directly on the orogenic platform, and the sedimentary package above consists of two shallowing upwards sequences starting with deepwater turbidites and finishing with shallow marine limestones (Puchkov 1997; Newell *et al.* 1999). The first cycle ends in the Sakmarian (Early Permian) and the second ends in the Kazanian (Early Permian) (Newell *et al.* 1999 Puchkov 1997).

Above, in the Tatarian, the sequence contains mostly alluvial red beds consisting of a variety of facies types: mudflat and floodplain interbedded sheet sandstones and mudstones, sandy distributary, small gravelly channels, and large gravelly channel systems (Newell *et al.* 1999; Tverdokhlebov *et al.* 2005; Surkov *et al.* 2007). Of these, the floodplain deposits show extensive paleosol development ranging from isolated root traces to indurated pedogenic calcretes (Newell *et al.* 1999; T.K. personal observations). The P/Tr boundary is marked by 'thick conglomerates' which are laterally extensive and up to 15m thick (Newell *et al* 1999; Tverdokhlebov *et al.* 2002; Tverdokhlebov *et al.* 2005). In the eastern sections these conglomerates comprise of 15m of erosionally-based conglomerates comprising of multiple, lenticular storeys containing gravel and cobble rounded clasts of up to 20cm sourced from the Ural Orogen (Newell *et al.* 1999; Tverdokhlebov *et al.* 2002). The conglomerate units are thought to be associated with a major fluvial conduit from an intra-orogen source deep in the Ural Mountains forming braided pattern channels at low flows similar to modern megafans (Newell *et al.* 1999; Benton *et al.* 2004).

The Late Permian and Early Triassic strata are unthrusted, and have been uplifted to their current position by post-depositional salt movement (Brunet *et al.* 1999 Newell *et al.* 1999; Newell *pers. comm.*). As such they are ideal for palaeoclimate and isotopic studies as they are more likely to retain their original isotopic values rather than a later diagenetic overprint.

3.2.1 Stratigraphic position

As discussed by other authors (Newell *et al.* 1999; Tverdokhlebov *et al.* 2002; Tverdokhlebov *et al.* 2005; Taylor *et al.* 2009) there has been much confusion about the stratigraphic positioning of Russian strata with respect to the international stratigraphic framework. Most of this confusion arises from the fact that traditional Russian stratigraphic units are not directly comparable with international units. The Russian system breaks both lithology and geological time into Svitas and Gorizonts (Tverdokhlebov *et al.* 2005). Gorizonts are the major regional stratigraphic units in the Russian system but, rather than referring to lithostratigraphic packages, they are defined primarily on their palaeontological characteristics (Tverdokhlebov *et al.* 2005). Svitas, on the other hand, are largely lithostratigraphic units and are defined by a mix of field lithological and biostratigraphic criteria (Tverdokhlebov *et al.* 2002). The Tatarian is divided into the Urzhumian, Severodvinian and Vyatkian Gorizonts, with the Vyatkian representing the uppermost Permian Gorizont (Figure 3.1). This is divided into two Svitas: the Kutulukskaya in the Volga–Ural Anticlise and the Kulchumovskaya in the Cis-Ural Trough (Tverdokhlebov *et al.* 2005). The Lower Triassic is divided into the Vetlugian Super Group, comprising the Vokhmian, Rybinskian, Sludkian, Ust-Mylian and the Yarenskian Gorizonts. These correspond to the Kopanskaya, Staritskaya, Kzylsaiskaya, Gostevskaya and Petropavlovskaya Svitas (Figure 3.1) (Tverdokhlebov *et al.* 2002).

Period	Epoch/ Stage	Gorizont		Svita
TRIASSIC	Olenekian	Yarenskian		**Petropavlovskaya**
		Vetlugian Supergorizont	Ust-Mylain	**Gostevskaya**
			Sludkian	**Kzylsaiskaya**
			Rybinskian	**Staritskaya**
	Induan		Vokhmian	**Kopanskaya**
PERMIAN	Lopingian	Tatarian	Vyatkian	**Kulchumovskaya**
	Guadalupian		Severodvinian	**Vyazovskaya**
			Urzhumian	**Urzhumian**

Figure 3.1 Stratigraphy of the Cis-Ural Trough (adapted from Tverdokhlebov *et al.* 2002, 2005).

Wardlaw *et al.* (2004) suggest that the top of the Tatarian in Russia corresponds to the top of the Guadalupian. Thus, they suggest there is a gap of approximately 11 million years between the youngest Permian rocks and the oldest Triassic rocks in Russia. Others, however, disagree

Tverdokhlebov *et al.* (2005) assign the beds below the thick conglomerates that cap the Permian succession to the Late Tatarian and the beds directly above this unit as Induan based on both and vertebrate fossils and microfossils (Tverdokhlebov *et al.* 2005). Furthermore, from both tetrapod and ostracod evidence, the Vyatkian Gorizont is inferred to be of equivalent age to the *Dicynodon* Assemblage Zone of South Africa (i.e. Changhsingian) (Benton *et al.* 2004; Surkov *et al.* 2007; Benton 2008). This interpretation implies that the Upper Tatarian is Changhsingian in age and within a million years of the P/Tr boundary (Tverdokhlebov *et al.* 2005).

There has been some debate over whether the multi-storey conglomerates represent the latest unit of the Permian or the youngest unit of the Triassic. Newell *et al.* (1999) suggested that because they sit below a structural unconformity they should be included in the Tatarian. Biostratigraphic studies, however, suggest the break in facies marks the P/Tr boundary and that the conglomerates are basal Triassic in age (Benton *et al.* 2004; Surkov *et al.* 2007).

This second interpretation has been further strengthened by recent magnetostatigraphic studies. Taylor *et al.* (2009) have shown that it is possible to correlate sections across the field area using a polarity transition from Reverse-Normal polarity zone which falls, in those sections where it is exposed, just before the onset of the thick conglomerates. They correlate the Russian magnetostratigraphic sections to the global correlation produced by Steiner (2006) in which the P/Tr boundary falls just after the start of this Normal. Thus, not only does this suggest that the Russian sections include almost all of the Late Permian (Lopingian), but also confirms that the thick conglomerates are the basal Triassic and the P/Tr boundary falls at, or just before, this facies change (Taylor *et al.* 2009).

3.2.2 Studied sections

In total 7 sections were identified and the paleosols within them studied; Vozdvizhenka (51° 42.651'N, 56° 23.034'E), Tuyembetka (51° 55.318'N, 56° 19.616'E), Sambullak (51° 52.922'N, 56° 13.098'E), Krasnogor (51° 33.378'N, 56° 4.820'E), Petropavlovka (52° 1.970'N, 55° 38.110'E) Mescheryakovka (51° 22.755'N, 55° 16.884'E), Boyevaya Gora (51° 17.883'N, 54° 54.569'E) (Figure 3.2). Of these sections Boyevaya Gora, Sambullak, Tuyembetka, Vozdvizhenka and Krasnogor all contain the boundary between the Tatarian and Early Triassic marked by the dramatic change to multi-storey conglomerates, while Mescheryakovka and Petropavlovka are Early Triassic sections (Figure 3.3).

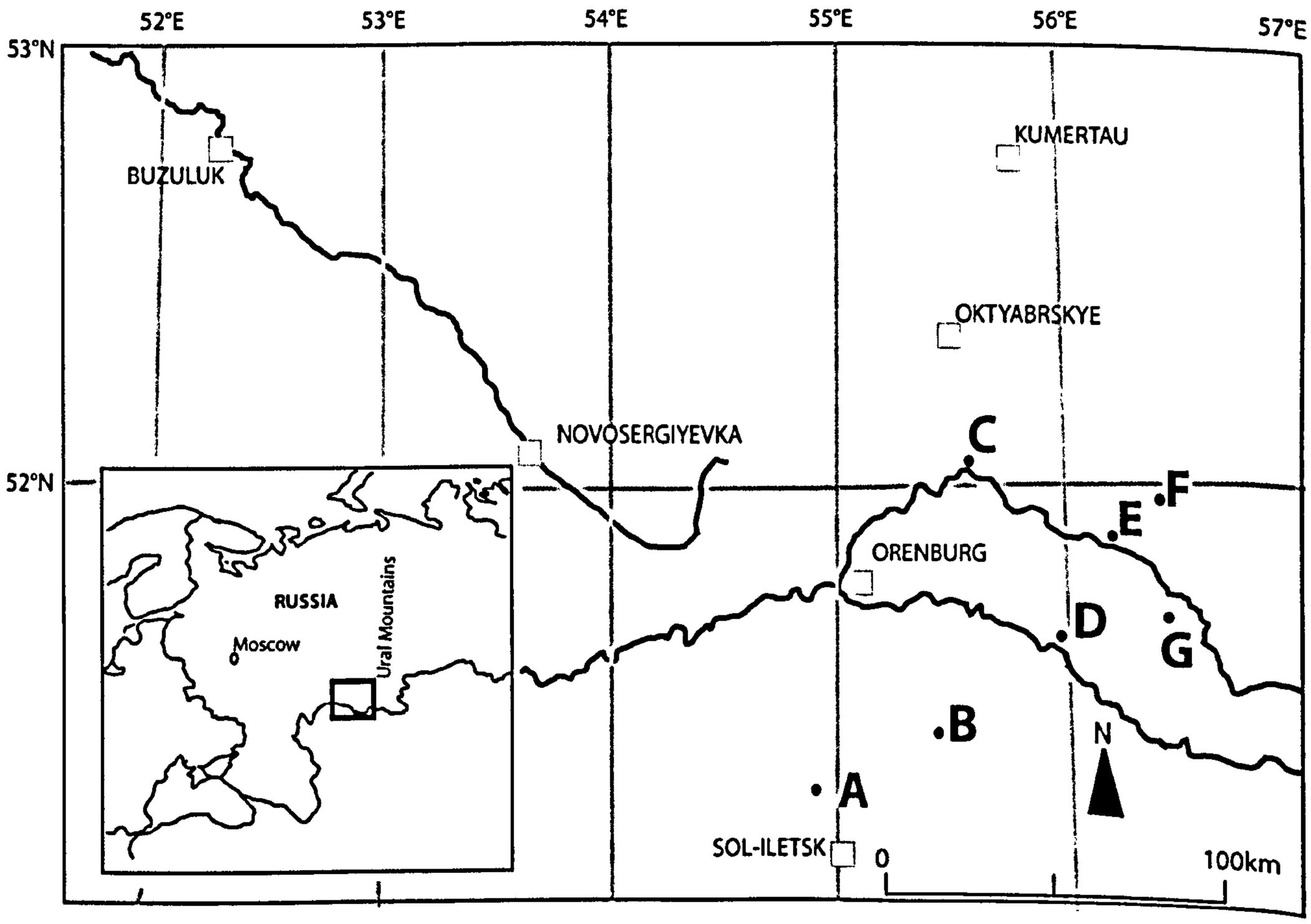

Figure 3.2 Field area in Southern Urals. A) Boyevaya Gora, B) Mescheryakovka, C) Petropavlovka, D) Krasnogor, E)Sambullak, F) Tuyembetka and G) Vozdvizhenka. The black lines represent major rivers (figure adapted from unpublished map by A. Newell).

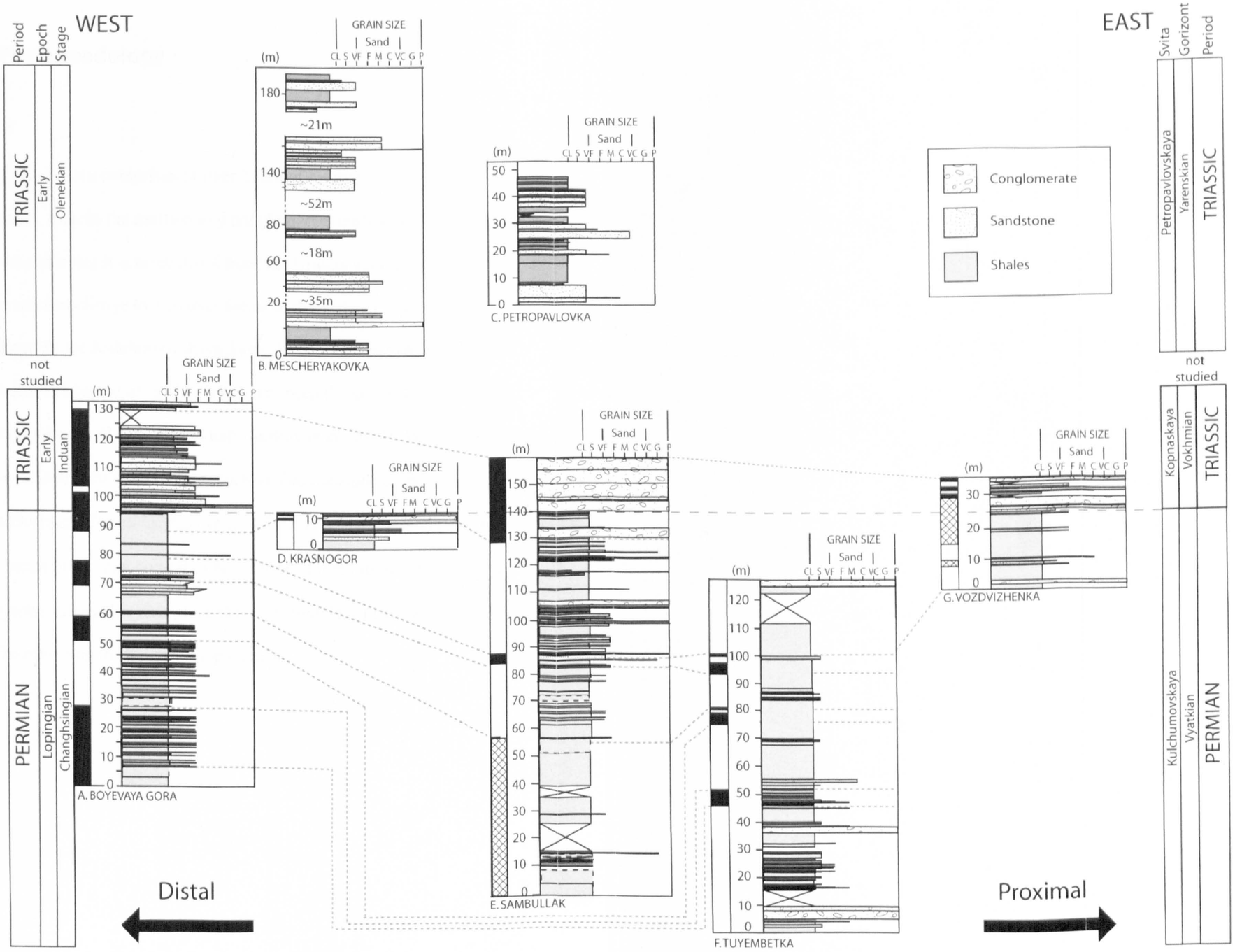

Figure 3.3 The stratigraphic position of all the sections studied in Russia. Sections A, D, E, F, G, are correlated using magnetostratigraphy defined by Taylor *et al.*(2008).The positioning of Triassic sections B and C is based on palaeontological data (Tverdokhlebov *et al.* 2002) Sections are arranges West to East across the basin, how the Svitas correspond to the global stages and epochs can be seen in Figure 3.1. (Sedimentological logs from unpublished field data by Dr A. Newell and Dr R. Twitchett).

3.3 Field results: Palaeopedology

3.3.1 Boyevaya Gora

The section studied at Boyevaya Gora comprises of over 132m of mudstones, siltstones, sandstones and conglomerates. It lacks the multi-storey conglomerate units seen in the east of the basin, probably due to the fact that it is more distal from the Uralian source (Surkov *et al.* 2007). However, there is a marked change to a coarser facies in the early Triassic. The lower part of the section is attributed to the Kulchumovskaya Svita, Vyatkian Gorizont by fish scales and skull bones (Tverdokhlebov *et al.* 2005). It has also been the site of large therapsid footprints interpreted as being produced by a dicynodont (Surkov *et al.* 2007). The section above the facies break has yielded vertebrate remains such as *Tupilakosaurus* and others of Early Triassic, Vokhmian Gorizont affinity (Surkov *et al.* 2007). The latest Permian fossils are found 22m below the facies break, and consist of both tetrapod remains and fish scales (Surkov *et al.* 2007). Magnetostratigraphic data place the P/Tr Boundary just below the facies break (Taylor *et al.* 2009) confirming the palaeontological data.

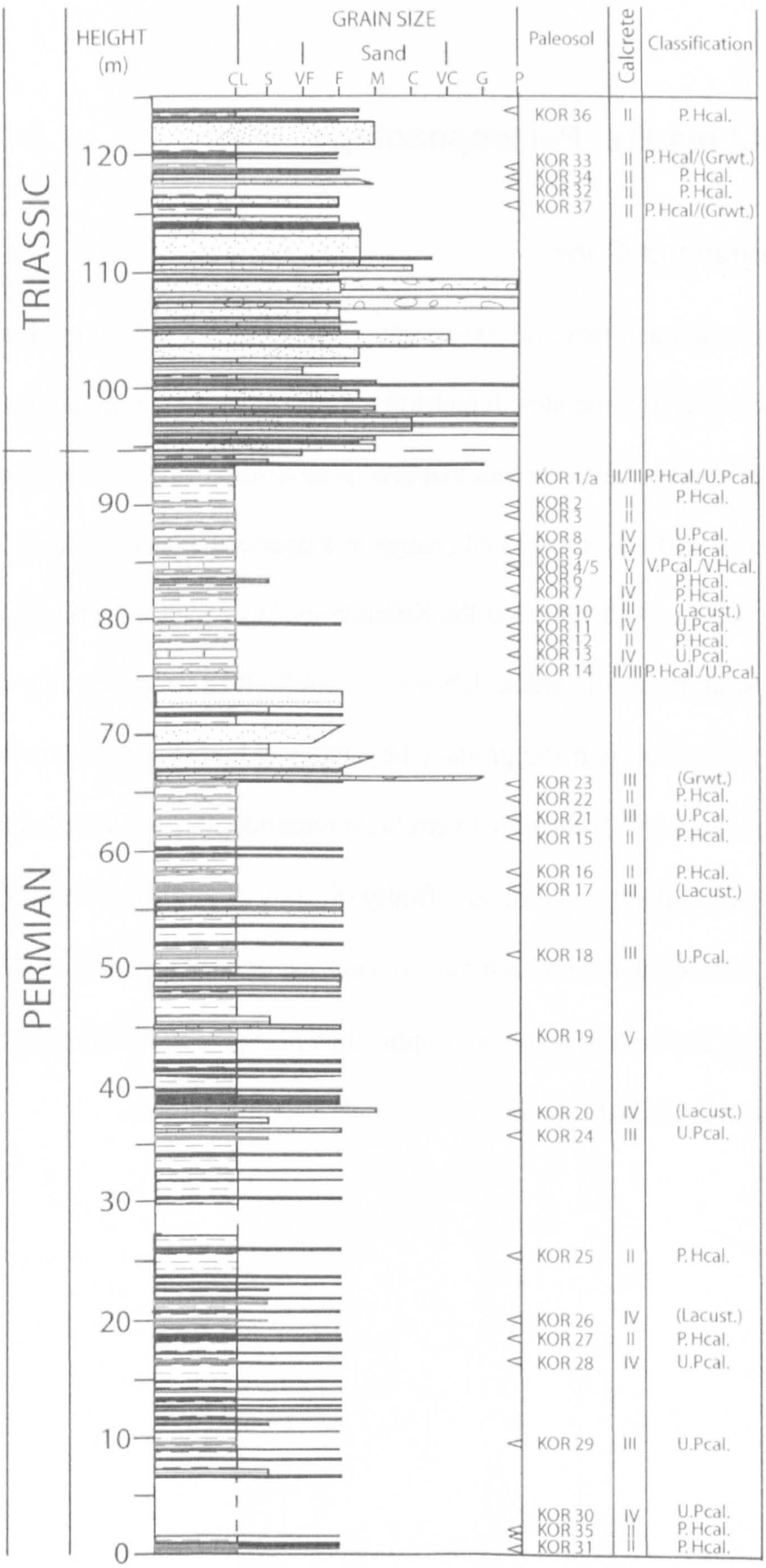

Figure 3.4 The studied section at Boyevaya Gora. The arrows (<) mark the position of the paleosols in the section. The calcrete column shows the relative development of the Bk horizons within the paleosols (see Table 2.2). Note the high density of soils just below the P/Tr boundary (Sedimentological for log from unpublished field data by Dr A. Newell and Dr R. Twitchett).

In total 37 paleosol horizons were identified at Boyevaya Gora (Figure 3.4, for individual paleosol descriptions see Appendix A1.1), interbedded with minor sand and gravel channels and associated over bank deposits. The thickness of the paleosols ranges from 15cm to 137cm. The more developed calcrete profiles appear to be marginally thicker (e.g. KOR 4) than the less developed paleosols (e.g. KOR 6), although this may be because the more developed calcretes are more resistant to erosion and compaction. Four of these paleosols (KOR 14) are part of stacked sequences where the paleosols below have been partially overprinted by the paleosols above producing compound horizons as described by Kraus (1999) in a period of steady deposition where the rate of sedimentation roughly matched the rate of deposition. Overall the paleosols are a uniform colour of 10R (ranging from moderate orange pink–10R 7/4 to greyish red –10R 4/2), although those above the P/Tr boundary show a marked colour change to 5GY (grey yellow).

All the paleosols have a grain size of either clay or silt and all but two (KOR 36 and KOR 9) have recorded root traces, although for some the rooting is restricted to the A horizon. These root traces primarily take the form of in fills of reddened clay, possibly formed by the oxidation of the original organic matter of the root (as suggested by Retallack 2001a), and are 2-6mm in width and have an obvious tapering and branching structure (Figure 3.5A). This would suggest an oxygenated environment and would explain the lack of preservation of organic matter.

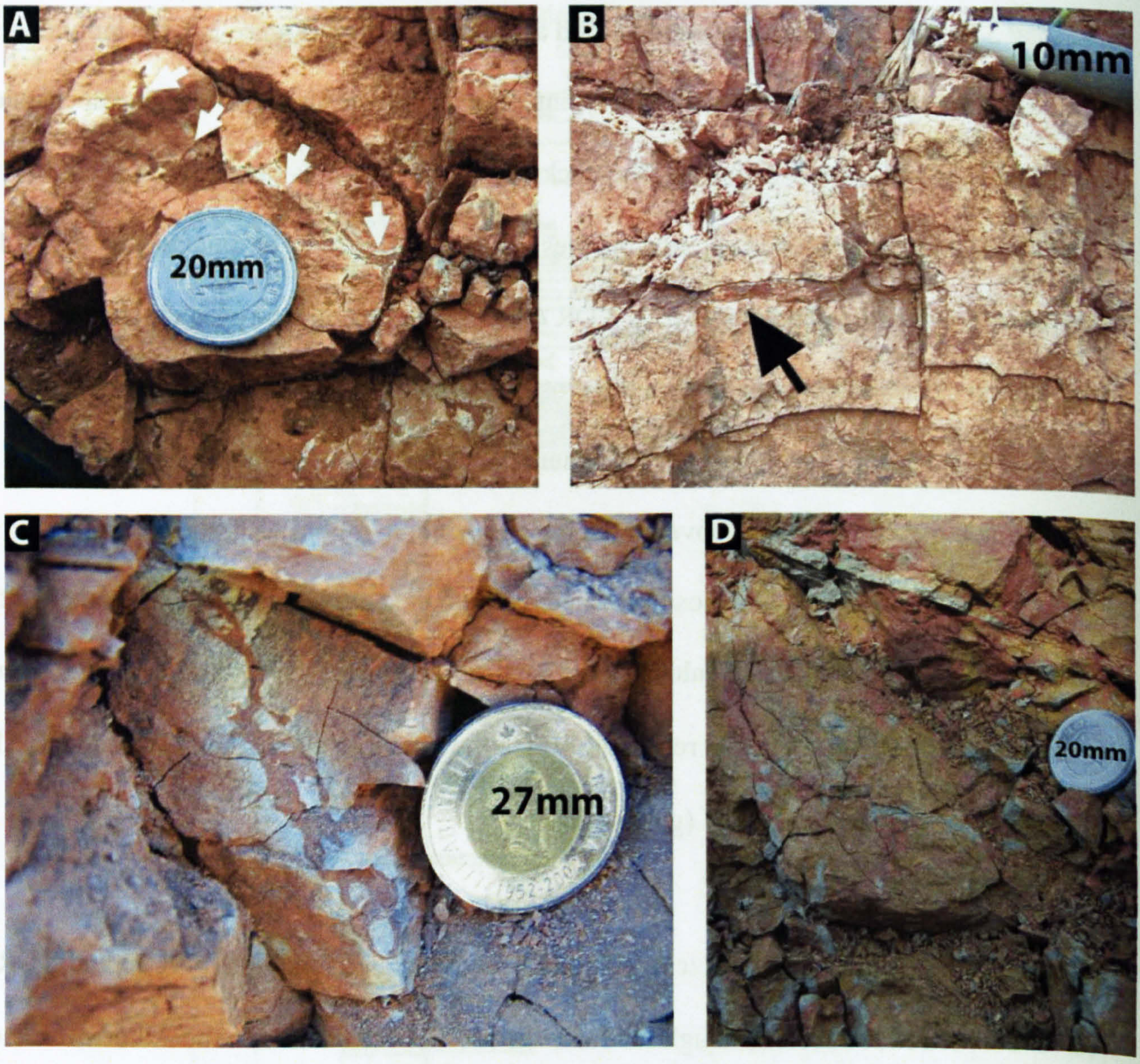

Figure 3.5 Root traces in Russia. A) are branching and tapering rootlets from Boyevaya Gora. B) is a tap root at Sambullak (SAM 5a) . C) and D) show drab root haloes at Boyevaya Gora and Mescheryakovka.

Most of the roots take the form of fibrous root systems (cf. Retallack 1997) which are mainly preserved as 20-50mm long traces. In those paleosols where the root networks are best preserved (KOR 4, KOR 11, KOR 17, KOR19, see Appendix 1 A1.1) it is possible to distinguish the nature of the rooting system. Those paleosols with a well-developed continuous calcrete layer (KOR 4 and KOR19) show a more tabular root system (Figure 3.5B) (cf. Retallack 1997), suggesting the calcrete layer is inhibiting water flow through the paleosol. In those horizons that have not developed a continuous calcrete layer (e.g. KOR 11, KOR 17 see Appendix A1.1) the roots have a more vertical orientation suggesting vertical

movement of water through the paleosol profile (Alonzo-Zarza 2003) and probably also sinker roots (Figure 3.5A) which would take advantage of deep groundwater during the dry season (Retallack 1997). Several horizons have roots showing drab-root halos (Figure 3.5C) (as defined by Retallack 2001a; Retallack 1997). These form ~1mm haloes around the root traces and are very pale blue (5B 8/2) to light bluish grey (5B 8/1). It is worth noting that in the Triassic at Boyevaya Gora there are no specific drab-root halos, although there is minor very light grey (N8) mottling in the sandstone above these horizons (Figure 3.5D).

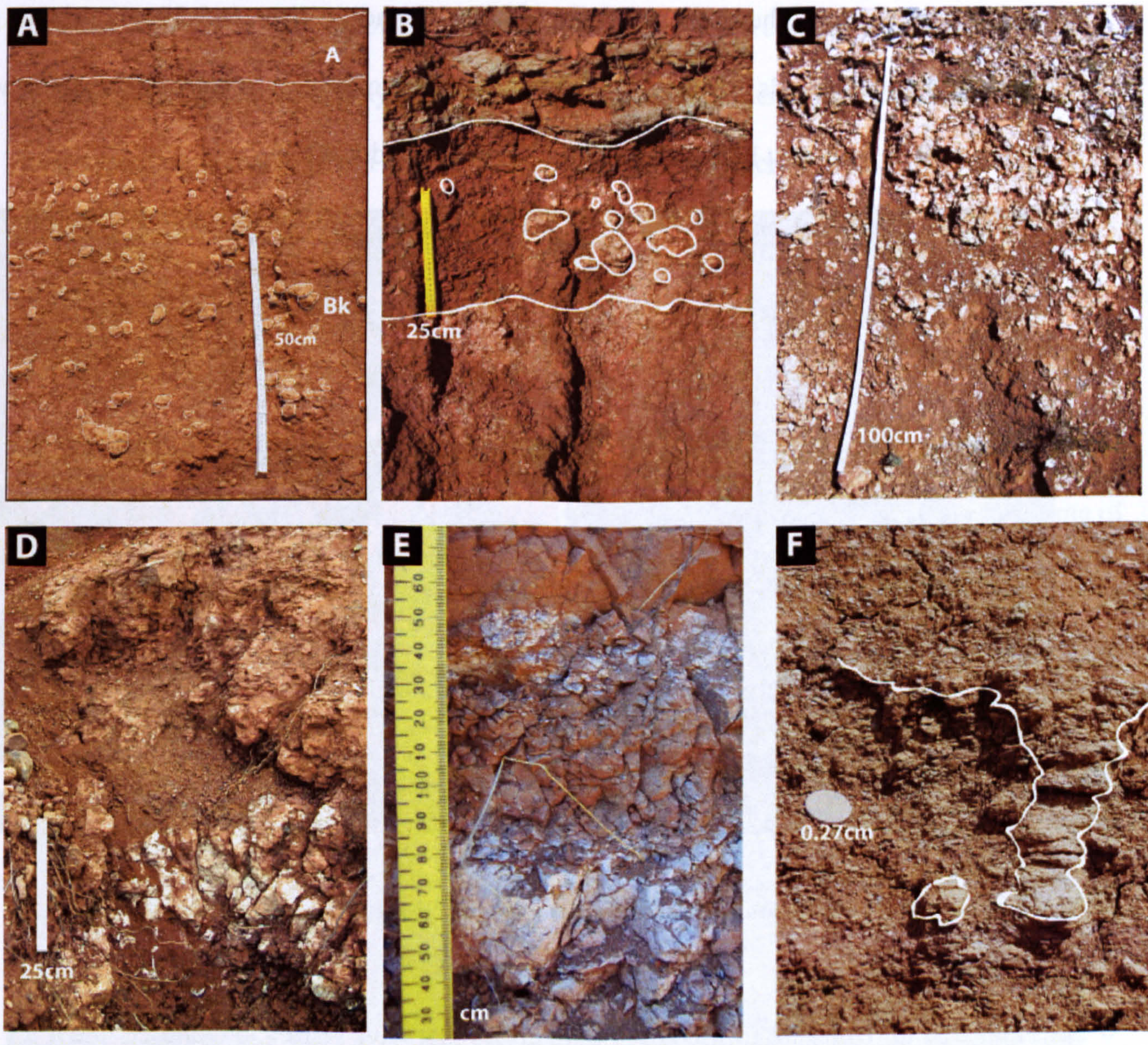

Figure 3.6 Bk horizon development stages in Russia: (A) a stage II nodular horizon from Boyevaya Gora with A and Bk horizons marked (KOR 6). (B) Is a stage III horizon with possible mixed groundwater/pedogenic influences at Boyevaya Gora (KOR 23). (C) is a stage III horizon at Tuyembetka (TUY55) and (D) is a Stage IV horizon from Sambullak (SAM 7). (E) is a particularly well exposed Stage V calcrete with brecciated top (KOR4). F) is a groundwater calcrete from Petropavlovka (PET2).

All paleosols at Boyevaya Gora have an evident Bk horizon with varying levels of maturity (see Table 2.2 for classification scheme). The maturity of Bk horizons range from nodules of 20-50mm in size (Stage II)(Figure 3.6A), through coalesced nodules forming a continuous carbonate layer (Stage III))(Figure 3.6B) and the start of formation of a solid carbonate layer with nodules beneath (Stage IV) (Figure 3.6E), to thick indurated calcrete horizons (Stage V) (Figure 3.6D) (classification after Wright and Tucker 1991; Retallack 2001a; Alonso-Zarza 2003 see Chapter 2 Table 2.2). Of these the stage II horizons are most prevalent and seen throughout the section. The stage II nodules are found either in discrete 5-30cm horizons or dispersed 50-100cm bands and may or may not contain root traces. In some cases root traces are preserved as drab-root haloes (e.g. KOR 19 see appendix A1.1).

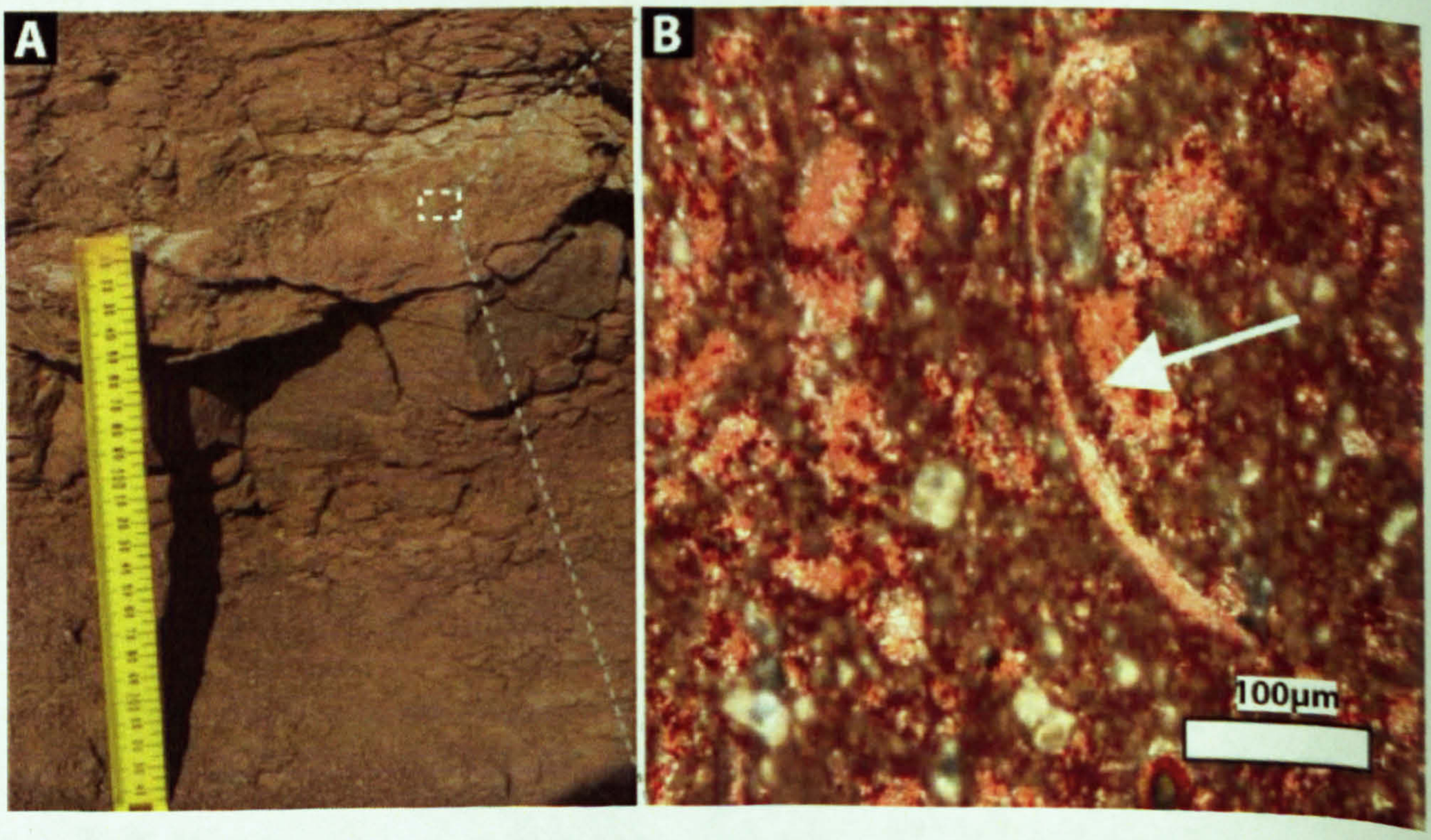

Figure 3.7 Ostracod in KOR17 suggesting a lacustrine environment and the bed it originated from (scale in 25 cm) (A) shows the carbonate horizon when the thin section was taken from (B) shows the ostracod fossil arrowed.

The stage III horizons are formed of nodule layers that have started to coalesce into a continuous calcrete horizon as a result of powdery calcite forming between the nodules (Wright and Tucker 1991). They form the second most prevalent stage of Bk horizon

development at Boyevaya Gora and are between 7-76cm thick, similar to the variations in thickness seen in the stage II nodules.

The stage IV horizons are defined by the occurrence of a laminated, solid calcrete top which is 8-16cm thick. Five of these maybe associated with ephemeral lakes (as described by Newell *et al.* 1999) and two of which (KOR 17 and KOR 25) have been found to contain ostracod fossils (Figure 3.7). They are also related to channel fills which have become calcified paleosols after the deposition of the channel fill (KOR 20) and contain desiccation cracks suggesting that the channel may have been waterlogged and then dried out (Figure 3.8A). These types of paleosol are not strictly speaking pedogenic calcretes, but instead are palustrine deposits (as described by Alonso-Zarza 2003). However, the thinness of these calcretes would suggest that they are related to ephemeral ponds, probably formed by sporadic intense rainfall (Gierlowski-Kordesch 1998). There are also examples of true pedogenic stage IV Bk horizons (as described by Alonso-Zarza 2003) for example KOR 3, KOR 8, KOR 11 and KOR 13 which all have rooted massive carbonate horizons and some of which show primary slickensides (KOR3) (Figure 3.8 B).

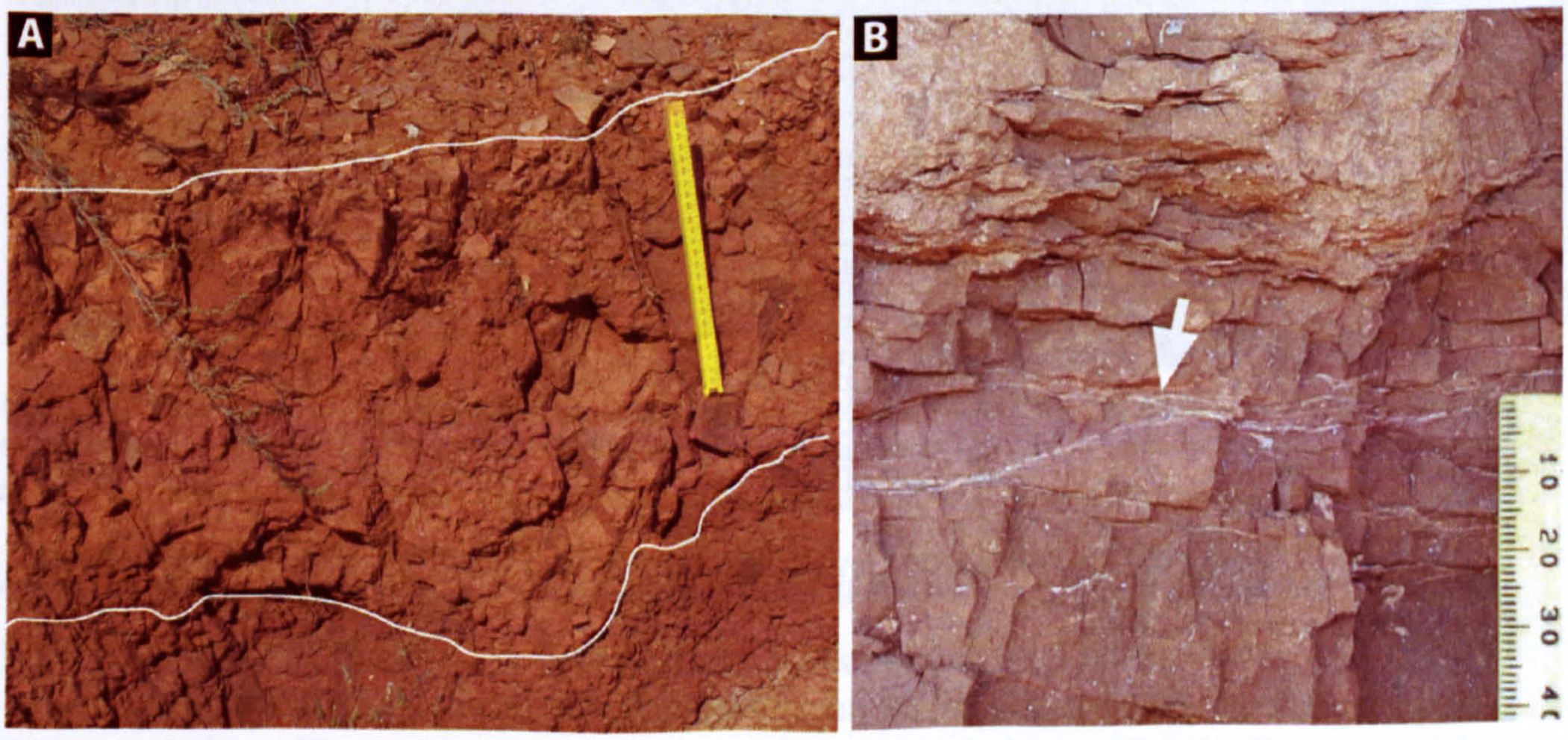

Figure 3.8 Paleosol developed on minor fluvial channels and pedogenic slickensides A) Shows a minor channel fill the top of which has become a paleosol (scale = 25cm). B) Wedge shaped peds (outlined by later sparry calcite) interpreted as pedogenic slickensides (scale in cm).

At Boyevaya Gora there are two Stage V horizons (KOR 4 and 19) of which one (KOR 4) is a spectacularly well-exposed example and comprises a 77cm thick, white (10R 7/4) calcrete unit which is predominantly massive although is cut by many iron-stained root traces (Figure 3.9). This is interpreted as a hardpan as described by Alonso-Zarza (2003). The top 5cm of the hardpan show minor brecciation with pisoliths of carbonate (Figure 3.6D) which were used to identify it as a stage V horizon (cf. Retallack 2001a). Above this there are lenses of reddened clay within the carbonate layers which are 16cm long and 8cm high and pinch in and out through the bed (Figure 3.9). These structures have been tentatively identified as shrink–swell structures (Dr N. Sheldon, *pers. comm.*) equivalent to the gilgai microtopography observed in modern Vertisols (Kovda and Wilding 2004).

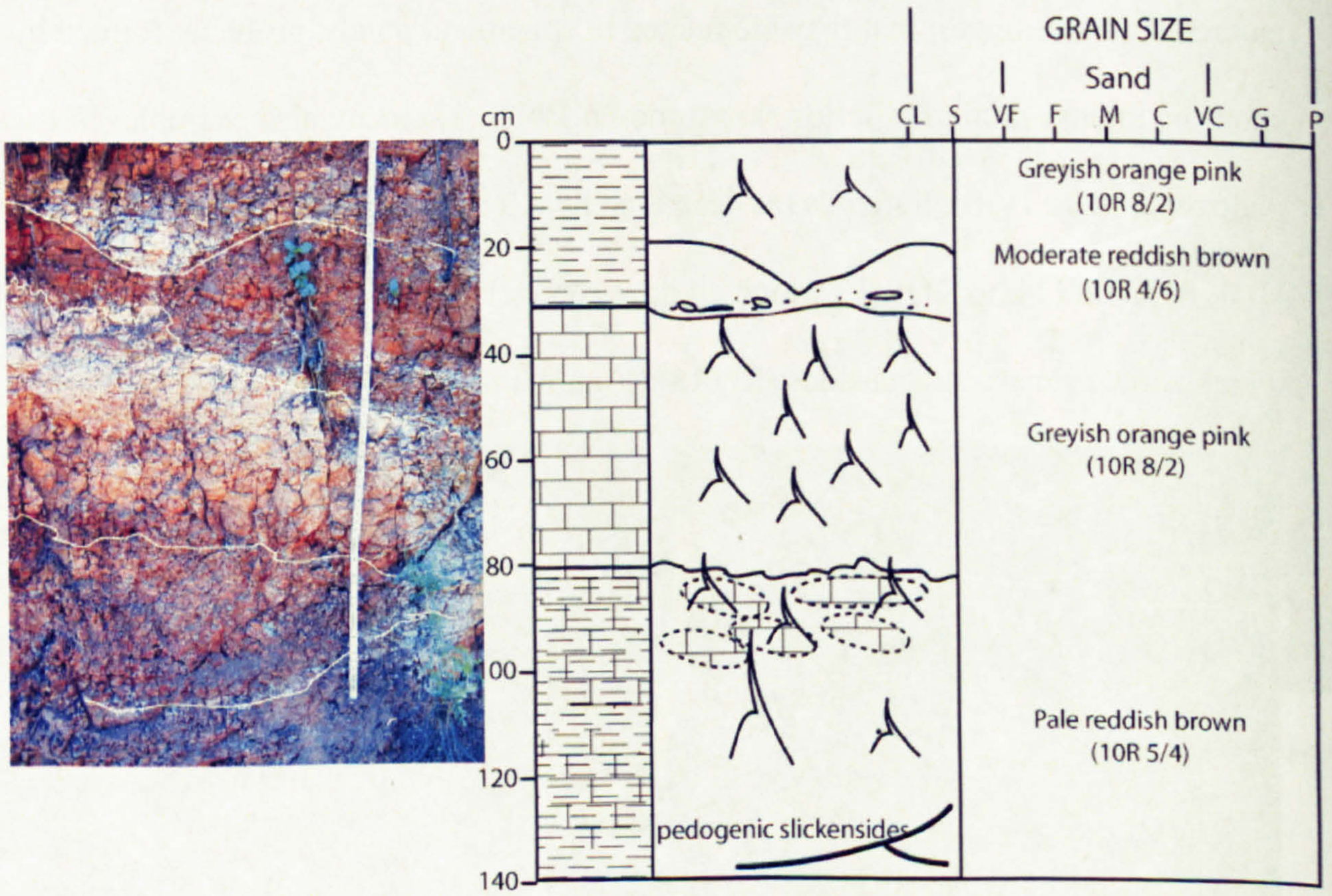

Figure 3.9 The Stage Vat Boyevaya Gora (KOR4), exhibiting possible gilgai microtopography on the top surface and pedogenic slickenside's at base.

The prevalence of stage II and III Bk horizons suggest that this was a relatively active floodplain as carbonate layers are thought to form at a relatively constant rate and more-developed Bk horizons take a longer time to develop and thus can be used to constrain periods

of non-deposition at the specific locality and constrain channel activity and flooding (Retallack 1997; Retallack 2001a). Retallack (1994, 2001) has suggested that it takes 10kyr to form a stage II calcic horizon and thus the Boyevaya Gora floodplain must have been relatively stable for at intervals of that duration at least.

Mottling and gleization is evident throughout the section, although it has different forms.). In many paleosols, (KOR2, KOR4, KOR6 KOR12, KOR14, KOR16, KOR18, KOR22, KOR28, KOR32) it takes the form minor mottles which are 1-2mm reduction spots (Figure 3.10C). These are thought to be caused by iron remobilisation within the paleosol or as reduction spots round degrading organic matter in the paleosol after burial during diagenesis (Retallack 2001a).

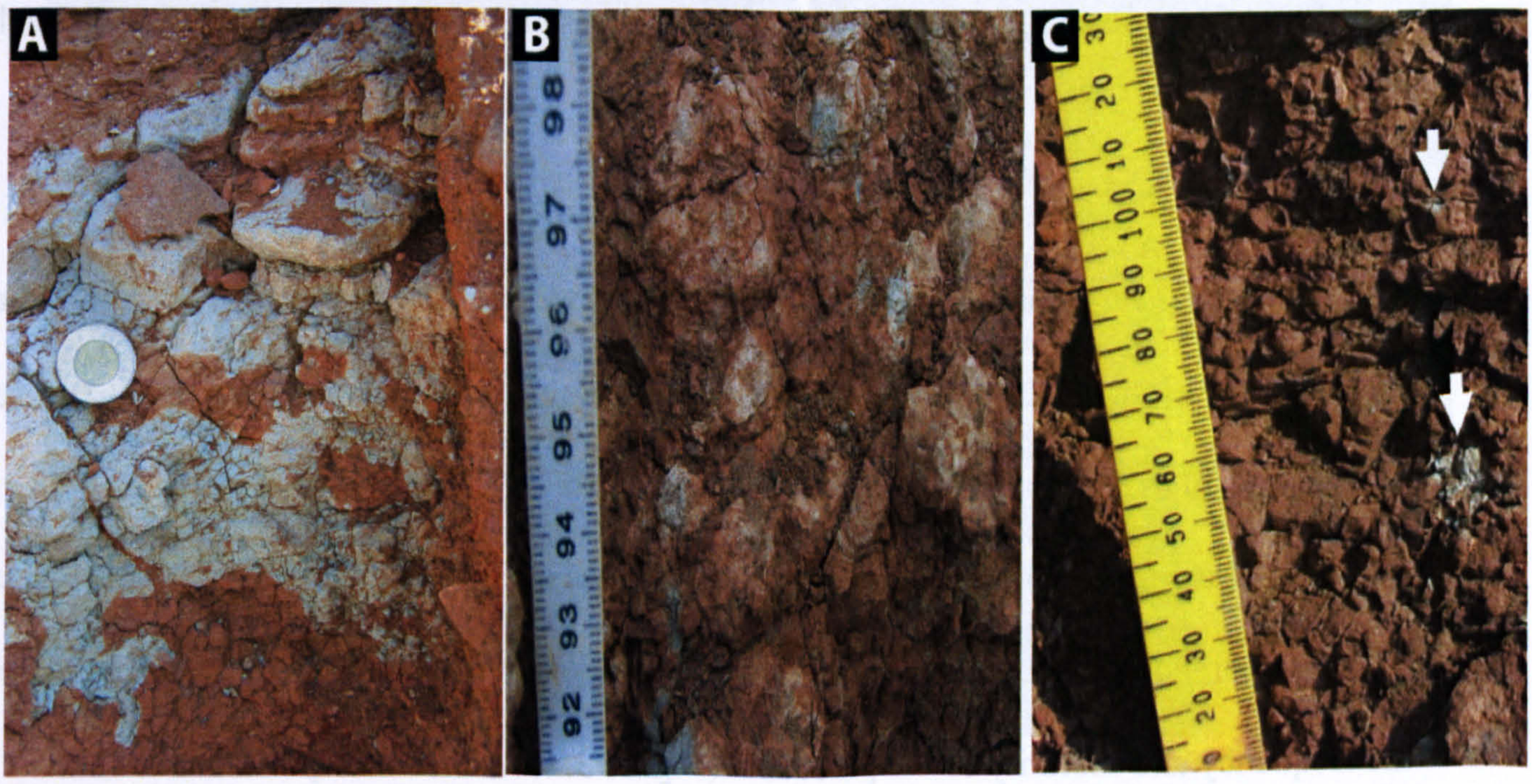

Figure 3.10 Variations of gley and mottles. A) the strongly gleyed top of KOR 1 at Boyevaya Gora. B) the mottles surrounding nodules in KOR 21 at Boyevaya Gora. C) Mottles seen in KOR2 The coin in photo A) is 27mm in diameter. The scale in B) and C) is in cm.

There are some paleosols which have distinct gleyed horizons (KOR1, KOR7, KOR10, KOR12, KOR15, and KOR28) ranging from 8-36cm thick, and normally associated with drab-root haloes. These primarily drab colours of very pale blue (5B 8/2), light greenish grey (5G 8/1), light grey (N7) and very light grey (N8). In the case of KOR1 this gley is quite

extensive and appears to be related to in filled desiccation cracks, although the gley continues down below these cracks for 14cm (Figure 3.10A). Several paleosols have overlying sandstones that are intensely gleyed (N8 and 5GY 8/1), contain drab-root haloes (see top of Figure 3.6B). KOR 15 and KOR 21 have nodules which themselves appear to be mottled (Figure 3.10B) possibly relating to drab-root haloes surrounding these nodules which were not visible in the field. This gley (opposed to the mottling) is associated with specific horizons, suggesting that its occurrence is related to pre-diagenetic processes. As such it probably represents the effects of periodic paleosol waterlogging as anaerobic microbes in poorly oxygenated water will reduce brown and red iron oxides and hydroxides from the ferric to ferrous states (Retallack 2001a). As these features are in the most part constrained to the upper horizons within the paleosol, it is plausible that they relate only to periodic waterlogging events, which is consistent with the presence of the ephemeral lakes (Newell *et al.* 1999).

There is vertical variation in the paleosol horizons at Boyevaya Gora. The paleosols at the bottom of the section are interbedded with numerous minor sand channels (Figure 3.4), some of which, as in the case of KOR 20, have undergone a level of paleosol development. Between 73 metres from the base of the section and the P/Tr boundary there is a change in both the sedimentation and paleosols: there is a lack of interbedded sands and an increase in the frequency and maturity of the paleosols (Figure 3.4). Also at this point there is the appearance of Vertisol-associated features (for example KOR4) suggesting periodic wetting and drying of the paleosol.

The paleosols of the earliest Triassic are significantly thinner than those of the Permian. The level of carbonate development is not greater than stage II and the nodules get no bigger than

30mm, with an average of 10mm. This is significantly smaller than the Permian average nodule size of 20-50mm. There is a shift in overall colour of the paleosol from brick red (10R), which dominates the Permian paleosols, to greyish yellow (5GY). Also, although the Triassic paleosols do show some evidence of root traces they are sparse and only preserved as drab root haloes (Figure 3.11A). Many of the overlying sandstone beds are gleyed, possibly suggesting they formed during flood events after which the water and sediment may have become anoxic (Figure 3.11B).

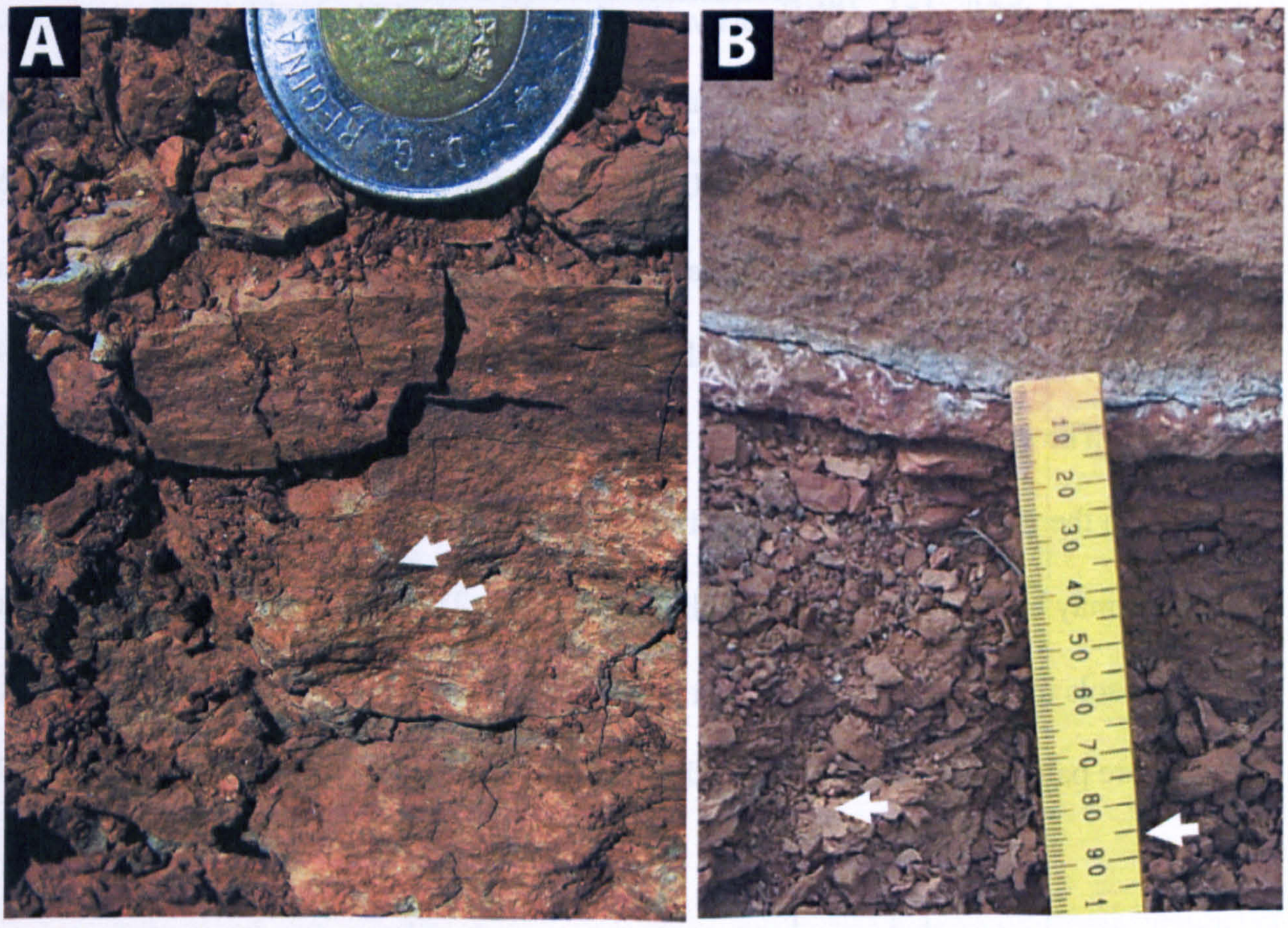

Figure 3.11 Root traces in Triassic paleosols at Boyevaya Gora; KOR37 (A) and KOR36 (B). A shows a minor drab root halo (coin 27mm in diameter) and B shows the gleyed sandstone (just above top of ruler) overlying a paleosol (scale in cm).

3.3.2 Sambullak

The section at Sambullak represents over 130 metres of interbedded muds, sandy channels, paleosols and lacustrine limestones capped by thick multi-storey conglomerates. The section

below the multi-storey conglomerates is the lowest part of the Kulchumovskaya Svita, Vyatkian Gorizont, by vertebrate bones (Tverdokhlebov *et al.* 2005). The Permian age is supported by palaeomagnetic data (Taylor *et al.* 2009) which places the P/Tr Boundary at the base of the conglomerate.

There are a total of 30 paleosols exposed at Sambullak, many of which are compound horizons, which are especially prevalent at the base of the studied section (Figure 3.12, for individual paleosol descriptions see Appendix A1.2). As with the paleosols at Boyevaya Gora the vertical thickness of the paleosols varies from 35cm to 164cm which also appears to be partially linked to the maturity of the calcrete layers within the paleosol and thus their age (cf. Wright and Tucker 1991; Retallack 2001a; Alonso-Zarza 2003). However, SAM2, SAM6, SAM8, SAM7, SAM17 and SAM21 have all been eroded by overlying conglomerate and sand channels therefore the measured thickness may not be representative of their original thickness. The grain size of the rock is uniformly of clay grain size in the lower part of the section. In the top 40 metres of the section average paleosol grain size increases to silt grain size, this may be related to increased channel activity. There is also a minor colour change in the paleosols up section: the lower part is predominantly moderate red (5R 5/4), those in the middle are pale brown (5YR 5/2) and those at the top are moderate reddish brown (10R 6/6).

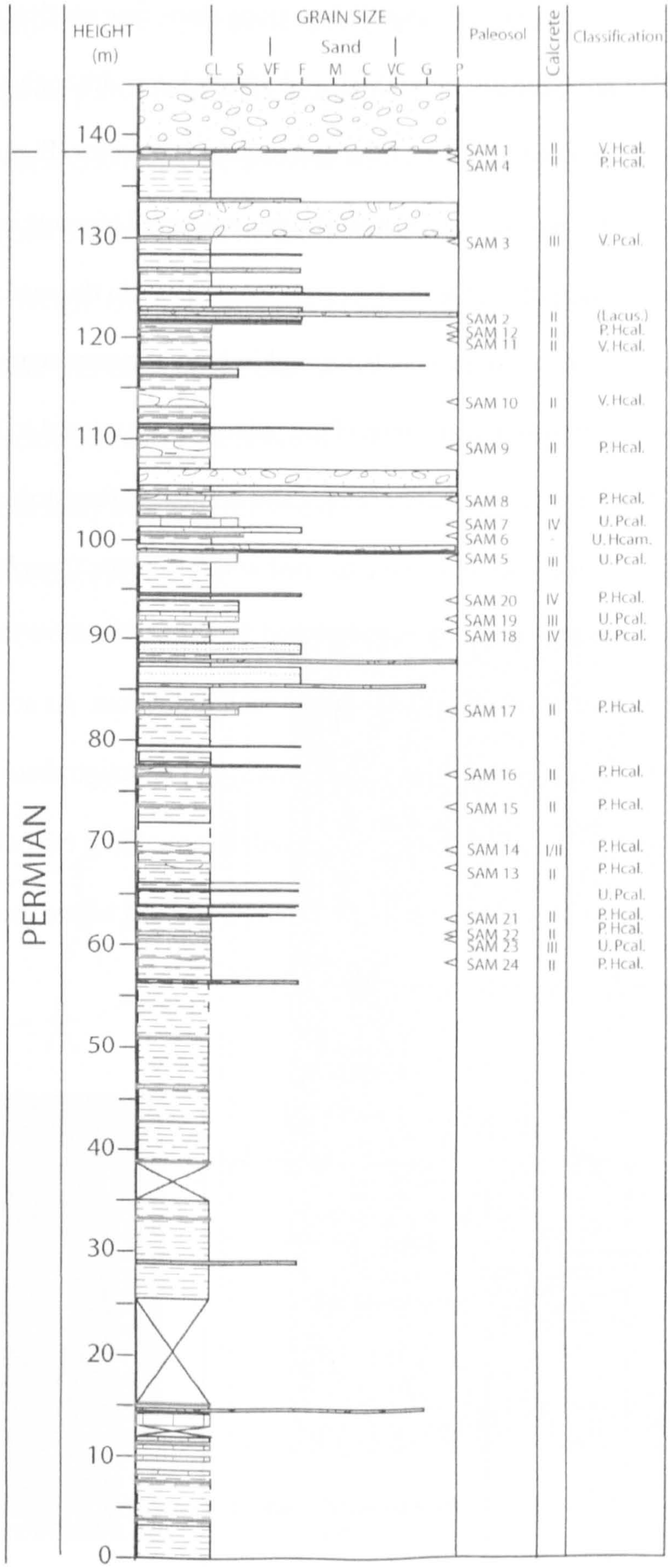

Figure 3.12 The studied section at Sambullak. The arrows (<) mark the position of the palaeosols in the section. The calcrete column shows the relative development of the Bk horizons within the paleosols and classification (see Table 2.2). P/Tr boundary is marked by the conglomerate at the top of the log (Sedimentological data for log from unpublished field data by Dr A. Newell and Dr R. Twitchett).

As at Boyevaya Gora, all the well-exposed sections show fine rootlets preserved as in fills of reddened clay that are typically 2mm thick and 30mm long, although some roots up to 300mm long are preserved in some of the more mature calcretes (Figure 3.5A). Similarly some of the Stage III calcretes (e.g. SAM 5) have preserved taproots which are thicker than the other rootlets (4mm) and have evident right-angles within the root structure (Figure 3.5B). This suggests that some of the paleosols formed in high or permanent water tables (Retallack 1997). There is also evidence that some of the paleosols are related to lacustrine deposits. For instance SAM 2 has evident limestone lenses and laminated limestones (25cm thick) (Figure 3.13) suggesting this paleosol may have formed with influence from lacustrine waters as described by Alonso-Zarza (2003). SAM 10 and SAM 19 also show similar features, although the rest of the other paleosols do not show any such influences. As at Boyevaya Gora some root traces are preserved as drab-root haloes (SAM 22) although these are rare (Figure 3.5C). Also, as at Boyevaya Gora, root traces are recorded throughout the paleosol apart from five horizons (SAM 1, SAM 8, SAM 12, SAM 21 and SAM 22) where root traces are only observed in the A horizon (see Appendix A1.2).

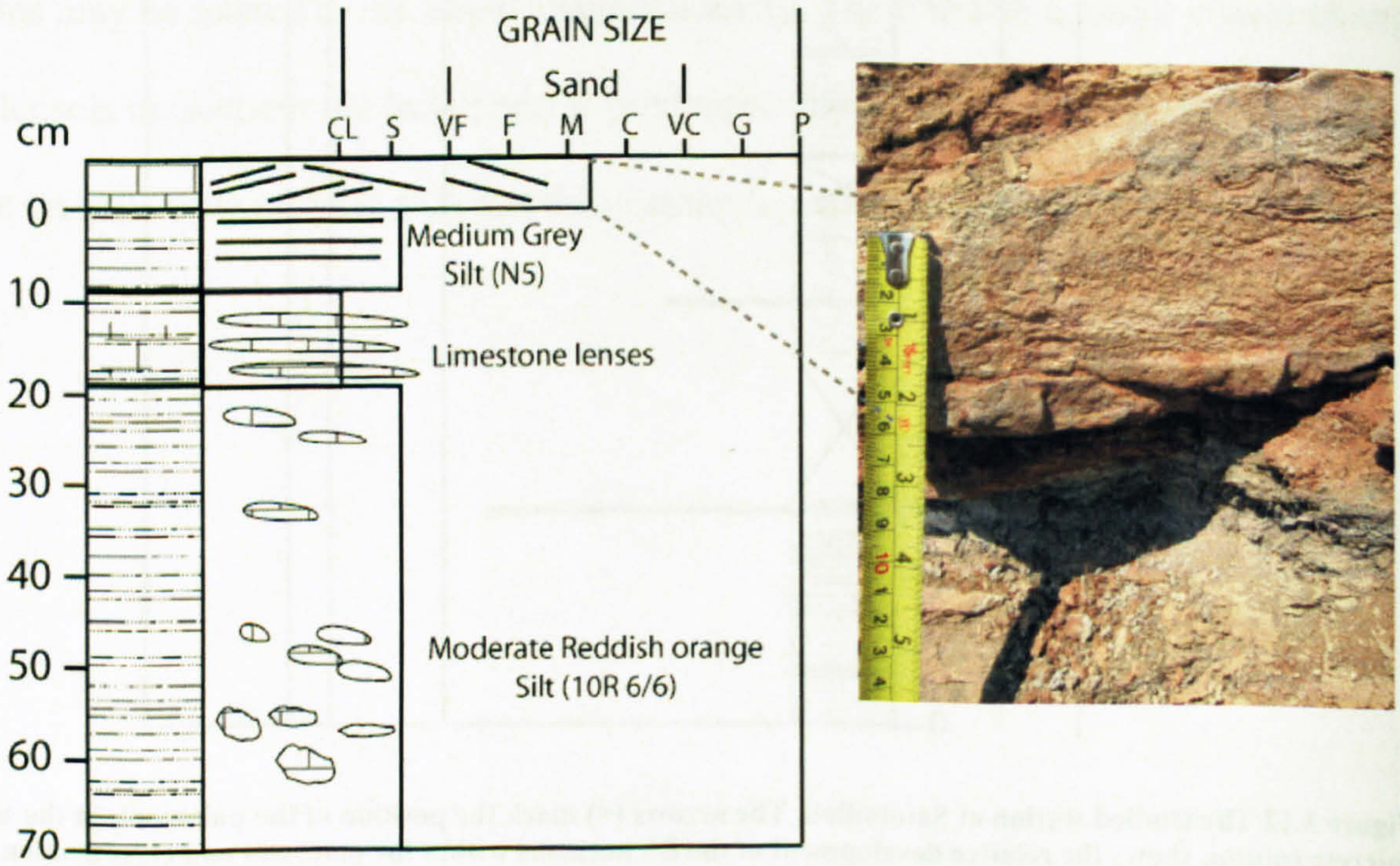

Figure 3.13 Palustrine associated paleosol (SAM2) with associated limestone lenses.

At Sambullak the majority of the paleosols have a developed Bk horizon, which range from 6-80cm thick, although they are not as well developed as the paleosols seen at Boyevaya Gora. There is one horizon (SAM6) which has no Bk horizon and a light coloured, but non calcified surface horizon (Figure 3.14). The Bk horizons that are present are mostly stage II horizons (classification after Wright and Tucker 1991; Retallack 2001a; Alonso-Zarza 2003). Possibly, the basin at Sambullak was more active than at Boyevaya Gora and the paleosols did not have as much time to develop extensive Bk horizons (cf. Retallack 1997; 2001a). The stage II horizons are predominantly 50-25cm thick and have a similar morphology to the dispersed nodular bands seen at Boyevaya Gora.

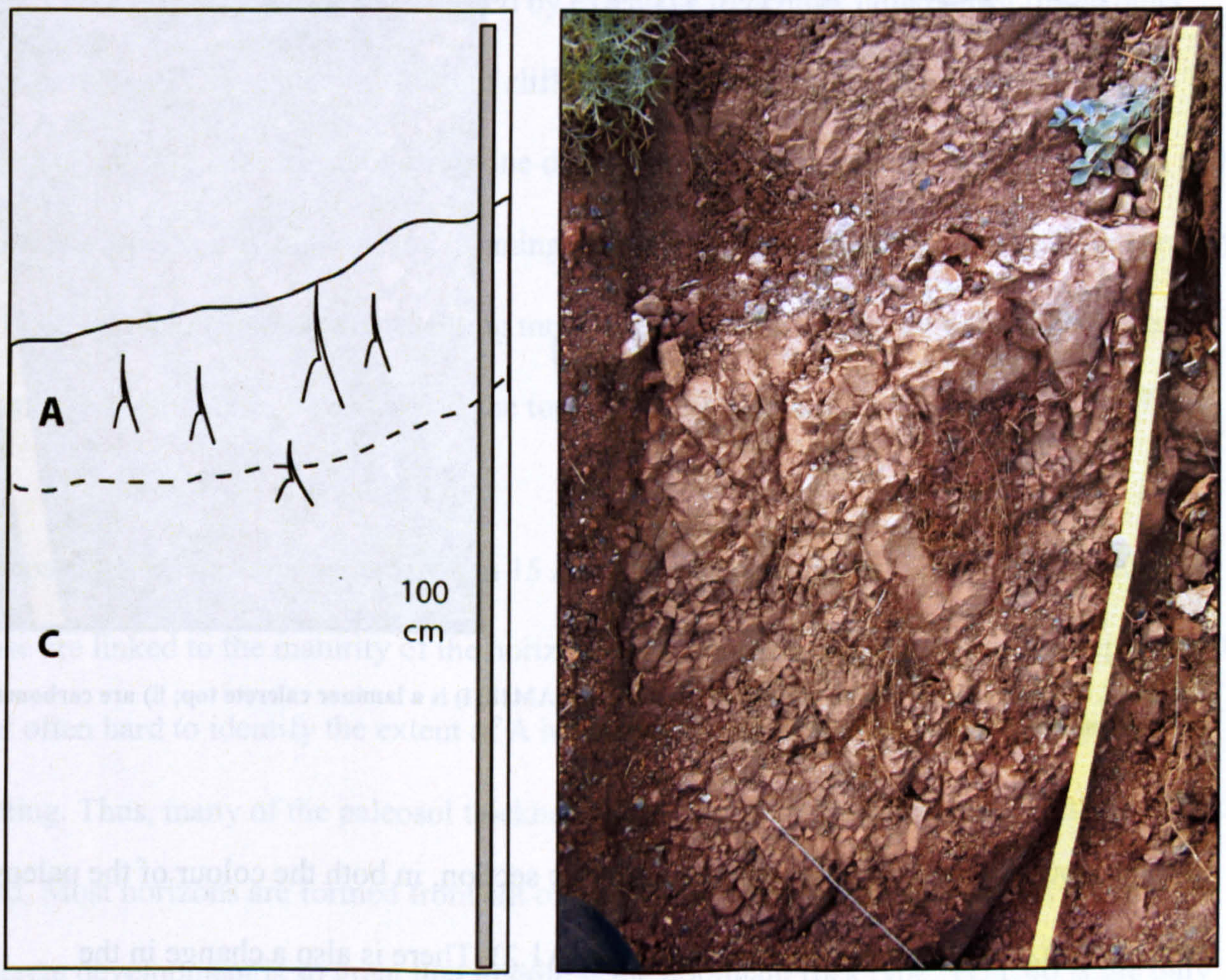

Figure 3.14 A poorly developed paleosol (SAM 6) with light coloured A horizon and no Bk development (the scale is a metre in length).

The stage III horizons are similar to those at Boyevaya Gora and range from 53-27cm in thickness. Some paleosols, such as SAM 5a, contain preserved tabular root systems (Figure 3.5A), suggesting that they formed in an area with a high water table (Retallack 1997). There

are two horizons (SAM 7 and SAM18) which have more developed Bk horizons. Both of these horizons were poorly exposed, but there was some evidence of laminar calcrete tops (of 10 and 17cm respectively, Figure 3.15) which would classify them at stage IV in Retallack's (2001) classification scheme or stage V as described by Alonso-Zarza (2003). However, SAM7 and SAM18 are both less developed as the Stage V Bk horizons at Boyevaya Gora.

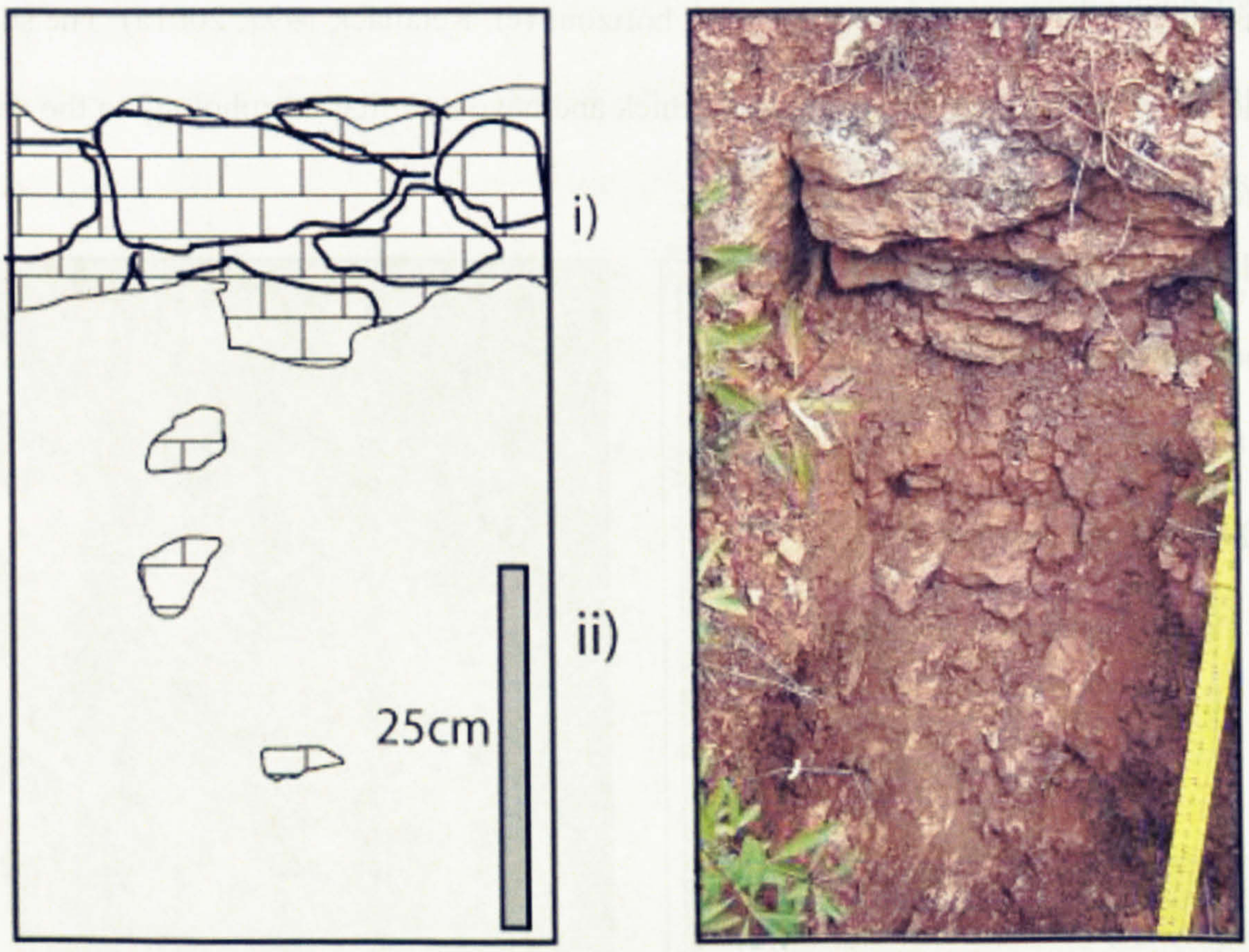

Figure 3.15 A stage IV carbonate horizon at Sambullak (SAM18) i) is a laminar calcrete top; ii) are carbonate nodules below. Ruler at side of trench = 25cm.

As previously stated there is some variation up section, in both the colour of the paleosols and the grain size of the sediment (see Appendix A1.2). There is also a change in the palaeoenvironment up section. The lower and mid parts of the section show evidence for minor temporary lacustrine influence, whereas two of the paleosols at the top of the section (SAM 1 and 3) below the start of the thick multi-storey have evidence of slickensides (Figure 3.8B) which implies drying out of the environment (cf. Kovda and Wilding 2004). There is

little variation in the development in the Bk horizons through the section, suggesting that this section had more active channels than seen at Boyevaya Gora and thus did not allow the paleosols as much time to develop (cf. Retallack 2001a).

3.3.3 Tuyembetka

Seventy one paleosols were identified at Tuyembetka in a section which is 111 metres thick, more than in any other section studied (Figure 3.16, for individual paleosol descriptions see Appendix A1.3). Unfortunately the exposure at Tuyembetka is relatively poor as the section occurs on a hillside, which was exposed by extensive trenching, unlike most of the other Russian sections which are exposed in cliffs and steam-cut gullies. So, for many of the paleosols, it is impossible to observe fine details and features recorded in other sections and many are obscured by modern soil-forming processes. The section is comprised of primarily of Permian rocks probably representing most of the Lopingian (Taylor *et al.* 2009). The P/Tr boundary is thought to lie just above the top of the exposed section (Taylor *et al.* 2009).

The paleosol thicknesses vary between 15 and 130cm thick and, as with the other sections, these are linked to the maturity of the horizons (see Appendix A1.2). Due to the exposure, it was often hard to identify the extent of A horizons as they were often obscured by modern rooting. Thus, many of the paleosol thicknesses may actually have been underestimated in the field. Most horizons are formed from silt or clay grade sediment. In some cases the level of calcrete development is so great that micrite is the dominant rock type. TUY 40 is the only horizon that is predominantly of a fine-sand grain size and may relate to a paleosol forming in a disused minor channel.

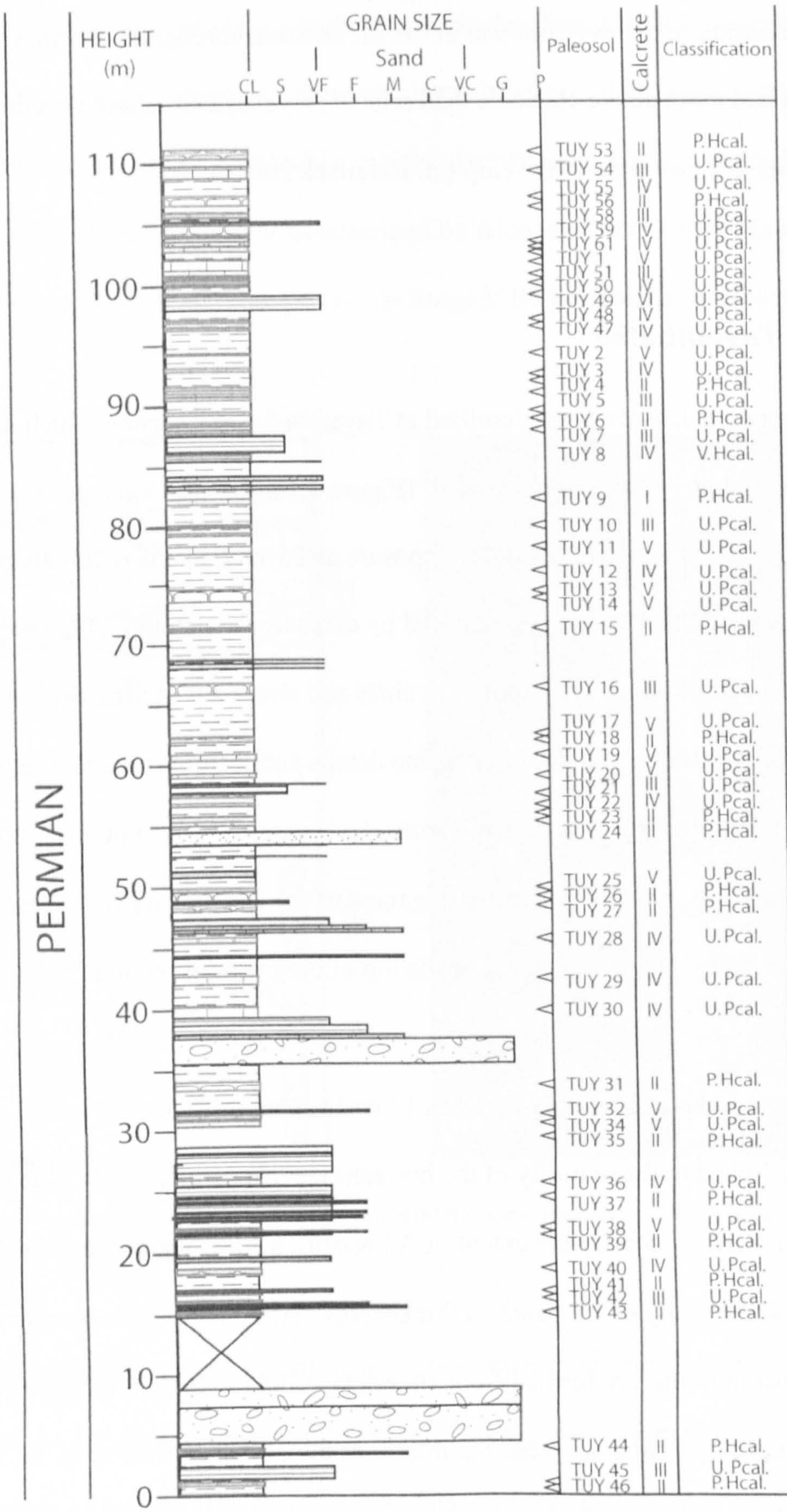

Figure 3.16 The studied section at Tuyembetka. The arrows (<) mark the position of the paleosols in the section. The calcrete column shows the relative development of the Bk horizons within the paleosols and classification (see Table 2.2). Note the relatively large number of paleosols per metre compared with other sections and the relative maturity of the carbonate within them (Sedimentological log data from unpublished field date by Dr A. Newell and Dr R. Twitchett).

As with the other sections, root traces were observed throughout the section. They were especially evident in the well-exposed examples of Stage V and VI horizons where they are preserved as iron-stained root traces. However, in some of lesser developed calcrete paleosols it is also possible to observe root traces in the A horizons (examples TUY 6, TUY9, TUY10, TUY26, TUY46, TUY56). These often take the form of deep vertical root traces (Figure 3.17) related to vertical movement of water through the paleosol profile (Alonzo-Zarza 2003) suggesting a prevalent dry season (Retallack 1997).

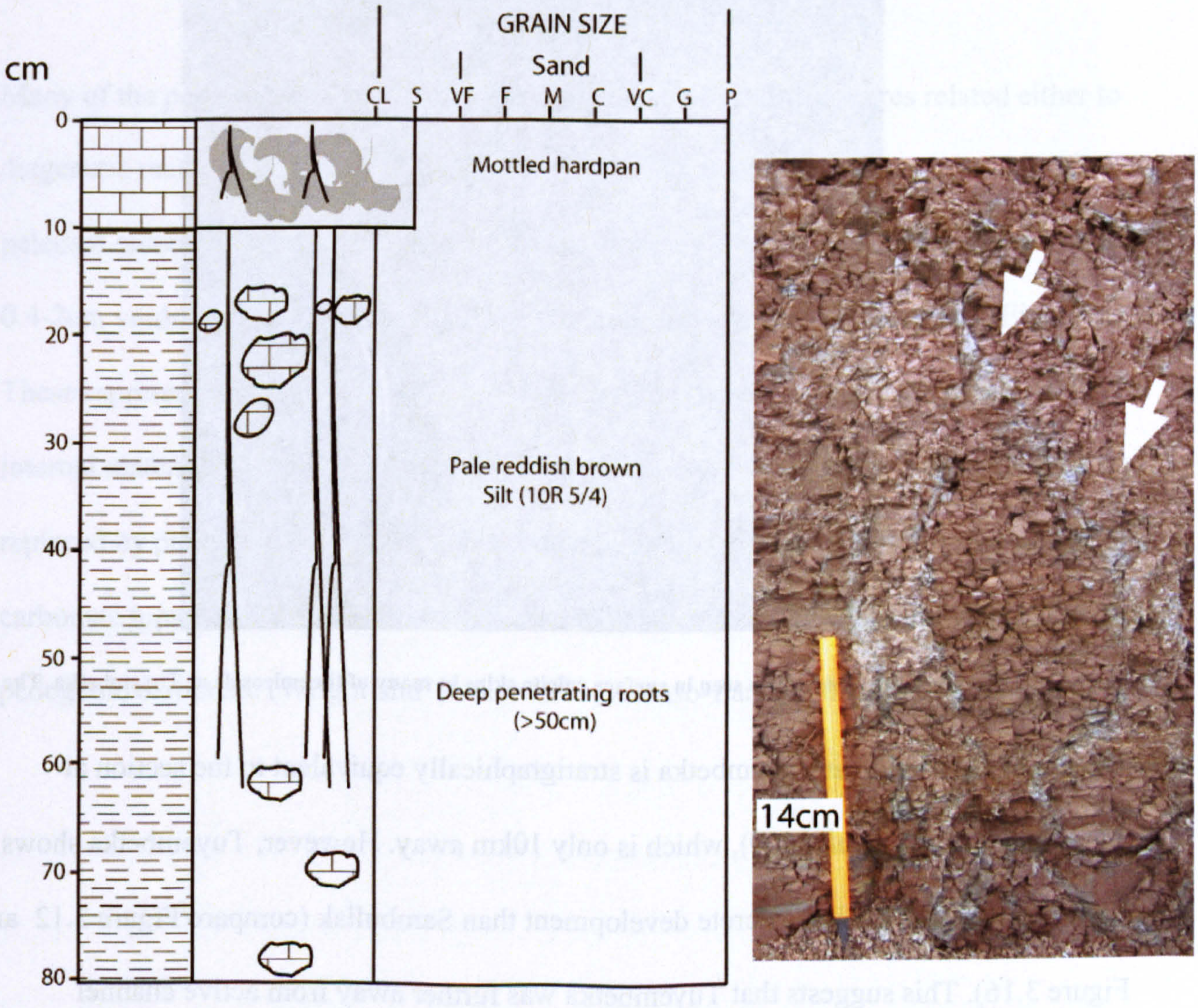

Figure 3.17 Deep root traces at Tuyembetka (TUY46) which penetrate over 50cm. Deep penetrating root traces arrowed.

The most evident feature of the paleosols at Tuyembetka is the level of calcrete development. Unlike the previous sections the average stage of Bk horizon development is stage IV. There is evidence of paleosols with stage VI Bk horizons (TUY 49 and 25) as described by

Retallack (2001). Both these horizons are relatively thin (53cm and 62cm respectively), although both show brecciated calcrete hardpans. There is also evidence in some of the calcrete hardpans of surface 'skins' (1-2mm thick) calcite with a characteristic 'knobbly' texture (Figure 3.18) possibly relating to repeated stages of recrystallisation. Even the stage II and III Bk horizons are more extensive and more indurated than those seen at any for the other sections in Russia (Figure 3.6C).

Figure 3.18 'Knobbly' surface texture seen in surface calcite skins in many of the paleosols at Tuyembetka. The coin is 20mm in diameter.

The top of the section at Tuyembetka is stratigraphically equivalent to the section at Sambullak (Taylor *et al.* 2009), which is only 10km away. However, Tuyembetka shows significantly more mature calcrete development than Sambullak (compare Figure 3.12 and Figure 3.16). This suggests that Tuyembetka was further away from active channel development, allowing more developed paleosols to form which were less likely to have been affected by groundwater originating from fluvial channels (Williams and Krause 1998). As these more mature paleosols take longer to form (Wright and Tucker 1991; Retallack 2001a; Alonzo-Zarza 2003).

The colour variation at Tuyembetka is also markedly different. Many of the paleosols are significantly redder than those elsewhere in Russia, and have chromae of 5R 8/2 – 5R 4/2 possibly relating to lack of moisture and organic matter relative to the other paleosols. Vertical variation seen at Tuyembetka is less evident than the other sections elsewhere in the basin. There is a decrease in the maturity of the calcretes in the lower parts of the section although this is not as marked as in other sections (Figure 3.16).

Many of the paleosols at Tuyembetka show evidence of calcitic features related either to diagenetic recrystallisation or to possible modern calcite formation (Figure 3.19A). The paleosol horizons with stage IV and above Bk horizons contain calcite-fills which manifest as 0.4-2cm voids that have been in filled by later euhedral sparry calcite crystals (Figure 3.19B). These represent original holes in the calcretes formed by roots or burrows of which the internal material has been removed by later diagenetic groundwater or diagenetic fluid and replaced by precipitated calcite crystals. Some paleosols (such as TUY 30) show diffuse carbonate tops and abrupt bases indicative of calcrete formed from groundwater rather than pedogenic carbonate (Wright and Tucker 1991; Alonso-Zarza 2003; Quast *et al.* 2006).

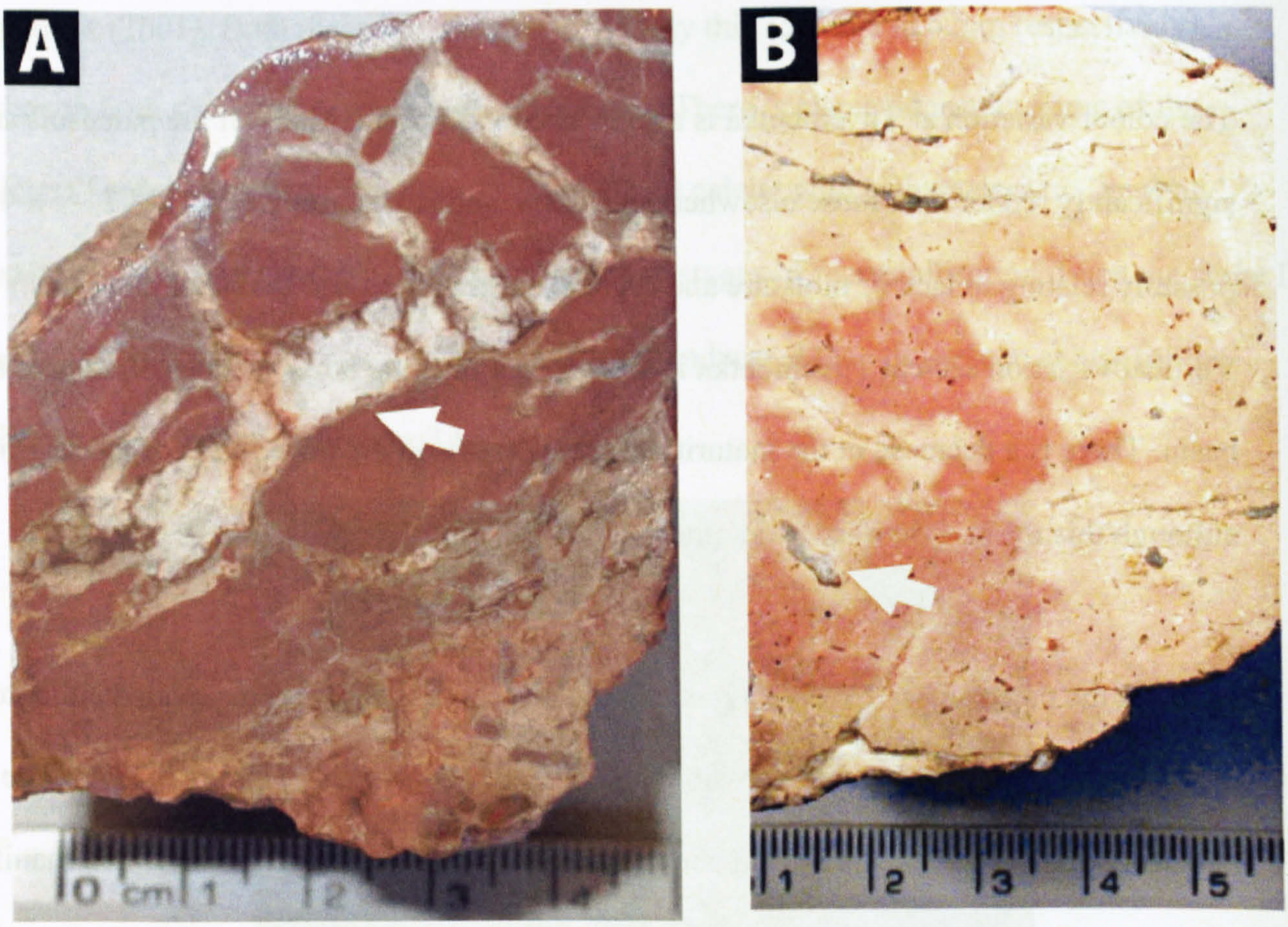

Figure 3.19 Large cracks (A) and voids (B) in filled with sparry calcite seen at Tuyembetka. These exist in other sections but only at Tuyembetka are they cm in scale. Scale in both photos in centimetres.

3.3.4 Vozdvizhenka

Vozdvizhenka is a shorter section than those thus far described (33m in thickness) (Figure 3.20, for individual paleosol descriptions see Appendix A1.4). In total 17 paleosols were identified at Vozdvizhenka. The section at Vozdvizhenka is thought to cross the P/Tr boundary although its exact position is still debated (Taylor *et al.* 2009). The most prominent feature of the paleosols at Vozdvizhenka is the substrate from which they formed. Unlike almost all the other Russian sections, which are primarily formed of siltstones and claystones, the paleosols at Vozdvizhenka are formed from fine to very fine sandstone and unconsolidated siltstones.

All the paleosols at Vozdvizhenka have Bk horizons. However, unlike Tuyembetka or Boyevaya Gora, there is only one example of a paleosol containing a Bk horizon developed above stage II, and that is only stage III (Figure 3.20). Many of these nodules are either very large (5-6cm) or almost blocky in shape (Figure 3.21), suggesting they may be formed by groundwater rather than pedogenic meteoric water (Khadkikar *et al.* 2000; Alonzo-Zarza 2003). This is supported by the presence of mottling and the relative coarseness of the sediment which would have allowed increased groundwater flow.

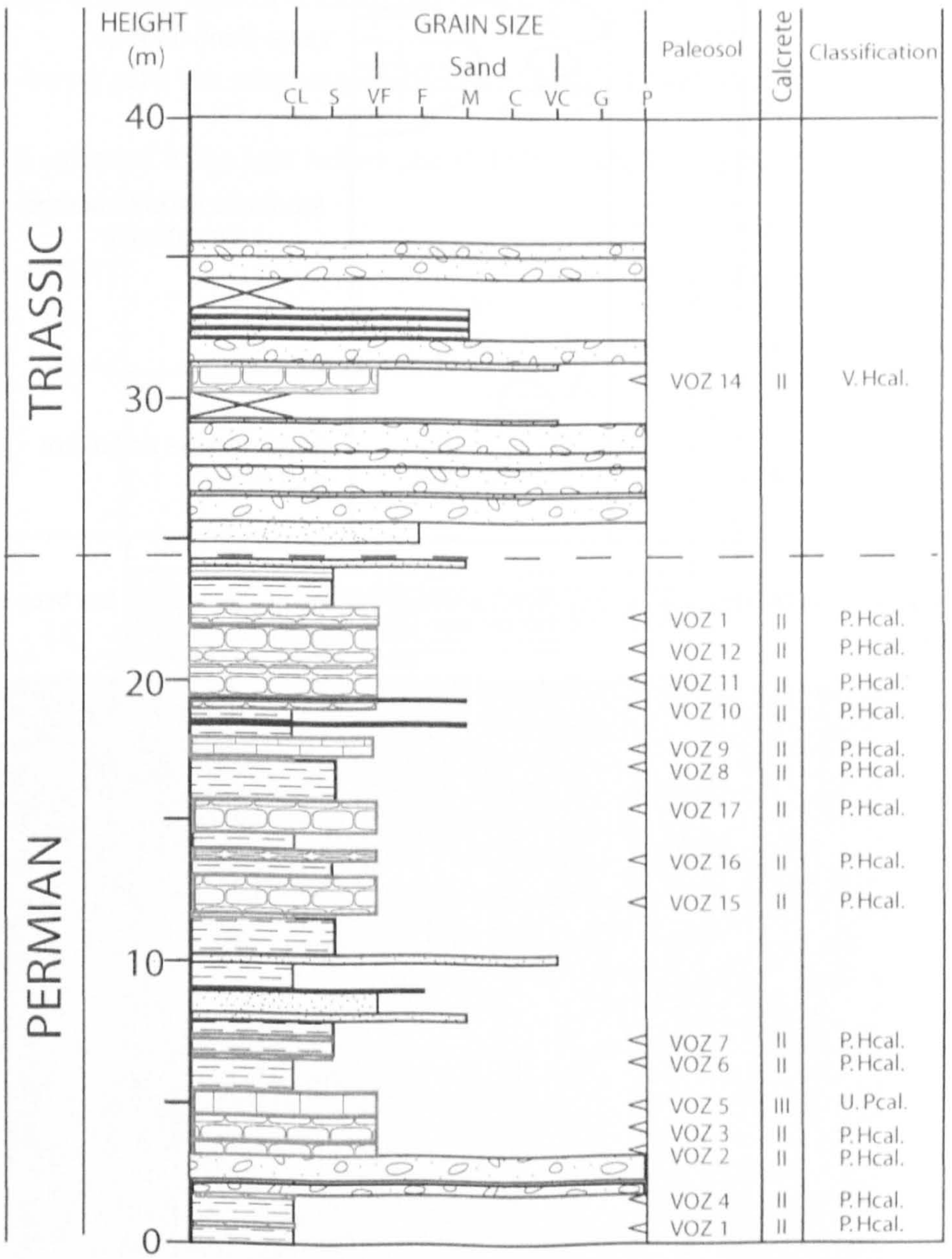

Figure 3.20 The studied section at Vozdvizhenka. The arrows (<) mark the position of the paleosols in the section. The calcrete column shows the relative development of the Bk horizons within the paleosols and classification (see Table2.2). P/Tr boundary based on magnetostratigraphy and sedimentology but due to poor magnetic recorded position of boundary is not precise (see Taylor *et al.* 2009). (Sedimentological data from unpublished field data by Dr A. Newell and Dr R. Twitchett).

There is, however, also evidence further up the section, 20cm below the P/Tr boundary, for pedogenic slickensides suggesting that there were periods when these paleosols must have periodically dried out. This paleosol (VOZ 14) also is capped by 3cm thick gravel beds (Figure 3.22) within which all clasts are well rounded and the lack of sorting would suggest a flash flood event (Leeder 1999).

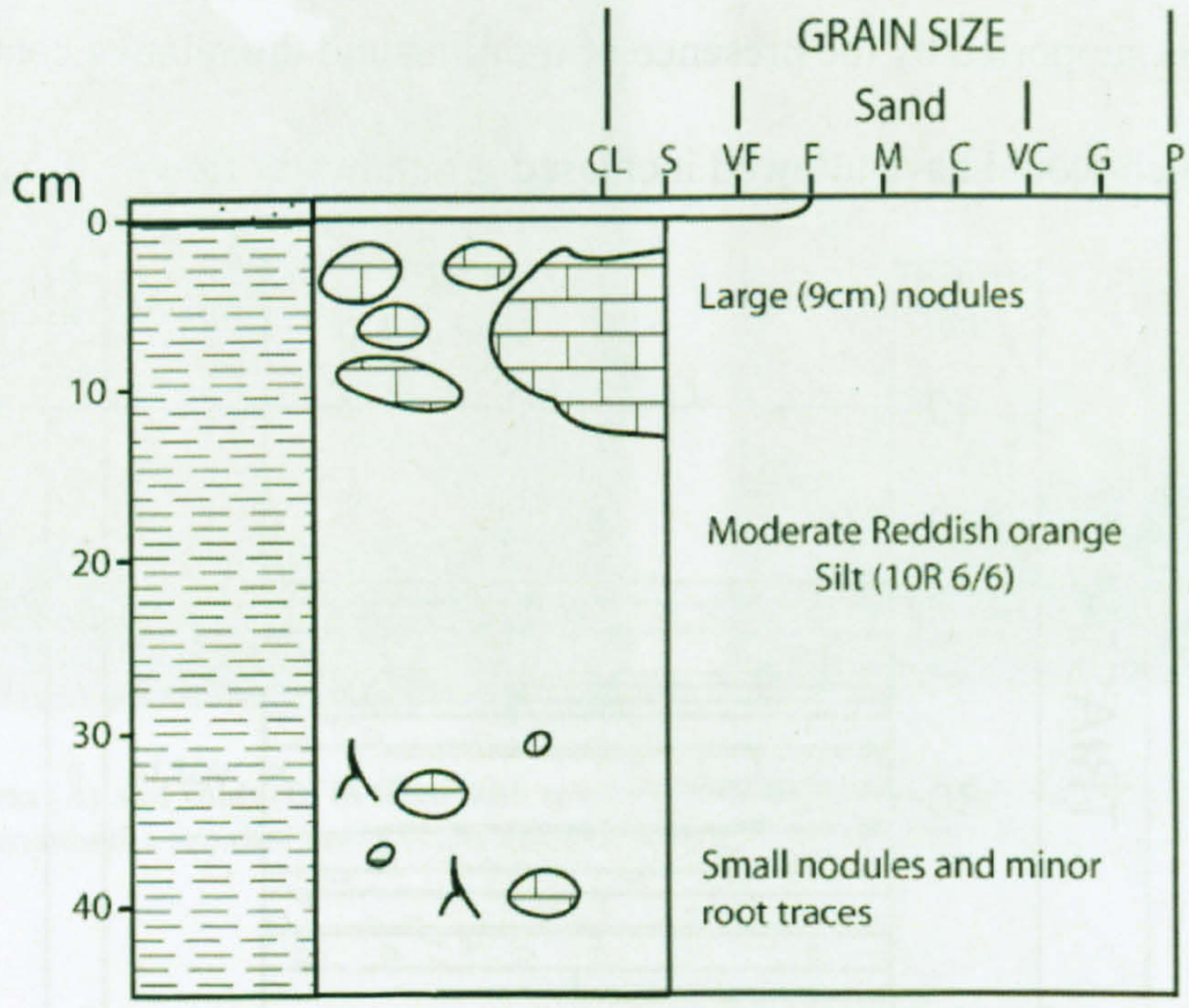

Figure 3.21 Paleosol VOZ9 with large blocky (9cm) nodules. The top of this horizon has been eroded by the overlying sandstone bed.

Figure 3.22 Paleosol VOZ14 at Vozdvizhenka capped by 3cm gravel. Scale in cm.

3.3.5 Krasnogor

Krasnogor is 20km further south than the sections of Sambullak, Tuyembetka and Vozdvizhenka (Figure 3.2). The P/Tr boundary is thought to be at the base the coarse facies (Figure 3.23), however, the Lower Triassic sandstones at Krasnogor have yielded *Benthosuchus* fossils which has been assigned to the Staritskaya Svita (Tverdokhlebov *et al.* 2002), which may suggest that first Gorizont of the Triassic is missing (Figure 3.2) (Taylor *et al.* 2009). This being said the magnetostratigraphy yields a well defined Reverse-Normal change which is inferred to be just below the P/Tr boundary (Figure 3.3).

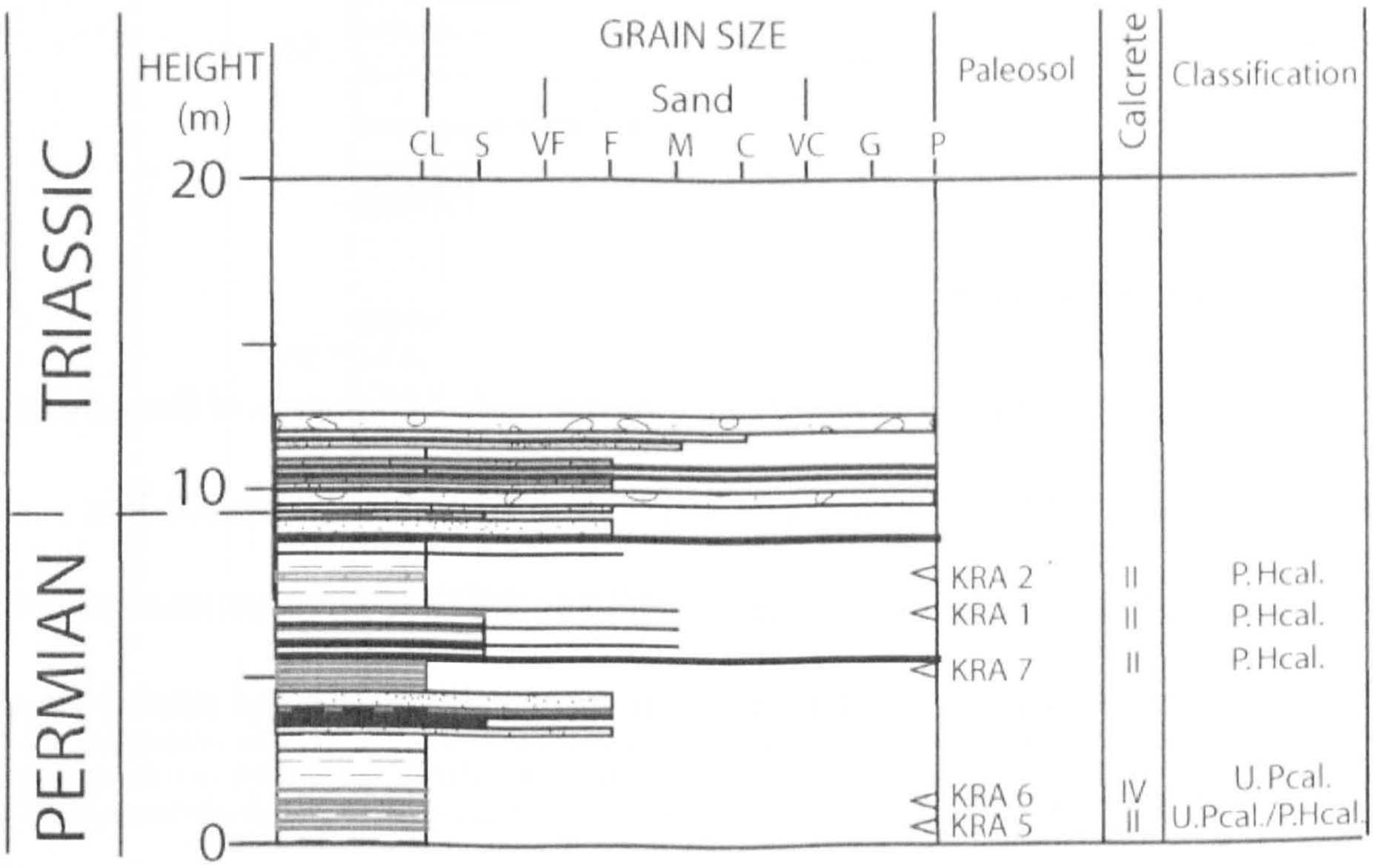

Figure 3.23 The studied section at Krasnagor. The arrows (<) mark the position of the paleosols in the section. The calcrete column shows the development of the Bk horizons within the paleosols and classification (see Table 2.2). (Sedimentological data from unpublished field data by Dr A. Newell and Dr R. Twitchett).

Krasnagor shows many similar pedogenic features to the paleosols further north in the basin. In a section 21m thick a total of 6 paleosol horizons where identified (Figure 3.23) and, like at Vozdvizhenka, the Krasnagor horizons all show a developed calcitic Bk horizon (Figure 3.23), for individual paleosol descriptions see Appendix A1.5). Although the majority of the

paleosols also have stage II Bk horizons, there is one horizon at Krasnagor that shows stage IV development (KRA 6). This paleosol is only 36cm thick but shows a calcrete laminar top with some evidence of brecciation.

Like Vozdvizhenka the paleosol substrate is markedly coarser than the rest of the sections. It is composed predominantly of very fine to fine sandstone, and it also shows large nodules (>6cm), intense gleys and blocky continuous sheets of nodules suggesting a predominantly groundwater source in the formation of the carbonate (cf. Khadkikar *et al.* 2000; Alonzo-Zarza 2003). However, many of the nodule horizons have preserved (5-2mm in width) root traces implying that at least at some points the water table must have been below the level the of Bk horizon (cf. Alonzo-Zarza 2003).

3.3.6 Petropavlovka

The section at Petropavlovka consists of approximately 100 metres of fluvial sandstones and mudstones along with channel deposits and occasional nodular paleosols. It is stratigraphically part of the Petropavlovskaya Svita which is the uppermost part of the Lower Triassic (Figure 3.3) and is constrained biostratigraphally by fish and amphibian remains (Tverdokhlebov *et al.* 2002).

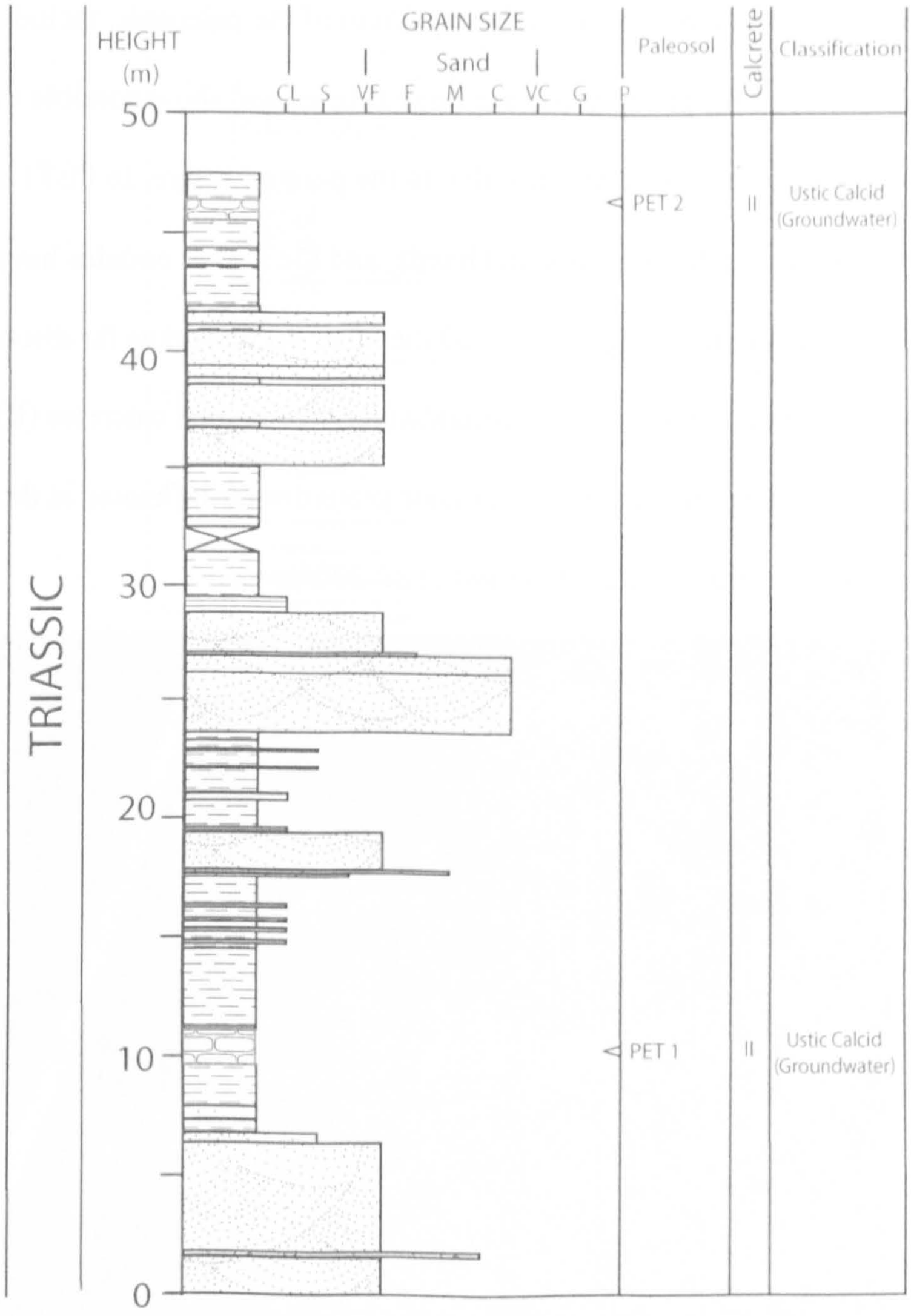

Figure 3.24 The section at Petropavlovka. The arrows (<) mark the position of the paleosols in the section. The calcrete column shows the relative development of the Bk horizons within the paleosols and classification (see table2.2). (Sedimentological data from unpublished field data by Dr A. Newell and Dr R. Twitchett).

The section is poorly exposed in a set of stream-cut gullies in the steppe and only yielded two identifiable paleosols (Figure 3.24, for individual paleosol descriptions see Appendix A1.6). All show green gleyed areas of up to 5cm (chromata 5G 8/1), which contrasts strongly with the moderate reddish orange (10R6/6) and light red (5R6/6) of the remaining paleosols (Figure 3.25). These gleys are concentrated in the top 10cm of the horizons although there are also mottled areas in the Bk horizons.

There is minor evidence of rooting in the top 25cm of the paleosols, including drab-root haloes. Also some of the Bk horizons are stage II level and show possible evidence of rooting, although identification is problematical due to the poor exposure. In PET1 in the lower part of the Bk horizon the nodules form distinct bands, and the higher nodules have gradational boundaries unlike the sharp edges observed the other sections thus far discussed (Figure 3.6 F). This is thought to be indicative of groundwater precipitated calcretes (Khadkikar *et al.* 2000). The excessive gleys also imply a major groundwater influence in the formation of the Bk horizons. (Khadkikar *et al* 2000; Quast *et al.* 2006).

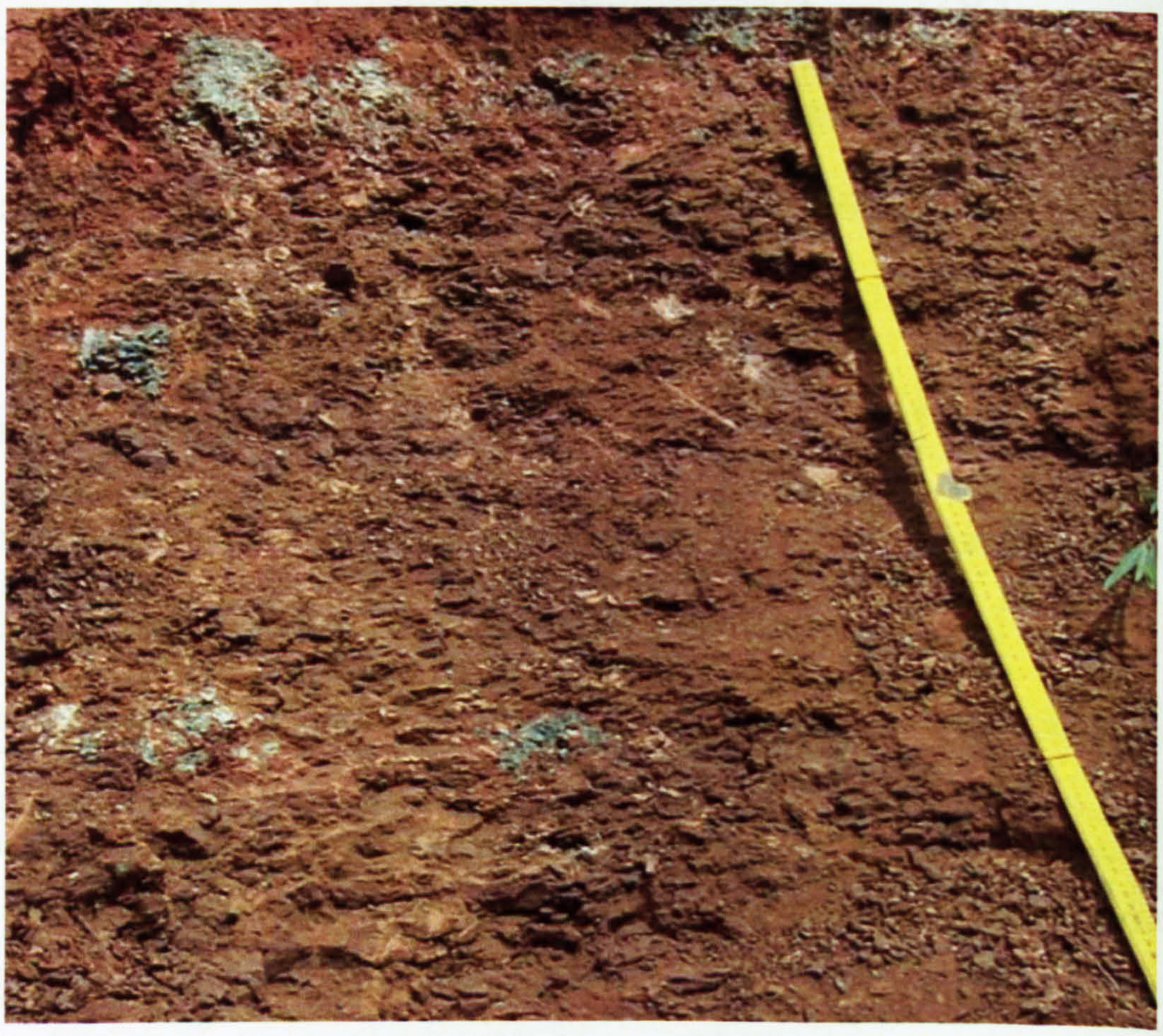

Figure 3.25 (5cm) mottles areas in the paleosols at Petropavlovka. Scale is 1metre in length.

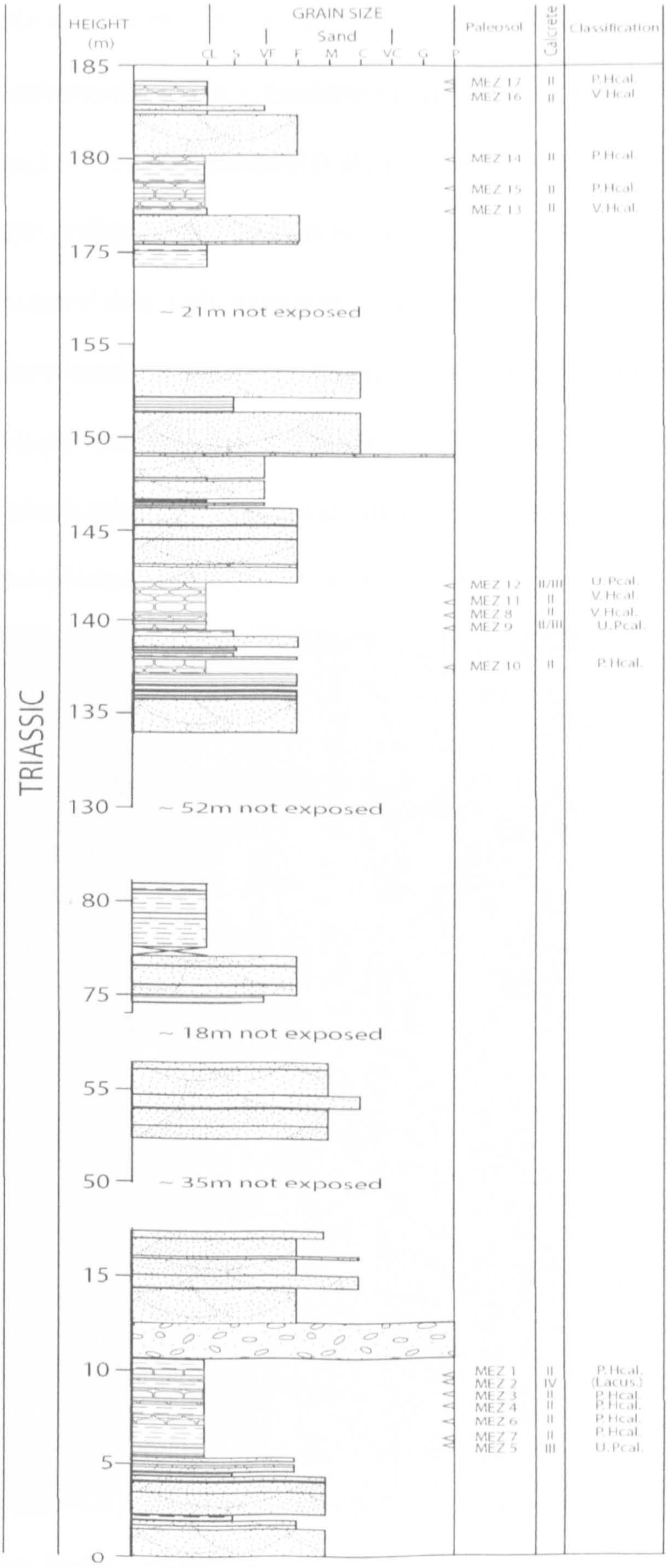

Figure 3.26 The studied section at Mescheryakovka. The arrows (<) mark the position of the paleosols in the section. The calcrete column shows the relative development of the Bk horizons within the paleosols and classification (see Table2.2). (Sedimentological data from unpublished field data by Dr A. Newell and Dr R. Twitchett).

3.3.7 Mescheryakovka

Mescheryakovka (184 metres thick) is assigned to the Petropavlovskaya Svita, Yarenskian Gorizont which is equivalent to top of the Olenekian (Figure 3.1) based on the occurrence of *Capitosauridae* and *Procolophoniae* (Tverdokhlebov *et al.* 2002). The section comprises of stacked sequences of tributary channels (Tverdokhlebov *et al.* 2002; Dr A. Newell and Dr R. Twitchett unpublished field data) and nodular paleosol horizons. There are 18 paleosol horizons (Figure 3.26, for individual paleosol descriptions see Appendix A1.7) which can be divided into two different pedotypes: the lower paleosols have similar affinities with paleosols from the Triassic of Boyevaya Gora, while the upper paleosols especially MES 16, have a morphology which is very different to anything else recorded in the Russian sections studied herein.

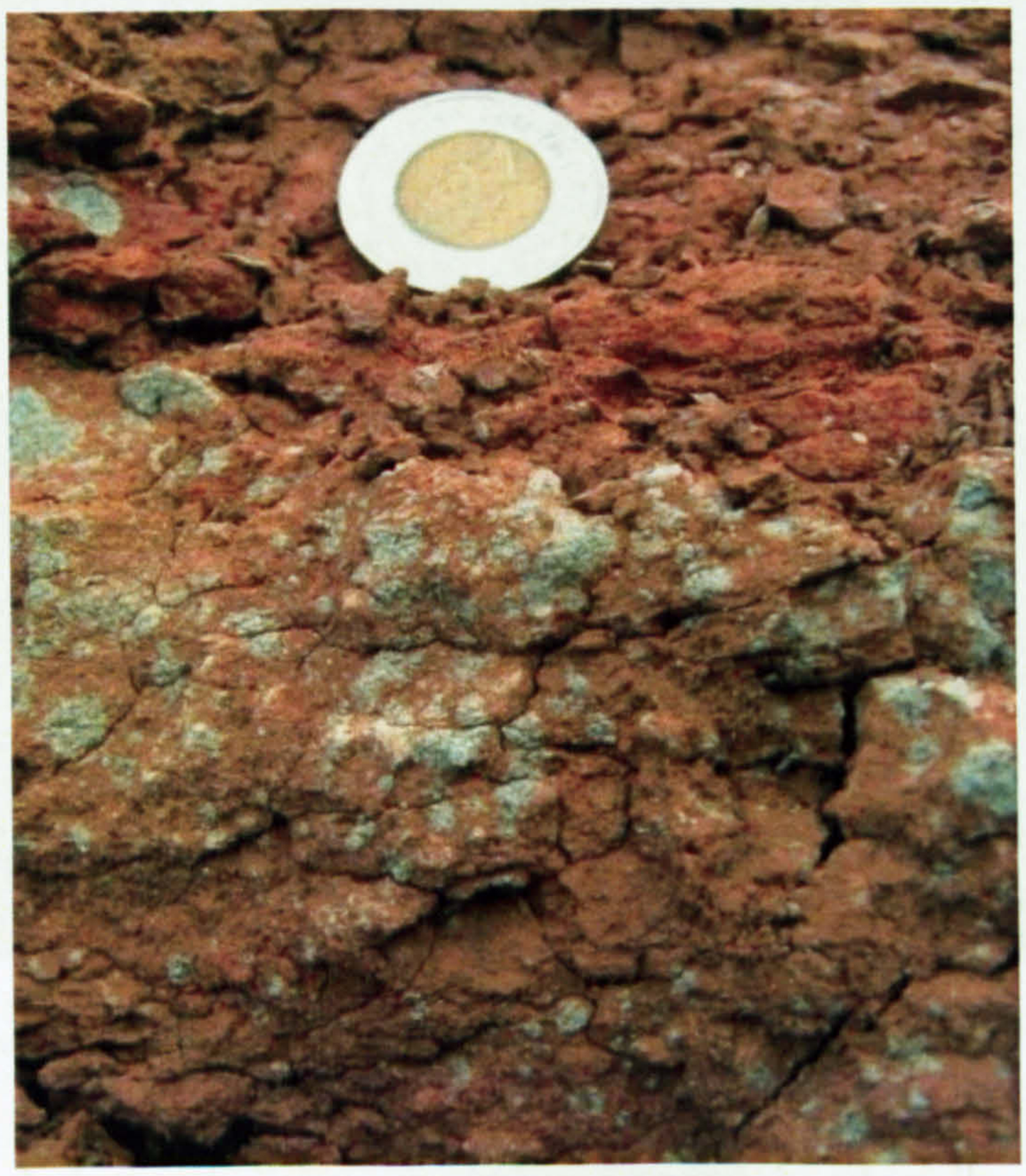

Figure 3.27 'Speckled' gley in the A horizon of MES8. Coin 27mm in diameter.

The lower paleosols (MES1, MES2, MES3, MES4, MES5, MES6, MES7, MES8 MES9, MES10, MES11, and MES12) are part of a stacked sequence made of siltstone. There is evidence for sparse root structures, although these only occur in the A horizons and never

penetrate the Bk horizons. The Bk horizons are only developed as far as stage II with relatively small (1-2cm) nodules and are confined to bands which are 10-40cm thick. Most of the A horizons have a light greenish grey gley (5G 8/1), while the lower horizons within the paleosol are a moderate yellowish brown (10YR 5/4) (Figure 3.27). In these lower paleosols there are some examples of deep (36cm) calcified rootlets (MES 8). From their irregular tubular shape and tapering appearance they have been tentatively identified as thick roots (after Retallack 1997). This is supported by the presence of calcite in these features which would suggest a rhizoconcretion, although an infilled crack could also act as a site for calcrete precipitation (Figure 3.28).

Figure 3.28 Tubular rhizoconcretion from Mescheryakovka. Coin is 27mm in diameter.

The upper paleosols at Mescheryakovka (MES14, MES15, MES16 and MES17) are quite different from anything else recorded in this study. The most striking feature is the change in colour: Rather than being shades of brick-red (10YR 5/4), like the rest of the Russian

paleosols, the colour of these paleosols is predominantly pale greenish yellow (10Y 7/2) and the A horizons are dominated by drab-root haloes of light red (5R6/6). The top 16cm of the paleosols have a gley of light bluish grey (5B 7/1) and contains possible desiccation cracks (Figure 3.29). The rooting in these horizons is dense (compared to previous paleosols) and extends from the paleosol surface down into the Bk horizon. The root traces are 10-15mm wide and show branching structures (Figure 3.29). They are preserved as drab haloes, suggesting waterlogging of the paleosol or a reducing environment allowing anaerobic bacteria to break down organic matter (Retallack 2001a).

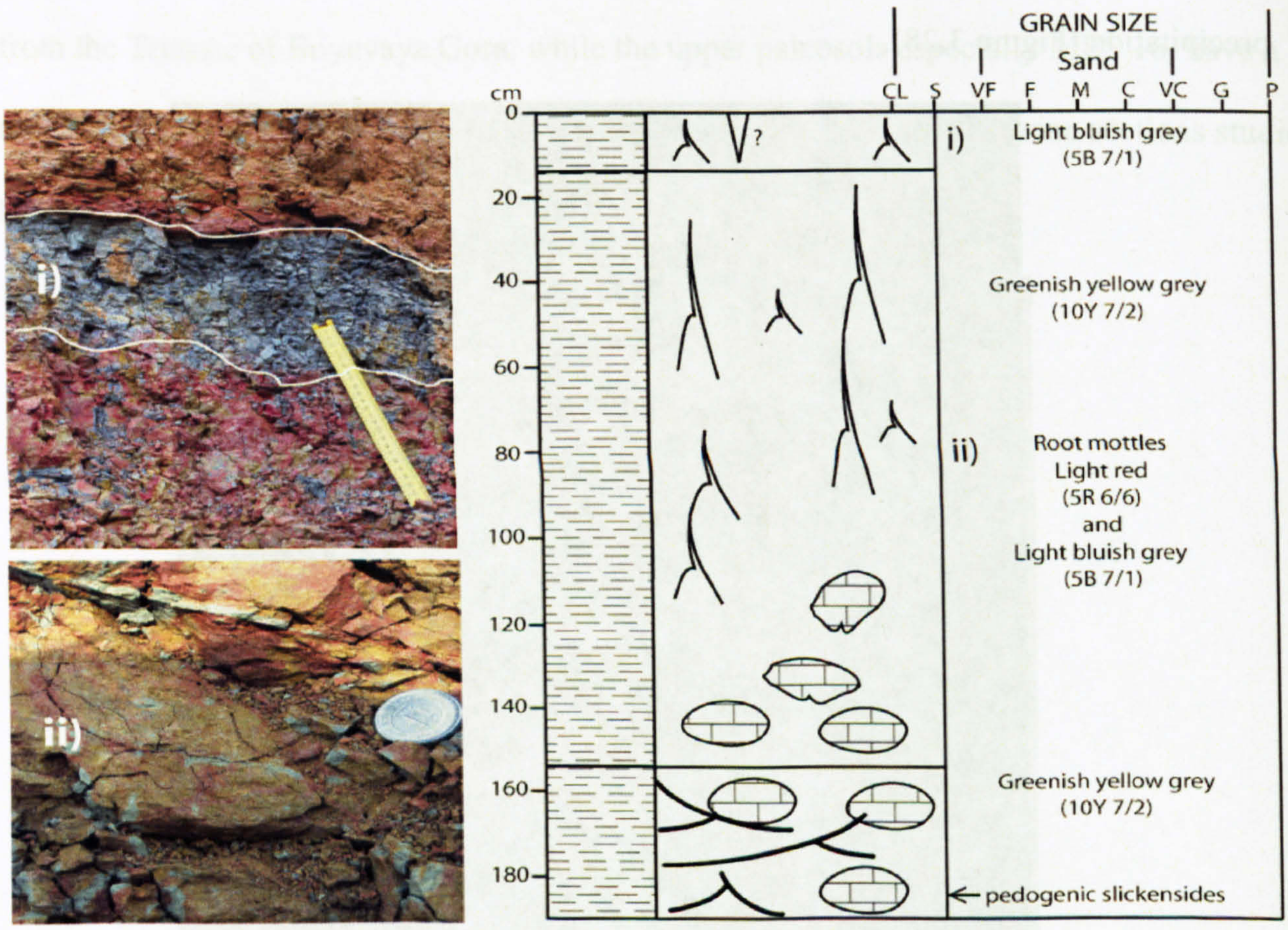

Figure 3.29 Gleyed paleosol at the top of Mescheryakovka (MES16) showing deep rooting structures and extreme gleys. The numerals i) an ii) represent where in the log those photos were taken from (the scale in i) = 25cm and the coin in ii) is 20mm in size).

Such gleys are commonly associated with swamp and fen facies (Retallack 1997). However, the Bk horizons directly below these gleyed horizons, contains evident pedogenic slickensides, which instead implies a periodic wetting and drying of the paleosol (cf. Kovda and Wilding 2004). The calcrete contained within the Bk horizon is of Stage II development

and is not concentrated within layers, nor does it show any other features associated with groundwater calcretes (cf. Khadkikar *et al* 2000; Quast *et al.*2006).

This apparent contradiction of associated gley and slickensides suggests that this is a pseudo-gley as described by Wright and Allen (1989). These form when the paleosols which are periodically, rather than permanently, waterlogged (Wright and Allen 1989). This would explain the juxtaposition of waterlogged features such as the gley, and features related to aridity (the developed Bk horizon and slickensides). It seems plausible that these paleosols formed in an arid environment allowing the formation of the deep root structure, slickensides and carbonate, and then the water table rose, or there was a period of intense rainfall which periodically flooded the paleosol creating anoxic conditions. Similar features have been recorded in the Plio-Pleistocene of Spain (Stokes and Mather 2000). Equally such features may be caused by reduction of iron hydroxides and oxides by anaerobic bacteria consuming organic matter while the paleosol is below the permanent water table (Retallack 2005a). These burial gleys can form in paleosols with no evidence of waterlogging and relate to the diagenetic process rather soil forming processes (Retallack 2005a). The reason for there limited occurrence within the upper paleosols at Mescheryakovka may be an increase in organic matter in these paleosols.

3.4 Discussion

3.4.1 Classification

Classification of paleosols, as described in Chapter 2, can be a controversial process. Based on the simplified identification key of Retallack (1993) used in the field (Chapter 2, Figure 2.1) the paleosols in Russia are classified as either Vertisols based on the presence of

slickensides; Aridisols based on the presence of a Bk horizon which is less than 1metre from the surface; Alfisols for those paleosols with a Bk horizon deeper than 1m or Inceptisols based on the lack of a Bk horizon and the presence of a cambic epipedon.

There are other features seen in the Russian paleosols that can be positively identified as belonging to certain modern soil types and thus can also be used in classification. Several of the carbonate nodules show a ped nucleus, a feature unique to Vertisols, with a primarily spherical morphology, and have sharp boundaries with the surrounding sediment suggesting a pedogenic source (Khadkikar *et al* 2000). Also KOR 4 (Figure 3.9) has features that can be interpreted as being gilgai microtopography which is found in modern Vertisols (Kovda and Wilding 2004, Dr Nathan Sheldon, *pers. comm.*). Several paleosols (SAM 1, 3, KOR 4) have evidence of slickensides (Figure 3.8B) and mud cracks (SAM 10, 20, KOR1,11, 26) which are related to primary shrinking and swelling of the paleosol as it is wetted in the rainy season and subsequently dries out. These factors have been attributed to Vertisols (Khadkikar *et al.* 2000).

Cleveland *et al.* (2008), however, suggest that terms such as Vertisol should not be used as the USDA Soil Taxonomy (Soil Survey Staff, 1999) defines these as containing seasonally opening cracks and although wedge-shaped slickensides (see Figure 3.8B) are interpreted to be seasonally active, this is still an interpretation and cannot be tested. In their classification, Cleveland *et al.* (2008) suggest that paleosols showing these features as defined are being 'Vertic' and the rest of their name is derived from other characteristics (Table 3.1). Although they concede that if these paleosols could have been observed while they were still active soils they would be defined as being a 'Vertisols'. It is possible to use the parameters used by Cleveland *et al.* (2008) to classify many of the paleosols seen in Russia (Table 3.1) and to

build on the system they use to classify paleosols seen in Russia that are not seen in New Mexico. For instance KOR 4 (Figure 3.9) could be classified as being a 'Vertic Petrocalcid' based on having both Vertisol features and a petrocalcitic horizon. A petrocalcitic horizon is a subsurface soil horizon cemented firmly with calcium carbonate (Soil Survey Staff, 1999) and thus is synonymous to a Bk horizon of stage IV and greater levels of development (see Chapter 2). Equally SAM 6 (Figure 3.14) would be defined as being a Ustic Haplocambid as it has a light-coloured, but non-calcified surface horizon (ochric epipedon) and darker sub-horizon with minor mottles (cambic horizon) (Soil Survey Staff, 1999)(Figure 3.14). This paleosol also lacked any evidence of a Bk horizon and contained evidence of fine (<2mm) root traces.

Soil order	Suborder	Classification	Diagnostic features	Russian soils showing similar features
Aridisols	Calcids	Ustic Haplocalcids	1) Calcic horizon with upper boundary within 100cm of soil surface 2) Do not have a petrocalcitic horizon within 150cm depth of the mineral soil surface 3) do not have intersecting pedogenic slickensides	e.g. KOR36, KOR2, KOR6, KOR15,
		Vertic Haplocalcids	1) Large 25cm thick layer of intersecting slickensides within 100cm of the mineral soil surface 2) have 30% of clay in all fine earth fraction 3) Calcic horizon with upper boundary within 100cm of soil surface	e.g. KOR 5, SAM1.
		Ustic Petrocalcids	1) have a calsic or petrocalcitic horizon within 100cm of soil surface 2) have petrocalcitic horizon within 150cm of base of section 3) do not have intersecting pedogenic slickensides	e.g. TUY47 TUY 2
	Cambids	Ustic Haplocambids	1)Have a subsurface cambic horizon within 100 cm of the mineral soil surface or its lower boundary at a depth of 25 cm 2) do not have a calcic or petrocalcic horizon unless its upper boundary is more than 100 cm below the mineral soil surface 3) do not have intersecting pedogenic slickensides	e.g. SAM6

Table 3.1 Classification used by Cleveland *et al.* (2008) in the Late Triassic of New Mexico being a simplification of the USDA Soil Taxonomy system (Soil Survey Staff, 1999). Also a list of Russian examples which show the features used by Cleveland *et al.* (2008).

However, the USDA Soil Taxonomy system (Soil Survey Staff, 1999) used by Cleveland *et al.* (2008) cannot be used to distinguish non lacustrine or groundwater paleosols from those with identifiable lacustrine and groundwater influenced paleosols such as those seen in some

of the Russian sections. This is because all these paleosols in Russia have a Bk horizon with a depth less than 1m and thus would be classified as Aridisols (after Retallack 1993) or Ustic Haplocalcids (after Cleveland *et al.* 2008). Differentiating of paleosols formed, or influenced by, lacustrine or groundwater processes is important when studying the geochemistry of carbonate material formed in these paleosols. This is because the isotopic composition in such paleosols is controlled by fractionated ground and lacustrine waters rather than meteoric waters (Cerling and Quade 1993; Alonso-Zarza 2003).

These paleosols can be identified in the field by being both rooted and having features that relate to a palustrine setting such as thin limestone beds containing ostracod fossils (KOR 17 and 25) and laminated limestone lenses (SAM 2) (see, Figure 3.7 and Figure 3.8). Equally paleosols dominated by groundwater processes can be identified by having nodules with diffuse boundaries that forming distinct bands (PET 1 and PET 2, Figure 3.6F), (Wright and Allen 1989; Khadkikar *et al.* 2000). Thus, new terms must be used to differentiate these paleosols.

Cleveland *et al.* (2008) suggests the presence of intense gleyed colours could be used to indicate waterlogging but some of the lacustrine associated paleosols (e.g. SAM2, Figure 3.13) have no evidence of gleyed colours.

Classification after Retallack [a]	Classification using USDA horizons [b]	Diagnostic features	Examples
Inceptisols	Ustic Haplocambids	1) Have some relict structures [a] 2) Does not have intersecting pedogenic slickensides [a+b] 3) Do not have a calcic or petrocalcic horizon [a+b] 4) Have a subsurface cambic horizon within 100 cm of the mineral soil surface or its lower boundary at a depth of 25 cm [b]	e.g. SAM6
Vertisols	Vertic Haplocalcids	1) Have no relict structures [a] 2) Large 25cm thick layer of intersecting slickensides within 100cm of the mineral soil surface [a+b] 3) Has have a calcic or petrocalcic horizon [a+b] 4) Calcic horizon with upper boundary within 100cm of soil surface [b] 5) have 30% of clay in all fine earth fraction	e.g. KOR5, SAM1
Vertisols	Vertic Petrocalcids	1) Have no relic structures [a] 2) Large 25cm thick layer of intersecting slickensides within 100cm of the mineral soil surface [a+b] 3) Have a calcic or petrocalcic horizon [a] 4) Calcic horizon with upper boundary within 100cm of soil surface [b] 5) have petrocalcic horizon within 150cm of base of section [b]	e.g. KOR4
Aridisols	Ustic Petrocalcids	1) Have no relict structures [a] 2) Does not have intersecting pedogenic slickensides within 100cm of the mineral soil surface or other shrink swelling structures [a+b] 3) Have a calcic or petrocalcic horizon [a] 3) Have a calsic or petrocalcic horizon within 100cm of soil surface [b] 4) Have petrocalcic horizon within 150cm of base of section [b]	e.g. TUY47 TUY2
Aridisols	Petronodic Haplocalcids	1) Have no relict structures [a] 2) Does not have intersecting pedogenic slickensides within 100cm of the mineral soil surface or other shrink swelling structures [a+b] 3) Have a calcic or petrocalcic horizon [a] 4) Calcic horizon with upper boundary within 100cm of soil surface [b] 5) Do not have a petrocalcic horizon within 150cm depth of the mineral soil surface [b] 6) One or more horizons, within 100 cm of the soil surface and with a combined thickness of 15 cm or more, that contain 20 percent or more (by volume) nodules or concretions [b]	e.g. KOR36, KOR2, KOR6, KOR15,
Aridisols/Alfisols	Ustic Calcids (Lacustrine)	1) Have no relict structures [a] 2) Does not have intersecting pedogenic slickensides within 100cm of the mineral soil surface or other shrink swelling structures [a+b] 3) Have a calcic or petrocalcic horizon [a] 4) Calcic horizon with upper boundary within 100cm of soil surface [b] 5) Have petrocalcic horizon within 150cm of base of section [b] 6) Is associated with lacustrine limestone; contains ostracods or forms in channel fills [c]	e.g. KOR17, SAM2,
Aridisols	Ustic Calcids (Groundwater)	1) Have no relict structures [a] 2) Does not have intersecting pedogenic slickensides within 100cm of the mineral soil surface or other shrink swelling structures [a+b] 3) Have a calcic or petrocalcic horizon [a] 4) Calcic horizon with upper boundary within 100cm of soil surface [b] 5) Have petrocalcic horizon within 150cm of base of section [b] 4) Carbonates which has diffuse boundaries and forms distinct lines [c]	e.g. PET 1, PET 2

Table 3.2 Paleosol classification used in this study and the equivalent classifications based on the Retallack (1993) classification and Soil Staff Survey (1999).The diagnostic features are primarily based on the definitions in the USDA Soil Taxonomy system classifications but with additions to differentiate groundwater and lacustrine related paleosols. The bracketed terms refer terms not used in the USDA classification or where the one of the classification terms is inferred.

[a] After a literal interpretation of Figure 2.1 (Chapter 2) from Retallack (1993, 1997, 2001) [b]After Soil Staff Survey (1999) Cleveland *et al.* (2008). [c] criteria used to differentiate between lacustrine and groundwater carbonates (see text).

Therefore in an attempt to encapsulate all this detail an abridged version of USDA Soil Taxonomy system as adapted by Cleveland *et al.* (2008) was used. For those paleosol types which are not adequately described by this method, as discussed above, modifiers were used. Lacustrine and groundwater derived carbonates have been divided for the reasons given above and are identified by placing "(lacustrine)" or "(groundwater)" after the USDA taxonomic name.

Finally it is possible that some of these paleosols may represent soil types which no longer have any direct modern analogue. For instance modern Mollisols are classified primarily on the presence of a mollic epipedon, which is a dark (organic-rich), well-structured surface horizon (Soil Survey Staff 1999; 2006; Retallack 2001a). This is directly related to an extensive and dense root network of grasses (Retallack 2001a). However, grasslands did not evolve until the middle Tertiary and it has been suggested that previously forests may have graded out into scrub and then to true desert vegetation (Retallack 2001a). Some of the palcosols (e.g. KOR6) in the Russian sections have features similar to those seen in Mollisols; for instance many of the lack any shrink–swell structures which would classify them as Vertisols and evidence of water saturation within 100cm of the palaeosurface (cf. Soil Survey Staff 1999). Therefore it may be possible that some of the paleosols represent a soil type that has become 'extinct' which, in the modern world, have been replaced by Mollisols.

3.4.2 Palaeoenvironmental interpretation

Palcosols are an extremely valuable tool for understanding palaeoenvironmental conditions. Using the environmental classification of Retallack (1994), the presence of such features as relatively abundant rooting traces of between 2-6mm wide, some of which are deeply penetrating, and a developed Bk horizon, would indicate that most of these Russian paleosols

formed in a brakeland, wooded grassland or desert shrubland environment. The extremely well developed Bk horizons in many Permian paleosols, some of which are shallow (e.g. KOR4) may point to desert shrubland as being the best modern analogue (cf. Retallack 1994). The Triassic paleosols, especially those of the Olenekian (Petropavlovka and Mescheryakovka) may represent dry woodlands, based on the presence of deeply penetrating roots and deep Bk horizons (cf. Retallack 1994) although this assumes modern environmental analogues are valid when applied to the Permian–Triassic periods.

The palaeoenvironment inferred from the paleosols agrees with previous interpretations which have concluded that in the Late Tatarian (Kulchumovskaya Gorizont) the palaeoenvironment of the South Urals shifted from lacustrine to meandering rivers. The over-bank deposits of this time are thought to have been dry, semi-arid steppe-land which was not flooded for thousands of years (Newell *et al.* 1999; Tverdokhlebov *et al.* 2005). A low-shrub Tatarian flora was thought to have made up the ground cover, which in some areas was dominated by herbaceous lycopods and horsetails and in others by conifers and gymnosperm flora (Tverdokhlebov *et al.* 2005; Dr. M. Stephenson, *pers. comm.*).

Section	Level of Calcrete development						Average depth to Bk horizon (cm)
	None	II	III	IV	V	VI	
Boyevaya Gora	_	20	9	9	2	_	22
Krasnogor	_	11	3	1	_	_	24
Sambullak	1	22	6	2	-		37
Tuyembetka	-	20	13	17	14	1	38
Vozdvizhenka	_	14	3	_	_	_	45
Mescheryakovka .	_	13	3	1	_	_	51
Petropavlovka	_	2	_	_	_	_	37

Table 3.3 Summary of the numbers of different levels of Bk development in the South Urals, Russia. See Appendix 1 for more detailed descriptions.

The variation in type and features of paleosols between sections gives a more detailed insight into the differences in palaeogeography across the basin in the Permian. As the level of calcrete development can be used as a proxy for time (Retallack 1994; Retallack 2001a), sections containing more mature paleosols were further away from areas of active channel development. At Sambullak and Krasnagor there are considerably fewer mature paleosols (greater than stage II development) than at Tuyembetka (Table 3.3) despite their relative geographical closeness (Figure 3.2). This suggests that Sambullak and Krasnogor were closer to the active river system, while Tuyembetka represents a part of the basin further away from the rivers, possibly on a palaeohigh. As such it was only affected by the most dramatic flood events and was drier, with time to form more mature calcrete profiles.

The uppermost Lower Triassic (Petropavlovskaya) is thought to be more arid than the Permian in the South Urals (Tverdokhlebov *et al.* 2002). This is confirmed by the evidence from Petropavlovka as the only carbonate material found formed by groundwater, rather than meteoric, based on the irregular nature of the nodules (Khadkikar *et al* 2000; Quast *et al.* 2006 see Figure 3.6F). The presence of only groundwater-related carbonate at this section may suggest a depressed water table, indicating more arid conditions (cf. Alonso-Zarza 2003). Mescheryakovka also shows evidence of deep rooting, slickensides, and carbonate related to arid environments (cf. Wright and Allen 1989;, Figure 3.29). However, Mescheryakovka also record the deepest average depth to Bk horizon when compared to the Permian sections (Table 3.3) suggesting this section was wetter (cf. Retallack *et al.* 2003). One solution is that there was an increase in seasonality and intensity of rainfall rather than a wetter climate (cf. Wright and Allen 1989).

3.4.3 Changes across the P/Tr boundary

The section at Boyevaya Gora has paleosols spanning the P/Tr boundary and records a distinct change in paleosol morphology between the last paleosols of the Permian and the first paleosols of the Triassic. Some of these changes are similar to changes reported from paleosols in both Antarctica and Karoo across the P/Tr boundary. The most striking similarity is the colour shift from a brick-red (10R) to a browner hue in the Triassic, seen in both Karoo (2.5.YR) (Retallack *et al.* 2003) and Russia (5GY) (Figure 3.30). Also, as in Antarctica and Texas (Retallack and Krull 1999; Krull and Retallack 2000; 2005c), the first paleosols of the Triassic are poorly developed and linked to an increase in coarse-grade sediments.

The Russian Late Permian paleosols have dispersed carbonate nodules, which in Karoo have been linked to the influence of monsoonal activity (Retallack *et al.* 2003; Retallack 2005b). However, unlike Karoo, the earliest Triassic carbonate nodules in Russia do not form deeper, well-focused zones; instead they become smaller and more ephemeral (Figure 3.30). This may suggest that, unlike Karoo, the Russia paleosols show an increase in rainfall earliest Triassic which causes a deepening of the Bk horizon (cf. Retallack 1994). The Triassic paleosols at Boyevaya Gora were, however, undoubtedly wetter than those of the Permian as roots are only poorly preserved as minor drab root haloes (Figure 3.11A) rather than as reddened clay in fills. This may be due to the Triassic paleosols being formed when the basin was more active and dominated by braided river channels increasing the amount of water present in the basin. This is supported by the fact that many of the Triassic paleosols are overlain by strongly gleyed sandstone beds (Figure 3.11 B), indicating flooding and waterlogging of the paleosols below.

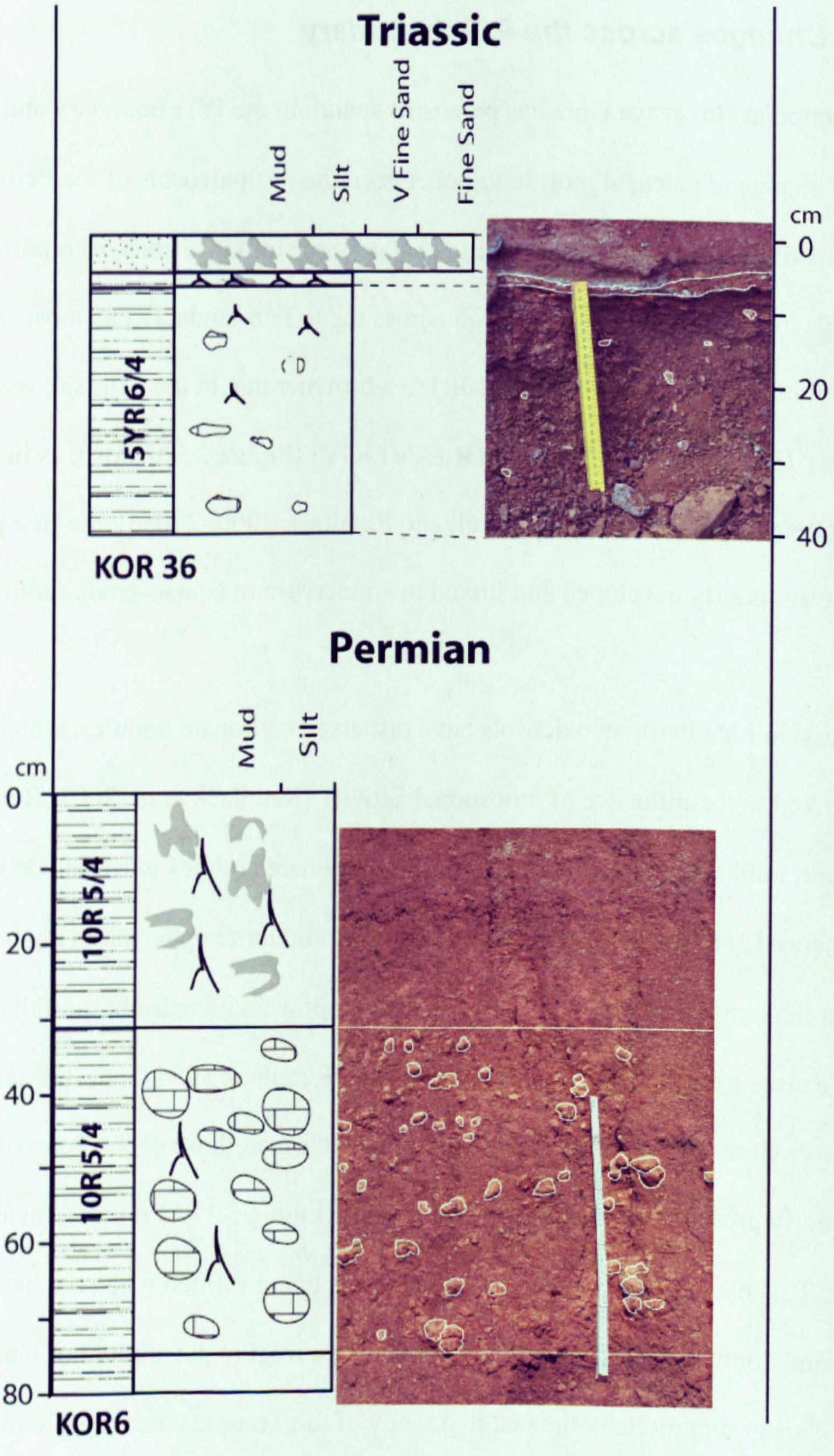

Figure 3.30 Typical Stage II paleosols from the Permian and Triassic of Boyevaya Gora. Note the change in colour and thickness between the paleosols.

In the interval just prior to the P/Tr boundary there is the appearance of pedogenic slickensides suggesting Vertisol forming conditions at Sambullak, Boyevaya Gora and

Krasnagor (see Figure 3.4, Figure 3.12, Figure 3.23). At Boyevaya Gora paleosols with Vertic features first appear ~210m before the boundary (Figure 3.4), while in the others these features first occurs 1-5metres before the P/Tr boundary. Vertisols are often interpreted as being associated with sub-humid climates (Khadkikar *et al.* 2000), although equally they may just suggest an increase in seasonality preceding the P/Tr boundary as the presence of pedogenic slickensides indicate repeated wetting and drying of the paleosol (Soil Staff Survey 1999; Khadkikar *et al.* 2000).

3.5 Summary

Overall the paleosol evidence from Russia suggests that the Permian represented a desert scrubland environment. In the Triassic this dry environment continued but the presence of possible depressed water suggest an increase in amount of waterlogging of the paleosols:

1. Similar to what is observed in Antarctica and the Karoo basin, there is a distinct change in paleosols across the P/Tr boundary itself from more stable, better-developed, paleosols to less-developed, less stable paleosols in the earliest Triassic. This change is related to a change in facies, from meandering fluvial systems to coarse conglomeratic fans;

2. Unlike the paleosols at Karoo, the earliest Triassic in Russia paleosols do not show a deep calcic horizon (although they are present at the top of the Early Triassic at Mescheryakovka) suggesting that the climate there was not an increase in rainfall just after the P/Tr boundary, as in Karoo;

3. Also in Russia Vertisols increase in the Latest Permian, suggesting that the palaeoclimate may have already started to change in the Southern Urals before the P/Tr boundary.

Chapter 4. Isotopic and mineralogical variation in paleosols from the Southern Urals

4.1 Introduction

There have been many studies that have used the stable isotopic composition of pedogenic carbonate from throughout the Phanerozoic to investigate changes in atmospheric CO_2, temperature and atmospheric chemistry (Cerling 1991; Mora *et al* 1991; Liu *et al.* 1996; Cerling and Quade 1993; Ekart *et al* 1999; Ghosh *et al.* 2001; Robinson *et al.* 2002; Dworkin *et al.* 2005; Prochnow *et al.* 2006; Quast *et al.* 2006; Tarbor *et al.* 2007). This is because pedogenic carbonate is formed in equilibrium with meteoric water at atmospheric temperatures and pCO_2 values, and thus is directly affected by changes in atmospheric chemistry (Cerling 1991; Mora *et al* 1991; Cerling and Quade 1993; Ekart *et al* 1999). However, all the authors listed above stress that efforts have to be made to discern between those isotopic values that reflect the primary pedogenic carbonate, and those that reflect later alteration, be it by groundwater fluids, diagenesis or even telogenesis, all of which can overprint the primary pedogenic values.

From the seven sections studied in the field (Chapter 3), the sections at Boyevaya Gora and Sambullak were chosen for rigorous isotopic study with the aim of recovering a palaeoclimatic signal. Preliminary investigation was carried out at Tuyembetka Krasnogor and Mescheryakovka. Boyevaya Gora and Sambullak were chosen for rigorous isotopic study because (1) they both represent the most extensive sections that either cross or come up to the P/Tr boundary, (2) the paleosols present did not exhibit strong groundwater morphologies, such as at Vozdvizhenka and Petropavlovka (see Chapter 3), and (3) they contain the highest proportion of stage II carbonate nodules, which have been identified as having the highest

potential to preserve palaeoclimatic data (Ekart *et al.* 1999; Alonso-Zarza 2003, Dworkin *et al.* 2005). In addition, preliminary assessments were made of paleosols at Tuyembetka to assess isotopic variation in drier sedimentary settings in the Permian, and at Krasnogor to look at variation across the basin. Also paleosols from Mescheryakovka to were analysed to gain insights into isotopic variation in the Olenekian.

4.2 Isotope results

At Boyevaya Gora micritic carbonate was analysed from a total of 37 paleosols (see Chapter 2), of which 33 were horizons from the Permian and 5 from the earliest Triassic (see Appendix A2.1). In addition; 47 paleosols from Sambullak, 19 at Tuyembetka and 8 at Krasnogor were analysed of which all were Permian. Figure 4.1(and Appendix A2.1) shows the unscreened isotopic results for the micritic carbonate analysed from the Permian sections. Also 8 paleosols from the Triassic section at Mescheryakovka were analysed (see Figure 4.2 and Appendix A2.1).

There are four excursion events identified in the isotopic results in the Permian (P1, P2, P3, P4,) and two in the Triassic (Tr1, Tr2) (Figure 4.1). P1, P2, P3 and Tr2 all occur in both the $\delta^{13}C_{carb}$ and $\delta^{18}O_{carb}$ values while P4 and Tr1 are only recorded in the $\delta^{18}O_{carb}$ values. P1 is only recorded at Boyevaya Gora, and represents an excursion of –9‰ in $\delta^{13}C_{carb}$ values and –4‰ in $\delta^{18}O_{carb}$ values. This excursion is constrained to the values within one paleosol (KOR35) (Appendix A2.1). P2 is also only recorded at Boyevaya Gora. The $\delta^{13}C_{carb}$ record has an excursion of –9‰ in a single paleosol horizon (KOR25) (Appendix A2.1) like P1. The $\delta^{18}O_{carb}$ shows the excursion starting slightly earlier in the three paleosols below (KOR26, KOR27 and KOR24; Appendix A2.1) and records an excursion of –8.00‰.

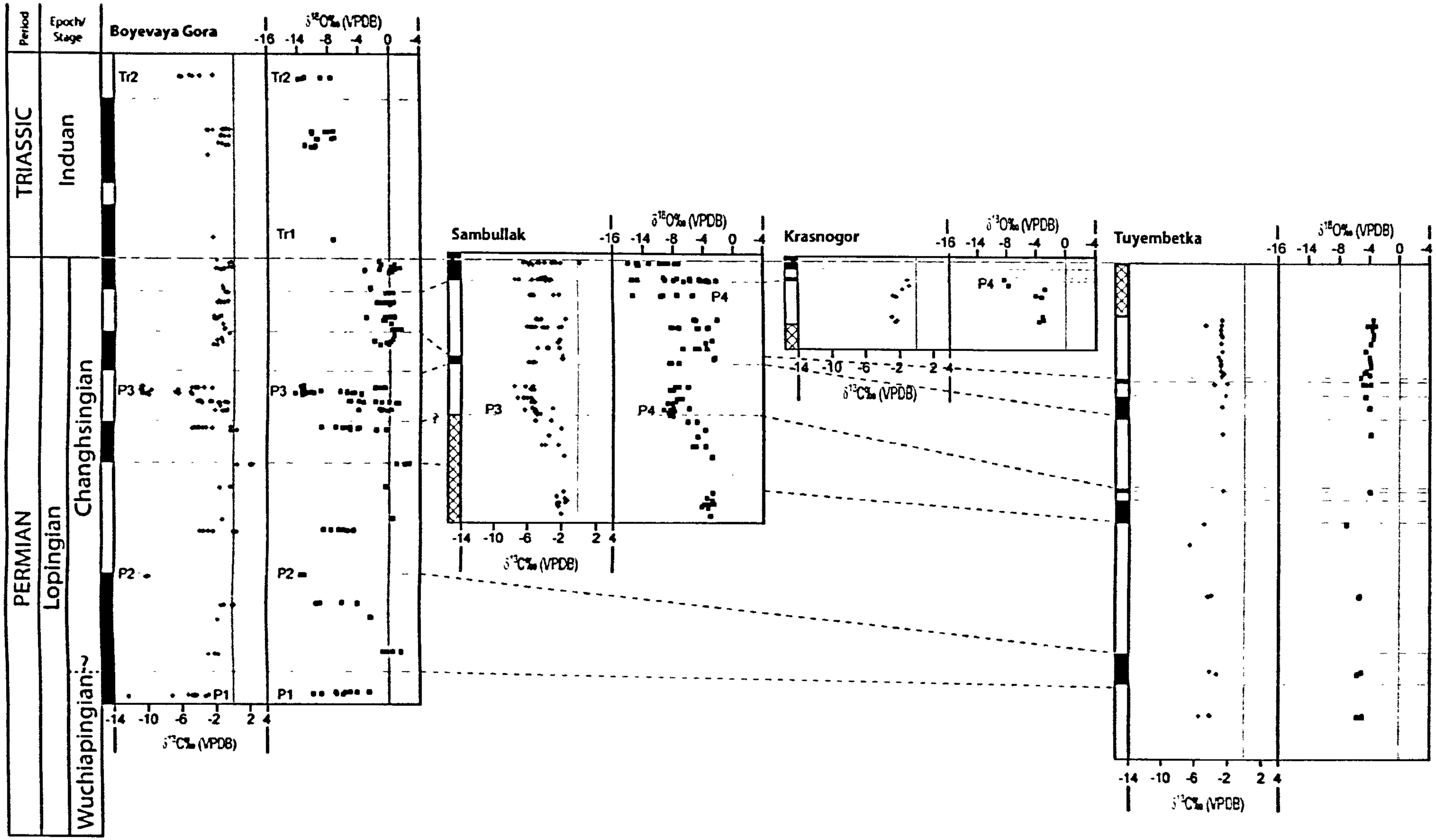

Figure 4.1 Micritic carbonate values from the Late Permian and earliest Triassic sections from the Southern Urals of Russia correlated using magnetostratigraphic data (Taylor *et al.* 2009 see Chapter 3 for stratigraphic information). Sections arranged west to east. See Appendix A2.1 for raw data.

P3 is recorded in both $\delta^{13}C_{carb}$ and $\delta^{18}O_{carb}$ values and is present at Boyevaya Gora and, to a lesser extent at Sambullak. At Boyevaya Gora it is constrained by 2 paleosols (KOR22, KOR23, see Appendix A2.1) with values as low as $\delta^{13}C_{carb}$ –11.06‰ and $\delta^{18}O_{carb}$ –11.30‰. The paleosol that contains these negative values (KOR22) also contains nodules which have isotopic values as positive as $\delta^{13}C_{carb}$ –4.90‰ and $\delta^{18}O_{carb}$ –4.91‰ (Figure 4.1, Appendix A2.1). At Sambullak the excursion is less pronounced in terms of magnitude and is spread over 10 paleosols (SAM17, SAM13, SAM14, SAM21, SAM22, SAM23, SAM24a, SAM24b, SAM24c, SAM24d, SAM24e, 04.7.24.a; Appendix A2.1). The excursion is as negative as $\delta^{13}C_{carb}$ –7.39‰ and $\delta^{18}O_{carb}$ –9.49‰ and while the $\delta^{13}C_{carb}$ values become more positive after the event the $\delta^{18}O_{carb}$ values stay negative.

P4 is only recorded at Sambullak and Krasnogor and is only observed in the $\delta^{18}O_{carb}$ values (Figure 4.1). At Sambullak it is recorded in 4 horizons (SAM12, SAM2, SAM3, SAM4, SAM1; Appendix A2.1) up to the P/Tr boundary. Like P3 at Boyevaya Gora the excursion manifests itself as an increase in the range of isotopic values rather than a shift in the mean. $\delta^{18}O_{carb}$ values range from –14.15‰ (SAM1) to as positive as –7.50‰ in the same paleosol (see Appendix A2.1). At Krasnogor P4 is only observed in two paleosols (KRA 2 and KRA1; Appendix A2.1) and the lowest $\delta^{18}O_{carb}$ values are –8.37‰ (KRA 2) which youngest Permian soil.

Only Boyevaya Gora has paleosols in the Induan (Figure 4.1) and while $\delta^{13}C_{carb}$ values (–0.10‰ to –4.90‰ see Appendix A2.1) are similar to those in the Permian (Figure 1) the $\delta^{18}O_{carb}$ values become more negative (Tr1; Figure 4.1) and become as negative –11.44‰

(KOR36). The negative value in KOR36, at the very top of the section, is also matched by a –2‰ excursion in $\delta^{13}C_{carb}$ values (Tr2).

The section at Mescheryakovka is the only analysed section in the Olenekian. There are no obvious trends in the section in either $\delta^{13}C_{carb}$ or $\delta^{18}O_{carb}$ (Figure 4.2), although this may be due to the fact that only 8 paleosols from this section were analysed (Appendix A2.1). Compared with the Permian and Early Triassic values (Figure 4.1) the isotope values have a more negative range in values, with a range for −6.42‰ to −10.62‰ and −1.53‰ to −17.66‰ for $\delta^{13}C_{carb}$ and $\delta^{18}O_{carb}$ respectively. These are the most negative micritic $\delta^{18}O_{carb}$ values of any section studied in Russia.

Before any detailed interpretation of the isotopic results can be carried out it is imperative to determine how much of the variation within the stable isotope signal is a result of later alteration and how much is related to the vadose pedogenic carbonate formed from meteoric water. Sources of alteration to the vadose pedogenic isotopic signature fall into three broad categories: (1) the effects of evaporation on the isotopic signal, (2) interactions with the phreatic groundwater table and surrounding rock, and (3) alterations caused during diagenesis. To assess the extent to which such factors may have affected the isotope signal a combination of petrographic, isotopic, X-ray diffraction (XRD) and scanning electron microscope techniques was used.

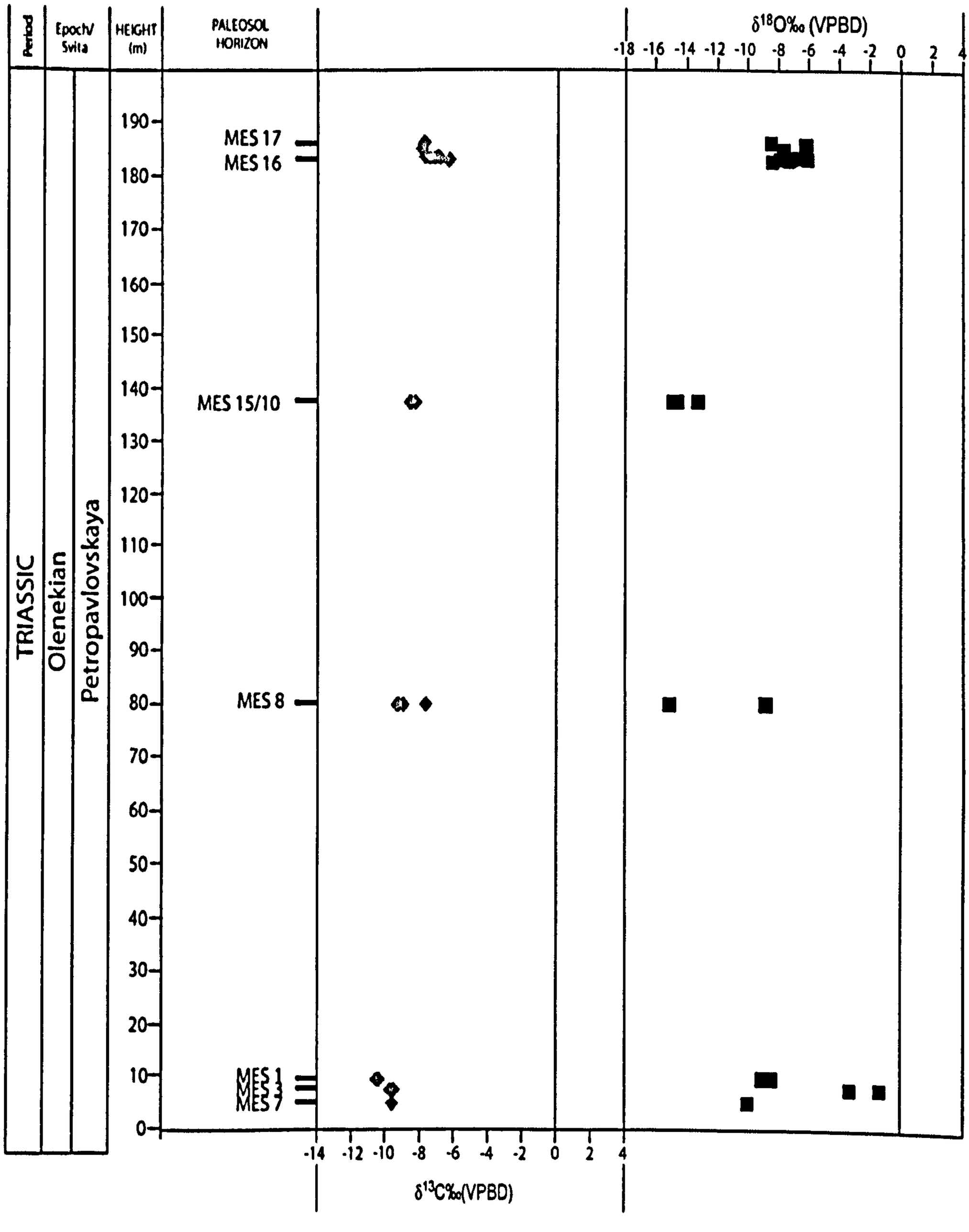

Figure 4.2 Micritic carbonate values from Mescheryakovka in the Olenekian (see Chapter 3 for stratigraphic information). See Appendix A2.1 for unscreened data.

4.3 Diagenesis and alteration of the isotope signal

Climate is only one of several factors that can affect the chemical characteristics of pedogenic calcretes. Other factors include the composition and texture of the parent material, landscape position, vegetation, latitudinal location, and the duration of soil development (Mack and

James 1994). All of these factors, especially the maturity of a soil and local influence of groundwater, have the effect of fractionating the isotopic signal such that the carbonate no longer represents equilibrium with vadose meteoric water (Quast *et al.* 2006). It has also been noted that many paleosol calcretes from the Palaeozoic have been altered both physically and geochemically by diagenesis (Quast *et al.* 2006). This problem has been encountered in other paleosol studies across the P/Tr boundary (e.g. Macleod *et al.* 2000) and therefore it is important to quantify the role of diagenesis in influencing the isotopic signal observed in the Russian paleosols.

4.3.1 Stage of calcrete development

Once a calcrete forms a solid layer its relative permeability decreases, this attenuated infiltration of meteoric water enhances the effect of evaporation (Liu *et al.* 1996; Ekart *et al.* 1999). As a result once the Bk horizon has become more mature than stage II the nodules are likely to become isotopically less negative as the light isotopes are selectively evaporated (Ekart *et al.* 1999). Equally any carbonate associated with palustrine or groundwater paleosols may be more likely to reflect the local evolved groundwater, or local lacustrine bodies which also have different isotopic compositions due to enhanced evaporation (Wright and Tucker 1991) and the effects of the breakdown of organic matter (Tabor *et al.* 2007).

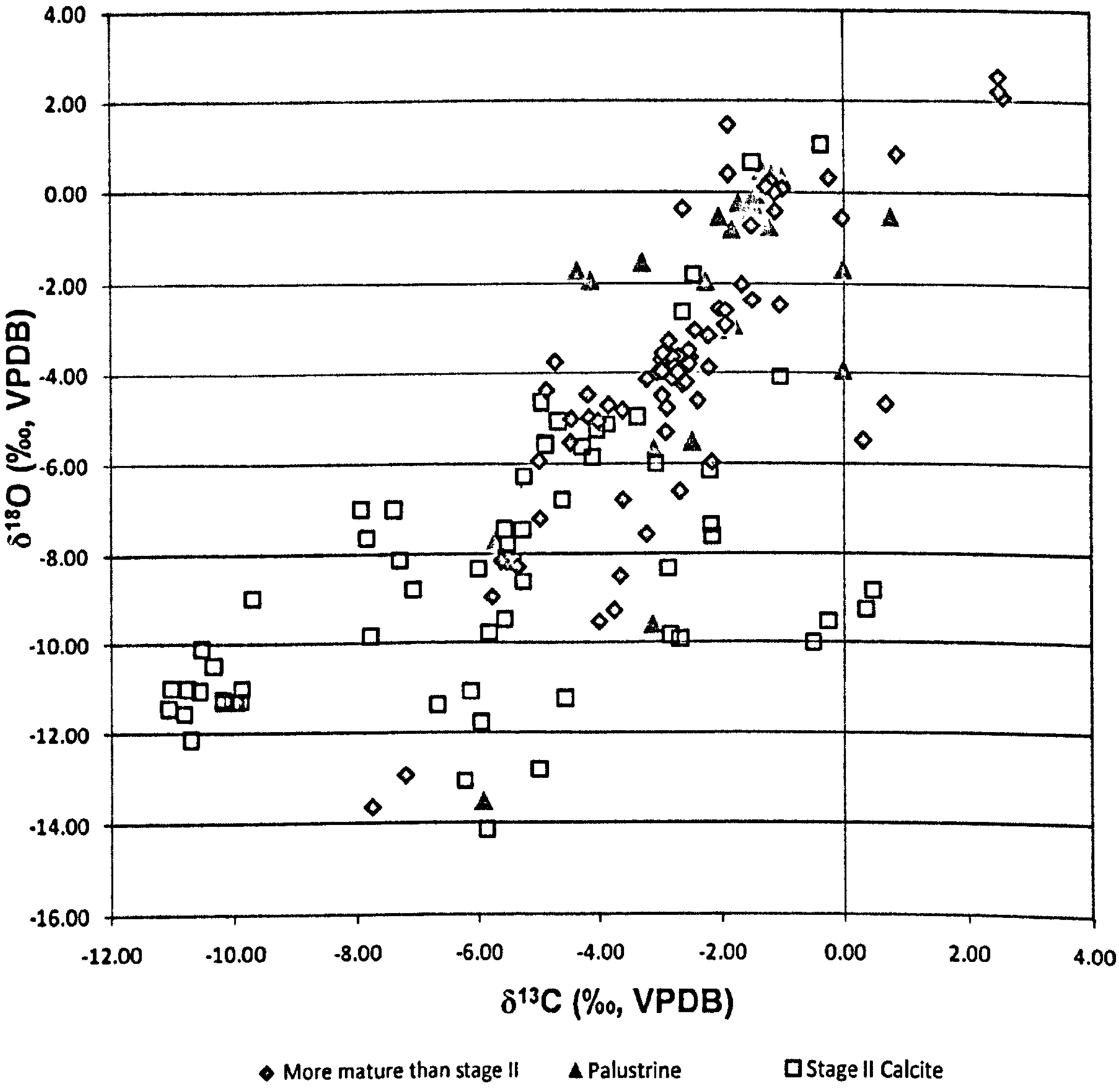

Figure 4.3 Cross plot of those micritic carbonate values from palustrine and mature micrite compared against micritic pedogenic values from stage II and I calcretes (see Table 1 and Appendix A2.1).

When the more mature calcretes are compared to the stage II nodules it is possible to see that the more mature calcretes are shifted towards the more positive end of the range of the values from the Stage II nodules (Figure 4.3) suggesting some influence of evaporation. However, the significant overlap suggests that evaporation may have only partially overprinted the more mature calcretes and the palustrine calcretes are also only partially affected by fractionated lacustrine waters. This is also true of the isotopic results from calcretes associated with palustrine paleosols (see Chapter 3). There is a positive covariance between $\delta^{13}C$ and $\delta^{18}O$ values. This has been observed in vadose pedogenic carbonates by other authors (Cerling 1991; Ghosh *et al.* 2001; Quast *et al.* 2001; Robinson *et al.* 2002) as well as in modern systems (Alonso-Zarza 2003).

4.3.2 Macromorphology

Pedogenic nodules

Throughout all the sections in Russia the micromorphologies of the pedogenic stage II nodules are remarkably similar. Those that are not associated with groundwater-influenced paleosols (see Chapter 3) all have a rounded to subrounded morphology and have sharp boundaries with the surrounding matrix suggesting a pedogenic origin (Wright and Tucker 1991; Alonso-Zarza 2003; Khadkikar *et al.* 2000). Many appear to have formed around a core of less consolidated soil matter (Figure 4.4A) which is a typical feature of pedogenic Vertisol nodules where a ped is used as a centre for nucleation (Khadkikar *et al* 2000). Nodules are primarily only cemented by cryptocrystalline carbonate and are very powdery, suggesting that they have not undergone much compaction or diagenesis since they formed (Figure 4.4B).

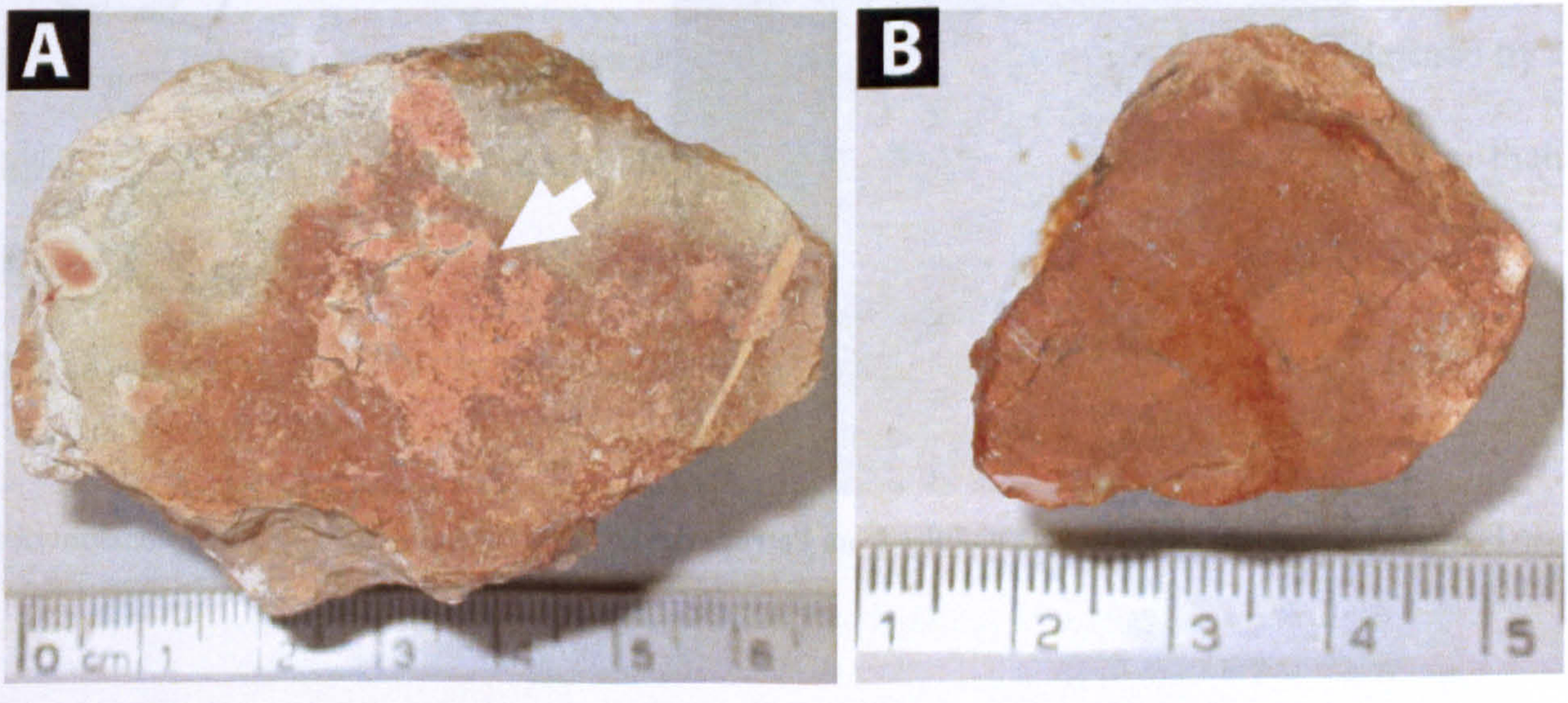

Figure 4.4 Internal macromorphology of pedogenic nodules. A) Appears to have formed around a core which has subsequently become compacted. B) Shows the typical poorly cemented nature of the majority of the nodules found in Russia. Scale in centimetres.

Groundwater nodules

Those carbonate nodules associated purely groundwater are easily distinguished from those formed from meteoric waters. The groundwater carbonates all show diffuse margins with the

surrounding sediment, rather than the smooth (Figure 4.5), sharp contacts of in pedogenic nodules (Khadkikar *et al*. 2000, Alonso-Zarza 2003). Both of these morphologies have been observed at Petropavlovka (Chapter 3), and include features such as nodules 1-4cm in width aligned in a continuous sheet that are indicative of vadose groundwater-formed calcretes (Khadkikar *et al*. 2000). These nodules are thought to record the groundwater isotopic values which may be highly fractionated from the atmospheric values caused by lack of recharge from the atmospheric system (Alonso-Zarza 2003) and thus must be discounted from any palaeoclimate analysis. Nodules with similar morphologies have been identified at Boyevaya Gora (i.e. KOR33, see Appendix A1.1)

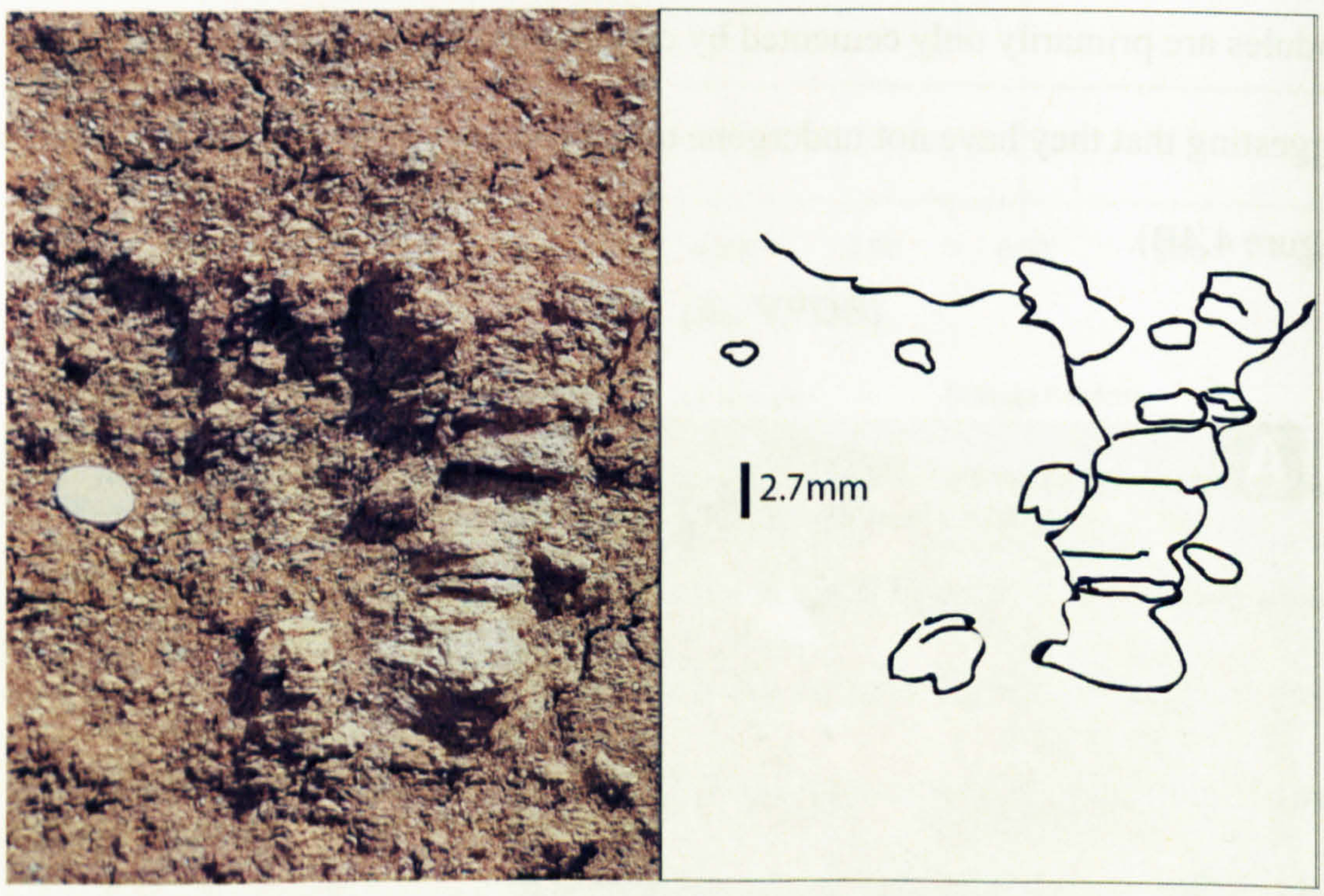

Figure 4.5 Groundwater carbonate nodules from Petropavlovka. Note the indistinct edges and non-spherical nature.

4.3.3 Micromorphology

One of the simplest ways to determine if the carbonate material has been altered by later recrystallisation and diagenesis is by petrographic screening of samples. Dworkin *et al.* (2005) suggest that the textures that are useful for indicating un-recrystallised pedogenic carbonates are: 1) anhedral grains of calcite in the micrite to microspar grain size, 2) crystic –

plasmic fabric (primarily fibrous and circumgranular textures), and 3) rhombic calcite crystals.

The nodular calcretes from Russia principally show features associated with primary pedogenic formation. 70% of the nodules are made of muddy crypto- to microcrystalline masses (the microcrystalline crystals being between 5 and16μm). Many nodules show a characteristic clotted texture of cryptocrystalline concretions surrounded by a coarser microcrystalline matrix (Figure 4.6A). This texture is commonly associated with vadose environments where nodules grow and coalesce (Wright and Tucker 1991; Quast *et al.* 2006). There are dark areas of mottled clays and iron oxides that are often found in the slides and these mask the optical properties of the calcite. There is also evidence for floating grains of very fine quartz which are not in contact with any other surrounding quartz grains (Figure 4.6 B). These represent clastic grains that have been displaced by the growth of carbonate and are also associated with the vadose zone carbonate formation (Khadkikar *et al.* 2000; Quast *et al.* 2006). All of the pedogenic carbonates show alpha calcrete micromophology as defined by Wright and Tucker (1991), and so are likely to be formed to pedogenic processes rather than biological processes. Similar micromorphologies have been seen in modern pedogenic nodules from grassland soils in the Kursk region of Russia (cf. Mikhailova *et al.* 2006).

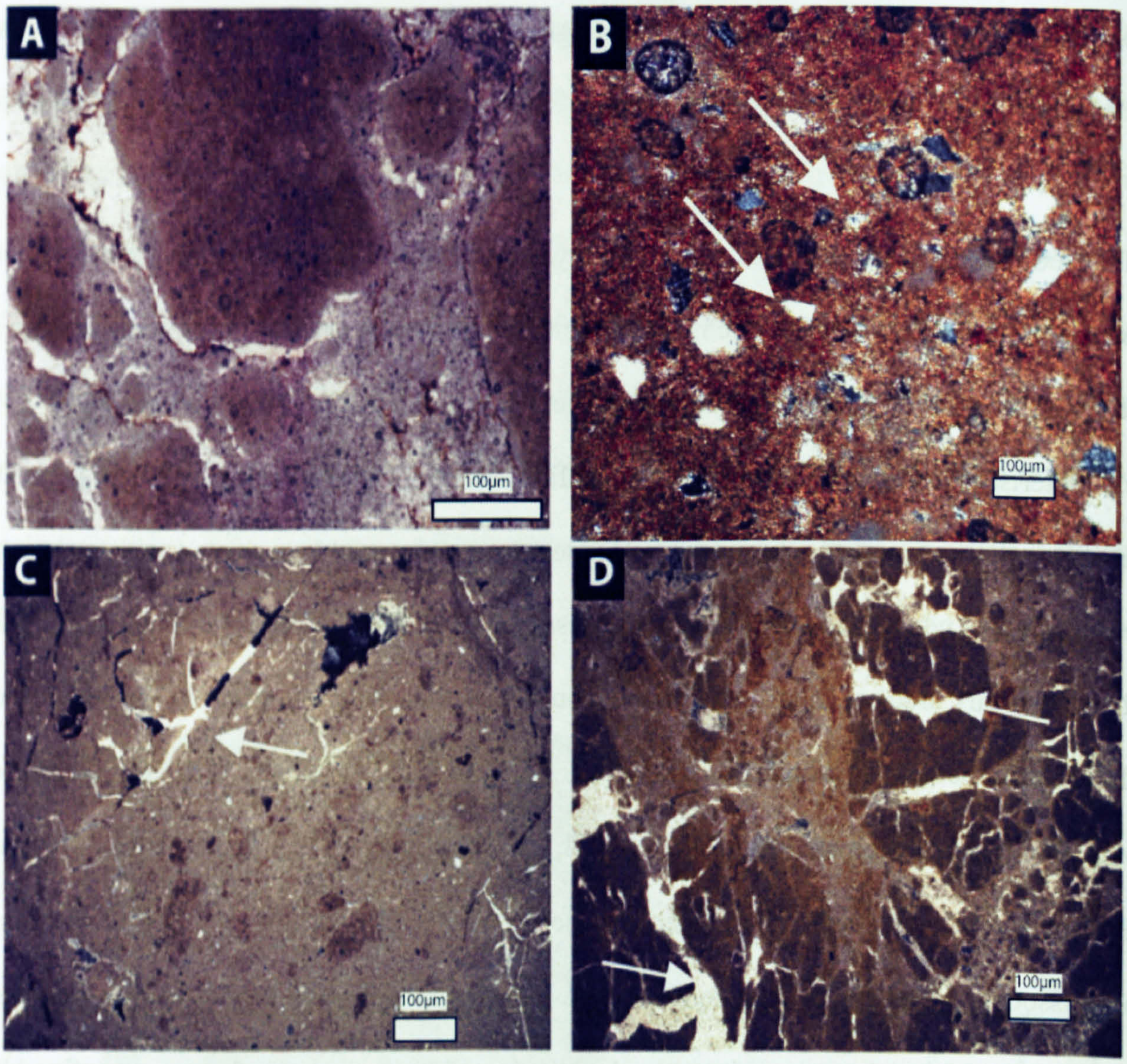

Figure 4.6 Photomicrographs of typical textures seen in the carbonate nodules. A) Shows a clotted texture seen in the micro and cryptocrystalline carbonates (KOR2). B) Floating grains of quartz (arrowed) in a carbonate matrix (KOR12). C) Anhedral to euhedral sinuous veins of calcite (KOR2). D) These veins cross cut earlier pedogenic structure (KOR1).

Sinuous veins of anhedral to euhedral calcite are found randomly cutting across most of the nodules. The veins are filled with different levels of crystal growth. Some are formed of single crystals which span the width of the vein; others are formed of smaller stubby crystals (Figure 4.6 C and D). The elongated crystals are 5-15µm in width and generally 150-50µm in length. The vein crystals have distinct boundaries from the surrounding micro- and cryptocrystalline groundmass, suggesting two distinct phases of crystallisation (Figure 4.6A and D). These veins are also seen to grow around patches of crypto- and microcrystalline micrite (Figure 4.6A), again suggesting that they postdate the formation of the micritic

component. The sinuous vein structures are most likely to be an infill of cavities created by shrinking and swelling of voids or by rootlet action (Wright and Tucker 1991; Khadkikar *et al.* 2000; Quast *et al.* 2006).

Nodules KOR2.4 and SAM2.2 show poikilotopic morphology (Friedman 1965; Quast *et al.* 2006, see Appendix A2.1), that is to say they formed as cement filling spaces between clastic grains (Figure 4.7A). This morphology is confined to the nodules formed in a fine or very fine sand substrate. They may represent nodules precipitated from phreatic water rather than meteoric (Quast *et al.* 2006), although it is highly plausible that in a soil where a calcrete hardpan had not yet developed which would, isolate the soil water from the meteoric system, that these two waters would have very similar chemistries.

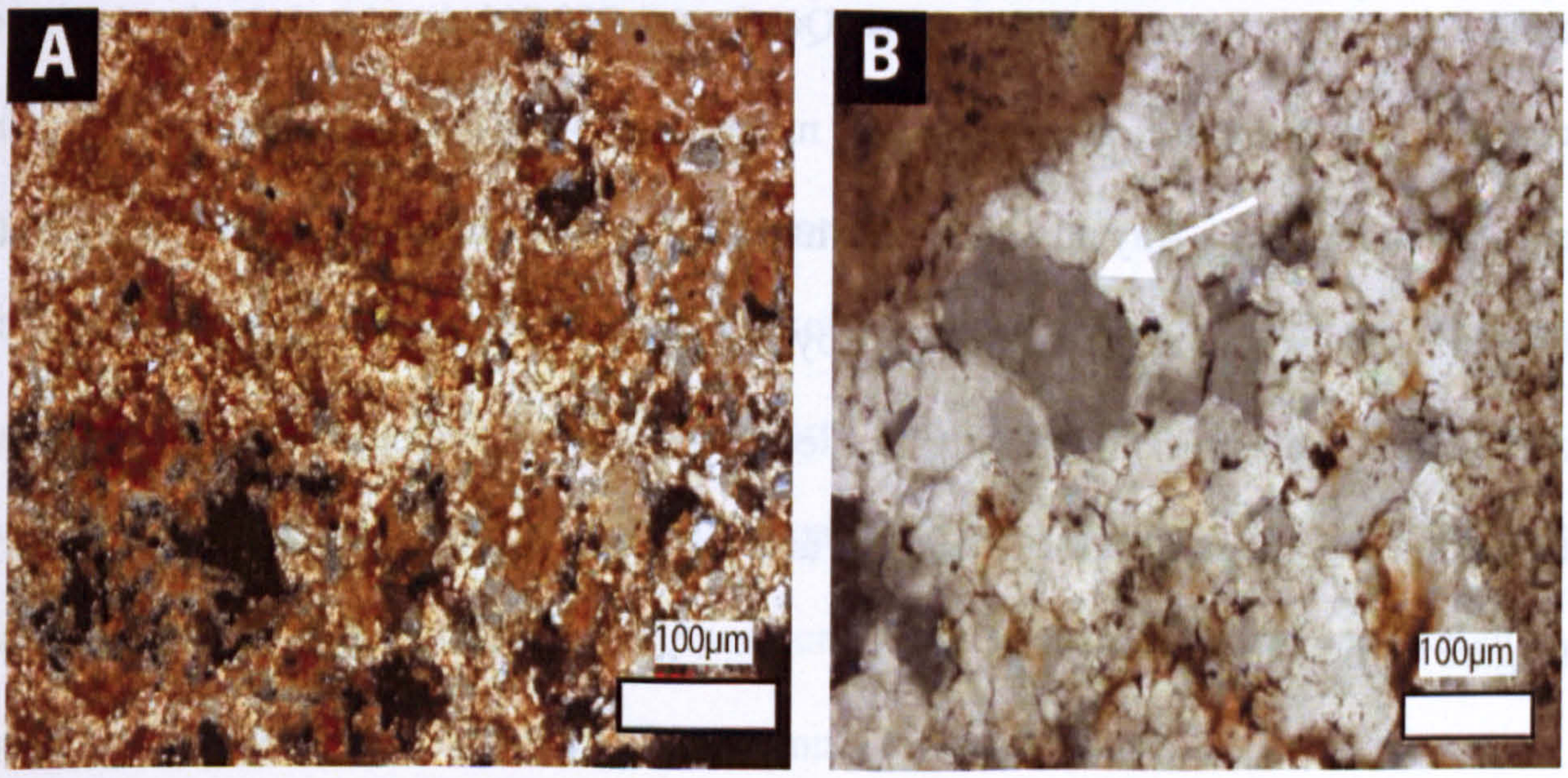

Figure 4.7 Diagenetic textures A) Poikilotopic morphology related to groundwaters (SAM2.2). B) Concavo-convex crystal contacts suggesting neomorphism (KOR 21.9).

There is evidence in some nodules (such as KOR21.9) of possible neomorphic features. Neomorphism and replacement within soil carbonate is common even when the soil is still part of the active vadose zone (Wright and Tucker 1991). However, it is also suggested to represent later diagenetic fabrics with characteristic concavo-convex crystal contacts (Figure

4.7B) which enclose smaller patches of crypto- and microcrystalline material (Quast *et al.* 2006). Diagenetic neomorphic features have been identified in only two horizons (SAM2 and KOR21) while the remaining horizons surrounding them show no such feature, which indicate that this texture may not be due to excessive burial but instead may be related to specific conditions within that nodule itself.

Petrographic analysis of the carbonate crystal structure can be used to divide all the calcrete samples analysed into crypto masses (Crp); cryptocrystalline masses containing sinuous veins (SpC); nodules where the calcite crystal size is above 20μm (MCr) and those nodules where the crystal size is above 20μm and contain sinuous veins (MCr/SpC) (Appendix A2.1).

As the sinuous veins are thought to represent a later phase digenetic or phreatic infill (Wright and Tucker 1991; Khadkikar *et al.* 2000; Quast *et al.* 2006) they were also sub-sampled to compare their isotopic composition to the micritic component of the nodule (see Chapter 2 and Appendix A2.1). Any nodules which have a calcite crystal size above 20μm are thought to be formed by groundwater rather than by pedogenic processes (Quast *et al.* 2006). Although the data from this study do not seem to support any significant difference between the crypto and microcrystalline carbonate and the calcite with a crystal size over 20μm (Figure 4.8).

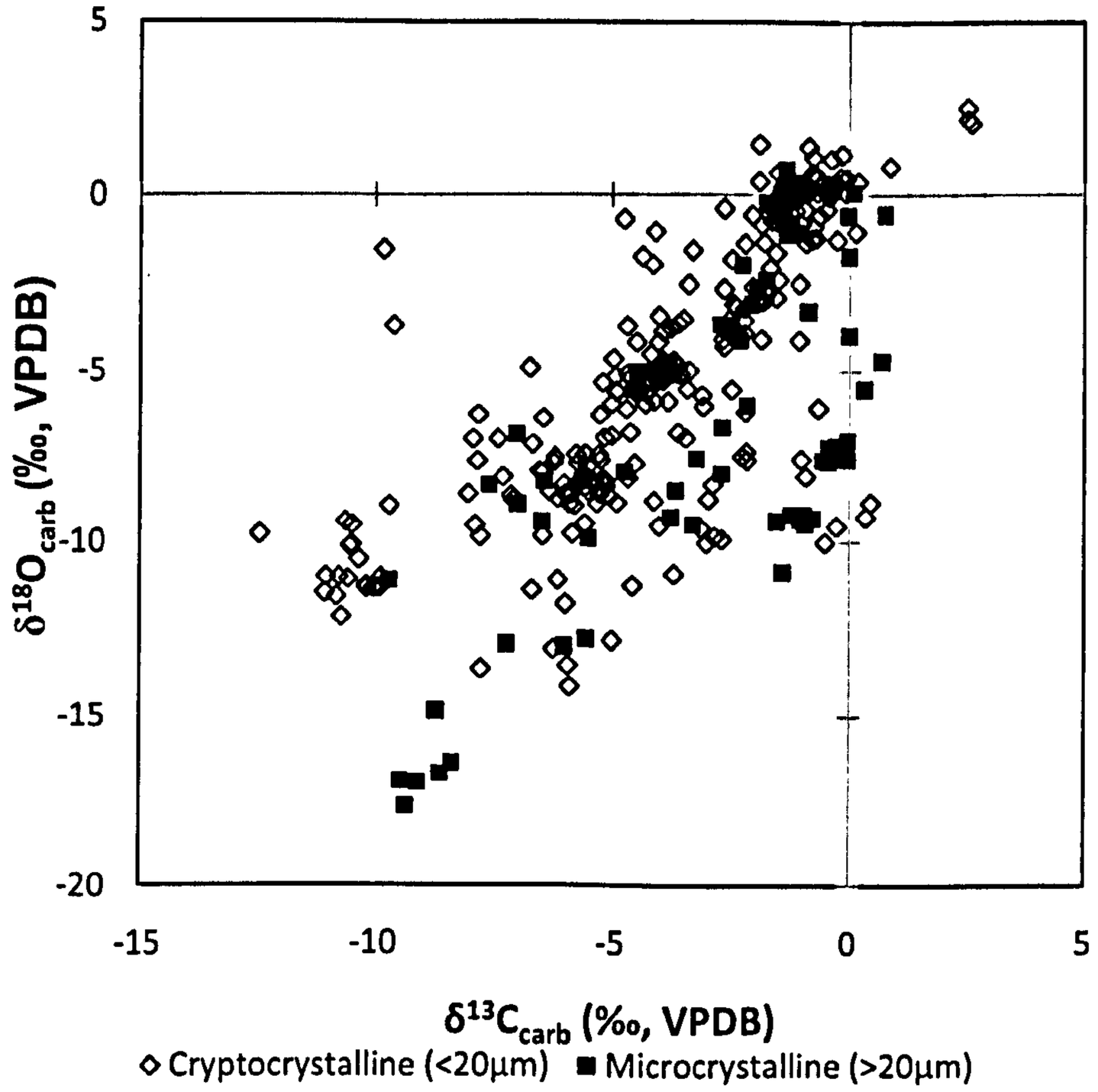

Figure 4.8 Cross plot of those micritic carbonate values from microcrystalline calcite nodules (crystal size >20μm) compared against finer pedogenic calcite values (see Table 1 and Appendix A2.1).

4.3.4 Isotopic composition of spar and micrite

It has been proposed that, by comparing the isotopic values of the cryptocrystalline micritic component of a nodule, with that from the sparry vein-filling calcite, it is possible to discern whether the micritic component has been isotopically overprinted (Quast *et al.*2006). For each sample containing both a cryptocrystalline micritic and a sparry vein component, both components were analysed to allow comparison between the two.

There are examples of paleosols where the isotopic composition of every micritic part of the nodule is isotopically similar to the spar component from that nodule. At Boyevaya Gora KOR33, KOR2, KOR16, show this, also SAM14 and SAM13 at Sambullak; TUY27 at Tuyembetka; all bar KRA7e at Krasnogor and MES1, MES3 at Mescheryakovka (Figure 4.9 and see Appendix A2.2). These suggest that even though the micritic component may appear

petrographically unaltered, it has been influenced by the spar-forming event. Equally there are many paleosols that show good separation between the spar and micritic values (Figure 4.9 and see Appendix A2.2) suggesting that the micritic component of these nodules are unaltered. In most cases the spar values are isotopically more negative than those of the micrite (Figure 4.9 and see Appendix A2.2).

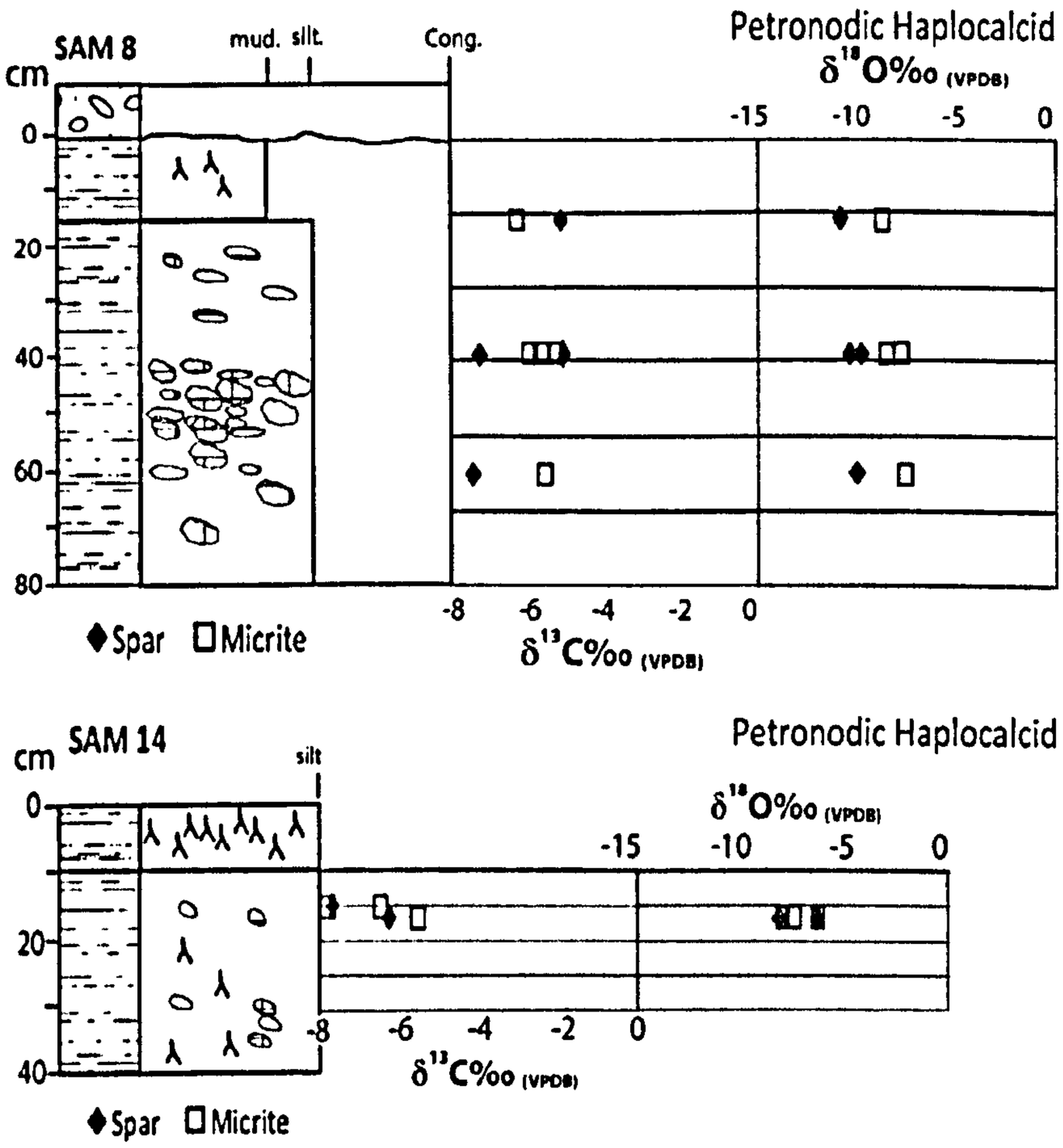

Figure 4.9 Two isotopic depth plots of micritic (open square) and spar components (closed diamond). SAM14 shows strong overlap between the spar and micritic components suggesting the micritic values are altered. KOR6 shows strong separation suggesting the micrite is not affected by the spar forming event.

To remove those nodules which the spar forming event had altered the micrite part of the nodule, all those nodules with spar and micritic values which were the same within 2 times experimental error (see Chapter 2) were deemed to be altered (cf. MacLeod *et al.* 2001; Quast *et al.* 2005; Dr Stephen Grimes *pers. comm.*) Those nodules that did not contain spar were compared against the average value of the other spar values from that horizon. This suggests that of the nodules at Boyevaya Gora 61 were affected by the later spar event; at Sambullak

42 were affected; at Tuyembetka 4 at Krasnogor all bar one; and at Mescheryakovka 14 were affected (see Appendix A2.2).

4.3.5 Variation with depth in paleosol

The depth at which carbonate samples are taken from within a paleosol is often considered important, as only below a certain depth do the effects of evaporation not affect the soil water (Cerling 1991; Li *et al.*1996; Ekart *et al.* 1999). It is reported that in the first 30–50cm of a soil horizon the isotopic values are out of equilibrium with the atmosphere due to the effects of evaporation and plant respired CO_2 altering the soil water down to this point (Liu *et al.*1996; Dr Nathan Sheldon *pers. comm.* 2008). However, in stacked paleosol sequences, the actual depth from the palaeosurface may have been shortened (see Chapter 5) due to overprinting of older soils by newer soils (Kraus 1999). To rectify this issue all the horizons containing stage II nodular calcrete were sampled stratigraphically, thus allowing for a reconstruction of the stable isotope curves with depth. It is therefore possible to recognise if the isotopic values within a paleosol have reached equilibrium even if the top of the horizon is overprinted. It has been suggested that these fractionated top zones, can show an $\delta^{13}C$ enrichment of 2-3‰ and a $\delta^{18}O$ enrichment of 4-10‰ in modern soils (Pendall *et al.* 1994; Liu *et al.* 1996; Huang *et al.* 2005).

Twenty four paleosols at Boyevaya Gora contain stage II calcite and are exposed well enough to accurately sample stratigraphically within them. This is also true for 21 paleosols at Sambullak; 3 paleosols at Tuyembetka and 5 paleosols at Mescheryakovka and thus it was impossible to investigate how the isotope signal varies with depth within each paleosol (see Appendix A2.2).

There are four distinct trends seen within the depth plots. The first shows a positive shift in both the $\delta^{13}C_{carb}$ and $\delta^{18}O_{carb}$ values towards the top of the paleosol (Figure 4.10 A). Examples of this are KOR2, KOR6, KOR10, and KOR36 (see Appendix A2.2). The second type shows a positive correlation with depth (Figure 4.10B). The third type shows a lot of variability between the nodules but no trend through the section – these can be very thin nodule bands or thicker sections (Figure 4.10C). The final type shows little internal variation within the section (Figure 4.10D).

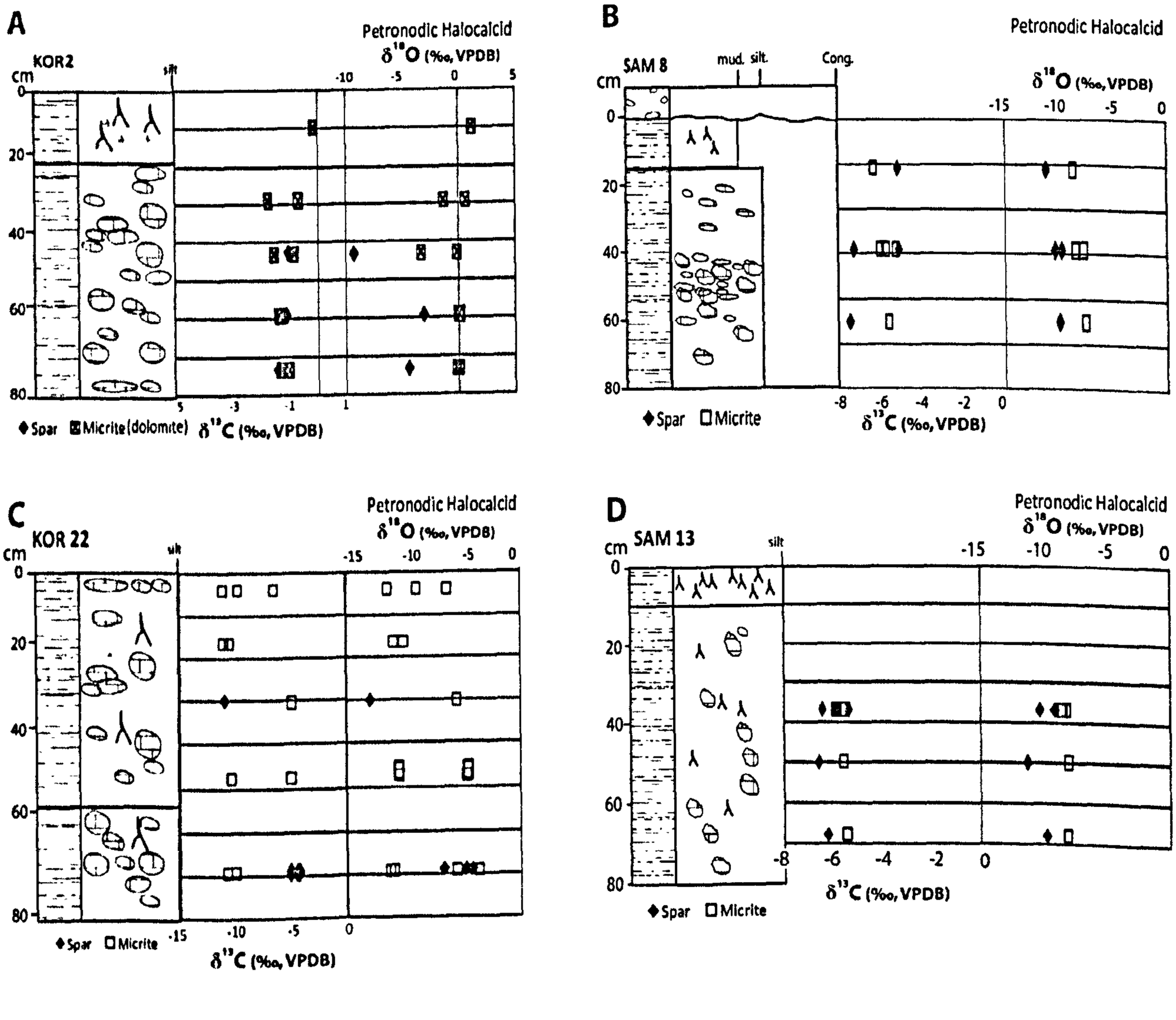

Figure 4.10 Isotopic depth plots of micritic (open square) and spar components (closed diamond) within individual paleosol horizons, the crosses denote dolomitic micrite. A) Shows a positive shift towards the top of the profile in the micritic values. B) Shows a positive correlation down profile in the micritic values. C) Shows no overall trend but a lot of variation. D) shows no overall trend and a tight cluster of values.

There are Russian paleosols (KOR2, KOR6, KOR10 and KOR36; see Appendix A2.2) that show positive values towards the top that become more negative and then stabilise with depth (Figure 4.10A; Appendix A2.2). This fits well with the diffusion-based model predicted by Cerling (1991) and observed by Liu *et al.* (1996). Most paleosols show little variation with depth which is interesting as these horizons often show a difference between the spar and micritic components (Figure 4.10 Table1) suggesting that they are probably not altered by diagenesis. Many of these paleosol horizons are overlain by sand channels (e.g. KOR10, KOR34 SAM8, SAM13 and SAM24, see Appendix A2.2) that may have eroded off the top part of the profile.

Trends with the opposite gradient to that observed in modern soils are harder to explain. For instance both the $\delta^{13}C_{carb}$ and $\delta^{18}O_{carb}$ values for SAM 8 show this pattern (Figure 4.10B). This horizon was eroded by conglomerate suggesting it became part of an active river system. In this case water from the active channel may have inundated the top of the paleosol and affected the geochemistry of the carbonate. There are other horizons, such as KOR22, which show a lot of internal variation (Figure 4.10C). It has been suggested that the fractionation model seen in modern soils is only found under relatively homogeneous climate condition (Pendall *et al.* 1994). Thus, those paleosols that show a large internal variation may have formed at times of climate change. This would also explain why those paleosols that show a negative excursion from the mean paleosol values in the section also have the greatest internal variation.

In summary, those nodules that show a fractionated (either positive or negatively) values at the top of the paleosol are probably out of equilibrium with the atmosphere and should not be used for palaeoclimate analysis. The paleosols that do not show a fractionated top are

assumed to have reached equilibrium and either the fractionated values were eroded or overprinted.

4.3.6 X-Ray diffraction results

All the micritic samples that were selected for isotopic analysis were also analysed using X-Ray Diffraction (XRD) (Appendix A2.4). This revealed that the nodules were made of one of two main components. The first of these components was interpreted to be calcite by both manual and electronic identification. It had a maximum peak at 29.29 °2θ (± 0.11, 1σ std) with a d-spacing of 3.05Å. This is almost identical to the laboratory standard (3.03 Å) and to published values for calcite and calcium carbonate (3.04 Å and 3.02 Å respectively) (Joint Committee on Powder Diffraction Standards 1971). The other main component of the micritic material was found to be dolomite. This has a maximum peak at 30.64 °2θ (± 0.30, 1σ std) and a d-spacing of 2.91Å. This is more positive than the laboratory standard (2.88Å) but is close to the published values for ferroan dolomite (2.90Å) (Joint Committee on Powder Diffraction Standards 1971).

To test further where the dolomite occurred within the nodules, three nodules from different paleosols (KOR2.4, KOR10.8 and KOR21.10), which showed the strongest dolomite response (Appendix A2.4), were sub-sampled (Table 4.1). Different analyses were taken from shallow drill sites, deep drill sites, areas of less consolidation/possible alteration, from the edge of the nodule and from areas with high amounts of spar present. In all cases the main peak was of dolomite and the variation between the measurements was less than that between the peaks of calcite and dolomite.

There were some nodules that showed both a calcite and dolomite peak (e.g. KOR 2.4 and KOR21.10, Table 2). In all cases the calcite was the secondary peak, after dolomite and there

are no cases where there was a secondary dolomite peak associated with a primary calcitic one (Appendix 2.4). There is a suggestion that the calcite may be related to the spar component as in KOR21.10 a calcite secondary peak was found in those areas that contain large amounts of spar (Table 4.1, Appendix A2.3). Equally, when a nodule was disaggregated there was no calcite present in the finest fractions (below <10μm Figure 11) (method after Kraimer *et al.* 2005). This also suggests that the coarse crystals are dominantly calcite while the finer ones are dominantly dolomite in nodules that show both a dolomite and calcite XRD response.

Sample		Main component	Main Peak	100% 2°θ	Secondary peak
KOR 2.4	Original	Dolomite	580	30.7749	Calcite III (29.4016)
	Shallow drill	Dolomite	796	30.7089	
	Deep drill	Dolomite	298	30.8873	Calcite III (29.5649)
	Edge of nodule	Dolomite	891	30.7478	Calcite III (29.3763)
	Repeat	Dolomite	933	30.8295	
KOR 10.8	Original	Dolomite	874.84	30.6249	Quartz High
	Shallow drill	Dolomite	1027.87	30.6143	Quartz
	Deep drill	Dolomite	506	30.7588	Quartz low
	Less consolidate	Dolomite	626.26	30.5844	Quartz
	Edge of nodule	Dolomite	579.23	30.5719	
KOR21.10	Original	Dolomite	896	30.7348	
	Shallow drill	Dolomite	636.92	30.6562	
	Edge of nodule B	Dolomite	616.59	30.6596	Quartz (50)
	High spar	Dolomite	510.2	30.7603	Calcite (100% 2°θ= 29.3826)
	Deep drill	Dolomite	777.8	30.6271	Quartz (31)

Table 4.1 Summary of multiple drill site XRD test. For further information see Appendix A2.3.

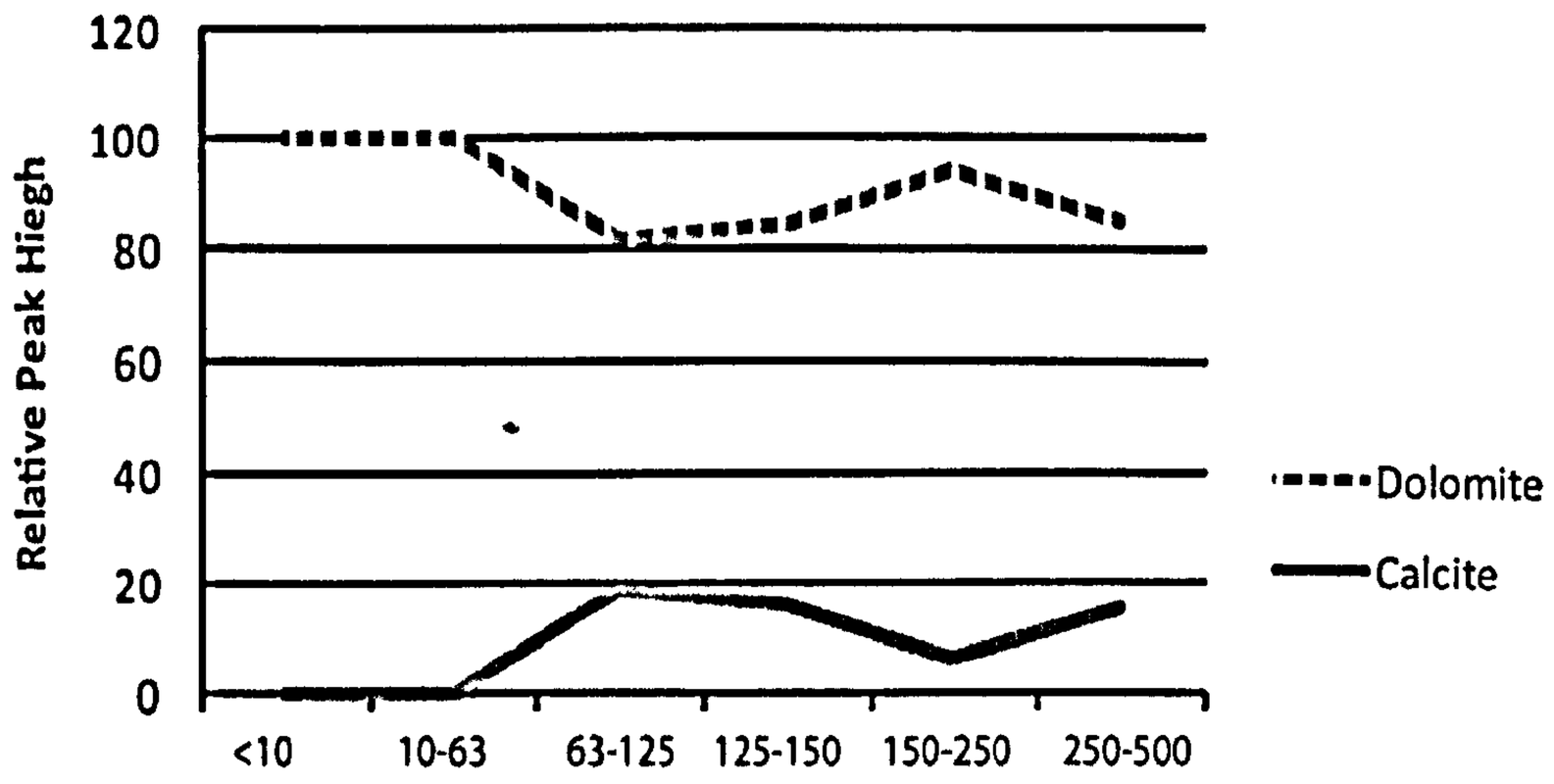

Figure 4.11 The relative peak heights between the dolomite response and the calcite response for different grain sizes of a nodule. Note the increase of the dolomite response at the lowest sizes suggesting the dolomite makes up the cryptocrystalline carbonate.

The presence of dolomite is also verified by the use of a dolomite-specific petrographic stain (Alkaline Alizian Red S). This stain selectively stains dolomite over calcite thus allowing identification of the part of the nodule fabric in which the dolomite is present. In the nodules containing dolomite it was the micro- and especially the cryptocrystalline parts of the fabric that took up most dolomite stain (Figure 4.12A). This suggests that the dolomite occurs in the primary pedogenic component of the nodule rather than as a result of a later recrystallisation event (cf. Quast *et al.* 2006). Those nodules which produced both a calcite and dolomite peak on the XRD were also stained with a calcite-specific stain (Alizian Red S). This showed that the calcite seems to be found in the sparry component of the nodule, suggesting a primary dolomite precipitation followed by calcitic phreatic water which filled in the veins forming the sparry crystals (Figure 4.12C).

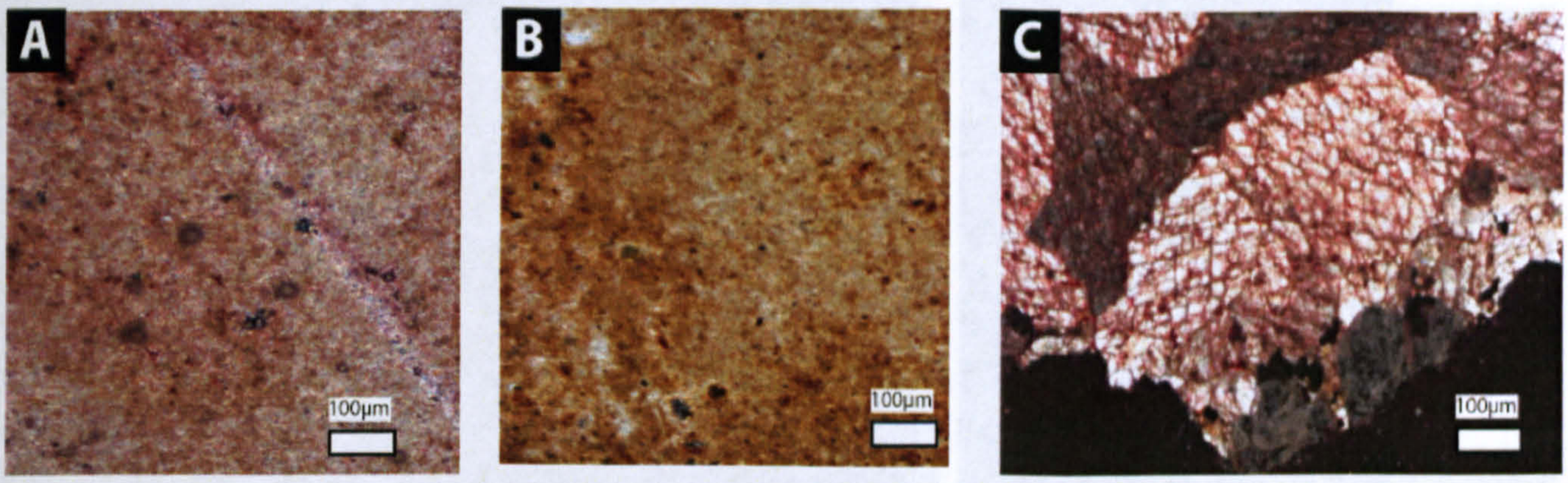

Figure 4.12 Effects of the dolomite, and calcite specific stains. A) produced an XRD response of dolomite and reacted to the stain with the dolomite specific stain (Alkaline Alizian Red S while B) was identified as calcite did not. C) Shows the sinuous vein crystals reacting to the calcite specific stain (Alizian Red S) (KOR14.1).

4.3.7 Scanning electron microscopy

The presence of iron oxides masks the crypto- and microcrystalline morphology in many of the nodules seen through a petrographic microscope, which hinders accurate identification of the finest fraction of the nodules. To determine further whether the dolomite was formed as a primary feature or a replacement of earlier precursor calcites, nodule KOR 2.4 was analysed with a backscatter scanning electron microscope as this nodule had one of the strongest dolomitic XRD responses (Appendix A2.4). This analysis revealed that the areas that make up the densest parts of the clotted texture in the nodule are made entirely of dolomite rhombs of about 2-5µm in size (Figure 4.13). Elemental analysis of these areas showed prominent peaks in calcium, oxygen and magnesium. The sparry vein fill, by contrast, lacks a prominent magnesium peak confirming it is indeed calcite as the petrographic analysis suggests. It is also evident that the calcitic crystals are enveloping the dolomite rhombs, supporting the hypothesis that the dolomite preceded the calcite formation (Figure 4.13ii).

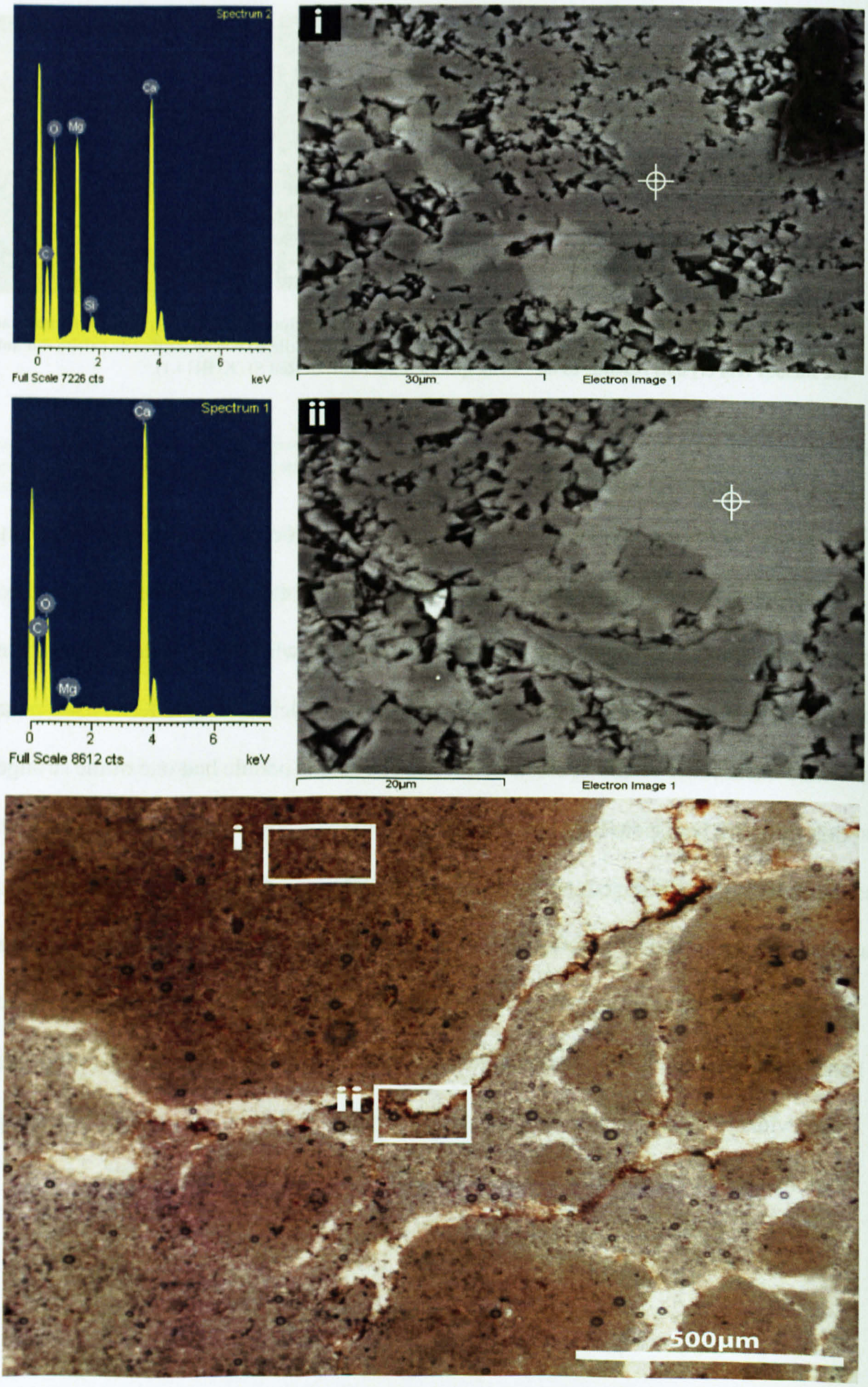

Figure 4.13 SEM analysis of a nodule (from KOR 2.4) which produced a dolomitic response on XRD. i) is from the inside of a cryptocrystalline area, elemental analysis of which shows a high Mg peak (top left hand panel). ii) is from a sinuous vein and the elemental analysis does not show an Mg peak (middle left hand panel). The lower panel is a photomicrograph showing where the two SEM photos were taken from.

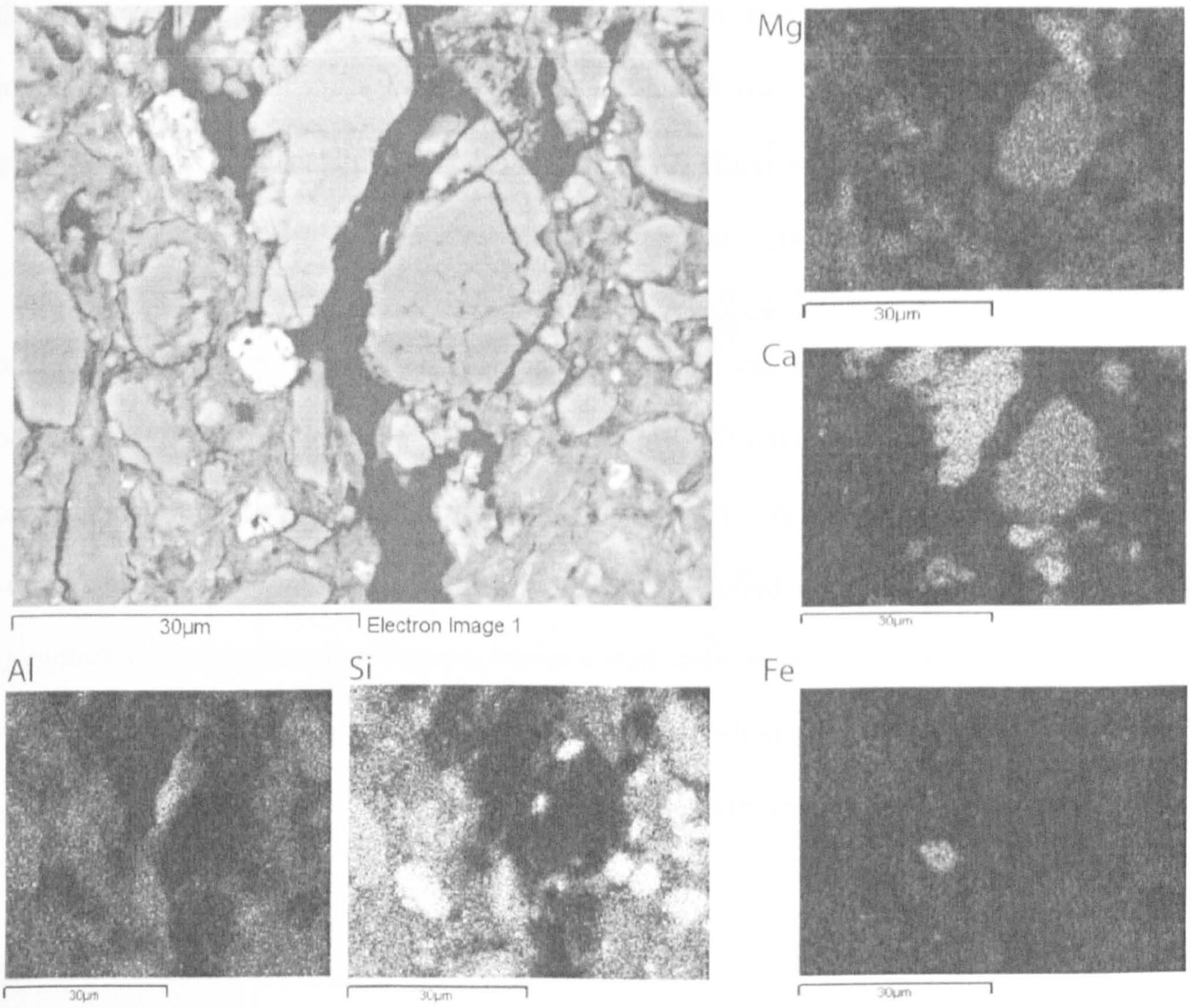

Figure 4.14 Elemental mapping of a calcitic nodule (KOR 22.6). The top left hand image is the SEM image and the surrounding panels are the individual element maps.

SEM analysis of a carbonate nodule which both XRD and staining techniques showed to be calcite (KOR 22.6) showed no evidence of dolomitic rhombs (Figure 4.14). Elemental mapping of the nodules reveals that the majority of the sample comprises areas of high silica content (interpreted as clays and quartz) surrounding areas of high calcium content (interpreted to be calcite) (Figure 4.14). Within the calcite areas there seems to be a variation in the amount of magnesium suggesting the presence of both high and low Mg calcite. However, the areas of clay also showed relatively high amounts of Mg (Figure 4.14 Mg). As this is only a semi-quantitative technique, this could be a result of different reflectance rates or interference from the clays. The Fe map attests to the presence of iron oxides which appear

to relate to the very bright parts of the images and slightly higher background values in the clay areas of the nodule (Figure 4.14 Fe). Other areas of the same nodule show submicron particles which are predominantly Al, Si, Mg and K, suggesting that they may also be areas of clays (Figure 4.14 Al, Si, Mg and K).

The carbonate found in the vast majority of paleosols in Russia is either dolomitic or calcitic. However, there is one exception at Boyevaya Gora. The paleosol horizon KOR 23 has both calcitic and dolomitic nodules (Figure 4.14). The distributions of the nodules are not random as the dolomitic part of the horizon is the lower part of the horizon while the upper part is calcitic. These are the horizons also show a mixed groundwater/pedogenic morphology (cf. Khadkikar *et al.* 2000) where the lower part of the section appears to be groundwater influenced and the upper is primarily pedogenic.

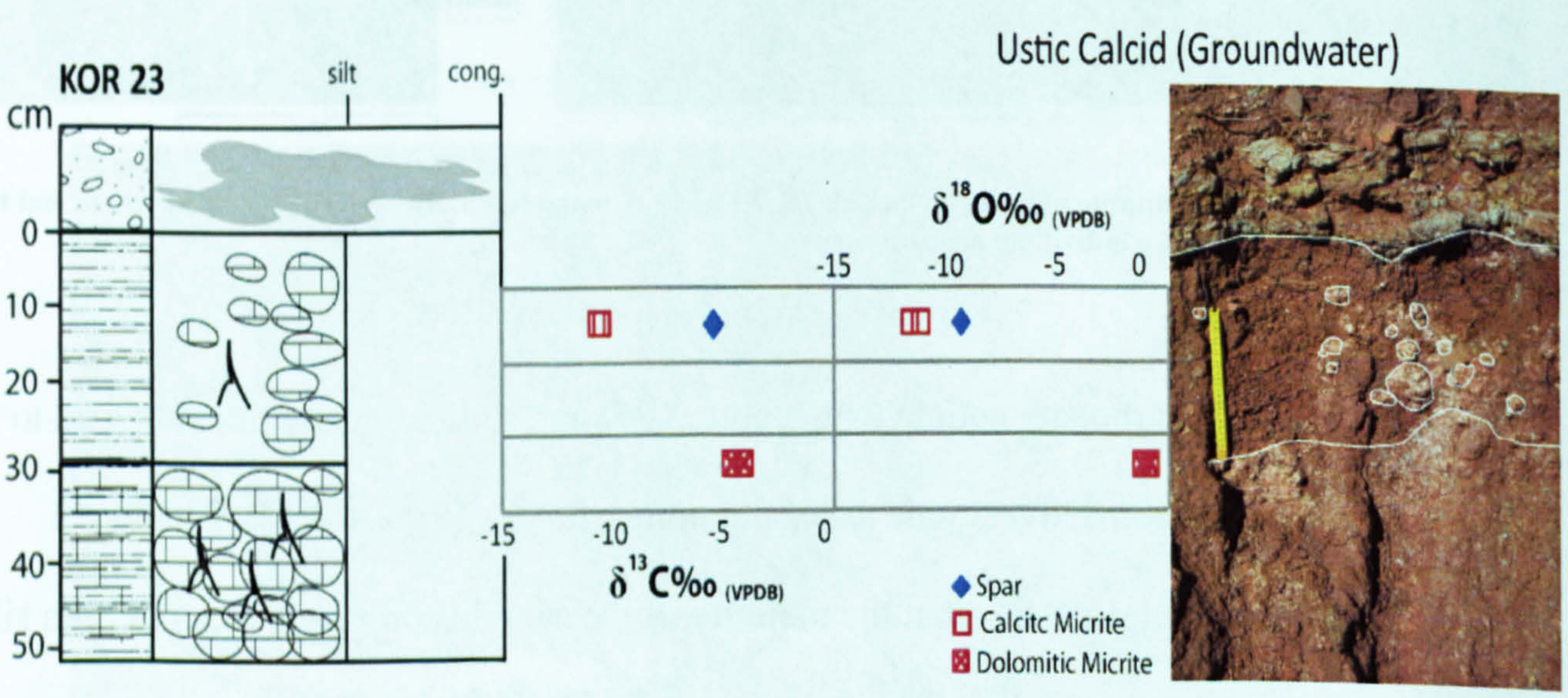

Figure 4.15 Paleosol at Boyevaya Gora which contained both dolomitic (squares with crosses) and calcitic nodules (open squares). Note how the dolomite is restricted to the base of the nodular horizons.

XRD results compared with isotope results

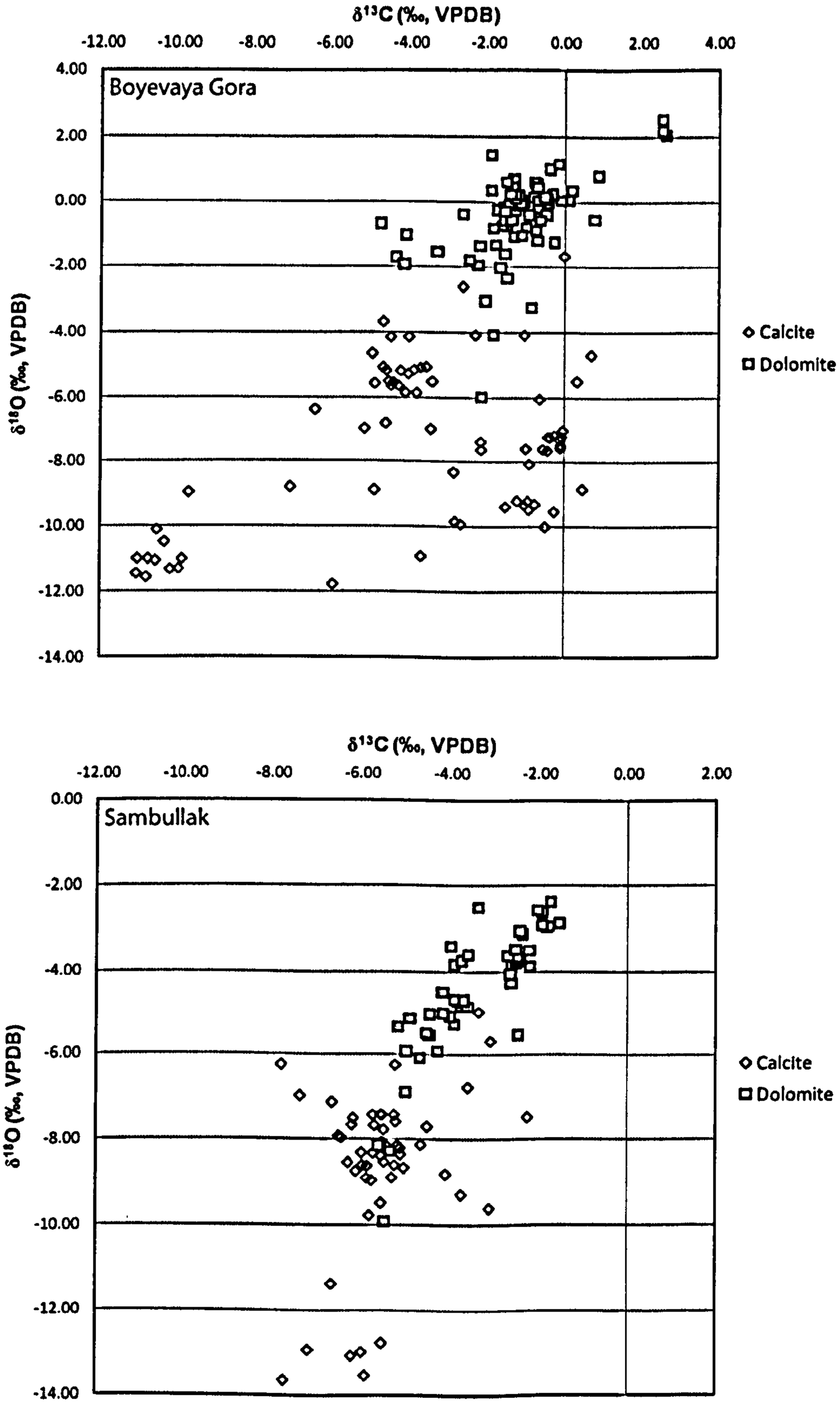

Figure 4.16 $\delta^{13}C$ and $\delta^{18}O$ cross plots for Boyevaya Gora (top) and Sambullak (bottom). The open diamonds are those nodules of which the micritic component is calcite and the closed squares are dolomite.

The XRD results show that the isotopically heavy values are primarily associated with the presence of dolomite while the lighter values are all related to calcite (Figure 4.16). In both localities there is an overlap between the dolocretes and calcretes suggesting possibly a similar origin for both the fluids that formed some of the dolomite and calcite. Also this overlap appears to be greater at Sambullak than at Boyevaya Gora.

4.4 Quantifying the effects of alteration on the isotope signature

As investigation into palaeoclimatic and palaeoatmospheric variation is the primary goal of this study it must be understood (a) how much of the isotope signature recorded at each section reflects the vadose pedogenic signal and (b) if any of the excursions identified in the primary data are the result of other influences or later alteration.

Table 4.1 shows the summary of the findings of Section 4.3 and the 4 criteria which will be used to assess the origins of the isotope results. These are:

(1) If the paleosol is associated with lacustrine units or the pedogenic carbonate shows ground water morphologies (section 4.3.2)

(2) If the calcrete is above or below stage II in development (section 4.3.1)

(3) Whether the micritic component was significantly different from the spar of the same nodule/horizon (Section 4.3.4)

(4) If the micritic component was dolomite or calcite (section 4.3.6 and 4.3.7)

(5) If the nodule was microcrystalline (greater than 20μm or not). (section 4.3.3)

Paleosol	Nodules	Not Groundwt. or Lacus.	Stage II or I	Significant difference between Micrite spar[a]	Calcite	Crystal size <20μm
KOR 36	KOR 36.1	✓	✓	✓✓	✓	✓
	KOR 36.2	✓	✓	××	✓	✓
	KOR 36.3	✓	✓	×	✓	✓
	KOR 36.4	✓	✓	✓	✓	✓

Paleosol	Nodules	Not Groundwt. or Lacus.	Stage II or I	Significant difference between Micrite spar[a]	Calcite	Crystal size <20µm
	KOR 36.5	✓	✓	✓	✓	✓
	KOR 36.6	✓	✓	✓	✓	✓
KOR 33	04.8.2.f	✓	✓	✓	✓	✓
	04.8.2.f	✓	✓	✓	✓	✓
	04.8.2.f	✓	✓	✓	✓	✓
	KOR 33.1	✓	✓	✓✓	✓	✓
	KOR 33.2	✓	✓	××	✓	✓
	KOR 33.3	✓	✓	××	✓	✓
KOR 37	KOR 37.1	✓	✓	?	✓	×
	KOR 37.2	✓	✓	?	✓	×
	KOR 37.3	✓	✓	?	✓	×
	KOR 37.4	✓	✓	?	✓	✓
	KOR 37.5	✓	✓	?	✓	✓
KOR 34	KOR 34.1	✓	✓	××	✓	×
	KOR 34.2	✓	✓	××	✓	×
	KOR 34.3	✓	✓	××	✓	×
	KOR 34.4	✓	✓	×	✓	×
	KOR 34.5	✓	✓	××	✓	×
	KOR 34.6	✓	✓	××	✓	×
	KOR 34.7	✓	✓	✓✓	✓	×
KOR 32	04.8.2.e	✓	✓	×	✓	×
	04.8.2.e.i	✓	✓	✓	✓	×
	04.8.2.e.ii	✓	✓	×	✓	×
	04.8.2.e.iii	✓	✓	✓	✓	×
	04.8.2.e.iv	✓	✓	✓	✓	×
	KOR 32.2	✓	✓	✓✓	✓	×
	KOR 32.7	✓	✓	✓✓	✓	×
	KOR 32.8	✓	✓	××	✓	×
KOR 1a	04.8.1.ac*	✓	✓	✓	×	✓
	04.8.1.ac.I	✓	✓	✓	×	✓
	04.8.1.ac.II	✓	✓	✓	×	✓
	KOR 1.10	✓	✓	✓	×	×
	KOR 1.7	✓	✓	××	×	✓
	KOR 1.8	✓	✓	✓	×	✓
	KOR 1.9	✓	✓	✓✓	×	✓
KOR 2	KOR 2.1	✓	✓	✓	×	✓
	KOR 2.2	✓	✓	×	×	✓
	KOR 2.3	✓	✓	×	×	✓
	KOR 2.4	✓	✓	××	×	×
	KOR 2.5	✓	✓	×	×	✓
	KOR 2.6	✓	✓	××	×	✓
	KOR 2.7	✓	✓	×	×	✓
	KOR 2.8	✓	✓	××	×	✓
	KOR 2.9	✓	✓	×	×	✓
KOR 8	04.8.1.aa	✓	×	?		✓

Paleosol	Nodules	Not Groundwt. or Lacus.	Stage II or I	Significant difference between Micrite spar[a]	Calcite	Crystal size <20µm
KOR 9	KOR 9.1	✓	✓	✓✓	×	✓
	KOR 9.2	✓	✓	✓	×	✓
	KOR 9.3	✓	✓	✓	×	✓
KOR 4	04.8.1.w	✓	×	?	×	✓
KOR 5	04.8.1.z	✓	✓	✓	×	✓
	KOR 5.1	✓	✓	✓	×	×
	KOR 5.2	✓	✓	××	×	✓
	KOR 5.3	✓	✓	✓	×	✓
	KOR 5.4	✓	✓	✓✓	×	✓
	KOR 5.5	✓	✓	✓✓	×	✓
KOR 6	KOR 6.2	✓	✓	✓✓	×	✓
	KOR 6.3	✓	✓	✓✓	×	✓
	KOR 6.4	✓	✓	✓✓	×	✓
	KOR 6.5	✓	✓	✓✓	×	✓
	KOR 6.6	✓	✓	✓✓	×	✓
	KOR 6.7	✓	✓	✓✓	×	✓
	KOR 6.8	✓	✓	✓✓	×	✓
KOR 10	04.8.1.x	×	×	✓	×	×
	KOR 10.1	×	×	✓✓	×	×
	KOR 10.11	×	×	××	×	×
	KOR 10.12	×	×	××	×	×
	KOR 10.2	×	×	××	×	×
	KOR 10.3	×	×	✓✓	×	×
	KOR 10.4	×	×	✓✓	×	×
	KOR 10.5	×	×	✓✓	×	✓
	KOR 10.6	×	×	×	×	✓
	KOR 10.7	×	×	××	×	×
	KOR 10.8	×	×	××	×	✓
KOR 11	04.8.1.w	✓	×	?	×	✓
KOR 12	04.8.1.v*	✓	✓	×	×	✓
	04.8.1.v.I	✓	✓	×	×	✓
	04.8.1.v.II	✓	✓	×	×	✓
	KOR 12.1	✓	✓	×	×	✓
	KOR 12.3	✓	✓	××	×	✓
KOR 13	04.8.1.u	✓	×	?	×	✓
KOR 14	04.8.1.t	✓	×	✓	×	✓
	KOR 14.10	✓	×	×	×	✓
	KOR 14.11	✓	×	✓	×	✓
	KOR 14.14	✓	×	✓✓	×	✓
	KOR 14.15	✓	×	✓✓	×	✓
KOR 14a	KOR 14.8	✓	✓	✓✓	×	✓
	KOR 14.9	✓	✓	✓	×	✓
KOR 14b	04.8.1.s	✓	✓	✓	×	✓
	KOR 14.1	✓	✓	××	×	✓
KOR 23	04.8.1.r*	×	✓	✓	×	×

Paleosol	Nodules	Not Groundwt. or Lacus.	Stage II or I	Significant difference between Micrite spar[a]	Calcite	Crystal size <20µm
	04.8.1.r.I	×	✓	✓	×	✓
	04.8.1.r.II	×	✓	✓	×	✓
	04.8.1.r.III	×	✓	✓	×	✓
	KOR 23.1	✓	✓	✓	✓	✓
	KOR 23.2	✓	✓	✓✓	✓	✓
	KOR 23.3	✓	✓	×	×	✓
	KOR 23.4	✓	✓	✓	×	✓
KOR 22	04.8.1.q	✓	✓	×	✓	✓
	04.8.1.q.I	✓	✓	✓	✓	✓
	04.8.1.q.II	✓	✓	✓	✓	✓
	04.8.1.q.III	✓	✓	×	✓	✓
	KOR 22.1	✓	✓	××	✓	✓
	KOR 22.10	✓	✓	✓	✓	✓
	KOR 22.11	✓	✓	✓	✓	✓
	KOR 22.12	✓	✓	✓	✓	✓
	KOR 22.13	✓	✓	×	✓	✓
	KOR 22.14	✓	✓	✓	✓	✓
	KOR 22.2	✓	✓	✓✓	✓	✓
	KOR 22.4	✓	✓	✓✓	✓	✓
	KOR 22.5	✓	✓	✓	✓	✓
	KOR 22.6	✓	✓	✓	✓	✓
	KOR 22.7	✓	✓	✓	✓	✓
	KOR 22.8	✓	✓	✓✓	✓	✓
KOR 21a	04.8.1.p	✓	✓	✓	×	✓
	KOR 21.10	✓	✓	✓✓	×	×
	KOR 21.4	✓	✓	×	✓	✓
	KOR 21.5	✓	✓	✓✓	✓	✓
	KOR 21.6	✓	✓	××	✓	✓
	KOR 21.7	✓	✓	✓✓	✓	×
	KOR 21.8	✓	✓	✓✓	✓	✓
	KOR 21.9	✓	✓	✓✓	✓	✓
KOR 21	KOR 21.1	✓	✓	✓✓	✓	✓
	KOR 21.2	✓	✓	✓✓	✓	×
	KOR 21.3	✓	✓	××	✓	×
KOR 15	04.8.1.o	✓	✓	✓	×	✓
	KOR 15.2	✓	✓	××	×	×
	KOR 15.3	✓	✓	✓✓	×	✓
	KOR 15.4	✓	✓	✓	×	✓
	KOR 15.5	✓	✓	✓✓	×	✓
	KOR 15.6	✓	✓	××	×	✓
	KOR 15.7	✓	✓	✓✓	×	✓
	KOR 15.8	✓	✓	××	×	×
	KOR 15.9	✓	✓	✓✓	×	✓
KOR 16	04.8.1.n*	✓	✓	✓	✓	✓
	KOR 16.10	✓	✓	××	✓	✓

Paleosol	Nodules	Not Groundwt. or Lacus.	Stage II or I	Significant difference between Micrite spar[a]	Calcite	Crystal size <20µm
	KOR 16.5	✓	✓	✓✓	✓	✓
	KOR 16.6	✓	✓	✓✓	✓	✓
	KOR 16.7	✓	✓	××	✓	✓
	KOR 16.8	✓	✓	××	✓	✓
	KOR 16.9	✓	✓	×	✓	✓
KOR 16 a	KOR 16.1	✓	✓	××	✓	✓
	KOR 16.2	✓	✓	××	✓	✓
	KOR 16.3	✓	✓	✓✓	✓	×
	KOR 16.4	✓	✓	✓✓	✓	✓
KOR 17	04.8.1.m*	×	×	×	✓	×
	KOR 17.2	×	×	×	✓	×
	KOR 17.3	×	×	✓✓	×	×
KOR 18	04.8.1.l	✓	×	?	×	✓
	04.8.1.l.I	✓	×	?	×	✓
	04.8.1.l.II	✓	×	?	×	✓
	04.8.1.l.III	✓	×	?	×	✓
KOR 19	04.8.1.k	✓	×	?		×
KOR 20	04.8.1.j	×	×	?		✓
KOR 24	04.8.1.l	✓	×	?	×	×
	04.8.1.l.I	✓	×	?	✓	×
	04.8.1.l.II	✓	×	?	✓	×
	04.8.1.l.III	✓	×	?	✓	×
	KOR 24.5	✓	×	?	✓	×
	KOR 24.6	✓	×	?	✓	×
KOR 25	KOR 25.1	✓	✓	✓✓	✓	✓
	KOR 25.3	✓	✓	✓		✓
	KOR 25.4	✓	✓	✓		✓
	KOR 25.5	✓	✓	✓	✓	✓
KOR 26	04.8.1.g*	×	×	?	✓	✓
KOR 27	04.8.1.f*	✓	✓	?	✓	✓
	KOR 27.2	✓	✓	?	✓	✓
	KOR 27.4	✓	✓	?	✓	✓
KOR 28	04.8.1.e	✓	×	?	×	✓
KOR 29	04.8.1.c	✓	×	?	×	✓
	04.8.1.c.I	✓	×	?	×	✓
	04.8.1.c.II	✓	×	?	×	✓
	04.8.1.c.III	✓	×	?	×	✓
KOR 31	04.8.1.b*	✓	✓	✓	✓	✓
	04.8.1.b.I	✓	✓	✓	✓	✓
	04.8.1.b.II	✓	✓	×	✓	✓
	04.8.1.b.III	✓	✓	×	✓	✓
	KOR 31.1	✓	✓	×	✓	✓
	KOR 31.2	✓	✓	×	✓	✓
	KOR 31.5	✓	✓	××	✓	✓
KOR 35	04.8.1.a	✓	✓	✓	✓	✓

Paleosol	Nodules	Not Groundwt. or Lacus.	Stage II or I	Significant difference between Micrite spar[a]	Calcite	Crystal size <20µm
	KOR 35.1	✓	✓	✓✓	✓	✓
	KOR 35.3	✓	✓	×	✓	✓
	KOR 35.5	✓	✓	✓✓	✓	✓
SAM 1	04.7.24.u	✓	✓	×	✓	✓
	04.7.24.u.I	✓	✓	✓	✓	✓
	04.7.24.u.II	✓	✓	✓	✓	✓
	SAM 1.1	✓	✓	××	✓	✓
	SAM 1.2	✓	✓	××	✓	✓
	SAM 1.3	✓	✓	✓✓	✓	✓
	SAM 1.4	✓	✓	××	✓	✓
	SAM 1.5	✓	✓	✓✓	✓	✓
SAM 4	04.7.24.t	✓	✓	?	✓	×
	04.7.24.t.I	✓	✓	?	✓	×
	04.7.24.t.II	✓	✓	?	✓	×
	04.7.24.t.III	✓	✓	?	✓	×
	SAM 4.3	✓	✓	?	✓	×
	SAM 4.4	✓	✓	?	✓	×
2004 field season	04.7.24.r	✓	×	?	?	✓
SAM 3	04.7.24.s	✓	×	✓	✓	×
	SAM 3.1	✓	×	✓	✓	×
	SAM 3.2	✓	×	××	✓	✓
	SAM 3.3	✓	×	✓	×	✓
	SAM 3.4	✓	×	✓	×	✓
	SAM 3.5	✓	×	✓	×	✓
2004 field season	04.7.24.q	✓	×	?	✓	✓
SAM 2	SAM 2.1	×	✓	✓	✓	✓
	SAM 2.2	×	✓	✓✓		✓
	SAM 2.3	×	✓	✓	✓	✓
	04.7.24.p	×	✓	✓✓	✓	✓
	SAM 2.4	×	✓	✓✓	✓	✓
SAM 12	SAM 12.1	✓	✓	?	✓	✓
	SAM 12.2	✓	✓	?	×	×
SAM 10	SAM 10.8	✓	✓	×	×	✓
	SAM 10.9	✓	✓	××	✓	✓
	SAM 10.7	✓	✓	×	×	✓
	SAM 10.6	✓	✓	✓✓	×	✓
SAM 10a	SAM 10.5	✓	✓	✓✓	×	✓
	SAM 10.3	✓	✓	××	×	✓
	SAM 10.4	✓	✓	✓	×	✓
	SAM 10.2	✓	✓	✓✓	×	✓
	SAM 10.1	✓	✓	✓✓	×	✓
SAM 9	04.7.24.m	✓	✓	✓	×	×
	SAM 9.3	✓	✓	✓✓	×	✓
	SAM 9.4	✓	✓	×	×	✓
	SAM 9.2	✓	✓	××	×	✓
SAM 8	SAM 8.5	✓	✓	××	✓	✓

Paleosol	Nodules	Not Groundwt. or Lacus.	Stage II or I	Significant difference between Micrite spar[a]	Calcite	Crystal size <20µm
	04.7.24.l	✓	✓	✓	×	✓
	SAM 8.2	✓	✓	××	✓	✓
	SAM 8.3	✓	✓	✓✓	✓	✓
	SAM 8.4	✓	✓	×	✓	✓
	SAM 8.1	✓	✓	✓✓	✓	✓
SAM 5a	04.7.24.k	✓	×	?	×	×
	04.7.24.k.I	✓	×	?	×	×
	04.7.24.k.II	✓	×	?	×	×
	04.7.24.k.III	✓	×	?	×	×
SAM 20	04.7.24.j	✓	✓	✓	×	✓
	SAM 20.2	✓	✓	✓	×	✓
	SAM 20.3	✓	✓	×	×	✓
	SAM 20.4	✓	✓	××	×	✓
	SAM 20.5	✓	✓	✓✓	×	✓
SAM 19a	04.7.24.i	✓	×	?	×	✓
SAM 18	04.7.24.h	✓	×	?	×	✓
2004 field season	04.7.24.g	✓	×	?	×	✓
2004 field season	04.7.24.f	✓	×	?	×	×
SAM 17	SAM 17.1	✓	✓	×	✓	✓
	SAM 17.2	✓	✓	✓✓	✓	✓
	SAM 17.3	✓	✓	×	✓	✓
	SAM 17.4	✓	✓	×	✓	✓
SAM 14	SAM 14.1	✓	✓	××	✓	✓
	SAM 14.2	✓	✓	××	✓	✓
	SAM 14.3	✓	✓	×	✓	✓
SAM 13	SAM 13.3	✓	✓	××	✓	×
	SAM 13.4	✓	✓	××	✓	✓
	SAM 13.5	✓	✓	××	✓	✓
	SAM 13.2	✓	✓	✓✓	✓	✓
	SAM 13.1	✓	✓	✓✓	✓	✓
SAM 21	SAM 21.1	✓	✓	×	✓	✓
	SAM 21.2	✓	✓	×	✓	✓
	SAM 21.3	✓	✓	×	✓	✓
	SAM 21.4	✓	✓	××	✓	✓
	SAM 21.5	✓	✓	✓	✓	✓
SAM 22	SAM 22.1	✓	✓	?	✓	✓
SAM 23	SAM 23.2	✓	×	××	×	✓
	SAM 23.3	✓	×	××	×	✓
SAM 24a	SAM 24.1	✓	✓	××	✓	✓
SAM 24b	SAM 24.3	✓	✓	?	✓	✓
	SAM 24.4	✓	✓	?	✓	✓
SAM 24c	SAM 24.5	✓	✓	××	✓	✓
	SAM 24.6	✓	✓	××	✓	✓
SAM 24d	SAM 24.8	✓	✓	××	✓	✓
	SAM 24.9	✓	✓	××	✓	✓
	SAM 24.10	✓	✓	✓✓	✓	✓
	SAM 24.11	✓	✓	××	✓	✓

Paleosol	Nodules	Not Groundwt. or Lacus.	Stage II or I	Significant difference between Micrite spar[a]	Calcite	Crystal size <20µm
SAM 24e	SAM 24.12	✓	✓	×	✓	✓
	SAM 24.13	✓	✓	××	✓	✓
	SAM 24.14	✓	✓	×	✓	✓
2004 field season	04.7.24.d	✓	✓	✓✓	✓	✓
2004 field season	04.7.24.d	✓	✓	✓	✓	✓
2004 field season	04.7.24.c	✓	×	?	×	✓
2004 field season	04.7.24.b	✓	×	✓✓	×	✓
2004 field season	04.7.24.a	✓	×	?	×	✓
2004 field season	04.7.24.a.I	✓	×	?	×	✓
2004 field season	04.7.24.a.II	✓	×	?	×	✓
2004 field season	04.7.23.o	✓	✓	✓✓	×	✓
2004 field season	04.7.23.n	✓	×	?	×	✓
2004 field season	04.7.23.l	✓	×	?	×	×
2004 field season	04.7.23.k	×	×	?	×	✓
2004 field season	04.7.23.j	✓	✓	✓✓	×	✓
2004 field season	04.7.23.h	✓	✓	✓✓	×	✓
2004 field season	04.7.23.I	✓	✓	✓✓	×	✓
2004 field season	04.7.23.i.I	✓	✓	×	×	✓
2004 field season	04.7.23.i.II	✓	✓	×	×	✓
2004 field season	04.7.23.g	✓	×	?	×	✓
2004 field season	04.7.23.f	✓	×	?	×	✓
TUY 53	04.7.26.b	✓	✓	?	×	✓
TUY 54	04.7.26.d	✓	×	?	×	✓
	04.7.26.c	✓	×	?	×	✓
	04.7.26.c.I	✓	×	?	×	✓
	04.7.26.c.II	✓	×	?	×	✓
TUY 55	04.7.26.f	✓	×	?	×	✓
	04.7.26.e	✓	×	?	×	✓
TUY 56	04.7.26.g	✓	✓	?	×	✓
TUY 57	04.7.26.h	✓	✓	?	×	✓
TUY 58	0.4.7.26.i	✓	×	?	×	✓
	0.4.7.26.j	✓	×	?	×	✓
TUY 59	0.4.7.26.k	✓	×	?	×	✓
TUY 61	0.4.7.26.l	✓	×	?	×	✓
TUY 1	0.4.7.26.o	✓	×	?	×	✓
	0.4.7.26.n	✓	×	?	×	✓
	0.4.7.26.m	✓	×	?	×	✓
TUY 52	0.4.7.26.p	✓	×	?	×	✓
TUY 56	0.4.7.26.q	✓	✓	?	×	✓
	04.7.26.q.I	✓	✓	?	×	✓
	04.7.26.q.II	✓	✓	?	×	✓
	04.7.26.q.III	✓	✓	?	×	✓
TUY 49	0.4.7.26.r*	✓	×	?	×	✓
TUY 2	0.4.7.26.s	✓	×	?	×	✓

Paleosol	Nodules	Not Groundwt. or Lacus.	Stage II or I	Significant difference between Micrite spar[a]	Calcite	Crystal size <20µm
TUY 3	0.4.7.26.t	✓	×	?	×	✓
TUY 54	04.7.26.u*	✓	×	?	×	✓
TUY 23	TUY 23.4	✓	✓	✓	×	✓
	TUY 23.2	✓	✓	××	×	✓
	TUY 23.3	✓	✓	✓✓	×	✓
TUY 27	TUY 27.3	✓	✓	××	×	✓
	TUY 27.7	✓	✓	××	×	✓
TUY 31	TUY 31.3	✓	✓	✓✓	×	✓
	TUY 31.4	✓	✓	××	×	✓
TUY 38	TUY 38.1	✓	×	✓✓	×	✓
KRA 2	KRA 2.2	✓	✓	××	✓	×
KRA 1	KRA 1.3	✓	✓	××	✓	×
KRA 7a	KRA 7.12	✓	✓	××	✓	×
KRA 7d	KRA 7.4	✓	✓	××	✓	×
KRA 7e	KRA 7.3	✓	✓	?	✓	×
KRA 5a	KRA 5.4	✓	×	××	✓	×
KRA 5c	KRA 5.11	✓	✓	××	✓	×
KRA 5d	KRA 5.14	✓	✓	××	×	×
MES 7	MES 7.2	✓	✓	?	✓	×
MES 3	MES 3.2	✓	✓	×	✓	✓
	MES 3.3	✓	✓	××	✓	✓
MES 1	MES 1.2	✓	✓	××	✓	✓
	MES 1.3	✓	✓	×	✓	✓
	MES 1.4	✓	✓	×	✓	✓
MES 8	MES 8.4	✓	✓	✓✓	✓	×
	MES 8.5	✓	✓	××	✓	×
	MES 8.2	✓	✓	✓✓	✓	✓
	MES 8.1	✓	✓	✓✓	✓	×
MES 10	MES 10.3	✓	✓	✓	✓	×
	MES 10.4	✓	✓	✓✓	✓	×
	MES 10.5	✓	✓	✓	✓	×
MES 15	MES 15.3	✓	✓	××	✓	×
	MES 15.5	✓	✓	××	✓	×
MES 16	MES 16.3	?	✓	××	✓	×
	MES 16.4	?	✓	××	✓	×
	MES 16.5	?	✓	××	✓	×
	MES 16.6	?	✓	✓✓	✓	✓
	MES 16.1	?	✓	✓✓	✓	✓
	MES 16.2	?	✓	×	✓	✓
MES 17	MES 17.10	?	✓	××	✓	✓
	MES 17.9	?	✓	✓✓	✓	✓
	MES 17.8	?	✓	××	✓	✓

Table 4.2 Summary of the screening results for all isotope results from Russia. Ticks refer to if the sample agrees with the statement in the column heading. In the significant difference between micrite and spar column two ticks is that the micrite from that nodule was significantly different from spar taken from the same nodule. One tick is that no spar was analysed from that nodule but the micrite was significantly different from the spar content of the nodules from the rest of the paleosol. One cross means the micritic values were the same as spar from the rest of the paleosol and two cross means the micritic component was the same as spar values from the same nodule .?refers to not enough data to make a classification (see Appendix A2.1 for values). [a]For explanations of significance see text (section 4.3.4).

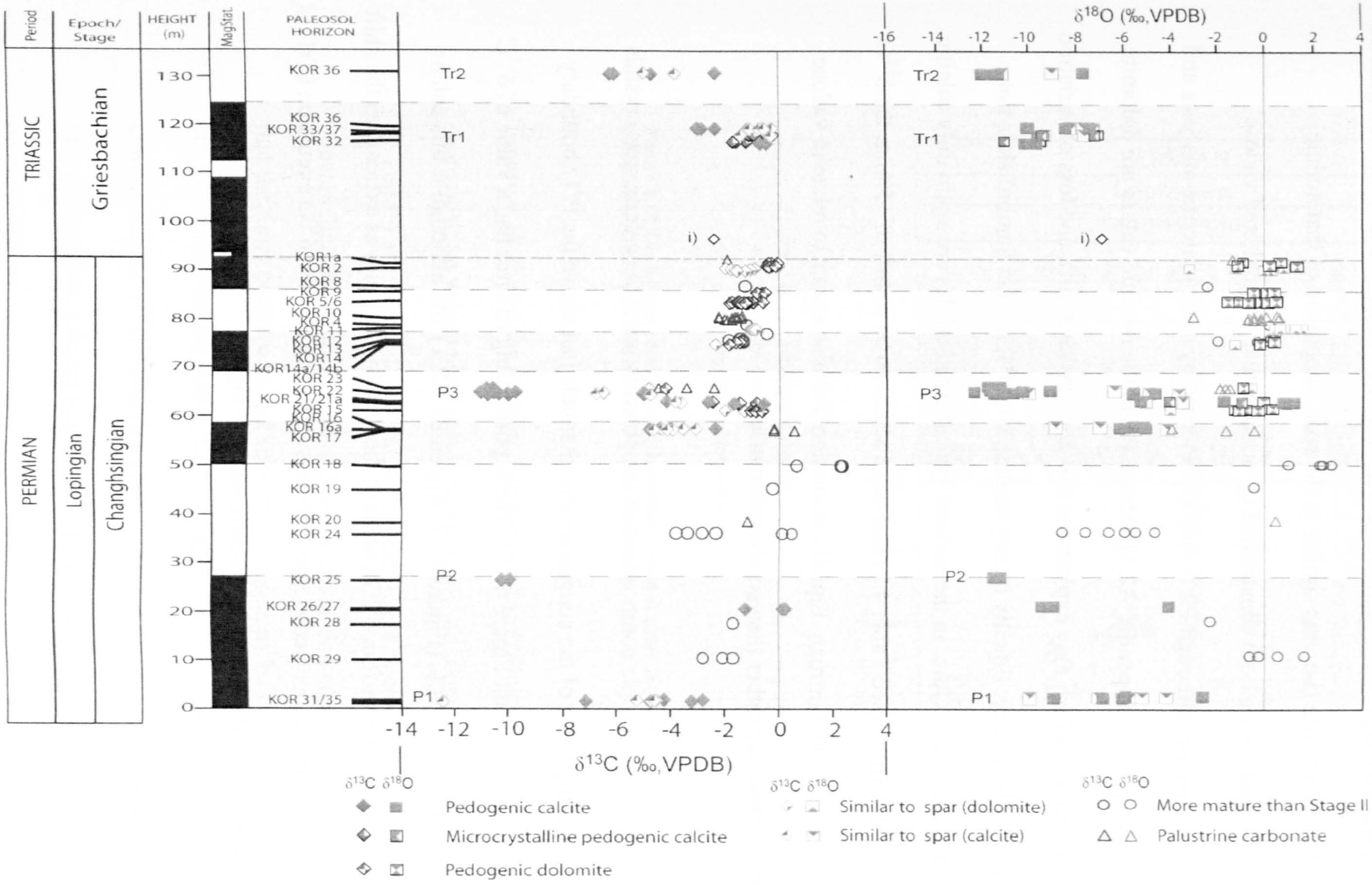

Figure 4.17 The isotope results from Boyevaya Gora screened using the criteria in Table 4.1. For descriptions of the paleosols and stratigraphic information see Chapter 3. i) the isotopic value of pore filling calcite from sandstones just above the P/Tr boundary.

Figure 4.17 shows the screened isotopic results from Boyevaya Gora. Using this screening it is now clear that magnitude excursion P1 is actually due to later diagenetic alteration of the micrite (i.e. it is similar to the spar component of that nodule). However, P2 and P3 are both constrained by nodules that are unaltered vadose pedogenic carbonate, although P2 is only represented by only 4 micritic analyses and one spar (Figure 4.17 Appendix A2.1). Above P3 all the micritic values are dolomite, rather than calcite, which may explain the apparent positive shift, and loss of variation up to the P/Tr boundary. Equally it may explain why P4, seen at Sambullak is not observed at Boyevaya Gora. In the earliest Triassic the nodules are again only calcitic rather than dolomitic (see Table 4.2) and there seems to be a shift of –5‰ in the $\delta^{18}O$ values relative to the Permian. Equally excursion Tr2 also seems to relate to vadose pedogenic carbonate rather than an alteration effect.

To investigate the isotopic composition of the phreatic water the calcite spar crystals found cementing some of the conglomeratic channels just above the P/Tr boundary were analysed (see (i) on Figure 4.17). These pore filling calcites had a value of $\delta^{13}C$ –2.21‰ and $\delta^{18}O$ –7.29‰ (Figure 4.17, Appendix A2.1) and although it this calcite does show a negative shift in $\delta^{18}O$ values in the Triassic, it is not as extreme as the shift in as the unaltered vadose pedogenic calcites suggesting that the $\delta^{18}O$ excursion (Tr1) is an atmospheric event rather than phreatic water overprint.

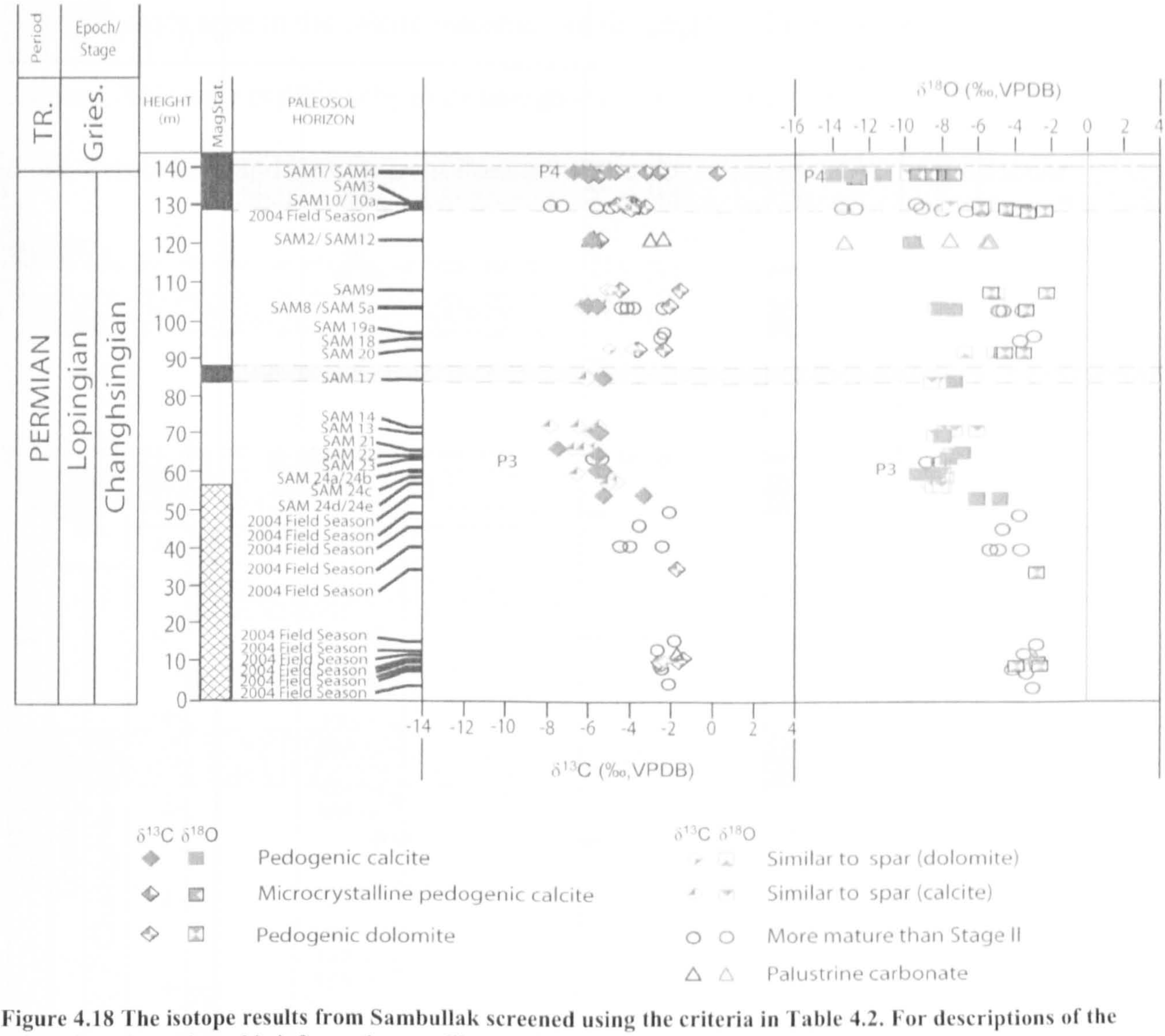

Figure 4.18 The isotope results from Sambullak screened using the criteria in Table 4.2. For descriptions of the paleosols and stratigraphic information see Chapter 3.

Figure 4.18 shows the isotopic variation at Sambullak. As with Boyevaya Gora the more positive values are a result of dolomite and more mature horizons. The excursions P3 and P4 are both still present in the vadose pedogenic micrite. Although below 50m it appears that all of the section is dolomitic (see Appendix A2.1) which would suggest that the more positive values seen below this may be related to this mineralogical change rather than an atmospheric change or an increase in paleosol maturity. When considering the $\delta^{18}O$ excursion (P4) it appears that the more positive values relate to the micro crystalline calcites and those that relate to the pedogenic calcite are the most negative values.

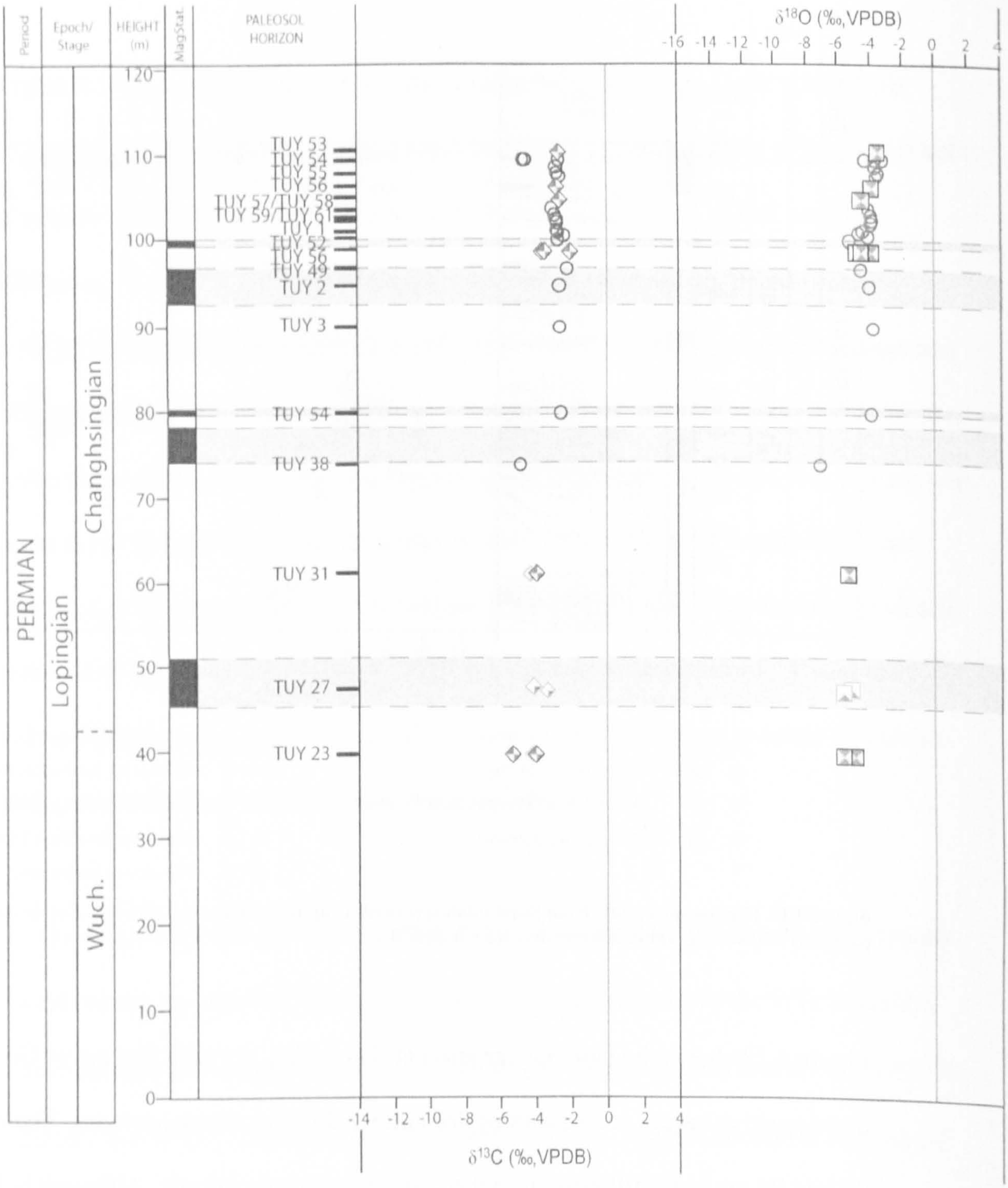

Figure 4.19 The isotope results from Tuyembetka screened using the criteria in Table 4.2. For descriptions of the paleosols and stratigraphic information see Chapter 3.

Tuyembetka has a restricted isotopic range compared with other sections and does not show any of the excursions seen in the other Permian sections (Figure 4.19). This is because the carbonate material from Tuyembetka is all dolomite rather than calcite (Appendix 2.1 and 2.4). As recorded in other sections, especially Boyevaya Gora (Figure 4.17), there is some isotopic variation within the dolomite which may follow the

isotopic trends seen in the calcite material, but the amount of variation is significantly reduced. This may explain why even though it overlaps with the sections at Boyevaya Gora, Sambullak, and Krasnogor it does not show any of the variation seen on those curves.

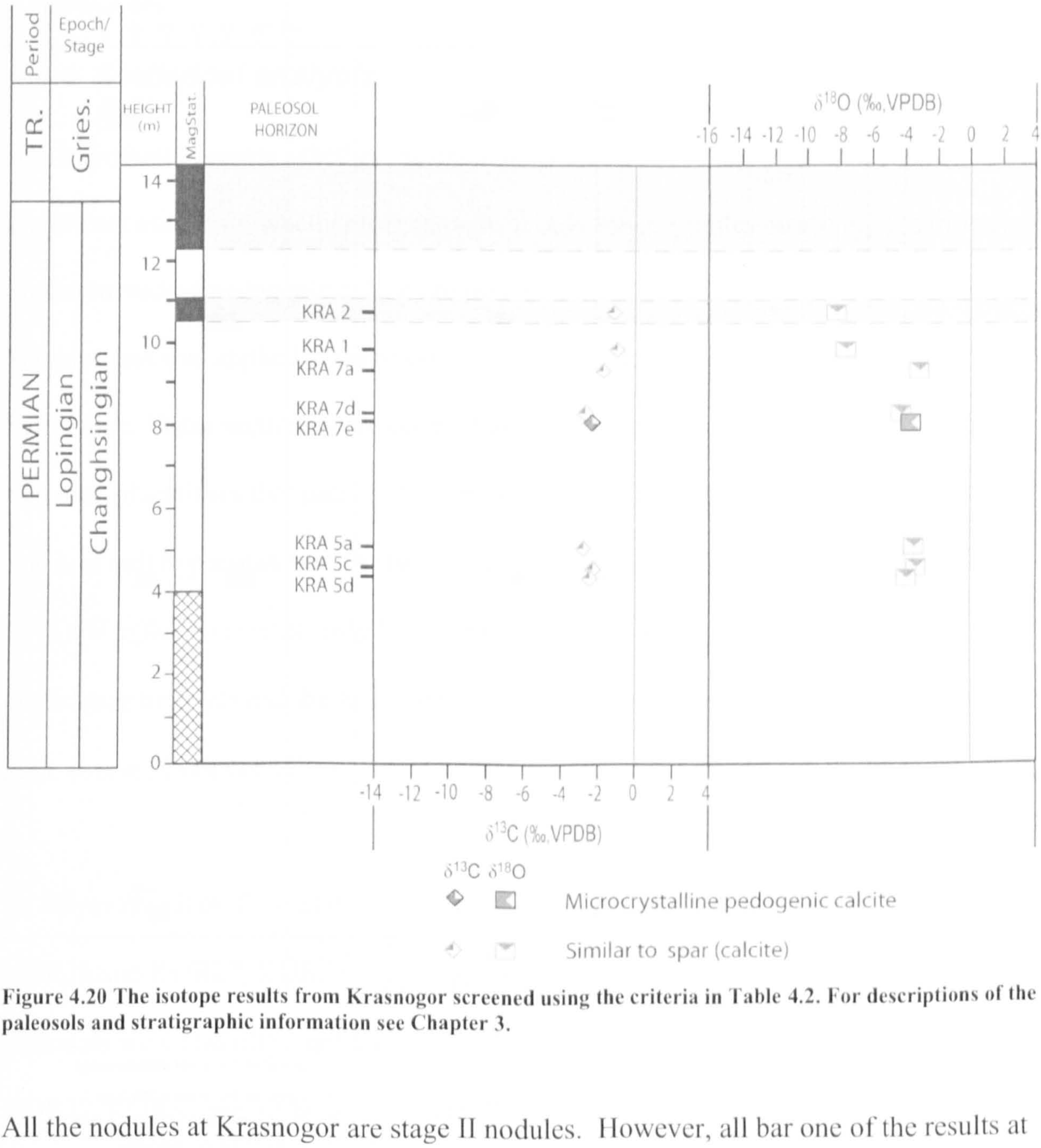

Figure 4.20 The isotope results from Krasnogor screened using the criteria in Table 4.2. For descriptions of the paleosols and stratigraphic information see Chapter 3.

All the nodules at Krasnogor are stage II nodules. However, all bar one of the results at Krasnogor appear to be over printed by the spar forming event. This is probably due to the fact that, as stated in Chapter 3, the Krasnogor palaeosols were formed on more porous fine sandstone rather than the mud and siltstone seen elsewhere in the basin. The one sample that has not been over printed by the spar forming event has values very

close to those which have been altered. This may suggest that this nodule was also altered but as it lacked any cracks or voids, there was nowhere for the spar to form. Alternatively the spar formed very early in the diagenetic history of the rock and had a similar geochemical signal to the meteoric water.

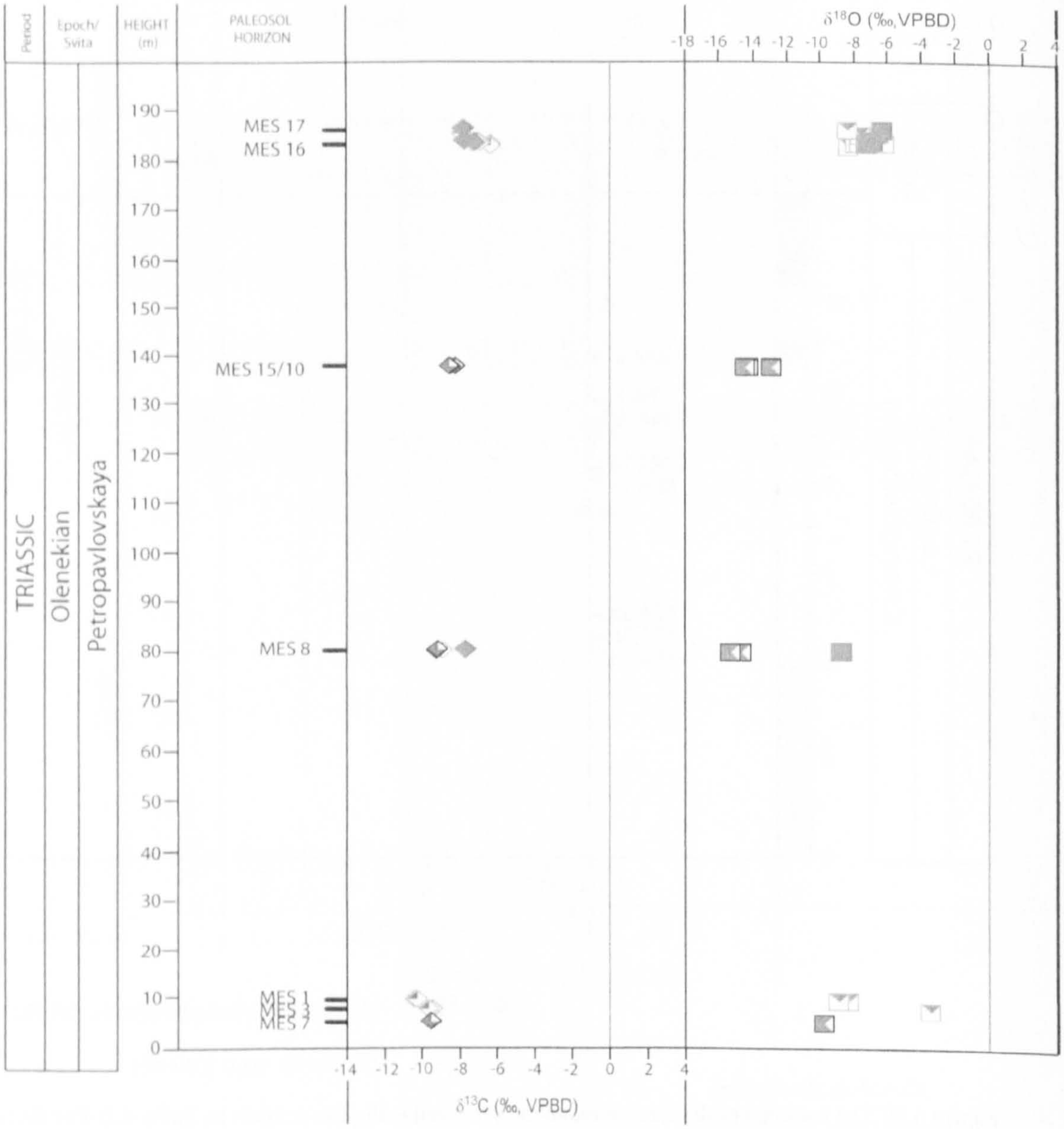

Figure 4.21 The isotope results from Mescheryakovka screened using the criteria in Table 4.2. For descriptions of the paleosols and stratigraphic information see Chapter 3.

Mescheryakovka is the only Olenekian section analysed and appears to have significantly more negative isotopic values than the Permian (minimum values of $\delta^{13}C$ –10.62‰ and $\delta^{18}O$ –17.66‰) (Figure 4.21). Figure 4.21 shows that most of these

extreme negative values are the result of a spar overprint or related to potential groundwater alteration. There are four analysis which have not been overprinted by the spar forming or groundwater alteration (MES8.2, MES16.6, MES16.1, MES17.9 see Table 1and Appendix 2.1). These have remarkably similar isotopic values of $\delta^{13}C$ –7.71‰ (±0.28‰ 1σ std) and $\delta^{13}C$ –8.15‰ (±1.22‰ 1σ std).

4.4.1 Statistical analysis

It is important to assess whether the excursions identified in the Russian data are significant and, if so, whether this changes if only those nodules positively identified as unaltered vadose pedogenic calcite are used (Table 4.2). For this purpose the Mann-Whitney test was applied to consecutive screened paleosols at Boyevaya Gora and Sambullak. These sections were selected as they are the only ones which had significant numbers of analyses that passed all screening tests. The Mann-Whitney test assumes that as a null hypothesis that the two datasets are from the same population (Conover 1971). If $p \leq 0.1$ it is statistically likely that the null hypothesis is invalid (to a 95% confidence interval) and the two datasets are from separate populations (Dr R. Moyeed *pers. comm.*; Conover 1971).

At Boyevaya Gora, P1 was defined as comprising paleosol KOR35; P2 as KOR25, KOR26 and KOR27, KOR24; and P3 as KOR22 and KOR23. All the rest of the paleosols were classified as 'Background Permian' apart from KOR36, KOR33, KOR37, KOR32 and KOR34 which are Triassic (see Figure 4.17 and Appendix 2.5 for full results). At Sambullak, P3 is defined as comprising SAM23, SAM22, SAM13, SAM14 and SAM17; and P4 is SAM1, SAM4, SAM3, SAM2 and SAM12. The rest of the isotopic values from the paleosols are defined as being 'Background Permian'

Section	Test	All data (p values)		Pedogenic calcite only (p values)	
		$\delta^{13}C$	$\delta^{18}O$	$\delta^{13}C$	$\delta^{18}O$
Boyevaya Gora	P1 (n=4,3) v 'Permian background' (n=119,13)	**0.0022**	**0.0011**	**0.0803**	0.1064
	P2 (n=4,3) v 'Permian background'(n=119,13)	**0.0007**	**0.0000**	**0.0693**	0.2528
	P3 (n=24,14) v 'Permian background' (n=119,13)	**0.0000**	**0.0000**	**0.0000**	**0.0005**
	Triassic (Tr1) (n=42,10) v 'Permian background' (n=119,13)	0.6073	**0.0000**	0.4757	**0.0003**
Sambullak	P3 (n=31,7) v "Permian background' (n=49,5)	0.5036	**0.0000**	1.0000	0.5160
	P4 (n=34,4) v 'Permian background' (n=49,5)	**0.0004**	**0.0000**	0.2703	**0.0200**

Table 4.3 Summary of statistical tests using the Mann-Whitney test (full results see Appendix 2.5) See section 1.2 for descriptions of the excursions. The bold values are those where there is a significant difference between the values of the excursions and those of the background (with a confidence interval of 95%). The n values are the numbers of analysis in the statistical test, the first is the unscreened number and the second is the screened number.

Table 4.3 shows the summary of all the statistical tests. When all the isotope results are compared anomalies P1, P2, P3 and P4 are significant when all the data is considered. When only those analyses that pass all the criteria described in Table 4.2 are subjected to statistical analysis the picture changes. At Boyevaya Gora (Table 4.3) it now appears that the $\delta^{18}O$ excursions P1 and P2 are no longer significant. However, P3 and the oxygen excursion into the Triassic (Tr1) are both still significant as is the upper oxygen excursion at Sambullak (P4). Equally so are the $\delta^{13}C$ excursions P1, P2, P3 and P4. Both the lower carbon and oxygen excursions at Sambullak (P3) are no longer significant to a 90% confidence interval. However, especially when comparing the screened values there are very small numbers of analyses (see Appendix A2.5) and at such low numbers of input values the test may not be accurate as the values measured may not represent the total population distribution of the data (Dr R. Moyeed *pers. comm.*). The screening proposed in Table 4.2 is to remove some of the statistically significant excursions identified in the isotope signal (section 4.2).

4.5 Discussion

4.5.1 Dolomite in the Russian sections

The vast majority of the carbonate material in the studied sections in the Southern Urals is formed primarily of poorly cemented micro- to cryptocrystalline micritic mud, suggesting a pedogenic origin for the calcrete in these sections (sees Section 4.3.3). This is supported by the predominance of carbonate nodules, rather than hardpans and the presence of floating grains and clotted textures within the nodules themselves (cf. Quast *et al.* 2006). Unstained petrographic observation of the micritic material supports this. XRD analyses of the micritic carbonate and subsequent dolomite-specific staining of the petrographic slides has revealed that some of the nodules contain micritic dolomite. Dolomite is commonly associated with diagenesis in sedimentary rocks (Leeder 1999) but this conflicts with the petrographic morphology observations of the nodules.

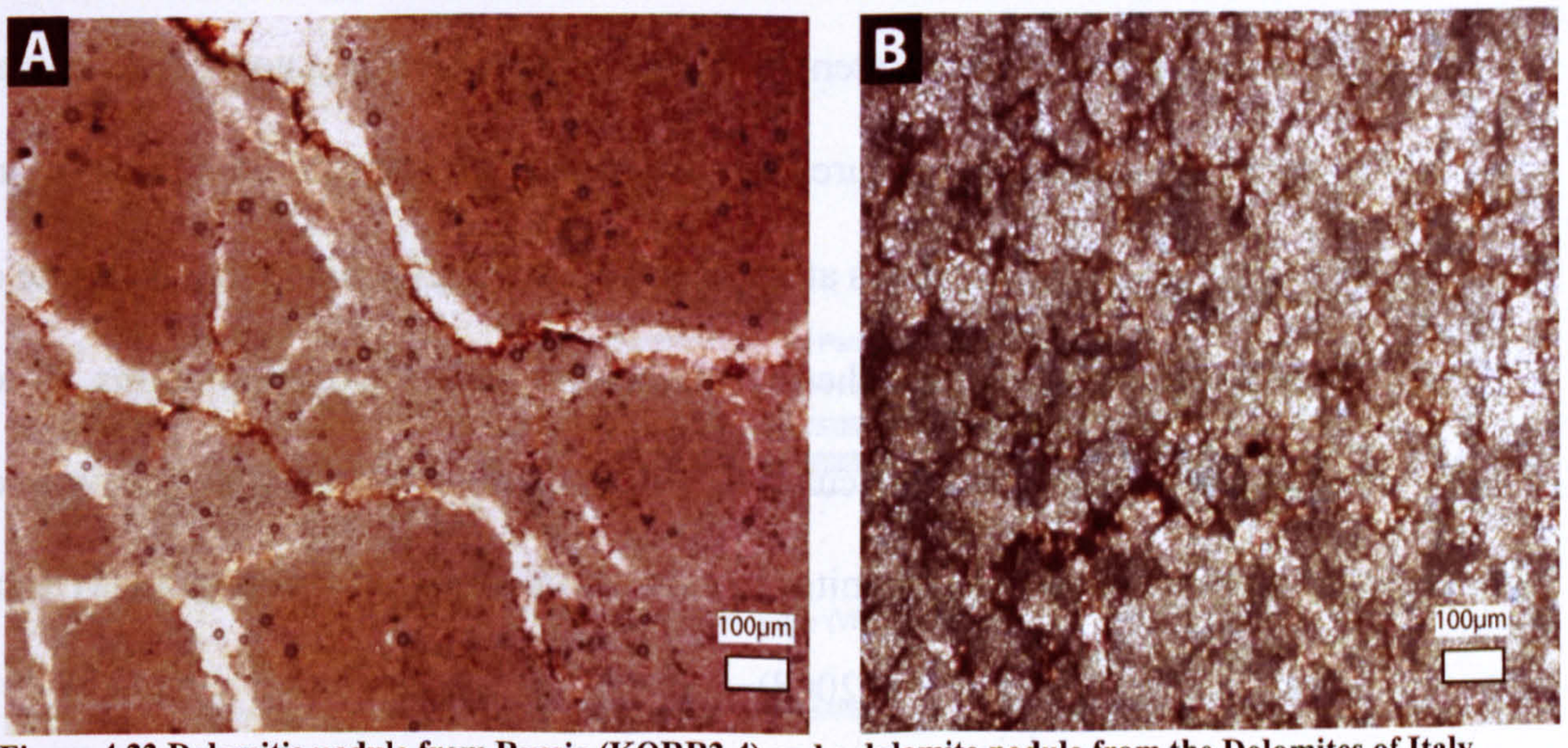

Figure 4.22 Dolomitic nodule from Russia (KORR2.4) and a dolomite nodule from the Dolomites of Italy (RDA 41) Scale bar = 100µm.

Comparing the texture of dolomitic nodules from Russia with diagenetically altered nodules from the Italian Dolomites (Figure 4.22, Appendix 5) shows that unlike the Italian dolocretes, those from Russia still preserve their primary pedogenic features (Figure 4.22) suggesting that the dolomite is not caused by diagenetic recrystallisation.

Another possibility is that the dolomite in Russian paleosols is derived from detrital dolomite from the source area of the fluvial sediments (in this case the Ural Mountains, see Chapter 3). This could explain the presence of dolomite in apparently pedogenic nodules (cf. Kraimer *et al.* 2005). The XRD analysis of different particle sizes within a nodule suggests that, unlike the nodules analysed by Kraimer *et al.* (2005), the dolomite derives primarily from the finest fraction which implies that it is related to the primary, micritic part of the nodule rather than clastic grains contained within matrix in which the nodules formed.

Primary pedogenic dolomite, formed through surface and groundwater processes rather than diagenetic or metamorphic processes has been recorded by several authors (Watts 1980, Wright and Tucker 1991, Colson and Cojan 1996; Alonso-Zarza *et al.* 1998; Capo *et al.* 2000; Bustillo and Alonso-Zarza 2007) and is usually associated with influence from lacustrine waters. Some have disputed if it is possible to crystallise dolomite at surface temperatures and pressures. Sherman and Barak (2000), in laboratory-based experiments at 25°C and 0.1 MPa CO_2 found that dolomite cannot directly precipitate at atmospheric temperatures and CO_2 concentrations. However, experiments using microbial cultures in both the field and laboratory have been shown to produce precipitated dolomites in natural waters at surface conditions (Roberts *et al.* 2004; Sánchez-Román *et al.* 2008).

There are two types of dolomitic paleosols present within the Russian sections: type A are those that are related to minor lacustrine limestones and as such are palustrine in origin (cf. Alonso-Zarza 2003); type B have no evidence of alteration or palustrine influence and yet the crypto- and microcrystalline component are formed principally dolomite.

Type A dolomitic profiles can be explained as there are many examples of such palustrine dolocretes in the geological record (Wright and Tucker 1991, Alonso-Zarza 2003). Similar examples have been recorded in Spanish Miocene dolocretes associated with groundwater and palustrine units (Alonzo-Zarza *et al.* 1998). Calvo *et al.* (1995) record dolomite occurring in soils close to lake margins that manifests as a crypto- to microcrystalline micrite nodules in the soil. It is thought that such asymmetric nodular dolocretes are precipitated in the vadose zone as the lacustrine body dried out (Colson and Cojan 1996; Quast *et al.* 2006). In semiarid climatic zones, evaporation of these ephemeral lakes would produce magnesium-rich waters which would precipitate dolomite rather than calcite (cf. Calvo *et al.* 1995). In such a system del Cura *et al.* (2001) suggest that cryptocrystalline (1-2μm crystals) dolomites can form directly from lake waters with an elevated carbonate/bicarbonate concentration. They suggest that the carbonate alkalinity will promote dolomite formation even at Mg/Ca ratios near 1, as there is plentiful CO_3^{2-} solute present.

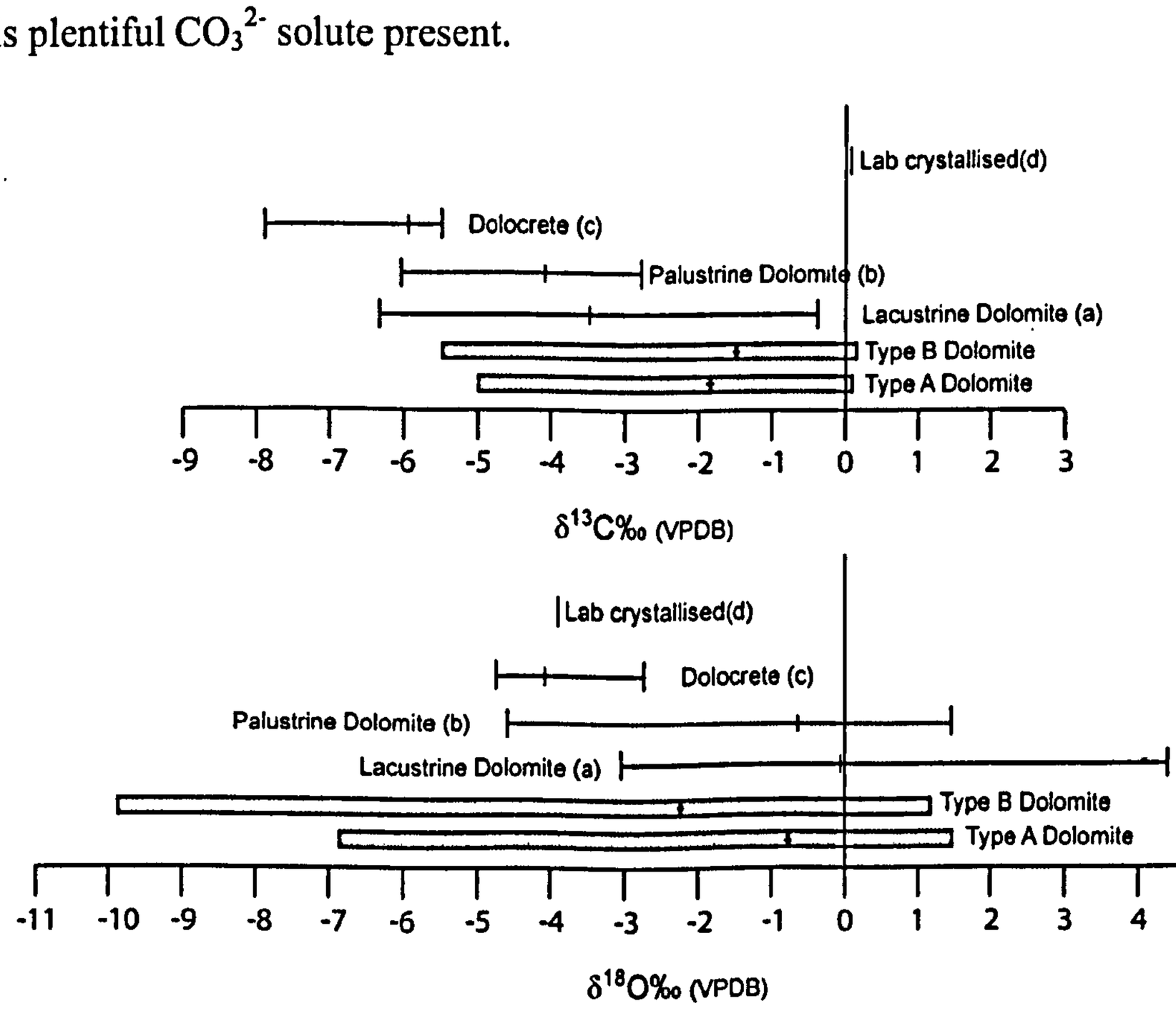

Figure 4.23 The ranges and medians (median represented by tick) of Type A and Type B dolomite from this study compared to isotope results from other studies. (a) is lacustrine dolomite from the Pliocene central Spain (del Cura *et al.* 2001). (b) is palustrine dolomite values from the Madrid basin in the Palaeogene (Bustillo *et al.* 2002). (c) is lake margin dolocretes from the Middle Miocene, in the Madrid basin Spain (Calvo *et al.* 1995). (d) are the values produced by lab based experiments using microbial precipitation (Roberts *et al.* 2004).

The $\delta^{13}C$ ranges of the Russian Type A dolomite fall within the ranges found in other lacustrine-formed dolomites (Figure 4.23). Similar values have been observed in the Pliocene of central Spain by del Cura *et al.* (2001). The relatively light $\delta^{13}C$ values (0 to–6‰) recorded in Russia (Figure 4.23) may suggest that plants had a role in the development of the dolomite (Calvo *et al.* 1995). Alternatively it may be a simple reflection of the more positive $\delta^{13}C$ atmospheric values in the Permian compared to the Cenozoic (cf. Veizer *et al.* 1999). Dolomite nodules associated with ephemeral lakes may have formed from a complex interplay between the desiccation of these bodies and the subsequent soil that formed after or during this process (Colson and Cojan 1996). The link between these type A dolomitic paleosols and lacustrine deposits is irrefutable as thin (5–6cm) limestones containing ostracods have been found as part of these soils.

A possible environmental analogue is the Loboi plain wetlands in Kenya (Bustillo and Alonzo-Zarza 2007). In periods of exceptionally heavy rainstorms, a river diversion takes place forming a wetland that becomes a shallow freshwater lake, which then evaporates producing progressively more saline waters. This saline water circulates through the surrounding soils and forms calcrete and dolocrete.

The $\delta^{18}O$ ranges of Type B dolomite sit partially outside the range of the lacustrine and lacustrine–associated dolomite (Figure 4.23). Equally the stratigraphic occurrence of Type B dolomite is harder to explain. Examples are found predominantly in paleosol horizons containing stage II carbonate nodules which are no different to their calcite counterparts. Equally they show no evidence of lacustrine influence, groundwater features or gleyed horizons (e.g. KOR6 Figure 4.24).

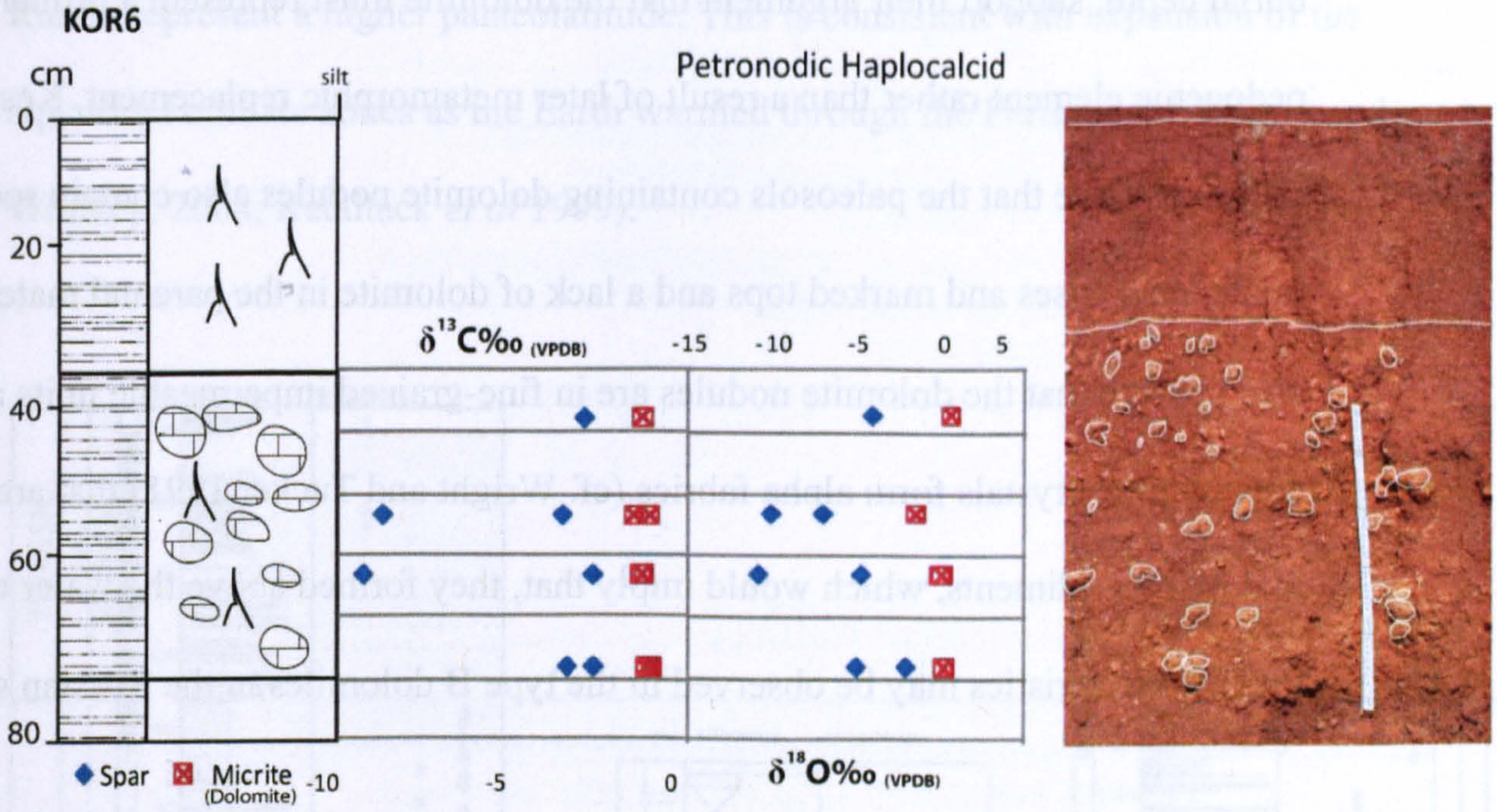

Figure 4.24 A typical paleosol containing Type B dolomitic nodules from Boyevaya Gora. Scale bar in photos is 50cm.

Type B dolomites are most evident in the 40 metres directly below the P/Tr boundary at Boyevaya Gora (Figure 4.17, Figure 4.25) where all the carbonate material is dolomite (see Appendix A2.1). This part of the section has the highest concentration of paleosols in the section. The paleosols have more developed Bk horizons than elsewhere in the section (up to stage V) and there is no evidence for ephemeral lakes associated with the paleosols. All paleosols are well rooted throughout with branching rootlets suggesting that the soil could not have been waterlogged for a prolonged period (Alonzo-Zarza 2003).

Paleosols showing a similar morphology as the Russian Type B dolomites have been previously identified in Vertisols from the Lower Permian (Wolfcampian to Leonardian) of New Mexico by Kessler *et al.* (2001) which at this time was at equatorial latitudes. These nodules are discrete, between <1cm to nearly 9cm in size, with a micritic texture to the dolomite crystals (≤30μm) and calcite filling the secondary veins. These observations, coupled with poor consolidation of the sediment and shallow

burial depth, support their argument that the dolomite must represent a primary pedogenic element rather than a result of later metamorphic replacement. Kessler *et al.* (2001) observe that the palcosols containing dolomite nodules also contain root traces, gradational bases and marked tops and a lack of dolomite in the parental material. They also observe that the dolomite nodules are in fine-grained impermeable units and that the dolomite crystals form alpha fabrics (cf. Wright and Tucker 1991) that are contained in dark red sediments, which would imply that, they formed above the water table. All these characteristics may be observed in the type B dolomites in the Russian sections.

Kessler *et al.* (2001) suggest that the origin of the dolomite crystallisation in their palcosols is a result of high Mg/Ca ratios caused by highly fluctuating water tables linked to high seasonality and a highly evaporative environment. Watts (1980) postulates that, in times of increased evaporation, magnesium will inhibit calcite nucleation and, if evaporation is greater than rate calcite nucleation, the Mg/Ca ratio would remain constant but the salinity would increase. Dolomite is then precipitated by 'forced crystallisation', and will thus not be in equilibrium with the precipitating fluids.

The type B dolocretes increase in occurrence after the negative $\delta^{13}C$ and $\delta^{18}O$ anomalies (excursion P3 see Figure 4.17) and below the P/Tr boundary at Boyevaya Gora and Sambullak (Figure 4.25). The soils of the lowest Triassic at Boyevaya Gora show no evidence ether Type A or B dolomite (Figure 4.25). This may suggest that the conditions that allowed the type B dolocrete to form may be directly related to the cause/consequences of the excursion P3. Using Kessler *et al.* (2001) as a guide, this suggests a dramatic increase in evaporation in the very latest Permian and a possible increase in seasonality. It must be noted that the example of Vertic dolosols in New Mexico is at near-equatorial palaeolatitude (Kessler *et al.* 2001) while the sections in

Russia represent a higher palaeolatitude. This is consistent with expansion of the equatorial climate zones as the Earth warmed through the Permian (cf. Kidder and Worsley, 2004; Retallack *et al* 1999).

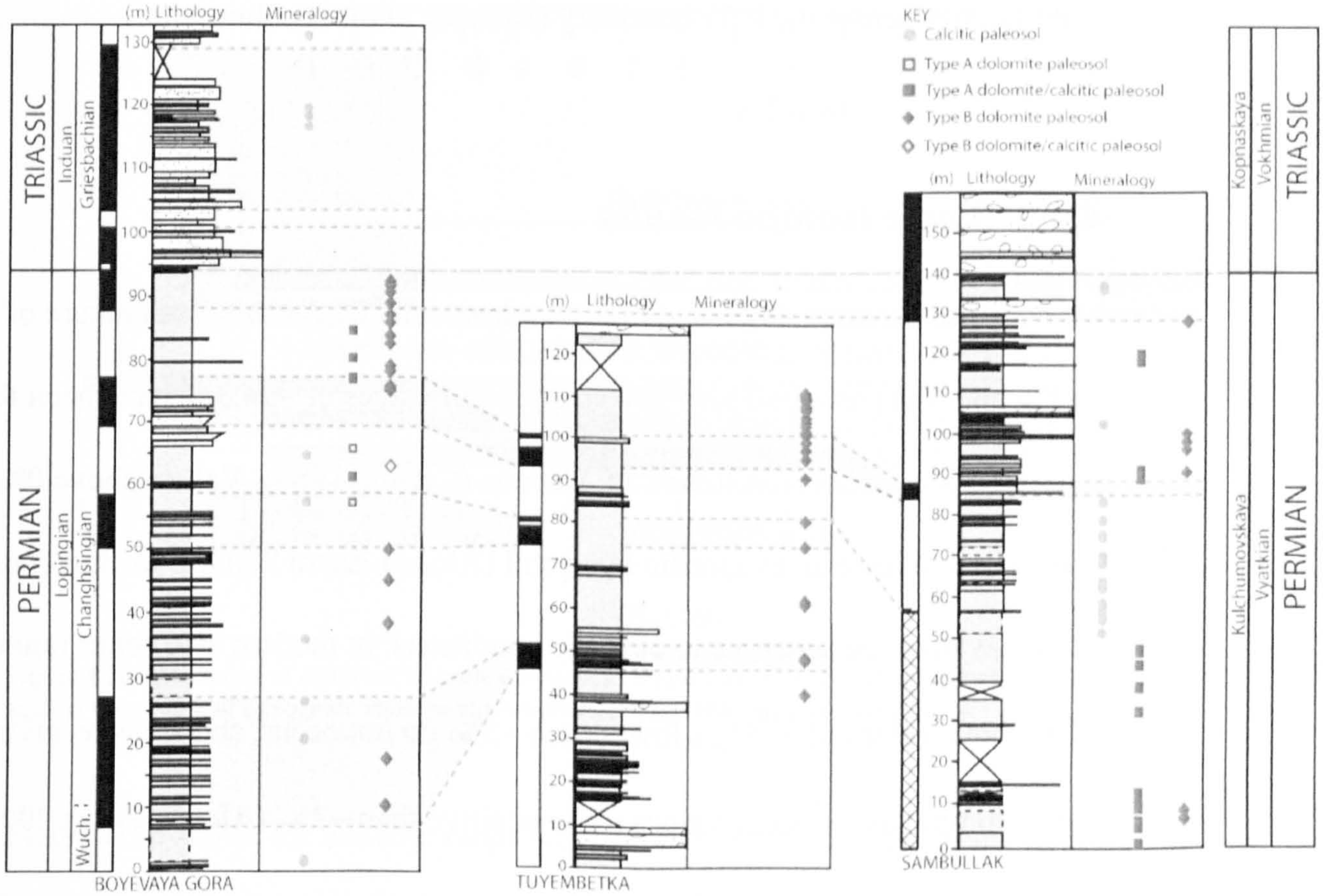

Figure 4.25 The distribution of Type A and B dolomite through the Permian sections in Russia. Note there is no pedogenic dolomite present in the Triassic (Kearsey et al. in submission).

The paleosols of the Triassic are, however, all calcitic and not dolomitic (Figure 4.21 and Figure 4.25), indicating that the specific conditions that resulted in the formation of primary, pedogenic dolomite peaked in the latest Permian, but did not continue in the Triassic. The complete absence of Lower Triassic dolocretes may indicate that evaporation rates, seasonality and monsoonal activity were reduced compared to the latest Permian. However, the Triassic paleosols at Mescheryakovka and Petropavlovka show evidence of fluctuating water tables, deep rooting, pedogenic slickensides, and pseudo-gleys, all indicating an increase in seasonality rather than a decrease (Chapter 3). An alternative hypothesis is that pedogenic dolomite formation is not linked to

extreme evaporation rates; rather it is reflecting a dramatic change in soil conditions across the P/Tr boundary. If bacteria were a key component in pedogenic dolomite formation (cf. Roberts *et al.* 2004, Sánchez-Román *et al.* 2008), then perhaps the disappearance of pedogenic dolocrete reflects a dramatic reduction in the soil microbial communities across the P/Tr boundary (Kearsey *et al.* in submission).

4.5.2 Stable isotope results

Modern and recent pedogenic carbonates have a $\delta^{18}O_{carb}$ isotopic signature of between −13‰ and 0‰ (Alonso-Zarza 2003), although values of −14.3‰ have been found in modern calcite from Saskatchewan, Canada (Cerling 1984). Values above 0‰ are considered to have an evaporitic overprint (Alonso-Zarza 2003; Dworkin *et al.* 2005). $\delta^{18}O_{carb}$ values are sensitive to climatic conditions: in modern arid zones (annual rainfall <250 mm), values of $\delta^{18}O_{carb}$ lower than −5‰ do not occur, and areas receiving less than 350mm have $\delta^{18}O_{carb}$ values more positive than −2‰ (Alonso-Zarza 2003). The only exceptions are areas influenced by monsoonal rains, which have especially negative isotopic values. Pedogenic carbonates from areas influence by monsoons can have $\delta^{18}O_{carb}$ values up to 6‰ more negative than carbonates of non-monsoonal areas (Alonso-Zarza 2003).

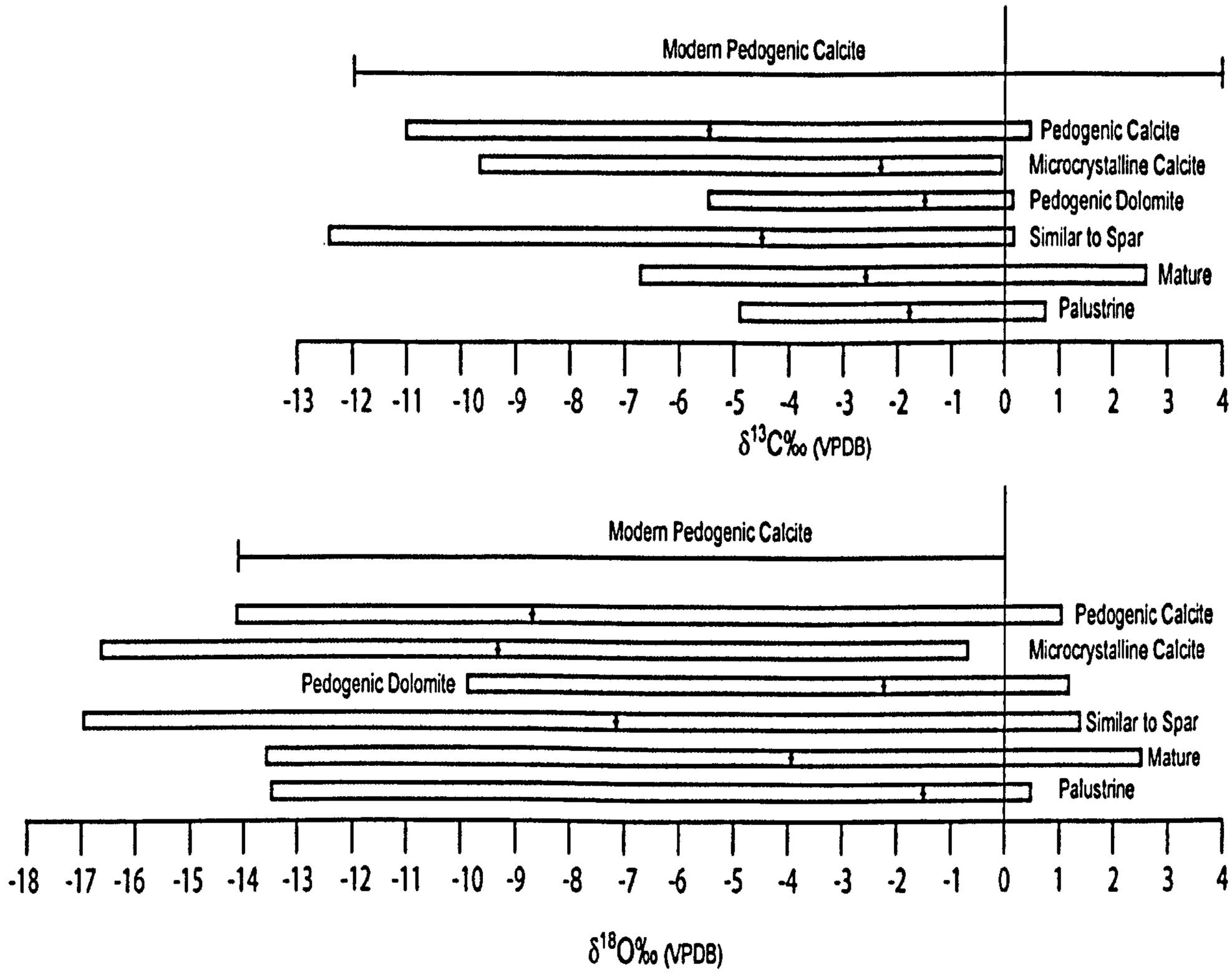

Figure 4.26 The ranges of different micritic carbonate components found in Russia (Appendix A2.1) plotted against the ranges of pedogenic modern carbonate (Cerling 1984, Alonso-Zarza 2003).

Figure 4.26 shows the isotopic ranges of the various types of carbonate identified in Table 4.2. from the Permian – Triassic paleosols of Russia. Apart from a few results from nodules where micritic values have been altered by the spar forming event, all values sit within the range of modern $\delta^{13}C_{carb}$ pedogenic calcite. The maximum $\delta^{18}O_{carb}$ values of the pedogenic calcite, pedogenic dolomite, mature calcrete and palustrine calcrete are within the range of modern calcite. However, all three types of carbonate have maximum values above 0‰ suggesting they may have been affected by evaporation. Those micritic values which were similar to the spar component of the nodule show the most negative isotopic values. This is similar to the observations of Cerling (1991) and Quast *et al.* (2006) where non-pedogenic and recrystallised calcretes are more negative than pedogenic values. In the three nodules where poikilotopic and neomorphic features were positively identified (SAM2.2, KOR2.4, KOR21.9) the spar component was significantly more negative than the micritic component (see Appendix

A2.1). For instance SAM2.2 has a micritic value of $\delta^{13}C_{carb}$ –2.48‰ and $\delta^{18}O_{carb}$ –5.52‰ and spar values of $\delta^{13}C_{carb}$ –4.24‰ and $\delta^{18}O_{carb}$ –10.66‰. The overlap between isotopic results from those nodules with micritic values similar to the spar component and those nodules which can be positively identified as being unaltered pedogenic calcite and dolomite (Figure 4.26) suggests that the spar-forming event happened at shallow depths or possibly even when the paleosol was active. This has been observed in modern Vertisols where microspars have grown in voids in an active soil (Ghosh *et al.* 2001). It also the micrite sampled from palustrine and paleosols more mature than stage II have a more positive range in $\delta^{18}O_{carb}$ than the other forms of carbonate observed in Russia (Figure 4.26) suggesting they are affected by evaporation to a greater extent than the stage II nodules, This was also recorded by Liu *et al.* (1996) and Ekart *et al.* (1999).

It is suggested that pedogenic carbonates with a crystal size >20μm are formed by groundwater rather than meteoric water (Quast *et al.* 2006), and it is evident that some of the microcrystalline carbonates have $\delta^{18}O_{carb}$ isotopic values which are more negative than those of the pedogenic calcite (Figure 4.26). This suggests that at least some of these calcretes may be formed from a different fluid to that which formed the pedogenic component. However, the fact that within many paleosol horizons, such as KOR15 (see Figure 4.17, Table 4.2 and Appendix A2.1), the vadose pedogenic values and microcrystalline values overlap suggesting they were formed from the same fluid.

	Age	Locality	$\delta^{13}C$ (‰,VPDB)	$\delta^{18}O$ (‰,VPDB)	Author
Triassic	234 Ma	Otter Sandstone (UK)	-9.9	-	Ekart *et al.* 2000
	Mid Triassic (240Ma)	Satpura basin, Central India	-5.8 to -7.2	-5.5 to -10.9	Ghosh *et al.*2001
	Lower Anisian (>242Ma)	Utah (USA)	-5.5 to -7.6	-3.7 to -6.2	Prochnow *et al.* 2006
	Upper Olenekian	Mescheryakovka	-7.29 to -7.92	-7.00 to -9.85	This Study
	Lowest Induan	Boyevaya Gora	-0.27 to -6.13	-7.36 to -11.77	This Study
	Earliest Triassic (28.0 metres [a])	Karoo (South Africa)	-5.2 to -5.7	-11.2 to -11.6	Tarbor *et al.*2007
Permian	Latest Permian (4.5 metres [a])	Karoo (South Africa)	-5.6 to -7.1	-13.4 to -14.1	Tarbor *et al.*2007
	Wuchiapingian to Changhsingian	Boyevaya Gora and Sambullak	0.46 to -11.06	1.03 to -14.15	This study
	251 Ma	Quartermaster (Texas)	-7.4	-	Ekart *et al.* 1999
	Mid-Permian (260mMa)	Satpura basin, Central India	-5.1 to -7.9	-8.4 to -14.4	Ghosh *et al.*2001

Table 4.4 Ranges from micritic pedogenic calcite values from other paleosol studies across the P/Tr boundary. [a] heights are from an arbitrary level placed at the bottom of Carlton heights, see Tarbor *et al.* (2007) for stratigraphic discussion. See figure 17, 18 and 21 and Appendix A2.1 for values from this study.

The negative (–14‰) $\delta^{18}O_{carb}$ unaltered pedogenic calcite values seen in the Permian at Sambullak and Boyevaya Gora compare well to previously published values which have been rigorously tested and identified as being pedogenic, especially the time equivalent values from the Karoo basin (Table 4.4). However, the positive end of this range is much greater than recorded in other studies, again suggesting that evaporation may have had some control over the isotope values recorded in Russia. Equally the range of $\delta^{13}C_{carb}$ unaltered pedogenic calcite values is greater in the Permian in Russia than in other studies (Table 4.4). In the lowest Triassic the $\delta^{18}O_{carb}$ values compare well with those from Karoo (Tarbor *et al.* 2007; Table 4.4) but the range of the $\delta^{13}C_{carb}$ is greater than that seen at Karoo (although the Karoo values are only based on two data points; cf. Tarbor *et al.* 2007). The $\delta^{13}C_{carb}$ values for the Olenekian from Russian compare well to those from the Lower Anisian of Utah while the $\delta^{18}O_{carb}$ values are slightly more negative than seen in Utah (Table 4.4).

Of the four excursions identified in the Permian (P1, P2, P3 and P4 – see Figure 4.17) P1 is probably a result of diagenetic alteration as the nodule that has the negative values (KOR 35.3) is within error of the spar values from that paleosol (Figure 4.17). P2 is

identified as being unaltered pedogenic calcite, although it is only constrained by two horizons (Figure 4.17; Appendix A2.1). The extremely negative values recorded at Boyevaya Gora for excursion P3 also appear to be pedogenic and many of the isotopically positive values recorded in the same paleosols (such as KOR22) are related to the spar forming event (Figure 4.17). P4 is also defined by unaltered pedogenic calcite at Sambullak (Figure 4.18). The reason it is not recorded at Boyevaya Gora is that at this point in the section all the pedogenic material is entirely dolomite rather than calcite, which shows more positive $\delta^{18}O_{carb}$ values than calcite (cf. Quast *et al.* 2006) (Figure 4.18). P4 at Krasnogor has the same isotopic values as the spar components of the same nodules suggesting that they are a result of the spar-forming event (Figure 4.20). However, the fact that P4 at Sambullak appears to be pedogenic, while at it Krasnogor is possibly altered, may suggest that the fluid that formed the spar at Krasnogor was similar to the pedogenic fluid at Sambullak as they both show the excursion. Finally, the Triassic excursion recorded at Boyevaya Gora in the $\delta^{18}O_{carb}$ values also appears to be pedogenic (Figure 4.17) especially as it is similar to vadose pedogenic values in Karoo of a similar age (Table 4.4).

Negative $\delta^{13}C_{carb}$ excursions in organic carbon, carbonate and bone, have been observed in many P/Tr sections round the world (e.g. Krull and Retallack 2001; deWit *et al.* 2002; Kidder and Woresley 2004; Payne *et al.* 2004; Retallack and Jahren 2008) and all have been linked to the cause or an effect of the mass extinction event. Most of these terrestrial excursions occur in the first few metres of the Triassic (cf. Retallack *et al.* 2005; Retallack and Jahren 2008).

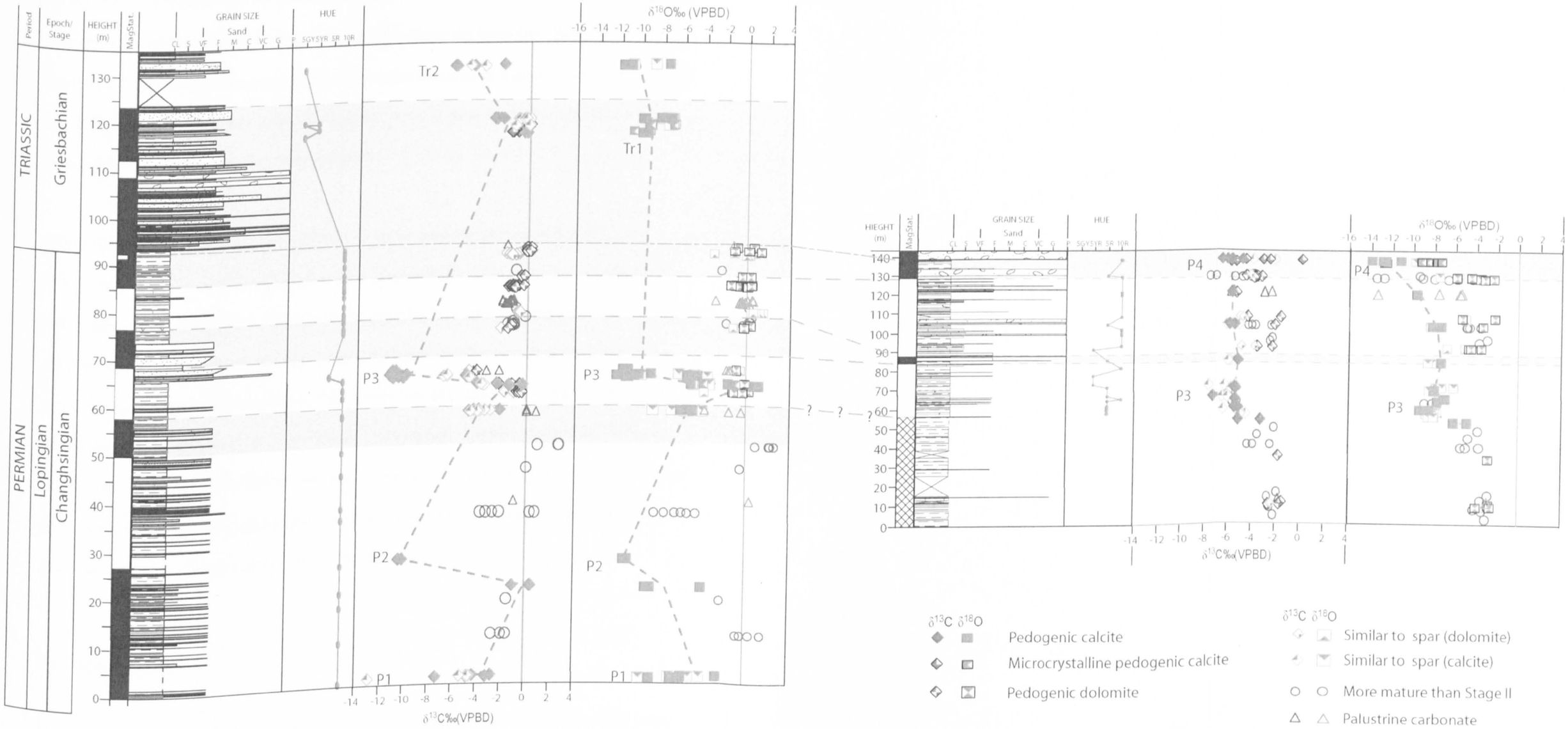

Figure 4.27 Screened data from Boyevaya Gora (left) and Sambullak (right) correlated using magnetostratigraphy from the same sections (Taylor *et al.* 2009). Lithological data from unpublished field data from Dr A Newell and Dr R. Twitchett.

No such excursion is seen in the basal Triassic in Russia (Figure 4.17). This is not to say that a negative excursion at the P/Tr boundary did not occur in Russia, but due to the change to coarser facies, there are no paleosols for 20 metres above the boundary. So it is possible that the global $\delta^{13}C_{carb}$ excursion seen in other areas also occurred in Russia in the basal Triassic, but as there was no carbonate being precipitated in the section studied or organic carbon preserved at that time, it has not been recorded.

In Russia, however, there is evidence for at least one negative excursion in $\delta^{13}C_{carb}$ and $\delta^{18}O_{carb}$ values in the mid-Changhsingian (P3) (Figure 4.27). This excursion is recorded in carbonate nodules which have not been overprinted by later spar forming events and show no groundwater or lacustrine associations or morphologies. Furthermore this excursion can be observed in the same magnetochron at both Sambullak and Boyevaya Gora (Figure 4.27) indicating that it is a basin wide event. Finally, this excursion is also statistically different from the background values, and the increase in the range of isotope values in paleosols that contain the excursion may indicate that they formed at a time of climate change rather than under homogenous climate conditions (cf. Pendall *et al.* 1994).

4.6 Summary

The stable isotopic composition of carbonate in paleosols is potentially influenced by many factors. Deciphering these factors is essential for any palaeoclimatic study, especially as they have an influence over whether the isotope results can be used for palaeotemperature and pCO_2 estimates (Ekart *et al.* 1999, Quast *et al.* 2006). While there is some evidence of minor alteration in the sections in Russia but it is possible to separate this from the primary pedogenic carbonate results. The similarity between some of the 'altered' results (especially

the microcrystalline carbonates) and the pedogenic carbonates isotope results suggests they are formed from the same fluid and may represent meteoric values or that some of the 'diagenetic' processes occurred when the paleosols were still active (cf. Ghosh *et al.* 2001):

1. There is evidence of an $\delta^{18}O_{carb}$ negative shift across the P/Tr boundary which starts in the last beds of the Permian (Sambullak P4) and continues into the Triassic (Boyevaya Gora, Tr1). There may have been a negative $\delta^{13}C_{carb}$ excursion at the P/Tr boundary, as recorded in the southern hemisphere, but this has to have occurred in the ~15m between the P/Tr boundary and the first Triassic paleosol (Figure 4.27);
2. However, there are four isotope excursions in the Changhsingian, identified in the Russian paleosols, which have not been recorded in the southern hemisphere. Of these, P3 is the best constrained. P3 can be identified in pedogenic calcite at Boyevaya Gora and, to a lesser extent, Sambullak and represents a negative shift of 6–4‰ in the $\delta^{13}C_{carb}$ and $\delta^{18}O_{carb}$ values;
3. There is evidence that the paleosols were affected by intense evaporation, recorded $\delta^{18}O_{carb}$ isotopic values greater than 0‰ and the occurrence of pedogenic dolomite. Pedogenic dolomite has been identified in the palaeo-equatorial Lower Permian (Kessler *et al.* 2001) but this is the first evidence of it at latitudes as high as 30-35°N at the P/Tr Boundary;
4. Also there may be a relation between the isotope anomalies and the appearance of pedogenic dolomite as at Boyevaya Gora as after the main Permian isotope excursion (P3) all the pedogenic carbonate above this point up to the P/Tr boundary is dolomite. This suggests that the excursion P3 marks the start of a period of extreme evaporation, and seasonality which continues up to the P/Tr boundary.

5 Palaeoclimatic analysis of the Southern Urals of Russia

5.1 Introduction

The variation in morphology and isotopic composition within paleosols can be used to investigate broad changes in climate and atmospheric conditions as described in previous chapters. However, it is also possible to use the relative depths of certain paleosol horizons and the isotope results as proxies for the amount of mean annual precipitation (MAP), mean annual temperatures (MAT) (e.g. Retallack 2005b and Dworkin *et al.* 2005). These can be used to investigate temperature and rainfall tends in the sections studied which are essential to test palaeoclimatic models (e.g. Ziegler *et al.* 1997: Kiehl and Shields 2005; Roscher and Schneider 2006).

5.1.1 Pedological and mineralogical indicators of changes in climate

Tracking sedimentological, pedological and mineralogical variation can be the most direct way of investigating how climate changes through the sections. The variation of such features, such as the presence or absence of pedogenic dolomite, can be used to indicate changes in the amount and intensity of evaporation (e.g. Kessler *et al.* 2001), and increase or decrease in ambient temperature through the section. These features can be used to test the results of any palaeotemperature estimates. Changes in soil colour and development and morphology of Bk horizons can also give an indication of changes in MAP and the intensity of monsoonal rains (Retallack 2005b).

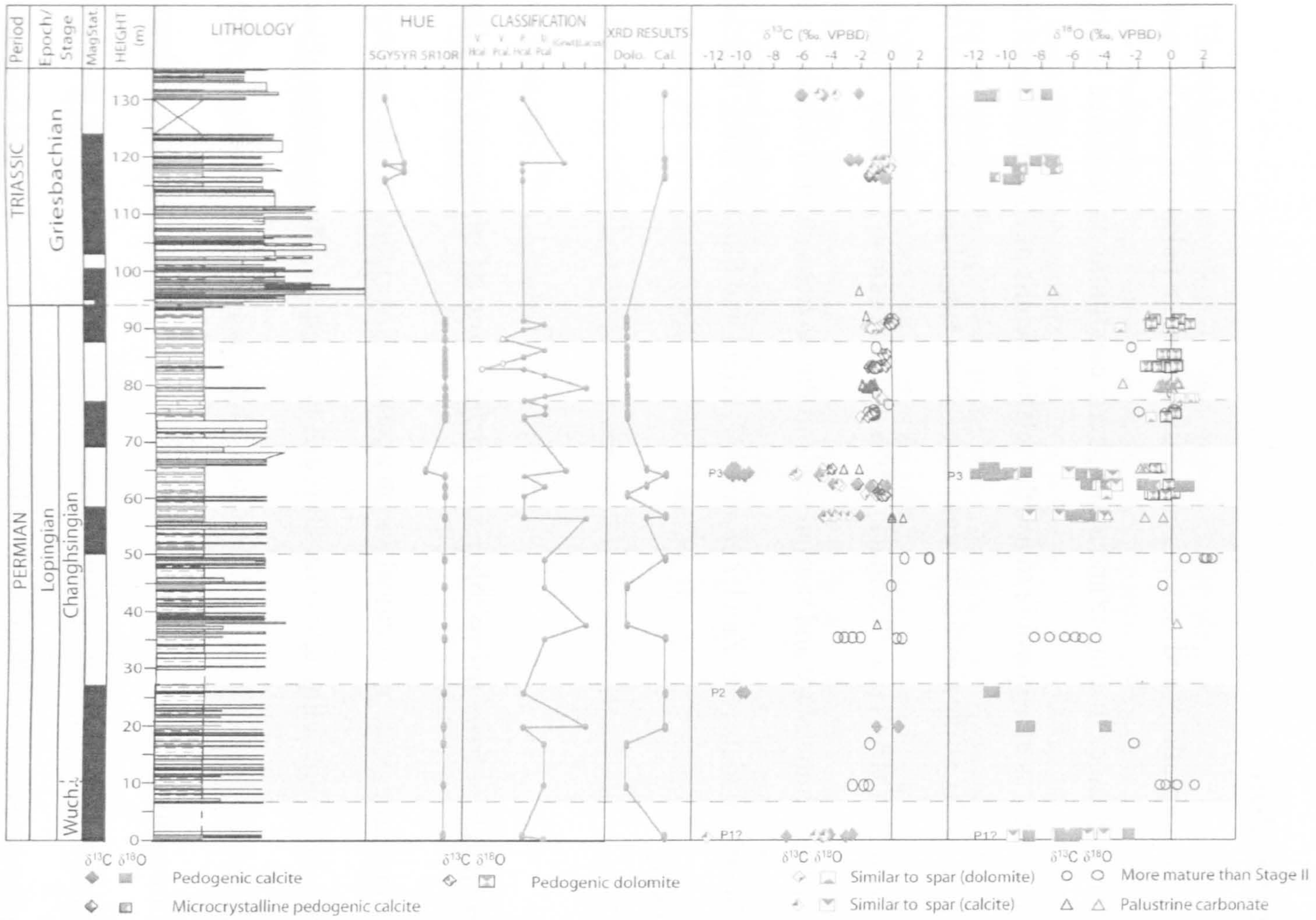

Figure 5.1 Summary of the pedological and isotopic features seen at Boyevaya Gora (see Chapter 3 and 4 for details).

Morphological changes in the type and development of paleosols have been observed in Antarctica (Retallack and Krull 1999; Retallack *et al.* 2007) and in the Karoo basin (Retallack *et al.* 2003) across the P/Tr boundary, associated with the isotopic anomalies seen in organic carbon (Retallack and Krull 2006) and pedogenic carbon (MacLeod *et al.*2000; Ward *et al.* 2000). As mentioned in Chapter 3, similar morphological features have observed at Boyevaya Gora (Figure 5.1) including a colour shift from a brick-red (10R) to a browner hue in the earliest (5GY). The first paleosols of the Triassic at Boyevaya Gora are poorly developed and associated with an increase in coarse-grade sediments. This also appears to be linked with a negative shift in the $\delta^{18}O$ isotope values in the earliest Triassic paleosols (Figure 5.1; Chapter 4). Equally at Boyevaya Gora, between the large $\delta^{13}C$ and $\delta^{18}O$ anomaly (P3, Figure 5.1), all the carbonate found in the paleosols is pedogenic dolomite, suggesting a rise in evaporation possibly initiated by the event that caused the isotopic excursions.

At Sambullak, while excursion P3 is present, there is no dominance of pedogenic dolomite after the excursion as at Boyevaya Gora (Figure 5.2). There are two possible explanations for this. Firstly, the dominance of pedogenic dolomite is a localised and restricted to Boyevaya Gora only. This appears unlikely as pedogenic dolomite was found at both sections. Another explanation for the dominance of dolomite is that it is linked to a rise in evaporation or a fall in river output. This would have affected Boyevaya Gora more dramatically as being further way from the Ural Mountains, where the fluvial systems originate, it would be affected first as the river output dwindles.

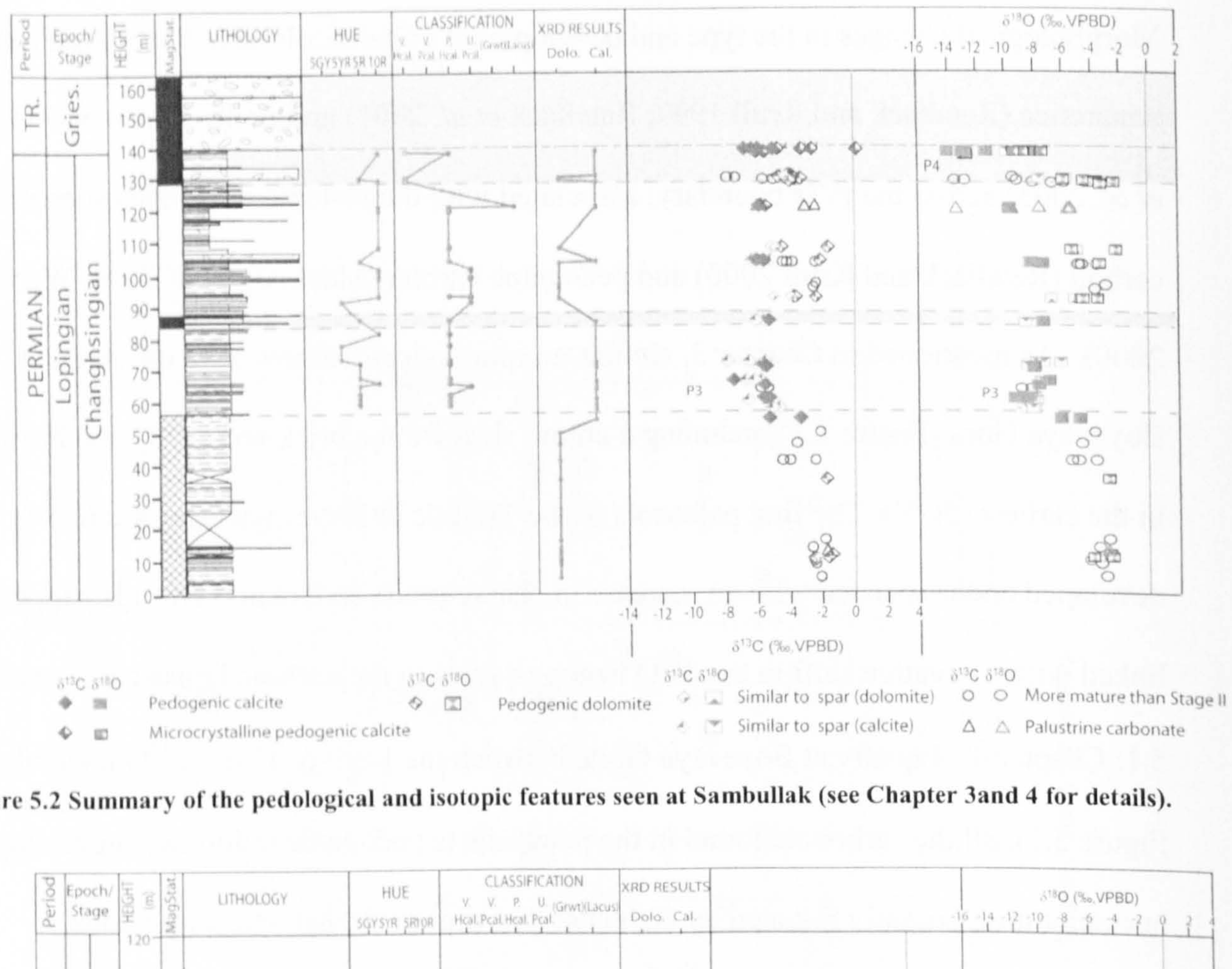

Figure 5.2 Summary of the pedological and isotopic features seen at Sambullak (see Chapter 3and 4 for details).

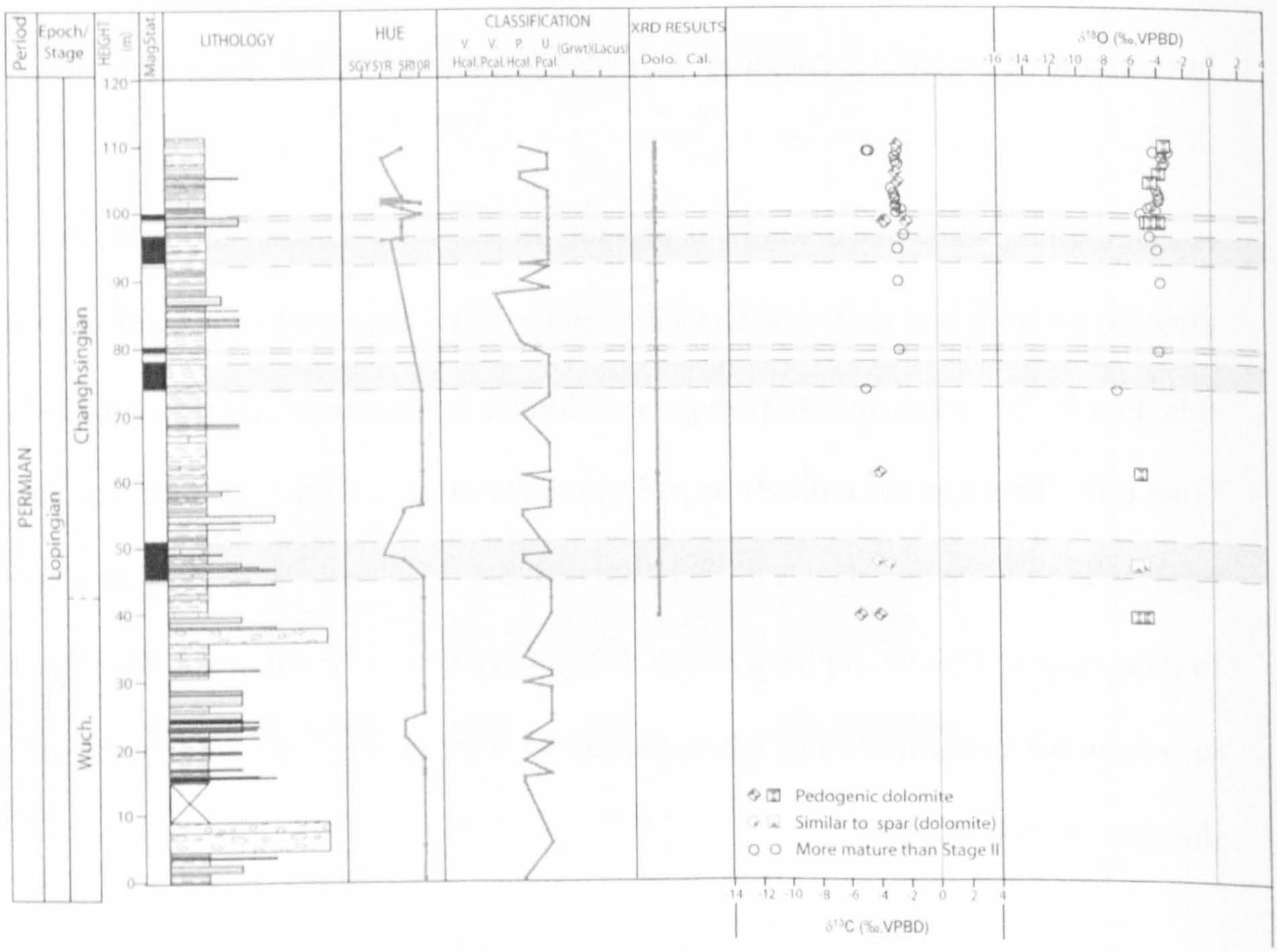

Figure 5.3 Summary of the pedological and isotopic features seen at Tuyembetka (see Chapter 3 and 4 for details).

Tuyembetka also covers this interval of time but as this section was probably on a palaeohigh (Chapters 3 and 4; and Taylor *et al.* 2009) it was already drier than the rest of the sections which explains why only dolomite was found there.

At Sambullak and Boyevaya Gora, in the interval just prior to the P/Tr boundary, there is an increase in the number of Vertisols again suggesting an increase in the amount of evaporation between P3 and the P/Tr boundary (Figure 5.1. and Figure 5.2).

By the upper Olenekian (Petropavlovskaya Svita) the basin has become more arid. For instance the carbonates found in the paleosols at Petropavlovka show groundwater morphologies suggesting that there was less influence from meteoric precipitation (Chapter 3). At Mescheryakovka, there is deep rooting, slickensides and carbonate related to arid environments (cf. Wright and Allen 1989; Stokes and Mather 2000). However, paleosols from Mescheryakovka also have the deepest average depth to Bk horizon which may indicate higher MAP (Chapter 3). The slickensides suggest that the paleosol must also have experienced times of drying and shrinking (Retallack 2001a; Kovda and Wilding 2005; Soil Survey Staff 2006) so perhaps the rains were more seasonal. This is supported by the strongly negative $\delta^{18}O$ values seen in this section (–14‰) possibly indicating monsoonal rains (cf. Alonso-Zarza 2003).

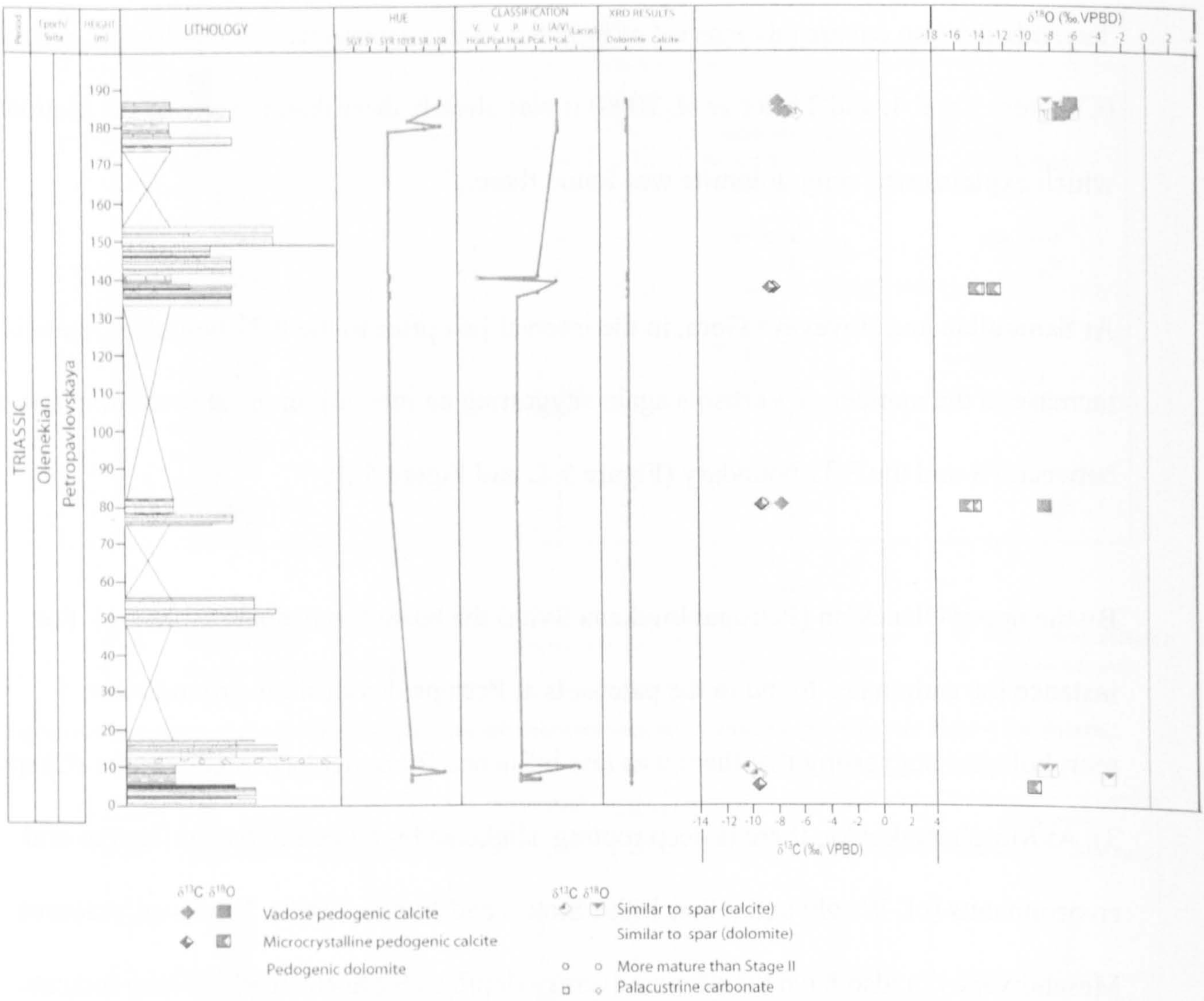

Figure 5.4 Summary of the pedological and isotopic features seen at Mescheryakovka (see Chapter 3 and 4 for details).

5.2 Palaeoprecipitation

The amount and severity of precipitation has a strong control on both the type of carbonate and the morphology of a paleosol. It has been suggested that the presence of carbonate in a paleosol indicates that the soil received between 100 and 1000mm of rainfall per year (Retallack 1994a, 2005a), although carbonate has been observed in modern Vertisols with a Mean Annual Precipitation (MAP) of 1400mm (Nordt *et al.* 2006).

It has also been observed that there is a quantitative link between the depth to the zone of carbonate (DTC) and mean annual precipitation (Jenny 1941; Retallack 1994a; 2001a; 2005b;

Nordt *et al.* 2006; Cleveland *et al.* 2008). This depth reflects the depth of biological respiration of the soil by available water during a year, and thus in years with less precipitation produces a shallower DTC. This relationship was first numerically described by Retallack (1994) based on 317 soils from the Quaternary. Since then this universal relationship has been revised with a more comprehensive dataset (Retallack 2005b). There have also been several models produced which link MAP to DTC for specific soil orders such as Vertisols (Nordt *et al.* 2006) and Aridisols (Cleveland *et al.* 2008).

The DTC can be hard to define as many nodule bands are diffuse rather than distinct horizons, particularly in monsoonal areas (Retallack 2005b). One definition of the DTC is the depth from the soil surface to the first occurrence of carbonate nodules; in monsoonal systems it is taken to be the zone of highest nodule abundance (Retallack 2005b). For this study the definition used will be that proposed by Nordt *et al.* (2006), which define the top of the DTC as the point in the paleosol when nodules make up 5% of the soil. 'Nodules' are defined as any form of carbonate segregation (nodule, soft mass, lump or concretion) (Nordt *et al.* 2006).

There is a question of the validity of applying the relationship between MAP and DTC to paleosols, especially Vertic-paleosols (Driese *et al.* 2000). This is partly because fluvial depositional sedimentary sequences are highly erosive, and while Bk horizons are relatively resistant to erosion, the A horizon is not and can be easily removed by overlying channels. In Vertisol sequences, layers that are several centimetres to a few decimetres thick have been observed to have been planed off by channel belt migration (Driese *et al.* 2000). There are other problems with the application of this relationship between the DTC and MAP to paleosol sequences. In fluvial stacked paleosol sequences, if the influx of sediment which buries a paleosol is less than the DTC, as controlled by precipitation, and a paleosol forms on

this new sediment the new paleosol can partially rework the top of the old paleosol, thus, truncating it without eroding it (Figure 5.5). Both erosion and this 'overprinting' have the effect of underestimating the DTC and thus the MAP. In the analysis of the Russian paleosols all those paleosols which had channels overlying them, or were part of a stacked paleosol sequence where there was no evident break between horizons, were noted as possible only representing the minimum rainfall.

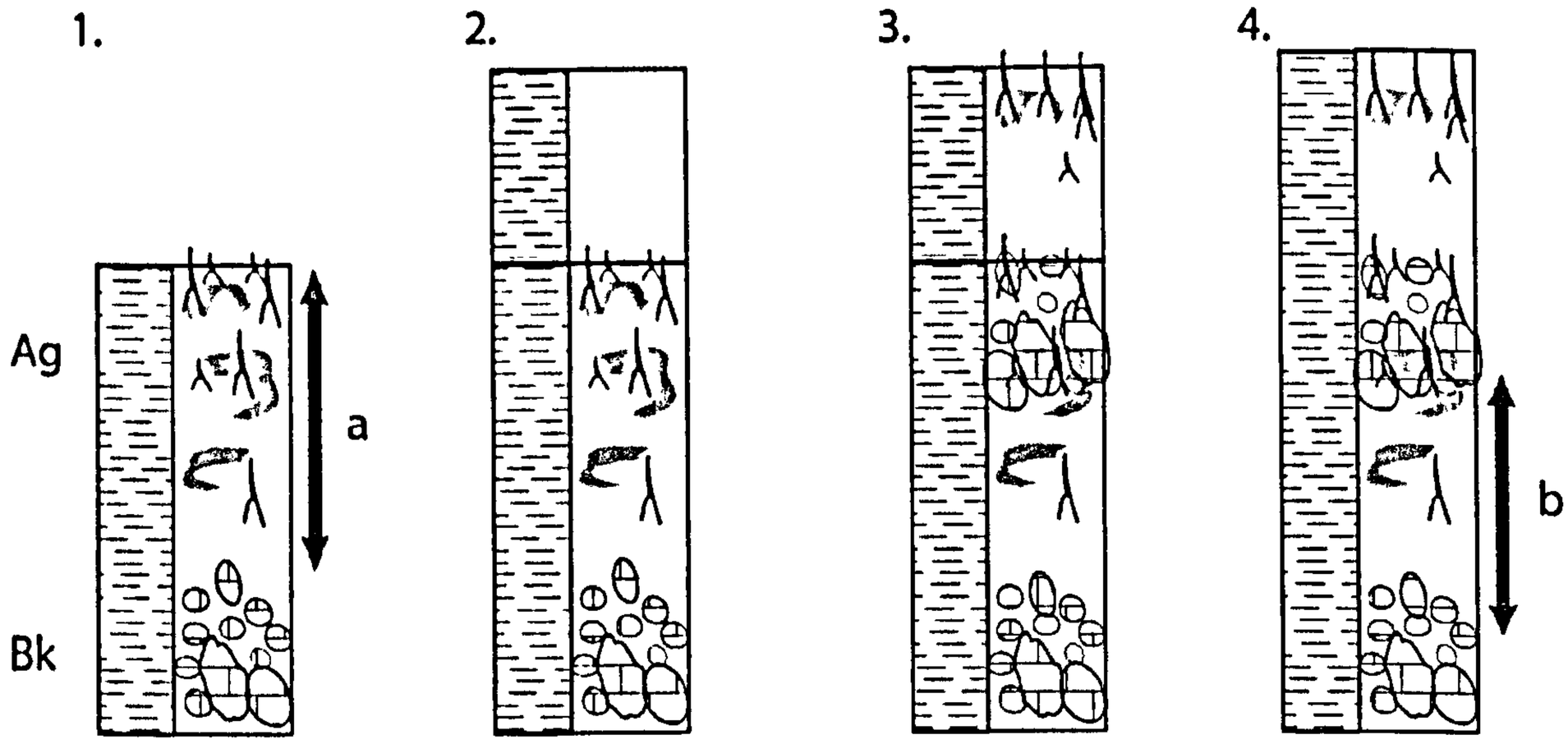

Figure 5.5 Illustration how the depth to Bk horizon can be overprinted in stacked paleosols sequences. a) refers to the depth to Bk horizon in the original soil which then becomes covered by flood-derived silt (2) and a new soil forms reworking part of the lower soil profile (3). Thus, the depth to Bk horizon (b) is reduced (compare a and b) (4).

The amount to which the paleosols have been compressed during lithification is another important factor to consider when applying precipitation estimates to paleosols. This study utilised the variant of the decompression algorithm proposed by Sheldon and Retallack (2001) for Aridisols (Equation 5.1). An estimated burial depth of 1.9km for the Russian sediments (Brunet *et al.* 1999; Andy Newell *pers. comm.*) was used in this equation.

$$C = \frac{-0.62}{\left[\left(\frac{0.38}{E^{0.17Dp}}\right) - 1\right]} \qquad (5.1)$$

C is the compression factor and Dp burial depth (km).

As mentioned previously, there are several variants of the palaeoprecipitation equation based on specific soil orders and overall relationships; this study utilises four of these. The first is the mean relationship proposed by Retallack (2005) based on a global dataset (Equation 5.2).

$$P=137.24+6.45D-0.013D^2 \qquad (5.2)$$

P is the MAP in millimetres and D is the DTC in centimetres.

A model specifically created for Vertisols was also used (Nordt *et al.* 2006). This equation comes in two variants, one for microlows (Equation 5.3) and another for microhighs (Equation 5.3a)

$$P=-4.00E-05D^2+4.251D+432.27 \qquad (5.3a)$$

$$P=-8.00E-04D^2+1.362D+1047.40 \qquad (5.3b)$$

P is the MAP in millimetres and D is the DTC in centimetres.

As these equations have been proposed purely for use in Vertisols, it has been suggested that they should only be used for DTC between 70 and 120cm (Cleveland *et al.* 2008).

Finally, the last relationship is the one formulated for Aridisols by Cleveland *et al.* (2008) (Equation 5.4). They suggest that this equation should only be applied to Aridisols with or paleosols containing pedogenic slickensides and that lack argillic horizons.

$$P=0.029(D-38)^2+2.7D+133 \qquad (5.4)$$

P is the MAP in millimetres and D is the DTC in centimetres.

It has been noted that in monsoonal conditions, Bk horizons become thicker reflecting the annual range of precipitation (Retallack 1991; Retallack 2005b). Retallack (2005b) uses this relationship to produce an equation that can predict the range of precipitation and thus the intensity of any monsoonal activity (Equation 5.5).

$$M=0.79T+13.71 \quad (5.5)$$

M is the mean annual range of precipitation in millimetres and T is the uncompressed thickness of the 'paleosol-with-nodules' in centimetres. The thickness of 'paleosol-with-nodules' in centimetres is defined as being the interval between the shallowest and deepest carbonate nodule (Retallack 2005b).

In the modern world the hydrological definition of monsoonal conditions is any region that receives the majority of its rain during a particular season (Webster 2005). For example, present day New Delhi (28° 34' 48" 77° 12' 00") has a mean annual range of precipitation of 235mm (based on 45-years' worth of measurements; IAEA/WMO, 2008) compared with Chihuahua in Mexico (28° 37' 48" -106° 4' 12") which has a range of 88mm (based on 27 years' worth of measurements; IAEA/WMO, 2008). Therefore, increases in mean annual range of precipitation can be seen as increases in seasonal conditions.

5.2.1 Palaeoprecipitation estimates for the Southern Urals, Russia

Palaeoprecipitation estimates were calculated from paleosols at Boyevaya Gora, Sambullak, Tuyembetka and Mescheryakovka. These sections were chosen because 1) they are primarily pedogenic rather than groundwater–related, and 2) they are long sections and thus it is possible to track changes over time.

Section	Average MAP (mm)			
	5.2	5.3a	5.3b	5.4
Boyevaya Gora (Permian)	344(±118)	293 (±74)	956 (±178)	217(±55)
Sambullak	411(±114)	268(±79)	989 (±31)	274(±63)
Tuyembetka	409(±189)	270(±102)	989(±41)	251(±89)
Boyevaya Gora (Triassic)	185(±23)	401(±15)	1037(±5)	180(±3)
Mescheryakovka	541(±269)	258(±43)	961(±58)	313(±151)

Table 5.1 The average MAP from the four longest Russian sections for the four different MAP equations (see Appendix 3.1 for calculations).

At Boyevaya Gora equations 5.2, 5.3a and 5.4 produce averages within error of each other (Table 5.1) suggesting an average MAP of 300mm. Equation 5.3b on the other hand seems to produce a much higher value (Table 5.1). This is probably due to the fact that Equation 5.3b models microhighs and Boyevaya Gora was probably an active river channel (Newell *et al.* 1999) and not a microhigh.

Equations 5.4 show a gradual rise in precipitation of 175mm at the base of the section up to the P/Tr boundary and then a drop of 200mm across into the Triassic (Figure 5.6). Equation 5.3a gives the inverse of this relationship with a fall of precipitation of about 150mm up to the boundary and a rise of 200mm across the boundary. Equation 5.3b shows very little variation across the whole curve.

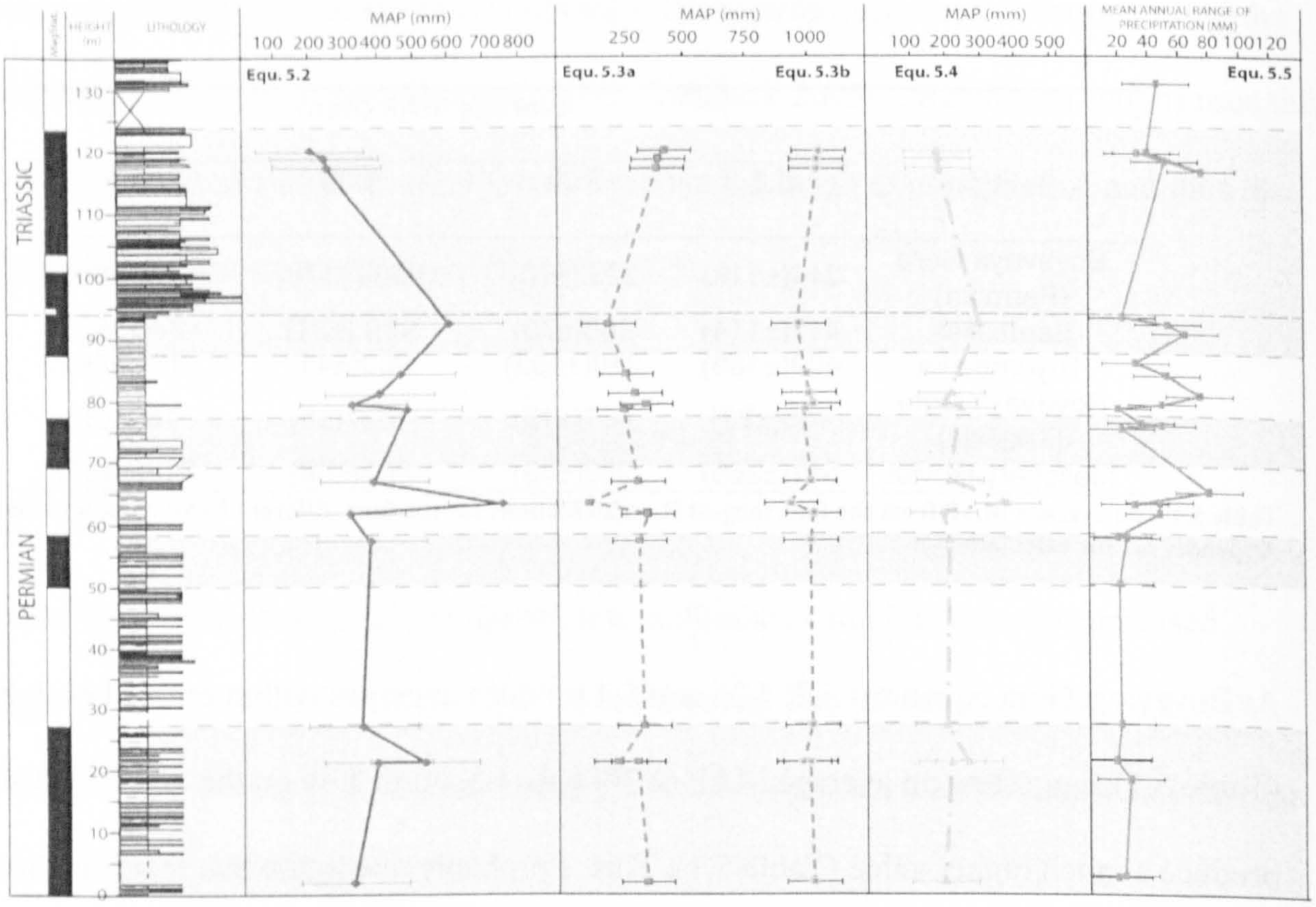

Figure 5.6 MAP and Mean Annual Range of Precipitation estimates using at Boyevaya Gora (see Appendix 3.1 and 3.2 for calculations).

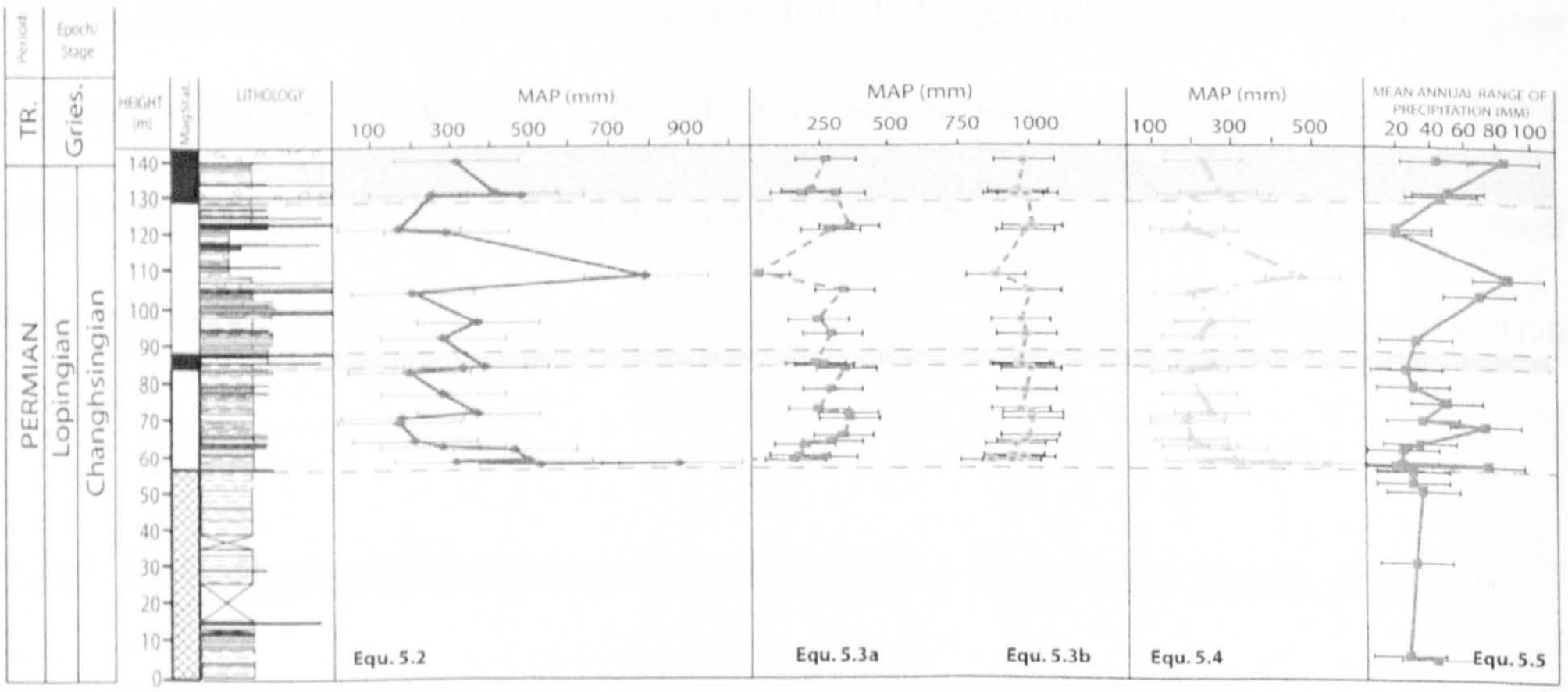

Figure 5.7 MAP and Mean Annual Range of Precipitation estimates using at Sambullak (see Appendix 3.1 and 3.2for calculations).

The average MAP values for Sambullak are greater than those seen at Boyevaya Gora (Table 5.1) and show a greater range of values, although a lot of the variation may be due to two anomalous paleosols, one at the base of the section and one at 110m which equation 5.2 and 5.4 models as a dramatic rise in MAP. Equations 5.2 and 5.4 show a minor rise in precipitation of 200mm as at Boyevaya Gora, while equation 4 shows a fall of about 200mm and equation 5.4 shows little variation. The mean annual range of precipitation shows a increase in the range in the last R-N-R-N magnetochrons of the Permian (Figure 5.7) which is similar to the average increase after the excursions seen at Boyevaya Gora (Figure 5.6), suggesting the increase in seasonality at Boyevaya Gora after P3 also occurred at Sambullak.

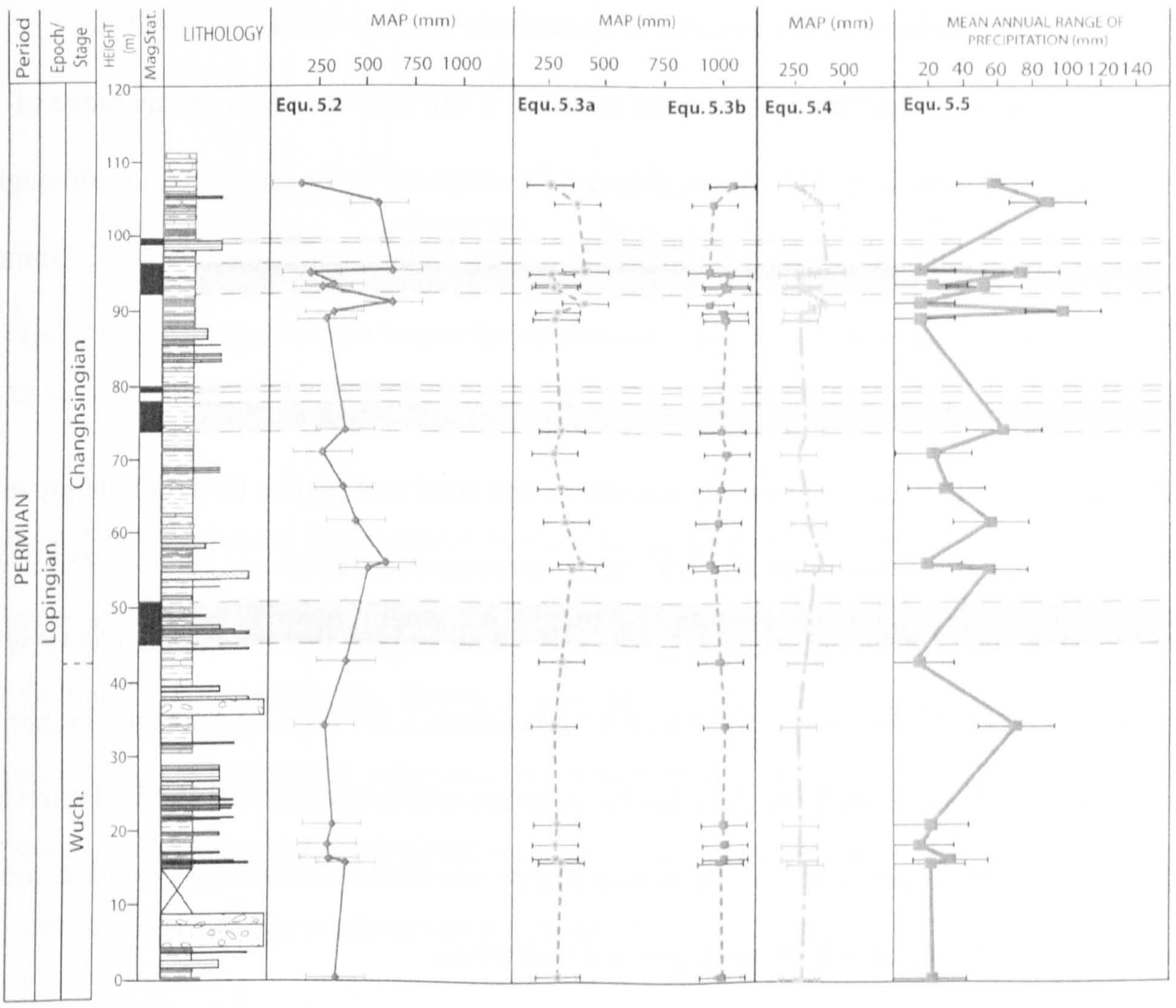

Figure 5.8 MAP and Mean Annual Range of Precipitation estimates using at Tuyembetka (see Appendix 3.1 and 3.2 for calculations).

The average values for Tuyembetka for equations 5.2 and 5.3b are similar to those for Boyevaya Gora and Sambullak which is expected as all three sections overlap stratigraphically. At the top of the section (above 90m, Figure 5.8) there appears to be an increase in MAP which may be linked to a rise in the mean annual range of precipitation seen at this point.

All three section show an increase in an increasing the range of mean annual precipitation (equation 5.5) up to the P/Tr boundary (Figure 5.6, Figure 5.7, Figure 5.8) from 17–44 (±22)mm range per year to 56–90 (±22)mm. Indicating an increase in seasonality up to the P/Tr boundary. Relative to the other three sections the average values for MAP at Mescheryakovka are elevated (apart from equation 5.3a). Also the mean annual range of precipitation is increased (134-18mm, Figure 5.9) compared to the other sections although this is not as in modern monsoonal climates (e.g. New Delhi mean annual range =235mm IAEA/WMO, 2008)

The Permian of Russia is interpreted as a steppe and semi-arid regime (Tverdokhlebov *et al.* 2005). Similar environments in modern steppe environments experience between 250-500mm MAP (McKnight 1999). Equations 5.2, 5.3a and 5.4 all suggest that the Permian MAP was between 227(±25)-500 (±144) mm (Table 5.1). Equation 5.3b, gives significantly higher estimates for all sections (Table 5.1), but his equation was formulated for Vertisol microhighs (Nordt *et al.* 2006) and there is no section in Russia where the sections were exposed well enough to positively identify microhighs and microlows.

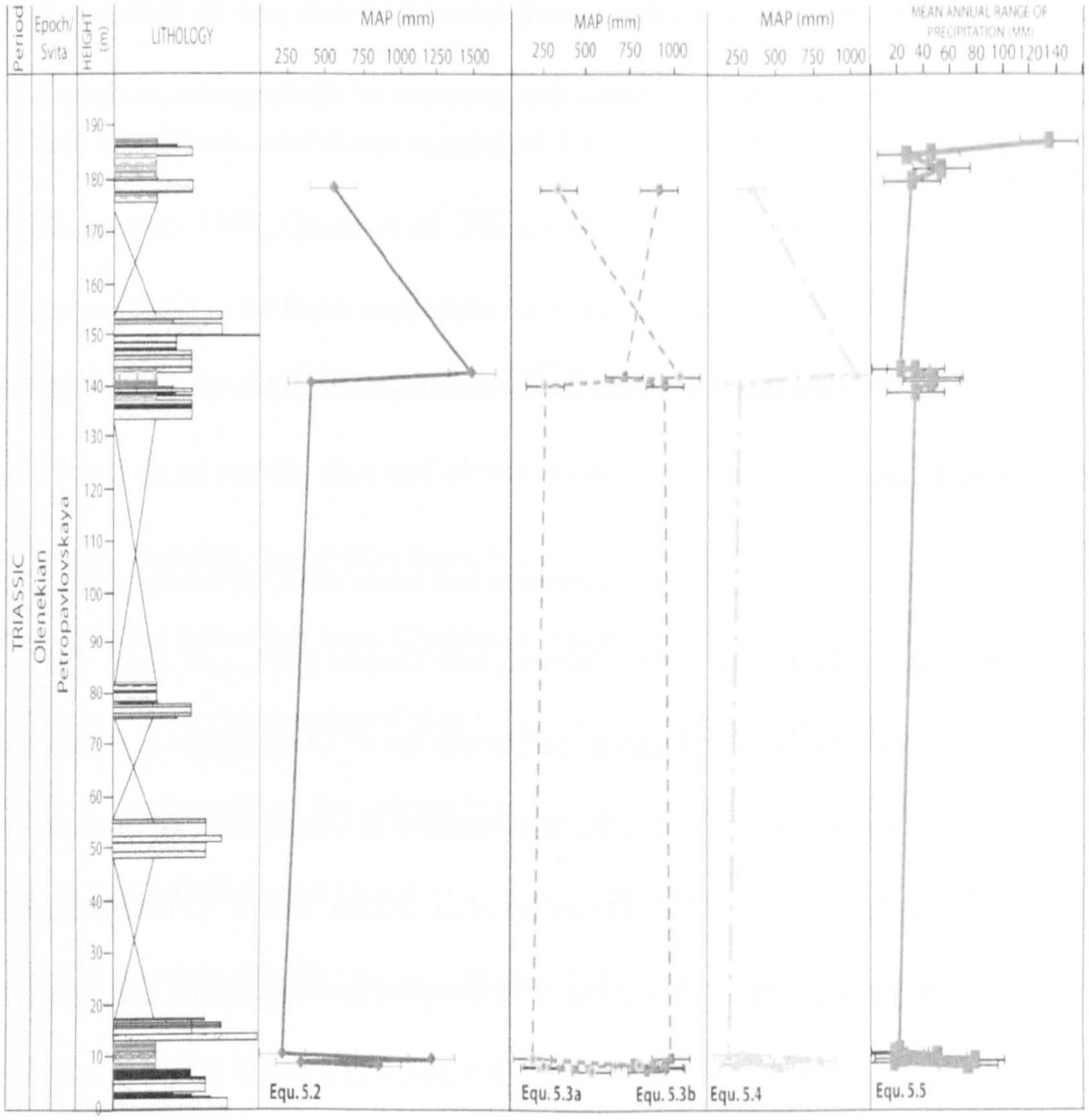

Figure 5.9 MAP and Mean Annual Range of Precipitation estimates using at Mescheryakovka (see Appendix 3.1 and 3.2 for calculations).

Both Tuyembetka and Boyevaya Gora show an increase in mean annual range of precipitation in the uppermost Permian (Figure 5.6, Figure 5.8). Boyevaya Gora also shows decrease in MAP in the earliest Triassic. However, this may be an erroneous result as the Triassic paleosols are all capped by sandstone beds which may have eroded the paleosols (Figure 5.6). The mean annual range of precipitation stays increased into the Triassic suggesting that the increase in seasonality continues in the earliest Triassic (Figure 5.6).

By the Olenekian it appears that both mean annual range of precipitation and MAP are elevated relative to the Permian and Earliest Triassic sections (Table 5.1, Figure 5.9).

This suggests both an increase in the overall amount of rain and an increase in the seasonality of that rain (Figure 5.9) which explains the presence of slickensides as deep as the Bk horizon (see Chapter 3).

5.3 Palaeotemperature and $\delta^{18}O$ composition of pedogenic carbonate

The $\delta^{18}O$ composition of pedogenic carbonate has been used for many years to estimate palaeotemperature (Mack *et al.* 1991; Wright and Tucker 1991; Liu *et al.* 1996; Dworkin *et al.* 2005). In primary vadose pedogenic carbonate the $\delta^{18}O$ signature is derived directly from meteoric precipitation (rainfall), and the temperature at which the carbonate formed (Cerling and Quade 1984; Mack *et al.* 1991; Dworkin *et al.* 2005). The $\delta^{18}O$ composition of the meteoric precipitation itself is a function of atmospheric temperature that precipitation formed at (Mack *et al.* 1991; Fricke O'Neil 1999). As such, it is a more useful palaeotemperature proxy than using $\delta^{18}O$ data derived from marine sediments as pedogenic carbonate is not affected by the isotopic fractionation in sea water (Wright and Tucker 1991; Dworkin *et al.* 2005).

Dworkin *et al* (2005) advise that, due to multiple different temperatures, chemistries and isotopic composition of the fluids from which pedogenic carbonate forms; particular attention must be taken to screening out these effects. They note that pedogenesis will 'pin' the oxygen isotopic composition to local precipitation and temperature so the most pressing issues are diagenetic modification and alteration in re-exposure. (Dworkin *et al* 2005). To this end only nodules that are made of anhedral grains of calcite of micritic or microspar size should be used for palaeotemperature analysis (c.f. Dworkin *et al* 2005).

Based on these conditions, and those suggested for screening paleosol carbonate for pCO_2 estimates (Ekart *et al.* 1999, Quast *et al.* 2006, see Chapter 4), only the isotope results which could be demonstrated to be from carbonate of Stage II and below, and not associated with palustrine carbonate, were used to calculate palaeotemperature estimates (see Chapter 4 Table 4.2). Similarly all those results that had similar isotopic values to the spar were excluded as, although the spar-forming event may have been very early, it may not represent active, vadose, soil-forming processes (see Chapter 4, Table 4.2). The pedogenic dolomite is also excluded as it has been demonstrated that $\delta^{18}O$ values from the dolomite are isotopically more positive relative to those from the calcite (see Chapter 4 Table 4.2). This is consistent with the findings of Land (1980) and Quast *et al.* (2006) that dolomitic $\delta^{18}O$ values are fractionated relative to the soil water. Finally, those nodules that show a microcrystalline texture are also problematic as they may be formed by groundwaters (Quast *et al.* 2006). However, the overlap with those nodules that were of unaltered cryptocrystalline micrite (see chapter 4) suggests that those nodules are also pedogenic, so they were included in the palaeotemperature estimates but only where they are similar to unaltered vadose pedogenic carbonate values from the same paleosol. As only Boyevaya Gora, Sambullak and Mescheryakovka have isotopic values that are definitely unaltered pedogenic calcite; these were used to calculate palaeotemperature estimates (see Chapter 4 Table 4.2).

5.3.1 Different Methods

Friedman and O'Neil (1986) described the relationship between the $\delta^{18}O$ value of calcite and temperature but their equation requites the isotopic value for the liquid from which that calcite precipitated from. To accurately estimate palaeotemperature, the effects of both meteoric

precipitation and temperature on the $\delta^{18}O$ of the pedogenic carbonate must be modelled. This relationship was first described by Friedman and O'Neil (1986):

$$\delta^{18}O_{carb} - \delta^{18}O_p = 2.78(10^6 T^2) - 2.89 \quad (5.6)$$

where $\delta^{18}O_{carb}$ is the isotopic composition of the pedogenic carbonate (relative to VSMOW) from the; $\delta^{18}O_p$ is the isotopic composition of the meteoric precipitation (relative to VSMOW) and T is the Mean Annual Temperature (°K). This is converted to °C using the conversion °C = °K – 273.15 (Bureau International des Poids et Measures 2008). This equation needs inputs of $\delta^{18}O_{carb}$ which is measured from the field data (Chapter 4) and $\delta^{18}O_p$ which has to be estimated.

It has been shown that the $\delta^{18}O$ of meteoric precipitation ($\delta^{18}O_p$) varies with latitude (Fricke and O'Neil 1999) and thus it is important to consider the palaeolatitude of the Southern Urals when trying to calculate palaeotemperature. In the Permian–Triassic period the Southern Urals were between 30–35 °N (Newell *et al.* 1999; Torsvik and Anderson 2002; Cocks and Torsvik 2007; Taylor *et al.* 2009). In the modern day rainfall from these latitudes has an isotopic range of between 11.06‰ and –15.51‰, (IAEA/WMO 2008). However, as SMOW is 1‰ any modern value greater than this must be fractionated by evaporation (Dr Stephen Grimes *pers. comm.*) and thus can be excluded, giving a range of –1.12 ‰ to –15.51‰ with a mean of –5.52‰ (Fricke and O'Neil 1999; IAEA/WMO 2008). Using the minimum, maximum and mean values for $\delta^{18}O_p$ and screened pedogenic carbonate values from Sambullak, Boyevaya Gora and Mescheryakovka, it is possible to produce temperature curves for the maximum, minimum and mean $\delta^{18}O_p$ curves using equation (5.6) (Figure 5.10)

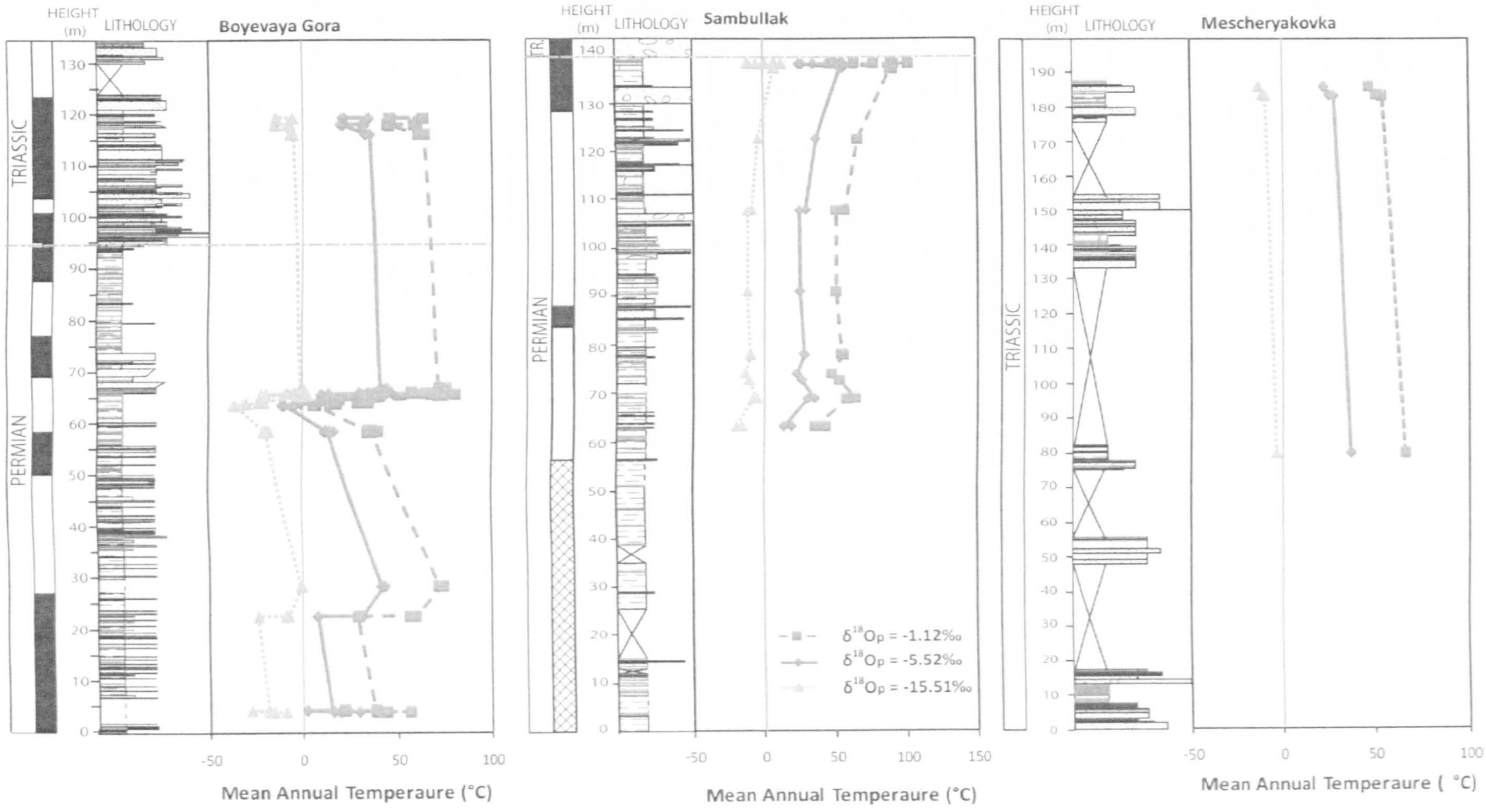

Figure 5.10 Palaeotemperatures produced by equations (5.6) using the max, min and mean modern values for $\delta^{18}O_p$ from 30–35°N (see Appendix 3.3 for calculations).

In all cases the minimum $\delta^{18}O_p$ value gives temperature values which are below freezing (averages of -9°C, -6°C, -7°C, for Boyevaya Gora, Sambullak and Mescheryakovka respectively see Figure 5.10). These are unrealistic as there is no evidence of ice wedging or prolonged formation in the Russian paleosols, suggesting that these paleosols never went below 0°C for a prolonged period of time. Equally the maximum modern $\delta^{18}O_p$ value for this latitude produces maximum temperatures that are unrealistically hot (ranges 6°C to 80°C, 6°C to 102°C, 48°C to 66°C for Boyevaya Gora, Sambullak and Mescheryakovka respectively, see Figure 5.10). The mean $\delta^{18}O_p$ value appears to produce realistic temperatures (Figure 5.10 and Figure 5.11) and suggests that there was an increase of 20°C and 26°C across the $\delta^{18}O_{carb}$ excursions seen at Boyevaya Gora (P3) and Sambullak (P4) respectively. However, this value also produced a large range in MAT estimates (ranges −11°C to 48°C, 14°C to 64°C, 48°C to 66°C for Boyevaya Gora, Sambullak and Mescheryakovka respectively, see Figure 5.11) some of which are below 0°C which again there is no physical evidence for in the sections.

Using a single value for $\delta^{18}O_p$ throughout a section may be problematic: firstly it assumes that using a modern average $\delta^{18}O_p$ value accurately represents the $\delta^{18}O_p$ of meteoric precipitation in the Permian–Triassic of Russia and, secondly, that $\delta^{18}O_p$ is unaffected by changes in atmospheric temperature.

Also at modern sites, there is a 5-10 per mil difference between the $\delta^{18}O$ of precipitation, between sites with the same mean annual temperature (MAT) (e.g. Rozanski *et al.*, 1993) and this would produce an uncertainty of ±5°C to any palaeotemperature estimates (Dr Nathan Sheldon *pers. comm.*).

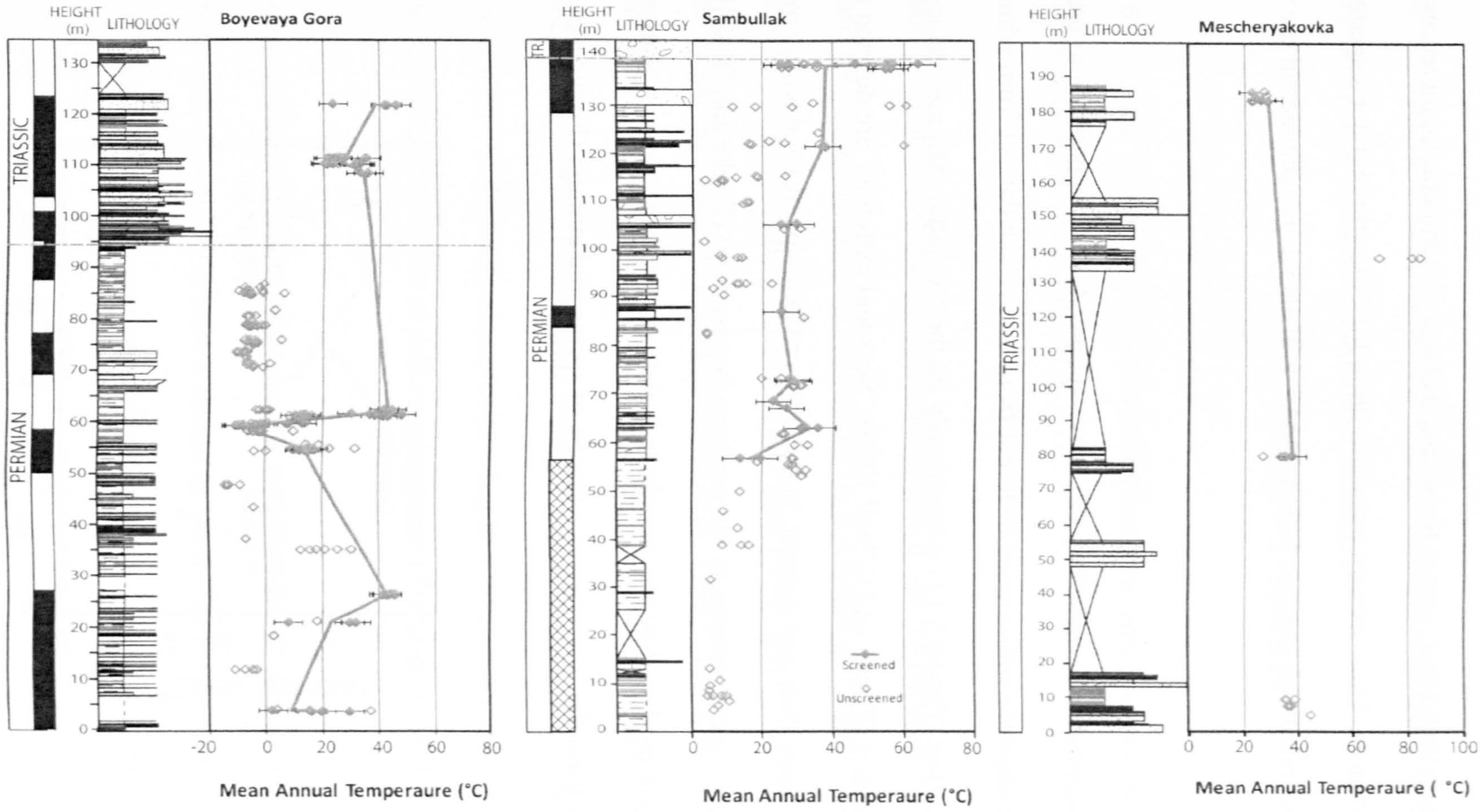

Figure 5.11 Palaeotemperature produced by equations (5.6) using the mean modern values for $\delta^{18}O_p$ from 30–35°N of –5.52‰ (Fricke and O'Neil 1999; IAEA/WMO, 2008) (see Appendix 3.3 for calculations).

Modelling the effect of temperature on meteoric precipitation, Fricke and O'Neil (1999) found that there was a positive relationship between the isotopic composition of meteoric precipitation ($\delta^{18}O_p$) and the local ground temperature in modern terrestrial environments (Figure 5.12). They found that, across the world, as local air temperature increases, the $\delta^{18}O_p$ becomes more positive. Thus, using a constant figure for $\delta^{18}O_p$ throughout a section will produce erroneous results as changes in local MAT will also cause changes in the value of $\delta^{18}O_p$.

By using the relationship described by this curve (Figure 5.12) it is possible to predict past $\delta^{18}O_p$ even if the absolute values were different from today. The dataset from which this relationship is derived (Figure 5.12) is based only on the 'seasonal extreme' values rather than the full annual dataset (Fricke and O'Neil 1999). 'Seasonal extremes' are defined as being the summer months (June, July and August, in the northern hemisphere) and winter months (December, January and February, in the northern hemisphere) (Fricke and O'Neil 1999). These months were used as they are thought to isolate seasonal extremes in climate variables and $\delta^{18}O_p$ values from the 'transitional' seasons of spring and autumn (Fricke and O'Neil 1999).

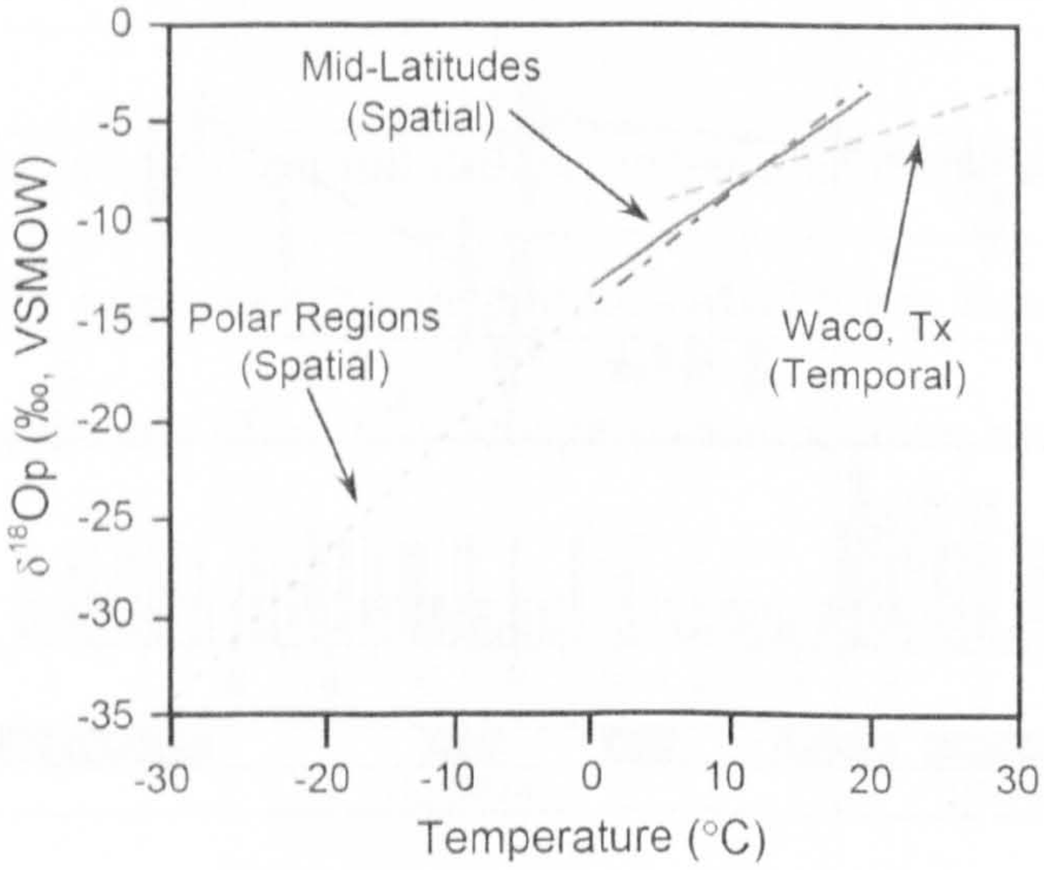

Figure 5.12 The modern day relationships between $\delta^{18}O_p$ and temperature described by Fricke and O'Neil (1999) and Dworkin *et al.* (2005) (figure adapted from Dworkin *et al.* 2005).

This relation between changes in MAT and $\delta^{18}O_p$ has been expressed as a 'spatial' relationship (equation 5.7a), referring to the relationship between long-term (annual) averages of $\delta^{18}O_p$ and surface air temperature at different latitudes round the globe (Rozanski *et al.* 1992; Fricke and O'Neil 1999; Dworkin *et al.* 2005).

$$\delta^{18}O_p = 0.50(T - 273) - 13.20 \qquad (5.7a)$$

where $\delta^{18}O_p$ is the isotopic composition of the meteoric precipitation (relative VSMOW) and T is the Mean Annual Temperature (°C).

It has also been observed that there is a difference in the relationship between surface air MAT and the long-term (annual) average $\delta^{18}O_p$ at a single geographical location when compared to the global pattern (Fricke and O'Neil 1999), and this relationship may be more relevant for palaeoclimate analysis (Rozanski *et al.* 1992). This is because the $\delta^{18}O_p$ of meteoric water at a given location is controlled by regional-scale processes, such as conditions at the source of the vapour, transport patterns of vapour in the atmosphere, average "rain-out history" of the air masses precipitating in a given place, and cloud-base temperature, and these have varying effects at different localities (Rozanski *et al.* 1992).

In their study Dworkin *et al.* (2005) use the modern summer and winter $\delta^{18}O_p$ data (method after Fricke and O'Neil 1999) from a station in Waco Texas (the closest modern weather station to their field area) to generate this relationship (equation 5.7b).

$$\delta^{18}O_p = 0.22(T - 273) - 8.31 \qquad (5.7b)$$

where $\delta^{18}O_p$ is the isotopic composition of the meteoric precipitation (relative VSMOW) and *T* is the Mean Annual Temperature (°C). This is referred to as a 'temporal' relationship (Rozanski *et al.* 1992; Fricke and O'Neil 1999; Dworkin *et al.* 2005). The closest modern weather station to the Russian field area which has records of $\delta^{18}O_p$ of rain water for over three consecutive years is at Saratov, in the Russian Federation (51° 34' 00" / 46° 1' 60" / altitude 166m), (using the Water Isotope System for Data Analysis, Visualization, and Electronic Retrieval Database, IAEA/WMO, 2008). Using the methods proposed by Fricke and O'Neil (1999) and Dworkin *et al.* (2005) based only on comparing $\delta^{18}O_p$ to air temperature from the summer and winter months (Figure 5.13) it is possible to produce an equivalent equation (5.7c) for Saratov.

$$\delta^{18}O_p = 0.278(T - 273) - 12.91 \qquad (5.7c)$$

where $\delta^{18}O_p$ is the isotopic composition of the meteoric precipitation (relative VSMOW) and *T* is the Mean Annual Temperature (°C).

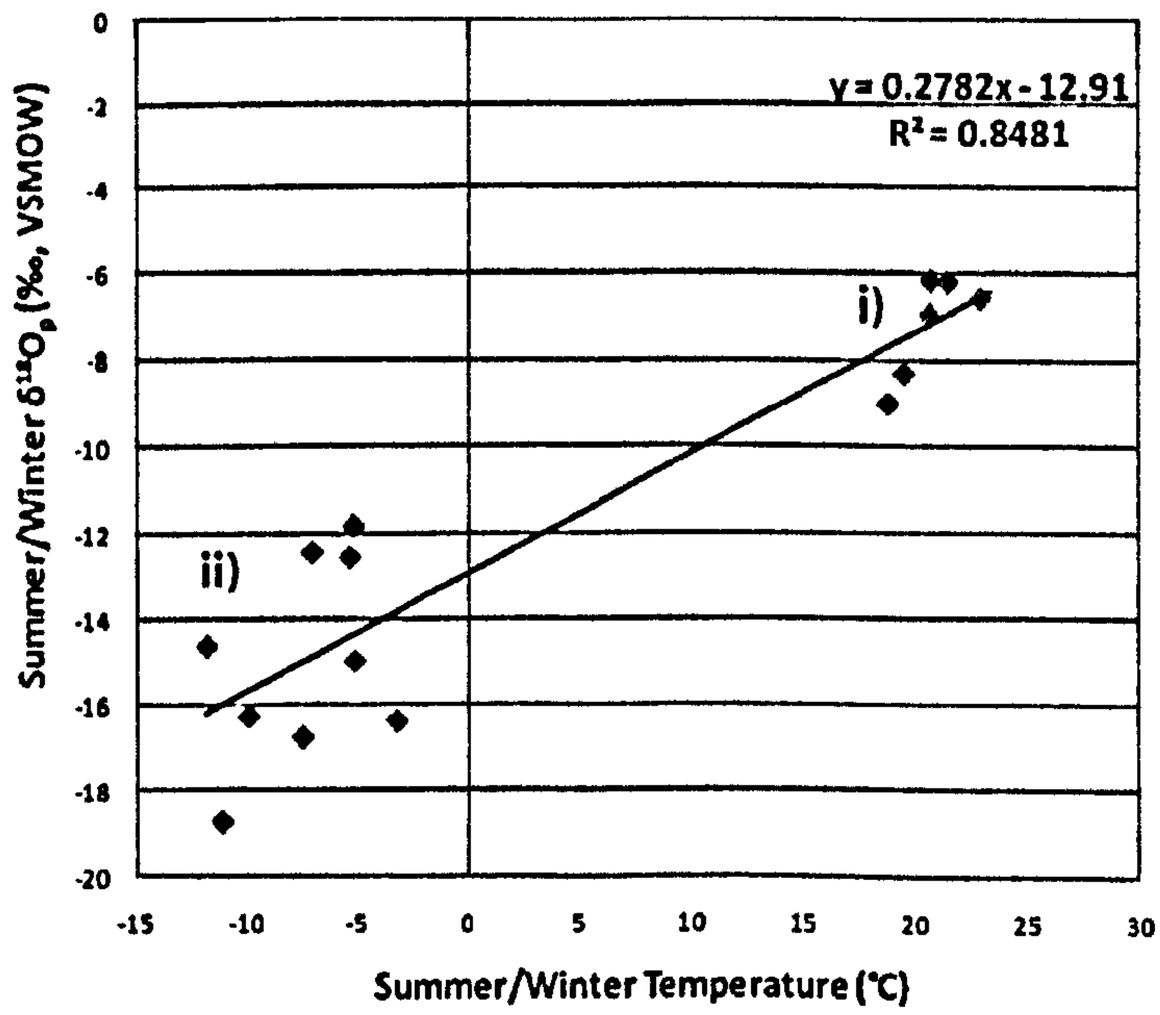

Figure 5.13 The summer/winter comparison from the same data used to produce equation (5.7c). i) is the summer data and ii) is the winter data following method from Fricke and O'Neil (1999).

Using equations (5.7a), (5.7b) and (5.7c) it is now possible to model how $\delta^{18}O_p$ changes with MAT in the Russian data. Combining these relationships with that described by Friedman and O'Neil (1977) (equation 5.6), Dworkin *et al.* (2005) and Prochnow *et al.* (2006) produced equations which can be used to model palaeotemperature without a known value for $\delta^{18}O_p$. They generate these equations by simultaneously solving equations (5.6) and (5.7a), and (5.7b) for temperature, and produce a third-order cubic polynomial for both a spatial relationship (5.8a) (Dworkin *et al.* 2005 and Prochnow *et al.* 2006) and a temporal relationship (5.8b) (Dworkin *et al.* 2005). Also, using the relationship created from the Saratov weather station (5.8c), it is possible to produce a temporal relationship specifically for the Russian field area (5.8c) following the method of Dworkin *et al.* (2005).

$$-0.50\,T^3+(\delta^{18}O_{carb}+152.04)\,T^2-2.78\times10^6=0 \quad (5.8a)$$

$$-0.22\,T^3+(\delta^{18}O_{carb}+61.99)\,T^2-2.78\times10^6=0 \quad (5.8b)$$

$$-0.28\,T^3+(\delta^{18}O_{carb}+92.24)\,T^2-2.78\times10^6=0 \quad (5.8c)$$

where $\delta^{18}O_{carb}$ is the isotopic composition of the pedogenic carbonate (relative to VSMOW); and T is the Mean Annual Temperature (°K). This is converted to °C using the conversion °C = °K – 273.15 (Bureau International des Poids et Mesures 2008).

When equation (5.8a) is applied to the pedogenic carbonate values from Sambullak, Boyevaya Gora and Mescheryakovka, all sections produce MAT values below 0°C, some as low as –28°C, (Figure 5.14). As previously mentioned, there is no evidence of these soils being below freezing for a prolonged period of time. It is also questionable whether carbonate

nodules will be able form in such cold mean annual conditions. Equation (5.8a) also models the negative $\delta^{18}O$ excursion seen at Boyevaya Gora and Sambullak as a fall in temperature (Figure 5.14). This is the opposite of what has been observed in the marine realm where the $\delta^{18}O_{carb}$ negative excursion is linked to a temperature rise (e.g. Magaritz and Holser 1991; Kidder and Worsley 2004) in the range of 5–6°C (Magaritz and Holser 1991), although this single result may be due to changes in rock type or salinity (see Twitchett 2007 and references therein). The estimated drop in temperature seen in Russia also appears incongruent with the observed rise in aridity and evaporation seen in the morphology and mineralogy of the paleosols related to the oxygen excursions. Thus, it is possible to reject this equation as not accurately modelling the Russian sections.

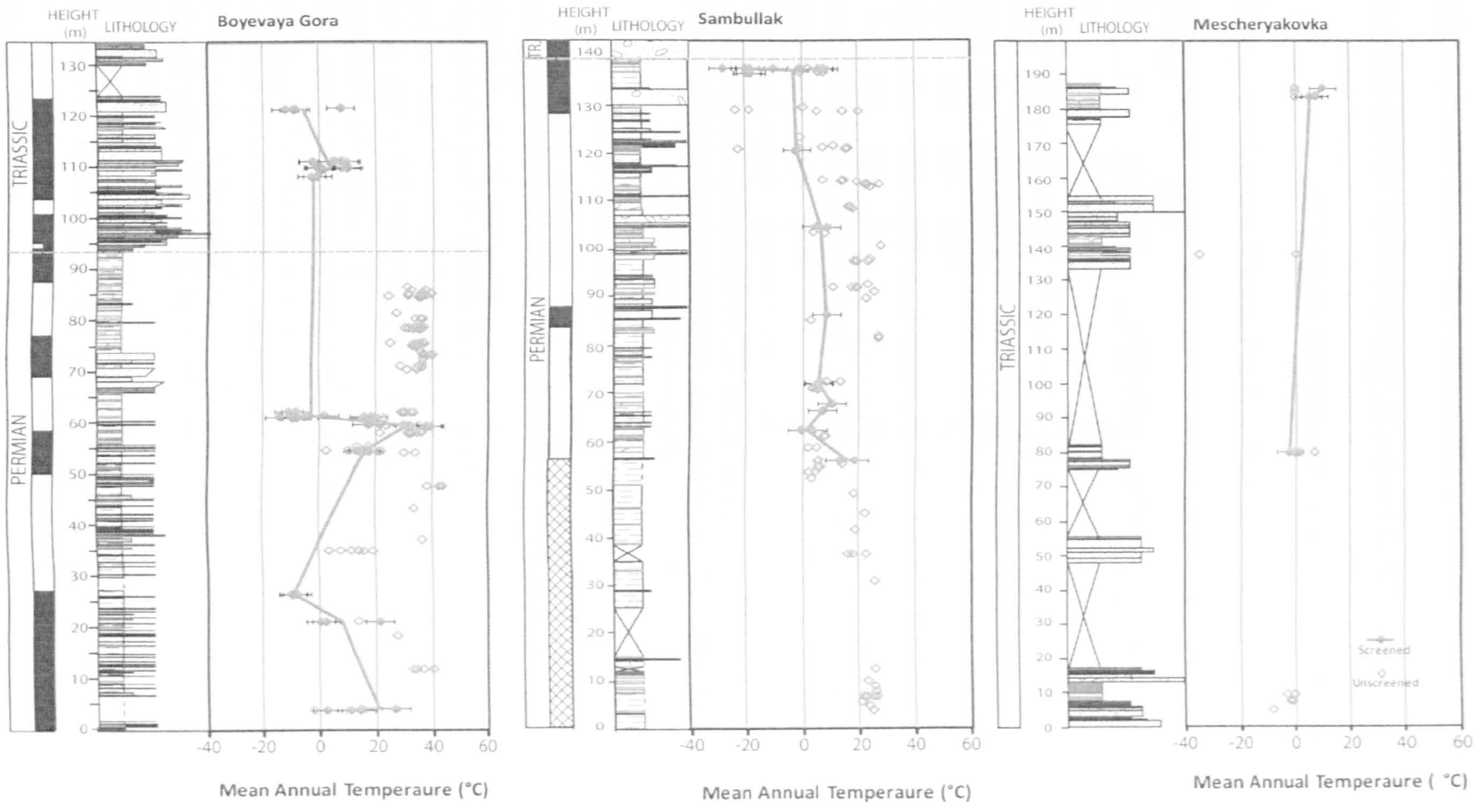

Figure 5.14 Palaeotemperature estimates using equation (5.8a) for Boyevaya Gora, Sambullak and Mescheryakovka. The open diamonds are the nodules that failed the at least one of the screening tests applied (see Appendix 3.3 for calculations).Modelled temperatures below 0°C are incompatible with paleosol morphology (see text) and so Equation 5.8a can be rejected.

When equation (5.8b) is applied to the screened pedogenic carbonate data from Russia, below pedogenic carbonate $\delta^{18}O$ values of –5 ‰ the equation produces temperature estimates of below –400°C, which is impossible (Table 5.2). This is also true for equation (5.8c) which exhibits this behaviour below values of –9‰ (VPDB) (Table 5.2).

		5.8b		5.8c	
$\delta^{18}O_{carb}$ (VPDB)	$\delta^{18}O_{carb}$ (VSMOW)	°K	°C	°K	°C
-3	28	342	69	346	72
-4	27	328	55	338	65
-5	26	304	31	330	57
-6	25	**-147**	**-420**	322	48
-7	24	**-148**	**-421**	312	39
-8	23	**-148**	**-421**	300	27
-9	22	**-149**	**-422**	279	6
-10	21	**-149**	**-422**	**-136**	**-409**
-11	20	**-150**	**-423**	**-136**	**-409**
-12	18	**-150**	**-423**	**-136**	**-410**

Table 5.2 The mean annual air temperatures (in °K and °C) for equations (5.8b) and (5.8c) at a range of $\delta^{18}O_{carb}$ values from 0‰ (VPDB) to –12‰ (VPDB). Note that below -5 ‰ (VPDB) for (8b) and -9‰ (VPDB) for (5.8c) the equations produce unrealistic results (i.e. below 0°K).

The reason for this sudden jump from positive values to extremely negative ones is due to the way a cubic polynomial is solved (see Chapter 2, mathematical methods for mathematical explanation). In the case of equations (5.8b) and (5.8c), below –5 ‰ (VPDB) and –9‰ (VPDB) the equations stop modelling the data in a realistic way (Table 5.2). As experimental values have been recovered from the pedogenic carbonate below these values, and since carbonate values below –5 ‰ (VPDB) and –9‰ (VPDB) are recorded in modern, unaltered pedogenic carbonates (Alonso-Zarza 2003; Dworkin *et al.* 2005), it is clear that these equations do not realistically model the relationship between temperature and $\delta^{18}O_{carb}$ in the Russian data and must also be rejected.

Dworkin *et al.* (2005) also produced an empirical method to calculate palaeotemperature from the modern linear relationship between MAT and modern pedogenic carbonates, from the data of Cerling and Quade (1993). This relationship is defined as:

$$\delta^{18}O_{carb} = 0.49(T) - 12.65 \quad (5.9)$$

where $\delta^{18}O_{carb}$ is relative to Vienna Pee Dee Belemnite (VPDB); and T is the Mean Annual Temperature (°C).

Equation (5.9), like equation (5.8a), models a negative excursion in $\delta^{18}O_{carb}$ as a drop in temperature (Figure 5.15). The values for all three sections are slightly warmer than those calculated from equation (5.8a) but with not quite the same range, that is to say the difference between the maximum and minimum estimates is not as great (Figure 5.15). However, as with equation (5.8a), this equation produces MAT estimates of below 0°C (see Sambullak Figure 5.15) and thus can be rejected as modelling MAT in the Russian sections.

The overall palaeotemperature estimates from the Russian P–Tr boundary produced from equations (5.8a) and (5.9) are not consistent with the pedological observations. That is to say they produce MAT estimates below 0°C as noted earlier, yet there is no evidence of freezing in the sections (see Chapter 3). This suggests that either:

(1) the $\delta^{18}O_{carb}$ values from the pedogenic carbonate were not formed from meteoric water,

(2) the relationship between $\delta^{18}O_{carb}$, $\delta^{18}O_p$, and MAT was different in the Permian –Triassic in the southern Urals, or,

(3) there are other factors influencing this relationship which the Dworkin *et al.* (2005) equations do not take into account.

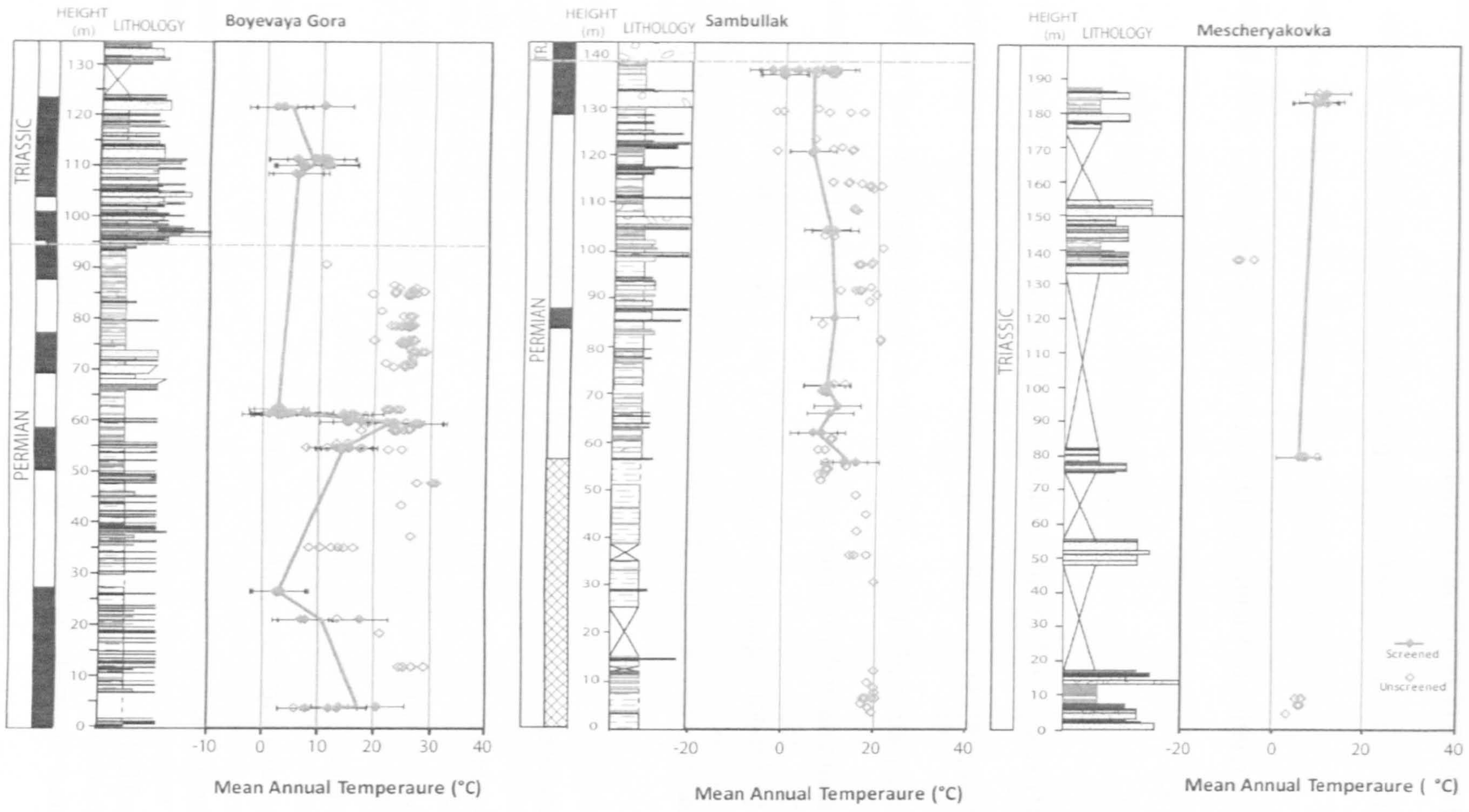

Figure 5.15 Palaeotemperature estimates using equation (5.9) for Boyevaya Gora, Sambullak and Mescheryakovka. The open diamonds are the nodules that failed the screening process (see Appendix 3.3 for calculations).

The screening criteria applied to the $\delta^{18}O_{carb}$ values (see Chapter 4) mean that point (1) can be rejected. The fact that equation (5.8a) has been successfully applied to similar paleosols in the Middle Triassic of Utah (Prochnow *et al.* 2006) suggests that the relationship described by equation (5.8a) is valid for at least some localities in the Triassic. Therefore it seems likely that another factor is influencing the $\delta^{18}O_{carb}$ composition of the pedogenic carbonate nodules in Russia which is causing equations (5.8a), (5.8b), (5.8c) and (5.9) either not to function or to produce anomalously cool temperatures.

The hypothesis that another factor not modelled by equations (5.8a), (5.8b), (5.8c) and (5.9) may also explain why these equations model a negative excursion in $\delta^{18}O_{carb}$ as a drop in temperature, rather than the expected rise. In order to produce a rise in temperature with a negative excursion in $\delta^{18}O_{carb}$ there must be a negative relationship between MAT and $\delta^{18}O_p$. This is the opposite of the relationship described by Fricke and O'Neil (1999). However, such relationships have been observed in the modern day. For instance in modern northern Italy it has been observed that a 3.5°C rise in temperature actually led to a $\delta^{18}O_p$ decrease of –3.82‰ in mean annual precipitation. The reason for this negative in northern Italy is because the rise in temperature caused a reduction in isotopically positive summer rain, shifting the weighted annual mean towards the isotopically negative autumn rains (Longinelli *et al.* 2006). This lowers the $\delta^{18}O$ of mean annual precipitation in the hotter years. This may suggest that in some localities just comparing the seasonal extremes to temperature (as proposed by Fricke and O'Neil 1999) fails to take into account when in the year the maximum precipitation falls and thus which isotopic composition is likely to have a controlling influence over the soil water.

This inverse relationship has also been observed at the Saratov weather station used to produce equation (5.7c), but only when the mean annual temperature is compared to the $\delta^{18}O_p$ of weighted mean annual precipitation (Figure 5.16). The method used to produce (5.7c) (as proposed by Fricke and O'Neil 1999) produces a positive relationship from the very same data (Figure 5.13).

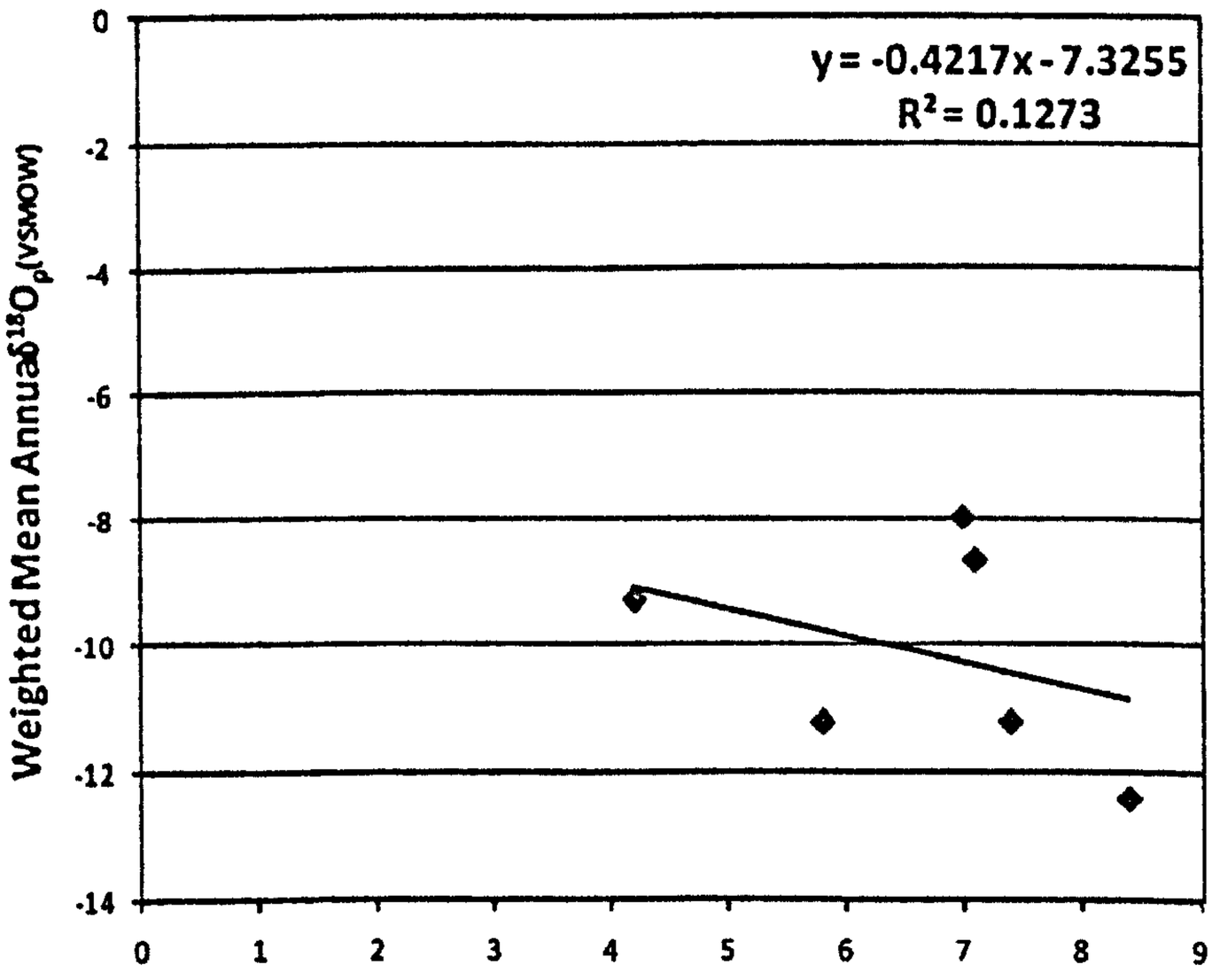

Figure 5.16 A. Weighted mean annual precipitation for 6 years plotted against Mean annual temperature for Saratov station (51° 34' 00" / 46° 1' 60" / 166m).

The reason for the difference between is that at Saratov (Figure 5.16), as in Italy (Longinelli *et al.* 2006), in the years with the highest MAT more precipitation falls in the winter, while in cooler years there is more precipitation in the summer months which is isotopically positive (Figure 5.17). This has the effect of shifting the annual mean of $\delta^{18}O_p$ negative while the actual isotopic values of summer and winter precipitation remain unchanged. Thus, it becomes essential to understand which of these methods best describes the $\delta^{18}O_p$ of soil water and thus that which is incorporated into pedogenic carbonate nodules.

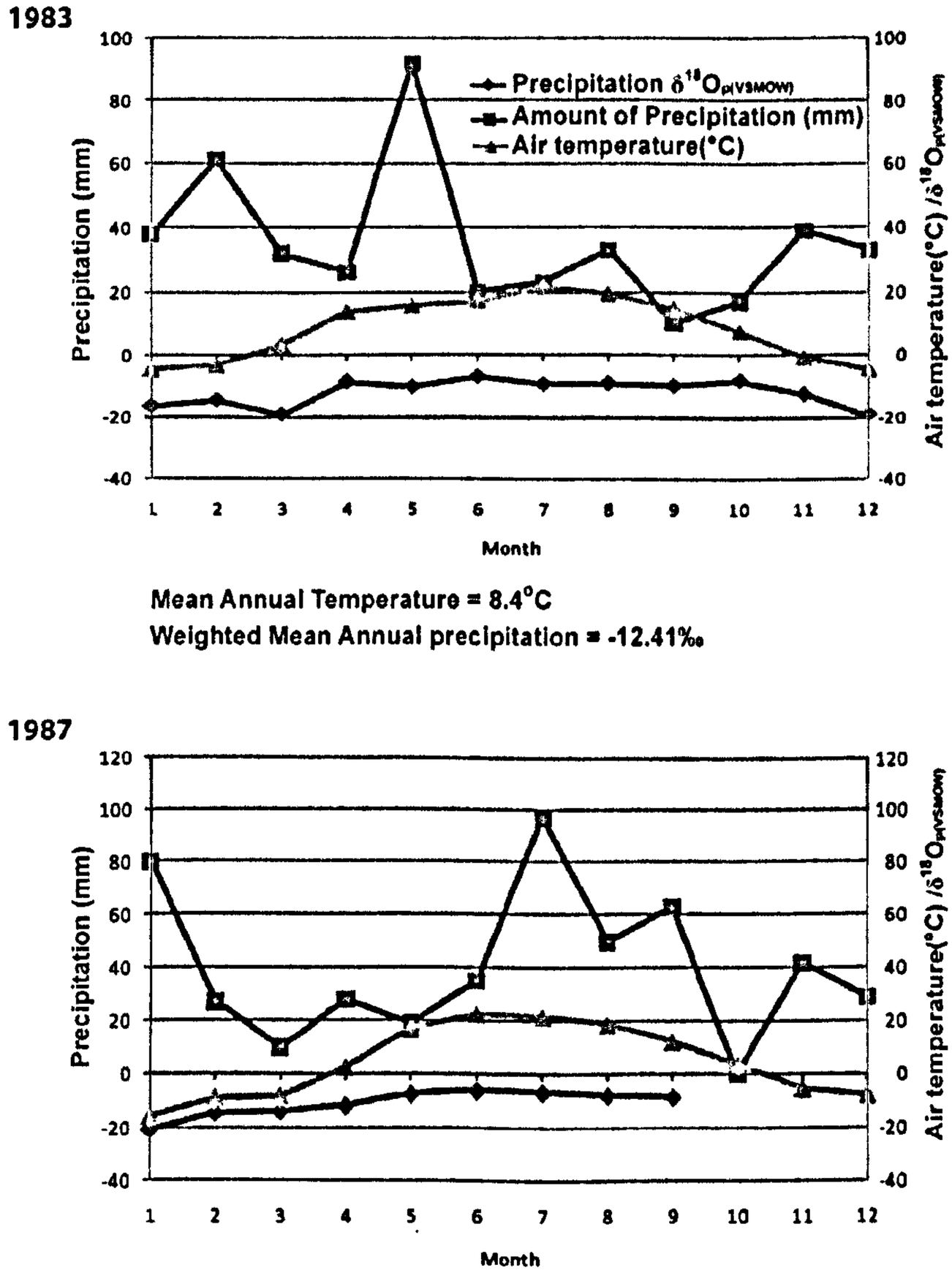

Figure 5.17 The plots of the monthly data collected at Saratov for the hottest year in the dataset (1983) and the coolest (1987). Note the reduction in summer precipitation in the hotter year (1983) leading to a more negative weighted Mean Annual precipitation (data from IAEA/WMO, 2008).

This negative relationship has also been observed in Russia (at Saratov and Rostov Na Donu), Japan (Ryori) and China (Chengdu, Hetian and Zhangye) (data from IAEA/WMO, 2008) (see Figure 5.18). However, when these values are all plotted together it is observed that although values from one locality may show a negative relationship over all they show a positive relationship with respect temperature. This suggests that the relationship described by Fricke and O'Neil (1999) is describing the global latitudinal variation of temperature and $\delta^{18}O_p$ while at single localities the opposite relationship may be true.

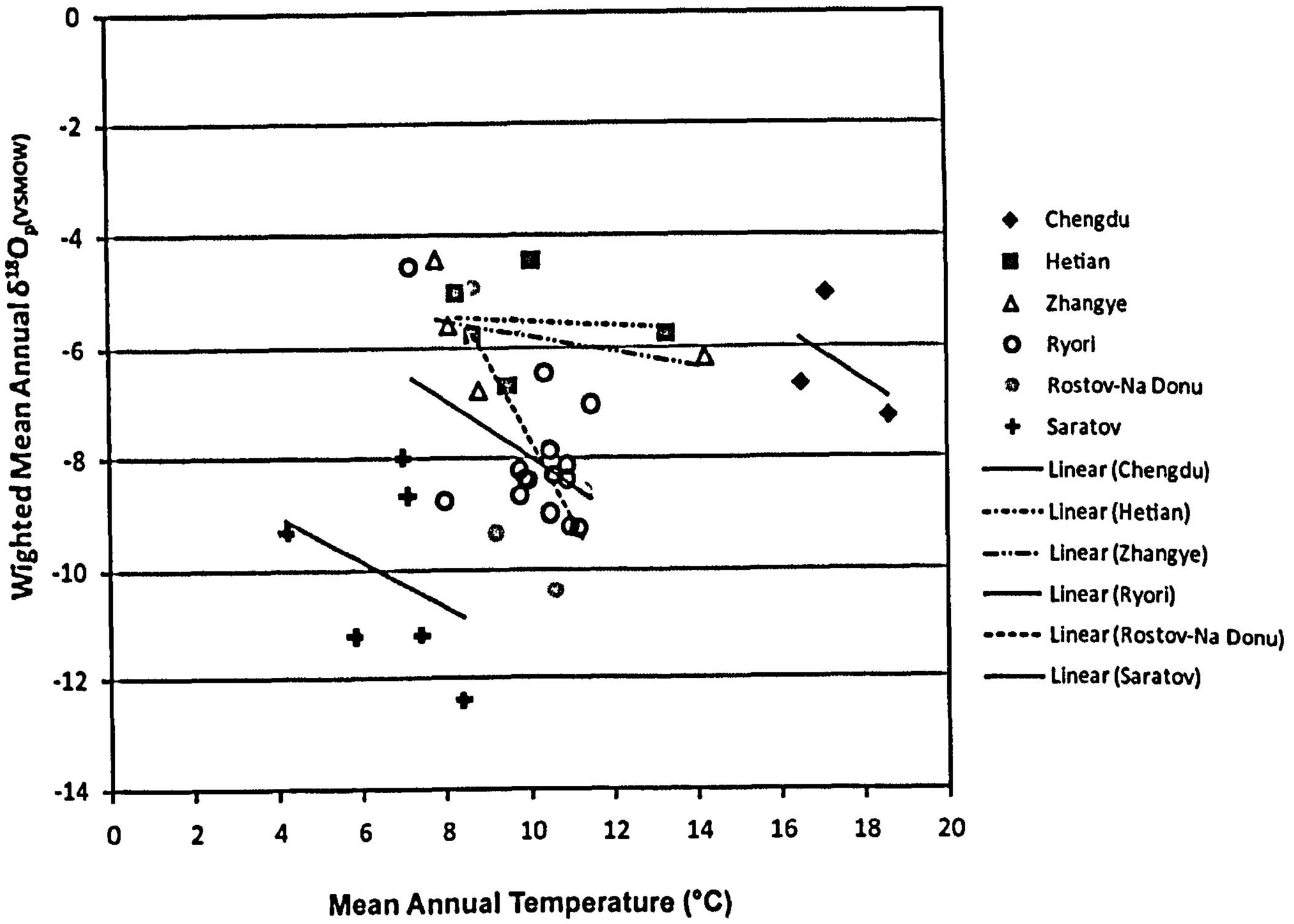

Figure 5.18 Weighted mean annual precipitation plotted against Mean annual temperature for Chengdu (30° 40' 12" / 104° 1' 12" / 506m), Hetian (37° 7' 60" / 79° 55' 60" / 1375m), Zhangye(38° 55' 48" / 100° 25' 48" / 1483m) in China; Ryori (39° 1' 48" / 141° 48' 36" / 260m) in Japan; and Rostov-Na Donu (47° 15' 00" / 39° 49' 12" / 77m) and Saratov (51° 34' 00" / 46° 1' 60" / 166m) in Russia (data from IAEA/WMO, 2008).

It has been suggested that long-term (inter-annual) changes in precipitation and surface air temperature are most appropriate for palaeoclimate reconstructions based on isotopic studies (Rozanski *et al.* 1992). In modern soils it has been observed that, in spite of significant seasonal variation in the isotopic value of the soil water at the surface, those nodules at depth show little inter-annual variation (Liu *et al.* 1996). This would suggest comparing MAT and MAP $\delta^{18}O_p$ rather than using the seasonal extremes as suggested by Fricke and O'Neil (1999), is more applicable to modelling the effect of $\delta^{18}O_p$ in soil carbonates. This approach has also been suggested by studies conducted on modern soils (Cerling and Quade 1993) which have

shown strong correlation between isotopic compositions of carbonate nodules and mean annual precipitation rather than seasonal extremes as used by Dworkin *et al.* (2005).

Using data from the MAT and weighted mean annual precipitation it is possible to model this relationship (Figure 5.16A). Combining this relationship with equation (5.6) it is possible to generate a temperature equation (5.10) that models the effect of reduction in isotopically heavy summer rain shifting the weighted annual mean at Saratov.

$$0.4217\,T^3 + (\delta^{18}O_{carb} - 124.88)\,T^2 - 2.78\times10^6 = 0 \qquad (5.10)$$

When applied to the Russian data this equation produces results that are not below 0°C and produces increases of temperature across the excursions rather than drops (Figure 5.19). Therefore, this method may more accurately model the results from Russia. However, the relative lack of data from the Saratov weather station and the weak coefficient of determination ($R^2 = 0.1273$) (Figure 5.16A) suggests that even though this relationship produces 'realistic' results (i.e. similar to what would be hypothesized) results may be treated with caution.

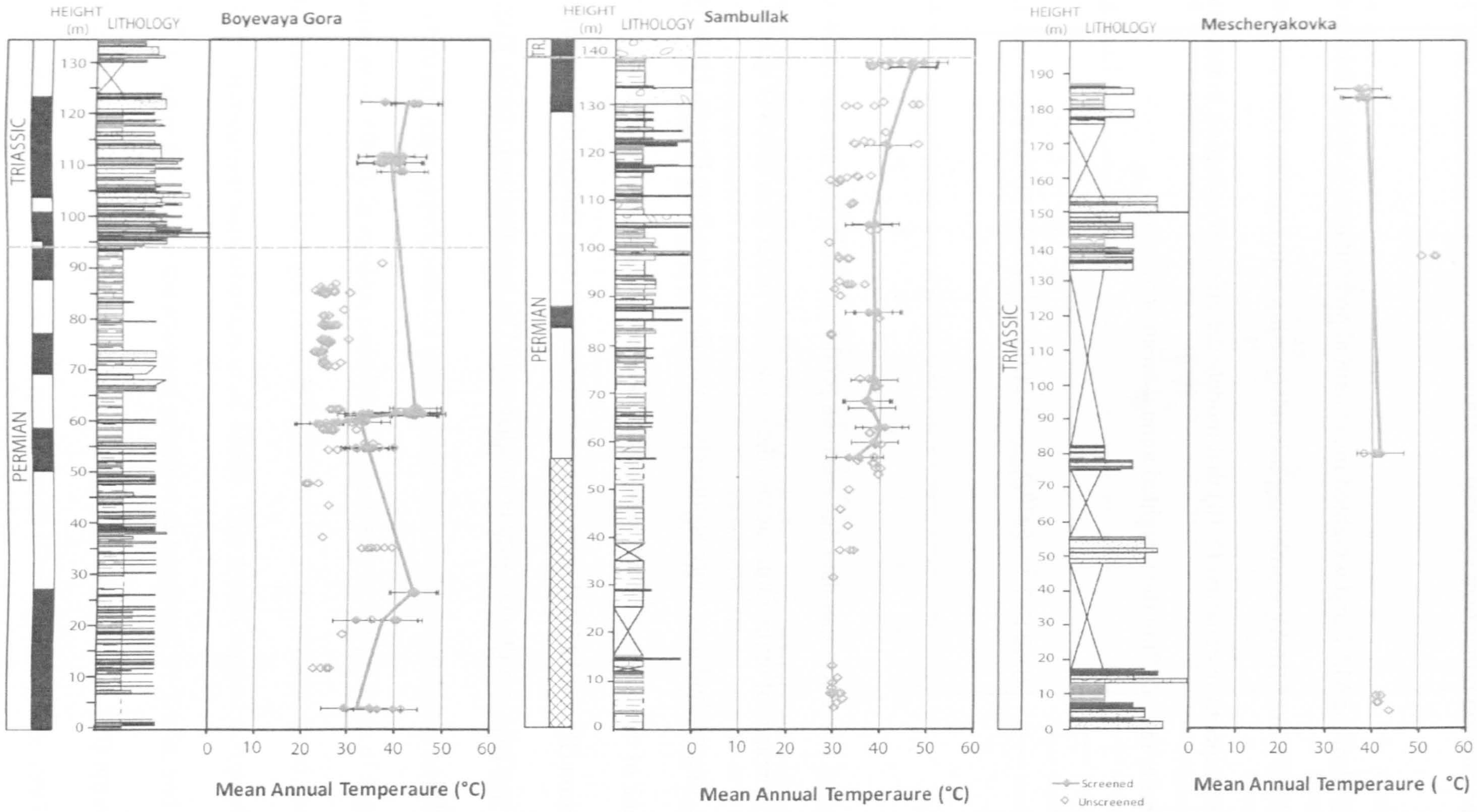

Figure 5.19 Palaeotemperature estimates using equation (5.10) for Boyevaya Gora, Sambullak and Mescheryakovka. The open diamonds are the nodules that failed the screening process. (See Appendix 3.3 for calculations.

5.3.2 Monsoonal effects on oxygen isotopes

Physical processes can change over time and it is possible that modern meteoric precipitation–temperature relationships may not be valid in the past or for a specific locality (Fricke and O'Neil 1999, Dworkin *et al.* 2005). For instance changes in the $\delta^{18}O$ of the palaeo-oceanic source region of precipitation and, changes in the temperature difference between ocean surface temperature at the vapour source and the air temperature at the site of interest, can affect the $\delta^{18}O_p$ versus MAT relationship (Dworkin *et al.* 2005).

The isotopic composition of monsoonal or highly seasonal rain does not correspond to temperature, due to the 'amount effect' where higher amounts of rainfall are associated with a lesser ^{18}O content in the rainwater because, unlike normal precipitation, the air masses move vertically rather than horizontally (Dansgaard 1964: Hoffmann and Heimann 1997; Yadava *et al.* 2007). This can disrupt the relationship seen by Fricke and O'Neil (1999), as rainfall, in these areas will record strongly depleted isotope signals at the period of highest rainfall (Hoffmann and Heimann 1997). In some areas the temperature effect (positive $d\,\delta^{18}O_p/dT$) has been known to partially cancel out the effect of precipitation (negative $d\,\delta^{18}O_p/dP$) as the time of highest rainfall coincides with the time of highest temperature (Johnson and Ingram 2004). In localities affected by the Asian monsoon the standard positive $\delta^{18}O_p$ versus MAT relationship may be nonexistent (Hoffmann and Heinemann 1997; Johnson and Ingram 2004; Li *et al* 2007). In these regions the $\delta^{18}O_{carb}$ can be ~6‰ lighter than in non-monsoonal areas (Alonso-Zarza 2003). Due to a pronounced 'amount effect', rather than producing more negative values at higher latitudes, similarly depleted $\delta^{18}O_p$ values are found at lower latitudes (Hoffmann and Heinemann 1997). This becomes even more problematic if the strength of the monsoon varies over time. It has been observed in modern China that, depending on the strength of the monsoon, the dominant control on $\delta^{18}O_p$ can switch back and forth between the

precipitation (the amount effect) and temperature (Johnson and Ingram 2004). This could produce erroneous palaeotemperature estimates using equations (5.8a), (5.8b), (5.8c), (5.9) and (5.10) if an increase in monsoonal, or seasonality, activities occurs at the same time as an increase in temperature, since it could potentially cancel out or even reverse the positive excursion caused by temperature.

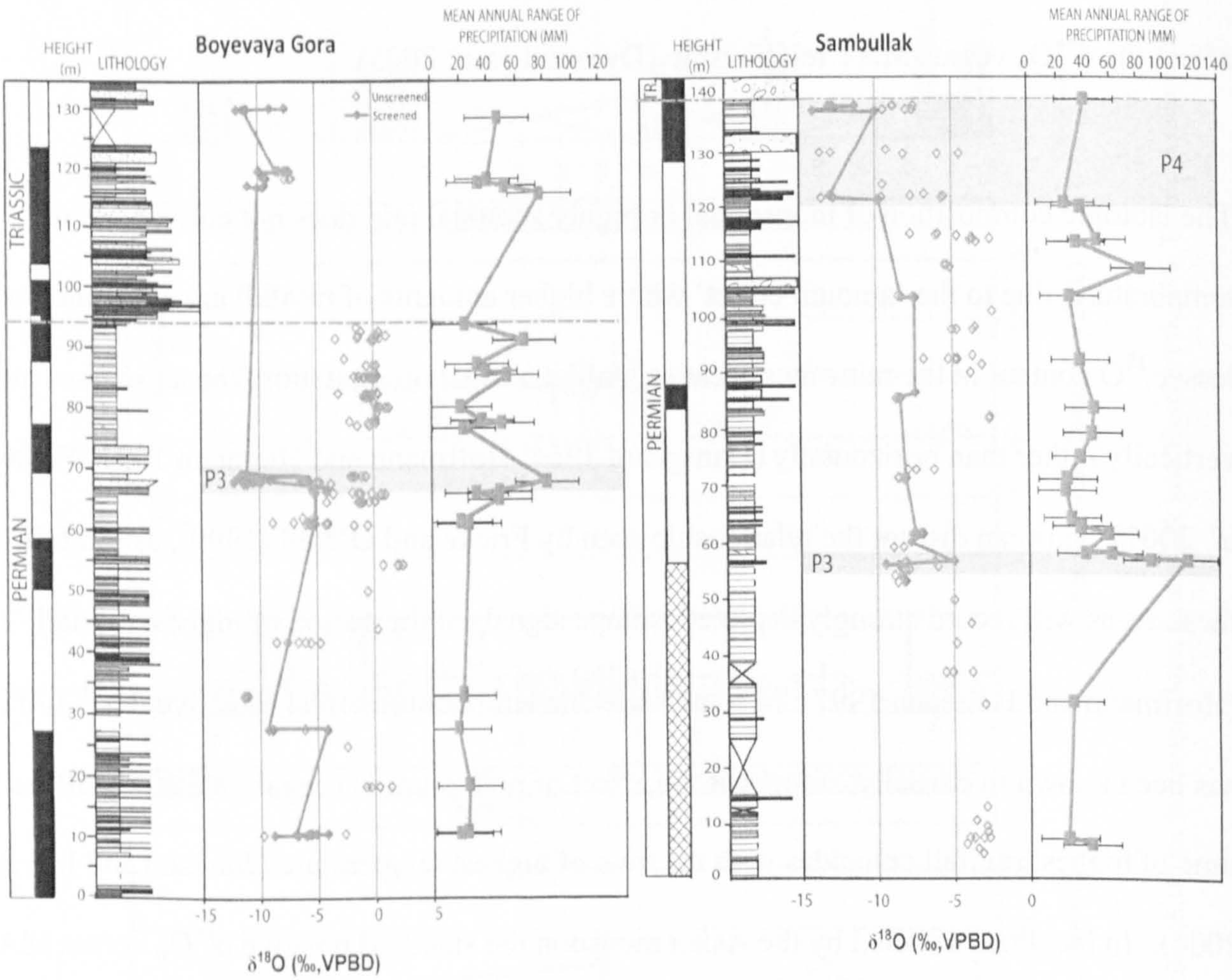

Figure 5.20 Variation in $\delta^{18}O_{carb}$ of pedogenic carbonate plotted next to mean annual range of precipitation at Boyevaya Gora and Sambullak. Note how there is an apparent increase in seasonality activity after the negative $\delta^{18}O_{carb}$ at Boyevaya Gora (see Appendix 3.2 and 3.3 for calculations).

If the annual range of precipitation is used as a proxy for changes in seasonality (cf. Retallack 2005b) and is plotted against the $\delta^{18}O_{carb}$ values it is notable that the negative excursion P3 is coincident with a marked rise in mean annual range of precipitation from 46mm (±22mm) to 76mm (±22mm) at Boyevaya Gora and 30mm (±22mm) to 90mm (±22mm) at Sambullak

(Figure 5.20). This is very similar to the difference in mean annual range of precipitation between monsoonal and non-monsoonal locations in the modern world (see Section 5.2) may suggests that the isotope excursion P3 may be caused by an increase in seasonality, and thus the influence of the amount effect, rather than temperature (Figure 5.20). Excursion P4, on the other hand, does not coincide with a rise in mean annual range of precipitation and thus probably relates to a change in temperature rather than seasonality activity (Figure 5.20).

5.4 Discussion

Some of the strongest evidence for environmental change associated with the P/Tr boundary is that from the palaeoprecipitation estimates. Using the palaeoprecipitation equation for Vertisol microlows (equation 5.3a) there is a 200mm rise in MAP across the P/Tr boundary compared to a rise of just less than 400mm across the P/Tr boundary recorded at Lootsberg Pass in the Karoo basin (Retallack 2003). However, the three other equations (5.2, 5.3 and5.5) all show the opposite relationship, suggesting a drop in MAP in the earliest Triassic. These three equations also all suggest an increase of MAP through the part of the section at Boyevaya Gora containing only pedogenic dolomite (Figure 1 and Figure 6) which may seem incongruous as pedogenic dolomite is probably linked to increases in evaporation (see Chapter 4). It has been noted that pedogenic dolomite in other sections is related to increased seasonality (Kessler *et al.* 2001), an observation borne out by the suggestion of an increase in the mean annual range of precipitation (seasonality) related to this rise in MAP (Figure 5.6). This increase in the mean annual range of precipitation is evident, both after the P3 event at Boyevaya Gora, over the P/Tr boundary and increasing into the Triassic, and is especially evident in the Olenekian where there is a strong increase in the range of mean annual precipitation. An increase in seasonality and MAP has also been observed at Karoo, in the

Earliest Triassic, (Retallack 2003) and in the Anisian of Utah in the USA. (Prochnow *et al.* 2006).

As stated by Retallack (1994), climate modelling can become very seductive and the results of any model must be tempered by real pedological and sedimentological data. This is especially pertinent when considering the results from the palaeotemperature equations. Thus, a holistic approach must be used, especially in cases where the evidence from different models is contradictory.

The pedological data and analysis of the sections in Russia (Chapter 3) suggest a steppe to semi-arid climate, as warm as or warmer than similar environments existing today. Modern dry steppe environments (BSh) have a MAT greater than 18°C (Peel *et al.* 2007). The increase in numbers of Vertic paleosols up to the P/Tr boundary seen in Russia suggests that the paleosols were being affected by more pronounced wetting and drying cycles, and the increase of pedogenic dolomite would suggest an increase in evaporation (Figure 1 and Chapter 4). This would all point to an increase in temperature up to the P/Tr boundary. Equally the evidence from the paleosols suggests that, by the Olenekian in the Early Triassic, the basin was more arid and possibly hotter than it was in the Permian. The occurrence of Triassic aeolian dunes in the Induan (Tverdokhlebov *et al.* 2002) would also indicate a hotter, more arid, climate in the Triassic than the Permian.

	Permian (°C)			Triassic (°C)		
Equation	Min	Mean	Max	Min	Mean	Max
5.6	-11	27	64	21	31	46
5.9	-3	10	28	2	8	12
5.10	23	38	49	37	40	45

Table 5.3 Values from the three palaeotemperature equations. Equation 5.6 uses a constant value of $\delta^{18}O_p = -5.52‰$) (see Appendix 3.3 for calculations).

Based on the results of computer climate modelling, it is suggested that in the latest Permian the Southern Urals area summer temperatures were between 35 – 40°C, winter temperatures were between 0 – 5°C (Kiehl and Shields 2005) and soil temps of ~30°C (Roscher *pers. comm.*). Others have suggested a slightly lower global temperature of 25°C (35°C at the equator and 15°C at the poles) in the Late Permian rising to a global average of 30°C (40°C at the equator and 20°C at the poles) (Kidder and Worsley 2004). Based on these models it appears that equation 5.10 best fits the range they predict (Table 5.3) although it is on the high end of the range of these predictions. Palaeotemperature estimates from paleosols in the Karoo basin, using different proxies (B horizon chemistry), suggest a rise from 9.9°C (±4.4) in the Permian to 10.3°C (±4.4) in the Triassic (Retallack *et al.* 2003). However, in their paper Retallack *et al.* (2003) suggest that diagenetic changes may have offset their estimates. Also the Karoo sections are at higher latitude than the Russian sections (50-60°S Retallack *et al.* 2003 compared with 30-35°N Taylor *et al.* 2009)

As noted in Chapter 4 there are two negative $\delta^{18}O_{carb}$ anomalies which are recorded in pedogenic calcite and defined by more than one paleosol in the South Urals sections; one just before the P/Tr boundary at Sambullak (P4) and one 40m below the P/Tr boundary (P3) at both Sambullak and Boyevaya Gora. Both of these excursions represent rises in temperature of ~7°C, using equation (5.10). However, it is possible that the excursions are linked to other processes such as an increase in highly fractionated seasonal precipitation rather than changes in temperature and, if these dominated, they could obscure any signal caused by changes in local air temperature.

These factors can be divided into local and global factors (Figure 5.21). Local factors include changes in evaporation, plant cover and waterlogging of the soil. With respect to the isotope

excursions recorded in Russia, the increase in aridity linked with the possible reduction in plant cover would cause an increase in evaporation which would preferentially remove the lighter isotopes producing a positive excursion rather than a negative one (Wright and Tucker 1991: Cerling and Quade 1993; Liu *et al.* 1996). The influence of groundwater is thought also to cause enrichment in ^{18}O from more evolved groundwaters (Wright and Tucker 1991) although it has been observed that pedogenic carbonate is enriched with respect to groundwater cavity fills (Quast *et al.* 2006). This effect was observed in the difference between the spar and micritic component of the Russian nodules so, by screening the data and excluding all the results where these values were within error of each other, the effect of groundwater has been removed (Chapter 4).

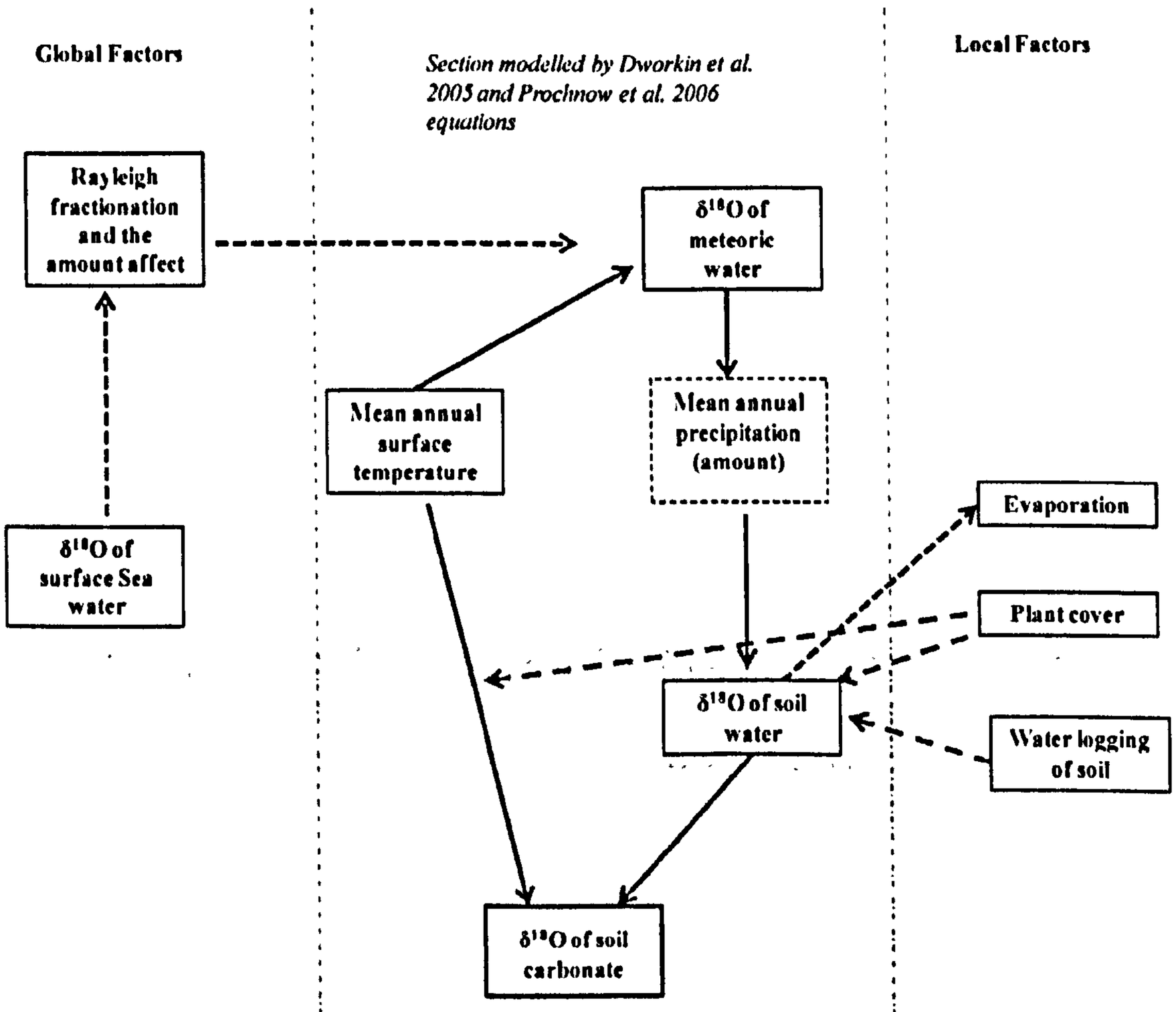

Figure 5.21 The factors that can affect the $\delta^{18}O$ of soil carbonate. The central panel contains the factors described in the equations created by Dworkin *et al.* (2005). The other two panels refer to other factors that can affect the $\delta^{18}O$ of soil carbonate that are not included in the equations. Global factors refer to factors that normally are constant but at a time of mass extinction may vary and local factors are those in the local environment that could also affect soil carbonate.

The global factors that could have obscured any change in local air temperature include changes in the $\delta^{18}O$ of the seawater source area and changes in circulation. However, it has been observed that changes in $\delta^{18}O$ of the seawater have only a minor effect on $\delta^{18}O_p$ (1–2‰ over geological scales) (Fricke and O'Neil 1999) compared to the effect caused by Rayleigh fractionation (the process of evaporation and condensation within the cloud base) which can vary up to 30‰ (Dansgaard 1964). One of the strongest influences of the $\delta^{18}O_{carb}$ of pedogenic carbonate is the effect of changes in monsoonal variability (Andrews *et al.* 1998; Alonso-Zarza 2003; Dworkin *et al.* 2005). The Russian paleosols of the Late Permian have dispersed carbonate nodules, which have been linked to the influence of monsoonal activity (Retallack *et al.* 2003; Retallack 2005b) and it has been suggested that there was an increase in monsoonal activity across the P/Tr boundary (Kidder and Worsley 2004). This increase in seasonal rain could have introduced isotopically lighter precipitation into the system, as has been recorded in the Late Pleistocene in India (Andrews *et al.* 1998) and in China (Johnson and Ingram 2004; Li *et al.* 2007).

The coincidence of a $\delta^{18}O_{carb}$ negative excursion (P3) with a marked increase in mean annual range of precipitation suggests that this excursion may be in part due to an increase in seasonality and thus the influence of the amount effect. It is possible to quantify the change in $\delta^{18}O_p$ that is needed to produce the recorded $\delta^{18}O_{carb}$ negative excursion, assuming temperature did not change, by using equation (5.6) (Table 5.4).

		$\delta^{18}O_{carb}$ (‰)		Temp	$\delta^{18}O_p$
		VPDB	VSMOW	°C	‰
Boyevaya Gora					
	Excursion	-9.46 (±7.48)	21.10 (±7.71)	30 (±12)	6.46 (±10.22)
	Pre excursion	-3.12 (±7.18)	27.65 (±7.41)	30 (±12)	-0.09 (±9.92)
Change in $\delta^{18}O_p$ needed to cause excursion					-6.54 (±0.31)
Sambullak					
	Excursion	-9.05 (±0.87)	21.53 (±0.90)	34 (±2)	5.15 (±1.32)
	Pre excursion	-5.63 (±1.29)	25.06 (±1.33)	34 (±2)	1.62 (±1.75)
Change in $\delta^{18}O_p$ needed to cause excursion					-3.53 (±0.43)

Table 5.4 The change in $\delta^{18}O_p$ to generate excursion P3 at Boyevaya Gora and Sambullak if temperature is held constant.

It is theoretically possible to produce the negative excursion P3 without any change in temperature simply by reducing $\delta^{18}O_p$ by –6.54‰ to –3.53‰. In modern monsoonal areas (e.g. New Delhi) there is a –8.4‰ difference between the $\delta^{18}O_p$ in monsoonal months compared to non monsoonal months (IAEA/WMO, 2008). Thus, it is possible that the excursion P3 may be purely due to a change to monsoonal conditions. However, the negative $\delta^{18}O_{carb}$ excursion occurs at the same time as a similar negative $\delta^{13}C_{carb}$ excursion, suggesting a change in atmospheric conditions (cf. Kidder and Woresley 2004; Retallack and Krull 2006; Payne and Kump 2007).

A negative $\delta^{18}O$ excursion in the composition of therapsid tusks has been observed at Karoo across the P/Tr boundary and has been interpreted as a rise in temperature (Smith and MacLeod 1998; MacLeod *et al.* 2000; Retallack *et al.* 2003). If this is indeed the case at these localities, then an inverse relationship between temperature and $\delta^{18}O_p$ (e.g. as observed at Saratov Figure 5.17 B) must have operated. As if the global positive relationship observed by Fricke and O'Neil (1999) controlled the composition of $\delta^{18}O_p$ then these excursions too would be caused by a fall in temperature rather than a rise. This underlines the fact that when

applying palaeotemperature equations to data from ancient terrestrial systems, the models that have been created for the modern day may not necessarily hold true in the past and that there may be local conditions that have a stronger influence on the isotopic composition than global ones especially at times of changes in the seasonality of rainfall as seen in Russia.

5.5 Summary

In summary, the period spanning the Permian–Triassic in Russia is characterised by dramatic climate change. This climate change, however, seems to have started prior to the P/Tr boundary in the South Urals and is linked to the large negative carbon and oxygen excursion (P3). The palaeoclimatic investigations have revealed the following:

1. The negative carbon and oxygen excursion (P3) is followed by a period of only type B dolomite at Boyevaya Gora and an increase in type B dolomite at Sambullak;
2. MAP for the Permian is 392mm (±158, 1σ std) (eq.5.2) to 242mm (±72, 1σ std) (eq.5.5) and a possible of drop in MAP into the earliest Triassic at Boyevaya Gora to 185mm (±48, 1σ std) (eq.5.2) to 180mm (±6, 1σ std) (eq.5.5) followed by an increase by the Olenekian to 541mm (±269, 1σ std) (eq.5.2) to 313mm (±151, 1σ std) (eq.5.5);
3. There is an increase in mean annual range of precipitation from the excursion P3 up to the P/Tr boundary and an even bigger increase in the Olenekian to annual ranges similar to modern-day monsoonal areas (New Delhi) suggesting an increase in seasonality in the Triassic;
4. If the $\delta^{18}O_{carb}$ isotopic values are completely controlled by temperature, it appears that the paleosols in Russia, as at Saratov today, showed a lack of summer rain with an increase in air temperature causing the weighting of the mean annual precipitation towards more negative $\delta^{18}O_p$ values for warmer years;

5. Using equation (5.10) suggests an average Permian temperature of 38°C (± 14) and 40°C (± 8) in the Triassic. The excursions at Sambullak and Boyevaya Gora (P3 and P4) represent a rise in MAT of 7°C, although the weakness of the MAT/$\delta^{18}O_p$ relationship (Figure 5.17) on which equation (5.10) is based urges caution in the use of this estimate;
6. It is possible that excursion P3 (but not P4) represents an increase in seasonality and thus the amount effect with or without a rise in temperature.

Chapter 6. Isotopic variation in marine carbonates of the Italian Dolomites[1]

6.1 Introduction

The potential multiple influences on the pedogenic $\delta^{18}O_{carb}$ values in Russia (see Chapter 5) means it is essential to understand whether the $\delta^{18}O_{carb}$ excursion seen in Russia are actually due to a change in temperature at P/Tr boundary or is due to another cause, such as changes in seasonality. Fossil brachiopods, due to their low-Mg calcite composition, which is a diagenetically more stable polymorph of calcite, have the potential to preserve a primary isotopic signal (Auclair *et al.* 2003). The comparison of the morphological and chemical structures of fossil brachiopods with modern brachiopods can thus determine if they have been recrystallised or altered by diagenesis (Auclair *et al.* 2003; Bojar *et al.* 2004; Korte *et al.* 2005a, b; van Geldern *et al.* 2006). As such they have been successfully used as proxies for both the $\delta^{13}C$ and $\delta^{18}O$ composition of ambient seawater (Popp *et al.* 1986; Veizer *et al.*1986; Grossman *et al.* 1996; Veizer *et al.* 1999; Brand 2004; Batt *et al.* 2007) and also to estimate palaeotemperature (Korte *et al.* 2005a, b; van Geldern *et al.* 2006) hence they could be used to test if the $\delta^{18}O$ excursion in the marine bulk rock record associated with the P/Tr boundary is a result of a change in temperature or a later diagenetic artefact.

In addition, understanding the $\delta^{13}C$ isotopic composition of palaeo-seawater is also essential when attempting to estimate pCO_2 from pedogenic carbonate from paleosols. This is because the paleosol pCO_2 model proposed by Cerling (1991) and modified by Ekart *et al.* (1999) needs an estimate of the $\delta^{13}C$ composition of the atmosphere ($\delta^{13}C_a$) which can be derived from the isotopic composition of carbonate precipitated in equilibrium with palaeo-seawater

[1] This chapter is adapted from a co-authored paper Kearsey *et al.* in review (see References)

(Mora *et al.* 1996; Ekart *et al.* 1999; Prochnow *et al.* 2006). Therefore, to produce an accurate pCO_2 estimate, especially over periods of extreme climatic change, accurate palaeo-seawater composition estimates are required.

The global marine negative carbon and oxygen isotope excursion associated with the P/Tr boundary has been observed in marine carbonate sections from the Italian and Austrian Dolomites (e.g. Magaritz *et al.* 1988; Baud *et al.*1989; Holser *et al.* 1991) which has been linked to a change rise in temperature (Holser *et al.* 1991). Equally, many of these sections have also been shown to contain brachiopod fossils (e.g. Posenato 2001; Chen *et al.* 2006). To investigate the difference between bulk rock and brachiopod isotope values the section at Val Brutta in the Italian Dolomites was micro-sampled and variations in lithology and recrystallisation were taken into consideration in order to determine whether lithology, diagenesis or primary processes were controlling the stable isotopic composition of the carbonates within the section. Biogenic calcite of brachiopod shells were recovered from this and another section (Tesero) to investigate how their isotopic composition compared with the bulk rock record with the aim of recovering a palaeotemperature and palaeo-seawater composition record.

6.2 Geological setting and stratigraphic position

The sampled localities for this study are Val Brutta (N 46° 0.539′, E 011° 26.685′) and Tesero (N 46° 17.191′, E 011° 31.211′) (Figure 1). The Val Brutta section has been previously described by Ghetti and Neri (1983) and Posenato (2001). It consists of 80 metres of shallow marine carbonates which extend through the upper part of the Bellerophon Formation and into the Tesero Member of the overlying Werfen Formation. The Bellerophon Formation consists

of interbedded grey micritic muds and recrystallised fossiliferous wackestones and packstones.

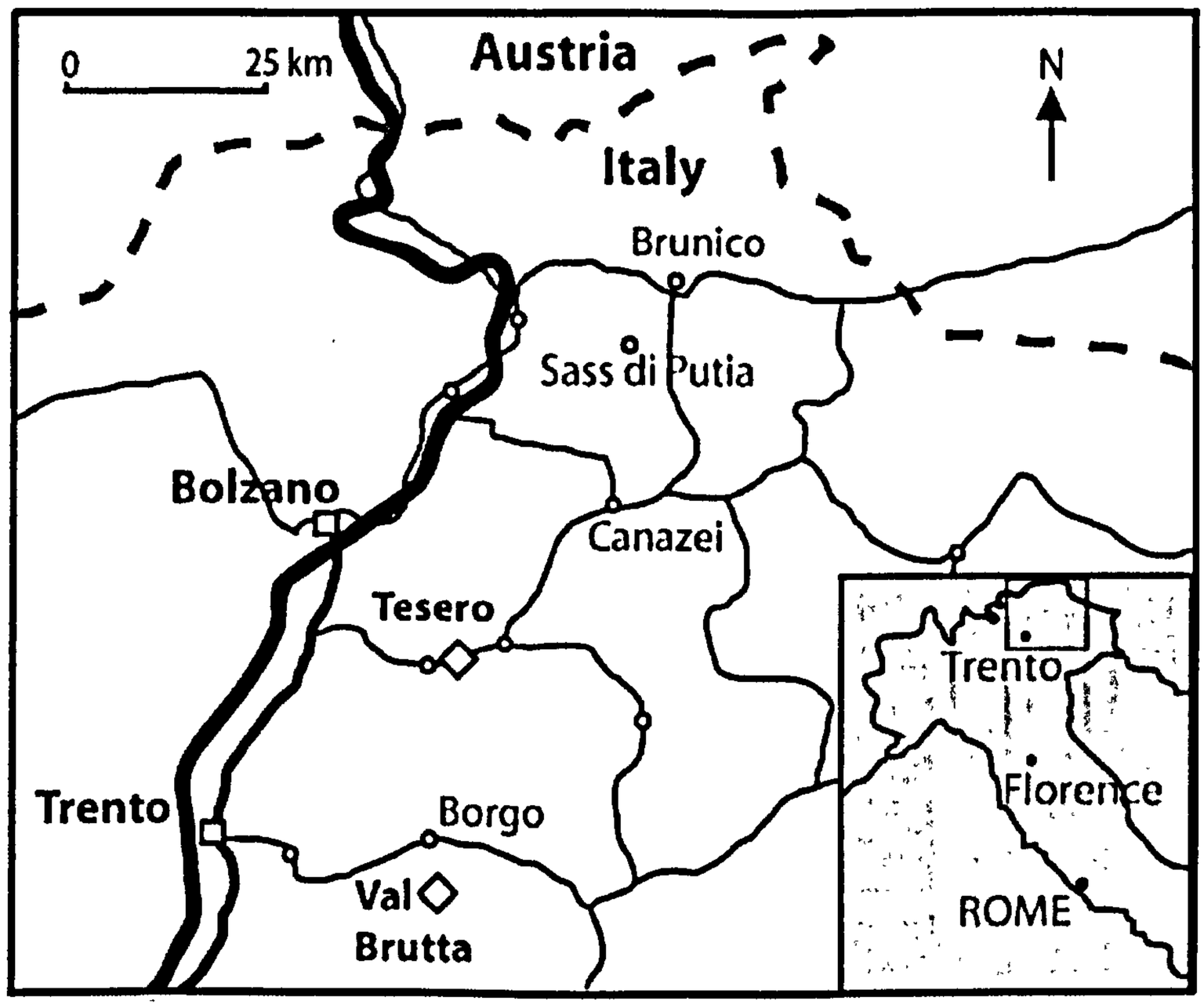

Figure 6.1 Map of the South Tyrol region of Northern Italy with the study localities (Val Brutta and Tesero) marked (diamonds).

The lower Tesero Member comprises thickly bedded oolitic grainstones which were deposited in sub-tidal, low energy, ooid shoals (Broglio Loriga *et al.* 1983; Farabegoli *et al.* 2007). The studied brachiopod material at Val Brutta has been mainly collected from the fossiliferous 'transitional beds' of Posenato (2001) between the Bellerophon and Werfen formations, which correspond to the Bulla Member of Farabegoli *et al.* (2007) (Figure 6.2). These beds consist of 0.30-0.24m of fossil rich bioclastic packstones, which are overlain by the first oolitic grainstones of the basal Tesero Member of the Werfen Formation.

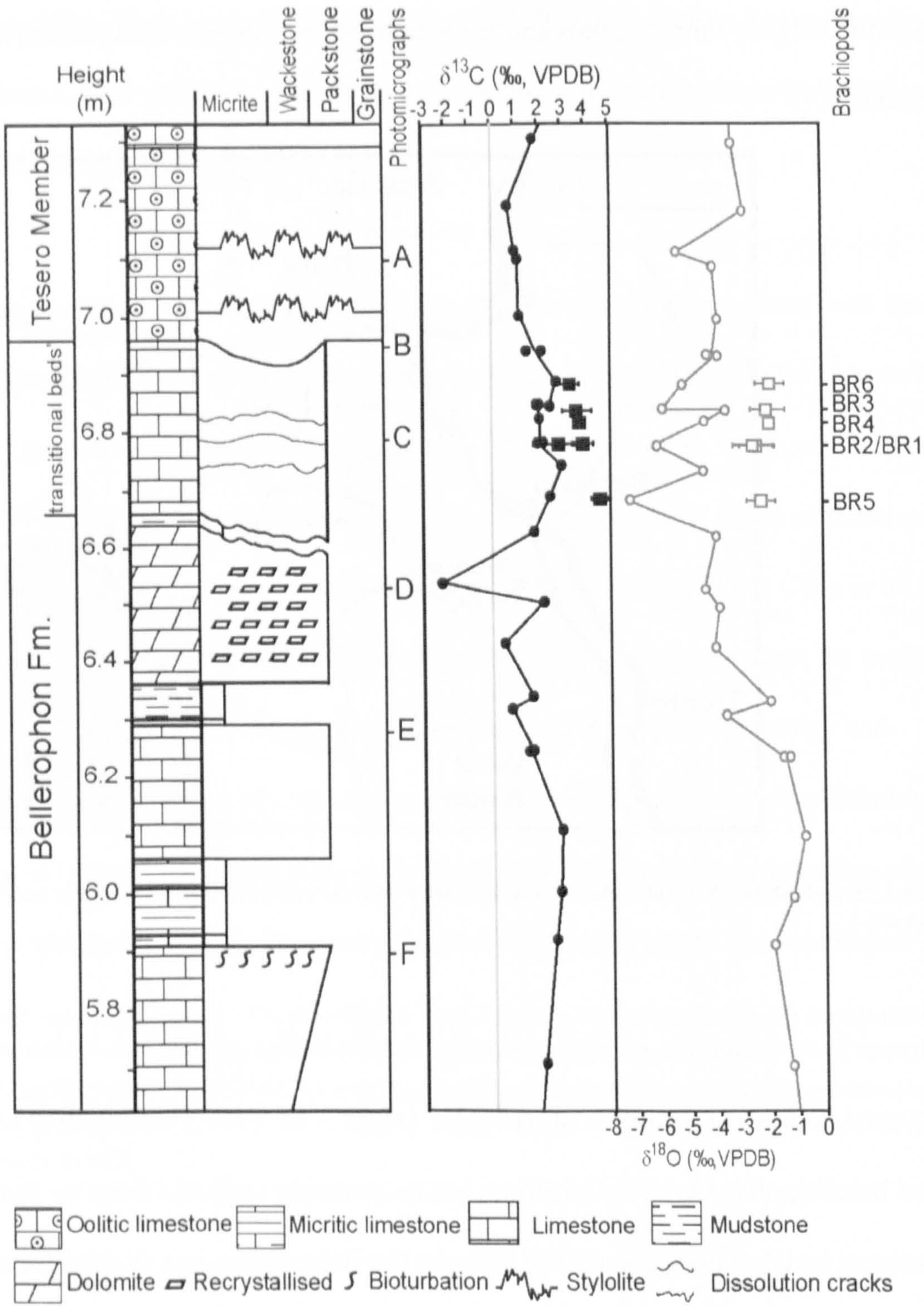

Figure 6.2 Detail of the beds around the Bellerophon Formation, Tesero Member boundary and especially the 'transitional beds' (of Posenato 2001). The photomicrographs referred to in the figure are seen in Figure 6.4. Stable isotope results for both the brachiopods (square) and bulk rock (circles) and the brachiopods results have the relevant sample number next to them.

The Tesero section has been previously described by Neri *et al.* (1986) and Broglio Loriga and Cassinis (1992). Only the uppermost Bellerophon Formation is exposed at Tesero and this consists of predominantly grey brown to whitish dolomites and shelly marls. Overlying this is a peloidal packstone which is taken to be the top of the Bellerophon Formation (Neri *et al.*

1986; Farabegoli *et al.* 2007). Above this point, as at Val Brutta, the peloidal packstone is overlain by the oolitic grainstones of the Tesero Member, interbedded with occasional ~10cm thick micritic mud bands. The brachiopod fossils were recovered from a micritic horizon 154cm above the base of Tesero Member.

Determining the precise position of the P/Tr boundary in the Southern Alps' sections has been problematic in the past, due to the absence of ammonoids in the lower Werfen Formation (e.g. Broglio Loriga *et al.* 1983). In marine Permian–Triassic sections conodonts are the preferred zone fossils of the P-Tr interval as the GSSP for the base of the Triassic is now defined as the first appearance datum of the conodont taxon *Hindeodus parvus* in Meishan, South China (Yin *et al.* 2001). However, due to the rarity of *H. parvus* in the Italian sections and the transgressive nature of the Tesero Member there is much debate about the position of the P/Tr boundary within the Werfen Formation. Wignall *et al.* (1996), placed the entire Tesero Member (= their Tesero Oolite Horizon) within the Changhsingian as they recorded *H. parvus* from the base of the Mazzin Member in the Tesero locality type section. In contrast, Farabegoli and Perri (1998, p. 302) placed the P/Tr boundary somewhat lower within the Tesero Member, following their analysis of the Bulla section. In southern Austria, *H. parvus* first appears at the top of Tesero Member in the Gartnerkofel-1 core, but at the base of the Tesero Member in the nearby outcrop sections (Holser *et al.* 1991).

Recently, Farabegoli *et al.* (2007) has correlated the Italian sections with the GSSP section in Meishan using a combination of facies interpretations and conodont biostratigraphy, and maintain that the P/Tr boundary lies within the Tesero Member. However, the extinction event occurs below the Bellerophon/Werfen Formation contact, with a further extinction horizon within the lower metres of the Tesero Member (Broglio Loriga and Cassinis 1992;

Cirilli *et al.* 1998; Rampino and Adler 1998). The brachiopods analysed in this study from Val Brutta derive from the Late Permian, just prior to the main local extinction event. The brachiopods recovered from the section at Tesero are from the Tesero Member, above the extinction horizon but below the first occurrence datum of *H. parvus* (Chen *et al.* 2006; Farabegoli *et al.* 2007).

6.3 Results – bulk rock stable isotopes

Bulk rock stable isotope analysis was undertaken at Val Brutta to pinpoint the isotope anomaly at that locality and to compare it to other Italian and global sections, and to the brachiopod values from the same locality (see Appendix A4.2 for results table).

At Val Brutta the $\delta^{13}C$ and $\delta^{18}O$ bulk rock values record a negative excursion which starts in the uppermost beds of the Bellerophon Formation (63m) (Figure 6.3). The $\delta^{18}O$ data record a negative excursion of –3.28‰ between 63m and 64m in the section. The $\delta^{18}O$ continue to record a negative trend of –1.58‰ up through the Tesero Member to the top of the section. The $\delta^{13}C$ data are more complicated. Coincident with the $\delta^{18}O$ excursion there is a $\delta^{13}C$ excursion of –2.04‰. Then at 65.6m there is an even greater excursion of –4.31‰, although this is only constrained by one analysis. By 67.6m the $\delta^{13}C$ values have returned to pre-excursion levels before showing a gradual negative shift of –2.58‰ into the Tesero Member and to the top of the section.

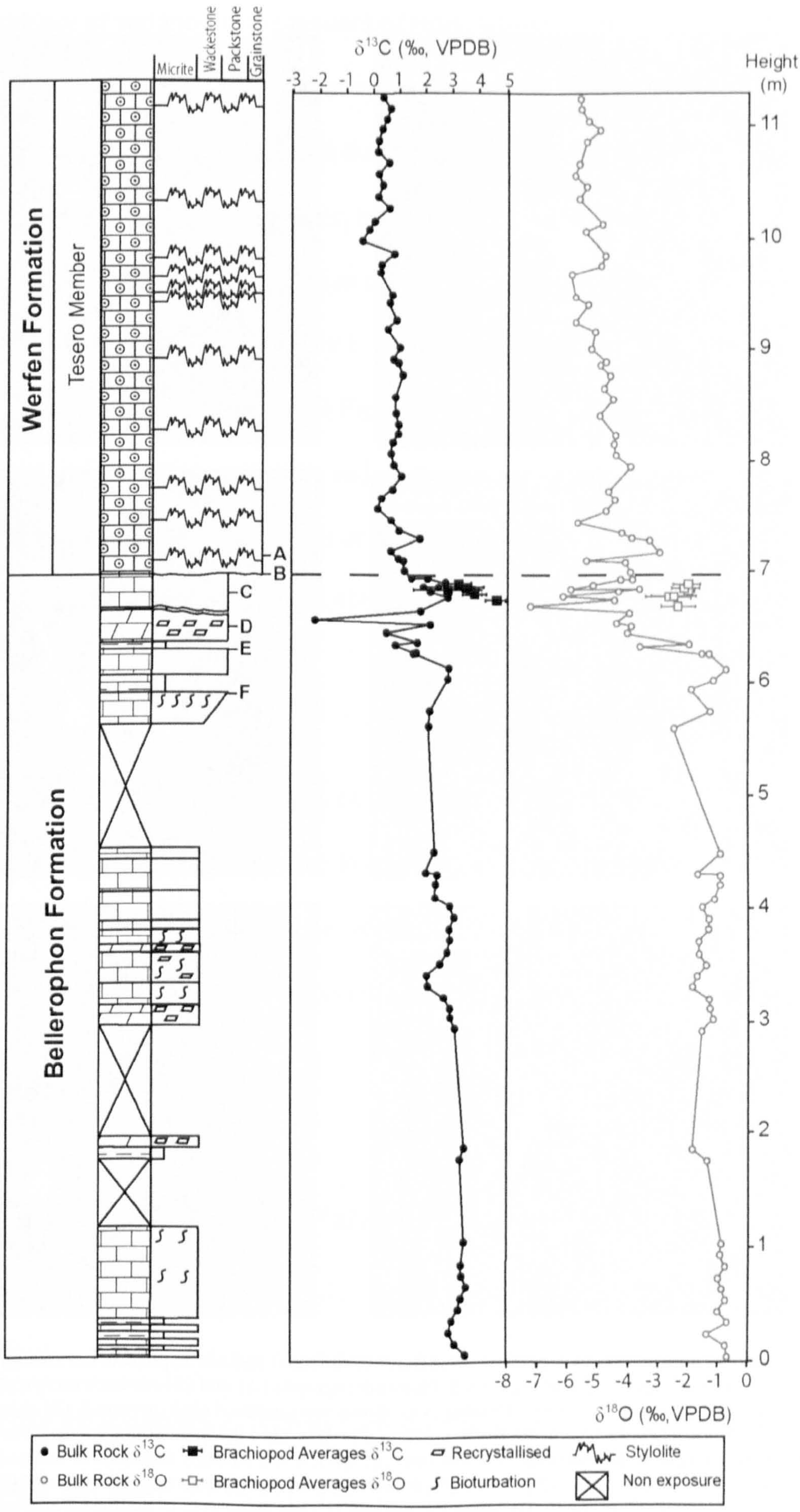

Figure 6.3 Stable isotope results for both the brachiopods (square) and bulk rock (circles) through the section at Val Brutta plotted against lithology. The Bellerophon Formation consists of recrystallised and bioturbated wackestones inter bedded with micrite and the Tesero Member consists of stylolite-rich oolitic grainstones. The letters (A-F) refer to the photomicrographs in Figure 6.4.

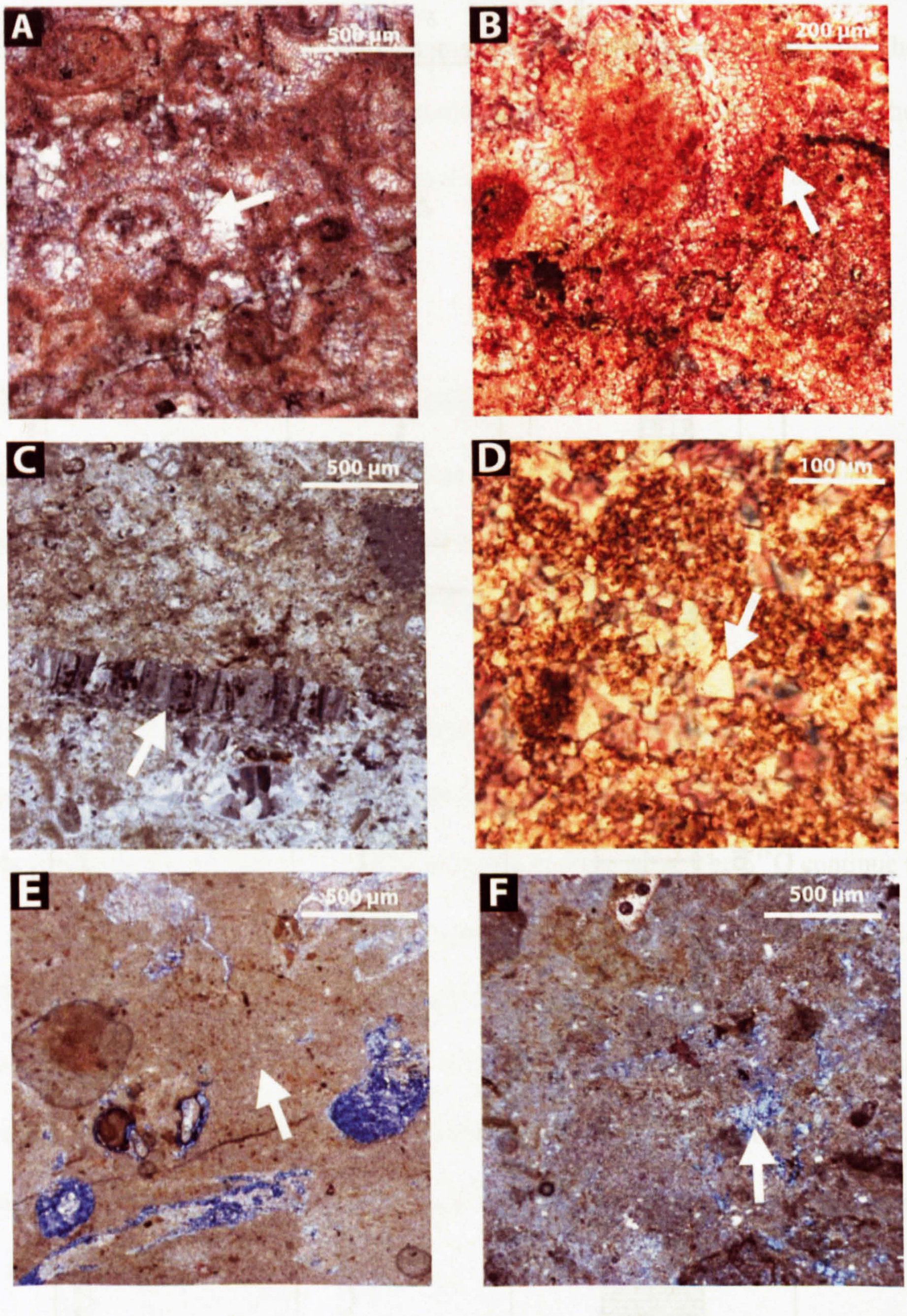

Figure 6.4 The photomicrographs represent the different lithologies and correspond to the stratigraphic heights on the section log seen in Figure 6.2 and Figure 6.3. Photomicrographs (A) and (B) are both recrystallised oolitic grainstones from the base of the Tesero Member; (A) shows recrystallised ooid (arrowed) (B) shows a stylolite (arrowed). Photomicrograph (C) is from the 'transitional beds' where the brachiopod fossils were sampled. The arrow points to a fragment of brachiopod. Photomicrograph (D) is a strongly dolomitised horizon, showing large dolomite crystals (arrowed). This bed is over 75% dolomite by area. Photomicrographs (E) and (F) are less recrystallised packstones from the Bellerophon Formation; (E) has large area of unaltered micrite shown by arrow. The arrowed section of (F) points to an area of small dolomite crystals (12% by area) which are present in both (E) and (F). Note changes in scale in photomicrographs (B) and (D).

There is evidence of variation in the amount of recrystallisation in the section. Petrographic analysis of the beds through the isotope excursions (Figure 6.4 and Figure 6.3) has revealed recrystallisation and dolomitisation in all the coarser-grained limestone samples (Figure 6.4 A and D). The amount of dolomitisation is, however, more variable throughout this part of the section. Within the Bellerophon Formation the wackestone beds that contain the excursions vary in the amount of dolomite rhomb by 12% – 75% by area of the slide (Photomicrograph E in Figure 6.4, and Photomicrograph D in Figure 6.4). There is a coincidence between the variation in amount of dolomite rhombs and the isotope signal. Petrographic analysis of bed that contains the negative $\delta^{13}C$ excursion at 65.6m above the base of the section shows it to contain 75% dolomite crystals (Figure 6.4D), while the bed directly beneath it only contains 12% (Figure 6.4E).

In the overlying Tesero Member there is an increase in the volume of dolomite crystals up to 19% (Figure 6.4b) and an increase in the level of recrystallisation (Figure 6.4b). Elemental analysis of bulk rock samples shows relative enrichment in Mn (178ppm) and Fe (945ppm) and depletion of Sr (330 ppm) with respect to the brachiopod samples from the same levels (Table 6.1).

6.4 Results – brachiopods stable isotopes

Six articulate brachiopods were analysed from Val Brutta including representatives of *Janiceps* and *Comelicania* and one from Tesero (*Crurithyris*). Brachiopods were recovered from just below the Bellerophon/Werfen Formation boundary (Figure 6.2) and from the Tesero Member just below the first appearance datum (FAD) of *H. parvus* as described by Farabegoli *et al.* (2007) (Figure 6.5). All of the brachiopods are more isotopically positive

than the equivalent bulk rock values at both localities (see Chapter 2 for preparation methods and Appendix A4.1 for results and Appendix A4.4 for the drill sites).

The brachiopod samples from Val Brutta $\delta^{18}O$ values range between –2.66‰ and –2.03‰ and $\delta^{13}C$ values between 4.65‰ and 2.83‰. This is quite different from the bulk isotope measurements from the same horizon which have average $\delta^{18}O$ values of –6.01‰ and $\delta^{13}C$ values of 2.39‰ (Figure 6.3). The brachiopod recovered from the Tesero section similarly has $\delta^{18}O$ values between –5.93‰ and –3.74‰ and $\delta^{13}C$ values between 1.13‰ and 1.74‰ compared to bulk rock values of $\delta^{18}O$ values of –6.6‰ and $\delta^{13}C$ values of 1.0‰ for the same horizon (Figure 6.5 and Appendix A4.1).

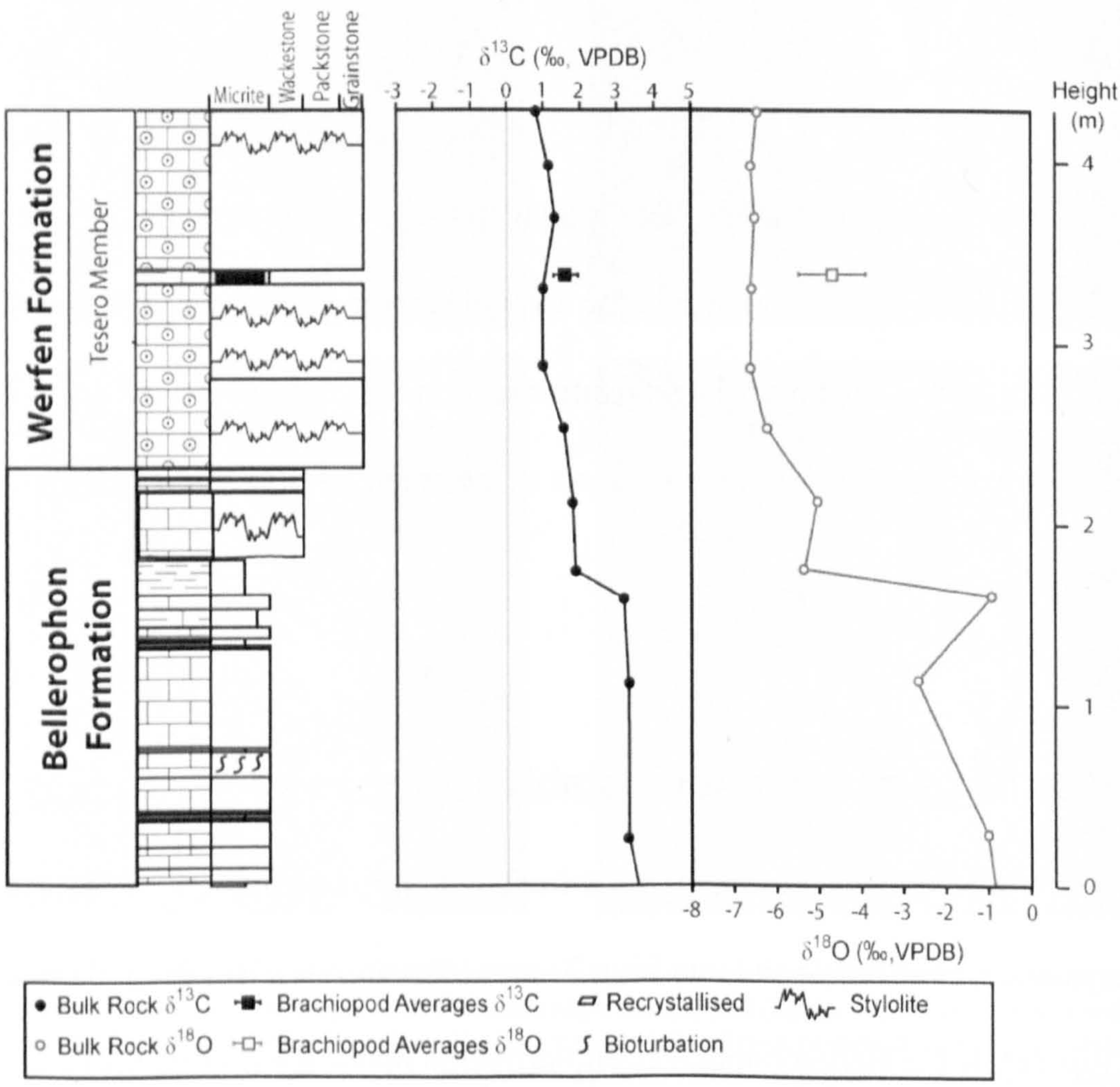

Figure 6.5 Stable isotope results for both the brachiopods (square) and bulk rock (circles) through the section at Tesero plotted against lithology (bulk rock values from Magaritz *et al.* 1988). The Bellerophon Formation consists of recrystallised and bioturbated wackestones interbedded with micrite and the Tesero Member consists of stylolite-rich oolitic grainstones.

6.4.1 Alteration of brachiopod shells

When using brachiopods to investigate temperature it is essential that the fossil material is not altered (Mii *et al.* 1997; Veizer *et al.* 1999; Korte *et al.* 2005a, b van Geldern *et al.* 2006; Batt *et al.* 2007). When the brachiopods were examined under a petrographic microscope it was possible to discern internal layers (Figure 6.6), analogous to the fibrous secondary layer and prismatic tertiary layer seen in modern brachiopods (Parkinson *et al.* 2005). In some samples a primary layer is also partially preserved, but in most cases this appears to have been removed by abrasion prior to burial (Figure 6.6). In the case of the brachiopod recovered from Tesero (TS1) it appears that both the primary and secondary layers had been removed (Figure 6.7), either by abrasion or prior to burial or in the processing of the fossil (see Chapter 2). All the brachiopods were subjected to Cathodoluminescence (CL) analysis (Appendix A4.1

All the shells are were primarily non-luminescent although all showed some areas of luminescence, which in most cases were concentrated around the umbo and the fibrous layer of the shell (Figure 6.6, Appendix A4.1). One of the 6 shells recovered from Val Brutta one (VB3) extensive luminescent areas to the extent it was impossible to isolate the non-luminescent areas for isotope analysis. Only the non-luminescent (NL, see Chapter 2 for full definitions of the CL classifications) areas were selected for sampling and isotopic analysis to avoid any diagenetic alteration affecting the primary signal. All the shells were significantly less luminescent than altered fossils (mostly foraminifera) in the surrounding matrix.

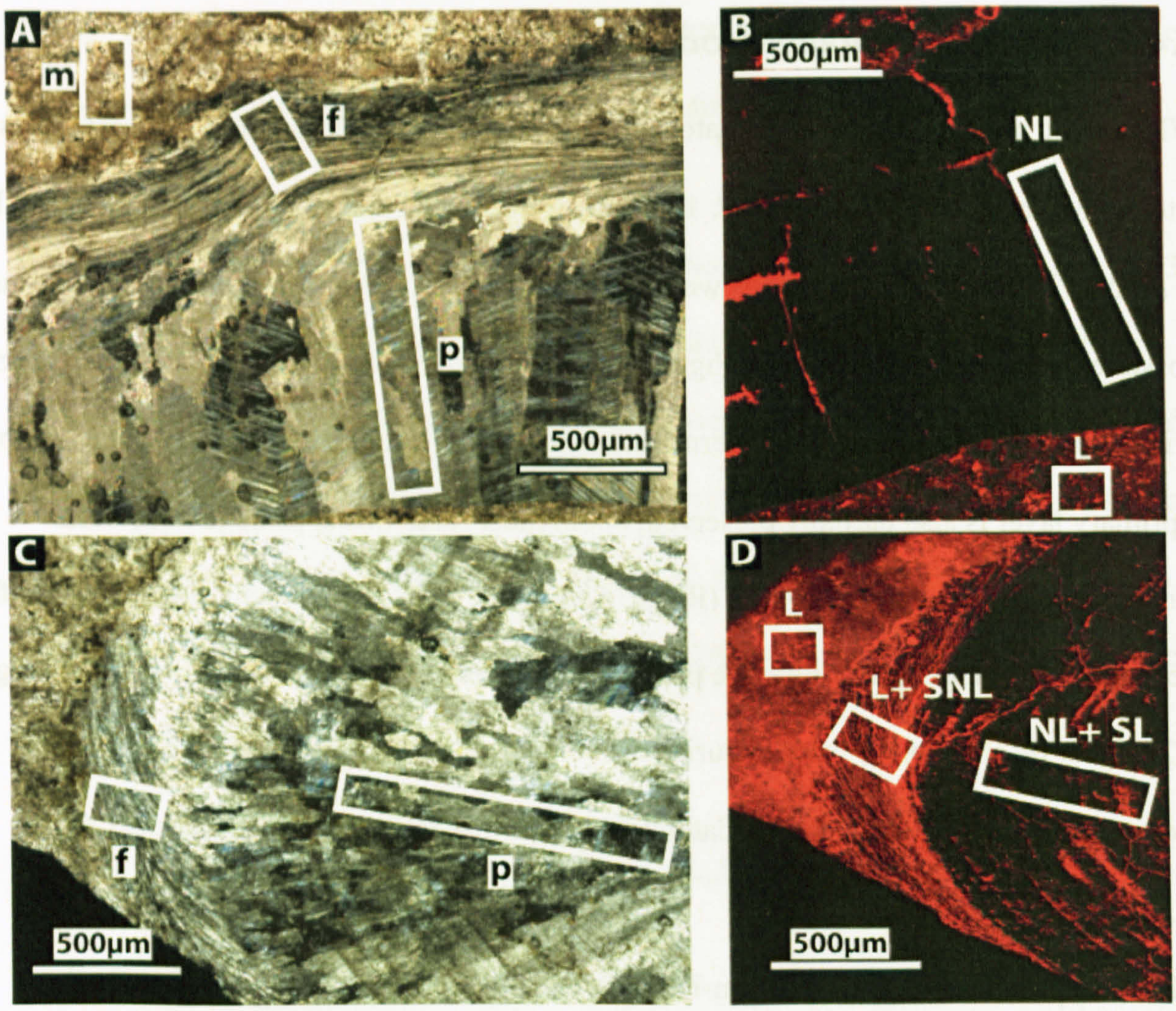

Figure 6.6 Petrographic and cathodoluminescent images of the brachiopod shells VB2 (A and B) and VB6 (C and D),(A) shows the distinct fibrous (f) and prismatic (p) layers representing the secondary and tertiary shell layers and surrounding bulk rock (m), (B) is the same brachiopod under CL showing the non luminescent (NL) brachiopod shell and the luminescent (L) bulk rock, (C) shows the umbo region of a more altered brachiopod with both fibrous (f) and prismatic (m) layers, (D) is the same brachiopod with the fibrous layer luminesce with slight non luminescence (L+SNL) and the prismatic layer showing non luminescence with slight luminescence (NL+SL).

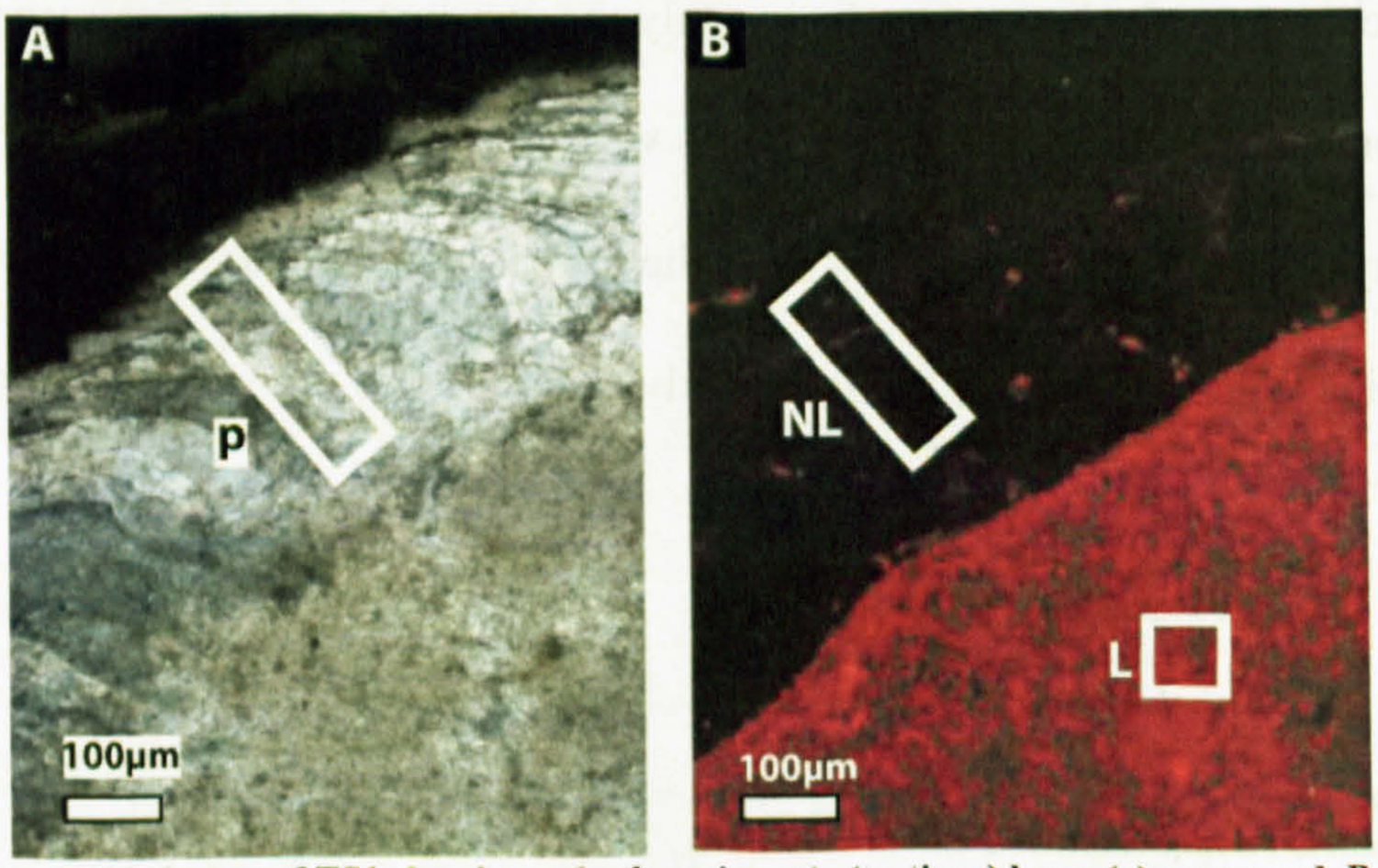

Figure 6.7 A. Petrographic image of TS1 showing only the prismatic (tertiary) layer (p) preserved. B. A cathodoluminescent image of the same brachiopod showing this layer is luminescent (NL) while the bulk rock is luminescent (L). Image (B) was taken by Nikita Jacobsen (unpublished data).

	ppm						
	Al	**Fe**	**Mg**	**Mn**	**Na**	**S**	**Sr**
Modern brachiopods (Brand *et al.* 2003)[2]		<140	600-17964	<80			450 - 1928
Criteria used by van Geldern *et al.*(2006)		<400		<100			>500
Criteria used by Korte *et al.* (2005a)				<250			>400
Criteria used by Mii *et al.* (1997)	700 +/- 300	270	860 +/- 1180	<190	1010 +/- 550	4150 +/- 1530	960 +/- 210

Specimen name	Species	CL results[1]	Al	Fe	Mg	Mn	Na	S	Sr
VB1	*Comelicania? sp.*	NL	35	43	911	25	1358	2521	484
VB1	*Comelicania? sp.*	NL+SL	73	28	654	10	1279	2351	481
VB2	*Janiceps aff.paracuta*	NL	32	104	1318	23	1346	1863	495
VB2	*Janiceps aff.paracuta*	NL	51	82	1500	30	1930	2189	535
VB3	*Comelicania? sp*	L+SNL	47	26	1068	8	1121	1639	461
VB3	*Comelicania? sp*	NL+SL	36	157	1356	56	1242	1970	473
VB4	*Comelicania? sp.*	NL+SL	69	115	1939	4	476	2442	542
VB5	*Janiceps sp.*	NL+SL	37	64	919	21	878	1493	440
VB6	*Comelicania sp.*	NL	77	84	1525	24	1128	1792	410
Bulk rock		**L**	**349**	**945**	**3750**	**178**	**734**	**852**	**330**

Table 6.1 Trace elemental analysis and cathodoluminescence results for the brachiopod fossils and bulk rock, compared against published ranges for modern and unaltered fossil brachiopods. NL – nonluminescent, NL +SL – nonluminescent with slight luminescence (>50% NL by area), L+SNL – luminescent with slight non luminescence (<50% NL by area), L – luminescent. [2] The modern brachiopods described by Brand *et al.* (2003) are from shallow water, mid-low latitudes. TS1 could not be analysed using this method as there was not enough sample to produce an accurate analysis (see Chapter 2) The bold type face highlights those analyses that fall outside the range of modern/unaltered brachiopods.

The trace element results for the brachiopods show a range of Mn values from 8–56 ppm, with the NL values clustering around a range of 4–56ppm. Fe has a range of between 26–157 ppm, again with the less-luminescent samples clustering closer to the lower values (Table 6.1). These fall within the ranges suggested for unaltered brachiopods (Brand *et al.* 2003; van Geldern *et al.* 2006; Korte *et al.* 2005a; Mii *et al.* 1997). Of all the specimens there is one (VB3) with Fe values above the limit advised by Brand *et al.* (2003) but below that suggested by van Geldern *et al.* (2006). Similarly there are two specimens (VB5 and VB6) with Sr values below that recommended by Brand *et al.* (2003), although still within that suggested by Korte *et al.* (2005a) and van Geldern *et al.* (2006). Both these samples have areas of L+SNL, NL+SL and NL (see Appendix A4.1) and these slightly negative Sr measurements represent both luminescent and non-luminescent areas.

Within individual brachiopods there is a $\delta^{18}O$ variation of between –4.30‰ and –2.33‰ from the outer to the inner part of the shell (Figure 6.8, and Appendix A4.3). This is only recorded in shells which show complete preservation of the fibrous and prismatic layers (VB2 and VB6). Within unaltered, non-luminescent shells the more negative isotope values are associated with the fibrous layers, a situation also observed in modern terebratulid brachiopods (Auclair *et al.* 2003).

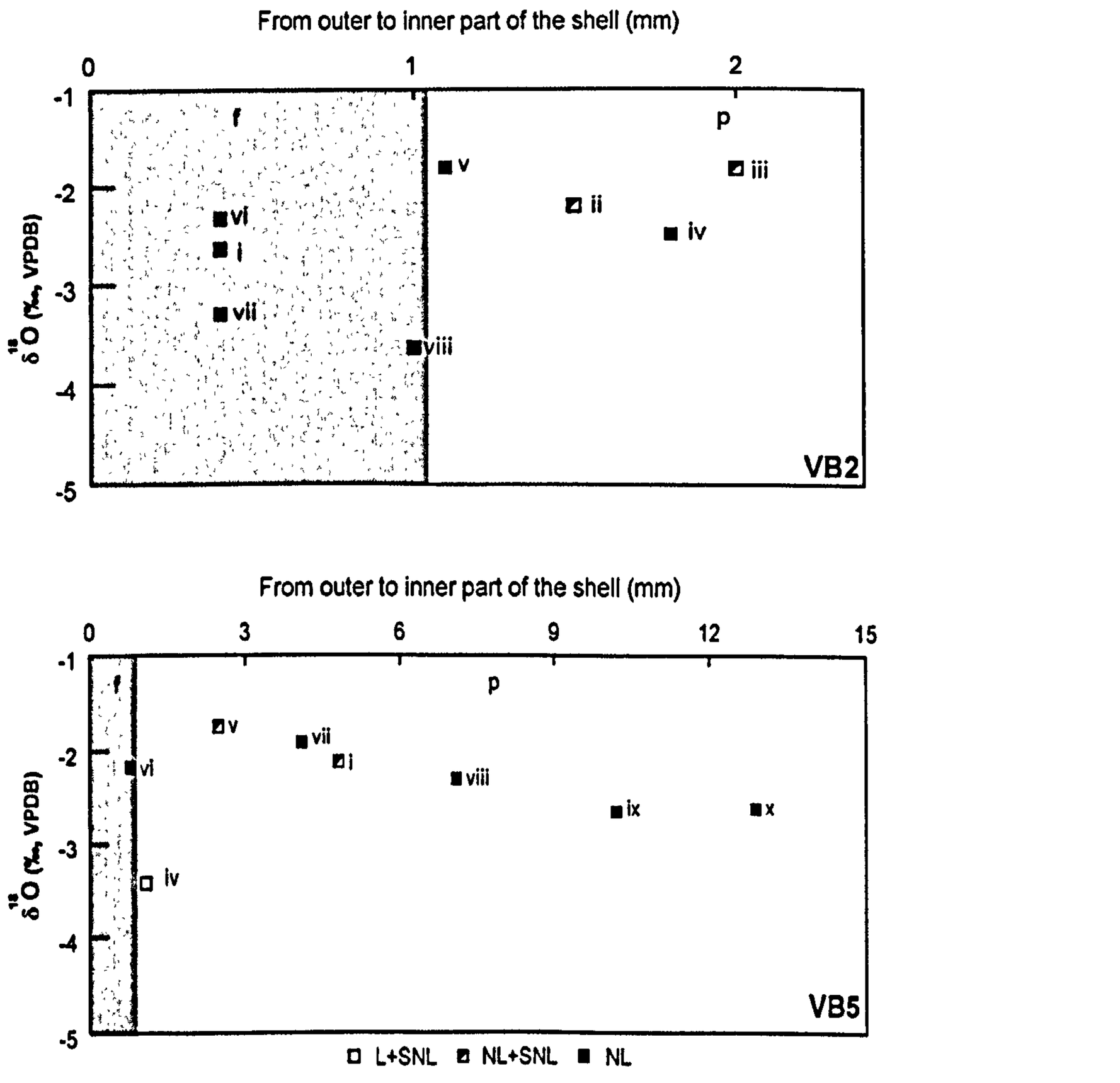

Figure 6.8 Variation in $\delta^{18}O$ ratios across the fibrous (f, shaded) and prismatic layers (p) within brachiopod fossils VB2 and VB5. The amount of luminescence in each isotope sample is also shown. Note change in scale; see Appendix A1 for positions of isotope samples.

6.5 Discussion

The $\delta^{13}C$ and $\delta^{18}O$ bulk rock excursions recorded at Tesero and Val Brutta have been observed elsewhere in Italy (Magaritz and Holser 1991; Broglio Loriga and Cassinis 1992;

Cirilli *et al.* 1998: Sephton *et al.* 2002; Newton *et al.* 2004; Horacek *et al.* 2007) (Figure 6.9) and globally (Baud *et al.* 1996; Jin *et al.* 2000; Musashi *et al.* 2001; Twitchett *et al.* 2001; Krystyn *et al.* 2003; Payne *et al.* 2004; Krull *et al.* 2004; Algeo *et al.* 2007) suggesting that the excursion is a global event rather than just a local diagenetic artefact (Figure 6.9). The high resolution sampling of the section at Val Brutta has revealed that in the Italian Dolomites the $\delta^{13}C$ and $\delta^{18}O$ excursions are synchronous and occur before the boundary between the Bellerophon and Werfen formation and below the FAD of *H. parvus* in Tesero (Figure 6.2, Figure 6.3)

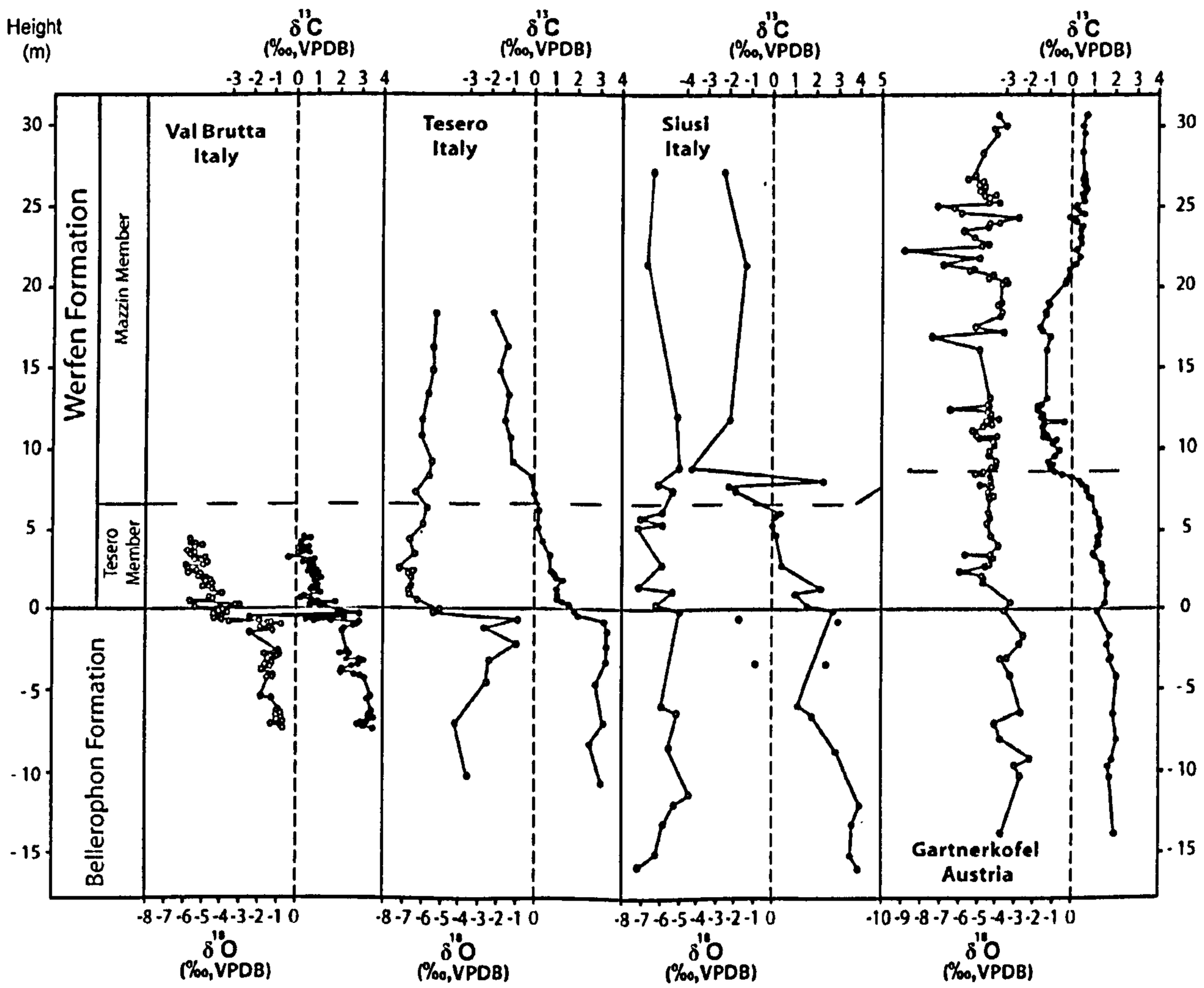

Figure 6.9 Carbonate isotope variations across the Permian /Triassic boundary in Italy and Austria. The grey open circles are the bulk rock $\delta^{18}O$ values and the filled black circles are the $\delta^{13}C$ values The Val Brutta curve is from this study. Data from Tesero is reproduced from Broglio Loriga and Cassinis (1992), the Siusi section from Newton *et al.* (2004) and the Garnerkofel section from Magaritz and Holser (1991). The two points excluded from both Siusi curves are heavily dolomitised (Newton *et al.* 2004).

It is generally assumed by many authors (Newton *et al.* 2004; Haas *et al.* 2006; Horacek *et al.* 2007; Algeo *et al.* 2007) that $\delta^{13}C$ values and excursions are unaffected by diagenesis as the carbon reservoir of the rock far outweighs the amount of carbon in a diagenetic fluid, and that alteration is likely to produce a positive excursion rather than a negative (Marshall 1992; Horacek *et al.* 2007). It has been noted that intense alteration of marine carbonates in the presence of meteoric water may lead to lower $\delta^{13}C$ values compared to unaltered carbonate (Haas *et al.* 2006).

Although the Tesero Member is intensely recrystallised there is no evidence of isopachous fringing cements (Figure 6.10) which would be indicative of the influence of meteoric waters (Tucker 2001). Equally those pore-filling cements that have not been completely recrystallised appear have been originally micritic muds which would have limited the ability of any potential meteoric fluids to penetrate the oolite.

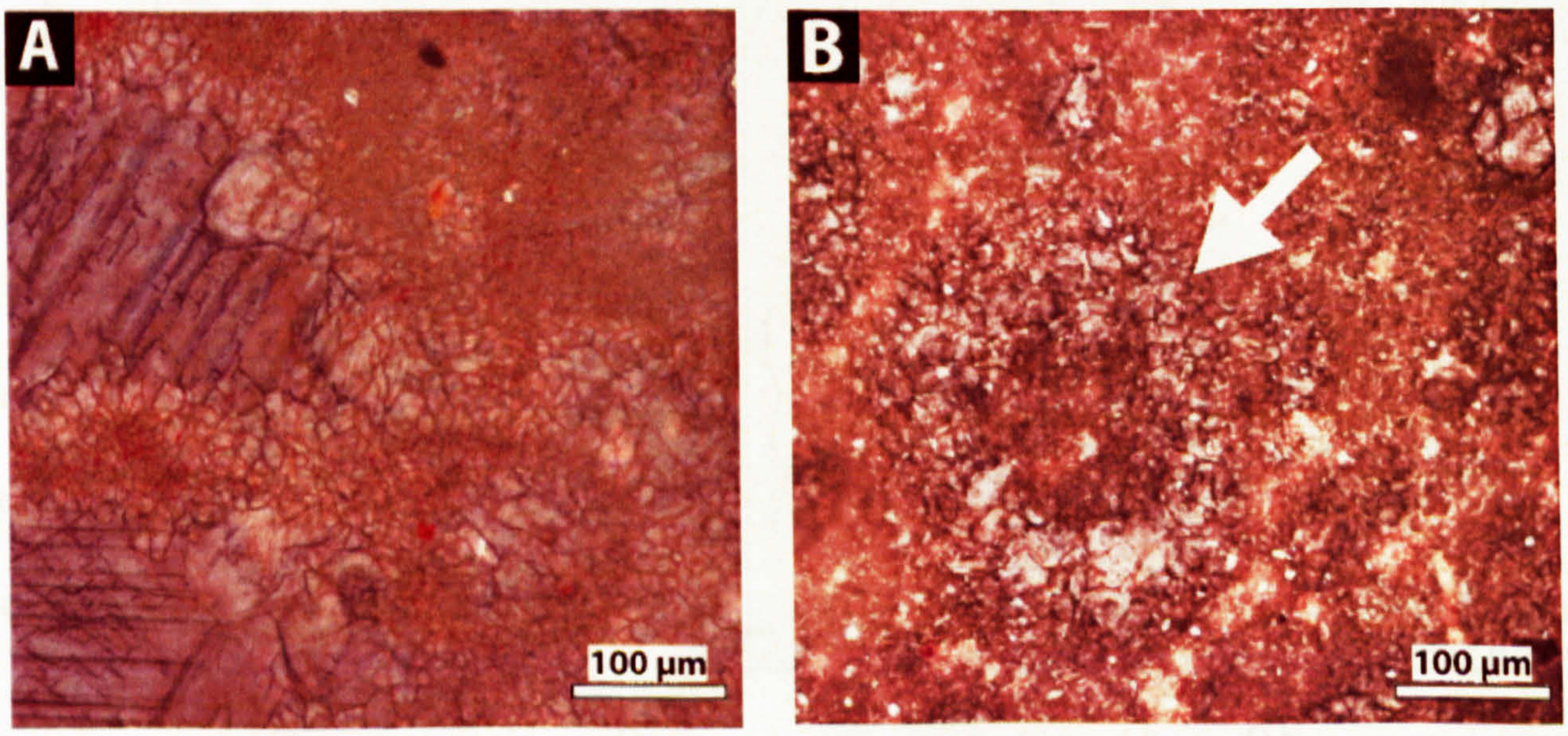

Figure 6.10 Recrystallisation textures in the Tesero Member. (A) shows a completely recrystallised bed with euhedral crystals filling in the space between ooids. (B) shows the outline of a recrystallised ooid (arrowed). (both slides are from the same stratigraphic height as photomicrograph A in Figure 6.2).

The petrographic data from the interval around the Bellerophon Formation-Tesero Member boundary at Val Brutta (Figure 6.4) shows that there is alteration present in all the coarse-

grained lithologies; although the amount of dolomite present in different beds varies from 12% to 75% by area. There is one incidence of a large negative point excursion in the $\delta^{13}C$ values of 4‰, 40cm below the Tesero Member (Figure 6.3), which coincides with a level dominated by large recrystallised rhombs (Figure 6.4d) which suggests that recrystallisation may be responsible for some of the changes in the $\delta^{13}C$ values. However, it is very hard to explain a negative excursion in terms of extensive dolomitisation as this produces positive rather than negative excursions (cf. Horacek *et al.* 2007; Algeo *et al.* 2007).

The potential influencing factors controlling the $\delta^{18}O$ values are much more various. Spötl *et al.* (1992) suggest that the $\delta^{18}O$ composition of the bulk rock can be affected by increases in water temperature; sulphate reduction; diagenetic recrystallisation under the influence of higher temperatures; or diagenetic re-equilibrium with fluids depleted in ^{18}O. It has been suggested that there is a sulphur reducing event associated with the Bellerophon/Tesero Oolite transition in the Italian Dolomites (Newton *et al.* 2004). Equally, the marked increase in recrystallisation in the Tesero Member may suggest the more porous oolites have been more affected by diagenetic fluids than the micrites below them, producing a negative excursion. However, the fact that the $\delta^{13}C$ and $\delta^{18}O$ excursions have been observed globally (cf. Kidder and Worsley 2004; Corsetti *et al.* 2005; Erwin 2006; Gorjan *et al.* 2008) indicate that even though the bulk rock is recrystallised the isotope values are still representative of the primary trends, if not the actual primary isotopic values. Equally, it has been observed that some limestones that have been metamorphosed at temperatures well in excess of 500°C can still preserve their original isotope composition or only partially re-equilibrate to diagenetic/metamorphic fluids (Melezhik *et al.* 2005).

In contrast to the bulk rock record, when all lines of evidence are considered, it seems very probable that all brachiopod shells analysed in this study contain large areas that are unaffected by diagenesis or dolomitisation and at least the non-luminescent areas retain a primary isotope signal. All shells show both the fibrous and prismatic layers (Figure 6.6; Figure 6.7) identical to the secondary and tertiary layers observed in modern brachiopods (cf. Parkinson *et al.* 2005). The trace element results show that all brachiopods have ranges similar to modern and unaltered brachiopods (Table 6.1) Finally the CL analysis (Figure 6.6) shows that although the matrix shows strong luminescence there was sufficient parts of all bar brachiopod VB3 and that did not luminesce to be isotopically sampled (Figure 6.6; Figure 6.7; Appendix 4.1) again indicating that the majority of the brachiopod fossils had not affected by recrystallisation. Only the NL areas of these shells were used in the palaeotemperature and $\delta^{13}C_a$ estimates. Finally, the $\delta^{13}C$ of the non-luminescent parts of the brachiopods fall within the ranges for unaltered samples as suggested by Korte *et al.* (2005a).

6.5.1 Disparity between bulk rock and brachiopod values

In other Permian localities it has been shown that while the bulk rock results show an isotope excursion the isotopic values from unaltered brachiopods from the same locality show no such excursion suggesting that the excursion is purely a diagenetic artefact rather than relating to primary processes (e.g. Mii *et al.* 1997).

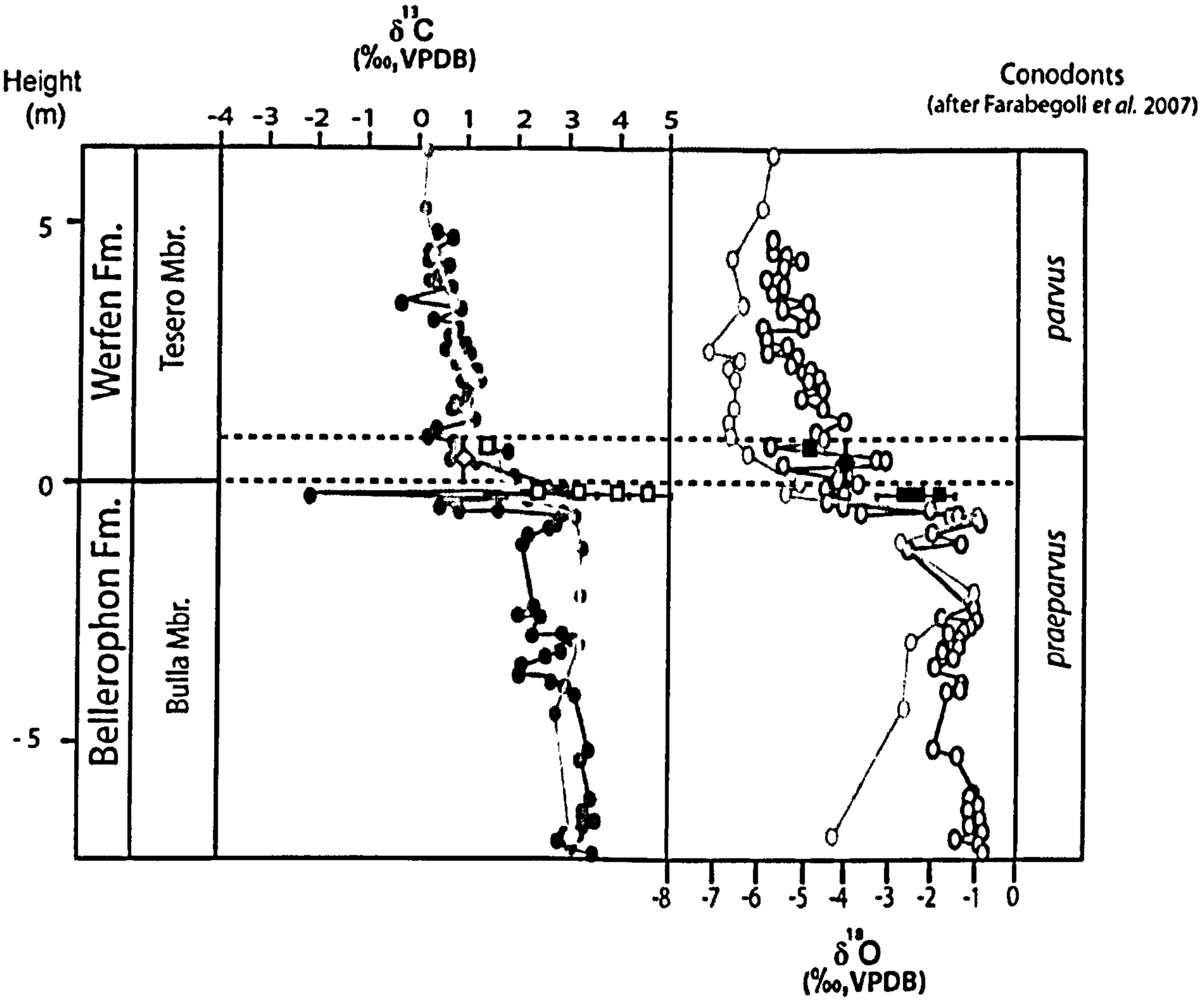

Figure 6.11 Brachiopod isotopic composition compared to bulk rock values from the Italian Dolomites. The squares are the un-altered isotopic values from brachiopods from this study, the diamonds are brachiopod values from Korte *et al.* (2005a) from Sass de Putia. The dark grey circles are the bulk rock values from Val Brutta while the light grey circles are from the Tesero section from Magaritz *et al.* (1988). The sections are correlated using the correlations of Farabegoli *et al.* (2007).

In both sections (Val Brutta and Tesero) the brachiopods have an isotopic value which is more positive than that of the bulk rock signal (Figure 6.3; Figure 6.5). The petrographic, CL and trace element evidence seem to indicate the brachiopods are not affected by the recrystallisation event. This may suggest the isotope values of the bulk rock have been altered by the recrystallisation event which has fractionated them relative to the unaltered brachiopods. This is plausible as it is known that early diagenetic stabilisation produces ^{12}C enrichment (Batt *et al.* 2007) which could produce a negative shift in values bulk rock. However, both the carbon and oxygen isotope values show a coincident excursion with P/Tr boundary sections worldwide (cf. Baud *et al.* 1989; Retallack and Krull 2006).

A comparison of the bulk rock values from Val Brutta and Tesero with brachiopods from Val Brutta, Tesero (both this study) and unaltered brachiopods from Sass di Putia (Korte *et al.* 2005a) reveal that although the brachiopods have a more positive isotopic value they show the same trend as the bulk rock values (Figure 6.11).

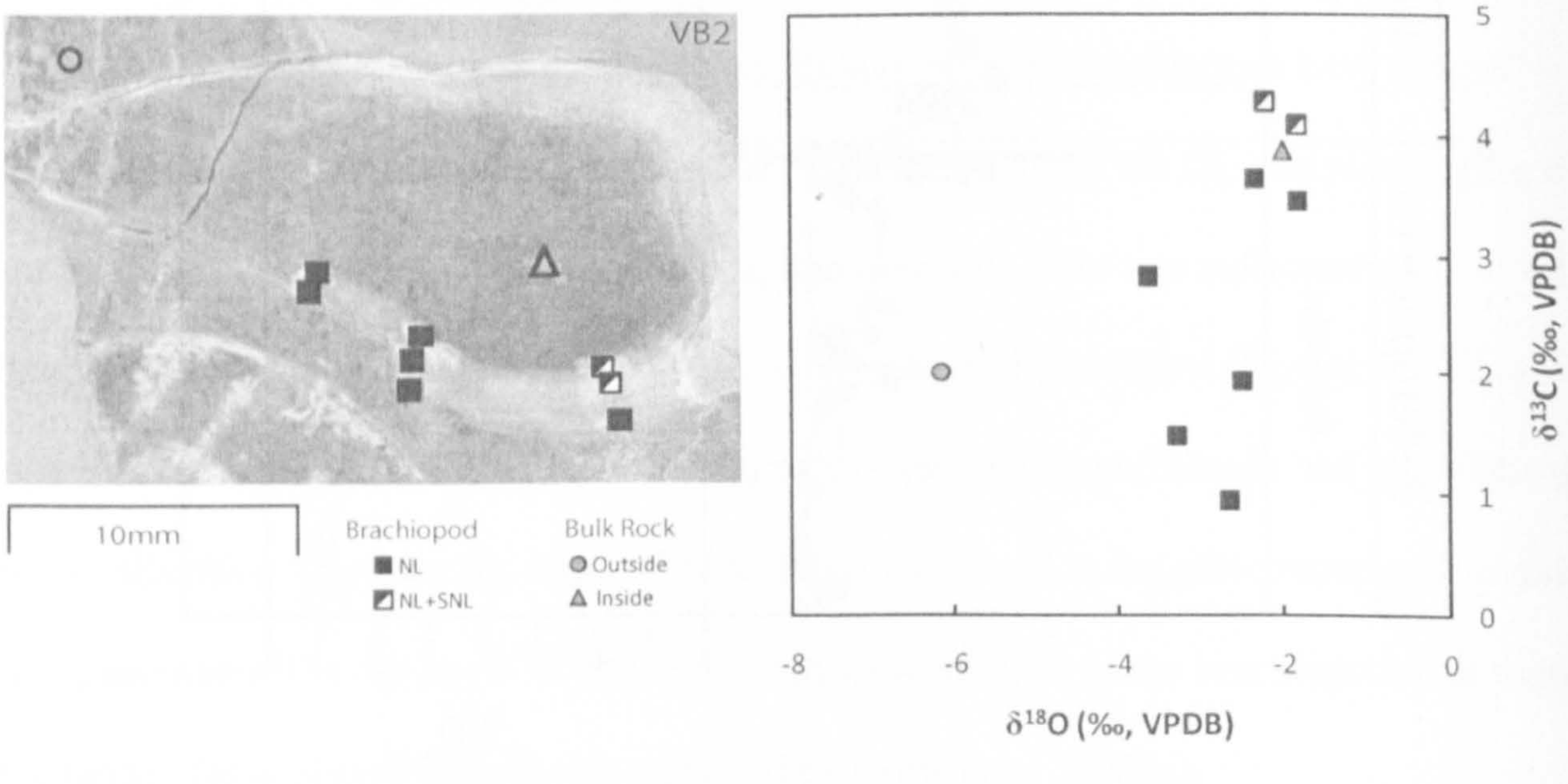

Figure 6.12 Comparison of the isotopic composition of micritic mud from within an articulated brachiopod and outside it with the isotopic.

Although all the brachiopods are isotopically more positive than the bulk rock that surrounds the fossils (Figure 6.2, Figure 6.3, Figure 6.5) in one of the articulated brachiopods (VB2), the micritic mudstone sampled from within between the two valves has a similar isotopic composition as the brachiopod shell while the micrite sampled from outside the shell is isotopically more negative (Figure 6.12). This suggests that the micritic muds outside the protection of the brachiopod shell have been slightly altered compared to the micrite protected by the shell. However, slight isotopic depletion seen in the bulk rock signal of micrite from outside the brachiopod, possibly caused by the recrystallisation event, has not been enough to completely overprint the pre-diagenetic/metamorphic signal and thus explaining why the isotopic trends in the brachiopod and bulk rock signal should mirror each other and that

although the bulk rock is still recording primary trends the absolute values are no longer representative of absolute value of palaeo-seawater.

6.5.2 Palaeotemperature estimates

Assuming the isotope ratios of the unaltered brachiopod shells reflect the isotopic composition of palaeo-seawater they can be used to track changes in palaeotemperature (e.g. Lavoie 1993; Mii and Grossman 1994; Grossman *et al.* 1996; Mii *et al.* 1997; Veizer *et al.* 1999; Bojar *et al.* 2004; Korte *et al.* 2005a and 2005b; van Geldern *et al.* 2006). Palaeotemperatures were calculated using the relationship between shell $\delta^{18}O$ calcite precipitation temperature as given by Anderson and Arthur (1983) and modified by Auclair *et al.* (2003) (Equation 6.1) and Parkinson *et al.* (2005) (Equation 6.2).

$$t\,(°C) = 16.9 - 4.14\,(\delta^{18}O_{calcite} - \delta^{18}O_{seawater}) + 0.13(\delta^{18}O_{Calcite} - \delta^{18}O_{seawater})^2 \quad (6.1)$$

$$t\,(°C) = 16.0 - 4.14\,(\delta^{18}O_{calcite} - \delta^{18}O_{seawater}) + 0.13(\delta^{18}O_{calcite} - \delta^{18}O_{seawater})^2 \quad (6.2)$$

$\delta^{18}O_{carb}$ is the oxygen isotope composition of the brachiopod shell calcite with respect to VPDB. $\delta^{18}O_{seawater}$ is the oxygen isotope composition of seawater relative to VSMOW (Standard Mean Ocean Water).

The $\delta^{18}O$ composition of the secondary and tertiary layers of modern Terebratulida form in equilibrium with seawater and thus can be used to estimate palaeotemperature (Parkinson *et al.* 2005). Only the $\delta^{18}O$ data from unaltered, nonluminescent areas of these layers were used to determine palaeotemperature values in this study (see Appendix A4.2). Finally, before a palaeotemperature can be calculated the $\delta^{18}O$ of the seawater from which the brachiopod

shells precipitated must be estimated. Korte *et al.* (2005a, 2005b) assume a $\delta^{18}O_{seawater}$ value of 0‰ for Tethyan tropical open marine basins and large intra-platformal basins in both the Permian and the Triassic.

Ocean salinity also has a direct effect on the $\delta^{18}O$ of seawater (Parkinson *et al.* 2005 and references therein). The rocks at Val Brutta and Tesero were deposited on a tropical subtidal shallow water carbonate ramp (Ghetti and Neri 1983). If surface water salinity is assumed to be 36‰, as seen in modern tropical oceans (Millero 2005), then the $\delta^{18}O_{seawater}$ would be 1.0‰ (cf. Parkinson *et al.* 2005). This also agrees with the lower estimate for the value of Hay *et al.* (2006) for the Early Triassic, ice free world of 37.32‰ which equal a salinity of 1.66‰ (method after Parkinson *et al.* 2005). Finally, there is no evidence of permanent ice sheets in the Late Permian and Early Triassic (Chumkov and Zharkov 2003; Kidder and Woresley 2004). In such an ice–free world it has been argued that $\delta^{18}O_{seawater}$ would be as low as -1‰ (Joachimski *et al.* 2006; Grossmann *et al.* 2008).

Using these three different estimates of $\delta^{18}O_{seawater}$, 0‰, 1‰ and –1‰ produces three different temperature estimates. Assuming a $\delta^{18}O_{seawater}$ of 0‰ and using the equation 6.1 produces average palaeotemperature estimate of 28°C (±3, 1σ std) across all the brachiopods at Val Brutta(see Table 6.2). The brachiopod from Tesero produces an average palaeotemperature estimate of 36°C (±2, 1σ std) (Table 6.2). Equation 6.2 produces an estimate of 27°C (±3, 1σ std) at Val Brutta and 35°C (±2, 1σ std) at Tesero, suggesting an 8°C rise in temperature across the excursion event. Assuming a $\delta^{18}O_{seawater}$ of 1‰ increases the temperature estimates by 5°C although the increase in temperature across the excursion event is still 8°C (Table 6.2). However, a using $\delta^{18}O_{seawater}$ of –1‰ produces estimates of 24°C (±3,

1σ std) at Val Brutta and 31°C (±2, 1σ std) at Tesero using equation 6.1 and equation 6.2 produces an estimate of 23°C (±3, 1σ std) at Val Brutta and 30°C (±2, 1σ std) at Tesero

Brachiopod	MAT (°C) $\delta^{18}O_{seawater}$ = 0‰		MAT (°C) $\delta^{18}O_{seawater}$ = 1‰		MAT (°C) $\delta^{18}O_{seawater}$ = -1‰	
	Equ. 6.1	Equ. 6.2	Equ. 6.1	Equ. 6.2	Equ. 6.1	Equ. 6.2
VB1	29 (±4)	29 (±4)	34 (±5)	33 (±5)	25 (±4)	24 (±4)
VB2	29 (±3)	28 (±3)	34 (±3)	33 (±3)	24 (±3)	23 (±3)
VB5	27 (±2)	26 (±2)	32 (±2)	31 (±2)	23 (±1)	22 (±1d)
VB6	27 (±3)	26 (±3)	32 (±3)	31 (±3)	22 (±3)	21 (±3)
TS1	36 (±2)	35 (±2)	41 (±3)	40 (±3)	31 (±2)	30 (±2)

Table 6.2 Palaeotemperature estimates from unaltered brachiopods at different salinity and thus $\delta^{18}O$ seawater compositions. Brachiopods VB3 and VB4 did not have large enough NL areas to be isotopically sampled. Errors given to 1σ std.

There is some independent corroboration which can be used to test which of these different $\delta^{18}O_{seawater}$ values is likely to be correct. Eighty kilometres to the north, at Sass di Putia (Figure 4.1), there is extensive gypsum precipitation in the Bellerophon Formation (Broglio Loriga *et al.* 1986; T.K. field observations). Gypsum forms in a temperature range of between 25-27°C in modern lagoon environments (Morris and Dickey 1957) and this correlates closest with the palaeotemperature estimate produced in this study with a $\delta^{18}O_{seawater}$ of 0‰. This palaeotemperature estimate also broadly agrees with that predicted by climate models of the late Permian and P/Tr boundary interval, which predict a temperature of 28-33°C for this palaeolatitude (e.g. Gibbs *et al.* 2002; Kiehl and Shields 2005; Winguth and Maier-Reimer 2005).

In contrast, the model of Kidder and Worsley (2004) assumed an equatorial ocean temperature of 35°C. From the isotope results from the brachiopods, the only way to generate a temperature of 35°C is to have much higher levels of salinity. Kidder and Worsley (2004), however, inferred a surface ocean water salinity of just 32‰. If this salinity is used to

generate a palaeotemperature estimate using the brachiopod isotope data, an temperature estimate of between 18-22°C is generated. This value is far cooler than the 35°C predicted by Kidder and Worsley (2004), and also cooler than predictions from other climate models (e.g. Gibbs *et al.* 2002; Kiehl and Shields 2005), suggesting that the surface salinity was not as low as 32‰ as they predict.

6.5.3 $\delta^{13}C$ of the Permian atmosphere

The $\delta^{13}C$ composition of brachiopod shells has been utilised by many studies to investigate changes in the isotopic composition of seawater (Veizer *et al.* 1999; Korte *et al.* 2005a, b; Batt *et al.* 2007; Jaffrés *et al.* 2007). It has been suggested that there is an −8‰ fractionation from marine seawater values to atmospheric $\delta^{13}C$ values (Ekart *et al.* 1999). This fractionation factor was derived by Ekart *et al.* (1999) based on the isotopic composition of pre-industrial carbon dioxide and contemporaneous values for surface ocean carbonates from the study of biogenic carbonate by Veizer *et al.* (1999). As such, this fractionation should be applicable to brachiopods as they were an integral part of the Veizer *et al.* (1999) dataset.

Korte *et al.* (2005a) note a rapid negative shift in brachiopod $\delta^{13}C$ values in the Changhsingian which they link to the negative excursion observed at the P/Tr boundary. They suggest (in Korte *et al.* 2005b) that this excursion culminated in the basal Triassic (base of the *Hindeodus parvus* zone and into the lower *Isarcicella isarcica* zone). This is recorded in both the brachiopod and bulk rock data from Val Brutta and Tesero. However, some of the mechanisms proposed as a cause of such an anomaly, such as influx of organic matter or ocean turnover, would have the effect of producing a negative anomaly in organic carbon without significant change in atmospheric $\delta^{13}C$ (cf. Sephton *et al.* 2005; Algeo *et al.* 2007). Using the fractionation factor suggested by Ekart *et al.* (1999) and the NL brachiopod values

produces and estimate of atmospheric $\delta^{13}C$ of –4.56‰ (±1.06, 1σ std) before the excursion, from Val Brutta, and –6.56‰ (±0.26, 1σ std) at Tesero, suggesting a –2‰ in atmospheric $\delta^{13}C$ values across the event. This is similar to the atmospheric change observed by others (e.g. Retallack and Jahren 2008).

It has been observed that although the $\delta^{18}O$ values from unaltered brachiopods may be in equilibrium with seawater, the $\delta^{13}C$ values maybe controlled by metabolic effects rather than simple equilibrium (Parkinson *et al.* 2005). Thus, it seems prudent to be cautious even of unaltered brachiopod $\delta^{13}C$ values when they show a different trend to the bulk rock values. However, as both follow the same trend in this study the use of the $\delta^{13}C$ composition of brachiopod shells as a proxy for atmospheric $\delta^{13}C$ is valid.

6.6 Summary

Detailed study of the bulk rock and brachiopod isotope compositions from Val Brutta and Tesero in the Italian dolomites has revealed that both the bulk rock and brachiopods record both the $\delta^{13}C$ and $\delta^{18}O$ excursion across the Permian/Triassic boundary. From this it is possible to conclude that:

1. Both the bulk rock and the brachiopods are recording the primary carbon and oxygen isotopic signals, although the bulk rock values may be depleted by the recrystallisation of these rocks;
2. The brachiopods from Val Brutta yield a palaeotemperature estimate of between 26-29°C, which is realistic for an equatorial seaway and agrees with other palaeotemperature estimates for this period. Although the method described by

Parkinson *et al.* (2005) assumes the $\delta^{18}O$ isotopic composition of the brachiopod shells were only controlled by temperature and there is no influence of vital affects;

3. The temperature, as recorded from the fossil brachiopods, rose by ~8°C across the bulk rock isotope excursion seen at the base of the Tesero Member. This is similar to the 5-6°C predicted from the bulk rock signal by Magaritz and Holser (1991). Also it is similar (within error) to that predicted at the P/Tr boundary in Russia (excursion P4, see chapter 6);
4. Although the palaeotemperature estimate agrees with modelled temperatures for this palaeolatitude, the reduced salinity values proposed for equatorial surface ocean waters by Kidder and Worsley (2004) are not supported by these results;
5. The $\delta^{13}C$ values of bulk rock, while undoubtedly recording changes in the global carbon cycle across the P/Tr boundary, may represent a fractionation of equilibrium seawater values. Thus, the use of bulk rock values to calculate absolute values for $\delta^{13}C$ of the atmosphere may lead to erroneous results and thus, the use of bulk rock values in models, such as for pCO_2 values from pedogenic carbonate (cf. Ekart *et al.* 1999), must be treated with caution and brachiopods provide a more realistic estimate of such values.

Chapter 7. Atmospheric carbon dioxide and the $\delta^{13}C$ composition of pedogenic carbonate

One of the principal factors in controlling the $\delta^{13}C$ signature of primary pedogenic soil carbonate is the partial pressure of carbon dioxide in the atmosphere (pCO_2) (Cerling 1991; Cerling and Quade 1993; Ekart *et al.* 1999). This relationship has been described by Cerling (1991) and modified by Ekart *et al.* (1999) and there are many examples where this has been successfully applied to paleosols (Mora *et al.* 1991; Ekart *et al.* 1999; Arens and Jahren 2000; Ghosh *et al.* 2001; Robinson *et al.* 2002; Prochnow 2006).

7.1 The model

As well as pCO_2 there are many other factors that can control the isotopic composition of pedogenic carbonate. These are all described in the pCO_2 equation as created by Cerling (1991) and modified by Ekart *et al.* (1999) based on modern-day relationships:

$$Ca = S_{(z)} \frac{(\delta^{13}C_s - 1.0044\ \delta^{13}C_\Phi - 4.4)}{\delta^{13}C_a - \delta^{13}C_s} \tag{7.1}$$

where Ca is atmospheric pCO_2 (ppmV); $S_{(z)}$ is the CO_2 contributed by soil respiration as a function of depth (ppmV); $\delta^{13}C_a$ is the isotopic composition of the atmosphere (‰); $\delta^{13}C_\Phi$ is the isotopic composition of respired soil CO_2 from plant matter in the soil (‰) and $\delta^{13}C_s$ is the isotopic composition of the soil water (‰).

7.1.1 Generating the variables

Today it is possible to measure each of these variables directly from the soil and atmosphere. However, when dealing with paleosols many of these variables must be generated from other proxies or estimated using modern analogues. All of these variables can bring levels of uncertainty into the estimates of pCO_2 which must be kept in mind when interpreting the results.

$S_{(z)}$ – Soil respiration

$S_{(z)}$ refers to the difference in concentration between the soil CO_2 and atmospheric CO_2 and depends on waterlogging, soil porosity, respiration rates and depth of CO_2 production (Ekart *et al.* 1999; Ghosh *et al.* 2001). It has been suggested that this may be calculated from rooting structures and depths, but at present no such model has been created (Ghosh *et al.* 2001). Most authors (Mora *et al.* 1991; Ekart *et al.* 1999, Arens and Jahren 2000, Ghosh *et al.* 2001; Robinson *et al.* 2002; Prochnow *et al.* 2006) use estimates based on measurements from modern soils in similar environments as the paleosols under study to generate this parameter. It has been suggested that desert soils have a range less than 3000ppmV (Ghosh *et al.* 2001), arid to semi-arid soils have a value of 4000ppmV; subhumid soils have a value of 5000ppmV (Prochnow *et al.* 2006) and waterlogged soils have a value of 10000ppmV (Robinson *et al.* 2002). Based on the arid to semi-arid environment suggested by the paleosols in this study (Chapter 3), the range between 3000ppmV and 4000ppmV was chosen as the best representative of the environment in the Southern Urals of Russia in the Permian-Triassic.

$\delta^{13}C_a$ – isotopic composition of the atmosphere

The isotopic carbon concentration of the atmosphere ($\delta^{13}C_a$) is another variable which cannot be directly measured from paleosols. There are two methods proposed for

estimating this variable, the first is using marine brachiopods or inorganic carbonate (Mora *et al.* 1996; Ekart *et al.* 1999); the second uses organic carbon in the paleosol (Ghosh *et al.* 2001). The first method assumes either a –8‰ fractionation from marine inorganic carbonate to atmospheric carbonate (Robertson *et al.* 2002; Cerling 1999; Ekart *et al.* 1999) or a –7‰ fractionation between shallow benthic marine inorganic carbonate and atmospheric carbonate (Driese and Mora 2002; Prochnow *et al.* 2006). It has been suggested that brachiopods could be used instead of marine inorganic carbonate (Mora *et al.* 1996; Ghosh *et al.* 2001). Brachiopods are likely to provide a better proxy for the isotope composition of sea water as it is easier to assess if they have been affected by alteration (Chapter 6). It has been shown that recent brachiopods secrete calcite in carbon isotopic equilibrium with ambient seawater (e.g. van Geldern *et al.* 2006, Lee and Wan 2000). In this study the isotopic compositions of brachiopods closest to the age of the relevant paleosols were used (Table 7.1).

	Age	Locality	$\delta^{13}C$ brachiopod shell (‰)		Source
			Brachiopod	Ave.	
Permian	Changhsingian *Janiceps* and *Comelicania*,	Val Brutta	3.44		Chapter 6
	Changhsingian (251.72)	Sass di Putia	0.86		Korte *et al.* (2005a)
	Changhsingian (252 37)	Meishan D	2.47		Korte *et al.*(2005a)
	Changhsingian (252 76)	Meishan D	4.51	**2.83**	Korte *et al.* (2005a)
Triassic	Induan *(Crurithyris sp.)*	Italy (Tesero)	1.44	**1.44**	Chapter 6
	Olenekian	Pietra del Saracini	4.2		Korte *et al.* (2005b)
	Olenekian	Pietra del Saracini	0.33	**2.27**	Korte *et al.* (2005b)

Table 7.1 $\delta^{13}C$ values of unaltered brachiopods from before and after the P/Tr boundary from published data and field data (see chapter 3). Species names listed where known. The bold values are the average of the brachiopod isotopic values from the same time period.

Using the averages for the Permian and Triassic brachiopod values this would produce $\delta^{13}C_a$ for the Permian of –5.17‰ (±1.55‰) and Triassic values of –6.56‰ (±0.26‰)

for the Induan and −5.74‰ (±2.74‰) for the Olenekian using a fractionation of −8‰ (Cerling 1999; Ekart *et al.* 1999; Robertson *et al.* 2002).

The second method for calculating $\delta^{13}C_a$ is to use the organic matter present in the paleosols. C_3 vegetation is depleted by an average of 21‰ from the atmospheric $\delta^{13}C$, thus adding this fractionation to the isotopic composition of organic carbon found in the soil will give an estimate of $\delta^{13}C_a$ (Ghosh *et al.* 2001). Using the organic carbon values found at Sambullak (Table 7.2) and using the fractionation factor described above (Ghosh *et al.* 2001) produces an estimate for $\delta^{13}C_a = -2.03‰ (\pm 1.55‰)$ which is two permil more positive than the estimate derived by the brachiopod fractionation method.

Sample	Height from based of section (m)	% Carbon	$\delta^{13}C_{org}$ (‰ VPDB)
06.7.21c	117.83	0.44	-22.11
06.7.20a	122.70	2.88	-22.45
06.7.20c	123.48	2.90	-24.55

Table 7.2 Values for organic carbon recovered from Sambullak.

The relationship between $\delta^{13}C_a$ and $\delta^{13}C_\Phi$ has been modelled by Arens *et al.* (2000) in equation (7.2). Using the organic carbon values found at Sambullak (Table 7.2) produces an estimate for $\delta^{13}C_a$ of −3.97‰ (±1.20‰ 1σ std).

$$\delta^{13}C_a = \frac{(\delta^{13}C_\phi + 18.67)}{1.10} \qquad (7.2)$$

$\delta^{13}C_\Phi$ – isotopic composition of soil organic matter

To estimate pCO_2 using equation 7.1 the isotopic composition of respired soil CO_2 from organic matter in the soil ($\delta^{13}C_\Phi$) also has be calculated. As with $\delta^{13}C_a$, there are two methods to calculate $\delta^{13}C_\Phi$. The first is by using the isotopic value of organic carbon found in the soil (e.g. Table 7.1). It is suggested that this can be used as a proxy for $\delta^{13}C_\Phi$ (Driese and Mora 2002; Ghosh *et al.* 2001). Organic carbon was recovered from

three carbon-rich beds at Sambullak (Table 7.2) which yield an average of –23.03‰ (± 1.32‰ 1σ std). This is well within the range of modern C_3 vegetation (Arens *et al.* 2000). However, no organic carbon was recovered from Boyevaya Gora in either the Permian or Triassic.

A second method to calculate $\delta^{13}C_\Phi$ has been proposed for sections where not enough organic carbon has been preserved which can be used for those parts of the sections where organic carbon has not been recovered, such as the Triassic in Russia. This method assumes a fractionation between $\delta^{13}C_a$ and $\delta^{13}C_\Phi$ (Cerling *et al.* 1999; Ekart *et al.* 1999; Robinson *et al.* 2002; Prochnow *et al.* 2006). Some authors assume a simple –18‰ fractionation between $\delta^{13}C_a$ and $\delta^{13}C_\Phi$ (Cerling *et al.* 1999; Ekart *et al.* 1999; Robinson *et al.* 2002). Prochnow *et al.* (2006) use the equation (7.2) and solving it for $\delta^{13}C_\Phi$. When both these techniques are applied to the $\delta^{13}C_a$ calculated from oceanic brachiopods (Table 7.1) estimates of $\delta^{13}C_\Phi = -23.17$ ‰, for the Permian, and $\delta^{13}C_\Phi = -25.71$ ‰, for the Triassic, are produced using the simple fractionation model of –18‰. While using equation (7.2) yields estimates of $\delta^{13}C_\Phi = -23.28$ ‰, for the Permian, and $\delta^{13}C_\Phi = -26.05$ ‰, for the Triassic. The Permian values produced by these techniques (–23.17 ‰, –23.28 ‰) produce values very close to the average value of organic matter from Sambullak (–23.03‰) this suggests that there is no contamination of younger organic matter.

$\delta^{13}C_s$ – isotopic composition of soil water

The final variable to be generated is the isotopic composition of the soil water ($\delta^{13}C_s$). This is directly measured from the isotopic composition of the pedogenic carbonate found in the soil which forms in equilibrium with such fluids (Cerling 1991; Cerling and Quade 1993; Ekart *et al.* 1999). There is a fractionation between the soil water and

pedogenic carbonate which varies with temperature (Ekart *et al.* 1999; Ghosh *et al.* 2001; Robinson *et al.* 2002; Prochnow *et al.* 2006). To account for this the temperature-dependent fractionation factor described by Romanek *et al.* (1992) (equation 7.3) is used to calculate the fractionation factor between the soil water and pedogenic carbonate.

$$\varepsilon_{cl\text{-}CO_2}=11.98(\pm0.13)-0.12(\pm0.01)T \quad (7.3)$$

where ε_{cl-CO_2} is the fractionation factor (‰) and T is temperature of precipitation (°C). Many authors use an average soil temperature of between 20 and 25°C, based on modern analogues (Ekart *et al.* 1999; Ghosh *et al.* 2001; Robinson *et al.* 2002). However, this could produce erroneous results if there is a major change in surface temperature. It has been shown that although there is much as 5°C difference between temperature at depth in a soil and surface air temperature within a year, interannual temperature averages are the same at depth as at the surface (Zhang *et al.* 2001; Smerdon *et al.* 2003). Prochnow *et al.* (2006) utilise the mean annual temperatures produced by equation (5.8a) to calculate their fractionation factor.

Ekart *et al.* (1999) suggest that only nodular (i.e. stage II) carbonates from Aridisols, Alfisols and Mollisols are suitable to be used for $\delta^{13}C_s$, although equation (7.1) has also been successfully applied to Vertisols (Prochnow *et al.* 2006; Ghosh *et al.* 2001). Ekart *et al.* (1999) also suggest a soil must be not formed in anaerobic or waterlogged conditions; be deeper than 20cm in the soil profile and not contain morphologies associated with burial diagenesis or groundwater origin.

The $\delta^{13}C$ values of a pedogenic carbonate can be controlled by both the atmospheric $\delta^{13}C$ and the $\delta^{13}C$ produced by in situ oxidation of organic matter (Cerling 1991), as described in equation (7.1). Tabor *et al.* (2007) argue that in the Karoo Basin across the P/Tr boundary the calcitic isotopic values only represent oxidation of biological matter and have no input from atmospheric carbon dioxide thus rendering them useless as an indicator of pCO_2. This is because the $\delta^{13}C$ of the pedogenic calcite is within +14.8‰ of the isotopic composition organic matter found at the section. This fractionation factor is derived from the 4.4‰ enrichment between carbonate and biologically derived CO_2 and additional 10.4‰ enrichment between the gas and carbonates (Tabor *et al.* 2007). It has been shown elsewhere that the theoretical minimum difference can be less than 4.4‰ if the difference between the biologically derived CO_2 and atmospheric CO_2 is small (Davidson 1995).

Age			$\delta^{13}C_{\Phi}$ (‰, VPDB)	$\delta^{13}C_{calcite}$ (‰, VPDB)
Permian	Changhsingian	Method 1	-23.17	-8.37
		Method 2	-23.26	-8.46
		Method 3	-23.03	-8.23
Triassic	Induan	Method 1	-25.71	-10.91
		Method 2	-26.05	-11.25
	Olenekian	Method 1	-23.36	-8.56
		Method 2	-23.50	-8.70

Table 7.3 Calculated values of $\delta^{13}C$ calcite if only formed from CO_2 produced from organic carbon present in the soil.

Although there is very little evidence of the intensive gleys associated with waterlogging, except at perhaps Mescheryakovka (see Chapter 3), Table 7.3 shows the theoretical values of pedogenic carbonate if it was only formed from biologically derived CO_2.

Based on these conditions only the isotope results which could be demonstrated to have passed all the screening criteria described in Chapter 4, Table 4.2, were used to calculate pCO_2 estimates (see Chapter 4, Table 4.2). The pedogenic dolomite is also

problematic, although it is possible that these represent the $\delta^{13}C$ of the active soil, because the $\delta^{18}O$ values are possibly fractionated (Land 1980). Quast *et al.* (2006) suggest that it not clear if ^{13}C-values of dolomites represent ^{13}C-values of soil CO_2 at higher soil levels. Those nodules that show a microcrystalline texture are also problematic as they may be formed by groundwaters (Quast *et al.* 2006). However, the overlap with those nodules that were of unaltered cryptocrystalline micrite (see chapter 4) suggests that those nodules are also pedogenic, so they were included in the palaeotemperature estimates but only where they are similar to unaltered vadose pedogenic carbonate values from the same paleosol. As only Boyevaya Gora, Sambullak and Mescheryakovka have isotopic values that are definitely unaltered pedogenic calcite; these were used to calculate pCO_2 estimates.

7.2 Application and results from Russia

As discussed in the previous section there are many ways of estimating the variables in equation 7.1. These different approaches all yield different pCO_2 estimates so they have been summed up in three different methods all of which were applied to the $\delta^{13}C_{carb}$ values from the Russian sections (Table 7.4). Method 1 is based on an approach used by Robinson *et al.* (2002) which calculates $\delta^{13}C_a$ from brachiopods using a fractionation factor of −8‰ and $\delta^{13}C_\Phi$ from a fractionation of −18‰ of $\delta^{13}C_a$. Method 2 is based on the approach of Prochnow *et al.* (2006) calculating $\delta^{13}C_a$ from brachiopods using a fractionation of −7‰ and $\delta^{13}C_\Phi$ from $\delta^{13}C_a$ using equation (7.2). Finally, Method 3 is based on the approach of Ghosh *et al.* (2001) who use organic carbon found in the soil to generate $\delta^{13}C_\Phi$ and $\delta^{13}C_a$ from a fractionation of 21‰ from $\delta^{13}C_\Phi$. Because no organic carbon was recovered from the Triassic, method 3 cannot be applied to the Triassic sections in Russia. It may be possible to estimate $\delta^{13}C_\Phi$ from other terrestrial sections in the Earliest Triassic. The Earliest Triassic is typified by many $\delta^{13}C_{org}$ organic

excursions (cf. Retallack and Krull 2006). As there are no extreme excursions in the Triassic at Boyevaya Gora it may be assumed that these excursions fall between or before the paleosols in the section.

Variable	Method 1	Method 2	Method 3
$S_{(z)}$	3000 – 4000ppmV	3000 – 4000ppmV	3000 – 4000ppmV
$\delta^{13}C_a$	Permian –5.17‰ Induan –6.56‰ Olenekian –5.74‰	Permian –4.17‰ Induan –5.56‰ Olenekian –4.74‰	Permian –2.03‰
$\delta^{13}C_\Phi$	Permian –23.17‰ Induan –24.17‰ Olenekian –23.74‰	Permian –23.26‰ Induan –24.79‰ Olenekian -23.88‰	Permian –23.03‰
$\delta^{13}C_s$	From $\delta^{13}C$ of pedogenic carbonate using equ.(8)	From $\delta^{13}C$ of pedogenic carbonate using equ.(8)	From $\delta^{13}C$ of pedogenic carbonate using equ.(8)

Table 7.4 The variables used in the three different methods used for generating the pCO_2 estimates. See text for details.

With all three methods, $\delta^{13}C_s$ was calculated from the screened unaltered pedogenic carbonate results using the temperature-controlled fractionation factor proposed by Romanek *et al.* (1992) (equation 7.3). The temperature estimates used in this equation were those generated from the $\delta^{18}O_{carb}$ results using equation (5.10) (Chapter 5). Although, as stated previously, there are potential issues with this equation (i.e. the low R^2 value of the underlying relationship), it represents the temperature estimate which fits closest to both the pedological evidence and the predicted values for the latest Permian (cf. Kiehl and Shields 2005) and successfully models the temperature rise of 7-8°C just prior to the P/Tr boundary observed in the Italian brachiopods (Chapter 6). For the pedogenic dolomites averaged estimated temperatures from calcite paleosols in the same magnetochron from both Boyevaya Gora and Sambullak were used to generate the fractionation factor.

7.2.1 Results

Section	$\delta^{13}C_{carb}$ (‰)	MAT °C (eq5)	pCO_2 estimate (ppmV) Method 1 (S_z) 3000 ppmV	Method 1 (S_z) 4000 ppmV	Method 2 (S_z) 3000 ppmV	Method 2 (S_z) 4000 ppmV	Method 3 (S_z) 3000 ppmV	Method 3 (S_z) 4000 ppmV
Permian								
Boyevaya Gora	−6.76 (± 3.08)	38 (±5)	3503 (± 2031)	4670 (± 2708)	2807 (± 1721)	2444 (± 1948)	1904 (± 1826)	2539 (± 2333)
Sambullak	−5.56 (± 1.02)	40 (±4)	2800 (± 955)	3733 (± 1274)	2530 (± 784)	3374 (± 1045)	1915 (± 535)	2554 (± 713)
Triassic								
Boyevaya Gora	−3.52 (± 2.59)	43 (±1)	13463 (±17162)	17951 (± 22883)	8200 (± 7049)	10933 (± 9398)	–	–
Mescheryakovka	−8.50 (± 0.81)	47 (±8)	1330 (±302)	1774 (± 403)	1271 (± 269)	1694 (±358)	–	–

Table 7.5 Summary of average atmospheric carbon dioxide calculations are based on stable carbon isotopes in pedogenic carbonate using the three different methods summarised in Table 3. Sz is soil CO_2 concentration (ppmv), $\delta^{13}C_{carb}$ is the isotopic measurement from the pedogenic carbonate (‰), and the average MAT is mean annual temperature (°C) calculated from $\delta^{18}O_{carb}$ using equation (10) (for full results see Appendix A3.3).

All pCO_2 estimates show a dramatic rise from the Permian in to the Triassic (Table 7.5).

There is also a large variation in the pCO_2 estimates between the three methods, for instance with the same input variables (Permian at Boyevaya Gora, with an $S_{(z)}$ of 3000ppmV) there is a difference of between 2766ppmV between the highest and lowest estimates (Table 7.5) although the variation between methods is not bigger than the increase in pCO_2 seen across the P/Tr boundary. Also there is a lot of variation both within the time-averaged estimates and within the horizons themselves (Figure 7.1). The variation in pCO_2 estimates within the Permian is as much as ±2333ppmV (1σ std). However, the overall trends are the same between the three methods.

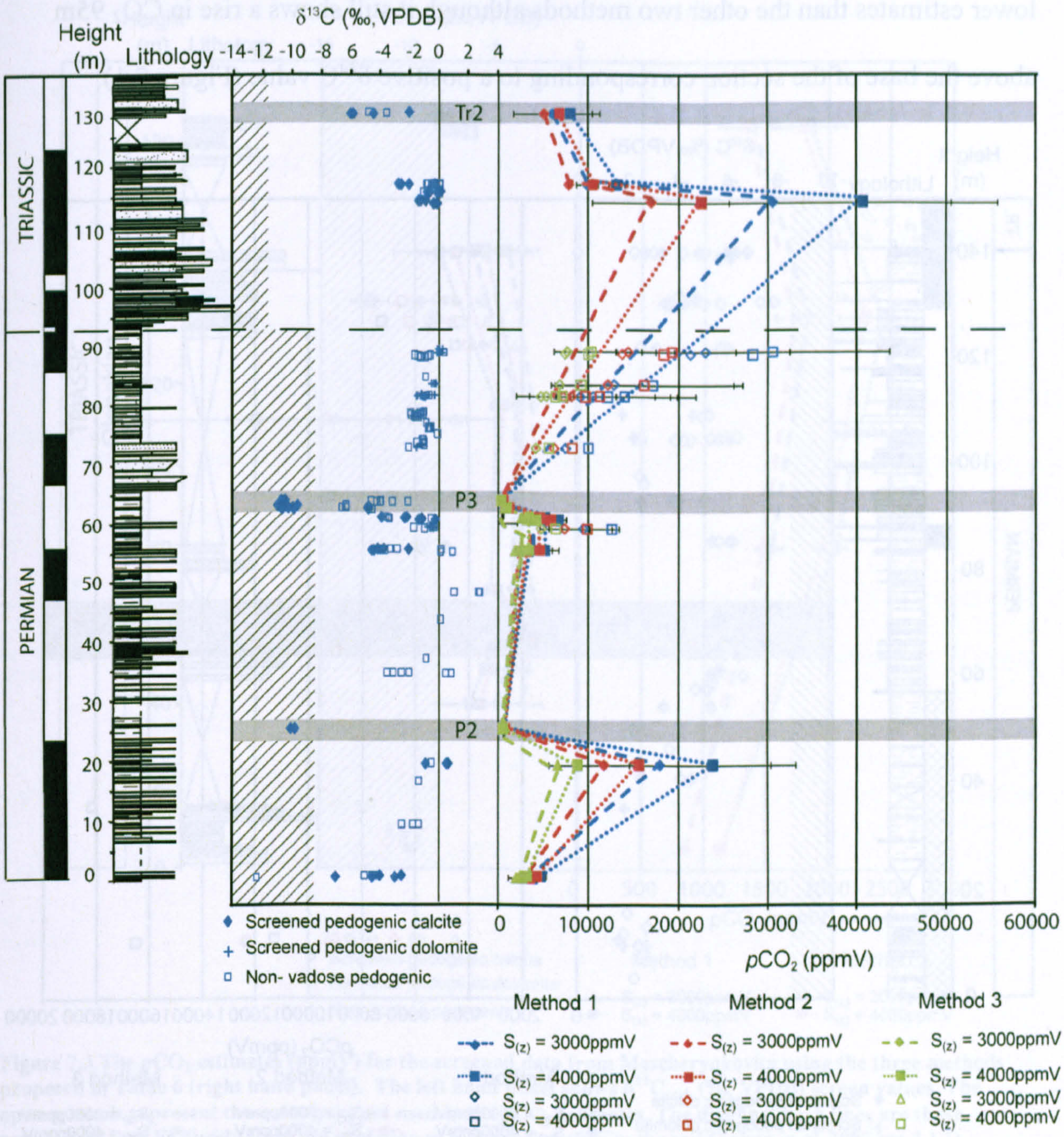

Figure 7.1 The pCO_2 estimates (ppmV) for the screened data from Boyevaya Gora using the three methods proposed in table 6 (right hand panel). The open symbols are those estimates from pedogenic dolomite nodules. The left hand panel shows $\delta^{13}C_{carb}$ (‰, VPDB) screen values the open symbols represent those analyses not used in the pCO_2 estimates and the crosses are pedogenic dolomite values. The diagonal hash lines mark the field in which the isotopic composition can be explained purely by the oxidation of biological matter in the soil (Tabor *et al.* 2007 see Section 7.1.1). The grey horizontal lines highlight the positions of the excursions that may not give accurate estimates if the system is out of equilibrium (Ekart *et al* 1999, see Section 7.3.2).

The estimates from Boyevaya Gora (Figure 7.1) show extreme variation in values, especially in the Triassic where Method 1 predicts values as high at 30000ppmV which is over 100 times greater than pre-industrial levels (Pre- industrial levels 280-380ppmV; Royer 2006). Method 3 (which can only be applied to the Permian) gives significantly

lower estimates than the other two methods although it still shows a rise in CO_2 95m above the base of the section corresponding to a positive $\delta^{13}C$ value (Figure 7.1).

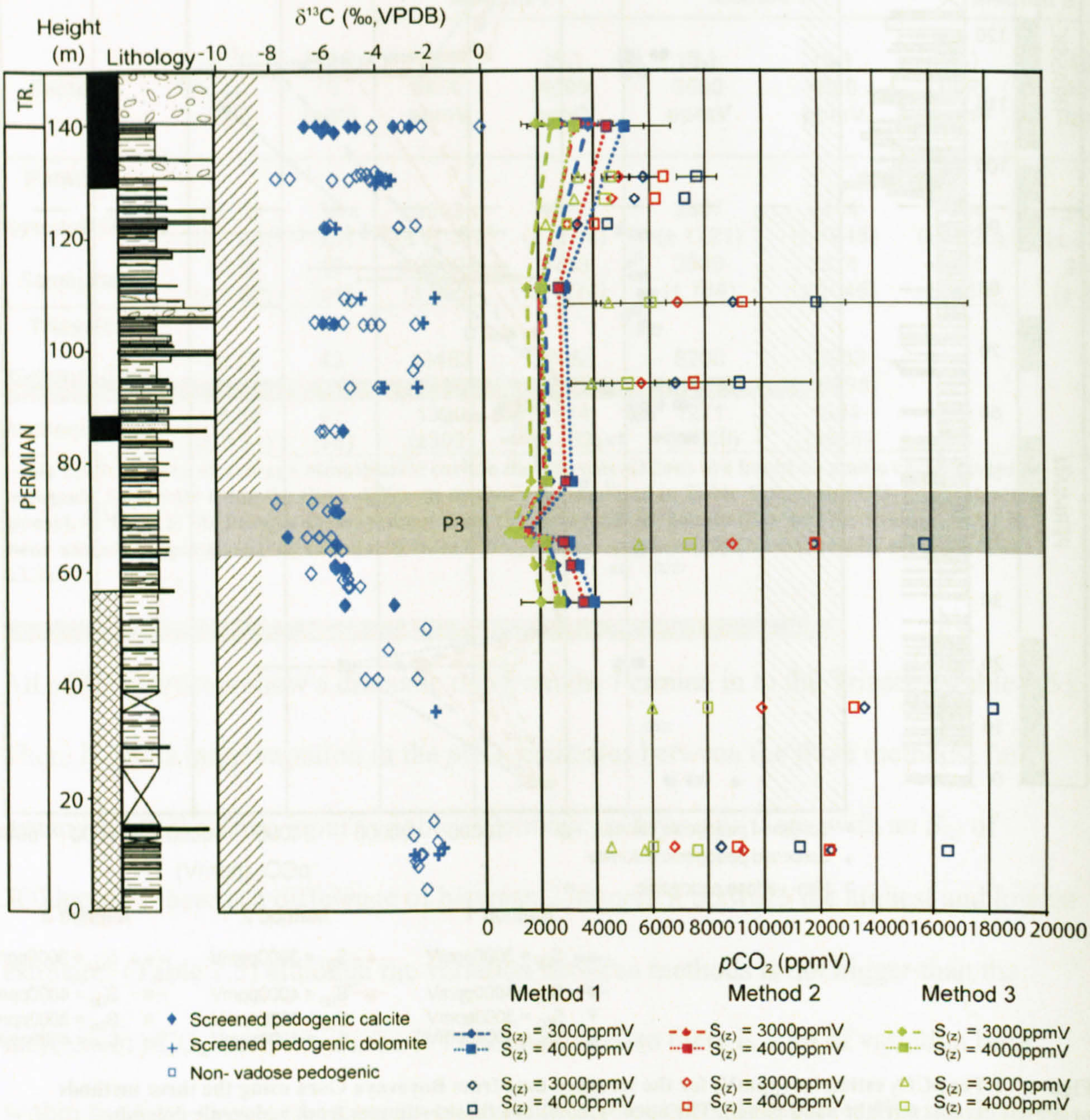

Figure 7.2 The pCO_2 estimates (ppmV) for the screened data from Sambullak using the three methods proposed in Table 6 . The open symbols are those estimates from pedogenic dolomite nodules. The left hand panel shows $\delta^{13}C_{carb}$ (‰, VPDB) screen values the open symbols represent those analyses not uses in the pCO_2 estimates and the crosses are pedogenic dolomite values The diagonal hash lines mark the field in which the isotopic composition can be explained purely by the oxidation of biological matter in the soil (Tabor *et al.* 2007 see Section 7.1.1). The grey horizontal lines highlight the positions of the excursions that may not give accurate estimates if the system is out of equilibrium (Ekart *et al* 1999, see 7.3.2).

The paleosols at Sambullak show much less variation (Figure 7.2) with the average within-paleosol variation being ± 541ppmV (1σ std) for all three methods (Method 1, ± 644ppmV 1σ std; Method 2, ± 539ppmV 1σ std; Method 3 ± 377ppmV 1σ std). Also, the pCO_2 estimates are all much reduced, being between 6 and 11 times pre-industrial levels (Pre industrial levels 280-380ppmV; Royer 2006) depending on the method used.

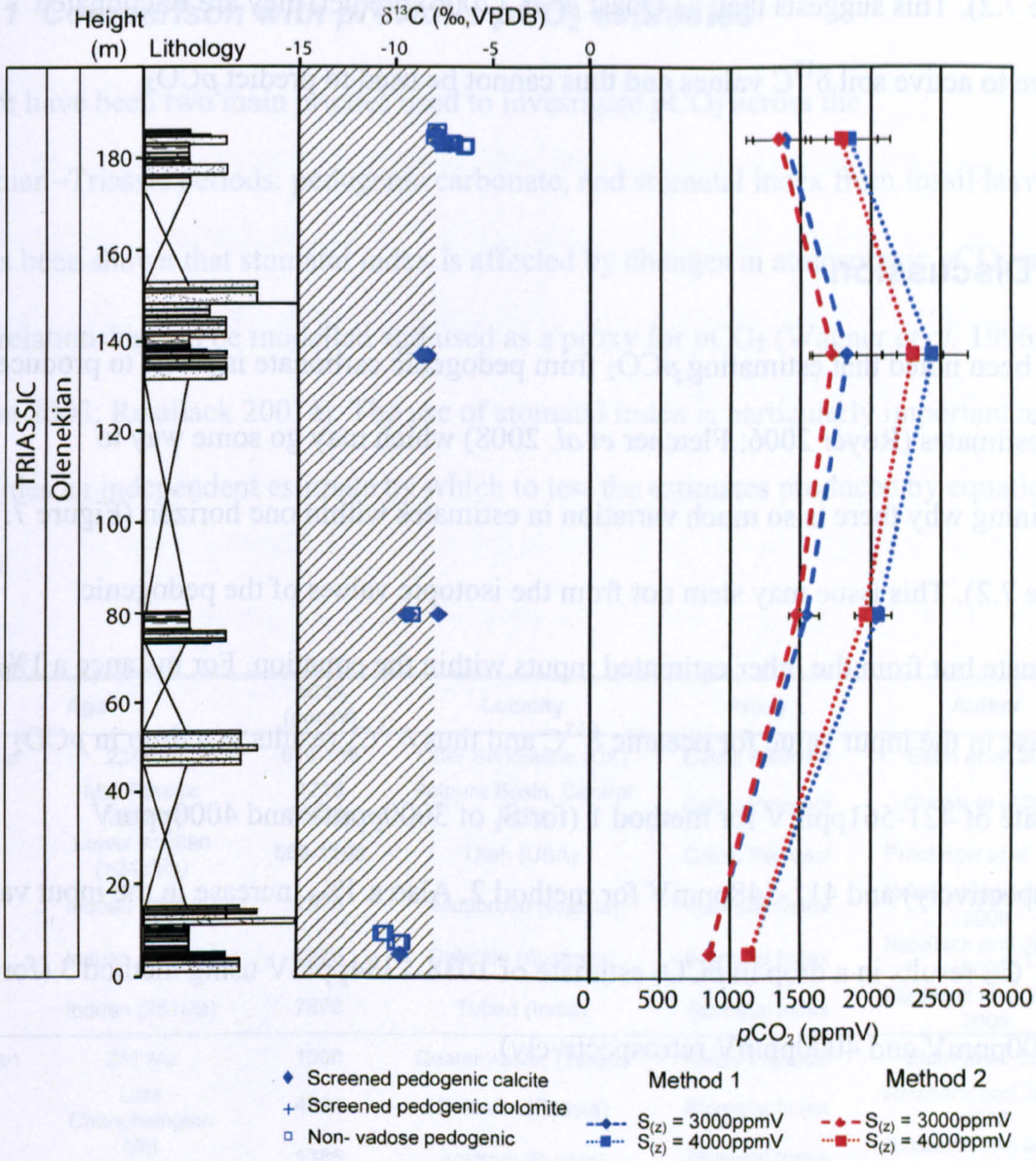

Figure 7.3 The pCO_2 estimates (ppmV) for the screened data from Mescheryakovka using the three methods proposed in Table 6 (right hand panel). The left hand panel shows $\delta^{13}C_{carb}$ (‰, VPDB) screen values. The open symbols represent those analyses not used in the pCO_2 estimates. The diagonal hash lines are those results that may be purely from the oxidation of biological matter in the soil (Tabor *et al.* 2007 see 7.1.1).

The values and within paleosol variation from Mescheryakovka (Figure 7.3) are much reduced compared to the Triassic values at Boyevaya Gora (Figure 7.1, Table 7.5).. However, many of the values could be explained purely by oxidation of biological matter (Figure 7.3) rather than atmospheric values.

The pedogenic dolomite values appear to produce significantly elevated pCO_2 estimates compared to the pedogenic calcite values from a similar stratigraphic level (Figure 7.1,

Figure 7.2). This suggests that, as Quast *et al.* (2006) predict, they are fractionated relative to active soil $\delta^{13}C$ values and thus cannot be used to predict pCO_2.

7.3 Discussion

It has been noted that estimating pCO_2 from pedogenic carbonate is prone to produce over-estimates (Royer 2006; Fletcher *et al.* 2008) which may go some way to explaining why there is so much variation in estimates within one horizon (Figure 7.1, Figure 7.2). This issue may stem not from the isotopic values of the pedogenic carbonate but from the other estimated inputs within the equation. For instance a 1‰ increase in the input value for oceanic $\delta^{13}C$ and thus $\delta^{13}C_a$ results in a drop in pCO_2 estimate of 421-561ppmV for method 1 (for S_z of 3000ppmV and 4000ppmV retrospectively) and 411-548ppmV for method 2. Also a 1‰ increase in the input value for $\delta^{13}C_\Phi$ results in a drop in pCO_2 estimate of 1038-1384ppmV using method 3 (for S_z of 3000ppmV and 4000ppmV retrospectively).

In comparison a 1‰ rise in $\delta^{13}C_s$ only produces a rise of 350-520ppmV across all three methods. This means that the input variables that are not measured from paleosols directly have an equal or greater control over the final pCO_2 estimate than those which were analytically measured. Equally, all three methods assume that the external variables are constant through the Permian and then change in the earliest Triassic. If there are changes in $\delta^{13}C_a$ and $\delta^{13}C_\Phi$ within the Permian or Triassic periods these can produce erroneous estimates. For example, if a negative excursion in $\delta^{13}C_s$ is caused by both a rise in pCO_2 and a fall in either $\delta^{13}C_a$ and $\delta^{13}C_\Phi$ it would make it impossible to estimate the pCO_2 values without some independent measure in the change in $\delta^{13}C_a$ and $\delta^{13}C_\Phi$ (see section 5.3.2).

7.3.1 Comparison with previous pCO_2 estimates

There have been two main proxies used to investigate pCO_2 across the Permian–Triassic periods: pedogenic carbonate, and stomatal index from fossil leaves. It has been shown that stomatal index is affected by changes in atmospheric pCO_2 and this relationship can be modelled and used as a proxy for pCO_2 (Wagner *et al.* 1996; Wynn 2003; Retallack 2001a). The use of stomatal index is particularly important as it provides an independent estimate by which to test the estimates produced by equation (7.1).

	Age	pCO_2 (ppmV)	Locality	Proxy	Author
Triassic	234 Ma	**610-710**	Otter Sandstone (UK)	Calcic Paleosol	Ekart *et al.* 2000
	Mid Triassic (240Ma)	**1210 (±424)**	Satpura Basin, Central India	Calcic Paleosol	Ghosh *et al.*2001
	Lower Anisian (>242Ma)	**600-1160**	Utah (USA)	Calcic Paleosol	Prochnow *et al.* 2006
	Induan (251Ma)	**7876**	Nedubrovo (Russia)	Stomatal Index	Retallack and Jahren 2008
	Induan (251Ma)	**7876**	Oakdale (Australia)	Stomatal Index	Retallack and Jahren 2008
	Induan (251Ma)	**7876**	Tubed (India)	Stomatal Index	Retallack and Jahren 2008
Permian	251 Ma	**1000**	Quatermaster (Texas)	Calcic Paleosol	Ekart *et al.* 1999
	Late Changhsingian	**4264**	Sokovka (Russia)	Stomatal Index	Retallack and Jahren 2008
	Mid Changhsingian	**1385**	Aristovo (Russia)	Stomatal Index	Retallack and Jahren 2008
	Early Changhsingian	**1034**	Aristovo (Russia)	Stomatal Index	Retallack and Jahren 2008
	mid Permian (260Ma)	**715 (±241)**	Satpura Basin, Central India	Calcic Paleosol	Ghosh *et al.*2001
	Early Permian (270Ma)	**300-1500**	Texas	Calcretes and Goethite	Tarbor *et al.* 2004

Table 7.6 Published pCO_2 estimates using both calcic paleosols (as in this study) and stomatal indexes across the Permian –Triassic period.

Table 7.6 shows pCO_2 estimates from other studies using both stomatal and pedogenic carbonate proxies. As Sambullak is Changhsingian in age and Boyevaya Gora spans the Changhsingian and earliest Induan (Chapter 3) these estimates are the most relevant to evaluate the results from this study. The published data shows a rise from 1385ppmV in the lower part of the Changhsingian to 4264ppmV in the Late Changhsingian and a dramatic rise of 7876ppmV in the lowest Triassic (Table 7.6). The estimates generated by method 3 are closest to those estimates predicted by other authors (Table 7.5, Figure

7.1 and Figure 7.2). This suggests that using locally derived values for $\delta^{13}C_{\Phi}$, rather than those derived from a fractionation of global averaged $\delta^{13}C_a$ values (as in methods 1 and 2), produce the most consistent results with the stomatal proxy estimates. This implies that knowledge of local soil conditions (e.g. soil organic matter) is imperative in pCO_2 estimates. Also that an $S_{(z)}$ of 3000ppmV produces values that are closer to those values predicted by others (Table 7.6).

Unfortunately method 3 cannot be applied to the Triassic of Boyevaya Gora as no organic carbon was recovered from this locality. However, the average values for the Earliest Triassic using method 2 and a $S_{(z)}$ of 3000ppmV produce an average of 8200ppmV (±7049), close to the 7876ppmV predicted by Retallack and Jahren (2008) for the earliest Triassic (Figure 7.4). This agreement between the pedogenic carbonate and stomatal proxies suggests that there indeed was rise in atmospheric pCO_2 in the earliest Triassic. The Russian data seems to show a minor rise in the mid to late Changhsingian to 4000ppmV, which is in agreement the stomatal data (Retallack and Jahren 2008, Retallack, www.uoregon.edu 2008) The paleosols then suggests a subsequent reduction before the massive increase in the early Triassic (Figure 7.4). There is one apparently anomalous estimate in the Permian from paleosol KOR 27, which gives an average of 7711ppmV (±6402) (method 3, Sz = 3000 ppmV). Such an anomaly cannot be explained by be explained by oxidation of biomass in the soil as this would cause a negative shift (cf. Tabor *et al.* 2007). Another way of explaining a positive $\delta^{13}C_{carb}$ shift is by increasing the amount of CO_2 in the soil by a change in grain size.

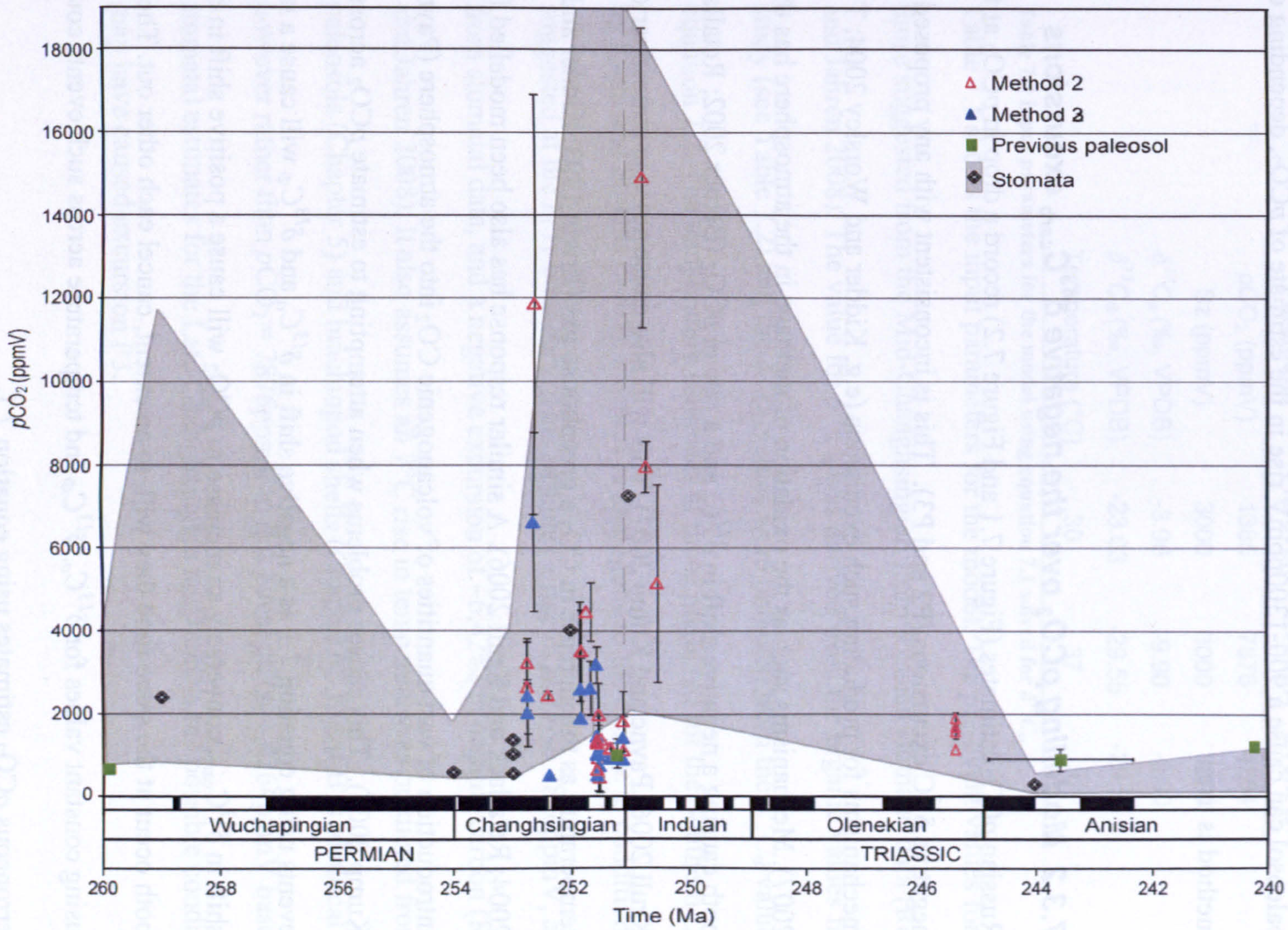

Figure 7.4 The *p*CO2 estimates from this study compared to previously published data. i) is stomatal records (Retallack and Jahren 2008, Retallack www.uoregon.edu 2008). (ii) other pedogenic carbonate estimates (Ekart *et al.*1999; Ghosh *et al.* 2001 and Prochnow *et al.* 2006). The open triangles are estimates using method 2 (Sz=3000ppmV) and the closed are using method 3 (Sz=3000ppmV). The data from this study is are stratigraphically arranged based on magnetic reversals (based on Taylor *et al.* 2009) apart from those in the Olenekian which are based on biostratigraphy (see Chapter 3).

However, KOR27 and those of the Triassic at Boyevaya Gora which contains the positive values are all the same siltstone grain size as the paleosols in the rest of the section (see Chapter 3, 4 and Appendix A2.1). More likely it may be due to local variation in organic matter in that paleosol as a –2‰ shift in the $\delta^{13}C_{\Phi}$ value in the paleosol can cause a 900-1300ppmV rise in the estimate of pCO_2, depending on which method is used.

7.3.2 Modelling pCO_2 over the negative $\delta^{13}C_{carb}$ excursions

Russian pCO_2 estimates (Figure 7.1 and Figure 7.2) record a drop in pCO_2 at the negative $\delta^{13}C$ excursions (P2 and P3). This is inconsistent with any proposed mechanisms for producing such excursions (e.g. Kidder and Worsley 2004; Twitchett 2007). Mechanisms such as the oxidation of methane in the atmosphere has the effect of both causing a negative shift in $\delta^{13}C_a$ and a rise in pCO_2 (Berner 2002; Retallack and Krull 2006; Payne and Kump 2007). This will also cause a rise in atmospheric temperature as the increase in CO_2 a greenhouse gas (Erwin 1993; Kidder and Worsley 2004; Retallack and Krull 2006). A similar response has also been modelled for the introduction of vast quantities of volcanogenic CO_2 into the atmosphere (Payne and Kump 2007). This causes problems when attempting to estimate pCO_2 across such events using equation 7.1 as a negative shift in $\delta^{13}C_a$ and $\delta^{13}C_{\Phi}$ will cause a negative shift in $\delta^{13}C_{carb}$, conversely an increase in pCO_2 will cause a positive shift in $\delta^{13}C_{carb}$. If both occur at the same time they will, to an extent, cancel each other out. Therefore using constant values for $\delta^{13}C_a$, $\delta^{13}C_{\Phi}$ and temperature across such events could lead to erroneous pCO_2 estimates using equation 7.1.

It is possible to theoretically model the pedogenic isotope signal of such an event in a paleosol by solving equation 7.1 for $\delta^{13}C_s$ and inputting pCO_2 values from stomatal data

whilst using $\delta^{13}C_{org}$ values to model the change in $\delta^{13}C_{\Phi}$, and thus $\delta^{13}C_a$ (using equation 7.2). The results from this model then can be compared to the real $\delta^{13}C_{carb}$ paleosol signal to see if it explains the variation seen.

Parameter	Pre event	Event A	Event B
pCO_2 (ppmV)	1385	7876	4264
Sz (ppmV)	3000	3000	3000
$\delta^{13}C_a$ (‰, VPDB)	-3.96	-9.90	-9.90
$\delta^{13}C_\Phi$ (‰, VPDB)	-23.03	-29.55	-29.55
Temperature (°C)	30	37	37

Table 7.7 Input parameters for the model using equation 7.1 solved for $\delta^{13}C_r$.

Table 7.7 shows the input parameters for the model. The pre-event values for pCO_2 those suggested from the Mid-Changhsingian from Russian stomatal data (Retallack and Jahren 2008). The value for $\delta^{13}C_\Phi$ was derived from the organic values from this study (see Table 7.2) and the $\delta^{13}C_a$ values were obtained from the $\delta^{13}C_\Phi$ values using equation 7.2. The temperature estimates at those predicted for the Southern Urals area by Kiehl and Shields (2005). Event A is analogous to the change in conditions suggested at the P/Tr boundary. This assumes a rise in pCO_2 to 7876ppmV, as observed from stomatal data, and a negative excursion of –6.42‰ in organic carbon (Retallack and Jahren 2008). It also assumes an 7°C rise in temperature as predicted from the paleosols (Chapter 5) and brachiopod shells (Chapter 6). Event B is identical to Event A however rather than pCO_2 = 7876ppmV at this event pCO_2 = 4264ppmV based on stomatal estimates for the Late Changhsingian and models the possible conditions that may have caused excursion P3.

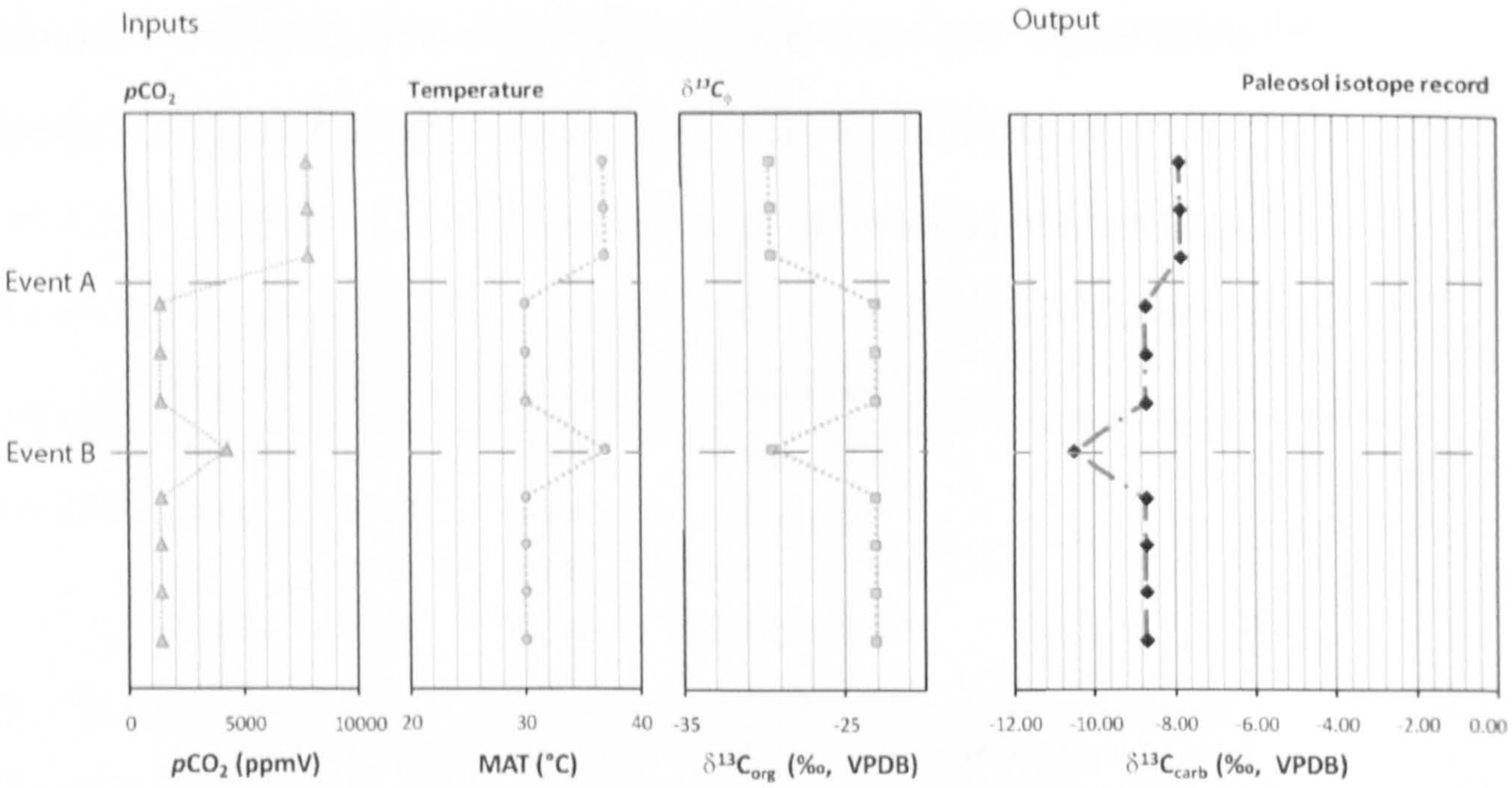

Figure 7.5 Results from the scenario described in Table 7.7. The pCO2, Temperature and $\delta^{13}C_\Phi$ graphs show how those variables change through both events. The output graph predicts how the $\delta^{13}C$ of pedogenic carbonate would vary through both events based using equation 7.1.

Figure 7.5 shows the results of this model. Event A, even though it includes a negative shift in $\delta^{13}C_\Phi$ and $\delta^{13}C_a$, does not produce a negative excursion in pedogenic carbonate values. Instead the massive increase in pCO_2 offsets this, producing a slight positive excursion of +2‰. This appears counter intuitive, but can be explained by the nature of the two component mixing model proposed by Cerling (1991) which underlies equation 7.1. This suggests there are two primary controls on the isotopic composition of pedogenic carbonate, $\delta^{13}C_\Phi$ and $\delta^{13}C_a$; as atmospheric pCO_2 increases there is a switch between $\delta^{13}C_\Phi$ and $\delta^{13}C_a$ being the dominant control on soil waters and thus pedogenic carbonate. In the modern world and at low pCO_2 values $\delta^{13}C_\Phi$ is the dominant control on the isotopic composition of soil water, but at times of extreme increases in pCO_2 this swaps over and thus the less negative $\delta^{13}C_a$ values dominate, producing a slight positive excursion in soil carbonates (Figure 7.6). The threshold between $\delta^{13}C_\Phi$ and $\delta^{13}C_a$ dominating, in the scenario describes in this model (Table 7.7 and Figure 7.5), is pCO_2 = ~6000ppmV and this explains why Event B, due to lower pCO_2 values (4264ppmV) shows a negative excursion rather than a positive one. In this case because $\delta^{13}C_\Phi$ is

dominating the composition of the soil water and thus the change in isotopic composition of the atmosphere is being recorded in the pedogenic carbonate.

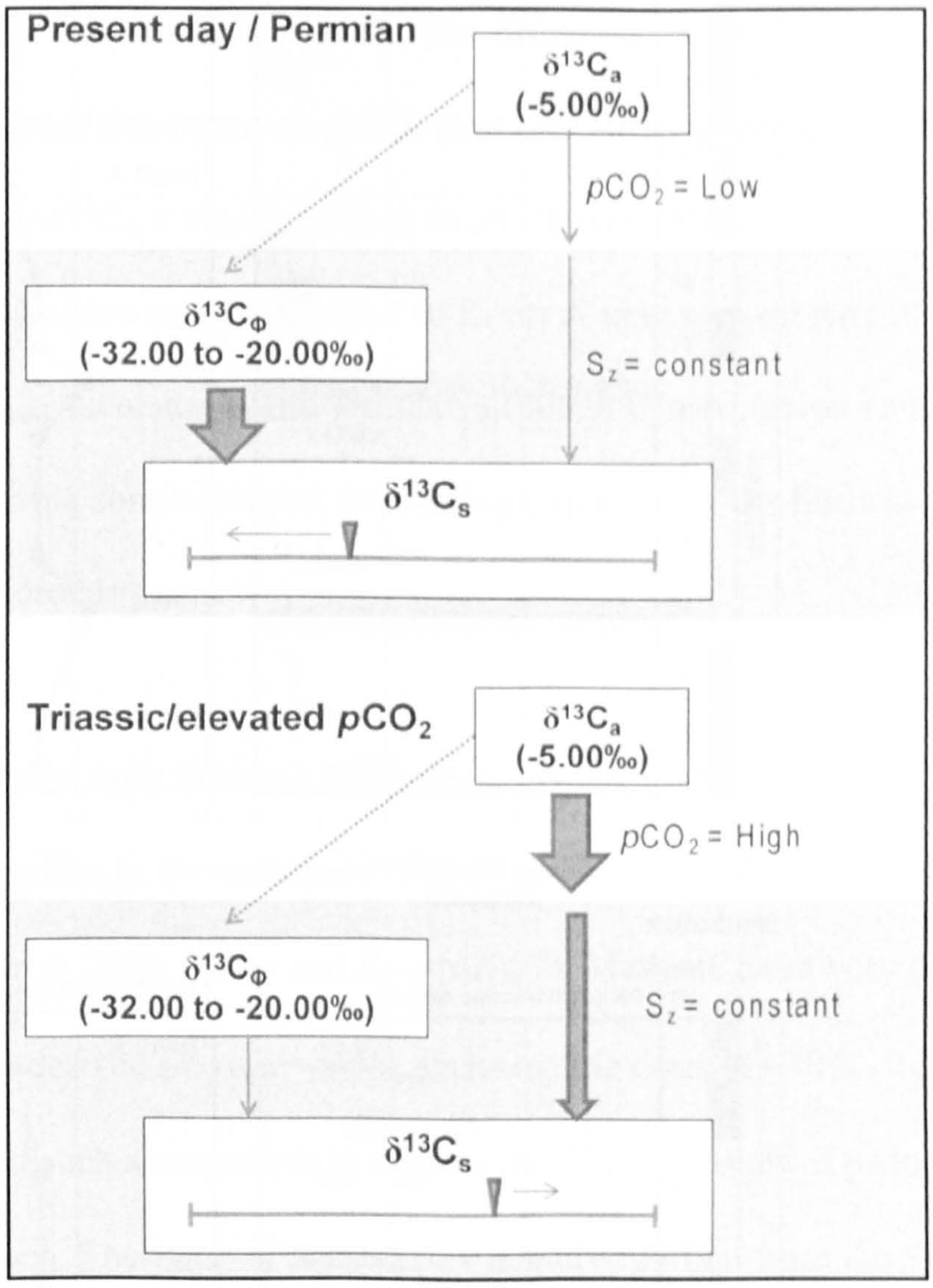

Figure 7.6 The dominance of the two component mixing model described by Cerling (1991) and Ekart *et al.*(1999). In present day/Permian conditions (top panel) $\delta^{13}C_{\Phi}$ has dominant control over $\delta^{13}C_s$ and because $\delta^{13}C_{\Phi}$ and $\delta^{13}C_a$ are linked negative excursions in $\delta^{13}C_a$ are recorded. However, in elevated pCO_2 conditions $\delta^{13}C_a$ is dominant and because it is isotopically more positive than $\delta^{13}C_{\Phi}$ it appears to produce a positive shift when switching between the control of $\delta^{13}C_{\Phi}$ and $\delta^{13}C_a$.

Like Event A (which is analogous to the P/Tr boundary), at Event B the value for the change in $\delta^{13}C_{\Phi}$ was assumed to be –6.42‰, however there is no experimental data to support this as there was no organic carbon recovered from the excursion P3 or any global values from elsewhere from which to model this event. It is equally possible to produce such results as modelled in Event B by the input of the same amount of CO_2 but a more isotopically negative source for that CO_2.

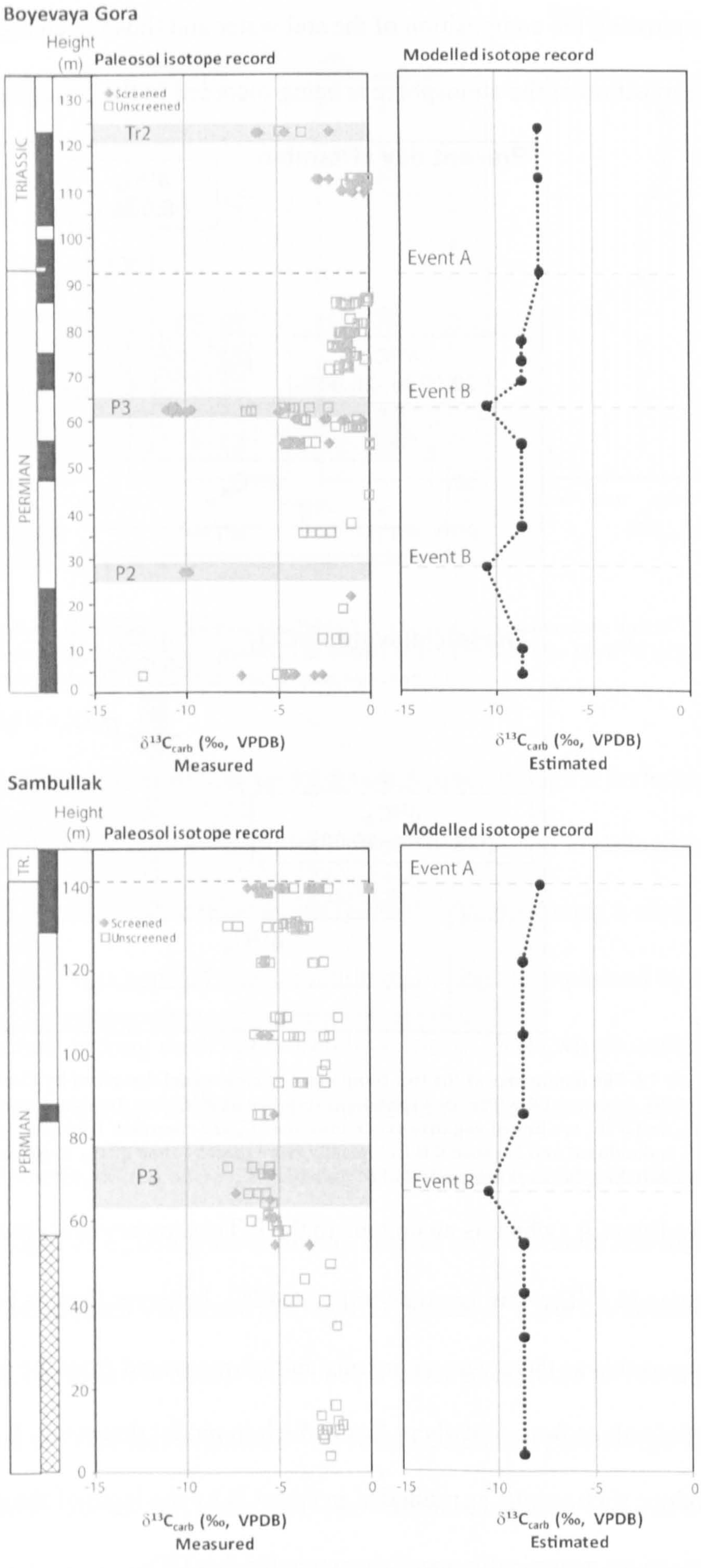

Figure 7.7 Comparison of modelled $\delta^{13}C_{carb}$ values using the parameters in Table 7.7 with recorded $\delta^{13}C_{carb}$ values from Boyevaya Gora and Sambullak. The change across the P/Tr boundary was modelled as an Event A while P2 and P3 were modelled as Event B excursions. Note excursions P4 and Tr1 are not shown as they are only recorded in the $\delta^{18}O_{carb}$ values.

Comparing these modelled values with the measured isotope record from the Russian sections (Figure 7.7) suggests that a scenario similar to that suggested in Event B may be responsible for excursions P2 and P3. The difference in absolute values may be due to the fact that Event B is based on global averages and does not take in to account local variations in S_z or $\delta^{13}C_{\Phi,}$ a 1‰ difference in which can alter the predicted $\delta^{13}C_{carb}$ value by ~1‰. Equally, this a scenario similar to Event A may suggest why there is no prominent $\delta^{13}C_{carb}$ excursion in the Triassic, although this excursion could occurred at the same time as the conglomerates were being deposited in the Earliest Triassic and thus was not recorded.

As previously stated both methane and volcanogenic CO_2 have been proposed as causes of negative anomalies in the carbonate record (Erwin 1993; Kidder and Woresley 2004; Retallack and Krull 2006; Payne and Kump 2007). Methane has a very negative $\delta^{13}C$ value (clathrates derived average –60‰; thermogenic derived –40‰, Retallack and Jahren 2008) and such a source could explain the $\delta^{13}C_{carb}$ values of pedogenic carbonate observed in Russia. The input of isotopically negative carbon from the Siberian Traps has also been postulated as a cause of the negative anomalies (e.g. Payne and Kump 2007) However, others have argued that volcanogenic emissions have an isotopic value of –5‰, which is close to the predicted atmospheric values of the Permian atmosphere (Retallack and Jahren 2008, Table 7.4). Thus, however much volcanic CO_2 is introduced into the atmosphere, it could not have caused the negative shift in atmospheric isotopic values (Retallack and Jahren 2008). This value of –5‰ is based on data collected from highly fractionated fumaroles at Mauna Loa in Hawaii in the 1950s (Faure 1986; Hansen 2006 and references therein). Hansen (2006) argues that CO_2 sampled directly from lava flows has a value of –24‰ ±2‰ and carbon recovered from lava flows, including the Deccan Traps from CO_2 in the lava, has values of between

−24.1‰ and −27.8‰. These more negative values could also be responsible for a negative excursion in $\delta^{13}C_{\Phi}$ of −6.42‰ assuming enough CO_2 is released.

The modelling of the isotope signal (Table 7.7 and Figure 7.5) shows that it is possible to explain why a dramatic rise in pCO_2 caused by input of isotopically negative CO_2 may not produce a negative excursion in the $\delta^{13}C_{carb}$ values of pedogenic carbonate. Also it suggests that the negative excursions seen in the pedogenic carbonate record in, such as P2 and P3 relate to either lesser inputs of CO_2 in to the atmosphere than at the P/Tr boundary, or they were caused by a different source which was more isotopically negative than that the source which caused the rise in pCO_2 observed at the P/Tr boundary.

7.4 Summary

There is much variation even between methods of generating the variables in the pCO_2 equation (7.1) and between and within individual paleosols. This variability must be considered when interpreting and using the pCO_2 estimates, as they are exactly that – estimates. With this consideration in mind there are several conclusions that can be drawn from the $\delta^{13}C_{carb}$ and pCO_2 modelling of the data from Boyevaya Gora and Sambullak.

1) There appears to be a dramatic rise in pCO_2 in the earliest Triassic which appears to be consistent with stomatal records of a similar age from Russia (Retallack and Jahren 2008). Although the extreme variation seen between methods may suggest the environment was not in equilibrium or that one of the other factors in the equation are not being accurately modelled.

2) The negative excursions (P2 and P3) observed at Boyevaya Gora and, to a lesser extent Sambullak, could be explained by a rise in pCO_2, but only if there is a

corresponding drop in the isotopic composition of organic carbon ($\delta^{13}C_{\Phi}$) at the same point in time.

3) A negative $\delta^{13}C$ excursion in the atmosphere will not necessarily cause a negative excursion in the $\delta^{13}C_{carb}$ record of pedogenic carbonate if it coincides with a dramatic rise in pCO_2 which is big enough to change the dominant control on the isotopic composition of pedogenic carbonate.

Chapter 8. Global comparisons

8.1 Introduction

In recent years there has been a move to correlate the various isotope records from around the globe across the Permian/Triassic boundary with a view to understanding how these events may have related to the mass extinction (deWit *et al.* 2002; Kidder and Worsley 2004; Erwin *et al.* 2006). There have also been attempts to map these anomalies, especially the $\delta^{13}C$ anomaly, to understand how the isotope excursions vary globally (Retallack and Krull 2006; Retallack and Jahren 2008). It has been suggested that the carbon isotope excursion is greater on land than in the sea (Retallack and Krull 2006; Retallack and Jahren 2008) and is more pronounced at high latitude than at low latitude (Krull *et al.* 2000; Krull *et al.* 2004; Retallack and Krull 2006; Retallack and Jahren 2008). It is important to understand how the new results from Russia and the Italian Dolomites fit into this emerging global picture.

It has been proposed that the mechanism which records the isotope signature in the material being analysed may also control the distribution or reason for the isotope anomaly. For instance marine carbonate values represent time averaging over millennia (Retallack and Jahren 2008); and paleosol carbonate nodules are thought to re-equilibrate isotopically through the time that a paleosol is active (Liu *et al.* 1996) and thus also represent an averaged signal. Organic carbon from terrestrial sections, on the other hand, records local annual–decadal values (Retallack and Krull 2006; Retallack and Jahren 2008). The same is true for carbonate isotope values recovered from vertebrate teeth and tusks (MacLeod *et al.* 2001).

The mechanisms that have been cited as causing the isotopic anomalies are different in different facies and sections. Marine carbonate and marine fossils are influenced by inputs of

organic carbon from land and influxes of anoxic bottom waters, along with direct changes in atmospheric chemistry (Hallam and Wignall 1997; Foster *et al.* 1997; Sephton *et al.* 2005; Algeo *et al.* 2007). Similarly, pedogenic carbonate can be influenced by changes in waterlogging (Tarbor *et al.* 2007), groundcover and meteoric source (Quast *et al.* 2006, see Chapter 5) as well as atmospheric changes. Even organic carbon, although thought to relate directly to the $\delta^{13}C$ composition of the atmosphere (Arens *et al.* 2000), can also be affected by changes in plant productivity, amount of wood and physiology (Foster *et al.* 1997; Krull and Retallack 2000; Retallack and Krull 2006).

With such varied potential influences controlling the isotope signal, knowing the relative timing of anomalies is imperative to understand and test proposed extinction mechanisms. For instance, if the marine $\delta^{13}C$ excursion is controlled by input of terrestrial organic material into the sediment caused by a die-off of land plants due to the terrestrial extinction (Foster *et al.*1997; Visscher *et al.* 2004; Sephton *et al.* 2005) then it must post-date the terrestrial $\delta^{13}C$ excursions as these are more likely to have been directly caused by changes in the atmospheric chemistry or plant cover. However, relative durations and sedimentation rates may make excursions appear synchronous without comprehensive stratigraphic control.

There is also debate over whether the excursion comes before or after the mass extinction event (Gorjan *et al.* 2008). In some localities, such as Jameson Land in Greenland, the $\delta^{13}C$ excursion occurs after the mass extinction (Looy *et al.* 2001; Twitchett *et al.* 2001) and is due either to changes caused by the mass extinction (as discussed in Chapter 7) or a mechanism which had little or no affect on the biotic crisis (Twitchett *et al.* 2001). However, there are other examples (e.g. Musashi *et al.* 2001; Dolenec *et al.* 2001; Krull *et al.* 2004) where the

extinction postdates the $\delta^{13}C$ excursion, suggesting that the excursion itself is linked to the cause of the mass extinction rather than the consequence.

Finally, there have been other $\delta^{13}C$ excursions observed below the excursion coincident with the P/Tr boundary. In northern Xinjiang in China two episodes of $\delta^{13}C$ depletion have been observed in the organic carbon in terrestrial and marine sequences (Cao *et al.* 2008; Hansen 2000). These have also been observed in Nelben in Germany 1 metre below the P/Tr excursion which has been correlated with the lower excursion seen at Xinjiang (Hansen *et al.* 2006). These excursions pre-date the P/Tr boundary excursions and are thought to be caused by onset of the latest Permian environmental stress linked to changes in the isotopic composition of the atmosphere (Cao *et al.* 2008). It must be remembered, however, that at the Global Stratotype Section and Point (GSSP) in Meishan the extinction occurs below the P/Tr boundary as defined by the FAD of *Hindeodus parvus*. There have also been $\delta^{13}C$ excursions observed in terrestrial and marine, organic and carbonate records coincident with the end-Guadalupian event (Retallack *et al.* 2005; Retallack *et al.* 2006). These have been observed in Karoo, Antarctica, Australia, Greece, and Slovenia and are thought to be caused by a mass methane release similar to the P/Tr boundary event (Retallack *et al.* 2006).

It is important to determine how the data from the Russian paleosols and Italian brachiopods fit within this global framework, especially with reference to how the isotope excursion observed in the mid-Changhsingian in Russia relates to the other global sections. Also, to track the changes in the environmental conditions, mean annual precipitation (MAP) and other climatic proxies will be compared to other paleosol sections from Antarctica (Retallack and Krull 1999), Australia (Retallack 1999) and the Karoo basin (Retallack *et al.* 2003). These will be used to test how the Russian excursions correlate with others and with the

Siberian Traps which are a proposed mechanism for the mass extinction (Erwin 1993; Kamo *et al.* 2003; Grard *et al.* 2005; Beerling *et al.* 2007; Payne and Kump 2007).

8.2 P/Tr Global correlations and stratigraphy

There are three main methods used to correlate between different Permian/Triassic sections: biostratigraphy (including conodonts, ammonoids, vertebrates and palynomorphs, see Gradstein and Ogg 2004), chemostratigraphy (matching the carbon isotope records, e.g. Retallack and Krull 2006; Retallack *et al.* 2006; Retallack and Jahren 2008) and magnetostratigraphy (e.g. Jin *et al.* 2000; Steiner 2006). Each technique has its own advantages and drawbacks, especially at times of mass extinction when fossil geographical ranges can change dramatically before they go extinct; isotope excursions can be caused by either the effects or the causes of the extinction, and erosion caused by facies changes associated with the extinctions (e.g. Ward *et al.* 2000; Benton *et al.* 2004) can remove magnetochrons.

The first appearance datum (FAD) of the conodont *Hindeodus parvus* was agreed as the marker for the base of the Triassic (Paull and Paull 1994; Yin *et al.* 2001) due to its global occurrence in both shallow and deep water facies (Yin *et al.* 2001). The GSSP was defined as the first appearance of the conodont *H. parvus* in bed 27c at Meishan section D in Changxing County in South China where the boundary is sandwiched between ash layers which can be used to date it at 251.0±0.4 Ma (Bowing *et al.* 1998; Gradstein *et al.* 2004). Since the definition of the GSSP newer U/Pb dates for the boundary at Meishan and terrestrial sections at Chahe (Guizhou Province in China) date main pulse of the extinction at 252.6 ±0.2 Ma and 252.6 ±2.8 Ma (Mundil *et al.* 2004; Yu *et al.* 2008). It was proposed that the $\delta^{13}C$ excursion

could act as an auxiliary marker for the P/Tr Boundary (Yin *et al.* 2001), although the excursion occurs below the FAD of *H. parvus* (Gradstein *et al.* 2004).

In terrestrial sediments, however, *Hindeodus parvus* cannot be used. As a result correlating terrestrial P/Tr stratigraphy with both marine sections and other global terrestrial sections is still problematic. As with the marine sections the extinction event appears to occur at dramatic a facies change. This manifests as a change from fluvial meandering rivers to coarse braided rivers which have been observed in the Southern Urals (Newell *et al.*1999; Benton *et al.* 2004), in the Karoo in South Africa (Ward *et al.* 2000), in Antarctica (Retallack 2005a; Retallack *et al.*2006; Retallack *et al.*2007) and Australia (Michaelsen 2002) (see Chapter1, Figure1.1 for palaeogeographical locations). There is also a global hiatus in coal formation and preservation at the P/Tr representing a dramatic change in the environment (Faure *et al* 1995, Retallack and Krull 2006). Although these changes are all attributed to be results of the extinction mechanism, it is hard to say whether these facies changes all occurred at one time or are diachronous and thus if the extinction influenced different latitudes and localities at different times.

Unlike the marine sections there is no global biomarker for terrestrial sections, thus correlations are far more complicated. The boundary is often defined by the last occurrence of the Permian zonal index fossil *Dicynodon* and the first occurrence of the vertebrate *Lystrosaurus* (Ward *et al.* 2005, Retallack *et al* 2005). However, Ward *et al.* (2005) have identified that, in the Karoo Basin in South Africa, *Lystrosaurus* is found in the *Dicynodon* zone. They explain this by suggesting that Triassic vertebrate fauna may have pre-dated the main Permian extinction pulse, similar to the pattern of mammalian radiation after the Cretaceous–Palaeogene extinction. An alternative hypothesis is that there was a migration of

the reptilian and amphibian fauna from South Africa to Antarctica in the Early Triassic (Collinson *et al.* 2006). Either way, this overlap causes great problems for correlative purposes as it is not seen in other world sections such as Antarctica (Collinson *et al.* 2006). Also, to date, *Lystrosaurus* has not been found in the Southern Urals (Russia) or in Australia (Retallack *et al.* 2005, Benton *et al.* 2004). Also, the use of *Dicynodon* as Late Permian zone fossil has been questioned due to its confusing taxonomic history and possible polyphyletic nature of the clade (Angielczyk and Kurkin 2003).

The other issue with using terrestrial vertebrates is that within terrestrial sedimentary sequences fossils can be scarce. For instance, at Boyevaya Gora in Russia, the first Triassic tetrapods are found within the basal strata of the Triassic as defined by magnetostratigraphy (Taylor *et al.* 2009), while the last Permian tetrapods and fishes are 22 metres below this point (Taylor *et al.* 2009). This can cause large areas of uncertainty and compound any issues resulting from extinction-induced migrations and localised extinction.

Palynology has also been used to correlate Indian and Madagascan terrestrial sections across the P/Tr boundary. However, in both these cases the pollen could only be used to identify the extinction within a basin rather than correlating between basins (de Wit *et al.* 2002). *Protohaploxypinus microcorpus* was used by Morante (1996) to define the P/Tr boundary in Australia. It has also been found in sections in Antarctica where it also occurs one metre above the last occurrence of *Glossopteris* fossils, which have been used locally to define the top of the Permian (Collinson *et al.* 2006, Retallack *et al.* 2005). In the Karoo Basin the top of the *P. microcorpus* biozone occurs over 20 metres above the major faunal extinction, just before the 'fungal spike' (Ward *et al.* 2005, Steiner *et al.* 2003).

The use of the $\delta^{13}C$ excursion itself as a chemostratigraphic marker has also been suggested as a global correlative tool between marine and terrestrial sections because the surface ocean mixes on a 10^4yr cycle and is in dynamic equilibrium with the atmosphere (MacLeod *et al.* 2000; Yin *et al* .2000). Thus, a global $\delta^{13}C$ excursion should be geologically simultaneous in terrestrial and marine sections (MacLeod *et al.* 2000). This technique has been used globally to correlate both marine and terrestrial sections (Retallack *et al.* 2006; Retallack and Krull 2006; Retallack and Jahren 2008).

However, this technique too has its drawbacks. Firstly, as with biostratigraphy, it assumes that the major extinction event occurred at the same time globally and that the excursion is geologically instantaneous. It has been observed that globally the excursion occurs both before and after the extinction event depending on locality (Gorjan *et al.* 2008) suggesting that at least one of these events is diachronous. Secondly, it only provides a datum on which to hang sections and gives little control over how time varies through a section. It has been suggested that there is a negative $\delta^{13}C$ excursion related to the end Guadalupian and this may be used as a lower correlative tool (Retallack *et al.* 2006). Finally, it has been suggested that some negative excursions are due to local factors and not global atmospheric changes (Tabor *et al.* 2007). Also, chemostratigraphy only works if both the marine and terrestrial $\delta^{13}C$ excursions are caused by the same mechanism (e.g. mass methane release or a volcanic eruption), or if the marine excursion is caused by influx of terrestrial organic matter (Foster *et al.* 1997; Visscher *et al.* 2004; Sephton *et al.* 2005).

All the techniques mentioned thus far are either biological or environmental, so are likely to be affected by an extinction event in different ways, such as migration of ranges and changes in facies. Magnetostratigraphy, however, reflects the changes in the polarity of the Earth's

magnetic field and thus should not be affected by the mass extinction event so providing an unbiased correlative tool. Equally, as reversals in polarity are typically less than 5000 years and are potentially recorded simultaneously globally, this is the most precise method available for global correlation (Ogg and Smith 2004). There have been several interbasinal magnetostratigraphic correlations between marine and terrestrial sections across the Permian/Triassic boundary (e.g. Szurlies *et al.* 2003; Molostovskii 2005; Szurlies 2007; Hounslow *et al.* 2008) and global correlations (e.g. Jin *et al.* 2000; Kozur and Bachmann 2005; Steiner 2006). Therefore, magnetostratigraphy should be a primary candidate for correlating between terrestrial sections and marine sections.

There are, however, issues with using magnetostratigraphy. Firstly, major terrestrial sections, such as Antarctica, do not have a reliable magnetostratigraphic record because of heating of the rocks by Jurassic diabase sills (Collinson *et al.* 2006). Likewise, it is suggested that the Karoo basin magnetostratigraphic record may have been affected by later diagenetic fluids and magmatic intrusions (de Wit *et al* 2002). Secondly, without corroborating fossil data it is possible to produce very different interpretations of magnetostratigraphic correlations such as for the Siberian Traps (compare Steiner 2006 and Dobretsov *et al.* 2007).

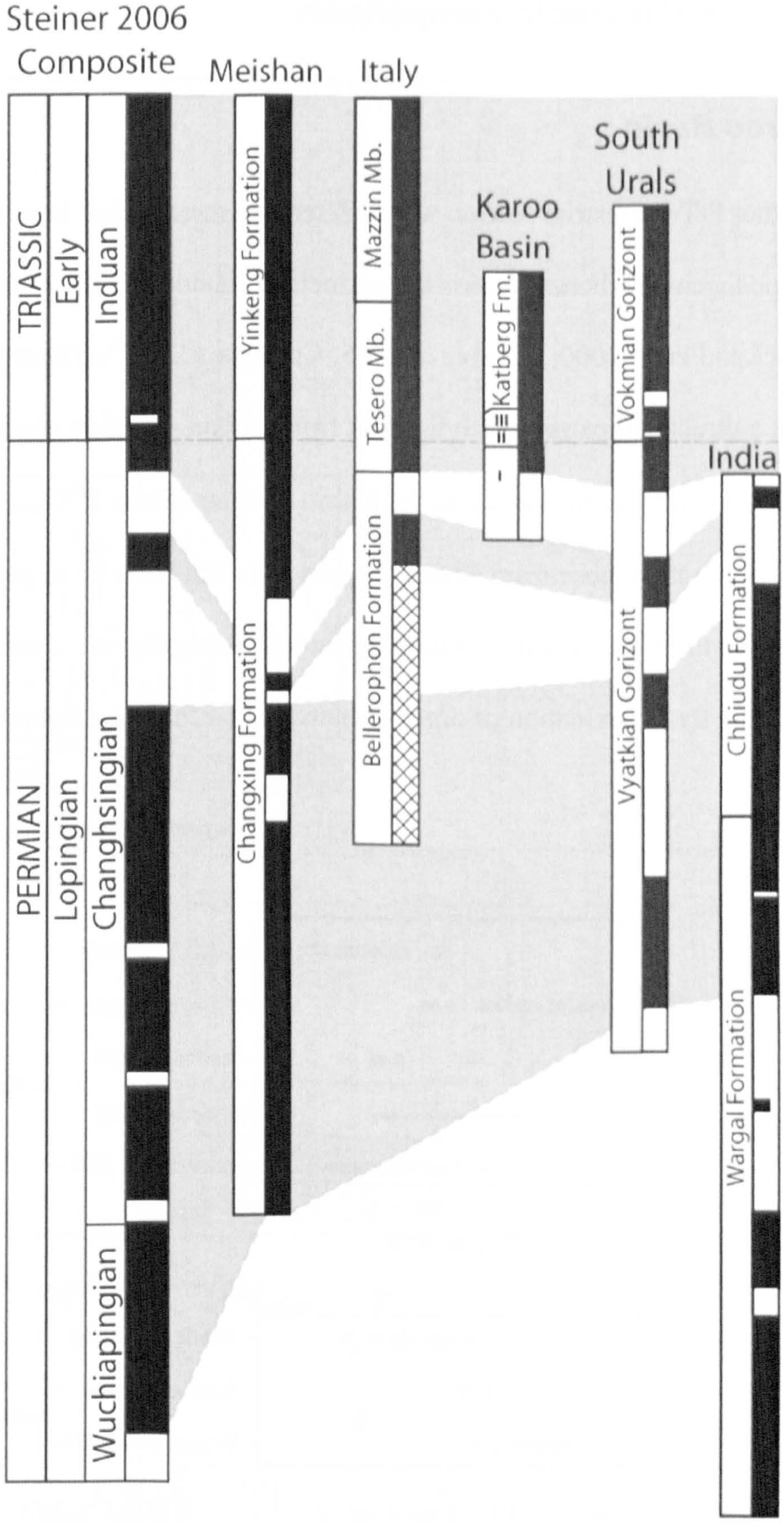

Figure 8.1 Magnetostratigraphic correlations used in this study. Correlations between sections from Steiner 2006 apart from the South Urals which was based on the correlation of Taylor *et al.* (2009) to Steiner's composite.

8.3 Terrestrial isotopic comparison

8.3.1 Karoo Basin

The only other P/Tr terrestrial section where extensive research has been undertaken in relation to pedogenic carbonate across the extinction boundary is the Karoo Basin in South Africa (MacLeod *et al.* 2000; Ward *et al* 2005; Coney *et al.* 2007; Tabor *et al.* 2007) and thus can provide a direct comparison with the data from Russia. The first observation that can be made from these isotope studies is that the Karoo nodular calcite $\delta^{13}C_{carb}$ and $\delta^{18}O_{carb}$ values are more negative than those from Russia (Figure 8.2). This may be in part due to waterlogging in the Karoo Basin in which the isotopic composition of carbonate nodules is controlled more by the oxidation of organic matter rather than atmospheric changes (Tabor *et al.* 2007).

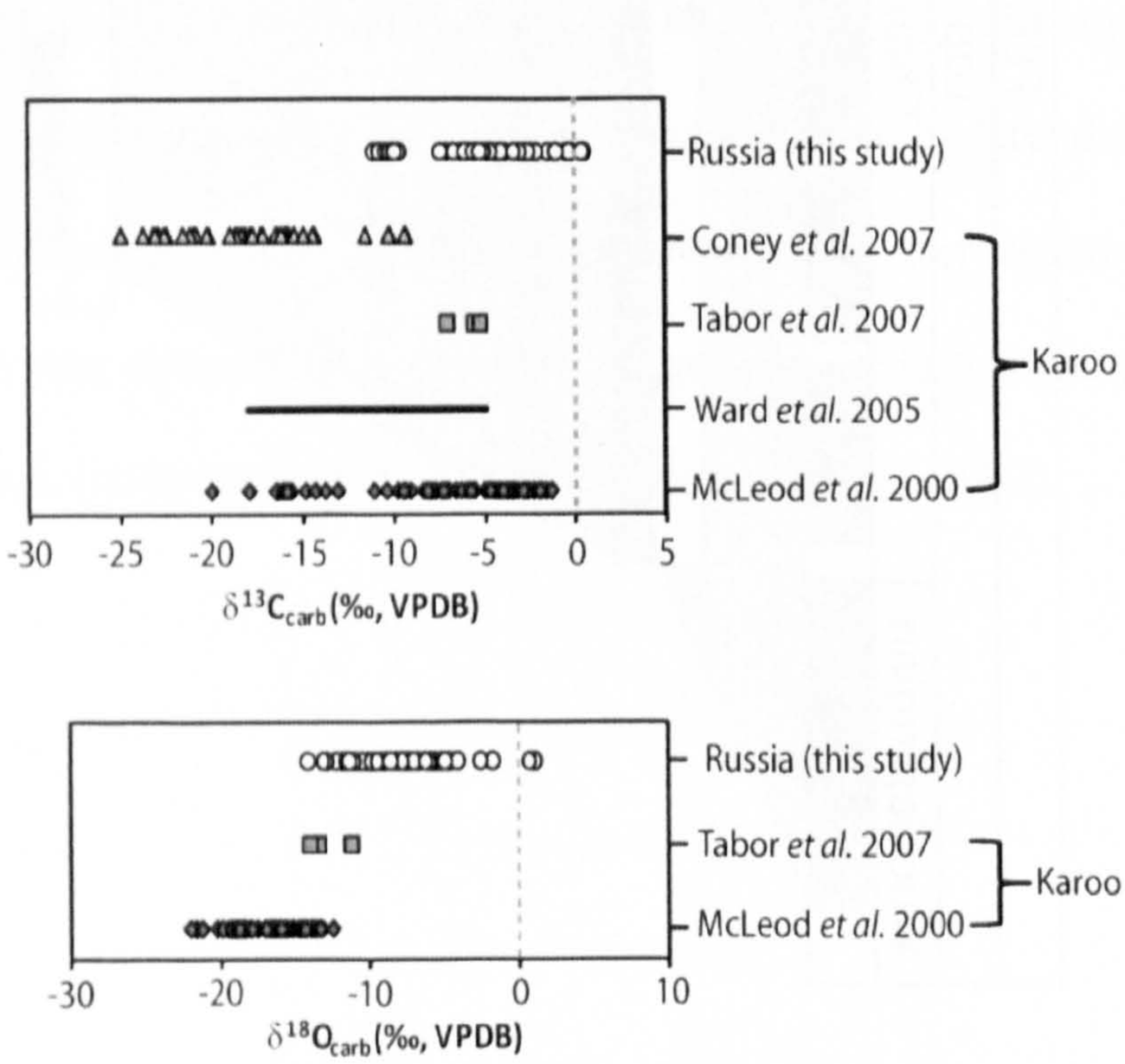

Figure 8.2 The ranges of other pedogenic carbonate studies across the Permian-Triassic boundary from the Karoo basin. Note the bar representing the values from Ward *et al.* (2005) is the range of values rather than the exact data points as these were not published. All the other values refer are those described as being 'primary and unaltered' by the papers from which the data are from.

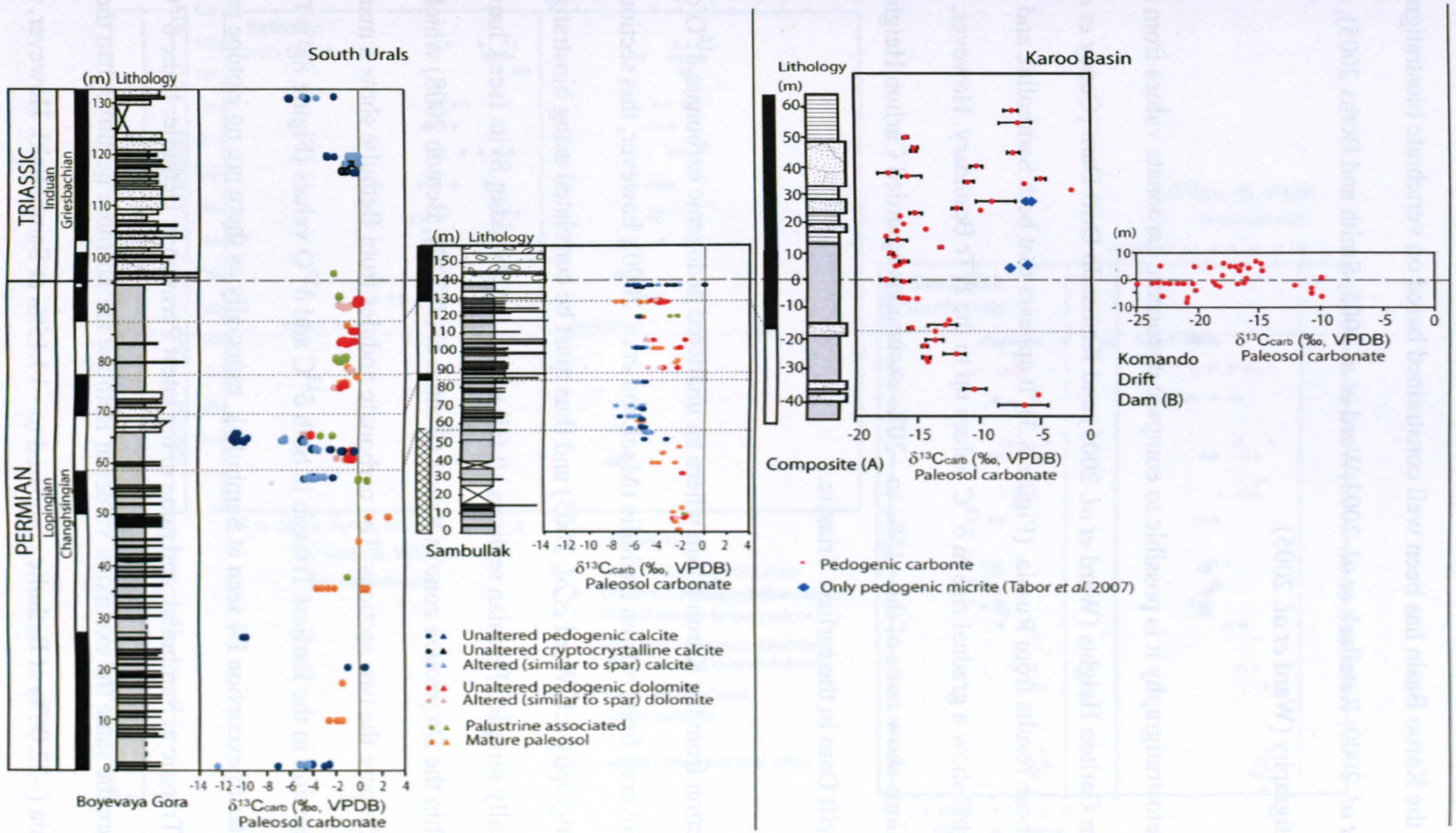

Figure 8.3 Pedogenic carbonate nodules from Russia (this study) and the Karoo basin (South Africa) correlated using magnetostratigraphic data (correlation based on Steiner 2006). A is the composite carbonate record of Ward *et al.* (2005) and their magnetostratigraphic data. Super imposed on this are micritic nodule values from Tabor *et al.* (2007) (blue diamonds) from Carlton heights. B are data from Komando Drift Dam recorded by Coney *et al.* (2007) correlated using magnetostratigraphic data from Ward *et al.* (2005).

When comparing the different isotope patterns observed in the Karoo region with Russia it is essential to understand how far in to the Permian the Karoo sections extend. The P/Tr boundary in the Karoo Basin has been well constrained based on vertebrate biostratigraphy (MacLeod *et al.* 2000; Retallack *et al.* 2003;Ward *et al* 2005; Smith and Botha 2005), and magnetostratigraphy (Ward *et al.* 2005).

Using magnetostratigraphy it is possible to compare pedogenic carbonate values from the sections from Carlton Heights (Ward *et al.* 2005) and Komando Drift Dam (Coney *et al.* 2007) with those results from Russia. (Figure 8.3). It appears that both Sambullak and Carlton heights show a gradual rise in $\delta^{13}C$ values up to the P/Tr Boundary. However, the Russian sections show none of the –15‰ to –20‰ excursions recorded Carlton Heights and Komando Drift Dam in the earliest Triassic.

The only section from the Karoo Basin where an unaltered pedogenic carbonate $\delta^{18}O$ curve has been recovered from is from Bethulie (MacLeod *et al.* 2000), however, this section lacks magnetostratigraphy (cf. Ward *et al.* 2005) and thus must be correlated using biostratigraphy. The isotopically sampled Permian sections all fall within the Vyatkian Svita (see Chapter 3) which is within the *Dicynodon* zone in Karoo (Benton *et al.* 2004; Benton 2008) which can be used to compare the two sections The carbonate nodules from Bethulie show a marked negative excursion in the Earliest Triassic in both $\delta^{13}C$ and $\delta^{18}O$ values (Figure 8.4). This may be similar to excursion P4 seen at Sambullak, especially as there are no isotope results in the Earliest Triassic at Sambullak and none in the latest Permian at Bethulie. If the $\delta^{18}O$ excursions are the same the excursion values at Bethulie are far more negative than those seen in Russia (–22.06‰ at Bethulie compared to –14.15‰ at Sambullak). However, the excursion at Sambullak (–6.76‰) is greater than that recorded at Bethulie (–4.98‰).

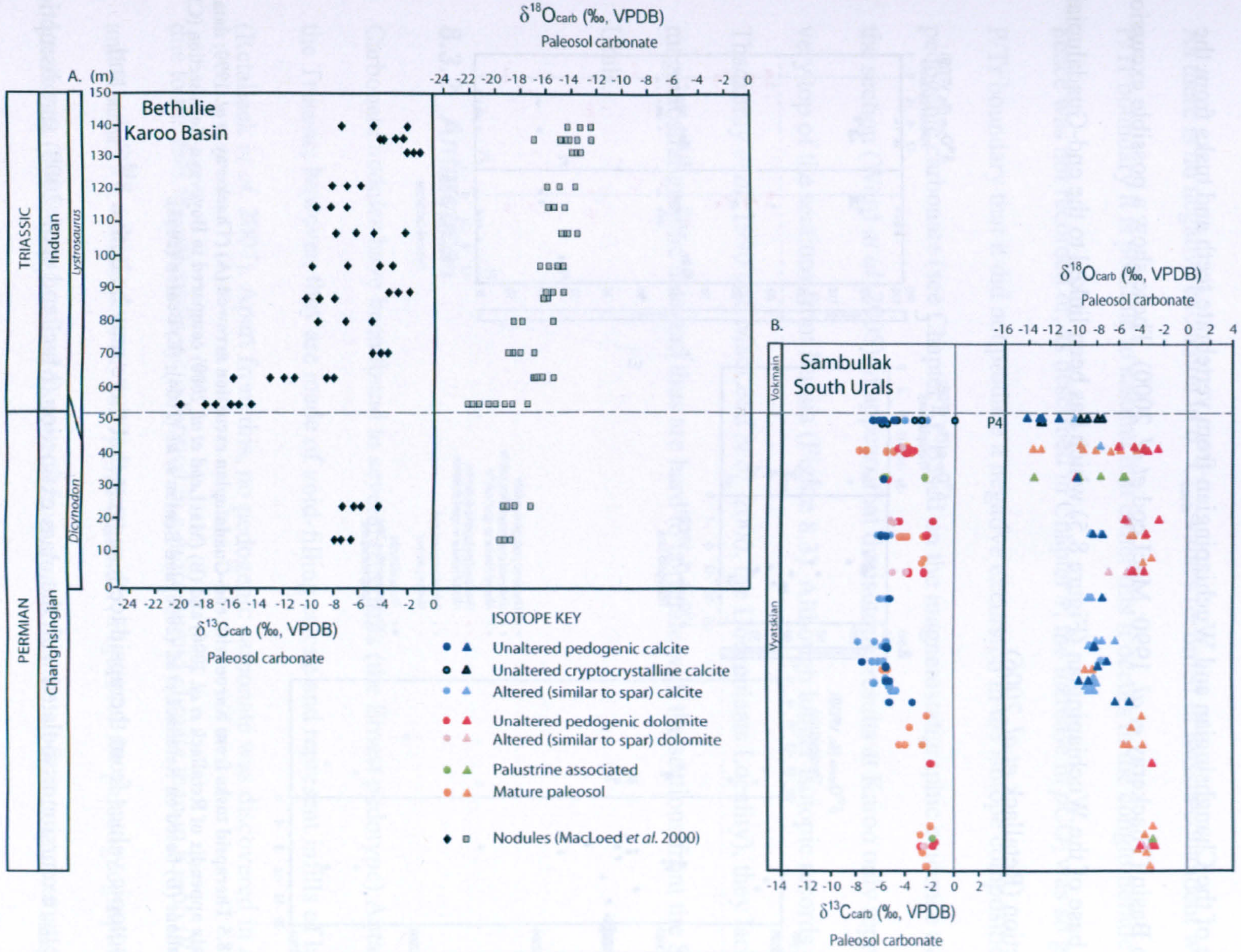

Figure 8.4 Pedogenic nodules from Bethulie section from the Karoo Basin (MacLeod *et al.* 2000) and Sambullak from the Southern Urals.

None of the sections which have had pedogenic carbonate analysis results extend far down into the Permian and thus are unlikely to contain the mid-Changhsingian excursion (P3) observed at Boyevaya Gora and Sambullak. There are, however, isotopic records spanning the whole of the Changhsingian and Wuchiapingian from vertebrate teeth and tusks from the Karoo Basin (Thackeray *et al.* 1990; MacLeod *et al.* 2000). These show a possible excursion at the base of the Wuchiapingian (Figure 8.5) which has been linked to the end-Guadalupian extinction (Retallack *et al.* 2006). .

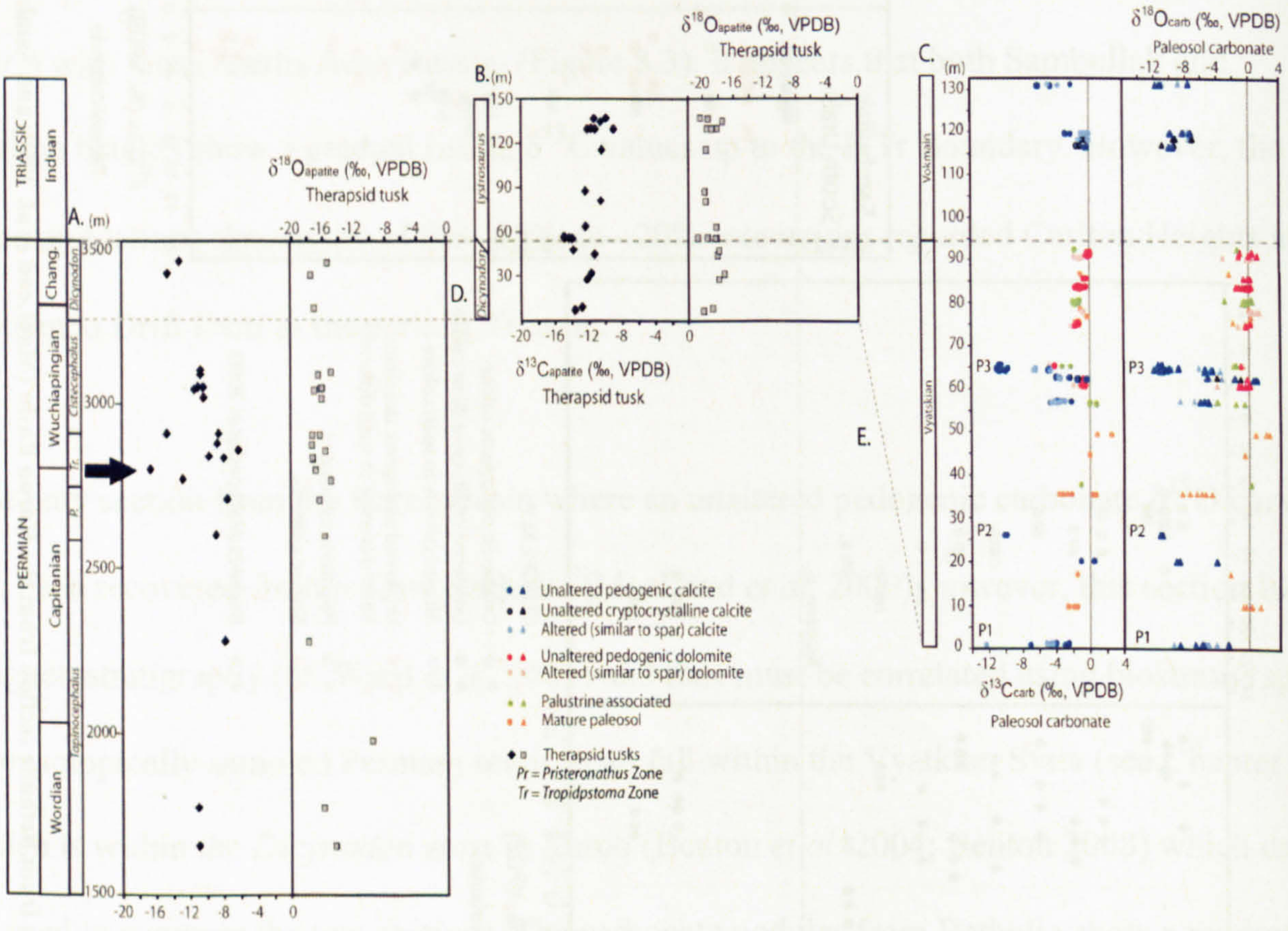

Figure 8.5 Therapsid tusks from Karoo with end-Guadalupian excursion arrowed (A) (Thackeray *et al.* 1990; data from data appendix of Retallack *et al.* 2006) and (B) (MacLeod *et al.* 2000) compared to Boyevaya Gora section (C). Correlations (D) based on Retallack *et al.* (2006) and Benton *et al.* (2004); (E) Benton (2008).

The isotopic values from therapsid teeth suggest that there may be both a $\delta^{13}C_{apatite}$ and $\delta^{18}O_{apatite}$ excursion associated with the mass extinction (MacLeod *et al.* 2000) and disruption in the $\delta^{13}C$ values throughout the *Dicynodon* zone (Thackeray *et al.* 1990). However, there is no evidence of any excursions in the Changhsingian to correspond with those seen in Russia, although there are only 10 analyses for this interval (Figure 8.5). Equally it is evident that the

negative $\delta^{13}C$ and $\delta^{18}O$ anomaly associated with the end-Guadalupian (Retallack *et al.* 2006) event is below the base of the Russian sections.

As there is no negative excursion in $\delta^{13}C_{carb}$ values recorded in Russia coincident with the P/Tr boundary it is possible to assume that either this it occurs in the conglomeratic units and hence was not recorded or, as described in Chapter 7, the increase in pCO_2 was so great at the P/Tr boundary that it did not produce a negative excursion in the isotope composition of the pedogenic carbonate (see Chapter 4). Based on the magnetostatigraphic evidence available for the section (Ward *et al.* 2005), it appears that the isotopic results at Karoo only represent the very top of the sections from Russia (Figure 8.3). Although longer isotopic records exist (e.g. Thackeray *et al.* 1990 and MacLeod *et al.* 2000, the Doornplaats Locality), they lack magnetostratigraphic data and thus are hard to correlate with the sections from the Southern Urals.

8.3.2 Antarctica

Carbonate nodules have been found in several paleosols (the Ernest pedotype) Antarctica in the Triassic; however, they are made of void-filling calcite and represent infills of large vugs (Retallack *et al.* 2007). Apart from this, no pedogenic carbonate was discovered in Antarctica due to the fact the paleosols were formed in a more humid climate than in Karoo (Retallack and Krull 1991; Retallack *et al.* 2007) (see Chapter1, Figure1.1 for palaeogeographical locations). The isotopic values recovered from Antarctica are all from organic matter contained in the paleosol (Krull and Retallack 2000; Retallack *et al.* 2005; Retallack and Krull 2006; Retallack *et al.* 2006 Retallack *et al.* 2007, see Chapter1, Figure1.1) and thus cannot be directly compared to those from Russia. The organic carbon recovered from Sambullak (Chapter 7) has an average of $\delta^{13}C_{org}$ –23.03‰ (±1.32, 1σ std), which is similar to the organic

carbon values observed in the Permian in Antarctica (Krull and Retallack 2000; Retallack *et al.* 2005; Retallack and Krull 2006; Retallack *et al.* 2006 Retallack *et al.* 2007).

The $\delta^{13}C_{org}$ record from Antarctica is marked by a dramatic isotope anomaly just before the P/Tr boundary (as defined by Collinson *et al.* 2006) of values as negative as –46.2‰ in the Graphite Peak section (Krull and Retallack 2001). This marks the start of a period of negative excursions in the earliest Triassic which last for about 10ky (Krull and Retallack 2000; Retallack *et al.* 2006; Retallack and Jahren 2008). There is also evidence of a Permian $\delta^{13}C_{org}$ isotope anomaly of up to –16‰ in several of the sections in Antarctica which has been related to an atmospheric disturbance related to the end-Guadalupian mass extinction event (Krull and Retallack 2000; Retallack and Krull 2006; Retallack *et al.* 2006, Figure 8.6).

These variations in $\delta^{13}C_{org}$ values from the paleosols are greater than anything that could be caused by either waterlogging or plant variation (cf. Arens *et al.* 2000). It is assumed that they must be documenting atmospheric $\delta^{13}C$ values or the reaction of methanotrophic bacteria (Krull and Retallack 2000). As discussed earlier, it is thought that the isotopic composition of C_3 organic matter from soils is directly related to the isotopic composition of the atmosphere rather than the influence of physiological or local factors (Arens *et al.* 2000). Therefore, as the $\delta^{13}C_{org}$ values in Antarctica are reacting to changes in atmospheric carbon, as are the $\delta^{13}C_{carb}$ values of pedogenic carbonates from Russia, it should be possible to compare the excursions between the two sections.

As previously stated there are no magnetostratigraphic data available for Antarctica (Collinson *et al.* 2006) so precise comparison of the Antarctic results with those from Russia is difficult.

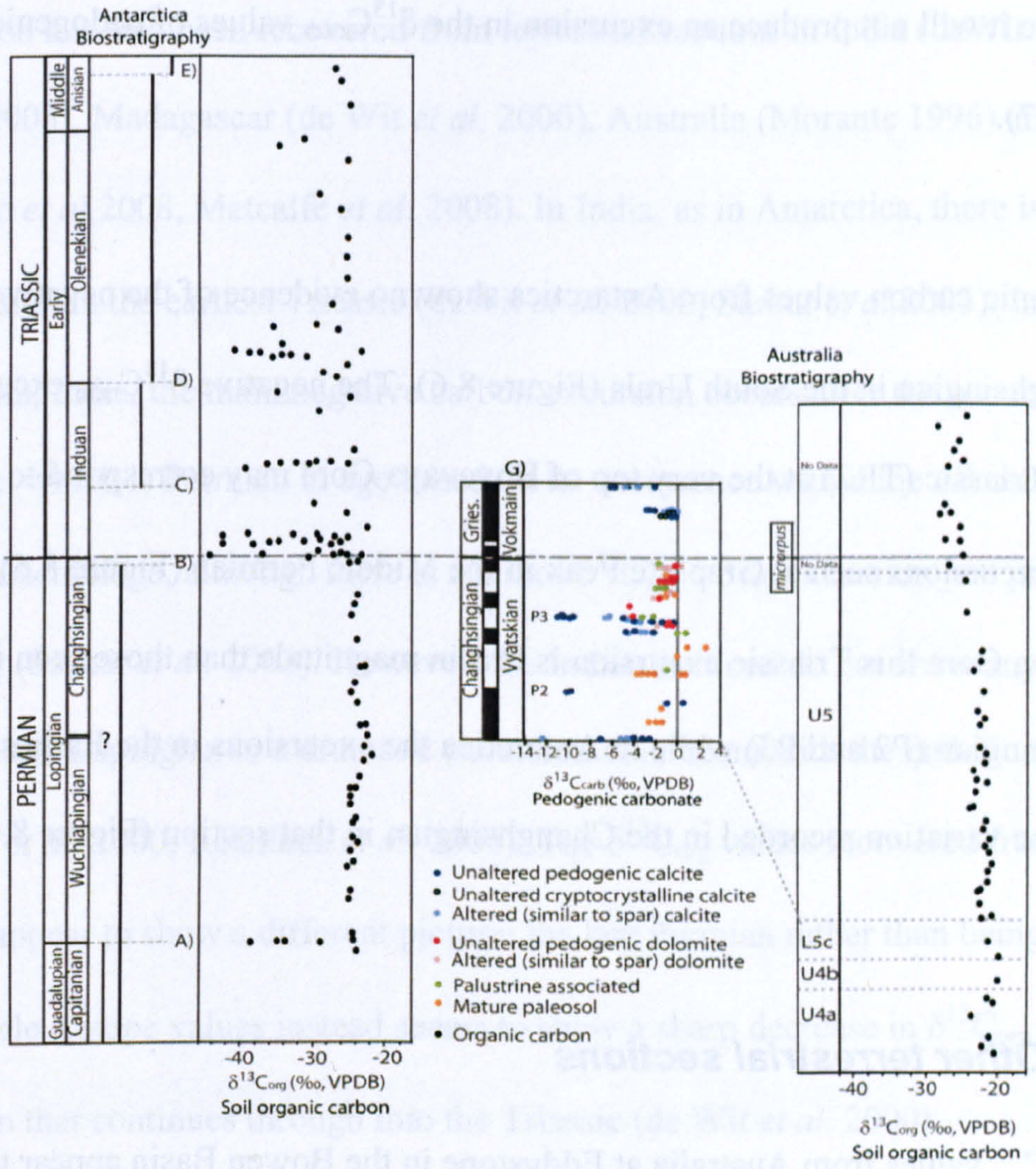

Figure 8.6 Organic carbon values from Graphite peak in Antarctica (Krull and Retallack 2001, left panel) and Eddystone Australia (Morante 1996) compared to Boyevaya Gora in Russia. Antarctica Biostratigraphy: A) Last occurrence of *Gangamopteris cyclopteroides* and *Palaeovittaria kurtz*i (Retallack and Jahren 2008), B) Last occurrence of *Glossopteris* and *Vertebraria* (Krull and Retallack 2000) C) Last occurrence of *Lystrosaurus* (Krull and Retallack 2000) D) First occurrence of *Dicroidium zuberi* (Krull and Retallack 2000). E) First occurrence of *Dicroidium odontopteroides* (Krull and Retallack 2000). The Russian stratigraphy is based on Surkov *et al.* 2007 (G). The correlation between the palynological zone U5 in Australia and the Vyatkian is based on Morante (1996) who correlates U5 to the *Dicynodon* zone in South Africa which is linked to Vyatkian Gorizont (Benton 2007).

The multiple negative $\delta^{13}C_{org}$ excursions observed in the earliest Triassic in Antarctica are not recorded in the Triassic at Boyevaya Gora (Figure 8.6). However, the Triassic paleosols from Boyevaya Gora have more positive $\delta^{13}C_{carb}$ values, possibly reflecting a rise in atmospheric pCO_2 (see Chapter 7). This may reflect the time averaging of the different materials, as organic matter is likely to record the ^{12}C release into the atmosphere (Retallack and Jahren 2008) while the paleosols if the ^{12}C release coincides with a dramatic rise in pCO_2 which is big enough to change the dominant control on the isotopic composition of pedogenic

carbonate it will not produce an excursion in the $\delta^{13}C_{carb}$ values of pedogenic carbonate (see Chapter 7).

The organic carbon values from Antarctica show no evidence of the negative excursions seen in Changhsingian in the South Urals (Figure 8.6). The negative $\delta^{13}C_{carb}$ excursion seen in the earliest Triassic (TR2) at the very top of Boyevaya Gora may correspond to the negative $\delta^{13}C_{org}$ excursions seen at Graphite Peak in the Middle Permian (Figure 8.6). However, at Boyevaya Gora this Triassic excursion is less in magnitude than those seen in the Changhsingian (P2 and P3) while in Antarctica the excursions in the Earliest Triassic dwarf any of the variation recorded in the Changhsingian in that section (Figure 8.6).

8.3.3 Other terrestrial sections

The $\delta^{13}C_{org}$ values from Australia at Eddystone in the Bowen Basin appear to show minor isotope anomalies before the P/Tr boundary and in to the Early Triassic (Morante 1996) (Figure 8.6). The P/Tr boundary is defined as being very near or at the base of the *Protohaploxypinus microcorpus* zone (Morante 1996). The lower excursions have been correlated with the first P/Tr excursion at Graphite Peak in Antarctica (Retallack *et al.* 2006). It has been observed that Upper Stage 5 which contains *Glossopteris* up to 25cm below the hiatus in the section (Morante 1996) and thus can be correlated with the *Dicynodon* zone in Karoo (Retallack *et al.* 2006) and thus the Vyatkian of Russia. Like Antarctica, there are no corresponding anomalies to those recorded in Russia in the Changhsingian. Unfortunately no comprehensive magnetostratigraphic data exist for Australia (cf. Steiner 2006) so it is impossible to test this correlation.

Organic carbon has also been recovered from terrestrial sections in India (deWit *et al.* 2000; Sarkar *et al.*2003), Madagascar (de Wit *et al.* 2000), Australia (Morante 1996) and Xinjiang in China (Cao *et al.*2008, Metcalfe *et al.* 2008). In India, as in Antarctica, there is a marked $\delta^{13}C_{org}$ excursion in the earliest Triassic (deWit *et al.* 2000; Sarkar *et al.*2003). In the Raniganj Basin, India, the main negative carbon excursion occurs after the occurrence of the conglomerate, which is Permian in age based on its occurrence within the *Glossopteris–Vertebraria* assemblage, although there is a minor $\delta^{13}C_{org}$ –3‰ excursion just prior to this conglomerate (Sarkar *et al.* 2003). However, the Indian sections do not show any dramatic excursions in the Lopingian or a dramatic excursion coincident with the end-Guadalupian event (deWit *et al.* 2000; Retallack *et al.* 2006). The $\delta^{13}C_{org}$ values recovered from Madagascar appear to show a different picture: the late Permian rather than being a period of relatively stable isotope values instead seems to show a sharp decrease in $\delta^{13}C_{org}$ values in the latest Permian that continues through into the Triassic (de Wit *et al.* 2000).

$\delta^{13}C_{org}$ values recovered from sections in the Tian Shan in Xinjiang Province, China appear to show two episodes of ^{13}C depletion (Cao *et al.* 2008). The lower of these is below the extinction horizon and is interpreted as an onset of environmental stress before the end-Permian mass extinction began (Cao *et al.* 2008). Global correlations using palynology, vertebrates, and conchostracans, place the sections from Tian Shan within the last reversal of the Permian and the P/Tr boundary normal (Metcalfe *et al.* 2008). This would mean that this lower ^{13}C depletion seen in Tian Shan does not correlate to the excursion (P3) seen in Russia. Furthermore, Metcalfe *et al.* (2008) argue that in their results they do not see two episodes of ^{13}C depletion, but rather multiple $\delta^{13}C_{org}$ negative excursions which they ascribe to multiple atmospheric perturbations.

8.4 Marine $\delta^{13}C$ comparisons

Comparing marine and terrestrial sections is notoriously difficult (cf. Retallack and Jahren 2008). Although some marine sections have terrestrial palynomorphs (e.g. Twitchett *et al.* 2001; Foster and Afonin 2005) which can be used to compare terrestrial sections, these data do not exist for the GSSP record at Meishan (Metcalfe *et al.* 2008). Correlating between terrestrial sequences and the GSSP record at Meishan is most accurately accomplished using magnetostratigraphy (Steiner 2006; Metcalfe *et al.* 2008).

The major boundary anomalies seen at Meishan occur within the normal polarity containing the P/Tr boundary (Yin *et al.* 2001; Metcalfe *et al.* 2008). Longer $\delta^{13}C_{carb}$ sections have been published by Jin *et al.* 2000 and correlating these with the magnetostratigraphy published in Yin *et al.* (2001), using the correlations of Steiner (2006), it is possible to compare these values with the Russian sections (Figure 8.7).

There is a suggestion that there is a very minor negative carbon anomaly concurrent with excursion (P3) at Meishan (Figure 8.7, arrowed). However, this correlation is debatable as there is evidence that some of the reversals, including the very brief reversal concurrent with the P/Tr (Figure 8.7), are actually remagnetised overprints (cf. Kozur and Bachmann 2005; Steiner 2006; Metcalfe *et al.* 2008). What is evident from the Meishan record is that there are negative, albeit noisy, $\delta^{13}C_{carb}$ excursions in the base of the section. These are Changhsingian in age as the base of the Changhsingian is defined as the first occurrence of *Clarkina wangi* in Bed 4 at Meishan D section (Jin *et al.* 2006) and these may be comparable with the excursions seen at the base of Boyevaya Gora (such as P2).

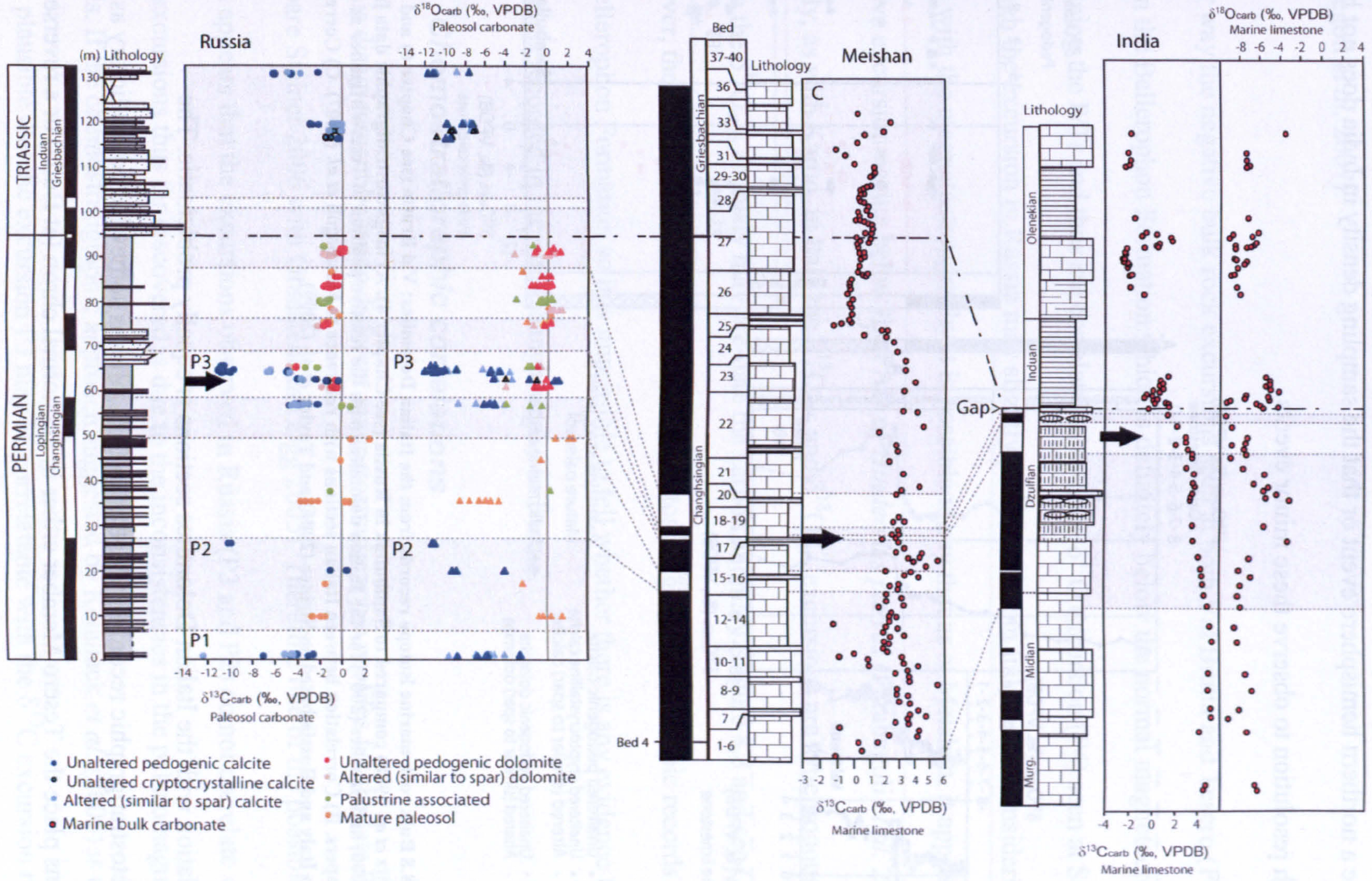

Figure 8.7 Russian section at Boyevaya Gora correlated with marine sections at Meishan (Jin *et al.* 2000, Yin *et al.* 2001) and India (Baud *et al.* 1996). Correlated using Steiner (2006). The arrow marks the level of excursion P3 at Boyevaya Gora. Bed 4 at Meishan is the base of the Changhsingian (Jin *et al.* 2006).

These lower excursions at Meishan are, however, not recorded globally. In northern India marine carbonate sections show none of this noise (see Baud *et al.* 1996), suggesting that it may be a northern hemisphere event or that the sampling density in India does not have enough resolution to observe these minor events.

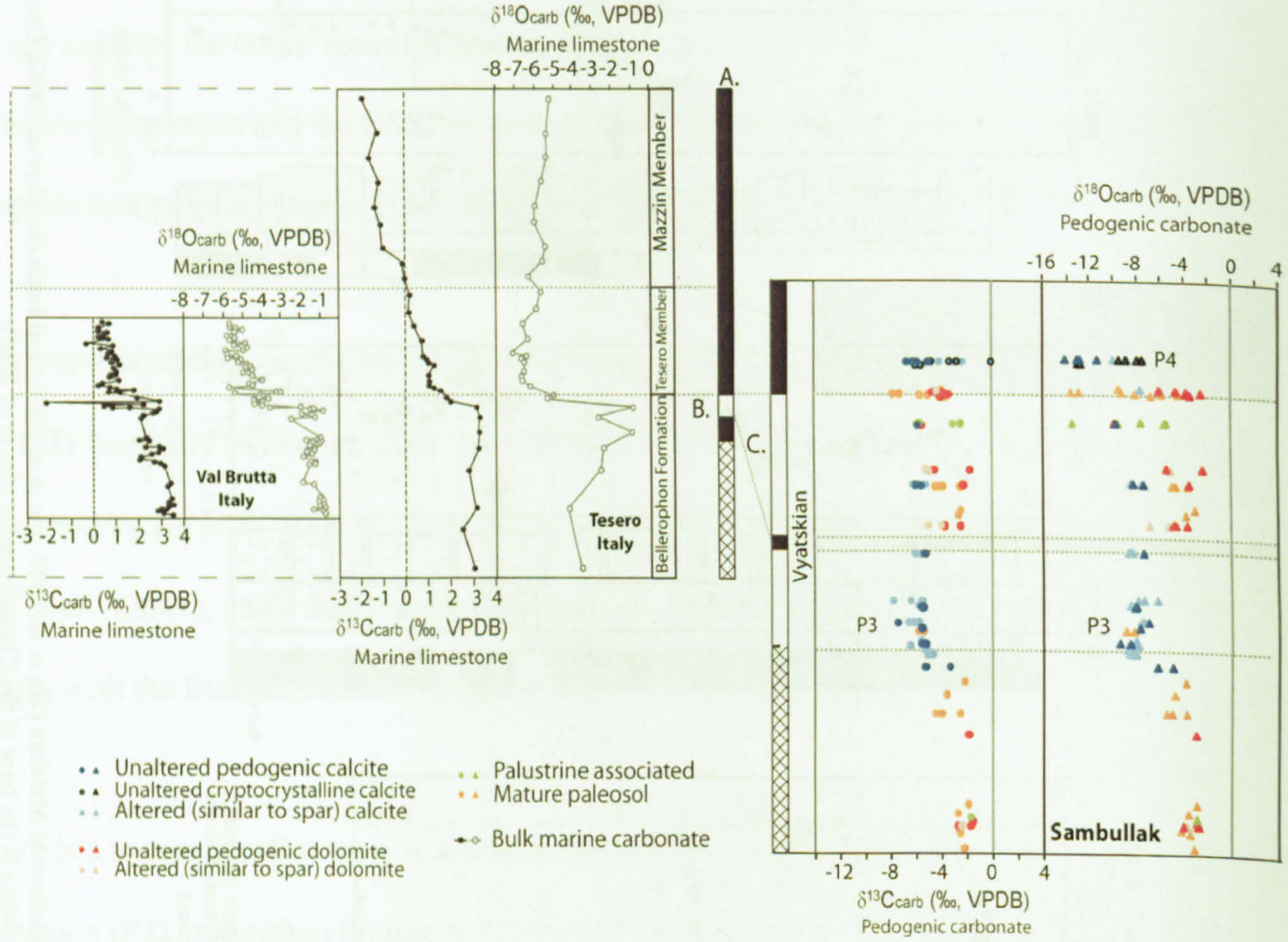

Figure 8.8 Bulk rock marine isotope records from the Italian Dolomites; Val Brutta (see Chapter 6) and Tesero (Magaritz *et al.* 1988) compared to Sambullak in Russia (see Chapter 4). A) magnetostratigraphic data from Scholger *et al.* (2000) and Szurlies (2007) for the Italian dolomites with the relative position of Tesero Member as described in those papers. B) Correlation between Italian sections with reference to Farabegoli *et al.* (2007). C) Correlation between Italy and Russia based on Steiner (2006) and Taylor *et al.* (2009).

Correlation with the Italian Dolomites sections is equally problematic. The magnetostratigraphic record for the Italian Dolomites is somewhat contradictory as different sections place the Tesero Member either in the normal chron (at Bulla) or a reversed chron (at Siusi) polarity (Scholger *et al.* 2000). Steiner (2006) suggests that some of the strata at Siusi are missing as the distinctive reversed polarity of the Late Changhsingian is not present and concludes that the Tesero Member is within the boundary normal event. Another explanation

for this is that the Tesero Member is a transgressive unit and thus is a different age in different parts of the basin at it transgressed from west to east (Broglio Loriga and Cassinis 1992; Farabegoli *et al.* 2007).

Either way the negative bulk rock excursions seen at both Val Brutta and Tesero (Figure 8.8) start in the Bellerophon Formation which is definitely below the normal magnetocron containing the P/Tr and thus are correlatable with the $\delta^{18}O$ excursion (P4) seen at Sambullak although the excursion in Russia may slightly post date that in Italy. Even considering these issues with the magnetostratigraphy it is possible to say that as at Meishan, it appears that the negative excursion occurs below the FAD of *Hindeodus parvus* (Farabegoli *et al.* 2007). Equally, as with Karoo, in Italy the $\delta^{13}C_{carb}$ and $\delta^{18}O_{carb}$ excursions are synchronous while in Russia the $\delta^{18}O_{carb}$ anomaly may pre-date the carbon anomaly (Figure 8.8 and see Chapter 5). However, the sections in Italy do not have magnetostratigraphic or isotopic records far in to the Bellerophon Formation so it is impossible to tell whether there is any evidence for the excursions recorded in the mid-Changhsingian in Russia.

8.4.1 Chemostratigraphic correlations

There is disagreement between different magnetostratigraphic profiles for the late Permian (compare Steiner 2006 with Gradstein and Ogg 2005). Therefore one of the possible reasons why it appears that the excursions observed in Russia (P3 and P2) do not correlate with any other excursions thus far discovered is due to the inconsistencies in the palaeomagnetic records. If the chemostratigraphic approach suggested by Retallack *et al.* (2006) is used it seems plausible that the excursion P3 may be correlatable with the $\delta^{13}C$ excursion recorded in bed 25 at Meishan (Figure 8.7) as it is known that the Meishan section is highly condensed (Prof. G.J. Retallack *pers. comm.*).

8.5 $\delta^{18}O$ and temperature

Understanding the correlation between $\delta^{18}O$ values and temperature globally is complicated. Many authors still contest that the $\delta^{18}O$ values from both marine carbonates and brachiopods do not represent variation in temperature (Spötl *et al.* 1992; Heydari *et al.* 2001; Batt *et al.* 2007). Equally, the $\delta^{18}O$ values of pedogenic carbonate in Russia could be explained by changes in seasonality rather than changes in temperature (see Chapter 5). This being said there is independent sedimentological evidence to suggest that there was a temperature rise up to the P/Tr, such as the increase in the number of Vertic paleosols and the prevalence of Type A dolomite (see Chapters 3 and 4). There is also global evidence for an increase in temperature across the P/Tr boundary, such as the migration of thermophilic plants into both the high latitudes of the northern and southern hemispheres (Retallack 1999, 2002, Retallack and Krull 1999 Looy 2001; Retallack and Krull 2006).

The oft-quoted temperature rise across the P/Tr boundary is 5–6°C (e.g. Erwin 1993; Benton and Twitchett 2003; Kidder and Worsley 2004) which is based on bulk rock analysis of the Gartnerkofel-1 core from Austria (Magaritz and Holser 1991). However, as discussed in Chapter 6, many authors have reservations about this estimate (e.g. Twitchett 2007). Negative excursions in $\delta^{18}O$ bulk rock values have been observed in China, Iran, Italy, Austria and India (Magaritz *et al.* 1988; Magaritz and Holser 1991; Baud *et al.* 1996; Dolenec *et al* 1999; Heydari *et al.* 2001).

The temperature rise predicted from the brachiopods at Val Brutta and Tesero suggest a rise of ~8°C just before the P/Tr boundary (Chapter 6). There is a marked $\delta^{18}O$ anomaly excursion in pedogenic carbonate just prior to the P/Tr boundary in Russia at Sambullak (P4, Chapter 4) which, assuming that the $\delta^{18}O$ values are not being controlled by changes in seasonality and

thus the influence of the amount effect, corresponds to a rise in MAT of ~7°C (see Chapter 5). Bearing in mind the potential issues with the Italian magnetostratigraphy (cf. Steiner 2006), it is possible to correlate the Italian brachiopod values with the boundary excursion at Sambullak (Figure 8.9). Both records seem to show an increase in temperature of 7-8°C just before the boundary. Comparing the Russian records also suggests a step-wise warming, culminating at the P/Tr boundary and then decreasing slightly into the Triassic (Figure 8.9). This being said, the $\delta^{18}O$ record in even unaltered pedogenic carbonate is a product of many factors, strongest among them being the isotopic composition of rainwater (see Chapter 5). Therefore, as with $\delta^{13}C$ values, global records need to be compiled to compare different basins and latitudes.

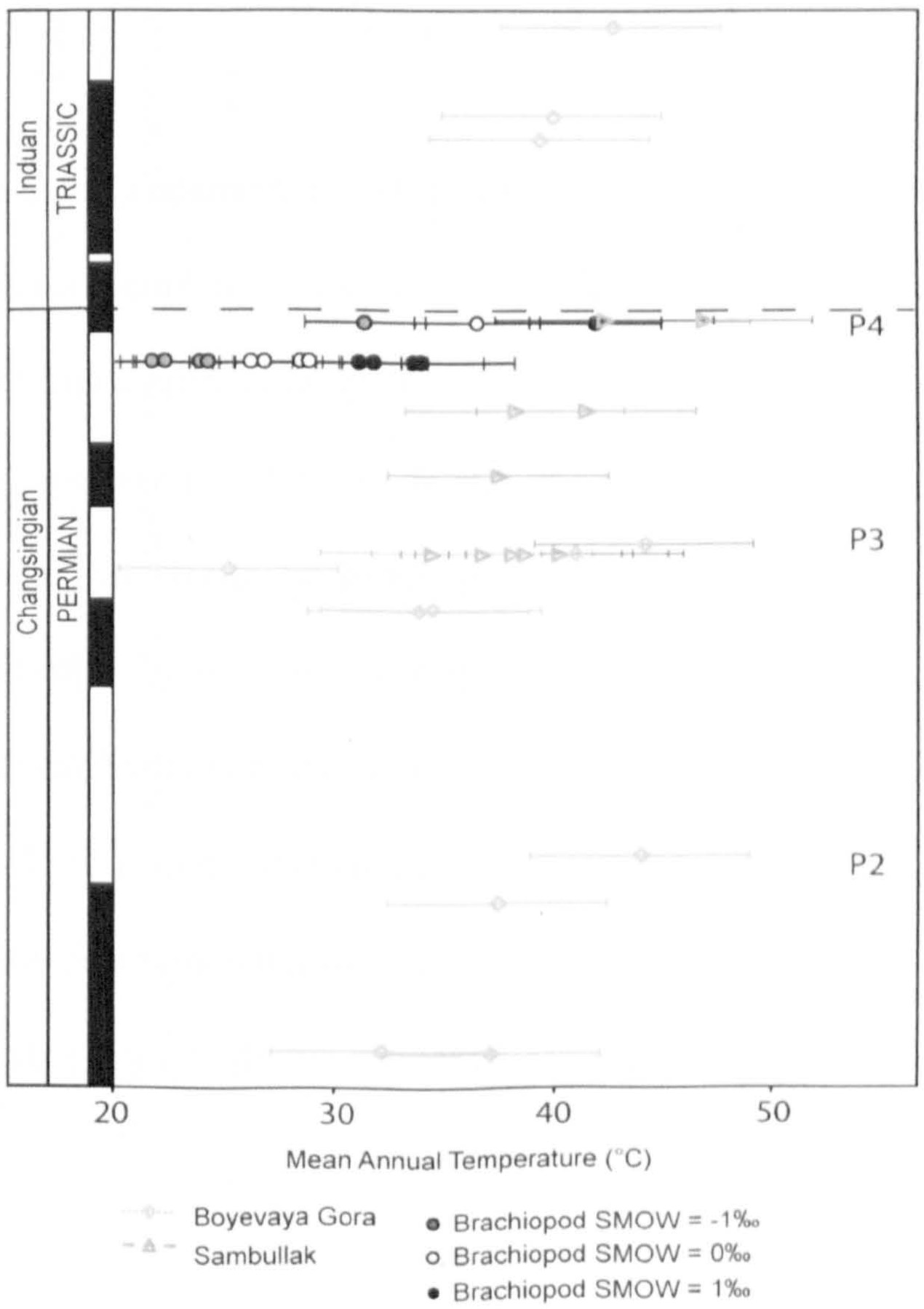

Figure 8.9 Temperature estimates from the Italian Brachiopods (Chapter 6) with the estimates for Boyevaya Gora and Sambullak using equation 5.10 (Chapter 5). Correlated using the magnetostratigraphic data from Scholger *et al.* (2000) and Szurlies (2007) and Steiner (2006) and Taylor *et al.* (2009).

8.6 Paleosol climate record

The P/Tr boundary has been linked to dramatic changes in terrestrial landscapes and paleosols in Antarctica (Retallack *et al.* 1998; Retallack and Krull 1999; Retallack *et al.* 2005; Retallack *et al.* 2007), Australia (Retallack 1999; Michaelsen 2002); and the Karoo Basin in South Africa (Ward *et al* 2000; Retallack *et al.* 2003). This study (see Chapter 3 and 5) and others conducted in the Southern Urals (Newell *et al.* 1999; Tverdokhlebov *et al.* 2005) have observed a similar dramatic shift in change in environment and paleosol type. Table 8.1 summarises the different changes in climate and paleosols across the P/Tr boundary in these four latitudinally different localities.

While it is evident that all of these localities show a dramatic change across the boundary, the type of change is not always the same. For instance, both Antarctica and Karoo show an increase in precipitation across the P/Tr boundary while Russia and Australia show a decrease. However, in Russia, the fact that all the earliest Triassic paleosols are capped by erosive sands which could have eroded and foreshortened the depth to Bk horizon creating an underestimate of MAP (Table 8.1). Therefore, this may suggest that the drop in precipitation observed is an underestimate. Also Russian paleosols from the Olenekian show a rise in MAP relative to the Permian and increase in seasonality (see Chapter 5). The paleosols from Antarctica, Karoo and Russia all show a change in soil colour across the boundary, although not in Australia (Table 8.1). This is probably due simply to locally distinct changes in environment and thus soil type across the boundary.

		Australia (65-85°S)	Antarctica (65-77°S)	Karoo (South Africa) (50-60°S)	Russia (30-35°N)
Triassic					
	Soil colour	5Y to 5GY	5Y to 10R	2.5YR	5GY
	MAP (mm)	800 to 1200	853(±175) -1159(±175)	732 (±141)	185(±48) - 180(±6)
	Nodule horizons	n/a	n/a	Deep well focused	Shallow poorly developed
	Climate regime	Cold temperate	Cold temperate (but warmer)	Semi-arid	Arid
	Inferred environment	Broad leaf and conifer forest	Conifer forest	Open woodland	Braided river flood plain
Thickness of boundary conglomerate/breccia (m)		0.3-1	0.7	5 to 10	5 to 20
Permian					
	Soil colour	5Y	5Y to 5bg	10R	10R
	MAP (mm)	1000 to 1300 (overlapping into earliest Triassic)	596(±175) -926(±175)	346 (±141)	392(±158) - 242(±72)
	Nodule horizons	n/a	n/a	Diffuse and shallow	Diffuse and shallow
	Climate regime	Cold temperate and marginally frigid	Cold temperate	Arid	Semi-arid /sub-humid
	Inferred environment	Swamp land	Broad leaf deciduous swap	Open shrub land/riparian woodland	Open shrub land/steppe

Table 8.1 Paleosol and palaeoclimate changes across the P/Tr boundary in terrestrial environments. Data for Australia is from Retallack (1999) and Michaelsen (2002); Karoo is from Ward *et al.* (2000), Retallack *et al* (2003); Antarctica is from Retallack and Krull (1999), Retallack *et al.* (2007). The data for Russia comes from this study (Chapter 3 and 5) and Newell *et al* 1990; Taylor *et al.* (2009).

Pedogenic carbonate nodules are only found in Russia and Karoo, and while they both show diffuse and shallow nodule horizons in the Permian suggesting monsoonal climates (cf. Retallack 2005b), in the Triassic nodule horizons in the Karoo basin become deep and well focused while in Russia they stay shallow but are poorly developed. Part of this change may be explained by the dramatic conglomerate fans seen in Russia (Newell *et al.* 1999; Benton *et al.* 2004) which mean that paleosols did not have time to form.

The inferred environments and climate regimes all show a shift to more active, less stable environments across the P/Tr boundary (Table 8.1). All the paleosols show a general warming of climate across the boundary (Retallack 1999; Retallack and Krull 1999; Retallack *et al.* 2003; Chapter 3 and 5). However, in Antarctica and Karoo the climate becomes wetter in the earliest Triassic. It is worth noting that both Karoo and Russia are thought to have an arid climate which suggest that arid zones extend to at least 50-60°S and 30-35°N at the present day these latitudes are dominated by temperate climate (cf. Peel *et al.* 2007). This probably reflects the extensive nature of dry continental interior related to the Pangaea landmass (Roscher and Schneider 2006; Deroin 2008).

The paleosols from Russia mirror the climatic and environmental changes inferred globally across the P/Tr boundary. The only area where Russia appears to show a difference from the trends in the southern hemisphere is that it does not show the increase in precipitation in the Triassic. However, the fact that no pedogenic dolomite is found in the Triassic soils suggests a higher moisture content in the soil and therefore a greater amount of water present in the fluvial system (Chapter 4 and 5). Also it appears that only in Russia is there evidence of changes in climate prior to the P/Tr boundary linked with isotope anomalies).

8.7 Siberian Trap correlation

Given the close proximity of the South Urals sections to the Siberian Traps, especially with the discovery that the Traps extend in to the Western Siberian basin under younger sediment cover (Figure 8.10; Reichnow *et al.* 2005; Saunders and Reichnow 2009), it would be expected that there should be some direct environmental impacts of the eruptions on the Russian sections. The Siberian Traps have often been linked to the mass extinction (Erwin 1993; Kamo *et al.* 2003; Grard *et al.* 2005; Beerling *et al.* 2007; Payne and Kump 2007), however, it has also been argued that the link to the mass extinction is purely on temporal relation (Heydari *et al.* 2008).

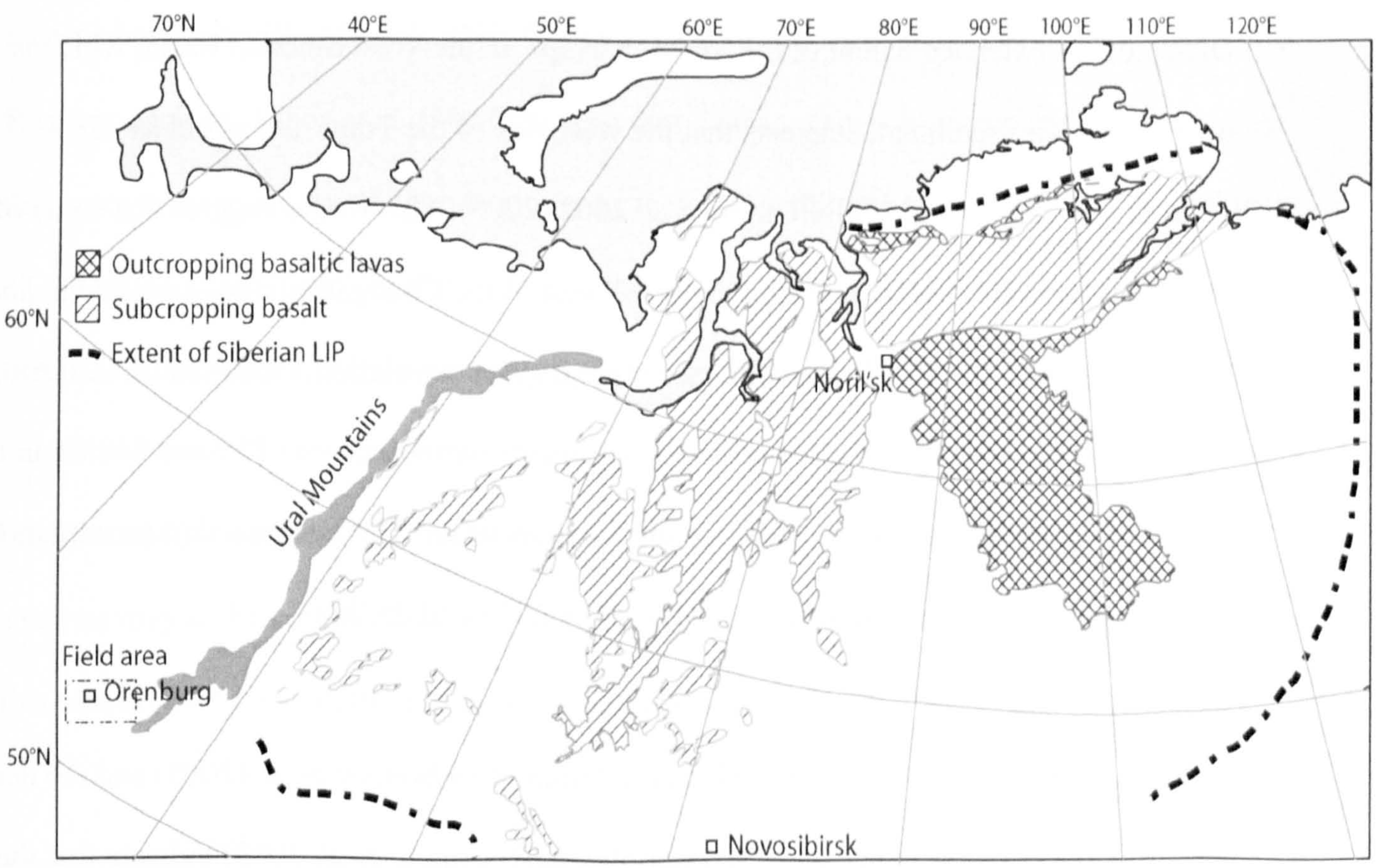

Figure 8.10 The extent of the Siberian large igneous province (LIP) in both surface outcrop and subcrop (adapted from Saunders and Reichnow 2009) and the field area of this study (see figure 3.2 localities of individual sections).

The precise timing of the Siberian Traps with reference to the P/Tr boundary is still an area of debate (cf. Reichnow *et al.* 2002 Kamo *et al.* 2003; Mundil *et al.* 2004 Steiner 2006;

Dobretsov *et al.* 2008). Steiner (2006) in her correlation uses the summary of $^{40}Ar/^{39}Ar$ results (from Kamo *et al.* 1996) and the patterns of reversals in the different palaeomagnetic sections from across the Siberian Traps to suggest that the volcanics were a long-lived event spanning much of the Lopingian and Induan. However, U-Pb dating from the Noril'sk section suggests the middle of this section to be 251.2±0.3 Ma in age and that the base of the section is no older that 251.7±0.3 Ma (Kamo *et al.* 2003). Kamo *et al.* (2003) argue that the main phase of the traps is coincident with the P/Tr boundary. However, more recent closed-system U/Pb dating of the P/Tr boundary by Mundil *et al.* (2005) has suggested an older date of 252.6 ±0.2Ma for the extinction but they still claim this is synchronous with the Siberian flood volcanism, and it occurred within the quoted uncertainty.

Dating of the extended extent of the Siberian Traps in the West Siberian Basin, which is overlain by later sediment, suggests that the west side of the Traps are as old as 253.4 ±0.3Ma and 252.4 ±1.5Ma (Reichnow *et al.*2002; 2005). This would suggest that some of the traps were active in the Changhsingian as the base of the Changhsingian is assigned to about 254Ma (Jin *et al.* 2006). In their magnetostratigraphic correlation, Dobretsov *et al.* (2008) suggest that the majority of the trap-based volcanism started between 251 and 248Ma in the Siberian Platform, West Siberian Basin and Kuzbass areas. They suggest that precursors to the main phase began in these areas from between 255 and 252Ma.

Based on both the magnetostratigraphic correlation of Dobretsov *et al.* (2008) and the dates proposed for the traps in the West Siberian Basin (Reichnow *et al.* 2002) indicate that there was active volcanism in the Siberian region in the Changhsingian. This may suggest that the negative excursion (P3) seen in both the $\delta^{13}C$ and $\delta^{18}O$ pedogenic carbonate records at Boyevaya Gora and Sambullak, and the time dominated by Type A dolomite in the South

Urals basin (Chapter 4 and 5) prior to the P/Tr boundary, are time equivalent to this initial stage of trap activity described by Reichnow *et al.* (2002; 2005) and that the main facies break at the P/Tr boundary is related to the onset of the main trap volcanism. This being said, the lack of agreement between different magnetostratigraphic correlations may cast doubt on this precise correlation.

8.8 Discussion

The Russian results indicate that the climatic changes in the terrestrial northern hemisphere were in some ways quite different from those seen in the southern hemisphere. Comparing the nodular carbonate isotopic values it is evident that the negative 10–15‰ $\delta^{13}C_{carb}$ anomaly recorded at Karoo (Ward *et al.* 2005; Coney *et al.* 2007). However, this is not recorded in the Russian sections. Tabor *et al.* (2007) suggest that $\delta^{13}C_{carb}$ values in Karoo are only recording the isotopic composition of organic matter as they fall within the range of calcite formed from CO_2 derived purely from organic matter. If this was an anoxic closed system, as they suggest, then it is isolated from the atmosphere and is not recording the variation the atmospheric $\delta^{13}C$ values. However, it has been shown that some plant matter (such as leaf tissue and cellulose based tissues) is affected by changes in atmospheric $\delta^{13}C$ (Arens *et al.* 2000) and thus the sections may still have the carbonate nodules at Karoo with some atmospheric variation, but this would purely be variation in the organic carbon content in the soil.

The terrestrial $\delta^{13}C_{org}$ record indicate that there are evident terrestrial excursions in Antarctica (Krull and Retallack 2001), India (deWit *et al.* 2000; Sarkar *et al.*2003), Madagascar (de Wit *et al.* 2000) and Australia (Morante 1996) but none of these coincide the anomalies seen in Russia (i.e. P3). There are also other northern hemisphere terrestrial sections such as Xinjiang

in China where there are multiple $\delta^{13}C_{org}$ anomalies in the normal polarity zone that contains the P/Tr boundary (Metcalfe *et al.* 2008) although not as pronounced as anything seen in the southern hemisphere. This may suggest that unlike the southern hemisphere, terrestrial sections in the north do no show a single marked $\delta^{13}C$ excursion just before the P/Tr Boundary. In the marine sections the $\delta^{13}C_{carb}$ bulk rock anomaly appears to occur within the normal polarity zone that contains P/Tr boundary, with the exception of Italy. However, as already stated, there may be stratigraphic issues with the magnetostratigraphic results from that the Italian Dolomites (cf. Steiner 2006).

The lack of any negative $\delta^{13}C_{carb}$ excursion in the normal polarity zone that contains the P/Tr boundary in any of the Russian sections is unexpected. As previously stated the simplest explanation for this is that the worldwide $\delta^{13}C$ excursion occurs in the period of conglomeratic and sandstone sedimentation in the South Urals and thus was not recorded. Those sections where paleosols were formed in the Earliest Permian, such as Boyevaya Gora (see Figure 8.3), do not show a prominent $\delta^{13}C$ excursion and if such an excursion did occur it must have happened before this point. However, there is a significant $\delta^{18}O_{carb}$ excursion at Sambullak recorded just prior to the tabular conglomerates boundary event and may be related to a rise in temperature linked to the P/Tr boundary. Therefore, the reason for the absence of a concurrent $\delta^{13}C_{carb}$ excursion at this point at Sambullak may be due to an large increase in atmospheric pCO_2 which if greater than a certain threshold will not cause a $\delta^{13}C_{carb}$ excursion (see Chapter 7). For this second hypothesis to be correct there must be a concurrent $\delta^{13}C_{org}$ excursion at the time of the excursion P4, however, due to the lack of organic carbon in the Russian paleosols at the times of the excursions, it was impossible to obtain $\delta^{13}C_{org}$ values for this paleosol using current techniques.

8.8.1 Palaeotemperature and palaeoenvironmental change

The evidence from the different terrestrial palaeoenvironmental indicators from the paleosols (Table 8.1) shows a much more coherent picture. By integrating the data from the Russian sections it is now possible to say that globally there is a dramatic shift in environmental conditions across the P/Tr boundary. This shift manifests itself in a change from a stable environment to more open and less stable one. The palaeoprecipitation results appear less coherent. While Russia show a fall in MAP, Australia Antarctica and Karoo show a rise (Table 8.1). As Antarctica and Australia are at almost the same latitude (Table 8.1), latitudinal variation can be ruled out. This may suggest the simple picture of a global rise or fall in MAP is overly simplistic. Kidder and Worsley (2004) suggest one of the aspects of warming is abundant rainfall at high latitudes which could explain this increase of rainfall in the high southern hemisphere but not at lower latitudes. This suggests that, whatever the extinction, mechanism it had a profound effect on global circulation patterns. There is evidence, in the form of diffuse carbonate nodules, at both Karoo and Russia to suggest the presence of monsoonal conditions in the Permian (Retallack *et al.* 2003; Retallack 2005b; Chapter 5). In Russia it appears that this monsoonal/seasonality increases after the $\delta^{13}C_{carb}$ and $\delta^{18}O_{carb}$ excursion (P3). This agrees with floral changes in the Upper Permian which indicate a severe climate with often changing temperatures and/or humidity/aridity (Kozur 1998). However, for the first time it is possible to observe a direct link between the isotopic anomalies and variations in seasonal activity (see Chapter 5).

What is constant across all four global terrestrial sections is the interpretation that the earliest Triassic is warmer than the Permian (see Table 8.1) which adds weight to the argument that the excursions in $\delta^{18}O_{carb}$ seen in the Russia palaeosols are linked to a rise in temperature. This interpretation is supported by the coincidence and similarity between the temperature

rise (7-8°C) observed in the Italian brachiopods and the excursion at Sambullak (P4) (Figure 8.9). However, it must always be remembered that there are many other influencing factors that can affect both brachiopods (cf. Spötl *et al.* 1992. Batt *et al.* 2007) and pedogenic carbonate (Dworkin *et al.* 2005; Quast *et al.* 2006) and can affect the estimates of exact temperature. This being said, the correlation with other indicators of temperature rise, such as those suggested from paleosols globally (Table 8.1), present a strong case for a sharp and dramatic temperature rise just before the major facies shift seen at the P/Tr boundary.

8.9 Summary

In summary, when comparing the data from the Russian paleosols and Italian brachiopods to the global picture it can be seen that:

1. The P/Tr $\delta^{13}C$ excursion observed in many global sections does not occur in Russia. It may have occurred at the same time as the conglomerates were being deposited. Alternatively, as described in Chapter 7, the rise in pCO_2 was so great that is did not cause a $\delta^{13}C_{carb}$ excursion in the pedogenic carbonate;
2. The mid-Changhsingian excursion (P3) at Boyevaya Gora and Sambullak is associated with the start of a period of extreme climate variation, including the increase of Type A dolomite and seasonal/monsoonal activity up to the facies break;
3. The temperature data suggest a rise of ~7°C preceding the P/Tr boundary, although there may be other factors that influenced both the brachiopods and paleosol estimates;
4. The paleosols show a similar change across the facies break to that observed in the Southern Hemisphere (Australia, Antarctica, and Karoo), including a shift to a less stable environment across the P/Tr boundary, and there are evident shifts in precipitation patterns and a general global environmental warming in the earliest Triassic;

5. Some of the environmental changes seen prior to the P/Tr boundary may relate to the initial eruptions of the Siberian Traps as they are time-equivalent.

Chapter 9. Conclusions

The aim of this project was to investigate the variations in paleosol morphology, stable isotopes, temperature, precipitation and carbon dioxide variation through the Late Permian and Early Triassic in sections in the northern hemisphere. These were used to produce a comprehensive understanding of how climate and atmospheric chemistry varied through this period which can be compared to previous studies in the southern hemisphere.

The paleosols of the South Urals of Russia represent a unique window into the northern hemisphere terrestrial climate across the Permian–Triassic boundary. In the Permian the paleosols suggest the area was primarily desert scrubland. In the Triassic this dry environment continued, but the presence of possible depressed water tables and pseudo-gleys suggest an increase in the amount of waterlogging of the paleosols (Chapter 3).

Like paleosols observed in Antarctica, the Karoo and Australia (e.g. Retallack 1999; Retallack and Krull 1999; Retallack *et al.* 1999), results from Russia show a marked change in paleosols across the P/Tr boundary, from more stable, better-developed paleosols to less-developed, less stable paleosols in the earliest Triassic. This is related to a change in facies, from meandering fluvial systems to coarse conglomeratic fans (Chapter 8). These changes are seen in parallel with a drop in mean annual precipitation in the earliest Triassic at Boyevaya Gora followed by a rise in the Olenekian. The variations in mean annual precipitation are also linked to changes in the annual range of precipitation which increases after excursion P3 and up to the P/Tr boundary with an even bigger increase in the Olenekian into ranges similar to modern-day monsoonal areas (New Delhi; IAEA/WMO, 2008) suggesting an increase in seasonality in the Triassic (Chapter 5).

There is evidence that the paleosols were affected by intense evaporation, both in the presence of $\delta^{18}O_{carb}$ isotopic values greater than 0‰ as well as the presence of pedogenic dolomite. Pedogenic dolomite has been identified in the equatorial Lower Permian (Kessler *et al.* 2001) but this is the first evidence of it at palaeolatitudes as high as 30-35°N during this period. The occurrence of this pedogenic dolomite ceases at the P/Tr boundary and there is no evidence of it in the Triassic, which may suggest an increase in available water in the Triassic which would inhibit the formation of dolomite. However, the Triassic paleosols show evidence of fluctuating water tables and deep-rooting, pedogenic slickensides and pseudo-gleys which suggests the opposite. An alternative hypothesis is that pedogenic dolomite formation is linked to other factors relating to changes in soil conditions across the P/Tr boundary. If bacteria are a key component in pedogenic dolomite formation (cf. Roberts et al. 2004; Sáchez–Román 2008), then perhaps the disappearance of pedogenic dolomite reflects serious depletion of the soil microbial communities in the Early Triassic (Chapter 4, Kearsey *et al.* in review).

It has been suggested that the complex interplay between groundwater, diagenesis and surface alteration can obliterate any meteoric pedogenic signal in Palaeozoic paleosols (Quast *et al.* 2006). While there is some evidence of alteration in the sections in Russia it is possible to separate this from the pedogenic carbonate results. Also the similarity between some of the 'altered' results (especially the microcrystalline carbonates) and the pedogenic carbonates suggests that they are formed from the similar fluid and may represent meteoric values rather than a later fractionated diagenetic fluid (Chapter 4).

There is evidence at Sambullak of an $\delta^{18}O_{carb}$ negative shift (P4) across the P/Tr boundary, although this excursion is not observed at Boyevaya Gora, presumably as just below the P/Tr

boundary the carbonate component of the paleosols is exclusively dolomite at this locality. There may have been a negative $\delta^{13}C_{carb}$ excursion at the P/Tr boundary in the South Urals, as recorded in the southern hemisphere, but this has to have occurred in the period dominated by conglomerates between the P/Tr boundary and the first Triassic paleosol and thus was not recorded. Alternatively, the increase in pCO_2 at the P/Tr was so great that it changes the dominant control on $\delta^{13}C_{carb}$ of pedogenic carbonate from the organic carbon content of the soil to the isotopic composition of the atmosphere and thus did not produce a negative excursion in the pedogenic carbonate (Chapter 7).

There are four isotope excursions in the Changhsingian identified in the Russian paleosols which have not been record in the southern hemisphere. Of these, excursion P3 is the best constrained. P3 can be identified in pedogenic calcite at Boyevaya Gora and, to a lesser extent, at Sambullak and represents a negative shift of 6–4‰ in the $\delta^{13}C$ and $\delta^{18}O_{carb}$ values in the mid Changhsingian. The negative carbon and oxygen excursions (P3) are followed by a period of only Type B dolomite at Boyevaya Gora and an increase in type B dolomite at Sambullak. These changes are linked with a rise in MAP and the Mean Annual Range of Precipitation which both increase after this point up to the facies break at the P/Tr boundary. This suggests that these excursions were related to changes in the climate and atmosphere rather than localised changes in paleosol conditions.

If the $\delta^{18}O_{carb}$ isotopic values are completely controlled by temperature, it appears that the paleosols in Russia, as at Saratov today, showed a lack of summer rain with an increase in air temperature causing the weighting of the mean annual precipitation towards more negative $\delta^{18}O_p$ values for warmer years. Using equation (5.10) suggests an average Permian temperature of 38°C (± 14) and 40°C (± 8) in the Triassic. The excursions at Sambullak and

Boyevaya Gora (P3 and P4) represent a rise in MAT of 7°C, although the weakness of the MAT/$\delta^{18}O_p$ relationship on which equation (5.10) is based urges caution in this estimate. It is equally possible that the excursion in $\delta^{18}O_{carb}$ values represents the onset of increased seasonal rainfall rather than a rise in temperature, or even both a rise and an onset of increased seasonal rainfall. However, independent temperature estimates from unaltered brachiopods from the Italian Dolomites (Chapter 6) indicate that just before P/Tr boundary there was a rise of 7°C, although the absolute ambient temperature estimates are dependent on the predicted salinities. This suggests that there was indeed a rise in temperature just before the P/Tr boundary and that excursion P4 in Russia at least corresponds to a rise in temperature.

Calculation of the variation in pCO_2 shows a dramatic rise in atmospheric CO_2 in the earliest Triassic, which appears to be consistent with stomatal records of a similar age from Russia (Retallack and Jahren 2008). The Russian sections also show fluctuations in pCO_2 in the Permian. The extreme variation seen between methods may suggest the environment was not in equilibrium or that the temperature estimates produced by equation (5.10) are overestimates or the lack of control over the variation in organic carbon in the sections. The negative $\delta^{13}C_{carb}$ excursions seen at Boyevaya Gora (P2 and P3) and, to a lesser extent, at Sambullak (P3) could be explained by a rise in pCO_2, but only if there is a corresponding drop in organic carbon at the same time or an input of isotopically negative $\delta^{13}C$ to the atmosphere (Chapter7).

Finally, this is the first time that a negative excursion has been definitively identified in the mid-Changhsingian in a terrestrial locality. This suggests that a different pattern of environmental change occurred in the northern hemisphere compared with the southern

hemisphere, and that the environment and climate started to change before the P/Tr boundary which is time equivalent to the first eruptions of the Siberian Traps (Chapter 9).

References

Algeo, T.J., Ellwood, B., Nguyen, T.K.T., Rowe, H. and Maynard, J.B., 2007. The Permian-Triassic boundary at Nhi Tao, Vietnam: Evidence for recurrent influx of sulfidic watermasses to shallow-marine carbonate platform. *Palaeogeography Palaeoclimatology Palaeoecology*, **252**: 304-327.

Allman, M. and Lawrence, D.F., 1972. *Geological laboratory techniques*, Blandford press, London, 335 pp.

Alonso-Zarza, A.M., 2003. Palaeoenvironmental significance of palustrine carbonates. *Earth-Science Reviews*, **60**: 261-298.

Alonso-Zarza, A.M., Sanz, M.E., Calvo, J.P. and Estevez, P., 1998. Calcified root cells in Miocene pedogenic carbonates of the Madrid Basin: evidence for the origin of *Microcodium* b. *Sedimentary Geology*, **16**: 81-97.

Anderson, T.F. and Arthur, M.A., 1983. Stable isotopes of oxygen and carbon and their application to sedimentological and paleoenvironmental problems. In: M.A. Arthur, T.F. Anderson, I.R. Kaplan, J. Veizer and L.S. Land (Editors), *Stable Isotopes in Sedimentary Geology, SEPM Short Course Notes,*. Society of Economic Paleontologists and Mineralologists, Tulsa, Oklahoma, pp. 1-151.

Andrews, J.E., Singhvi, A.K., Kailath, A.J., Kuhn, R., Dennis, P.F., Tandon, S.K. and Dhir, R.P., 1998. Do stable isotope data from calcrete record Late Pleistocene monsoonal climate variation in the Thar Desert of India? *Quaternary Research*, **50**: 240-251.

Angielczyk, K.D. and Kurkin, A.A., 2003. Phylogenetic analysis of Russian Permian dicynodonts (Therapsida: Anomodontia): implications for Permian biostratigraphy and Pangaean biogeography. *Zoological Journal of the Linnean Society*, **139**: 157–212.

Arche, A. and López-Gómez, J., 2005. Sudden changes in fluvial style across the Permian-Triassic boundary in the eastern Iberian Ranges, Spain: Analysis of possible causes.

Palaeogeography, Palaeoclimatology, Palaeoecology, **229**: 104-126.

Arens, N.C. and Jahren, A.H., 2000. Carbon isotope excursion in atmospheric CO_2 at the Cretaceous-Tertiary boundary: Evidence from terrestrial sediments. *Palaios*, **15**: 314-322.

Auclair, A.-C., Joachimski, M.M. and Lecuyer, C., 2003. Deciphering kinetic, metabolic and environmental controls on stable isotope fractionations between seawater and the shell of *Terebratalia transversa* (Brachiopod). *Chemical Geology*, **202**: 59-78.

Banner, J.L. and Hanson, G.L., 1990. Calculation of simultaneous isotopic and trace element variations during water-rock interactions with applications to carbonate diagenesis. *Geochimca et Cosmochimica Acta*, **54**: 3123-3137.

Batt, L.S., Montañez, I.P., Isaacson, P., Pope, M.C., Butts, S.H. and Abplanalp, J., 2007. Multi-carbonate component reconstruction of mid-carboniferous (Chesterian) seawater $\delta^{13}C$. *Palaeogeography Palaeoclimatology Palaeoecology*, **256**: 298-318.

Baud, A., Atudorei, V. and Sharp, Z., 1996. Late Permian and Early Triassic evolution of the Northern Indian margin: carbon isotope and sequence. *Geodinamiça Acta (Paris)*, **9**: 57-77.

Baud, A., Magaritz, M. and Holser, W.T., 1989. Permian - Triassic of the Tethys - Carbon Isotope Studies. *Geologische Rundschau*, **78**: 649-677.

Beauchamp, B. and Baud, A., 2002. Growth and demise of Permian biogenic chert along northwest Pangea: evidence for end-Permian collapse of thermohaline circulation. *Palaeogeography Palaeoclimatology Palaeoecology*, **184**: 37-63.

Becker, L., Poreda, R.J., Basu, A.R., Pope, K.O., Harrison, T.M. and Nicholson, C., 2004. Bedout: A possible end-Permian impact crater offshore of Northwestern Australia. *Science*, **304**: 1469-1476.

Becker, L., Poreda, R.J., Hunt, A.G., Bunch, T.E. and Rampino, M., 2001. Impact event at the

Permian-Triassic boundary: Evidence from extraterrestrial noble gases in fullerenes. *Science*, **291**: 1530-1533

Beerling, D.J., Harfoot, M., Lomax, B. and Pyle, J.A., 2007. The stability of the stratospheric ozone layer during the end-Permian eruption of the Siberian Traps. *Philosophical Transactions of the Royal Society of London Series A*, **365**: 1843-1866.

Benito, M.I., de la Horra, R., Barrenechea, J.F., López-Gómez, J., Rodas, M., Alonso-Azcárate, J., Arche, A. and Luque, J., 2005. Late Permian continental sediments in the SE Iberian Ranges, eastern Spain: Petrological and mineralogical characteristics and palaeoenvironmental significance. *Palaeogeography Palaeoclimatology Palaeoecology*, **229**: 24-39.

Benton, M.J., 1995. Diversification and extinction in the history of life. *Science*, **268**: 52-58.

Benton, M.J., 2008. The end-Permian mass extinction - events on land in Russia. *Proceedings of the Geologists' Association*, **119**: 119-136.

Benton, M.J., Tverdokhlebov, V.P. and Surkov, M.V., 2004. Ecosystem remodelling among vertebrates at the Permian–Triassic boundary in Russia. *Nature*, **432**: 97-100.

Benton, M.J. and Twitchett, R.J., 2003. How to kill (almost) all life: the end-Permian extinction event. *TRENDS in Ecology and Evolution*, **18**: 358-365.

Berner, R.A., 2002. Examination of hypotheses for the Permo - Triassic boundary extinction by carbon cycle modeling. *Proceedings of the National Academy of Sciences of the United States of America*, **99**: 4172 - 4711.

Bojar, A.V., Hiden, H., A.Fenninger and Neubauer, F., 2004. Middle Miocene seasonal temperature changes in the Styrian basin, Austria, as recorded by the isotopic composition of pectinid and brachiopod shells. *Palaeogeography, Palaeoclimatology, Palaeoecology*, **203**: 95-105.

Bojar, A.V., Hiden, H., Fenninger, A. and Neubauer, F., 2004. Middle Miocene seasonal

temperature changes in the Styrian basin, Austria, as recorded by the isotopic composition of pectinid and brachiopod shells. *Palaeogeography, Palaeoclimatology, Palaeoecology*, **203** 95-105.

Broglio Loriga, C. and Cassinis, G., 1992. The Permo-Triassic Boundary in the Southern Alps (Italy) and in adjacent Periadratic regions. In: W.C. Sweet, Y. Zungi, J.M. Dickens and Y. Hongfu (Editors), *Permo-Triassic Events in the Eastern Tethys*. Cambridge University Press, Cambridge, U.K., pp. 78-97.

Boucot, A.J. and Gray, J., 2001. A critique of Phanerozoic climatic models involving changes in the CO_2 content of the atmosphere. *Earth-Science Reviews*, **56**: 1-159.

Bowring, S.A., Erwin, D.H., Jin, Y.G., Martin, M.W., Davide, K. and Wang, W., 1998. U/Pb Zircon Geochronology and Tempo of the End-Permian Mass Extinction. *Science*, **280**: 1039-1045.

Broglio Loriga, C., Fontana, D., Massari, F., Neri, C., Pasini, M. and Posenato, R., 1986. The Upper Permian Sequence and the P/T Boundary in the Sass de Putia Mountains (Dolomites), *Permian and Permian -Triassic boundary in the southern Alpine segment of western tethys*. IGCP Project 203, Brescia, pp. 73 -90.

Brand, U., Logan, A., Hiller, N. and Richardson, J., 2003. Geochemistry of modern brachiopods: applications and implications for oceanography and paleoceanography. *Chemical Geology*, **198**: 305-334.

Brasier, M.D., 1980. *Microfossils*. Allen and Unwin, London, 193 pp.

Broglio Loriga, C. and Cassinis, G., 1992. The Permo-Triassic Boundary in the Southern Alps (Italy) and in adjacent Periadratic regions. In: W.C. Sweet, Y. Zungi, J.M. Dickins and Y. Hongfu (Editors), *Permo-Triassic Events in the Eastern Tethys*. Cambridge University Press, Cambridge, U.K., pp. 78-97.

Broglio Loriga, C., Fontana, D., Massari, F., Neri, C., Pasini, M. and Posenato, R., 1986. The

Upper Permian Sequence and the P/T Boundary in the Sass de Putia Mountains (Dolomites), *Permian and Permian -Triassic boundary in the southern Alpine segments of western tethys*. IGCP Project 203, Brescia, pp. 73 -90.

Brownlow, A.H., 1996. *Geochemistry*. Prentice-Hall, Upper Saddle River, New Jersey, 580pp.

Brunet, M.-F., Volozh, Y.A., Antipov, M.P. and Lobkovsky, L.I., 1999. The geodynamic evolution of the Precaspian Basin (Kazakhstan) along a north–south section. *Tectonophysics*, **313**: 85-106.

Bryan, S.E. and Ernst, R.E., 2008. Revised definition of large igneous provinces (LIPs) *Earth Science Reviews*, **86**: 175-202.

Budd, D.A., Pack, S.M. and Fogel, M.L., 2002. The destruction of paleoclimatic isotopic signals in Pleistocene carbonate soil nodules of Western Australia. *Palaeogeography, Palaeoclimatology, Palaeoecology*, **188**: 249-273.

Bureau International des Poids et Mesures, 2008, Unit of thermodynamic temperature (Kelvin): *http://www1.bipm.org/en/si/si_brochure/chapter2/2-1/2-1-1/kelvin.html.*

Bustillo, M.A. and Alonso-Zarza, A.M., 2007. Overlapping of pedogenesis and meteoric diagenesis in distal alluvial and shallow lacustrine deposits in the Madrid Miocene Basin, Spain. *Sedimentary Geology*, **196**: 255-271.

Bustillo, M.A., Arribas, M.E. and Bustillo, M., 2002. Dolomitization and silicification in low-energy lacustrine carbonates (Paleogene, Madrid Basin, Spain). *Sedimentary Geology*, **151**: 107-126.

Calvo, J.P., Jones, B.F., Bustillo, M.A., Fort, R., Alonso-Zarza, A.M. and Kendall, C., 1995. Sedimentology and Geochemistry of Carbonates from Lacustrine sequences in the Madrid Basin, Central Spain. *Chemical Geology*, **123**: 173-191.

Cao, C., Wang, W., Liu, L., Shen, S. and Summons, R.E., 2008. Two episodes of ^{13}C-

depletion in organic carbon in the latest Permian: Evidence from the terrestrial sequences in northern Xinjiang, China. *Earth and Planetary Science Letters*, **270**: 251-257.

Capo, R.C., Whipkey, C.E., Blachère, J.R. and Chadwick, O.A., 2000. Pedogenic origin of dolomite in a basaltic weathering profile, Kohala peninsula, Hawaii. *Geology*, **28**: 271-274.

Cerling, T.E., 1984. The stable isotopic composition of modern soil carbonate and its relationship to climate. *Earth and Planetary Science Letters*, **71**: 229-240.

Cerling, T.E., 1991. Carbon Dioxide in the Atmosphere: Evidence from Cenozoic and Mesozoic Paleosols. *American Journal of Science*, **291**: 377-400.

Cerling, T.E. and Quade, J., 1993. Stable Carbon and Oxygen Isotopes in Soil Carbonates In: P.K. Swart, K.C. Lohmann, J. McKenzie and S. Savin (Editors), *Climate Change in Continental Isotope Records*. American Geophysical Union, pp. 217-239.

Chen, Z.Q., Kaihlo, K., George, A.D. and Tong, J.N., 2006. Survival brachiopod faunas of the end-Permian mass extinction from the southern Alps (Italy) and South China. *Geological Magazine*, **143**: 301-327.

Chenet, A.-L., Fluteau, F. and Courtillot, V., 2005. Modelling massive sulphate aerosol pollution, following the large 1783 Laki basaltic eruption. *Earth and Planetary Science Letters*, **326**: 721-731.

Chumakov, N.M. and Zharkov, M.A., 2003. Climate during the Permian-Triassic Biosphere Reorganizations. Article 2. Climate of the Late Permian and Early Triassic: General Inferences. *Stratigraphy and Geological Correlation*, **11**: 361-375.

Cirilli, S., Radrizzani, C.P., Ponton, M. and Radrizzani, S., 1998. Stratigraphical and palaeoenvironmental analysis of the Permian-Triassic transition in the Badia Valley (Southern Alps, Italy). *Palaeogeography, Palaeoclimatology, Palaeoecology*, **138**: 85-

113.

Cleveland, D.M., Nordt, L.C. and Atchley, S., 2008. Paleosols, trace fossils, and precipitation estimates of the uppermost Triassic strata in northern New Mexico. *Palaeogeography Palaeoclimatology Palaeoecology*, **257**: 421-444.

Cocks, L.R.M. and Torsvik, T.H., 2007. Siberia, the wandering northern terrain, and its changing geography through the Palaeozoic. *Earth-Science Reviews*, **82**: 29-74.

Collinson, J.W., Hammer, W.R., Askin, R.A. and Elliot, D.H., 2006. Permian - Triassic boundary in the central Transantarctica Mountains, Antarctica. *Geological Society of America Bulletin*, **118**: 747 - 763.

Colson, J. and Cojan, I., 1996. Groundwater dolocretes in a lake-marginal environment: An alternative model for dolocrete formation in continental settings (Danian of the Provence Basin, France). *Sedimentology*, **43**: 175-188.

Coney, L., Reimold, W.U., Hancox, P.J., Mader, D., Koeberl, C., McDonald, I., Struck, U., Vajda, V. and Kamo, S.L., 2007. Geochemical and mineralogical investigation of the Permian–Triassic boundary in the continental realm of the southern Karoo Basin, South Africa. *Palaeoworld*, **16**: 67-107.

Conover, W.J., 1971. *Practical Nonparametric Statistics,* John Wiley and Sons, New York, 462 pp.

Coplen, T.B., Kendall, C. and Hopple, J., 1983. Comparison of stable isotope reference samples. *Nature*, **302**: 236-238.

Corsetti, F.A., Baud, A., Marenco, P.J. and Richoz, S., 2005. Summary of Early Triassic carbon isotope records. *Comptes Rendus Palevol*, **4**: 473-486.

Dahams, D.E. and Holliday, V.T., 1998. Soil Taxonomy and Paleoenviromental Reconstruction: A Critical Commentary. *Quaternary International*, **51/52**.

Dansgaard, W., 1964. Stable isotopes in precipitation. *Tellus*, **4**: 436-468.

de Wit, M.J., Ghosh, J.G., de Villiers, S., Rakotosolofo, N., Alexander, J., Tripathi, A. and Looy, C., 2002. Multiple organic carbon isotope reversals across the Permo-Triassic boundary of terrestrial Gondwana sequences: Clues to extinction patterns and delayed ecosystem recovery. *Journal of Geology*, **110**: 227-246.

Del Cura, M.A.G., Calvo, J.P., Ordonez, S., Jones, B.F. and Canaveras, J.C., 2001. Petrographic and geochemical evidence for the formation of primary bacterially induced lacustrine dolomite; La Roda 'white earth' (Pliocene, central Spain). *Sedimentology*, **48**: 897-915.

Deroin, J.-P., 2008. Permian and Quaternary playas, a discussion based on climatic, tectonic and palaeogeographic settings. *Journal of Iberian Geology*, **34**: 11-28.

Deutz, P., Montanez, I.P., Monger, H.C. and Morrison, J., 2001. Derivation of a palaeoenvironmental record from pedogenic carbonates in buried and relict Quaternary soils, Rio Grande Rift, New Mexico. *Palaeogeography, Palaeoclimatology, Palaeoecology*, **171**: 85-87.

Dickson, J.A.D., 1966. Carbonate identification and genesis as revealed by staining. *Journal of Sedimentary Petrology*, **36**: 491-505.

Dobretsov, N.L., Kirdyashkin, A.A., Kirdyashkin, A.G., Vernikovsky, V.A. and Gladkov, I.N., 2008. Modelling of thermochemical plumes and implications for the origin of the Siberian traps *Lithos*, **100**: 66-92.

Dolenec, T., Lojen, S., Buser, S. and Dolence, M.J., 1999. Stable isotope event markers near the Permo-Triassic Boundary in the Karavanke Mountains (Slovenia). *Geologia Croatica*, **52**: 77-81.

Dolenec, T., Lojen, S. and Ramovs, A., 2001. The Permian-Triassic boundary in Western Slovenia (Idrijca Valley section): magnetostratigraphy, stable isotopes and elemental variations. *Chemical Geology*, **175**: 175-190.

Driese, S.G. and Mora, C.I., 2002. Paleopedology and stable-isotope geochemistry of late Triassic (Carnian-Nordian) paleosols, Durham sub-basin, North Carolina, U.S.A.: Implications for paleoclimate and paleoatmospheric pCO_2. In: R.W. Renaut and G.M. Ashley (Editors), *Sedimentation in Continental Rifts*. SEPM Special Publications No. 73, pp. 207-218.

Dunham, R.J., 1962. Classification of carbonate rocks according to depositional texture. In: W.E. Ham (Editor), *Classification of carbonate rocks*. American Association of Petroleum Geologists Memoir 1, pp. 108-121.

Dworkin, S.I., Nort, L. and Atchley, S., 2005. Determining terrestrial paleotemperatures using the oxygen isotopic composition of pedogenic carbonate. *Earth and Planetary Science Letters*, **237**: 56– 68.

Ekart, D.D., Cerling, T.E., Montanez, I.P. and Tarbor, N.J., 1999. A 400 million year carbon isotope record of pedogenic carbonate: Implications for paleoatmospheric carbon dioxide. *American Journal of Science*, **299**: 805-827.

Elkins-Tanton, L.T., Draper, D.S., C.B, A., Jewell, J., Thorpe, A. and Hess, P.C., 2007. The last lavas erupted during the main phase of the Siberian flood volcanic province: results from experimental petrology *Contributions to Mineralogy and Petrology*, **153**: 191-209.

Enogoren, M., 2004. Vertebrate extinction across the Permian-Triassic boundary in Karoo Basin, South Africa: Discussion. *GSA Bulletin*, **116**: 1294-1296.

Erwin, D.H., 1993. *The Great Paleozoic crisis: Life and death in the Permian* Columbia University Press, New York, 327 pp.

Erwin, D.H., 2006. *Extinction: How life on earth nearly ended 250 million years ago.* Princeton University Press, Princeton, 296 pp.

Farabegoli, E., Perri, M.C. and Posenato, R., 2007. Environmental and biotic changes across

the Permian-Triassic boundary in western Tethys: The Bulla parastratotype, Italy *Global and Planetary Change*, **55**: 109-135.

Farley, K.A., Ward, P.D., Garrison, G.H. and Mukhopadhyay, S., 2005. Absence of extraterrestrial ^{3}He in Permian–Triassic age sedimentary rocks. *Earth and Planetary Science Letters*, **240**.

Faure, G., 1986. *Principles of Isotope Geology*. John Wiley and Sons, New York. 608 pp.

Faure, G. and Mensing, T.M., 2005. *Isotopes: Principles and applications* Wiley Hoboken, New Jersey, 897 pp.

Faure, K., deWit, M.J. and Willis, J.P., 1995. Late Permian Global Coal Hiatus Linked to C^{13} Depleted CO_2 Flux into the Atmosphere During the Final Consolidation of Pangea. *Geology*, **23**: 507-510.

Foster, C.B. and Afonin, A., 2005. Abnormal pollen grains: an outcome of deteriorating atmospheric conditions around the Permian–Triassic boundary. *Journal of the Geological Society*, **162**: 653–659.

Foster, C.B., Logan, G.A., Summons, R.E., Gorter, J.D. and Edwards, D.S., 1997. Carbon isotopes, kerogen types and the Permian - Triassic boundary in Australia: Implications for Exploration. *APPEA Journal*, **37**: 472-488.

Fricke, H.C. and O'Neil, J.R., 1999. The correlation between $^{18}O/^{16}O$ ratios of meteoric water and surface temperature: its use in investigating terrestrial climate change over geologic time. *Earth and Planetary Science Letters*, **170**: 181-196.

Friedman, G.M., 1965. Terminology of crystallisation textures and fabrics in sedimentary rocks. *Journal of Sedimentary Petrology*: 35: 643-655.

Friedman, I. and O'Neil, J.R., 1977. *Compilation of stable isotope fractionation factors of geochemical interest*, 440-KK. U.S. Geological Survey Professional Paper, 12 pp.

Ghosh, P., Ghosh, P. and Bhattacharya, S.K., 2001. CO_2 levels in the Late Palaeozoic and

Mesozoic atmosphere from soil carbonate and organic matter, Satpura basin, Central India. *Palaeogeography Palaeoclimatology Palaeoecology*, **170**: 219-236.

Gibbs, M.T., Rees, P.M., Kutzbach, J.E., Ziegler, A.M., Behling, P.J. and Rowley, D.B., 2002. Simulations of Permian climate and comparisons with climate-sensitive sediments. *Journal of Geology*, **110** 33-55.

Gierlowski-Kordesch, E.H., 1998. Carbonate deposition in an ephemeral siliciclastic alluvial system: Jurassic Shuttel Meadow Formation, Newark Supergroup, Hartford Basin, USA. *Palaeogeography, Palaeoclimatology, Palaeoecology*, **140**: 161-184.

Gomez-Gras, D. and Alonso-Zarza, A.M., 2003. Reworked calcretes: their significance in the reconstruction of alluvial sequences (Permian and Triassic, Minorca, Balearic Islands, Spain). *Sedimentary Geology,* **158**: 299-319

Gorjan, P., Kaihlo, K. and Chen, Z.Q., 2008. A carbon-isotopic study of an end-Permian mass-extinction horizon, Bulla, northern Italy: a negative $\delta^{13}C$ shift prior to the marine extinction. *Terra Nova*, **20**: 253-258.

Gradstein, F., Ogg, J. and Smith, A., 2004. *A Geologic Time Scale 2004*. Cambridge University Press, Cambridge, 589 pp.

Grard, A., L.M., F., Dessert, C., Dupre, B. and Godderis, Y., 2005. Basaltic volcanism and mass extinction at the Permo-Triassic boundary: Environmental impact and modeling of the global carbon cycle. *Earth and Planetary Science Letters*, **234**: 207-221.

Grasby, S.E. and Beauchamp, B., 2008. Intrabasin variability of the carbon-isotope record across the Permian–Triassic transition, Sverdrup Basin, Arctic Canada. *Chemical Geology*, **253**: 141-140.

Grice, K., Cao, C., Love, D.G., Böttcher, M.E., Twitchett, R.J., Grosjean, E., Summons, R.E., Turgeon, S.C., Dunning, W. and Jin, Y., 2005. Photic zone euinia during the Permian-Triassic superanoxic event. *Science*, **307**: 706-709.

Grossman, E.L., Mii, H.S., Zhang, C. and Yancey, T.E., 1996. Chemical Variation in Pennsylvanian Brachiopods shells - Diagenetic, Taxonomic, Microstructural, and seasonal effects. *Journal of Sedimentary Research*, **66**: 1011-1022.

Grossman, E.L., Yancey, T.E., Jones, T.E., Bruckschen, P., Chuvashov, B., Mazzullo, S.J. and Mii, H.S., 2008. Glaciation, aridification, and carbon sequestration in the Permo-Carboniferous: The isotope record from low latitudes *Palaeogeography Palaeoclimatology Palaeoecology*, **268**: 222-233.

Hallam, A. and Wignall, P.B., 1997. *Mass Extinctions and Their Aftermath*. Oxford University Press, Oxford, 320 pp.

Hansen, H.J., 2006. Stable isotopes of carbon from basaltic rocks and their possible relation to atmospheric isotope excursions. *Lithos*, **92**: 105-119.

Haas, J., Demény, A., Hips, K. and Vennemann, T.W., 2006. Carbon isotope excursions and microfacies changes in marine Permian-Triassic boundary sections in Hungary. *Palaeogeography Palaeoclimatology Palaeoecology*, **237**: 160-181.

Hay, W.W., Migdisov, A., Balukhovsky, A.N., Wold, C.N., Flogel, S. and Soding, E., 2006. Evaporites and the salinity of the ocean during the Phanerozoic: Implications for climate, ocean circulation and life. *Palaeogeography Palaeoclimatology Palaeoecology*, **240**: 3-46.

Heydari, E., Arzani, N. and Hassanzadeh, J., 2008. Mantle plume: The invisible serial killer - Application to the Permian-Triassic boundary mass extinction. *Palaeogeography Palaeoclimatology Palaeoecology*, **264**: 147-162.

Heydari, E., Wade, W.J. and Hassanzadeh, J., 2001. Diagenetic origin of carbon and oxygen isotope compositions of Permian-Triassic boundary strata. *Sedimentary Geology*, **143**: 191-197.

Hoffmann, G. and Heimann, M., 1997. Water isotope modeling in the Asian monsoon region.

Quaternary International, **37**: 115-128.

Holser, W.T., Schonlaub, H.P. and Klein, P., 1991. The Permian-Triassic boundary in the Gartnerkofel Region of the Carnic Alps (Austria). Introduction. In: W.T. Holser and H.P. Schonlaub (Editors), *The Permian-Triassic boundary in the Carnic Alps of Austria (Gartnerkofel Region)*. Abhandlungen der Geologischen Bundesansalt, pp. 5-16.

Horacek, M., Brandner, B. and Abart, R., 2007. Carbon isotope record of the P/T boundary and the Lower Triassic in the Southern Alps: Evidence for rapid changes in storage of organic carbon. *Palaeogeography, Palaeoclimatology, Palaeoecology*, **252:** 347-354.

Hounslow, M.W., Peters, C. and Mørk, A., 2008. Biomagnetostratigraphy of the Vikinghøgda Formation, Svalbard (Arctic Norway), and the geomagnetic polarity timescale for the Lower Triassic. *GSA Bulletin*, **120**: 1305-1325.

Huang, C.-M., Wang, C.-S. and Tang, Y., 2005. Stable carbon and oxygen isotopes of pedogenic carbonate in Ustic Vertisols: Implications for Paleoenvironmental Change. *Pedosphere*, **15**: 539-544.

Huey, R.B. and Ward, P.D., 2005. Hypoxia, Global Warming, and Terrestrial Late Permian Extinctions. *Science*, **308**: 398-401.

IAEA/WMO, 2008, Water Isotope System for Data Analysis, Visulation and Electronic Retrieval: *http://nds121.iaea.org/wiser.*

Isozaki, Y., 1997. Permo- Triassic Boundary Superanoxia and stratified superocean: Records from Lost Deep Sea. *Science*, **276**: 235-238.

Jenny, H.J., 1941. *Factors of soil formation* McGraw-Hill, New York, 281 pp.

Jin, Y., Wang, Y., Henderson, C., B.R., W., Shen, S. and Cao, C., 2006. The Global Boundary Stratotype Section and Point (GSSP) for the base of the Changhsingian Stage (Upper Permian). *Episodes*, **29**: 175-182.

Jin, Y.G., Wang, Y., Wang, W., Shang, Q.H., Cao, C.Q. and Erwin, D.H., 2000. Pattern of marine mass extinction near the Permian-Triassic boundary in South China. *Science*, **289**: 432-436.

Joachimiski, M.M., von Bitter, P.H. and Buggisch, W., 2006. Constraints on Pennsylvanian glacioeustatic sea-level changes using oxygen isotopes of conodont apatite. *Geology*, **34**: 277-280.

Johnson, K.R. and Ingram, B.L., 2004. Spatial and temporal variability in the stable isotope systematics of modern precipitation in China: implications for paleoclimate reconstructions. *Earth and Planetary Science Letters*, **220**: 365-377.

Joint Committee on Powder Diffraction Standards, 1971. *Inorganic Index to the Powder Diffraction File* Joint Committee on Powder Diffraction Standards, Pennsylvania, 1322 pp.

Kamo, S.L., Czamanske, G.K., Amelin, Y., Fedorenko, V.A., Davis, D.W. and Trofimov, V.R., 2003. Rapid eruption of the Siberian flood-volcanic rocks and evidence for coincidence with Permian-Triassic boundary and mass extinct at 251 Ma. *Earth and Planetary Science Letters*, **214**: 71-91.

Kamo, S.L., Czamanske, G.K. and Krogh, T.E., 1996. A minimum U-Pb age Siberian flood-basalt volcanism. *Geochimca et Cosmochimica Acta*, **60**: 3505-3511.

Kearsey, T., Twitchett, R.J., Price, G.D., Grimes, S.T., Isotope excursions and paleotemperature estimates from the Permian/Triassic Boundary in the Italian Dolomites. *Palaeogeography Palaeoclimatology Palaeoecology*, in review.

Kearsey, T., Twitchett, R.J., Newell, A.J., The origin and significance of pedogenic dolomite from the Upper Permian of the South Urals of Russia. *Geology,* in submission.

Kershaw, S., Li, Y., Crasquin-Soleau, S., Feng, Q., Mu, X., Collin, P.-Y., Reynolds, A. and Guo, L., 2007. Earliest Triassic microbialites in the South China block and other

areas: controls on their growth and distribution. *Facies*, **53**: 409-425.

Kessler, J.L.P., Soreghan, G.S. and Wacker, H.J., 2001. Equatorial aridity in western Pangea: Lower Permian loessite and dolomitic paleosols in northeastern New Mexico, USA. *Journal of Sedimentary Research*, **71**: 817-832.

Khadkikar, A.S., Chamyal, L.S. and Ramesh, R., 2000. The character and genesis of calcrete in Late Quaternary alluvial deposits, Gujartat, western India, and its bearing on the interpretation of ancient climates. *Palaeogeography, Palaeoclimatology, Palaeoecology*, **162**: 239-261.

Kidder, D.L. and Worsley, T.R., 2004. Causes and consequences of extreme Permo-Triassic warming to globally equable climate and relation to the Permo-Triassic extinction and recovery. *Palaeogeography, Palaeoclimatology, Palaeoecology*, **203**: 207-237.

Kiehl, J.T. and Shields, C.A., 2005. Climate simulation of the latest Permian: Implications for mass extinction. *Geology*, **33**: 757-760.

Koeberl, C., Farley, K.A., Peucker-Ehrenbrink, B. and Sephton, M.A., 2004. Geochemistry of the end-Permian extinction event in Austria and Italy: No evidence for an extraterrestrial component. *Geology*, **32**: 1053-1056.

Korte, C., Jasper, T., Kozur, H.W. and Veizer, J., 2005a. $\delta^{18}O$ and $\delta^{13}C$ of Permian brachiopods: A record of seawater evolution and continental glaciation. *Palaeogeography, Palaeoclimatology, Palaeoecology*, **224**: 333-351.

Korte, C., Kozur, H.W. and Veizer, J., 2005b. $\delta^{13}C$ and $\delta^{18}O$ values of Triassic brachiopods and carbonate rocks as proxies for coeval seawater and palaeotemperature. *Palaeogeography, Palaeoclimatology, Palaeoecology*, **226**: 287-306.

Korzur, H.W., 1998. Some aspects of the Permian-Triassic boundary (PTB) and of the possible causes for the biotic crisis around the boundary. *Palaeogeography, Palaeoclimatology, Palaeoecology*, **143**: 227-272.

Kovda, I., Mora, C.I. and Wilding, L.P., 2006. Stable isotope compositions of pedogenic carbonates and soil organic matter in a temperate climate Vertisol with gilgai, southern Russia. *Geoderma*, **136**: 423-435.

Kovda, I.V. and Wilding, L.P., 2005. Vertisols: Problems of Classification, Evolution and Spatial Self-Organization. *Eurasian Soil Science*, **37**: 1507-1518.

Kozur, H.W. and Bachmann, G.H., 2005. Correlation of the Germanic Triassic with the international scale. *Albertiana*, **32**: 21-35.

Kraimer, R.A., Monger, H.C. and Steiner, R.L., 2005. Mineralogical distinctions of carbonates in desert soils. *Soil Science Society of America Journal.* **69**:1773-1781

Krasilnikov, P.V. and Calderón, N., 2006. Valintin Tverdokhlebov. *Quaternary International*, **156:** 176-188.

Kraus, M.J., 1999. Paleosols in clastic sedimentary rocks: their geological applications. *Earth-Science Reviews*, **47**: 41-70.

Krull, E.S., Lehremann, D.J., Druke, D., Kessel, B., Yu, Y.-Y. and Li, R., 2004. Stable carbon isotope stratigraphy across the Permian-Triassic boundary in shallow marine carbonate platforms, Nanpanjiang Basin, south China. *Palaeogeography Palaeoclimatology Palaeoecology*, **204**: 297-315.

Krull, E.S. and Retallack, G.J., 2000. $\delta^{13}C$ depth profiles from paleosols across the Permian-Triassic boundary: Evidence for methane release. *GSA Bulletin*, **112**: 1459-1452.

Krystyn, L., Richoz, S., Baud, A. and Twitchett, R.J., 2003. A unique Permian-Triassic boundary section from the Neotethyan Hawasina Basin, Central Oman Mountains. *Palaeogeography, Palaeoclimatology, Palaeoecology*, **191**: 329-344.

Lavoie, D., 1993. Early Devonian marine isotopic signatures: Brachiopods from the Upper Gaspe Limestones, Gaspe Peninsula, Quebec, Canada. *Journal of Sedimentary Petrology* **63**: 620-627.

Lee, X. and Wan, G., 2000. No vital effect on $\delta^{18}O$ and $\delta^{13}C$ values of fossil brachiopod shells, Middle Devonian of China. *Geochimca et Cosmochimica Acta*, **15**: 2649-2664.

Leeder, M., 1999 *Sedimentology and Sedimentary Basins: From Turbulence to Tectonics*. Blackwells Science Ltd., Oxford, 592 pp.

Liu, B., Phillips, F.M. and Campbell, A.R., 1996. Stable carbon and oxygen isotopes of pedogenic carbonates, Ajo Mountains, southern Arizona: implications for paleoenvironmental change. *Palaeogeography, Palaeoclimatology, Palaeoecology*, **124**: 233-246.

Longinelli, A., Anglesio, E., Flora, O., Iacumin, P. and Selmo, E., 2006. Isotopic compost ion of precipitation in Northern Italy: Reverse effect of anomalous climatic events. *Journal of Hydrology*, **329**: 471-476.

Looy, C.V., Twitchett, R.J., Dilcher, D.L., Van Konjneburg-Van Cittert, J.H.A. and Visscher, H., 2001. Life in the end-Permian dead zone. *Proceedings of the National Academy of Sciences of the United States of America*, **98**: 7879-7883.

Loriga, C.B. and Cassinis, G., 1992. The Permo-Triassic boundary in the Southern Alps (Italy) and in adjacent Periadriatic regions. In: W.C. Sweet, Y. Zunyi, J.M. Dickins and Y. Hongfu (Editors), *Permo-Triassic events in the Eastern Tethys*. Cambridge University Press, Cambridge pp. 78-97.

Machette, M.N., 1985. Calcic soils of southwestern United States. In: D.L. Weide (Editor), *Soil and Quaternary Geology of the Southwestern United States*. Special Paper, Geological Society of America, pp. 1-21.

Mack, G.H., Cole, D.R., Giordano, T.H., Schaal, W.C. and Barcelos, J.H., 1991. Paleoclimatic controls on stable oxygen and carbon isotopes in caliche of the Abo Formation (Permian), South-Central New Mexico, U.S.A. *Journal of Sedimentary Petrology*, **61**: 458 - 472.

Mack, G.H. and James, W.C., 1994. Paleoclimate and the Global Distribution of Paleosols. *Journal of Geology*, **102**: 360-366.

Mack, G.H., James, W.C. and Monger, H.C., 1993. Classification of Paleosols. *Geological Society of America Bulletin*, **105**: 129-136.

MacLeod, K.G., Smith, R.M.H., Koch, P.L. and Ward, P.D., 2000. Timing of mammal-like reptile extinctions across the Permian-Triassic boundary in South Africa. *Geology*, **28**: 227-230.

Magaritz, M., Bar, R., Baud, A. and Holser, W.T., 1988. The Carbon-Isotope Shift at the Permian Triassic Boundary in the Southern alps is gradual. *Nature*, **331**: 337-339.

Magaritz, M. and Holser, W.T., 1991. The Permian-Triassic of the Gartnerkofel -1 Core (Carnic Alps, Austria): Carbon and Oxygen Isotope Variation. In: W.T. Holser and H.P. Schonlaub (Editors), *The Permian-Triassic boundary in the Carnic Alps of Austria (Gartnerkofel Region)*. Abhandlungen der Geologischen Bundesansalt, pp. 5-16.

Magaritz, M., Krishnamurthy, R.V. and Holser, W.T., 1992. Parallel trends in organic and inorganic carbon isotopes across the Permian/Triassic Boundary. *American Journal of Science*, **292**: 727-739.

Marshall, J.D., 1992. Climatic and oceanographic isotope signals from carbonate rock and their preservation *Geological Magazine*, **292**: 143-160.

McLoughlin, S., S., L. and Drinnan, A.N., 1997. Gondwanan floristic and sedimentological trends during the Permian-Triassic transition: new evidence from the Amery group northern Prince Charles Mountains, East Antarctica. *Antarctic Science*, **9**: 281-298.

Melezhik, V.A., Fallick, A.E., Smith, R.A. and Rosse, D.M., 2007. Spherical and columnar, septarian, 18O-depleted, calcite concretions from Middle–Upper Permian lacustrine siltstones in northern Mozambique: evidence for very early diagenesis and multiple

fluids. *Sedimentology*, **54**: 1389-1416.

Melezhik, V.A., Roberts, D., Fallick, A.E., Gorokhov, I.M. and Kusnetzov, A.B., 2005. Geochemical preservation potential of high-grade calcite marble versus dolomite marble: implication for isotope chemostratigraphy. *Chemical Geology*, **216**: 203-224.

Metcalfe, I., Foster, C.B., Afonin, S.A., Nicoll, R.S., Mundil, R.W., Wang, X. and Lucas, S.G., 2008. Stratigraphy, biostratigraphy and C-isotopes of the Permian-Triassic non-marine sequence at Dalongkou and Lucaogou, Xinjiang Province, China. *Journal of Asian Earth Sciences*. **doi:10.1016/j.jseaes.2008.06.005.**

Michaelsen, P., 2002. Mass extinction of peat-forming plants and the effect on fluvial styles across the Permian-Triassic boundary, northern Bowen Basin, Australia. *Palaeogeography Palaeoclimatology Palaeoecology*, **179**: 173-188.

Mii, H.S. and Grossman, E.L., 1994 Late Pennsylvanian seasonality reflected in the O-18 and elemental composition of a brachiopod shell *Geology*, **22**: 661-664.

Mii, H.S., Grossman, E.L. and Yancey, T.E., 1997. Stable carbon and oxygen isotope shifts in the Permian seas of West Spitsbergen - Global change or diagenetic artefact? *Geology*, **25**: 227-230.

Mikhailova, E.A. and Post, C.J., 2006. Stable carbon and oxygen isotopes of soil carbonates at depth in the Russian Chernozem under different land use. *Soil Science*, **171**: 334-340.

Mikhailova, E.A., Post, C.J., Magrini-Bair, K. and Castle, J.W., 2006. Pedogenic Carbonate Concretions in the Russian Chernozem. *Soil Science*, **171**: 981-991.

Miller, J., 1988. Microscopical techniques I. Slices, slides, stains and peels. In: M.E. Tucker (Editor), *Techniques in Sedimentology*. Blackwell Science Oxford.

Minitab Inc., 2006. Mintab Help File.

Molostovskii, E.A., 2005. Magnetostratigraphic Correlation of Upper Permian Marine and

Continental Formations. *Stratigraphy and Geological Correlation*, **13**: 49-58.

Mora, C.I., Driese, S.G. and Seager, P.G., 1991. Carbon-dioxide in the Paleozoic atmosphere - Evidence from carbon-isotope compositions of pedogenic carbonate. *Geology*, **19**: 1017-1020.

Mora, C.I., Sheldon, B.T., Elliott, W.C. and Driese, S.G., 1998. An oxygen isotope study of illite and calcite in three appalachian paleozoic vertic paleosols. *Journal of Sedimentary Research*, **68**: 456-464.

Morante, R., 1996. Permian and Early Triassic Isotopic Records of Carbon and Strontium in Australia and a Scenario of Events About The Permian-Triassic Boundary. *Historical Biology*, **11**: 289-310.

Morris, R.T. and Dickey, P.A., 1957. Modern Evaporate Deposition in Peru. *AAPG Bulletin* **41**: 2467-2474.

Müller, R.D., Goncharov, A. and Kritski, A., 2005. Geophysical evaluation of the enigmatic Bedout basement high, offshore northwestern Australia. *Earth and Planetary Science Letters*, **237**: 264-284.

Mundil, R.W., Ludwig, K.R., Metcalfe, I. and Renne, P.R., 2004. Age and timing of the Permian Mass extinctions: U/Pb dating of closed-system zircons. *Science*, **305**: 1760-1763.

Musashi, M., Isozaki, Y., Koike, T. and Kreulen, R., 2001. Stable carbon isotope signature in mid-Panthalassa shallow-water carbonates across the Permo-Triassic boundary: evidence for ^{13}C depleted superocean. *Earth and Planetary Science Letters*, **191**: 9-20.

National Climatic Data Centre, 2007, Global Measured Extremes of Temperature and Precipitation: *http://www.ncdc.noaa.gov/oa/climate/globalextremes.html.*

Neri, C., Pasini, M. and Posenato, R., 1986. The Permian/Triassic boundary and Early Scythian sequence - Tesero Section, Dolomites In: I.I. Group (Editor), *Field*

Conference on Permian-Triassic Boundary in the South-Alpine Segment of the Western Tethys, Field Guide-Book. Società Geologica Italiana, Brescia, pp. 111-130.

Nettleton, W.D., Brasher, B.R., Benham, E.C. and Ahrens, R.J., 1998. A classification system for buried paleosols. *Quaternary International*, **51**: 175-183.

Nettleton, W.D., Olson, C.G. and Wysocki, D.A., 2000. Paleosol classification: problems and solutions. *Catena*, **41**: 61-92.

Newell, A.J., Tverdokhlebov, V.P. and Benton, M.J., 1999. Interplay of tectonics and climate on a transverse fluvial system, Upper Permian, Southern Uralian Foreland Basin, Russia. *Sedimentary Geology*, **127**: 11–29.

Newton, R.J., Pevitt, E.L., Wignall, P.B. and Bottrell, S.H., 2004. Large shifts in the isotopic composition of seawater sulphate across the Permo-Triassic boundary in northern Italy. *Earth and Planetary Science Letters*, **218:** 331-345.

Nordt, L.C., M., O., Driese, S.G. and Tubbs, J., 2006. Vertisol carbonate properties in relation to mean annual precipitation: Implications for paleoprecipitation estimates. *Journal of Geology*, **114**: 501-51.

Ogg, J. and Smith, A.G., 2004. The geomagnetic polarity timescale. In: F. Gradstein and J. Ogg (Editors), *A Geological Time Scale 2004*. Cambridge University Press, Cambridge.

Parkinson, D., Curry, G.B., Cusack, M. and Fallick, A.E., 2005. Shell structure, patterns and trends of oxygen and carbon stable isotopes in modern brachiopod shells. *Chemical Geology*, **219**: 193-235.

Payne, J.L. and Kump, L.R., 2007. Evidence for recurrent Early Triassic massive volcanism from quantitive interpretation of carbon isotope fluctuation. *Earth and Planetary Science Letters*, **256**: 264-277.

Payne, J.L., Lehremann, D.J., Wei, J.Y., Orchard, M.J., Schrag, D.P. and Knoll, A.H., 2004.

Large perturbations of carbon cycle during recovery from the end-Permian extinction. *Science*, **305**: 506-509.

Pearson, P.N., Ditchfield, P.W., Singano, J., Harcourt-Brown, K.G., Nicholas, C.J., Olsson, R.K., Shackleton, N.J. and Hall, M.A., 2001. Warm tropical sea surface temperatures in the Late Cretaceous and Eocene epochs. *Nature*, **413**: 481-487.

Peel, M.C., Finlayson, B.L. and McMahon, T.A., 2007. Updated world map of the Koppen-Geiger climate classification. *Hydrology and Earth System Science*, **11**: 1633-1644.

Pendall, E.G., Harden, J.W., Trumbore, S.E. and Chadwick, O.A., 1994. Isotopic approach to soil carbonate dynamics and implications for palaeoclimate interpretations. *Quaternary Research*, **42**: 60-71.

Posenato, R., 2001. The Athyridoids of the Transitional Beds between Bellerophon and Werfen Formations (Uppermost Permian, Southern Alps, Italy) *Rivista Italiana di Paleontologia e Stratigrafia*, **107**: 197-226.

Poulsen, C.J., Pollard, D., Montañez, I.P. and Rowley, D.B., 2007. Late Paleozoic tropical climate response to Gondwanan deglaciation. *Geology*, **35**: 771-774.

Prochnow, S.J., Nordt, L.C., Athchley, S.C. and Hudec, M.R., 2006. Multi-proxy paleosol evidence for middle and late Triassic climate trends in eastern Utah. *Palaeogeography Palaeoclimatology Palaeoecology*, **232**: 53-72.

Quast, A., Hoefs, J. and Paul, J., 2006. Pedogenic carbonates as a proxy for palaeo-CO2 in the Palaeozoic atmosphere. *Palaeogeography, Palaeoclimatology, Palaeoecology*, **242**: 110-125.

Rahimpour-Bonab, H., Bone, Y. and Moussavi-Harmi, R., 1997. Stable isotope aspects of modern molluscs, brachiopods, and marine cements from cool-water carbonates, Lacepede Shelf, South Australia. *Geochimca et Cosmochimica Acta*, **61**: 207-218.

Rampino, M.R., Prokoph, A. and Adler, A., 2000. Tempo of the end-Permian event: High-

resolution cyclostratigraphy at the Permian-Triassic boundary. *Geology*, **28**: 643-646.

Rantitsch, G., 2007. Robust sequential Factor Analysis of geochemical data from the Permian-Triassic Gartnerkofel-1 core (Southern Alps): the geochemical response to changing paleo-oceanographic conditions in shallow-marine carbonate platforms. *Facies*, **53**: 129-140.

Raup, D.M., 1979. Size of the Permo-Triassic bottleneck and its evolutionary implications. *Science*, **206**: 217-218.

Reichow, M.K., Saunders, A.D., White, R.V., Al'Mukhamedov, A.I. and Medvedev, A.Y., 2005. Geochemistry and petrogenesis of basalts from the Western Siberian Basin: an extension of the Permo-Triassic Siberian Traps, Russia. *Lithos*, **79**: 425-452.

Reichow, M.K., Saunders, A.D., White, R.V., Pringle, M.S., Al'Mukhamedov, A.I., Medvedev, A.Y. and Kirda, P.K. 2002. $^{40}Ar/^{39}Ar$ Dates from West Siberia Basin: Siberian flood basalt province doubled. *Science*, **296**: 1846-1849.

Renne, P.R., Melosh, H.J., Farley, K.A., Reimold, W.U., Koeberl, C., Rampino, M., Kelly, S.P. and Ivanov, B.A., 2004. Is Bedout an Impact Crater? Take 2. *Science*, **306**: 610-611.

Retallack, G.J., 1993. Classification of paleosols: discussion. *Geological Society of America Bulletin*, **105**: 383-400.

Retallack, G.J., 1994a The environmental factor approach to the interpretation of paleosols. In: R. Amundson, J. Harden and M. Singer (Editors), *Factors in Soil Formation: and Fiftieth Anniversary Retrospective*. Soil Science Society of America Special Publication. **33:** 31-64.

Retallack, G.J., 1994b. A pedotype approach to latest Cretaceous and earliest Tertiary paleosols in eastern Montana. *GSA Bulletin*, **106**: 1377-1397.

Retallack, G.J., 1997. *A Colour Guide to Paleosols*. Wiley, Chichester, 175 pp.

Retallack, G.J., 1999. Postapocalyptic greenhouse paleoclimate revealed by earliest Triassic paleosols in the Sydney Basin, Australia *GSA Bulletin*, **111**: 52-70.

Retallack, G.J., 2001a. *Soils of the Past - An Introduction to Paleopedology*. Blackwell Science, Oxford 404 pp.

Retallack, G.J., 2001b. A 300-million-year record of atmospheric carbon dioxide from fossil plant cuticles. *Nature*, **411**: 287-289.

Retallack, G.J., 2005a. Earliest Triassic claystone breccias and soil erosion crisis. *Journal of Sedimentary Research*, **75**: 663-679.

Retallack, G.J., 2005b. Pedogenic carbonate proxies for amount and seasonality of precipitation in paleosols. *Geology*, **33**: 333-336.

Retallack, G.J., 2005c, Permian greenhouse crises, In: Lucas, S.G. and Ziegler, K.E., (Editors), *The nonmarine Permian.* Bulletin New Mexico Museum of Natural History and Science 30, 256-269.

Retallack, G.J., 2008. Ginkgo stomatal index data updated to 2008, http://www.uoregon.edu/~dogsci/directory/faculty/greg/downloadable_data.

Retallack, G.J. and Krull, E.S., 1999. Landscape ecological shift at the Permian-Triassic boundary in Antarctica. *Australian Journal of Earth Sciences*, **46**: 785-812.

Retallack, G.J. and Krull, E.S., 2006. Carbon isotopic evidence for terminal -Permian methane outbursts and their role in extinctions of animals, plants, coral reefs, and peat swamps. In: S.F. Greb and W.A. DiMichele (Editors), *Wetlands through time: Geological Society of America Special Paper*. **399**: 249-268.

Retallack, G.J. and Jahren, A.H., 2008. Methane Release from Igneous Intrusion of Coal during Late Permian Extinction Events. *Journal of Geology*, **116**: 1-20.

Retallack, G.J., Veevers, J.J. and Morante, R., 1996. Global coal gap between Permian-Triassic extinction and Middle Triassic recovery of peat forming plants. *GSA Bulletin*,

108: 195-207.

Rétallack, G.J., Seyedolali, A., Krull, E.S., Holser, W.T., Ambers, C.P. and Kyte, F.T., 1998. Search for evidence of impact at the Permian-Triassic boundary in Antarctica and Australia. *Geology* **26**: 979-982.

Retallack, G.J., Smith, R.M.H. and Ward, P.D., 2003. Vertebrate extinction across Permian-Triassic boundary in Karoo Basin, South Africa. *Geological Society of America Bulletin*, **115**: 1133-1152.

Retallack, G.J., Sheldon, N.D., Cogoini, M. and Elmore, R.D., 2003b. Magnetic susceptibility of early Paleozoic and Precambrian paleosols. *Palaeogeography, Palaeoclimatology, Palaeoecology*, **198**: 373-380.

Retallack, G.J., Jahren, A.H., Sheldon, N.D., Chakrabarti, R., Metzger, C.A. and Smith, R.M.H., 2005. The Permian-Triassic boundary in Antarctica. *Antarctica Science*, **17**: 241-258.

Retallack, G.J., Metzger, C.A., Greaver, T., Jahren, A.H., Smith, R.M.H. and Sheldon, N.D., 2006. Middle-Late Permian mass extinction on land. *GSA Bulletin*, **118**: 1398-1411.

Retallack, G.J., Greaver, T. and Jahren, A.H., 2007. Return to Coalsack Bluff and the Permian - Triassic boundary in Antarctica. *Global and Planetary Change* **55**: 90-108.

Roberts, J.A., Bennett, P.C., Gonzalez, L.A., Macpherson, G.L. and Milliken, K.L., 2004. Microbial precipitation of dolomite in methanogenic groundwater. *Geology*, **32**: 277-280.

Robinson, S.A., Andrews, J.E., Hesselbo, S.P., Radley, J.D., Dennis, P.F., Harding, I.C. and Allen, P., 2002. Atmospheric pCO_2 and depositional environment from stable-isotope geochemistry of calcrete nodules (Barremian, Lower Cretaceous, Wealden Beds, England). *Journal of the Geological Society, London*, **159**: 215-224.

Romanek, C.S., Grossman, E.L. and Morse, J.W., 1992. Carbon isotopic fractionation in

synthetic aragonite and calcite: Effects of temperature and precipitation rate. *Geochimica et Cosmochimica Acta*, **56**: 419-430.

Roscher, M. and Schneider, J.W., 2006. Permo-Carboniferous climate: Early Pennsylvanian to Late Permian climate development of central Europe in a regional and global context. In: S.G. Lucas, G. Cassinis and J.W. Schneider (Editors), *Non-Marin Permian Biostratigraphy and Biochronology*. . Geological Society, London Special Publications, pp. 95-136.

Ross, P.-S., I.U., P., McClintock, M.K., Xu, Y.G., Skilling, I.P., White, J.D.L. and Houghton, B.F., 2005. Mafic volcaniclastic deposits in flood basalt provinces: A review. *Journal of Volcanology and Geothermal Research*, **145**: 281-314.

Rowley, D.B.,2008, 2003 Revised Permian Paleogeographic maps: *http://geosci.uchicago.edu/~rowley/Rowley/Revised_Permian_Maps.html*

Royer, D.L., 2006. CO_2-forced climate thresholds during the Phanerozoic. *Geochimca et Cosmochimica Acta*, **70**: 5665-5675.

Rozanski, K., Araguás-Araguás, L. and Gonfiantini, R., 1992. Relation between long-term trends in oxygen -18 isotope composition of precipitation and climate. *Science*, **258**: 981-984.

Sánchez-Román, M., Vasconcelos, C., Schmid, T., Dittrich, M., McKenzie, J.A., Zenobi, R. and Rivadeneyra, M.A., 2008. Aerobic microbial dolomite at the nanometer scale: Implications for the geologic record. *Geology*, **36**: 879–882

Sarkar, A., Yoshioka, H., Ebihara, M. and Naraoka, H., 2003. Geochemical and organic carbon isotope studies across the continental Permo-Triassic boundary if the Raniganj Basin, eastern India. *Palaeogeography Palaeoclimatology Palaeoecology*, **191**: 1-14.

Saunders, A., and Reichow, M., 2009. The Siberian Traps and the End-Permian mass extinction: a critical review. *Chinese Science Bulletin*, **54:** 20-37.

Scarciglia, F., de Rosa, R., Vecchio, G., Apollaro, C., Robustelli, G. and Terrasi, F., 2007. Volcanic soil formation in Calabria (southern Italy): The Cecita Lake geosol in the lat Quaternary geomorphological evolution of the Sila uplands. *Journal of Volcanology and Geothermal Research*. **177**: 101-117.

Schmid, S., Worden, R.H. and Fisher, Q.J., 2006. Sedimentary facies and the context of dolocrete in the Lower Triassic Sherwood Sandstone group: Corrib Field west of Ireland. *Sedimentary Geology*, **187**: 205–227.

Scholger, R., Maurtisch, H.J. and Brandner, R., 2000. Permian-Triassic boundary magnetostratigraphy from the Southern Alps (Italy). *Earth and Planetary Science Letters*, **176**: 495-508.

Self, S., Thordarson, T. and Widdowson, M., 2005. Gas Fluxes from Flood Basalt Eruptions. *Elements*, **1**: 283-287.

Sephton, M.A., Looy, C., Brinkhuis, H., Wignall, P.B., de Leeuw, J.W. and Visscher, H., 2005. Catastrophic soil erosion during the end-Permian biotic crisis. *Geology*, **33**: 941-944.

Sheldon, N.D., 2005. Do red beds indicate paleoclimatic conditions?: A Permian case study. *Palaeogeography, Palaeoclimatology, Palaeoecology*, **228**: 305-319.

Sheldon, N.D., 2006. Abrupt chemical weathering increase across the Permian-Triassic boundary. *Palaeogeography, Palaeoclimatology, Palaeoecology*, **231**: 315-321.

Sheldon, N.D. and Retallack, G.J., 2001. Equation for compaction of paleosols due to burial:. *Geology*, **29**: 247-250.

Sheldon, N.D. and Retallack, G.J., 2002. Low oxygen levels in earliest Triassic soils. *Geology*, **30**: 919-922.

Sherman, L.A. and Barak, P., 2000. Solubility and dissolution kinetics of dolomite in Ca-Mg-HCO_3/CO_3 solutions at 25 degrees C and 0.1 MPa carbon dioxide. *Soil Science*

Society of America Journal, **64**: 1959 1968.

Smith, R. and Botha, J., 2005. The recovery of terrestrial vertebrate diversity in the South African Karoo Basin after the end-Permian extinction *Comptes Rendus Palevol*, **4**: 623-636.

Soil Survey Staff, 1999. *Soil Taxonomy: A Basic System of Soil Classification for Making and Interpreting Soil Surveys*, Agriculture Handbook Number 436. United States Department of Agriculture Natural Resources Conservation Service 871 pp.

Soil Survey Staff, 2006. *Keys to Soil Taxonomy*. United States Department of Agriculture Natural Resources Conservation Service, 332 pp.

Soreghan, G.S., Elmore, R.D. and Lewchuk, M.T., 2002. Sedimentologic-magnetic record of western Pangean climate in upper Paleozoic Loessite (Lower Cutler beds, Utah). *GSA Bulletin*, **114**: 1019 - 1035.

Sperling, E.A. and Ingle, J.C., 2006. A Permian-Triassic boundary section at Quinn River Crossing, northwestern Nevada, and implications for the cause of the Early Triassic chert gap on the western Pangean margin. *Geological Society of America Bulletin*, **118**: 733-746.

Spötl, C. and Wright, V.P., 1992. Groundwater Dolocretes from the Upper Triassic of the Paris Basin, France - a case-study of an Arid, Continental Diagenetic Facies *Sedimentary Geology*, **39**: 1119-1136.

Steiner, M.B., 2006. The magnetic polarity time scale across the Permian-Triassic Boundary. In: S.G. Lucas, G. Cassinis and J.W. Schneider (Editors), *Non-Marine Permian Biostratigraphy and Biochronology* Geological Society, London, Special Publications, pp. 15-38.

Steiner, M.B., Estet, Y., Rampino, M.R. and Schwindt, D.M., 2003. Fungal abundance spike and the Permian - Triassic boundary in Karoo Supergroup (South Africa).

Palaeogeography Palaeoclimatology Palaeoecology, **194**: 405 - 414.

Stokes, M. and Mather, A.E., 2000. Response of Plio-Pleistocene alluvial systems to tectonically induced base-level changes, Vera Basin, SE Spain. *Journal of the Geological Society*, **157**: 303-316.

Surkov, M.V., Benton, M.J., Twitchett, R.J., Tverdokhlebov, V.P. and Newell, A.J., 2007. First Occurrence of Footprints of Large Therapsids from the Upper Permian of European Russia *Palaeontology* **59**: 641-652.

Szurlies, M., 2007. Latest Permian to Middle Triassic cyclo-magnetostratigraphy from the Central European Basin, Germany: Implications for the geomagnetic polarity timescale. *Earth and Planetary Science Letters*, **261**: 602-619.

Szurlies, M., Bachmann, G.H., Menning, M., Nowaczyk, N.R. and Kading, K.C., 2003. Magnetostratigraphy and high-resolution lithostratigraphic of the Permian-Triassic boundary interval in Central Germany. *Earth and Planetary Science Letters*, **212**: 263-278.

Tabor, N.J., Montanez, I.P. and Southard, R.J., 2002. Paleoenvironmental reconstructions from chemical and isotopic compositions of Permo-Pennsylvanian pedogenic minerals. *Geochimca et Cosmochimica Acta*, **66**: 3093-3107.

Tabor, N.J., Montanez, I.P., Steiner, M.B. and Schwindt, D., 2007. delta C-13 values of carbonate nodules across the Permian-Triassic boundary in the Karoo Supergroup (South Africa) reflect a stinking sulfurous swamp, not atmospheric CO2. *Palaeogeography Palaeoclimatology Palaeoecology*, **252**: 370-381.

Taylor, G.K., Tucker, C., Twitchett, R.J., Kearsey, T., Benton, M.J., Newell, A.J., Surkov, M.V. and. Tverdokhlebov, V.P., 2009. Magnetostratigraphy of Permian/Triassic boundary sequences in the Cis-Urals, Russia: No evidence for a major temporal hiatus. *Earth and Planetary Science Letters*, **281**: 36-47.

The Rock Color Chart Committee, U.S.G.S., 1997. Rock Color Chart: with genuine Munsell color chips. The Geological Society of America, Boulder, Colorado.

Therckray, J.F., van de Merwe, N.J., Lee-Thorp, J.A., Sillen, A., Lanham, J.L., Smith, R., Keyser, A. and Monteiro, P.M.S., 1990. Changes in carbon isotope ratios in the Late Permian recorded in therapsid tooth apatite. *Nature*, **347**: 751-753.

Tomašových, A. and Farkaš, J., 2005. Cathodoluminescence of Late Triassic terebratulid brachiopods: implications for growth patterns. *Palaeogeography, Palaeoclimatology, Palaeoecology*, **216** 215-233.

Torsvik, T.H. and Andersen, T.B., 2002. The Taimyr fold belt, Arctic Siberia: timing of prefold remagnetisation and regional tectonics. *Tectonophysics*, **352**: 335-348.

Tucker, M.E., 2001. *Sedimentary Petrology*. Blackwell Science, Oxford, 272 pp.

Tucker, M.E., 2003. *Sedimentary Rocks in the Field*. Wiley Chichester, 234 pp.

Tucker, M.E. and Wright, V.P., 1990. *Carbonate Sedimentology*. Wiley Blackwell Oxford 496 pp.

Tverdokhlebov, V.P., Tverdokhlebov, G.I., Surkov, M.V. and Benton, M.J., 2003. Tetrapod localities from Triassic of the SE of European Russia. *Earth Science Reviews*, **60**: 1-66.

Tverdokhlebov, V.P., Tverdokhlebova, G.I., Minikh, A.V., Surkov, M.V. and Benton, M.J., 2005. Upper Permian vertebrates and their sedimentological context in the Southern Urals, Russia. . *Earth-Science Reviews*, **69**: 27-77.

Twitchett, R.J., 2006. The palaeoclimatology, palaeoecology and palaeoenvironmental analysis of mass extinction events. *Palaeogeography, Palaeoclimatology, Palaeoecology*, **232**: 190-213.

Twitchett, R.J., 2007. Climate change across the Permian/Triassic boundary. In: M. Williams, A.M. Haywood, F.J. Gregory and S. D.T. (Editors), *Deep-Time Perspective on*

Climate Change: Marrying the Signal from Computer Models and Biological Proxies. The Micropalaeontological Society, Special Publications, The Geological Society, London, pp. 191-200.

Twitchett, R.J., Looy, C.V., Morante, R., Visscher, H. and Wignall, P.B., 2001. Rapid and synchronous collapse of marine and terrestrial ecosystems during the end-Permian biotic crisis. *Geology*, **29**: 351-354.

van Geldern, R., Joanchimski, M.M., Day, J., Jansen, U., Alvarez, F., Yolkin, E.A. and Ma, X.-P., 2006. Carbon, oxygen and strontium isotope records of Devonian brachiopod shell calcite. *Palaeogeography, Palaeoclimatology, Palaeoecology*, **240**: 47-67.

Veizer, J., 1983. Chemical diagenesis of carbonates: theory and application of trace element techniques In: M.A. Arthur, T.F. Andersen, I.R. Kaplan, J. Veizer and L.S. Land (Editors), *Stable isotopes in Sedimentary Geology*. SEPM Short Course, pp. 3-100.

Veizer, J., Ala, D., Azmy, K., P., B., Buhl, D., Buhl, F., Carden, G.A.F., Deiner, A., Ebneth, S., Godderis, Y., Jasper, T., Korte, C., Pawellek, F., Podlaha, O.G. and Strauss, H., 1999. $^{87}Sr/^{86}Sr$, $\delta^{13}C$ and $\delta^{18}O$ evolution of Phanerozoic seawater. *Chemical Geology*, **161**: 59-88.

Visscher, H., Looy, C., Collinson, M.E., Brinkhuis, H., Van Cittert, J.H.A., Kurschner, W.M. and Sephton, M.A., 2004. Environmental mutagenesis during the end-Permian ecological crisis. *Proceedings of the National Academy of Sciences of the United States of America*, **101**: 952-956.

Wagner, F., Below, R., DeKlerk, P., Dilcher, D.L., Joosten, H., Kurschner, W.M. and Visscher, H., 1996. A natural experiment on plant acclimation: Lifetime stomatal frequency response of an individual tree to annual atmospheric CO_2 increase. *Proceedings of the National Academy of Sciences of the United States of America* **93**: 11705-11708.

Wang, K., Geldsetzer, H.H.J. and Krouse, H.R., 1994. Permian-Triassic extinction: Organic $\delta^{13}C$ evidence from British Columbia, Canada. *Geology*, **22**: 580-584.

Ward, P.D., Botha, J., Buick, R., De Kock, M.O., Erwin, D.H., Garrison, G.H., Kirschvink, J.L. and Smith, R., 2005. Abrupt and gradual extinction among Late Permian land vertebrates in the Karoo Basin, South Africa. *Science*, **307**: 709-714.

Ward, P.D., Montgomery, D.R. and Smith, R., 2000. Altered river morphology in South Africa related to the Permian-Triassic extinction. *Science*, **289**: 1740-1743.

Watts, N.L., 1980. Quaternary pedogenic calcretes from the Kalahari (southern Africa): mineralogy, genesis and diagenesis. *Sedimentology* **27**: 661-686.

Webster, P.J., 2005. Oceans and Monsoon. In: C.-P. Chang, W. B. and L. N.-C.G. (Editors), *The Global Monsoon System: Research and Forecast*. Secretariat of the World Meteorological Organization, Geneva, pp. 253-298.

Wignall, P.B., 2001. Large igneous provinces and mass extinctions. *Earth Science Reviews*, **53**: 1-33.

Wignall, P.B., 2007. The End-Permian mass extinction - how bad did it get? *Geobiology*, **5**: 303-309.

Wignall, P.B. and Newton, R.J., 2003. Contrasting Deep-water Records from the Upper Permian and Lower Triassic of South Tibet and British Columbia: Evidence for a Diachronous Mass Extinction. *Palaios*, **18**: 153-167.

Wignall, P.B., Thomas. B., Willink, R., Wating, J., Becker, R.J. and Pope, K.O.,2004. Is Bedout an Impact Crater? Take 1. *Science*, **306**: 609.

Wignall, P.B. and Twitchett, R.J., 1996. Oceanic anoxia and the end Permian mass extinction *Science*, **272**: 1155-1158.

Wignall, P.B. and Twitchett, R.J., 1999. Unusual intraclastic limestones in Lower Triassic carbonates and their bearing on the aftermath of the end-Permian mass extinction.

Sedimentology, **45**: 303-316.

Williams, A., Carlson, S.J., Brunton, C.H.C., Holmer, L.E. and Popov, L., 1996. A supra-ordinal classification of the Brachiopoda. *Philosophical Transactions of the Royal Society of London Series B-Biological Sciences*, **351**: 1171-1193.

Williams, C.A. and Krause, F.F., 1998. Pedogenic-phreatic carbonates on a Middle Devonian (Givetian) terrigenous alluvial-deltaic plain, Gillwood member (Watt Mountain formation), northcentral Alberta, Canada. *Sedimentology*, **45**: 1105-1124.

Winguth, A.M.E. and Maier-Reimer, E., 2005. Causes of the marine productivity and oxygen changes associated with the Permian-Triassic boundary: A revaluation with ocean general circulation models. *Marine Geology*, **217**: 283-304.

Woan, G., 2000. *The Cambridge Handbook of Physics Formulas*. Cambridge University Press, Cambridge, 219 pp.

Wright, D.T. and Wacey, D., 2005. Precipitation of dolomite using sulphate-reducing bacteria from Coorong Region, South Australia: significance and implications. *Sedimentology*, **52**: 987-1008.

Wright, V.P. and Allen, J.R.L., 1989. Palaeosols in Silici-clastic sequences PRIS Short Course Notes No.001 University of Reading, pp. 98.

Wynn, J.G., 2003. Towards a physically based model of CO_2-induced stomatal frequency response. *New Phytologist*, **157**: 394-398.

Xu, D.-Y., Yan, Z., Zhang, Q.-W. and Sun, Y.-Y., 1986. Three main mass extinctions-significant indicators of major natural divisions of geological history in the Phanerozoic *Marine Geology*, **10**: 365-375.

Yadava, M.G., Ramesh, R. and Pandarinath, K., 2007. A positive 'amount effect' in the Sahayadri (Western Ghats) rainfall. *Current science*, **93**: 560-564.

Yin, H.F., Zhang, K.X., Tong, J.N., Yang, Z.Y. and Wu, S.B., 2001. The Global Stratotype

Section and Point (GSSP) of the Permian-Triassic Boundary. *Episodes*, **24**: 102-114.

Yu, J.X., Li, H.M., Zhang, S.X., Yang, F.Q., Feng, Q.L. 2008. Timing of the terrestrial Permian-Triassic boundary biotic crisis: Implications from U-Pb dating of authigenic zircons. *Science in China Series D: Earth Science*, **51**: 1633-1645.

Ziegler, A.M., Hulver, M.L. and Rowley, D.B., 1997. Permian world topography and climate In: I.P. Martini (Editor), *Late glacial and postglacial Environmental Change: Quaternary, Carboniferous-Permian and Proterozoic*. Oxford University Press, Oxford, pp. 111-146.

Appendix 1

Paleosol feature descriptions and field data

(Chapter 3)

A1.1

Pedological features of paleosols from Boyevaya Gora.

Horizon	Total thickness (cm)	Colour	Grain Size	Contains a mottled horizon/ other alteration controls	Presence of Roots recorded	Nodule stage	Depth to Bk Horizon (cm)	Notes	Classification
KOR 36	39	5GY 8/1 - 10R 6/6 - 5YR 6/4	Siltstone	Sandstone above gleyed (N8)	Only in A horizon	II	2		Petronodic Haplocalcid
KOR 33	32	10R 6/6 and 5YR 6/4	Siltstone	Sandstone above gleyed (N8)	Throughout	II	3	Nodules 'flattened' becomes platy at base	Petronodic Haplocalcid/ Ustic Calcids (Groundwater)
KOR 37	80	5GY 8/1 - 10R 5/4 - 5YR 6/5	Siltstone	Sandstone above gleyed (N8)	Throughout	II	9	Many nodules appear flattened in top section v poor nodule development	Petronodic Haplocalcid
KOR 34	34	5GY 8/1 and 5YR 6/4	Fine sandstone and Siltstone	Sandstone above gleyed (N8)	Throughout	II	eroded		Petronodic Haplocalcid
KOR 32	51	5R 5/4 5YR 6/4	Siltstone	Minor	Throughout	II	8	Appears to contain diagenetic calcite	Petronodic Haplocalcid
KOR 1	59	10R 4/6 and 7/4 (nod horizons)	Siltstone in rooted zones/VF sand in nod bands	Blue green mud cracked area extensively mottled minor mottling in rooted area	Throughout	II	49	Mud cracks on the top surface with strong mottles (top 10cm)	Petronodic Haplocalcid
KOR 1a	105	10R 4/6 and 7/4 (nod horizons)	Siltstone in rooted zones/VF sand in nod bands	Minor reductions spots	In rooted and un rooted areas	III	23		Ustic Petrocalcid
KOR 2	83	10R 5/4	Siltstone	Minor reductions spots	Only in A horizon	II	25		Petronodic Haplocalcid.
KOR 3	45	top 10R 5/6 Bk - 10R 7/4	Mudstone	Minor reductions spots	Throughout	IV	8	Slickenside	Vertic Petrocalcid
KOR 8	27	10R 7/4	Siltstone	Mottled roots	Throughout	IV	Eroded	Drab root haloes	Ustic Petrocalcid
KOR 9	20	10R 6/6	Mudstone	Minor reductions spots	Throughout	II	Eroded		Petronodic Haplocalcid.

Horizon	Total thickness (cm)	Colour	Grain Size	Contains a mottled horizon/ other alteration controls	Presence of Roots recorded	Nodule stage	Depth to Bk Horizon (cm)	Notes	Classification
KOR 4	137	10R 7/4 - 10R 5/4	Siltstone	None	Throughout	V	18	Shows hummocky brecciated top	Vertic Petrocalcid
KOR 5	27	10R 5/4	Siltstone	None	Throughout	II	eroded	Probably affected/part of by soil above	Vertic Haplocalcid
KOR 6	88	10R 5/4	Siltstone	Minor reductions spots	Throughout	II	34		Petronodic Haplocalcid
KOR 7	72	10R 8/2 and 10R 7/4	Siltstone	Mottled -5B 8/2 mottled roots	Throughout	IV	28		Ustic Petrocalcid
KOR 10	96	10R 6/6	Siltstone	Mottled -5B 8/2 top like 1	Throughout	III	27	Top boundary indistinct may have mud cracks	Ustic Calcid (Lacustrine)
KOR 11	58	10R 7/4 - 10R 8/2	Siltstone	Drab root haloes	Throughout	IV	18	Patch calcification	Ustic Petrocalcid
KOR 12	42	10R 7/4	Siltstone	Mottled roots 5G 8/1	Only in A horizon	II	36	Very thin Bk horizon	Petronodic Haplocalcid
KOR 13	86	10R 8/2 10R 7/4	Siltstone	None	Only in A horizon	IV	eroded	white limestone cemented top bed	Ustic Petrocalcid
KOR 14	50	10R 5/4	Siltstone	None	Only in A horizon	III	26	Stacked horizons min 2 or 4 and possible rooted hard ground	Ustic Petrocalcid.
KOR 14a	48	10R 5/4	Very fine sandstone	None	Throughout	II	8	Stacked horizons min 2 or 4 and possible rooted hard ground	Petronodic Haplocalcid
KOR 14b	27	10R 5/4 base 10R 8/4	Siltstone	None	Throughout	II	18	Stacked horizons min 2 or 4 and possible rooted hard ground	Petronodic Haplocalcid
KOR 23	51	5R 5/4	Mudstone	Erosive Gleyed sand above	Throughout	III	28	Possibly waterlogged horizon??	Ustic Calcid (Groundwater)
KOR 22	76	10R 5/4	Mudstone	None	Throughout	II	64.5	Laterally variable 23 - 70 cm thick	Petronodic Haplocalcid
KOR 21	61	10R 5/4	Mudstone	None	Throughout	III	eroded		Ustic Petrocalcid
KOR 15	55	10R 5/4 - N7	Top VF sandstone and Siltstone	N7 -in mottled top - nodules mottled	Only in A horizon	II	17	Top possibly like 17	Petronodic Haplocalcid
KOR 16	19	10R 4/1	Siltstone	Minor reductions spots	In nodule zones	II	13	Stacked horizon	Petronodic Haplocalcid

Horizon	Total thickness (cm)	Colour	Grain Size	Contains a mottled horizon/ other alteration controls	Presence of Roots recorded	Nodule stage	Depth to Bk Horizon (cm)	Notes	Classification
KOR 16a	27	10R 4/2	Siltstone	Minor reductions spots	In nodule zones	II	14	Stacked horizon	Petronodic Haplocalcid
KOR 17	31	top 5YR 8/4 10R 6/2	Top VF sandstone and Siltstone	N7 in rooted area	Only 'A' Horizon	III	24	Contains ostracods - lacustrine. Not very laterally continuous	Ustic Calcid (Lacustrine)
KOR 18	19	10R 5/4	Siltstone	Minor reductions spots	Only 'A' Horizon	III	12	Note 18.1-4 are different horizons than 18.5-9	Ustic Petrocalcid
KOR 19	79	10R 8/2 - 10R7/4 below	Siltstone	Drab root haloes	Throughout	V	21		Ustic Petrocalcid
KOR 20	59	10R 6/6 and 10R 5/4	Fine sandstone	None	None	IV	Calcified channel	Calcified channel	Ustic Calcid (Lacustrine)
KOR 24	15	10R 6/6 and 10R 5/4	Mudstone / VF Sandstone	None	Throughout	III	15		Ustic Petrocalcid
KOR 25	29	10R 5/4		None	None	II	21		Petronodic Haplocalcid
KOR 26	46	top N8 and 10R 5/4	Siltstone t/VF sandstone	Strongly mottled throughout (N8)	Throughout	IV	41	Contains ostracods - lacustrine Not very laterally continuous	Ustic Calcid (Lacustrine)
KOR 27	30	top 10R 6/2 and	Siltstone t/VF sandstone	Minor reductions spots	Only 'A' Horizon	II	26		Petronodic Haplocalcid
KOR 28	15	10R 5/4 and 10R 7/4	Mudstone / Siltstone	Top 2cm mottled N8 but strongly rooted	In Bk horizon	IV	Eroded		Ustic Petrocalcid
KOR 29	16	10R 8/2 and 10R 5/4	Siltstone	None	Throughout	III	Eroded	Desiccation cracks on top	Ustic Petrocalcid
KOR 30	24	10R 5/4 and 10R 6/2	Silt and VF sand	None	Throughout	IV	18	Poor exposure	Ustic Petrocalcid
KOR 31	28	5YR 8/1 and 10R 5/4	Fine sand and clay	Sand above strongly mottled	None recorded	II	Eroded	possibly waterlogged horizon (12cm)	Petronodic Haplocalcid.
KOR 35	23	10R 5/4	Mudstone	None	None recorded	II	Eroded		Petronodic Haplocalcid.

A1.2

Pedological features of paleosols from Sambullak.

Horizon	Total thickness (cm)	Colour	Grain Size	Contains a mottled horizon/ other alteration controls	Presence of Roots recorded	Nodule stage	Depth to Bk Horizon (cm)	Notes	Classification
SAM 1	66	10R 7/4, 10R 3/4, 10R 5/4	Siltstone	Calcite filled slickenside at top	Only in A horizon	II	31		Vertic Haplocalcid
SAM 4	80	10R 6/6	Siltstone		None observed	II	eroded	Weakly developed	Petronodic Haplocalcid
SAM 3	129	10R 6/6, 10R 5/4	Siltstone	Slickenside at top of profile mottled round nodules	None observed	III	49	Presence of pedogenic slickensides	Vertic Haplocalcid
SAM 2	68	10R 6/6,	Siltstone	Lacustrine carbonate above	None observed	II	Lacust.	Top lacustrine limestone so probably palustrine	Ustic Calcid (Lacustrine)
SAM 12	20	10R 5/4	Mudstone	Mottled top	Only in A horizon	II	14	Rootlets rare	Petronodic Haplocalcid
SAM 11	34	10R 5/4 and 5GY 8/1	Mudstone	Calcite vein	Throughout	II	28	Poorly exposed	Petronodic Haplocalcid
SAM 10	145	10R 5/4,	Mudstone	Calcified top mottled	Throughout	II	42	Presence of pedogenic slickensides	Vertic Haplocalcid
SAM 10a	103	5R 5/4,	Mudstone	Calcified top mottled	Throughout	II	24	Presence of pedogenic slickensides	Vertic Haplocalcid
SAM 9	164	10R 8/2, 5R 5/4, 10R 6/2	Mudstone	Mottles in A horizon	Throughout	II	80		Petronodic Haplocalcid
SAM 8	83	5R 8/2	Siltstone	None	Only in A horizon	II	18	Top may be eroded by overlying conglomerate	Petronodic Haplocalcid
SAM 7	48	10R 8/2	Mudstone	None	Throughout	IV	eroded	Top may be eroded by overlying conglomerate	Ustic Petrocalcid
SAM 6	50		Siltstone	Minor mottles with mottled zone at top	Throughout	none	No Bk.		Ustic Haplocambid
SAM 5	94	10R 6/2, , 10R 4/6,	Mudstone	None	Throughout possible tap root/burrow	III	37		Ustic Petrocalcid
SAM 5a	84	5YR 5/6, 10R 8/2	Siltstone	None	Throughout	III	25		Ustic Petrocalcid
SAM 20	47	10R 8/2, 10R 7/4, 10R 6/2	Mudstone	Slight mottles in A horizon	Throughout	II	27	This horizon may be a weakly calcified (A) rooted horizon and not a nodule horizon	Petronodic Haplocalcid
SAM 19	59	10R 7/4, 5Y 8/1,	Mudstone	Top A horizon strongly mottled	Throughout	III	33		Ustic Petrocalcid

Horizon	Total thickness (cm)	Colour	Grain Size	Contains a mottled horizon/ other alteration controls	Presence of Roots recorded	Nodule stage	Depth to Bk Horizon (cm)	Notes	Classification
SAM 19a	101	10R 7/4, 5R 4/2	Mudstone	Minor mottling in A	Throughout	III	12		Ustic Petrocalcid
SAM 18	46	5YR 8/1, 5R 7/4	Mudstone	None	Throughout	IV	17	Below possible lacustrine limestone	Ustic Petrocalcid
SAM 17	52	N7, 5R 5/4	Mudstone	Bleached 2cm under conglomerate	Throughout	II	39	Top eroded by overlying conglomerate	Petronodic Haplocalcid
SAM 16	56	5Y 8/1, 10R 4/6	Mudstone	Mottled top	Only in BK	II	37		Petronodic Haplocalcid
SAM 15	65	5YR 5/2, 5YR 6/5	Mudstone	None	Throughout	II	27	High degree of modern pedogenesis	Petronodic Haplocalcid.
SAM 14	40	5YR 5/2, 5YR 6/4	Mudstone	Bk horizon mottled	Throughout	I/II	15	Poorly exposed	Petronodic Haplocalcid
SAM 13	83	5R 4/3, 5R 5/4	Mudstone	None	Throughout	II	14	Small nodules	Petronodic Haplocalcid
SAM 21	42	5R 5/4	Mudstone	Very minor mottles	Only in A horizon	II	19		Petronodic Haplocalcid
SAM 22	35	5R 5/4, 10R 5/4,	Mudstone	Drab root haloes mottled A horizon	Only in A horizon	II	27		Petronodic Haplocalcid
SAM 23	83	5R 5/4	Mudstone	Minor mottles	Throughout	III	47		Ustic Petrocalcid
SAM 24a	61	5R 5/5	Mudstone	None	None observed	II	51	Poorly exposed	Petronodic Haplocalcid
SAM 24b	102	5R 5/6	Mudstone	None	None observed	II	31	Poorly exposed	Petronodic Haplocalcid
SAM 24c	60	5R 5/7	Mudstone	None	None observed	II	54	Poorly exposed	Petronodic Haplocalcid
SAM 24d	146	5R 5/8	Mudstone	None	None observed	II	88	Poorly exposed	Petronodic Haplocalcid
SAM 24e	133	5R 5/9	Mudstone	None	None observed	II	119	Poorly exposed	Petronodic Haplocalcid

A1.3

Pedological features of paleosols from Tuyembetka.

Horizon	Total thickness (cm)	Colour	Grain Size	Presence of Roots recorded	Nodule stage	Depth to Bk Horizon (cm)	Notes	Classification
TUY 53	73	5R 4/2	*Siltstone*		II	Eroded	Layered groundwater nodules	Petronodic Haplocalcid

Horizon	Total thickness (cm)	Colour	Grain Size	Presence of Roots recorded	Nodule stage	Depth to Bk Horizon (cm)	Notes	Classification
TUY 54	130	5YR 6/1	Mudstone		III	Eroded	Lots of spars present carbonate	Ustic Petrocalcid
TUY 55	85		Siltstone		IV	37		Ustic Petrocalcid
TUY 56	55		Mudstone	Some evidence	II	3	Weakly developed	Petronodic Haplocalcid
TUY 57	57		Mudstone		II	53		Petronodic Haplocalcid
TUY 58	98	5R 4/2, 10R 4/2	Siltstone	Throughout	III	54		Ustic Petrocalcid
TUY 59	23	5R 6/1, 5YR 4/2	Mudstone	Some evidence	IV	Eroded		Ustic Petrocalcid
TUY 60	32	5R 6/1, 5YR 4/3	Mudstone	Some evidence	IV	Eroded		Ustic Petrocalcid
TUY 61	34	10R 6/2, 5YR 6/1	Siltstone	Only in A horizon	IV	Eroded		Ustic Petrocalcid
TUY 1	74		Micrite	Some observed	V	Eroded	Laminated	Ustic Petrocalcid
TUY 52	20	5R 6/2	Mudstone	Only in A horizon	IV	Eroded	Fused nodules	Ustic Petrocalcid
TUY 51	15	10R 6/2	Mudstone	Some evidence	III	Eroded	Poor exposure	Ustic Petrocalcid
TUY 50	39	5R 8/3	Mudstone	Only in A horizon	IV	Eroded	Mottled horizon	Ustic Petrocalcid
TUY 49	52	5R 8/2	Mudstone	Only in A horizon	VI	Eroded	Brecciated top -	Ustic Petrocalcid
TUY 48	15	5R 5/4 5YR 6/1	Mudstone	Some evidence	IV	Eroded	Vugs	Ustic Petrocalcid.
TUY 47	80		Mudstone		IV	Eroded	Welded calrete horizons	Ustic Petrocalcid
TUY 2	82	5R 8/2	Siltstone	None observed	V	62	Laminated	Ustic Petrocalcid
TUY 3	48		Mudstone	None observed	IV	36		Ustic Petrocalcid
TUY 4	12		Siltstone	Only in A horizon	II	26		Petronodic Haplocalcid
TUY 5	26		Mudstone	Some observed	III	18		Ustic Petrocalcid
TUY 6	107		Mudstone	Only in A horizon (vertical)	II	62	Smallest nodule 1cm diffuse pattern	Petronodic Haplocalcid
TUY 7	120		Mudstone	Throughout	III	26		Ustic Petrocalcid

Horizon	Total thickness (cm)	Colour	Grain Size	Presence of Roots recorded	Nodule stage	Depth to Bk Horizon (cm)	Notes	Classification
TUY 8	60		Mudstone	Some observed	IV	21	Evidence of heave cracks on surface	Vertic Petrocalcid
TUY 9	43		Mudstone	Some observed	I	Poor exp.		Petronodic Haplocalcid
TUY 10	199		Mudstone	Some observed	III	Poor exp	Sparry calcite in cracks	Ustic Petrocalcid
TUY 11	85		Mudstone	Throughout	V	Laminated		Ustic Petrocalcid
TUY 11a	95		Mudstone	Throughout	V	Laminated	Laminated top	Ustic Petrocalcid
TUY 12	98		Mudstone	Throughout	V	45	Sparry calcite in voids	Ustic Petrocalcid
TUY 13	87	10R6/2, 3/4	Mudstone	Only in A horizon	IV	33	Sparry calcite in voids	Ustic Petrocalcid
TUY 14	84		Mudstone	Some observed	V	Eroded	Sparry calcite in voids	Ustic Petrocalcid
TUY 15	27	10R 5/2	Mudstone	Sparsely	II	Eroded	Poorly exposed	Petronodic Haplocalcid
TUY 15a	18	10R 5/2	Mudstone	Sparsely	II	18		Petronodic Haplocalcid
TUY 15b	18	10R 5/2	Mudstone	Sparsely	III	16		Ustic Petrocalcid
TUY 16	50		Mudstone	Throughout	III	120		Ustic Petrocalcid
TUY 16a	36		Mudstone	Throughout	III	25	Poor exposure	Ustic Petrocalcid
TUY 16b	36	10R6/2	Mudstone	Throughout	III	32	Poor exposure	Ustic Petrocalcid
TUY 17	80	5B 9/1	Mudstone	Roots not continuous	V	Eroded	Cracks infilled with calcite	Ustic Petrocalcid
TUY 18	17	10R 4/2	Mudstone	Sparsely	II	44		Petronodic Haplocalcid
TUY 19	64		Fine sandstone	Some observed	V	42		Ustic Petrocalcid.
TUY 20	12		Mudstone	Some observed	V	Eroded		Ustic Petrocalcid
TUY 20a	55		Mudstone	Some observed	V	Eroded	Top may be brecciaed - modern weathering	Ustic Petrocalcid
TUY 21	36		Siltstone	Only in A horizon	III	Eroded	Poor exposure	Ustic Petrocalcid
TUY 22	55	10R 5/4, 5R 6/2	Mudstone	Throughout	IV	Eroded		Ustic Petrocalcid

Horizon	Total thickness (cm)	Colour	Grain Size	Presence of Roots recorded	Nodule stage	Depth to Bk Horizon (cm)	Notes	Classification
TUY 23	61	5R 5/4	Mudstone	Only in A horizon	II	58	Poor exposure	Petronodic Haplocalcid
TUY 24	97	5R 4/2	Siltstone	Throughout	II	48	Sparry calcitic veins	Petronodic Haplocalcid
TUY 25	62		Siltstone	Throughout	V	100	Mottling in lower horizon Cherty	Ustic Petrocalcid
TUY 26	76	5YR 6/1	Mudstone	Throughout	II	Eroded	Nodules possibly drift	Petronodic Haplocalcid
TUY 27	130	5R 4/2	Siltstone	Throughout	II	Eroded	Layered nodules	Petronodic Haplocalcid
TUY 28	118	10R 5/4, 10R 4/2	Mudstone	Throughout	IV	34	Hard calcified top	Ustic Petrocalcid
TUY 29	102	10R 5/4	Siltstone	Well rooted	IV	Poor exp.		Ustic Petrocalcid
TUY 30	98		Siltstone	In Bk Horizon	IV	Poor exp	Mottled rooted top	Ustic Petrocalcid
TUY 31	67		Mudstone	Throughout	II	20		Petronodic Haplocalcid
TUY 32	30		Mudstone		V	Eroded	Dark shale above	Ustic Petrocalcid
TUY 34	58	N8	Mudstone	Some observed	V	Eroded	Calcite filled voids	Ustic Petrocalcid
TUY 35	155	10R 4/2	Siltstone		II	Eroded	Evidence of carbonate veneer	Petronodic Haplocalcid
TUY 36	73	10R 6/2	Mudstone	Only in A horizon	IV	Eroded	Calcified layer with 'rooted' horizon top	Ustic Petrocalcid
TUY 37	17	5R 4/2	Mudstone		II	Eroded	V cemented mud	Ustic Petrocalcid
TUY 38	15	5R 6/2	Micrite/clay	Rooted micrite	V	Eroded	Layers of modern calcite	Ustic Petrocalcid
TUY 39	10		Siltstone		II	25	Very thin and diffuse hard to identify institute nodules	Petronodic Haplocalcid
TUY 40	180	10R 3/4, 5YR 8/1	VF sand	Only in A horizon	IV	22	Multiple horizons, some evidence of mottling	Ustic Petrocalcid
TUY 41	15	10R 4/2	Mudstone		II	23	Mottled horizons	Petronodic Haplocalcid
TUY 42	41	10R 4/2	Mudstone		III	34		Ustic Petrocalcid
TUY 43	23		Mudstone	Some evidence	II	Eroded	Mottled horizon	Petronodic Haplocalcid
TUY 44	55	10R 5/6	Mudstone		II	Eroded	V diff from anything else I have seen some modern calcification	Petronodic Haplocalcid

Horizon	Total thickness (cm)	Colour	Grain Size	Presence of Roots recorded	Nodule stage	Depth to Bk Horizon (cm)	Notes	Classification
TUY 45	22		Mudstone		III	31	Nodules very large (8-10cm)	Ustic Petrocalcid
TUY 46	80	10R 5/4	Mudstone	Deep rooting	II	10	Many alteration mottled top	Petronodic Haplocalcid

A1.4

Pedological features of paleosols from Vozdvizhenka.

Horizon	Total thickness (cm)	Colour	Grain Size	Contains a mottled horizon/ other alteration controls	Presence of Roots recorded	Nodule stage	Depth to Bk Horizon)	Notes	Classification
VOZ 14	44	10R 4/6	Mudstone	Mottled above	Some evidence	II	30	Thin gravel above and slickensides	Vertic Haplocalcid
VOZ 13	130	10R 5/4	V Fine sandstone	Mottled above	Some evidence	II	90	Above the powdery clay	Petronodic Haplocalcid
VOZ 12	128	10R 6/6	V Fine sandstone	Mottled	Some evidence	II	Eroded.	Outcrop quite weathered	Petronodic Haplocalcid
VOZ 11	140	10R 5/4	V Fine sandstone at base		Some evidence	II	Eroded.	Diffuse	Petronodic Haplocalcid
VOZ 10	23	10R 6/6	Siltstone		Some evidence	II	Eroded.	Diffuse small nodules under blocky micaceous top	Petronodic Haplocalcid
VOZ 9	45	10R 6/6	Siltstone		Some evidence	II	Eroded.	Very large 5cm top medium sand	Petronodic Haplocalcid
VOZ 8	24	10R 8/2	Siltstone	0.5/1mm reduction spots	None observed	II	Eroded.	Very large 5cm top medium sand	Petronodic Haplocalcid
VOZ 17	260	10R 4/6	V Fine sandstone Mudstone		Some evidence	II	30	Large defuse horizon - fines upwards	Petronodic Haplocalcid
VOZ 16	42	10R 4/2	Mudstone		Some evidence	II	50		Petronodic Haplocalcid
VOZ 15	159	10R 4/2	V Fine sandstone Mudstone	Mottled	Some evidence	II	40	Some mottles higher up	Petronodic Haplocalcid
VOZ 7	44	10R 6/4	Siltstone		Very fine	II	35	Top eroded	Petronodic Haplocalcid.
VOZ 6	95	10R 5/4	V Fine sandstone	Mottled	Some evidence	II	Eroded.	Overlain by micaceous horizon	Petronodic Haplocalcid

Horizon	Total thickness (cm)	Colour	Grain Size	Contains a mottled horizon/ other alteration controls	Presence of Roots recorded	Nodule stage	Depth to Bk Horizon)	Notes	Classification
VOZ 5	167	5R 4/2			Some evidence	III	Eroded.		Ustic Petrocalcid
VOZ 3	80	5R 3/4	Siltstone		Some evidence	II	Eroded.		Petronodic Haplocalcid
VOZ 2	94	5R 5/4	Fine sandstone and pebble		Some evidence	II	Eroded.	In a conglomerate lag	Petronodic Haplocalcid
VOZ 4	15	5R 5/4	V Fine sandstone and silt		None observed	II	Eroded.	top eroded	Petronodic Haplocalcid
VOZ 1	105	10R 4/2	Siltstone		Some evidence	II	Eroded.		Petronodic Haplocalcid

A1.5

Pedological features of paleosols from Krasnogor.

Horizon	Total thickness (cm)	Colour	Grain Size	Contains a mottled horizon/ other alteration controls	Presence of Roots recorded	Nodule stage	Depth to Bk Horizon (cm)	Notes	Classification
KRA 2	43	10R 5/4	VF and Fine sandstone	Mottled	Some evidence	II	22		Petronodic Haplocalcid
KRA 1	39	10R 4/6	VF and Fine sandstone	Mottled	Some evidence	II	27	Base of Triassic	Petronodic Haplocalcid
KRA 7	32	10R 6/6	Siltstone			II	18	Exposure very poor	Petronodic Haplocalcid
KRA 7a	24	10R 6/6	Siltstone			II	20		Petronodic Haplocalcid
KRA 7b	27	10R 6/6	Siltstone			II	10		Petronodic Haplocalcid
KRA 7c	206	10R 6/6	V fine sandstone			II	18		Petronodic Haplocalcid
KRA 7d	46	10R 7/4	V fine sandstone			II	31		Petronodic Haplocalcid
KRA 7e	21	10R 7/4	V fine sandstone			II	13		Petronodic Haplocalcid
KRA 7f	24	10R 7/4	V fine sandstone			II	14		Petronodic Haplocalcid
KRA 6	36	10R 5/4	Siltstone		Some evidence	IV	102	Poorly weak developed calcified tops	Ustic Petrocalcid
KRA 5	34	10R 4/2	VF sandstone and Siltstone	Reduction spots	Some evidence	III	35	Stacked sequence	Ustic Petrocalcid

Horizon	Total thickness (cm)	Colour	Grain Size	Contains a mottled horizon/ other alteration controls	Presence of Roots recorded	Nodule stage	Depth to Bk Horizon (cm)	Notes	Classification
KRA 5a	12	10R 6/6	VF sandstone and Siltstone		Some evidence	III	5	Stacked sequence	Ustic Petrocalcid
KRA 5b	25	10R 4/2	VF sandstone and Siltstone			III	16	Stacked sequence	Ustic Petrocalcid
KRA 5c	23	10R 7/4	VF sandstone and Siltstone		Some evidence	II	7	Stacked sequence	Petronodic Haplocalcid
KRA 5d	22	10R 7/4	VF sandstone and Siltstone			II	15	Stacked sequence	Petronodic Haplocalcid

A1.6

Pedological features of paleosols from Petropavlovka.

Horizon	Total thickness (cm)	Colour	Grain Size	Contains a mottled horizon/ other alteration controls	Presence of Roots recorded	Nodule stage	Depth to Bk Horizon (cm))	Notes	Classification
PET 2a	47	10R 6/6	Fine sandstone to mudstones at base	Mottled sand top	Some evidence	II	26		Ustic Calcid (Groundwater)
PET 2b	43	10R 6/6	Mudstone	Mottled in the nodular horizon	Some evidence	II	20		Ustic Calcid (Groundwater)
PET 2c	49	10R 6/6	Siltstone	Mottled top with minor mottling throughout	Some evidence	II	49		Ustic Calcid (Groundwater)
PET 1	167	5R 6/6	Mudstone	Mottled top with minor mottling throughout	Some evidence	II	51	Lower part nodules form in bands	Ustic Calcid (Groundwater)

A1.7

Pedological features of paleosols from Mescheryakovka.

Horizon	Total thickness (cm)	Colour	Grain Size	Contains a mottled horizon/ other alteration controls	Presence of Roots recorded	Nodule stage	Depth to Bk Horizon (cm)	Notes	Classification
MES 1	34	10YR 5/4	Siltstone		Some evidence	II	24	V. weakly Developed	Petronodic Haplocalcid
MES 2	34	10YR 5/4	Siltstone		Some evidence	IV	28	Lacustrine	Ustic Calcid (Lacustrine)
MES 3	169	10YR 5/4	Siltstone	Yes	Minor	II	121		Petronodic Haplocalcid
MES 4	56	10R 5/4	Siltstone	Yes	None recorded	II	43		Petronodic Haplocalcid
MES 5	127	10YR 5/4	Siltstone	Yes mottled above	Some evidence	III	45		Ustic Petrocalcid
MES 6	76	10YR 5/4	Siltstone			II	Eroded		Petronodic Haplocalcid
MES 7	108	10YR 5/4	Siltstone		Some evidence	II	Eroded		Petronodic Haplocalcid
MES 8	89	5YR 4/6	Siltstone	Pseudo - Gley	Drab root halos	II	44	Deep rooted (36cm) top strongly mottled	Vertic Haplocalcid
MES 9	37	5YR 4/6	VF sandstone	Mottled	Some evidence	II-III	Eroded	Top eroded	Ustic Petrocalcid
MES 10	32	5YR 4/6	Siltstone		Some evidence	II	Eroded	Top eroded	Petronodic Haplocalcid
MES 11	172	5YR 4/6	Mudstone	Mottled	Some evidence	II	Eroded	Pedogenic slickensides	Vertic Haplocalcid
MES 12	23	5YR 4/6	Mudstone	Pseudo - Gley	Some evidence	II-III	Eroded	Large Nodules just below erosive sand	Ustic Petrocalcid
MES 13	80	5YR 6/4	Siltstone	Mottled nodules	Drab root halos	II	16	Slickensides (calcitic)	Vertic Haplocalcid
MES 14	46	10R 6/6	Siltstone	Pseudo - Gley	Drab root halos	II	38	Large stage 2 nodules vertically orientated	Petronodic Haplocalcid
MES 15	59	5R	Siltstone	Pseudo - Gley	Drab root halos	II	Eroded	Slickensides (calcitic)	Petronodic Haplocalcid
MES 16	187	10Y 7/2	Siltstone	Pseudo - Gley	Drab root halos	II	100	Slickensides at base	Vertic Haplocalcid
MES 17	140	10R 4/2	silt	Pseudo - Gley	Drab root halos	II	Eroded	Mostly nodules scattered throughout section	Petronodic Haplocalcid

Appendix 2

Paleosol isotope data, XRD data and statistical data

(Chapter 4)

A2.1

Table of all isotope analysis from the Southern Urals of Russia. Those analyses are starting 04. (e.g. 04.8.2.f) are from the 2004 field season. No within paleosol depths were recorded in this field season so the depth recorded is the middle of the paleosol horizon. Crp = cryptocrystalline; SpC = contains sinuous veins; MCr = microcrystalline (crystals above 20μm); MCr/SpC = microcrystalline (crystals above 20μm) and contains sinuous veins. All depths to Bk horizon are uncompressed depths using a burial depth of 1.9km for the Russian sediments (Brunet *et al.* 1999) and the decompression ratio calculator proposed by Sheldon and Retallack (2001). 2004 F/S = 2004 field season, see Chapter 2.

										Micrite		Spar	
Horizon	Classification	Calcrete stage	Depth to Bk horizon (cm)	Sample	Section height (m)	Paleosol depth (m)	XRD Result	Texture	Date run	$\delta^{13}C‰$ VPDB	$\delta^{18}O‰$ VPDB	$\delta^{13}C‰$ VPDB	$\delta^{18}O‰$ VPDB
KOR 36	Petronodic Haplocalcid	II	2	SU06 KOR 36.1	211.10	0.07	Calcium Carbonate	SpC	05/09/07	-2.16	-7.60	-3.14	-8.68
				SU06 KOR 36.2	211.10	0.07	Calcite	SpC	19/09/07	-4.90	-8.88	-3.10	-9.54
				SU06 KOR 36.3	210.94	0.24	Calcite	SpC	19/09/07	-3.70	-10.91	–	–
				SU06 KOR 36.4	210.82	0.37	Quartz	SpC	19/09/07	-4.57	-11.25	–	–
				SU06 KOR 36.5	210.82	0.37	Calcite	SpC	19/09/07	-5.97	-11.77	–	–
				SU06 KOR 36.6	210.82	0.37	Quartz	SpC	19/09/07	-6.13	-11.09	–	–
KOR 33	Petronodic Haplocalcid/ Ustic Calcid (Lacustrine)	II	3	04.8.2.f	199.33	0.16	Calcite, magnesian	SpC	24/03/05	-2.18	-7.36	–	–
				04.8.2.f	199.33	0.16	Calcite, magnesian	SpC	10/05/06	-2.69	-9.92	–	–
				04.8.2.f	199.33	0.16	Calcite, magnesian	SpC	10/05/06	-2.84	-9.84	–	–
				SU06 KOR 33.1	199.41	0.16	Calcite, magnesian	SpC	05/09/07	-2.87	-8.32	-0.26	-9.55
				SU06 KOR 33.2	199.41	0.16	Calcium Carbonate	SpC	05/09/07	-1.00	-7.57	-0.75	-8.71
				SU06 KOR 33.3	199.41	0.16	Calcite	SpC	05/09/07	-0.91	-8.07	-0.88	-8.35
KOR 37	Petronodic Haplocalcid	II	9	SU06 KOR 37.1	196.58	0.17	calcite	MCr	19/09/07	-1.04	-9.34	–	–
				SU06 KOR 37.2	196.58	0.17	Quartz	MCr	19/09/07	-1.40	-10.85	–	–
				SU06 KOR 37.3	196.58	0.17	calcite	MCr	19/09/07	-1.53	-9.39	–	–
				SU06 KOR 37.4	196.12	0.68	calcite	SpC	19/09/07	-0.50	-10.01	–	–
				SU06 KOR 37.5	196.12	0.68	calcite	SpC	19/09/07	-0.27	-9.54	v	

Horizon	Classification	Calcrete stage	Depth to Bk horizon (cm)	Sample	Section height (m)	Paleosol depth (m)	XRD Result	Texture	Date run	Micrite		Spar	
										$\delta^{13}C‰$ VPDB	$\delta^{18}O‰$ VPDB	$\delta^{13}C‰$ VPDB	$\delta^{18}O‰$ VPDB
KOR 34	Petronodic	II	eroded	SU06 KOR 34.1	199.46	0.02	Calcite	MCr/SpC	05/09/07	-0.45	-7.64	0.39	-8.04
	Haplocalcid			SU06 KOR 34.2	199.40	0.09	Calcite	MCr/SpC	05/09/07	-0.10	-7.46	-0.83	-8.40
				SU06 KOR 34.3	199.40	0.22	Calcite	MCr/SpC	05/09/07	-0.56	-7.59	-0.22	-8.20
				SU06 KOR 34.4	199.28	0.22	Calcite	MCr/SpC	05/09/07	-0.12	-7.29	–	–
				SU06 KOR 34.5	199.35	0.14	Calcite, magnesian	MCr/SpC	05/09/07	-0.08	-7.19	-0.48	-10.34
				SU06 KOR 34.6	199.35	0.14	Calcite	MCr/SpC	05/09/07	-0.38	-7.22	-1.21	-8.14
				SU06 KOR 34.7	199.35	0.14	Calcite	MCr/SpC	05/09/07	-0.42	-7.21	-2.35	-8.96
KOR 32	Petronodic	II	8	04.8.2.e	198.01	0.17	Calcite	MCr	10/05/06	-1.23	-9.20	–	–
	Haplocalcid			04.8.2.e.i	198.01	0.17	Calcite	MCr	10/05/06	-0.92	-9.48	–	–
				04.8.2.e.ii	198.01	0.17	Calcite	MCr	10/05/06	-1.23	-9.20	–	–
				04.8.2.e.iii	198.01	0.17	Calcite	MCr/SpC	10/05/06	-0.95	-9.21	–	–
				04.8.2.e.iv	198.01	0.17	Calcite	MCr	10/05/06	-0.77	-9.31	–	–
				SU06 KOR 32.2	198.08	0.16	Calcite	MCr	05/09/07	-0.04	-7.01	-2.93	-8.69
				SU06 KOR 32.7	197.95	0.31	Calcite	MCr/SpC	05/09/07	-0.27	-7.15	-2.55	-8.71
				SU06 KOR 32.8	197.95	0.31	Calcite	MCr/SpC	05/09/07	-0.11	-7.55	0.12	-8.03
KOR 1a	Ustic	III	23	04.8.1.ac*	171.16	0.50	–	SpC	24/04/5	-0.07	0.50	–	–
	Petrocalcid			04.8.1.ac.I	171.16	0.50	–	SpC	10/05/06	-0.20	0.52	–	–
				04.8.1.ac.II	171.16	0.50	–	SpC	10/05/06	0.14	-1.03	–	–
				SU06 KOR 1.10	170.46	0.94	Dolomite	MCr	24/03/05	0.08	0.08	–	–
				SU06 KOR 1.7	170.46	0.94	Dolomite	SpC	24/03/05	0.18	0.38	-0.09	0.55
				SU06 KOR 1.8	170.46	0.94	Dolomite	SpC	25/08/07	-0.09	0.07	–	–
				SU06 KOR 1.9	170.46	0.94	Dolomite	SpC	25/08/07	-0.27	-1.25	-2.90	-8.85
KOR 2	Petronodic	II	25	SU06 KOR 2.1	170.38	0.11	Dolomite	Crp	25/08/07	-0.16	1.16	–	–
	Haplocalcid			SU06 KOR 2.2	169.99	0.32	Dolomite	Crp	25/08/07	-0.74	0.61	–	–
				SU06 KOR 2.3	169.99	0.32	Dolomite	Crp	25/08/07	-1.79	-1.33	–	–
				SU06 KOR 2.4	169.85	0.47	Dolomite	MCr/SpC	25/08/07	-0.86	-3.26	-1.09	-9.23

Horizon	Classification	Calcrete stage	Depth to Bk horizon (cm)	Sample	Section height (m)	Paleosol depth (m)	XRD Result	Texture	Date run	Micrite		Spar	
										$\delta^{13}C‰$ VPDB	$\delta^{18}O‰$ VPDB	$\delta^{13}C‰$ VPDB	$\delta^{18}O‰$ VPDB
				SU06 KOR 2.5	169.85	0.47	Dolomite	Crp	25/08/07	-1.57	-0.12	–	–
				SU06 KOR 2.6	169.69	0.64	Dolomite	SpC	25/08/07	-1.37	-0.01	-1.16	-3.07
				SU06 KOR 2.7	169.69	0.64	Dolomite	Crp	25/08/07	-1.43	0.13	–	–
				SU06 KOR 2.8	169.55	0.80	Dolomite	SpC	25/08/07	-1.06	0.06	-1.46	-4.41
				SU06 KOR 2.9	169.55	0.80	Dolomite	Crp	25/08/07	-1.36	-0.20	–	–
KOR 8	Ustic Petrocalcid	IV	27	04.8.1.aa	166.13	0.15	–	SpC	24/03/05	-1.05	-2.49	–	–
KOR 9	Petronodic	II	Eroded	SU06 KOR 9.1	164.92	0.11	Dolomite	SpC	25/08/07	-0.44	-0.03	-2.03	-6.10
	Haplocalcid			SU06 KOR 9.2	164.92	0.11	Dolomite	Crp	25/08/07	-0.64	-0.57	–	–
				SU06 KOR 9.3	164.92	0.11	Dolomite	Crp	25/08/07	-0.33	0.26	–	–
KOR 4	Vertic Petrocalcid	V	18	04.8.1.w	157.95	0.57	Dolomite	SpC	24/03/05	-1.01	0.07	–	–
KOR 5	Vertic	II	Eroded	04.8.1.z	162.86	0.42	–	SpC	24/03/05	-0.79	-1.23	–	–
	Haplocalcid			SU06 KOR 5.1	162.91	0.26	Quartz	MCr	25/08/07	-0.41	0.33	–	–
				SU06 KOR 5.2	162.90	0.27	Dolomite	SpC	25/08/07	-0.81	0.17	-1.57	-2.83
				SU06 KOR 5.3	162.90	0.27	Dolomite	Crp	25/08/07	-0.94	-0.40	–	–
				SU06 KOR 5.4	162.77	0.42	Dolomite	SpC	25/08/07	-1.63	-0.72	-2.55	-5.56
				SU06 KOR 5.5	162.77	0.42	Dolomite	SpC	25/08/07	-1.01	-0.80	-2.41	-4.19
KOR 6	Petronodic	II		SU06 KOR 6.2	163.04	0.58	Dolomite	SpC	25/08/07	-1.31	0.36	-2.96	-4.15
	Haplocalcid			SU06 KOR 6.3	162.88	0.40	Dolomite	SpC	25/08/07	-1.12	0.09	-3.60	-7.09
				SU06 KOR 6.4	162.88	0.40	Dolomite	SpC	25/08/07	-1.55	-1.61	-9.20	-10.94
				SU06 KOR 6.5	162.78	0.29	Dolomite	SpC	25/08/07	-1.36	-0.11	-8.63	-10.18
				SU06 KOR 6.6	162.78	0.29	Dolomite	SpC	25/08/07	-1.29	-0.24	-2.72	-4.84
				SU06 KOR 6.7	162.63	0.13	Dolomite	SpC	25/08/07	-1.21	-0.09	-2.71	-2.18
				SU06 KOR 6.8	162.63	0.13	Dolomite	SpC	25/08/07	-1.07	0.00	-3.46	-5.13
KOR 10	Ustic Calcid	III		04.8.1.x	159.40	0.67	–	MCr/SpC	24/03/05	-1.23	-0.77	–	–
	(Lacustrine)			SU06 KOR 10.1	159.86	0.04	–	MCr	25/08/07	-1.18	0.36	-3.92	-7.29
				SU06 KOR 10.11	158.97	1.00	Dolomite	MCr	25/08/07	-1.73	-0.24	-2.48	-3.65

Horizon	Classification	Calcrete stage	Depth to Bk horizon (cm)	Sample	Section height (m)	Paleosol depth (m)	XRD Result	Texture	Date run	Micrite		Spar	
										$\delta^{13}C‰$ VPDB	$\delta^{18}O‰$ VPDB	$\delta^{13}C‰$ VPDB	$\delta^{18}O‰$ VPDB
				SU06 KOR 10.12	158.97	1.00	Dolomite	MCr	25/08/07	-1.57	-0.56	-1.93	-1.78
				SU06 KOR 10.2	159.72	0.19	Dolomite	MCr/SpC	25/08/07	-2.06	-3.05	-2.46	-4.74
				SU06 KOR 10.3	159.72	0.19	Dolomite	MCr	25/08/07	-1.45	-0.06	-3.98	-8.23
				SU06 KOR 10.4	159.59	0.33	Dolomite	MCr	25/08/07	-1.38	-0.56	-2.67	-2.43
				SU06 KOR 10.5	159.59	0.33	Dolomite	SpC	25/08/07	-1.34	0.46	-3.42	-6.86
				SU06 KOR 10.6	159.40	0.53	Quartz	SpC	25/08/07	-2.05	-0.55		
				SU06 KOR 10.7	159.40	0.53	Dolomite	MCr	25/08/07	-1.55	-0.28	-1.99	-3.31
				SU06 KOR 10.8	159.10	0.86	Dolomite	SpC	25/08/07	-1.84	-0.83	-2.48	-6.78
KOR 11	Ustic Petrocalcid	IV	18	04.8.1.w	157.95	0.41	–	SpC	29/03/05	-1.01	0.07	–	–
KOR 12	Petronodic	II	36	04.8.1.v*	157.13	0.43	–	Crp	24/03/05	-0.89	0.24	–	–
	Haplocalcid			04.8.1.v.I	157.13	0.43	–	Crp	10/05/06	-0.85	1.38	–	–
				04.8.1.v.II	157.13	0.43	–	SpC	10/05/06	-0.76	1.08	–	–
				SU06 KOR 12.1	157.17	0.43	Dolomite	SpC	25/08/07	-0.77	0.63	–	–
				SU06 KOR 12.3	157.17	0.43	Dolomite	SpC	25/08/07	-0.71	0.47	-1.02	1.29
KOR 13	Ustic Petrocalcid	IV	Eroded	04.8.1.u	156.08	0.15	–	Crp	24/03/05	-0.25	0.31	–	–
KOR 14	Ustic Petrocalcid	III	26	04.8.1.t	154.35	0.41	–	SpC	24/03/05	-1.13	-0.42	–	–
				SU06 KOR 14.10	154.65	0.41	Dolomite	SpC	10/09/07	-1.67	-2.04	–	–
				SU06 KOR 14.11	154.65	0.41	Dolomite	SpC	10/09/07	-1.14	-0.02	–	–
				SU06 KOR 14.14	155.03	0.41	Dolomite	SpC	10/09/07	-1.21	0.24	-2.07	-2.50
				SU06 KOR 14.15	155.03	0.41	Dolomite	SpC	10/09/07	-1.28	0.11	-2.92	-10.58
KOR 14a	Petronodic	II	8	SU06 KOR 14.8	154.35	0.13	Dolomite	SpC	10/09/07	-1.28	0.25	-5.49	-4.02
	Haplocalcid			SU06 KOR 14.9	154.35	0.13	Dolomite	SpC	10/09/07	-1.41	0.25	–	–
KOR 14b	Petronodic	II	18	04.8.1.s	153.83	0.25	–	SpC	24/03/05	-1.66	-0.34	–	–
	Haplocalcid			SU06 KOR 14.1	153.83	0.25	Dolomite	SpC	25/08/07	-2.20	-1.36	-2.67	-0.69
KOR 23	Petronodic	III	Eroded	04.8.1.r*	144.56	0.15	Dolomite	MCr/SpC	24/03/05	-2.26	-1.96	–	–

Horizon	Classification	Calcrete stage	Depth to Bk horizon (cm)	Sample	Section height (m)	Paleosol depth (m)	XRD Result	Texture	Date run	Micrite		Spar	
										$\delta^{13}C‰$ VPDB	$\delta^{18}O‰$ VPDB	$\delta^{13}C‰$ VPDB	$\delta^{18}O‰$ VPDB
	Haplocalcid			04.8.1.r.I	144.56	0.15	Dolomite	SpC	10/05/06	-3.30	-1.55	–	–
				04.8.1.r.II	144.56	0.15	Dolomite	SpC	10/05/06	-4.36	-1.73	–	–
				04.8.1.r.III	144.56	0.15	Dolomite	SpC	10/05/06	-4.14	-1.95	–	–
				SU06 KOR 23.1	144.76	0.05	Calcite, magnesian	Crp	05/09/07	-10.81	-11.55	–	–
				SU06 KOR 23.2	144.76	0.05	Calcite, magnesian	SpC	05/09/07	-10.56	-11.05	-5.48	-9.26
				SU06 KOR 23.3	144.57	0.26	Dolomite	Crp	05/09/07	-4.75	-0.68	–	–
				SU06 KOR 23.4	144.57	0.26	Dolomite	Crp	05/09/07	-4.09	-1.03	–	–
KOR 22	Petronodic	II	64.5	04.8.1.q	143.54	0.41	–	SpC	05/04/06	-6.46	-9.84	–	–
	Haplocalcid			04.8.1.q.I	143.54	0.41	–	SpC	10/05/06	-10.71	-12.14	–	–
				04.8.1.q.II	143.54	0.41	–	SpC	10/05/06	-10.03	-11.30	–	–
				04.8.1.q.III	143.54	0.41	–	SpC	10/05/06	-6.73	-4.91	–	–
				SU06 KOR 22.1	143.26	0.13	Calcite ($CaCO_3$)	SpC	05/09/07	-4.68	-3.70	-4.98	-4.37
				SU06 KOR 22.10	143.78	0.70	Calcite	Crp	05/09/07	-11.03	-10.99	–	–
				SU06 KOR 22.11	143.78	0.70	Calcite, magnesian	Crp	05/09/07	-10.53	-10.12	–	–
				SU06 KOR 22.12	143.89	0.82	Calcite	Crp	05/09/07	-11.06	-11.45	–	–
				SU06 KOR 22.13	143.89	0.82	Calcite	Crp	05/09/07	-6.44	-6.38	–	–
				SU06 KOR 22.14	143.89	0.82	Calcite, magnesian	Crp	05/09/07	-9.70	-8.96	–	–
				SU06 KOR 22.2	143.26	0.13	Calcite (Mg, $CaCO_3$)	Crp	05/09/07	-9.97	-11.30	-4.44	-6.79
				SU06 KOR 22.4	143.26	0.13	Calcite, magnesian	Crp	05/09/07	-10.76	-11.00	-4.24	-4.88
				SU06 KOR 22.5	143.26	0.13	Quartz	SpC	05/09/07	-4.90	-5.60	–	–
				SU06 KOR 22.6	143.47	0.36	Calcite	Crp	05/09/07	-4.96	-4.66	–	–
				SU06 KOR 22.7	143.47	0.36	Calcite	SpC	05/09/07	-10.34	-10.49	–	–
				SU06 KOR 22.8	143.64	0.55	Calcite	Crp	05/09/07	-4.90	-5.57	-10.87	-12.91
KOR 21	Ustic Petrocalcid	II	Eroded	04.8.1.p	141.58	0.23	Dolomite	SpC	24/03/05	-0.69	-0.18	–	–
				SU06 KOR 21.10	141.35	0.59	Dolomite	MCr/SpC	10/09/07	-1.33	0.73	-3.20	-6.34
				SU06 KOR 21.4	141.67	0.24	Dolomite	SpC	10/09/07	-3.57	-5.06	–	–

Horizon	Classification	Calcrete stage	Depth to Bk horizon (cm)	Sample	Section height (m)	Paleosol depth (m)	XRD Result	Texture	Date run	Micrite		Spar	
										$\delta^{13}C‰$ VPDB	$\delta^{18}O‰$ VPDB	$\delta^{13}C‰$ VPDB	$\delta^{18}O‰$ VPDB
				SU06 KOR 21.5	141.67	0.24	Dolomite	SpC	10/09/07	-2.47	-1.81	-4.31	-7.74
				SU06 KOR 21.6	141.55	0.37	Quartz	SpC	10/09/07	-3.50	-3.50	-4.17	-5.46
				SU06 KOR 21.7	141.55	0.37	Dolomite	MCr/SpC	10/09/07	-1.32	-1.09	-4.87	-5.90
				SU06 KOR 21.8	141.35	0.59	Dolomite	SpC	10/09/07	-0.39	1.03	-4.09	-9.31
				SU06 KOR 21.9	141.35	0.59	Dolomite	SpC	10/09/07	-1.51	0.64	-3.06	-3.00
KOR 21a	Ustic Petrocalcid	II	Eroded	SU06 KOR 21.1	141.80	0.10	Calcite (Mg)	SpC	10/09/07	-4.04	-5.27	-5.08	-6.45
				SU06 KOR 21.2	141.80	0.10	Calcite, magnesian	MCr/SpC	10/09/07	-2.32	-4.10	-3.99	-7.48
				SU06 KOR 21.3	141.80	0.10	Calcite ($CaCO_3$)	MCr/	10/09/07	-3.72	-5.08	-4.17	-7.37
KOR 15	Petronodic	II	17	04.8.1.o	139.97	0.39	–	SpC	29/03/05	-0.91	-1.33	–	–
	Haplocalcid			SU06 KOR 15.2	140.08	0.23	Dolomite	MCr/SpC	10/09/07	-0.46	0.11	-1.09	-0.16
				SU06 KOR 15.3	140.08	0.23	Dolomite	SpC	10/09/07	-0.68	0.07	-2.94	-8.89
				SU06 KOR 15.4	140.08	0.23	Dolomite	SpC	10/09/07	-0.52	0.17	–	–
				SU06 KOR 15.5	139.96	0.36	Dolomite	SpC	10/09/07	-0.76	-0.88	-3.54	-13.39
				SU06 KOR 15.6	139.96	0.36	Dolomite	SpC	10/09/07	-1.85	-4.07	-1.78	-2.90
				SU06 KOR 15.7	139.79	0.55	Dolomite	SpC	10/09/07	-0.71	-1.20	-1.74	-3.99
				SU06 KOR 15.8	139.79	0.55	Dolomite	MCr/SpC	10/09/07	-1.12	-1.03	-1.18	-1.22
				SU06 KOR 15.9	139.79	0.55	Dolomite	SpC	10/09/07	-0.48	-0.39	-3.27	-10.12
KOR 16	Petronodic	II	13	04.8.1.n*	136.10	0.22	–	SpC	10/09/07	-2.20	-6.16	–	–
	Haplocalcid			SU06 KOR 16.10	136.20	0.33	Calcite, magnesian	SpC	10/09/07	-2.97	-8.76	-3.44	-8.78
				SU06 KOR 16.5	136.20	0.33	Calcite, magnesian	SpC	10/09/07	-4.28	-5.64	-3.33	-6.52
				SU06 KOR 16.6	136.20	0.33	Calcite, magnesian	SpC	10/09/07	-3.89	-5.15	-2.90	-6.32
				SU06 KOR 16.7	136.20	0.33	Calcite	SpC	10/09/07	-3.42	-5.50	-3.13	-7.15
				SU06 KOR 16.8	136.20	0.33	Calcite, magnesian	SpC	10/09/07	-4.23	-5.18	-3.66	-7.06
				SU06 KOR 16.9	136.20	0.33	Calcite, magnesian	SpC	10/09/07	-3.45	-6.96	–	–
KOR 16 a	Petronodic	II	14	SU06 KOR 16.1	135.97	0.22	Calcite, magnesian	SpC	10/09/07	-3.83	-5.86	-4.03	-6.41
	Haplocalcid			SU06 KOR 16.2	135.97	0.22	Calcite, magnesian	SpC	10/09/07	-4.02	-4.16	-3.47	-6.84

Horizon	Classification	Calcrete stage	Depth to Bk horizon (cm)	Sample	Section height (m)	Paleosol depth (m)	XRD Result	Texture	Date run	Micrite		Spar	
										$\delta^{13}C‰$ VPDB	$\delta^{18}O‰$ VPDB	$\delta^{13}C‰$ VPDB	$\delta^{18}O‰$ VPDB
				SU06 KOR 16.3	135.97	0.22	Calcite	MCr	10/09/07	-4.54	-5.51	-3.05	-7.57
				SU06 KOR 16.4	135.97	0.22	Calcite, magnesian	SpC	10/09/07	-4.68	-5.08	-3.10	-7.16
KOR 17	Ustic Calcid	III	24	04.8.1.m*	136.10	0.30	–	MCr	29/03/05	-0.01	-3.96	–	–
	(Lacustrine)			SU06 KOR 17.2	135.68	0.24	Calcite	MCr	10/09/07	-0.02	-1.70	–	–
				SU06 KOR 17.3	135.68	0.24	Dolomite	MCr	10/09/07	0.75	-0.54	-0.75	-2.36
KOR 18	Ustic Petrocalcid	III	12	04.8.1.I	128.42	0.19	Dolomite	Crp	29/03/05	0.86	0.82	–	–
				04.8.1.I.I	128.42	0.19	Dolomite	Crp	10/05/06	2.60	2.07	–	–
				04.8.1.I.II	128.42	0.19	Dolomite	Crp	10/05/06	2.52	2.52	–	–
				04.8.1.I.III	128.42	0.19	Dolomite	Crp	10/05/06	2.53	2.20	–	–
KOR 19	Ustic Petrocalcid	V	21	04.8.1.k	123.57	0.00	–	MCr/SpC	29/03/05	-0.04	-0.56	–	–
KOR 20	Ustic Calcid(Lacustrine)	IV	59	04.8.1.j	116.70	0.00	–	SpC	29/03/05	-1.01	0.30	–	–
KOR 24		III	15	04.8.1.i	114.34	0.25	Dolomite	MCr	10/05/06	-2.16	-5.97	–	–
				04.8.1.i.I	114.34	0.25	–	MCr	10/05/06	-2.69	-6.61	–	–
				04.8.1.i.II	114.34	0.25	–	MCr	10/05/06	-3.23	-7.56	–	–
				04.8.1.i.III	114.34	0.25	–	MCr	10/05/06	-3.67	-8.50	–	–
				SU06 KOR 24.5	114.23	0.36	Calcite	MCr	05/09/07	0.31	-5.49	–	–
				SU06 KOR 24.6	114.23	0.36	Calcite, magnesian	MCr	05/09/07	0.68	-4.70	–	–
KOR 25	Ustic Petrocalcid	II	21	SU06 KOR 25.1	104.66	0.27	Calcite	SpC	05/09/07	-10.18	-11.31	-9.05	-12.24
				SU06 KOR 25.3	104.66	0.27	–	Crp	05/09/07	-10.18	-11.24	–	–
				SU06 KOR 25.4	104.66	0.27	–	Crp	05/09/07	-9.90	-11.29	–	–
				SU06 KOR 25.5	104.66	0.27	Calcite, magnesian	Crp	05/09/07	-9.88	-11.01	–	–
KOR 26	Ustic Calcid(Lacustrine)	IV	41	04.8.1.g*	98.73	0.00	Calcite	SpC	29/03/05	-0.65	-6.04	–	–
KOR 27	Petronodic	II	26	04.8.1.f*	98.59	0.31	Calcite	SpC	29/03/05	-1.05	-4.10	–	–
	Haplocalcid			SU06 KOR 27.2	98.59	0.31	Calcite	SpC	28/11/07	0.46	-8.84	–	–
				SU06 KOR 27.4	98.59	0.31	Quartz	SpC	28/11/07	0.36	-9.26	–	–

Horizon	Classification	Calcrete stage	Depth to Bk horizon (cm)	Sample	Section height (m)	Paleosol depth (m)	XRD Result	Texture	Date run	Micrite		Spar	
										$\delta^{13}C‰$ VPDB	$\delta^{18}O‰$ VPDB	$\delta^{13}C‰$ VPDB	$\delta^{18}O‰$ VPDB
KOR 28	Ustic Petrocalcid	IV	Eroded	04.8.1.e	95.56	0.08	Dolomite	SpC	29/03/05	-1.50	-2.38	–	–
KOR 29	Ustic Petrocalcid	III	Eroded	04.8.1.c	88.20	0.11	Dolomite	Crp	10/05/06	-1.52	-0.75	–	–
				04.8.1.c.I	88.20	0.11	Dolomite	Crp	10/05/06	-1.90	1.45	–	–
				04.8.1.c.II	88.20	0.11	Dolomite	Crp	10/05/06	-1.90	0.38	–	–
				04.8.1.c.III	88.20	0.11	Dolomite	Crp	10/05/06	-2.64	-0.37	–	–
KOR 31	()	II	Eroded	04.8.1.b*	79.51	0.23	Calcite	SpC	10/05/06	-2.64	-2.64	–	–
	Haplocalcid			04.8.1.b.I	79.51	0.23	Calcite	SpC	10/05/06	-4.11	-5.85	–	–
				04.8.1.b.II	79.51	0.23	Calcite	SpC	10/05/06	-4.42	-5.54	–	–
				04.8.1.b.III	79.51	0.23	Calcite	SpC	10/05/06	-4.48	-5.64	–	–
				SU06 KOR 31.1	79.51	0.23	Calcite, magnesian	SpC	05/09/07	-4.61	-5.17	–	–
				SU06 KOR 31.2	79.51	0.23	Calcite	SpC	05/09/07	-4.49	-4.17	–	–
				SU06 KOR 31.5	79.51	0.23	Calcite	SpC	05/09/07	-5.15	-6.95	-5.13	-8.09
KOR 35	Petronodic	II	Eroded	04.8.1.a	79.22	0.25	–	SpC	29/03/05	-3.07	-6.00	–	–
	Haplocalcid			SU06 KOR 35.1	79.22	0.25	Calcite, magnesian	SpC	05/09/07	-4.62	-6.79	-8.42	-8.94
				SU06 KOR 35.3	79.22	0.25	Quartz	Crp	05/09/07	-12.44	-9.76	–	–
				SU06 KOR 35.5	79.22	0.25	Calcite, syn	SpC	05/09/07	-7.07	-8.79	-8.50	-9.88

Sambullak

Horizon	Classification	Calcrete stage	Depth to Bk horizon (cm)	Sample	Section height (m)	Paleosol depth (m)	XRD Result	Texture	Date run	Micrite		Spar	
										$\delta^{13}C‰$ VPDB	$\delta^{18}O‰$ VPDB	$\delta^{13}C‰$ VPDB	$\delta^{18}O‰$ VPDB
SAM 1	Vertic	II	31	04.7.24.u	131.13	0.52	–	SpC	29/03/06	-3.00	-10.03	–	–
	Haplocalcid			04.7.24.u.I	131.13	0.52	–	SpC	10/05/06	-5.88	-14.15	–	–
				04.7.24.u.II	131.13	0.52	–	SpC	10/05/06	-5.00	-12.82	–	–
				SU06 SAM 1.1	131.13	0.52	Calcite, magnesian	SpC	11/11/07	-4.12	-8.81	-2.80	-8.21
				SU06 SAM 1.2	131.13	0.52	Calcite	SpC	11/11/07	-2.26	-7.50	-2.08	-7.09

Horizon	Classification	Calcrete stage	Depth to Bk horizon (cm)	Sample	Section height (m)	Paleosol depth (m)	XRD Result	Texture	Date run	Micrite		Spar	
										$\delta^{13}C‰$ VPDB	$\delta^{18}O‰$ VPDB	$\delta^{13}C‰$ VPDB	$\delta^{18}O‰$ VPDB
				SU06 SAM 1.3	131.13	0.52	Calcite	SpC	11/11/07	-6.23	-13.07	-5.23	-11.26
				SU06 SAM 1.4	131.13	0.52	Calcite	SpC	11/11/07	-5.89	-8.91	-5.23	-11.33
				SU06 SAM 1.5	131.13	0.52	Calcite, magnesian	SpC	11/11/07	-6.68	-11.38	-4.30	-8.45
SAM 4	Petronodic	II	eroded	04.7.24.t	131.1	0.35	–	MCr	29/03/06	-3.31	-9.50	–	–
	Haplocalcid			04.7.24.t.I	131.1	0.35	–	MCr	10/05/06	-4.74	-7.95	–	–
				04.7.24.t.II	131.1	0.35	–	MCr	10/05/06	-2.71	-7.99	–	–
				04.7.24.t.III	131.1	0.35	–	MCr	10/05/06	-0.04	-7.57	–	–
				SU06 SAM 4.3	130.22	0.53	Calcite, magnesian	MCr	12/11/07	-6.00	-12.98	–	–
				SU06 SAM 4.4	130.14	0.61	Calcite	MCr	12/11/07	-5.55	-12.77	–	–
2004F/S		III?		04.7.24.r	123.68		–	SpC	21/03/05	-4.01	-9.54	–	–
SAM 3	Vertic	III	49	04.7.24.s	122.62	0.325	Calcite	MCr	21/03/05	-3.77	-9.29	–	–
	Haplocalcid			SU06 SAM 3.1	122.62	0.83	Calcite, magnesian	MCr	11/11/07	-7.21	-12.93	–	–
				SU06 SAM 3.2	122.62	0.83	Calcite	SpC	11/11/07	-7.76	-13.64	-8.18	-12.94
				SU06 SAM 3.3	122.33	1.12	Dolomite	SpC	11/11/07	-5.00	-5.94	–	–
				SU06 SAM 3.4	122.33	1.12	Dolomite	SpC	11/11/07	-5.62	-8.15	–	–
				SU06 SAM 3.5	122.33	1.12	Dolomite	SpC	11/11/07	-4.19	-4.50	–	–
2004F/S		IV		04.7.24.q	121.96		Calcite, magnesian	SpC	21/03/05	-3.62	-6.80	–	–
SAM 2	Ustic Calcid	II	Lacust.	SU06 SAM 2.1	114.84	0.11	Calcite, magnesian	SpC	12/11/07	-5.71	-7.69	–	–
	(Lacustrine)			SU06 SAM 2.2	114.72	0.23	Dolomite	SpC	12/11/07	-2.48	-5.52	-4.24	-10.66
				SU06 SAM 2.3	114.51	0.44	Calcite, magnesian	SpC	12/11/07	-3.10	-5.69	–	–
				04.7.24.p	114.48	0.35	Calcite	SpC	21/03/05	-3.13	-9.61	-4.68	-11.92
				SU06 SAM 2.4	114.48	0.47	Calcite, magnesian	SpC	12/11/07	-5.92	-13.53	-4.76	-11.88
SAM 12	Petronodic	II	14	SU06 SAM 12.1	114.38	0.17	Calcite	Crp	11/11/07	-5.83	-9.78	–	–
	Haplocalcid			SU06 SAM 12.2	114.38	0.17	Dolomite	MCr	11/11/07	-5.49	-9.90	–	–
SAM 10		II	42	SU06 SAM 10.8	123.28	0.555	Dolomite	SpC	12/11/07	-4.31	-5.93	–	–

Horizon	Classification	Calcrete stage	Depth to Bk horizon (cm)	Sample	Section height (m)	Paleosol depth (m)	XRD Result	Texture	Date run	Micrite		Spar	
										$\delta^{13}C‰$ VPDB	$\delta^{18}O‰$ VPDB	$\delta^{13}C‰$ VPDB	$\delta^{18}O‰$ VPDB
	Vertic Haplocalcid			SU06 SAM 10.9	123.28	0.555	Calcite, magnesian	SpC	12/11/07	-4.53	-7.72	-4.65	-6.03
				SU06 SAM 10.7	123.07	0.805	Dolomite	SpC	12/11/07	-4.70	-6.09	–	–
				SU06 SAM 10.6	122.94	0.99	Dolomite	SpC	12/11/07	-3.93	-4.68	-5.32	-9.02
SAM 10a	Vertic	II	24	SU06 SAM 10.5	122.6	0.27	Dolomite	SpC	11/11/07	-3.76	-3.75	-5.48	-11.39
	Haplocalcid			SU06 SAM 10.3	122.44	0.39	Dolomite	SpC	11/11/07	-3.61	-3.62	-4.49	-6.00
				SU06 SAM 10.4	122.44	0.41	Dolomite	Crp	11/11/07	-3.39	-2.52	–	–
				SU06 SAM 10.2	122.3	0.54	Dolomite	SpC	11/11/07	-3.93	-3.85	-7.45	-6.57
				SU06 SAM 10.1	121.89	1	Dolomite	SpC	11/11/07	-4.01	-3.41	-6.67	-6.36
SAM 9	Petronodic	II	80	04.7.24.m	102.48	0.65	Dolomite	MCr	21/03/05	-1.75	-2.39	–	–
	Haplocalcid			SU06 SAM 9.3	102.48	0.81	Dolomite	Crp	12/11/07	-4.55	-5.49	-6.00	-11.34
				SU06 SAM 9.4	102.48	0.81	Dolomite	SpC	12/11/07	-5.18	-5.33	–	–
				SU06 SAM 9.2	102.14	0.47	Dolomite	SpC	12/11/07	-4.92	-5.14	-5.20	-5.36
SAM 8	Petronodic	II	18	SU06 SAM 8.5	98.61	0.49	Calcite	SpC	11/11/07	-6.31	-8.55	-5.51	-11.00
	Haplocalcid			04.7.24.l	98.43	0.5	Dolomite	SpC	21/03/05	-2.22	-3.52	–	–
				SU06 SAM 8.2	98.43	0.31	Calcite	SpC	11/11/07	-5.24	-7.61	-5.47	-9.65
				SU06 SAM 8.3	98.43	0.31	Calcite	SpC	11/11/07	-6.00	-8.32	-7.65	-10.20
				SU06 SAM 8.4	98.43	0.31	Calcite, magnesian	Crp	11/11/07	-5.74	-8.33	–	–
				SU06 SAM 8.1	98.27	0.15	Calcite, magnesian	SpC	11/11/07	-5.57	-7.45	-7.84	-9.83
SAM 5a	Ustic	III	25	04.7.24.k	98.13	0.72	Dolomite	MCr	21/03/05	-2.51	-3.67	–	–
	Petrocalcid			04.7.24.k.I	98.13	0.72	Dolomite	MCr	10/05/06	-3.86	-4.73	–	–
				04.7.24.k.II	98.13	0.72	Dolomite	MCr	10/05/06	-4.46	-5.03	–	–
				04.7.24.k.III	98.13	0.72	Dolomite	MCr	10/05/06	-4.17	-5.00	–	–
SAM 20	Petronodic	II	27	04.7.24.j	87.76	0.36	Dolomite	Crp	21/03/05	-2.47	-3.69	–	–
	Haplocalcid			SU06 SAM 20.2	87.76	0.36	Dolomite	Crp	12/11/07	-3.77	-4.85	–	–
				SU06 SAM 20.3	87.76	0.36	Dolomite	SpC	12/11/07	-5.00	-6.90	–	–
				SU06 SAM 20.4	87.76	0.36	Dolomite	SpC	12/11/07	-3.93	-5.26	-4.27	-5.93

Horizon	Classification	Calcrete stage	Depth to Bk horizon (cm)	Sample	Section height (m)	Paleosol depth (m)	XRD Result	Texture	Date run	Micrite		Spar	
										$\delta^{13}C$‰ VPDB	$\delta^{18}O$‰ VPDB	$\delta^{13}C$‰ VPDB	$\delta^{18}O$‰ VPDB
				SU06 SAM 20.5	87.76	0.36	Dolomite	SpC	12/11/07	-3.71	-4.69	-5.45	-6.72
SAM 19a	Ustic Petrocalcid	III	12	04.7.24.i	91.88	0.46	Dolomite	SpC	21/03/05	-2.44	-3.06	–	–
SAM 18	Ustic Petrocalcid	IV	17	04.7.24.h	90.53	0.315	Dolomite	SpC	21/03/05	-2.62	-3.83	–	–
2004F/S		IV		04.7.24.g		0.125	Dolomite	SpC	21/03/05	-2.04	-2.58	–	–
2004F/S		IV		04.7.24.f		0.325	Dolomite	MCr/SpC	21/03/05	-1.94	-2.62	–	–
SAM 17	Petronodic Haplocalcid	II	39	SU06 SAM 17.1	80.435	0.065	Calcite	SpC	11/11/07	-5.98	-8.61	–	–
				SU06 SAM 17.2	80.435	0.065	Calcite	SpC	11/11/07	-5.27	-7.46	-6.32	-9.97
				SU06 SAM 17.3	80.435	0.065	Calcite	SpC	11/11/07	-5.57	-8.40	–	–
				SU06 SAM 17.4	80.435	0.065	Calcium Carbonate	SpC	11/11/07	-6.13	-8.75	–	–
SAM 14	Petronodic Haplocalcid	I/II	15	SU06 SAM 14.1	68.205	0.125	Calcite, magnesian	SpC	12/11/07	-7.82	-6.27	-7.72	-6.35
				SU06 SAM 14.2	68.205	0.125	Calcite, magnesian	SpC	12/11/07	-6.46	-7.97	-6.29	-8.12
				SU06 SAM 14.3	68.205	0.125	Calcite, magnesian	Crp	12/11/07	-5.54	-7.45	–	–
SAM 13	Petronodic Haplocalcid	II	14	SU06 SAM 13.3	66.8	0.33	Calcite, magnesian	SpC (MCr areas)	12/11/07	-5.63	-8.23	-6.28	-10.41
				SU06 SAM 13.4	66.8	0.33	Calcite, magnesian	SpC	12/11/07	-5.50	-8.54	-5.77	-9.14
				SU06 SAM 13.5	66.8	0.33	Calcite, magnesian	SpC	12/11/07	-5.88	-8.63	-6.64	-10.41
				SU06 SAM 13.2	66.67	0.2	Calcite, magnesian	SpC	12/11/07	-5.55	-8.08	-6.80	-11.43
				SU06 SAM 13.1	66.49	0.02	Calcite	SpC	12/11/07	-5.43	-8.18	-6.38	-9.87
SAM 21	Petronodic Haplocalcid	II	19	SU06 SAM 21.1	62.44	0.3	Calcite	Crp	11/11/07	-6.22	-7.68	–	–
				SU06 SAM 21.2	62.44	0.3	Calcite, magnesian	Crp	11/11/07	-5.75	-7.45	–	–
				SU06 SAM 21.3	62.44	0.3	Calcite, magnesian	Crp	11/11/07	-6.67	-7.15	–	–
				SU06 SAM 21.4	62.44	0.3	Calcite	SpC	11/11/07	-6.19	-7.53	-5.81	-8.25
				SU06 SAM 21.5	62.44	0.3	Calcium Carbonate	Crp	11/11/07	-7.39	-7.00	–	–
SAM 22	Petronodic Haplocalcid	II	27	SU06 SAM 22.1	60.97	0.33	Calcite, magnesian	Crp	11/11/07	-5.51	-7.79	–	–
SAM 23	Petronodic Haplocalcid	III	47	SU06 SAM 23.2	60.15	0.7	Dolomite	SpC	11/11/07	-5.35	-8.28	-6.13	-10.69
				SU06 SAM 23.3	60.15	0.7	Calcite	SpC	11/11/07	-5.78	-8.96	-6.11	-10.87

Horizon	Classification	Calcrete stage	Depth to Bk horizon (cm)	Sample	Section height (m)	Paleosol depth (m)	XRD Result	Texture	Date run	Micrite		Spar	
										$\delta^{13}C‰$ VPDB	$\delta^{18}O‰$ VPDB	$\delta^{13}C‰$ VPDB	$\delta^{18}O‰$ VPDB
SAM 24a	Petronodic Haplocalcid	II	51	SU06 SAM 24.1	57.44	1.36	Calcite	SpC	12/11/07	-5.61	-8.21	-5.59	-8.74
SAM 24b	Petronodic Haplocalcid	II		SU06 SAM 24.3	57.02	1.78	Calcite	Crp	12/11/07	-5.57	-9.49	–	–
				SU06 SAM 24.4	56.945	1.855	Calcite	SpC	12/11/07	-5.26	-8.62	–	–
SAM 24c	Petronodic Haplocalcid	II		SU06 SAM 24.5	57.61	1.19	Calcite, magnesian	SpC	12/11/07	-5.60	-8.12	-5.28	-8.63
				SU06 SAM 24.6	56.29	2.51	Calcite	SpC	12/11/07	-6.52	-7.93	-5.82	-10.03
SAM 24d	Petronodic Haplocalcid	II		SU06 SAM 24.8	56.28	3.47	Calcite, magnesian	SpC	12/11/07	-5.19	-8.16	-5.30	-8.60
				SU06 SAM 24.9	55.27	3.53	Calcite	SpC	12/11/07	-5.13	-8.36	-5.55	-10.05
				SU06 SAM 24.10	55.58	3.59	Calcite	SpC	12/11/07			-5.04	-8.21
				SU06 SAM 24.11	55.21	3.59	Calcite, magnesian	SpC	12/11/07	-5.32	-8.90	-5.52	-9.18
SAM 24e	Petronodic Haplocalcid	II		SU06 SAM 24.12	54.06	4.74	Calcite	SpC	12/11/07	-4.67	-8.14	–	–
				SU06 SAM 24.13	54	4.8	Calcite	SpC	12/11/07	-5.05	-8.67	-5.26	-8.62
				SU06 SAM 24.14	53.95	4.85	Calcite	SpC	12/11/07	-5.13	-8.22	–	–
2004F/S	II			04.7.24.d	50.91	0.285	Calcite, magnesian	SpC	10/05/06	-3.38	-4.98	-6.37	-8.86
2004F/S	II			04.7.24.d	50.91	0.285	Calcite, magnesian	SpC	10/05/06	-5.24	-6.27	–	–
2004F/S	III			04.7.24.c	46.93	0.15	Dolomite	SpC	21/03/05	-2.21	-3.89	–	–
2004F/S	III			04.7.24.b	43.53	0.05	Dolomite	Crp	21/03/05	-3.62	-4.84	-6.09	-5.77
2004F/S	III			04.7.24.a	38.61	0.08	Dolomite	SpC	29/03/06	-2.53	-3.81	–	–
2004F/S	III			04.7.24.a.I	38.61	0.08	Dolomite	SpC	10/05/06	-4.02	-5.08	–	–
2004F/S	III			04.7.24.a.II	38.61	0.08	Dolomite	SpC	10/05/06	-4.48	-5.54	–	–
2004F/S	II			04.7.23.o	33.13	0.10	Dolomite	Crp	21/03/05	-1.85	-2.97	-4.27	-7.88
2004F/S	IV			04.7.23.n	15.11	0.13	Dolomite	Crp	21/03/05	-1.94	-2.93	–	–
2004F/S	IV			04.7.23.l	12.74	0.04	Dolomite	MCr	21/03/05	-2.71	-3.64	–	–
2004F/S	V/lacustrine			04.7.23.k	11.63	0.08	Dolomite	SpC	21/03/05	-1.80	-2.95	–	–
2004F/S	II			04.7.23.j	10.58	0.08	Dolomite	Crp	21/03/05	-1.55	-2.87	-3.07	-4.42

Horizon	Classification	Calcrete stage	Depth to Bk horizon (cm)	Sample	Section height (m)	Paleosol depth (m)	XRD Result	Texture	Date run	Micrite		Spar	
										$\delta^{13}C‰$ VPDB	$\delta^{18}O‰$ VPDB	$\delta^{13}C‰$ VPDB	$\delta^{18}O‰$ VPDB
2004F/S		II		04.7.23.h	9.53	0.15	Dolomite	SpC	21/03/05	-2.67	-4.07	-3.95	-1.34
2004F/S		II		04.7.23.i	9.53	0.15	–	SpC	21/03/05	-1.75	-2.75	-2.79	-4.14
2004F/S		II		04.7.23.i.I	9.53	0.15	Dolomite	SpC	10/05/06	-2.44	-3.75	–	–
2004F/S		II		04.7.23.i.II	9.53	0.15	Dolomite	SpC	10/05/06	-2.38	-3.14	–	–
2004F/S		IV		04.7.23.g	8.45	0.1	Dolomite	SpC	21/03/05	-2.64	-4.28	–	–
2004F/S		IV		04.7.23.f	7.58	0.18	Dolomite	SpC	21/03/05	-2.54	-3.50	–	–
2004F/S		IV		04.7.23.e	3.75	0.15	Dolomite	SpC	21/03/05	-2.22	-3.17	–	–

Tuyembetka

Horizon	Classification	Calcrete stage	Depth to Bk horizon (cm)	Sample	Section height (m)	Paleosol depth (m)	XRD Result	Texture	Date run	Micrite		Spar	
										$\delta^{13}C‰$ VPDB	$\delta^{18}O‰$ VPDB	$\delta^{13}C‰$ VPDB	$\delta^{18}O‰$ VPDB
TUY 53	Petronodic Haplocalcid	II	Eroded	04.7.26.b	110.49	0.20	Dolomite	SpC	21/03/06	-2.85	-3.61	–	–
TUY 54	Ustic Petrocalcid	III	Eroded	04.7.26.d	108.64	0.30	Dolomite	MCr	21/03/05	-2.98	-3.72	–	–
				04.7.26.c	109.51	0.30	Dolomite	MCr	21/03/05	-2.86	-3.29	–	–
				04.7.26.c.I	109.51	0.72	Dolomite	MCr	10/05/06	-4.87	-4.40	–	–
				04.7.26.c.II	109.51	0.72	Dolomite	MCr	10/05/06	-4.73	-3.76	–	–
TUY 55	Ustic Petrocalcid	IV	37	04.7.26.f	107.49	0.47	Dolomite	MCr	21/03/05	-2.81	-3.65	–	–
				04.7.26.e	107.89	0.13	Dolomite	SpC	21/03/05	-2.96	-3.57	–	–
TUY 56	Petronodic Haplocalcid	II	3	04.7.26.g	106.29	0.16	Dolomite	SpC	21/03/05	-2.94	-3.96	–	–
TUY 57	Petronodic Haplocalcid	II	53	04.7.26.h	104.86	0.29	Dolomite	MCr	21/03/05	-2.79	-4.62	–	–
TUY 58	Ustic Petrocalcid	III	54	0.4.7.26.i	103.74	0.25	Dolomite	MCr	21/03/05	-3.23	-4.16	–	–
				0.4.7.26.j	103.09	0.72	Dolomite	MCr	29/03/06	-3.05	-4.01	–	–
TUY 59	Ustic Petrocalcid	IV	Eroded	0.4.7.26.k	102.56	0.20	Dolomite	MCr	29/03/06	-2.98	-3.96	–	–
TUY 61	Ustic Petrocalcid	IV	Eroded	0.4.7.26.l	102.21	0.18	Dolomite	SpC	29/03/06	-2.97	-3.98	–	–

Horizon	Classification	Calcrete stage	Depth to Bk horizon (cm)	Sample	Section height (m)	Paleosol depth (m)	XRD Result	Texture	Date run	Micrite		Spar	
										$\delta^{13}C‰$ VPDB	$\delta^{18}O‰$ VPDB	$\delta^{13}C‰$ VPDB	$\delta^{18}O‰$ VPDB
TUY 1	Ustic Petrocalcid	V	Eroded	0.4.7.26.o	100.74	0.50	Dolomite	MCr	29/03/06	-2.58	-4.22	–	–
				0.4.7.26.n	101.04	0.50	Dolomite	SpC	29/03/06	-2.89	-4.79	–	–
				0.4.7.26.m	101.34	0.50	Dolomite	SpC	29/03/06	-2.97	-4.52	–	–
TUY 52	Ustic Petrocalcid	IV	Eroded	0.4.7.26.p	100.24	0.20	Dolomite	SpC	29/03/06	-2.91	-5.32	–	–
TUY 56	Petronodic Haplocalcid	II	Eroded	0.4.7.26.q	98.91	0.29	Dolomite	MCr	29/03/06	-2.24	-3.96	–	–
				04.7.26.q.I	98.91	0.29	Dolomite	MCr	10/05/06	-3.80	-4.60	–	–
				04.7.26.q.II	98.91	0.29	Dolomite	MCr	10/05/06	-3.66	-4.88	–	–
				04.7.26.q.III	98.91	0.29	Dolomite	MCr	10/05/06	-3.67	-4.65	–	–
TUY 49	Ustic Petrocalcid	VI	Eroded	0.4.7.26.r*	96.81	0.28	Dolomite	MCr	29/03/06	-2.39	-4.63	–	–
TUY 2	Ustic Petrocalcid	VI	62	0.4.7.26.s	94.79	0.70	Dolomite	MCr	29/03/06	-2.81	-4.14	–	–
TUY 3	Ustic Petrocalcid	IV	36	0.4.7.26.t	89.98	0.24	Dolomite	MCr	29/03/06	-2.76	-3.88	–	–
TUY 54	Ustic Petrocalcid	III	17	04.7.26.u*	79.78	0.75	Halite?	MCr	29/03/06	-2.72	-4.00	–	–
TUY 23	Petronodic Haplocalcid	II		TUY 23.4	39.59	0.05	Dolomite	MCr	21/05/08	-4.15	-5.06		
				TUY 23.2	39.565	0.03	Dolomite	MCr	21/05/08	-4.28	-5.73	-4.80	-5.53
				TUY 23.3	39.565	0.03	Dolomite	MCr	21/05/08	-5.50	-5.74	-12.22	-11.56
TUY 27	Petronodic Haplocalcid	II		TUY 27.3	47.46	0.77	Dolomite	SpC	21/05/08	-4.28	-5.25	-4.83	-5.78
				TUY 27.7	47.07	1.16	Dolomite	SpC	21/05/08	-3.46	-5.78	–	–
TUY 31	Petronodic Haplocalcid	II	20	TUY 31.3	61.0875	0.50	Dolomite	SpC	21/05/08	-4.12	-5.43	-5.39	-11.08
				TUY 31.4	60.92	0.67	Dolomite	SpC	21/05/08	-4.48	-5.46	-5.35	-11.27
TUY 38	Ustic Petrocalcid	V		TUY 38.1	73.84	0.15	Dolomite	SpC	21/05/08	-4.98	-7.22	-10.26	-11.82

Krasnogor

Horizon	Classification	Calcrete stage	Depth to Bk horizon (cm)	Sample	Section height (m)	Paleosol depth (m)	XRD Result	Texture	Date run	Micrite		Spar	
										$\delta^{13}C‰$ VPDB	$\delta^{18}O‰$ VPDB	$\delta^{13}C‰$ VPDB	$\delta^{18}O‰$ VPDB
KRA 2	Petronodic Haplocalcid	II	22	KRA 2.2	7.08	0.36	calcite	MCr	21/05/08	-1.01	-8.37	-1.36	-8.57
KRA 1	Petronodic Haplocalcid	II	27	KRA 1.3	6.07	0.22	calcite	MCr	21/05/08	-0.84	-7.76	-0.80	-8.51
KRA 7a	Petronodic Haplocalcid	II	20	KRA 7.12	5.49	0.23	–	MCr	21/05/08	-1.67	-2.83	-1.19	-3.88
KRA 7d	Petronodic Haplocalcid	II	31	KRA 7.4	4.35	0.34	–	MCr	21/05/08	-2.76	-4.05	-2.91	-7.36
KRA 7e	Petronodic Haplocalcid	II	13	KRA 7.3	4.12	0.16	–	MCr	21/05/08	-2.40	-3.36	–	–
KRA 5a	Ustic Petrocalcid	III	5	KRA 5.4	0.82	1.15	–	MCr	21/05/08	-2.94	-3.15	-1.83	-2.47
KRA 5c	Petronodic Haplocalcid	II	7	KRA 5.11	0.27	0.14	–	MCr	21/05/08	-2.32	-3.01	-2.60	-3.72
KRA 5d	Petronodic Haplocalcid	II	15	KRA 5.14	0	0.15	Dolomite	MCr	21/05/08	-2.53	-3.60	-1.18	-4.06

Mescheryakovka

Horizon	Classification	Calcrete stage	Depth to Bk horizon (cm)	Sample	Section height (m)	Paleosol depth (m)	XRD Result	Texture	Date run	Micrite		Spar	
										$\delta^{13}C‰$ VPDB	$\delta^{18}O‰$ VPDB	$\delta^{13}C‰$ VPDB	$\delta^{18}O‰$ VPDB
MES 7	Petronodic Haplocalcid	II	Eroded	MES 7.2	4.87	0.97	Calcite	MCr	12/12/07	-9.70	-11.09	–	–
MES 3	Ustic Calcid	II	121	MES 3.2	7.44	1.42	–	SpC	12/12/07	-9.60	-3.68	–	–
	(Lacustrine)			MES 3.3	7.44	1.42	Calcite	SpC	12/12/07	-9.82	-1.53	-9.77	-7.75
MES 1	Petronodic Haplocalcid	II	24	MES 1.2	9.35	0.31	Calcite (mg)	SpC	12/12/07	-10.48	-9.52	-10.66	-9.14
				MES 1.3	9.35	0.31	Calcite	SpC	12/12/07	-10.62	-9.43	–	–
				MES 1.4	9.35	0.31	Calcite	SpC	12/12/07	-10.49	-10.08	–	–
MES 8	Vertic)	II	44	MES 8.4	79.82	0.58	Calcite	MCr	09/12/07	-9.45	-16.93	-8.28	-16.13
	Haplocalcid			MES 8.5	79.82	0.58	Calcite (mg)	MCr	09/12/07	-9.09	-16.96	-9.26	-17.15
				MES 8.2	79.87	0.52	Calcite	SpC	09/12/07	-7.78	-9.85	-10.99	-14.38
				MES 8.1	79.89	0.50	Calcium Carbonate	MCr	09/12/07	-9.34	-17.66	-8.54	-16.54
MES 10	*Petronodic Haplocalcid*	II	*Eroded*	MES 10.3	137.454	0.55	Calcite	MCr	12/12/07	-8.38	-16.39	–	–

Horizon	Classification	Calcrete stage	Depth to Bk horizon (cm)	Sample	Section height (m)	Paleosol depth (m)	XRD Result	Texture	Date run	Micrite		Spar	
										$\delta^{13}C‰$ VPDB	$\delta^{18}O‰$ VPDB	$\delta^{13}C‰$ VPDB	$\delta^{18}O‰$ VPDB
				MES 10.4	137.454	0.55	Calcite	MCr	12/12/07	-8.62	-16.71	-11.90	-12.87
				MES 10.5	137.454	0.55	Calcite	MCr	12/12/07	-8.71	-14.85	–	–
MES 15	Petronodic	II	Eroded	MES 15.3	183.114	0.16	Calcite (mg)	MCr	12/12/07	-6.42	-8.25	-6.93	-7.83
	Haplocalcid			MES 15.5	182.814	0.49	–	MCr	12/12/07	-6.48	-9.44	-6.82	-9.74
MES 16	Vertic	II	100	MES 16.3	183.354	1.83	–	MCr	09/12/07	-7.58	-8.35	-5.92	-8.59
	Haplocalcid			MES 16.4	183.354	1.83	Calcite	MCr	12/12/07	-6.98	-8.92	-7.84	-9.58
				MES 16.5	183.354	1.83	Calcite	MCr	12/12/07	-7.00	-6.86	-7.14	-6.00
				MES 16.6	183.354	1.83	Calcite	SpC	12/12/07	-7.29	-8.12	-7.70	-7.30
				MES 16.1	183.634	1.53	Calcite (mg)	MCr/SpC	09/12/07	-7.83	-7.64	-7.52	-9.50
				MES 16.2	183.634	1.53	–	SpC	09/12/07	-7.12	-8.66	–	–
MES 17	Petronodic	II	Eroded	MES 17.10	185.054	0.98	–	MCr/SpC	12/12/07	-8.03	-8.62	-8.45	-8.23
	Haplocalcid			MES 17.9	186.034	1.09	Calcite (mg)	MCr/SpC	12/12/07	-7.92	-7.00	-9.01	-10.00
				MES 17.8	186.234	1.31	–	MCr/SpC	12/12/07	-7.88	-9.54	-8.46	-9.72

A2.2

Variation in stable isotope results for individual paleosols. Paleosols from Boyevaya Gora, Sambullak, Tuyembetka and Mescheryakovka which contained three or more isotope analysis are displayed here

Key to Diagrams

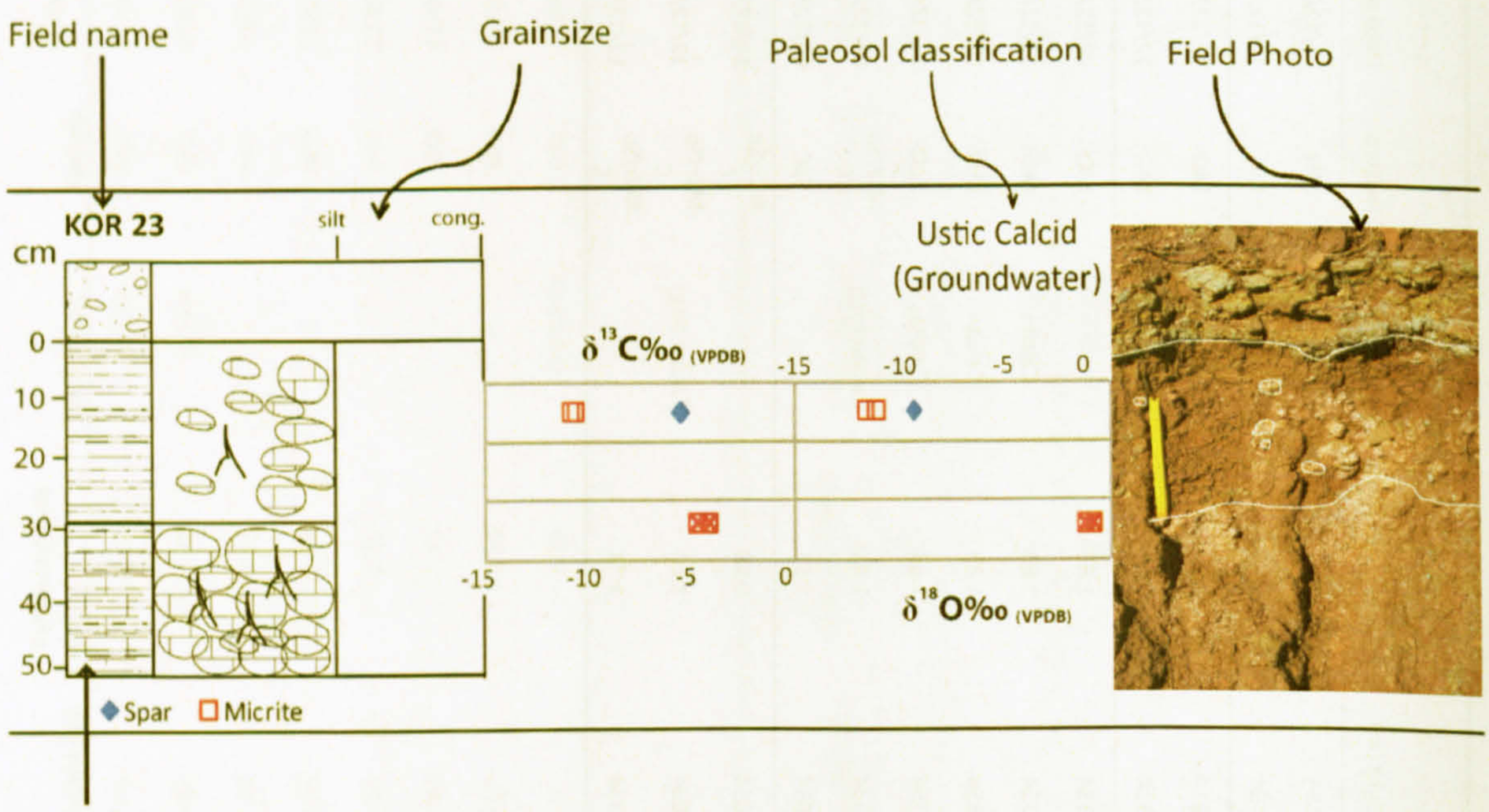

Paleosol features

- Pseudo-Gley
- Minor mottelling
- Drab root halos
- Root traces
- Desiccation cracks
- Parallel lamination
- Pedogenic slickensides
- Carbonate nodule
- Ephemeral nodule
- Coalesced nodules

Isotope results

- Dolomite micrite isotopic values
- Calcite micrite isotopic values
- Spar isotopic values from sinous veins

Lithological Key

- Mudstone/Siltstone
- Sandstone
- Conglomerate
- Calcified horizons (above 50% carbonate)
- Limestone

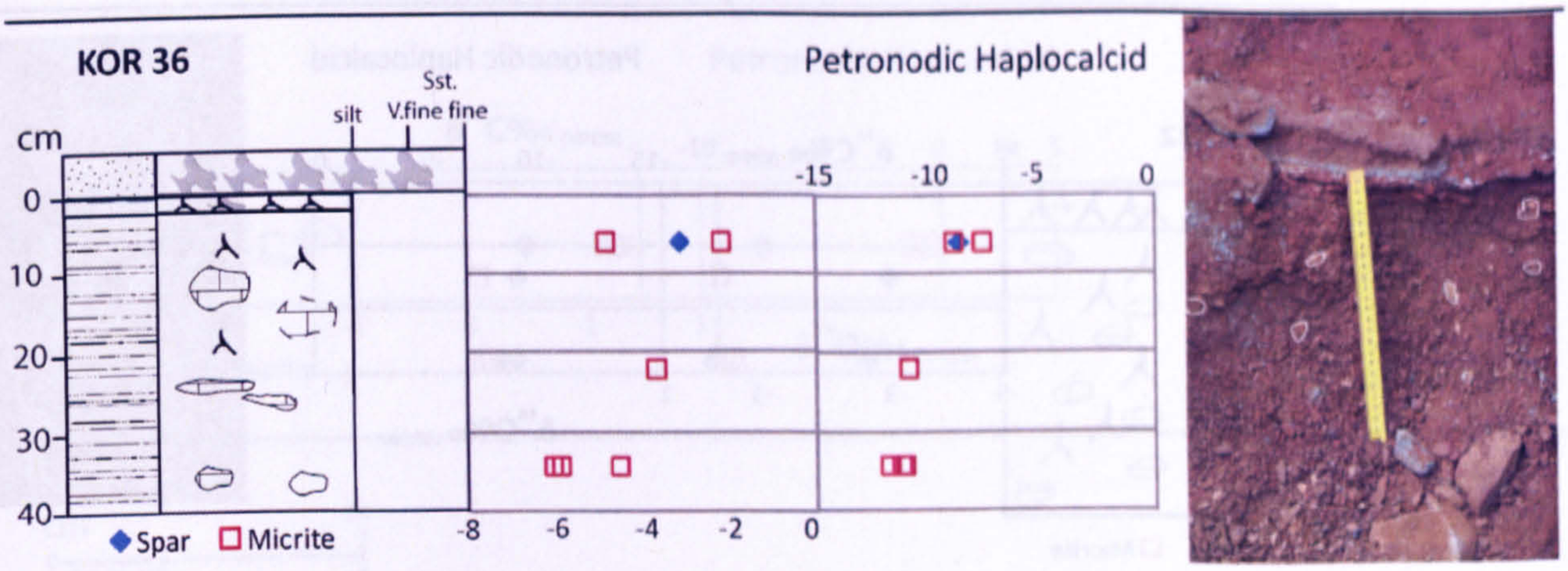
KOR 36
Petronodic Haplocalcid
Sst.
silt
V.fine fine
cm
0
10
20
30
40
-15
-10
-5
0
-8
-6
-4
-2
0
Spar
Micrite

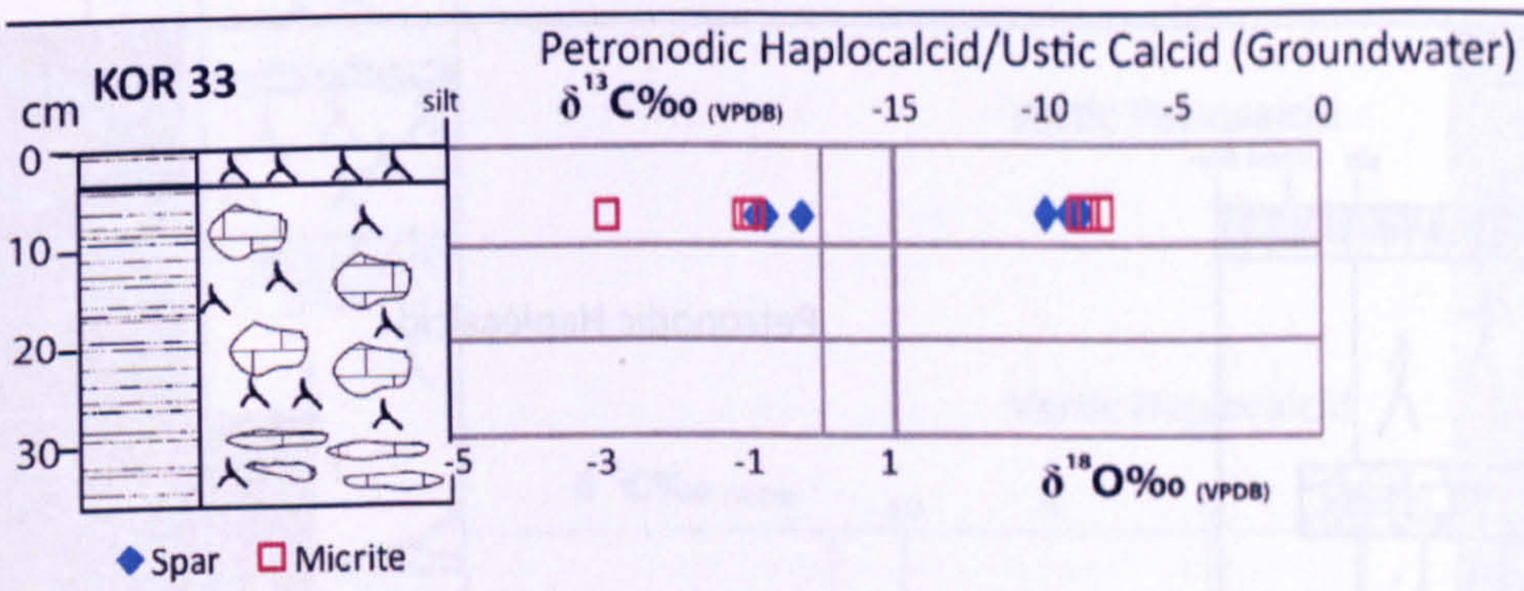
Petronodic Haplocalcid/Ustic Calcid (Groundwater)
KOR 33
cm
silt
δ13C‰ (VPDB)
-15
-10
-5
0
0
10
20
30
-5
-3
-1
1
δ18O‰ (VPDB)
Spar
Micrite

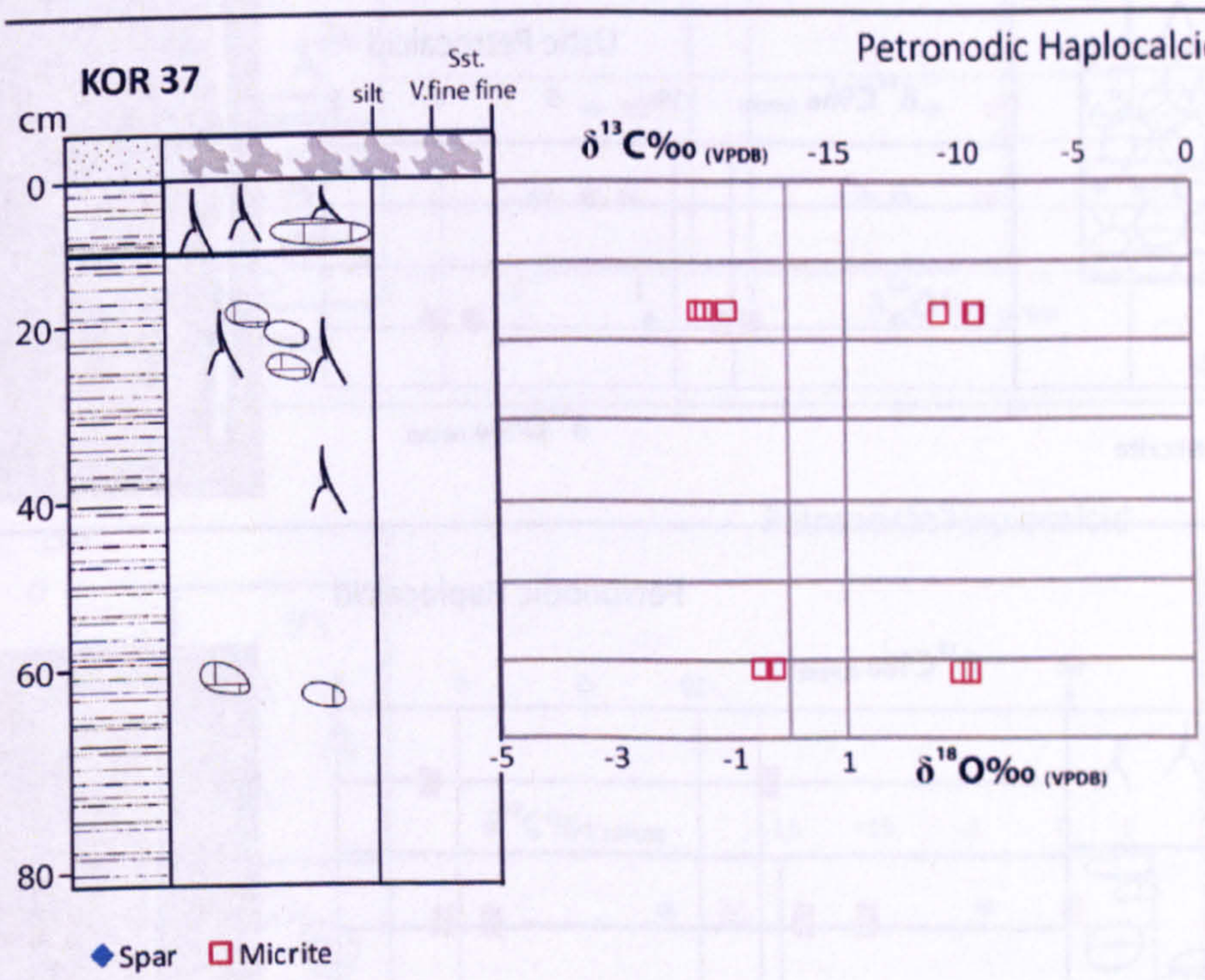
KOR 37
Petronodic Haplocalcid
Sst.
silt
V.fine fine
cm
δ13C‰ (VPDB)
-15
-10
-5
0
0
20
40
60
80
-5
-3
-1
1
δ18O‰ (VPDB)
Spar
Micrite

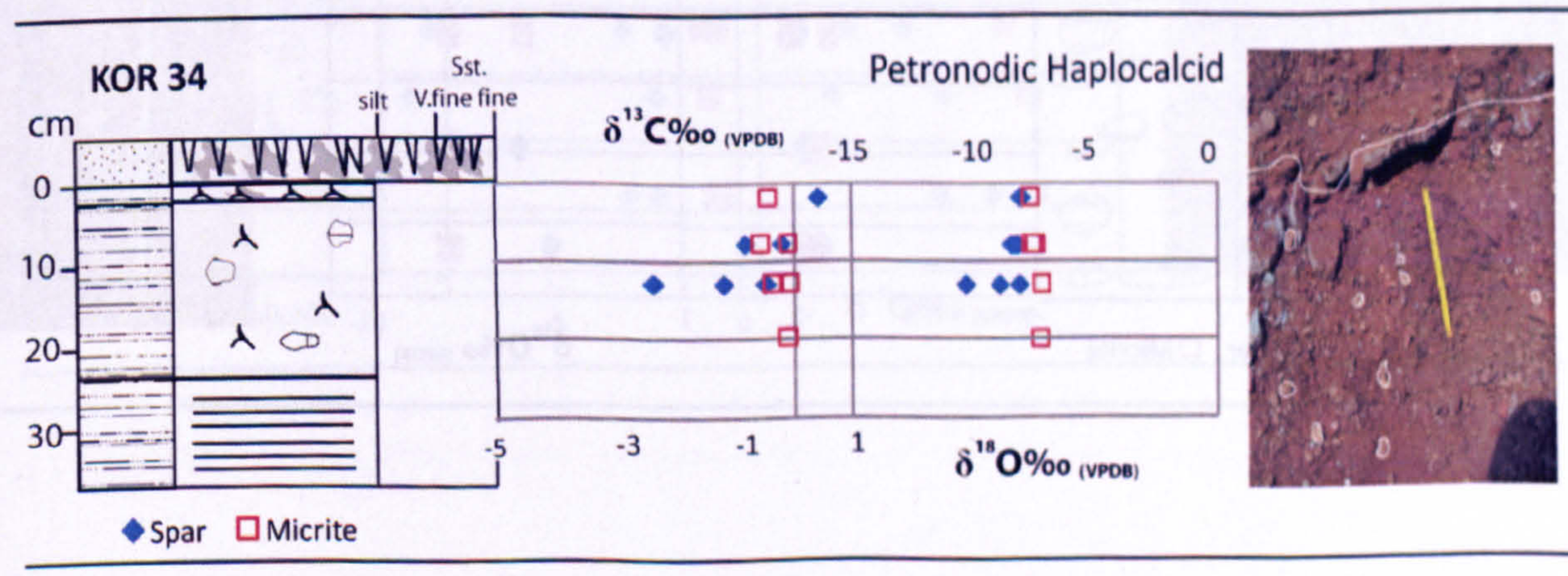
KOR 34
Petronodic Haplocalcid
Sst.
silt
V.fine fine
cm
δ13C‰ (VPDB)
-15
-10
-5
0
0
10
20
30
-5
-3
-1
1
δ18O‰ (VPDB)
Spar
Micrite

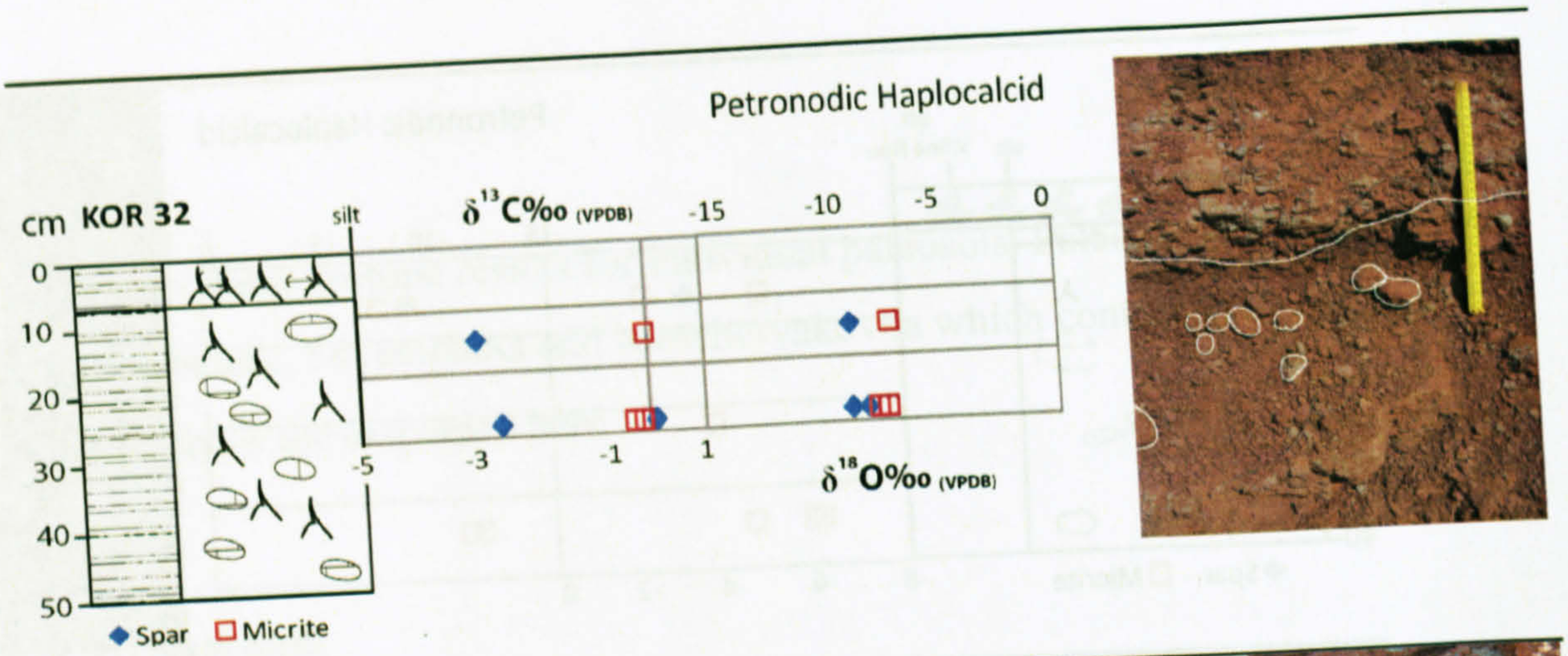
Petronodic Haplocalcid
cm KOR 32
silt
δ13C‰ (VPDB)
-15
-10
-5
0
0
10
20
30
40
50
-5
-3
-1
1
δ18O‰ (VPDB)
Spar
Micrite

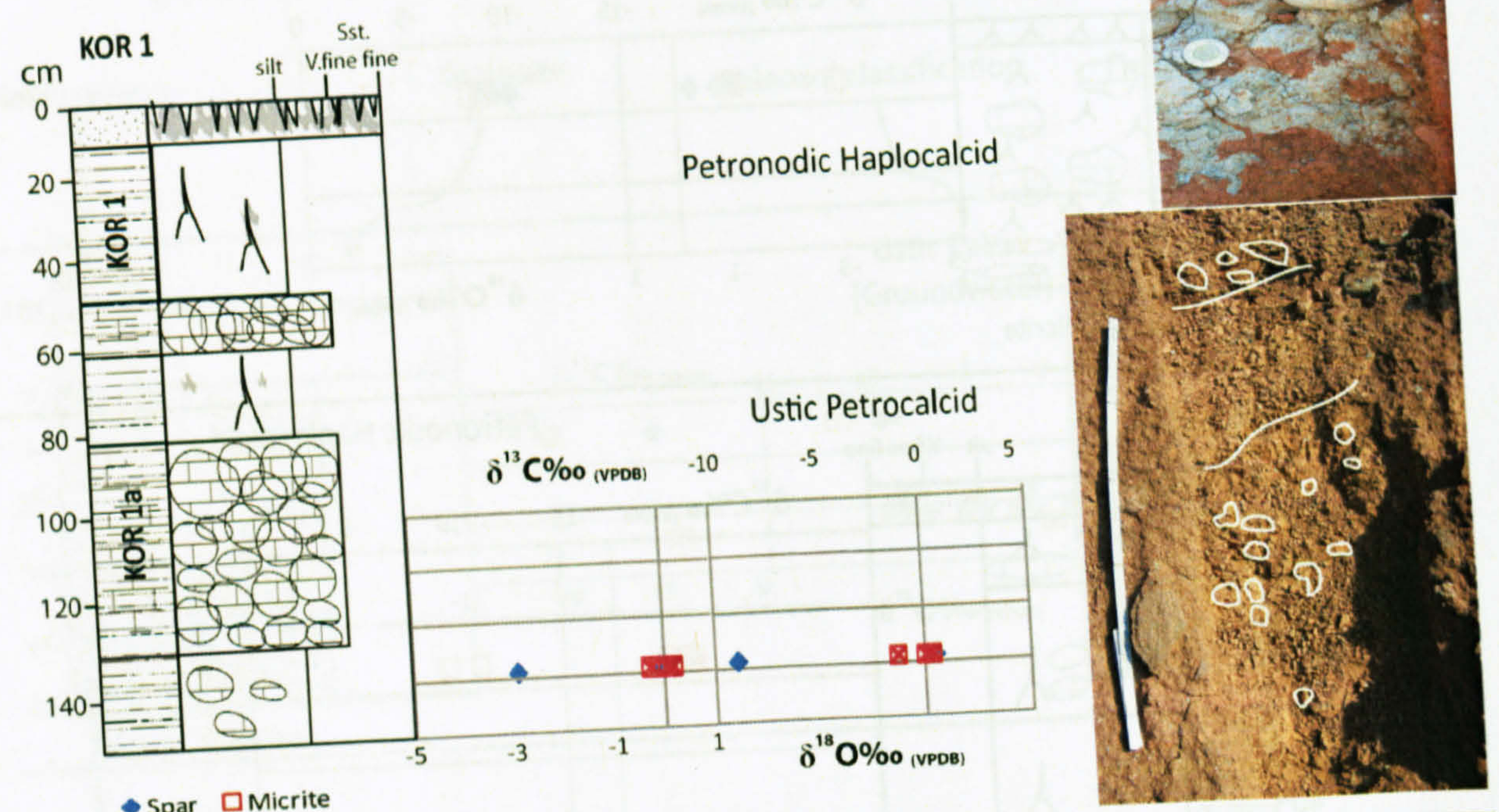
KOR 1
cm
silt
Sst.
V.fine fine
0
20
40
60
80
100
120
140
KOR 1
KOR 1a
Petronodic Haplocalcid
Ustic Petrocalcid
δ13C‰ (VPDB)
-10
-5
0
5
-5
-3
-1
1
δ18O‰ (VPDB)
Spar
Micrite

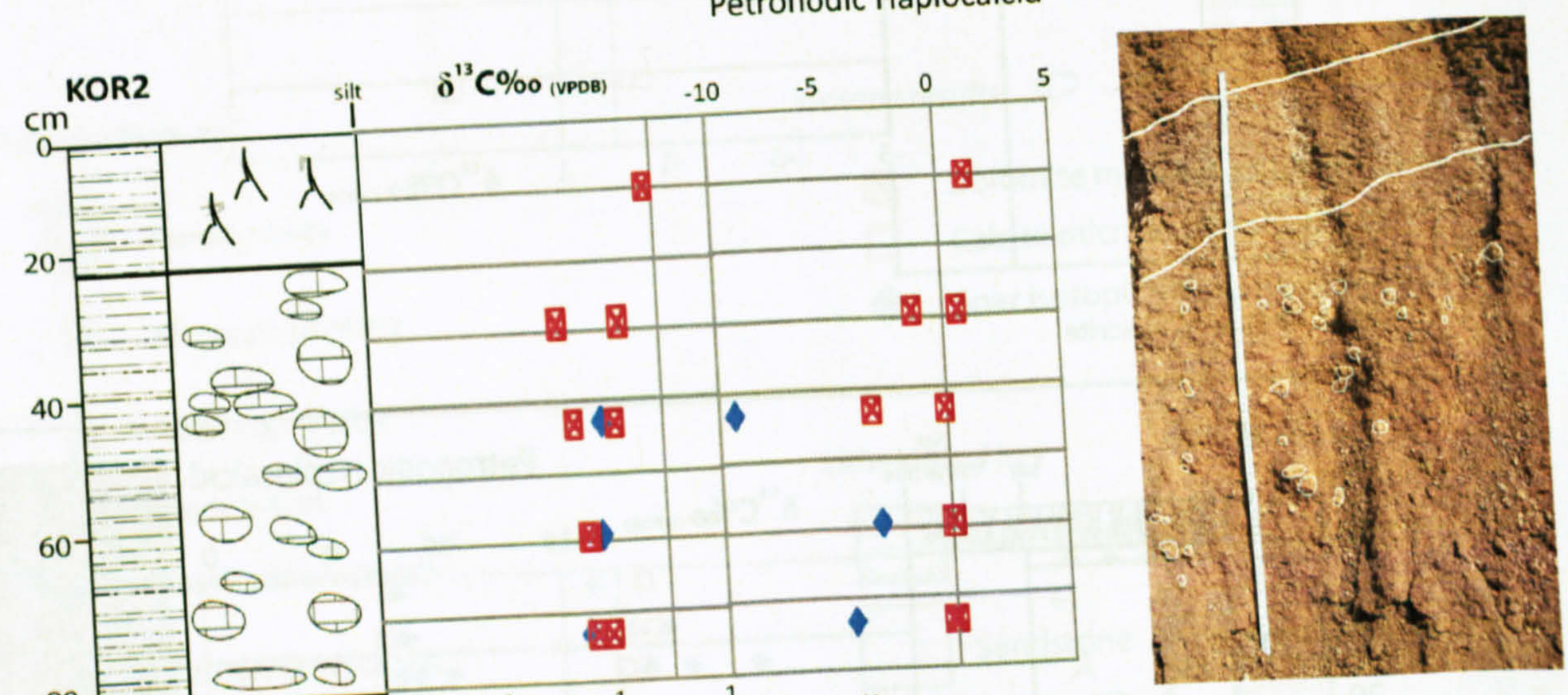
Petronodic Haplocalcid
KOR2
cm
silt
δ13C‰ (VPDB)
-10
-5
0
5
0
20
40
60
80
-5
-3
-1
1
δ18O‰ (VPDB)
Spar
Micrite

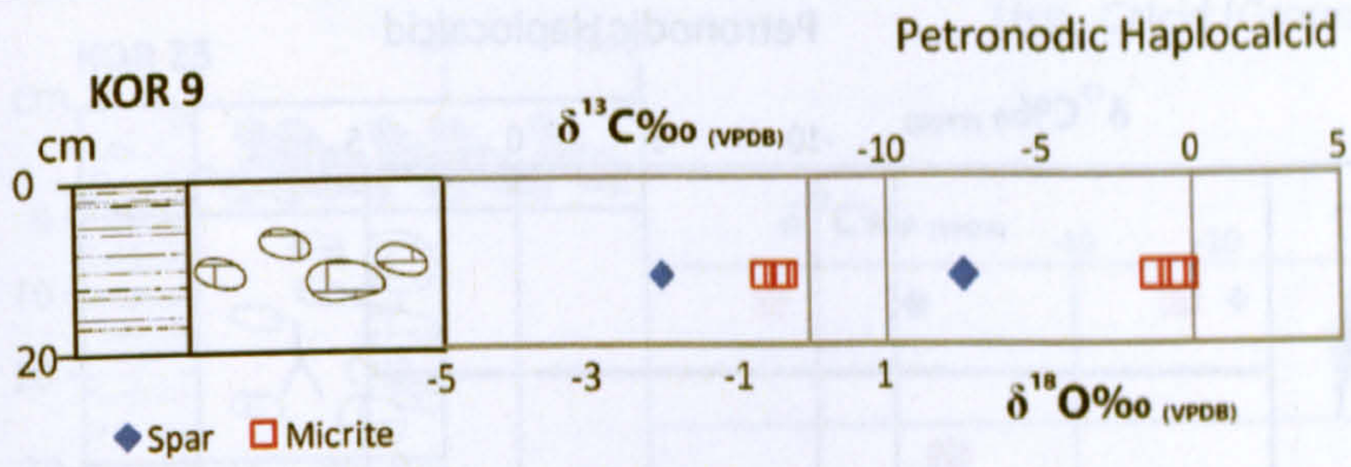
KOR 9
Petronodic Haplocalcid
cm
0
20
δ13C‰ (VPDB)
-10
-5
0
5
-5
-3
-1
1
δ18O‰ (VPDB)
Spar
Micrite

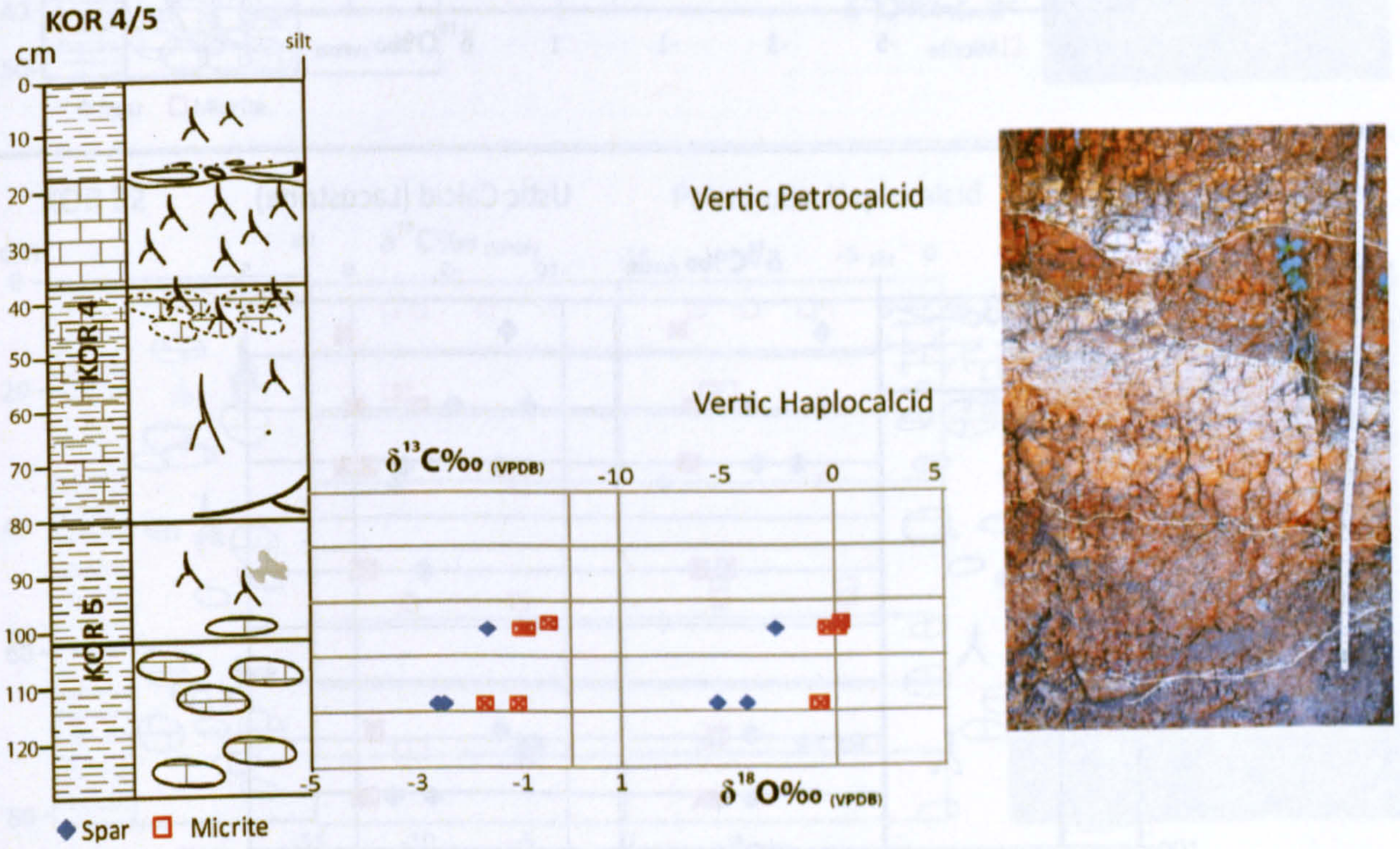
KOR 4/5
cm
silt
0
10
20
30
40
50
60
70
80
90
100
110
120
KOR 4
KOR 5
Vertic Petrocalcid
Vertic Haplocalcid
δ13C‰ (VPDB)
-10
-5
0
5
-5
-3
-1
1
δ18O‰ (VPDB)
Spar
Micrite

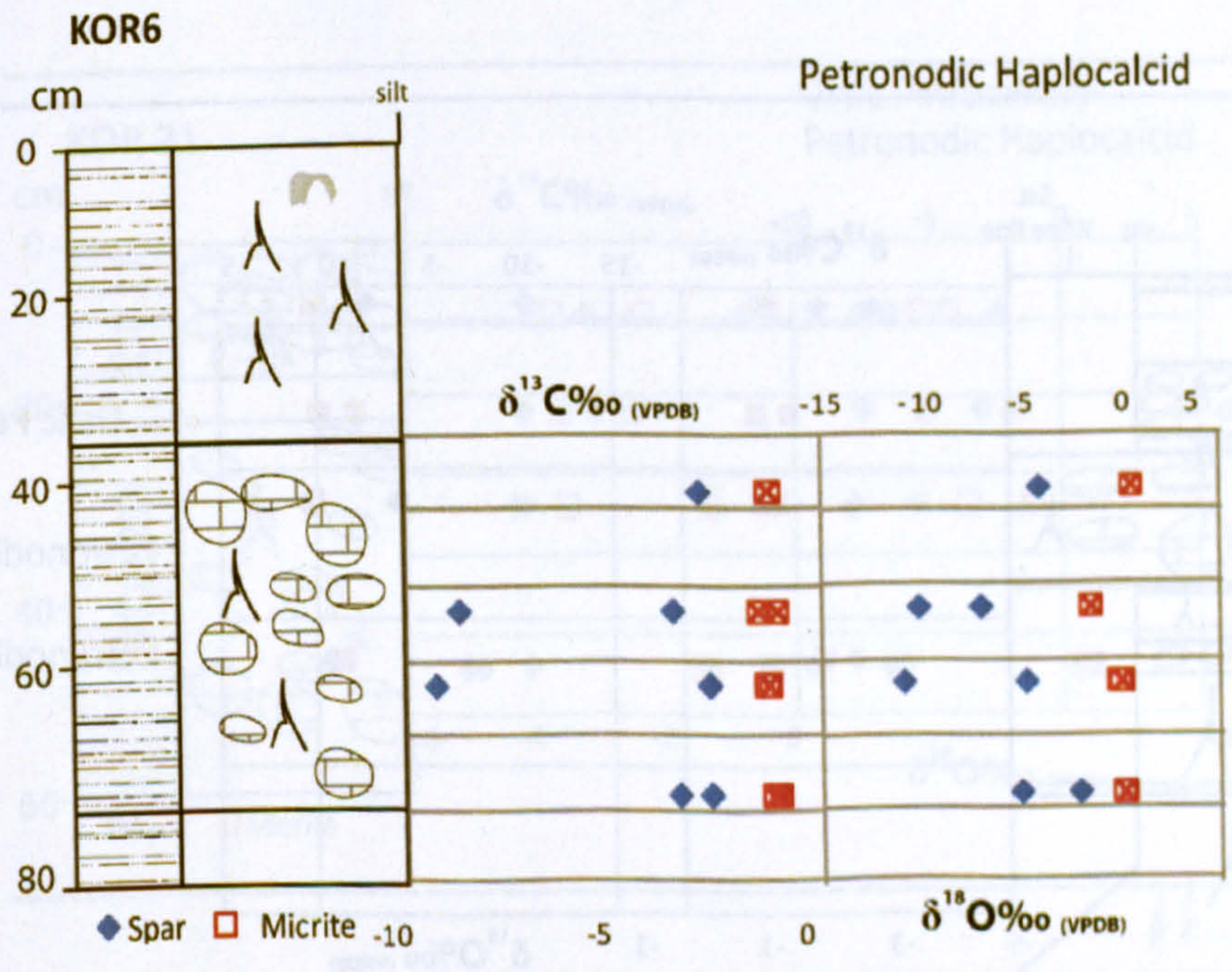
KOR6
cm
silt
0
20
40
60
80
Petronodic Haplocalcid
δ13C‰ (VPDB)
-15
-10
-5
0
5
-10
-5
0
δ18O‰ (VPDB)
Spar
Micrite

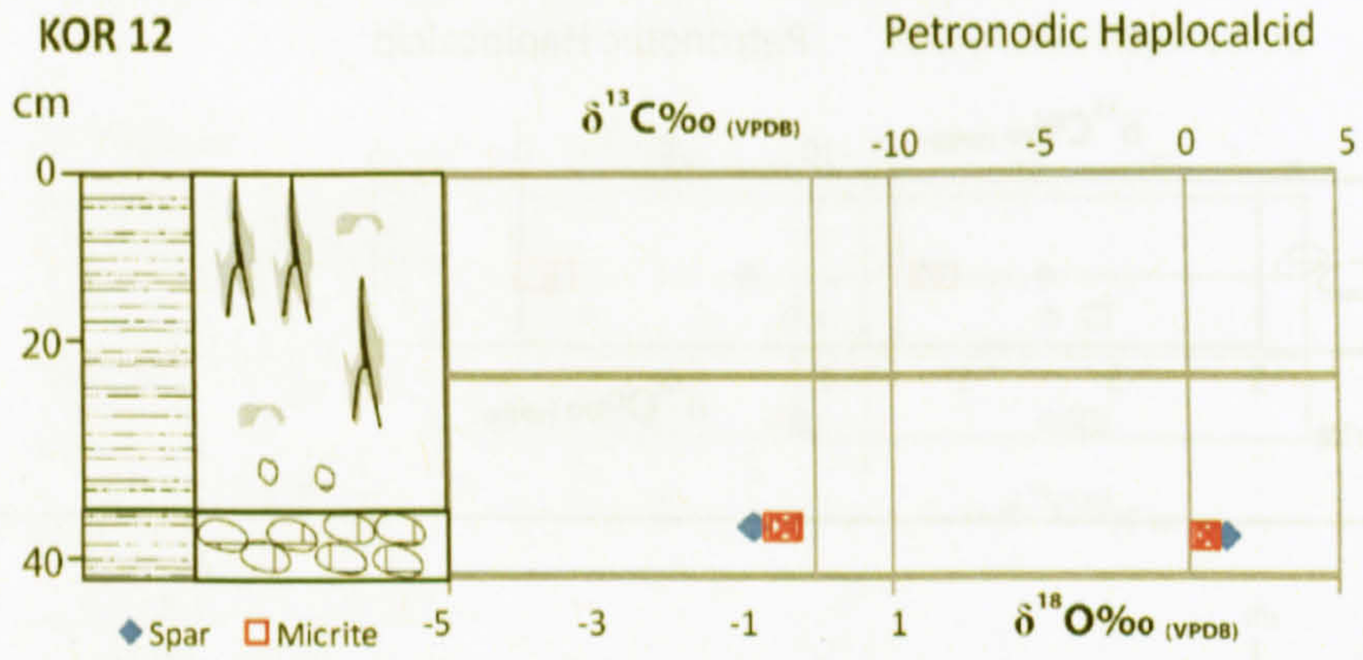
KOR 12
Petronodic Haplocalcid
cm
δ13C‰ (VPDB)
-10
-5
0
5
0
20
40
-5
-3
-1
1
δ18O‰ (VPDB)
Spar
Micrite

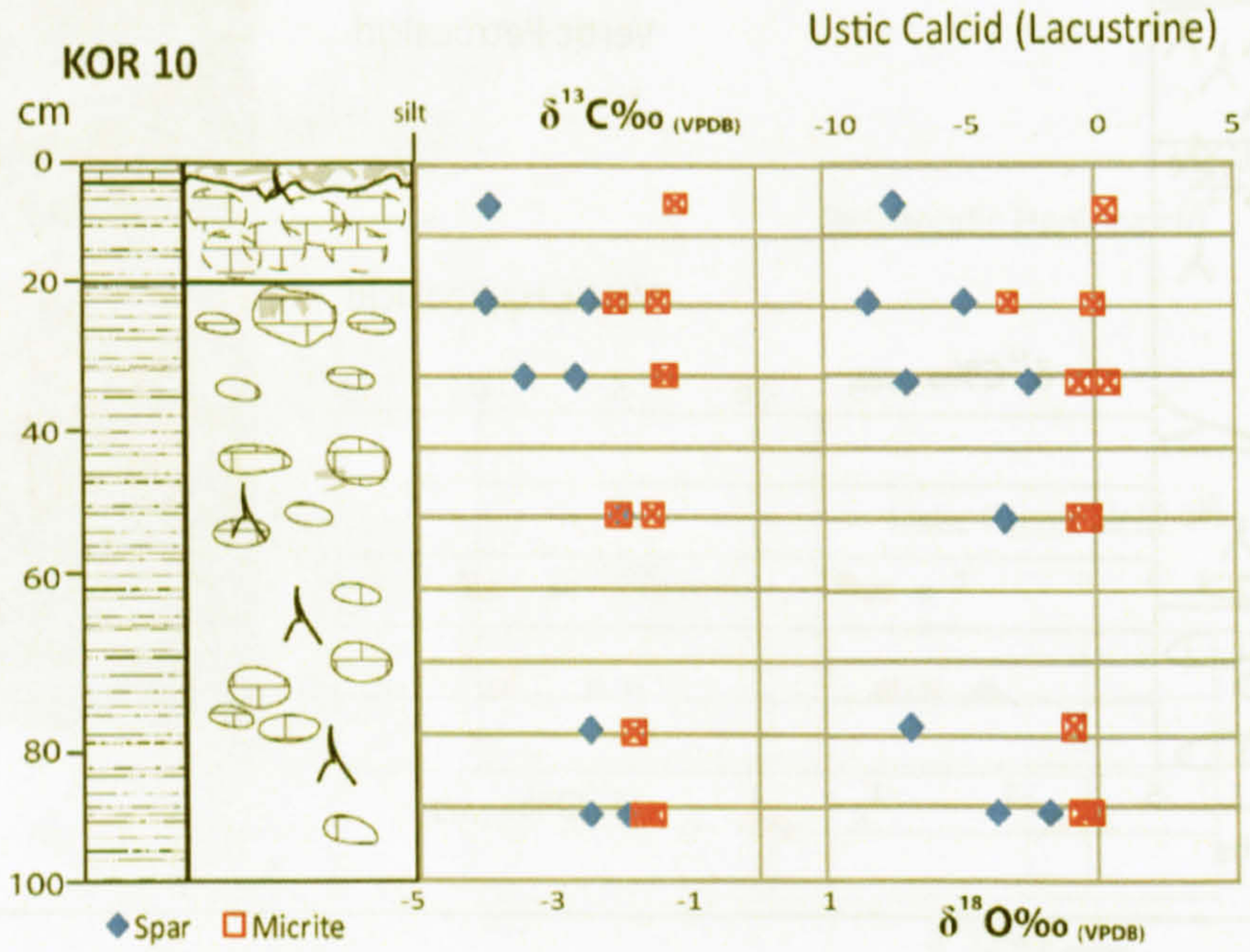
KOR 10
Ustic Calcid (Lacustrine)
cm
silt
δ13C‰ (VPDB)
-10
-5
0
5
0
20
40
60
80
100
-5
-3
-1
1
δ18O‰ (VPDB)
Spar
Micrite

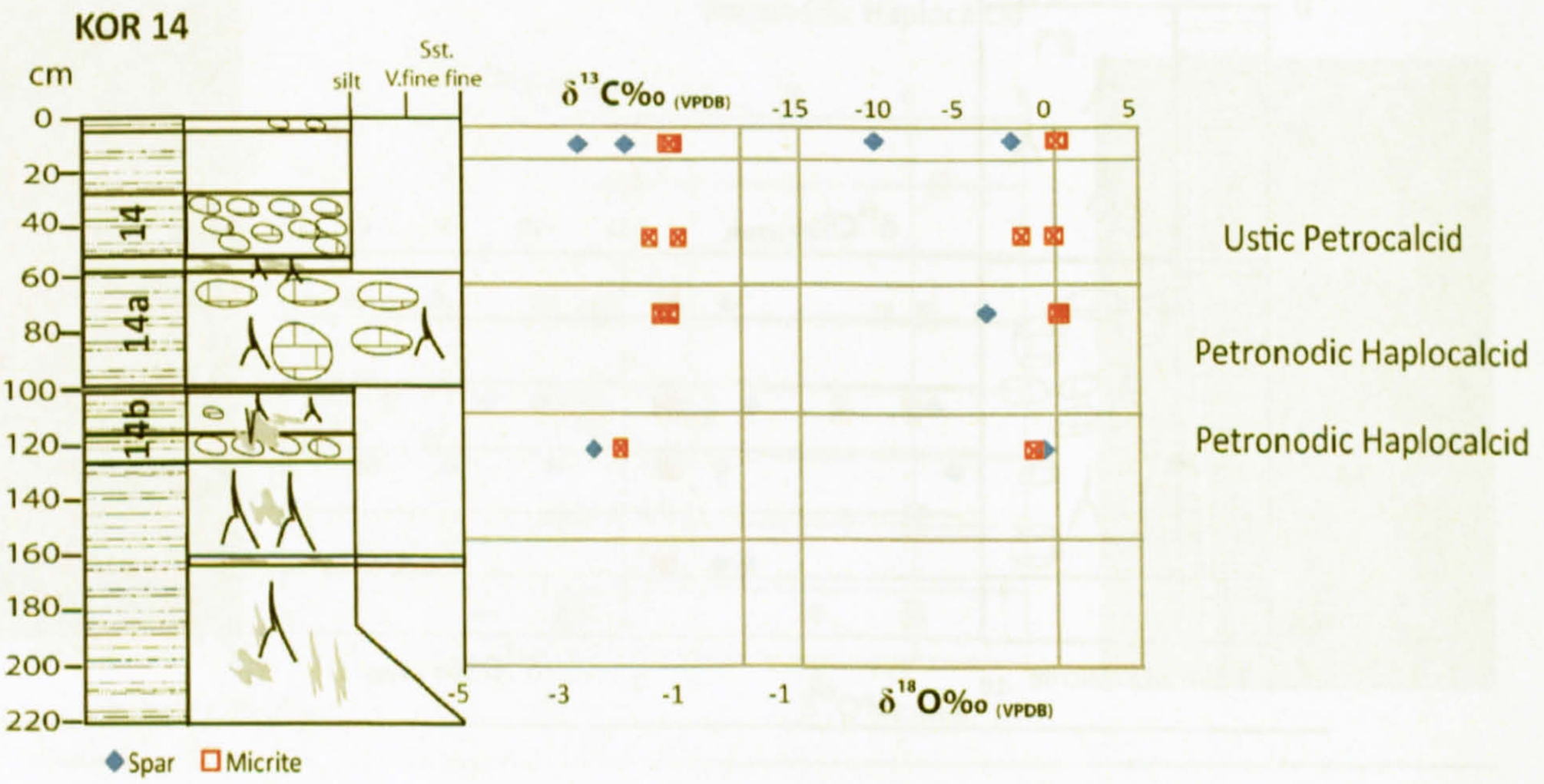
KOR 14
cm
silt
Sst.
V.fine fine
δ13C‰ (VPDB)
-15
-10
-5
0
5
0
20
40
60
80
100
120
140
160
180
200
220
14
14a
14b
-5
-3
-1
-1
δ18O‰ (VPDB)
Spar
Micrite
Ustic Petrocalcid
Petronodic Haplocalcid
Petronodic Haplocalcid

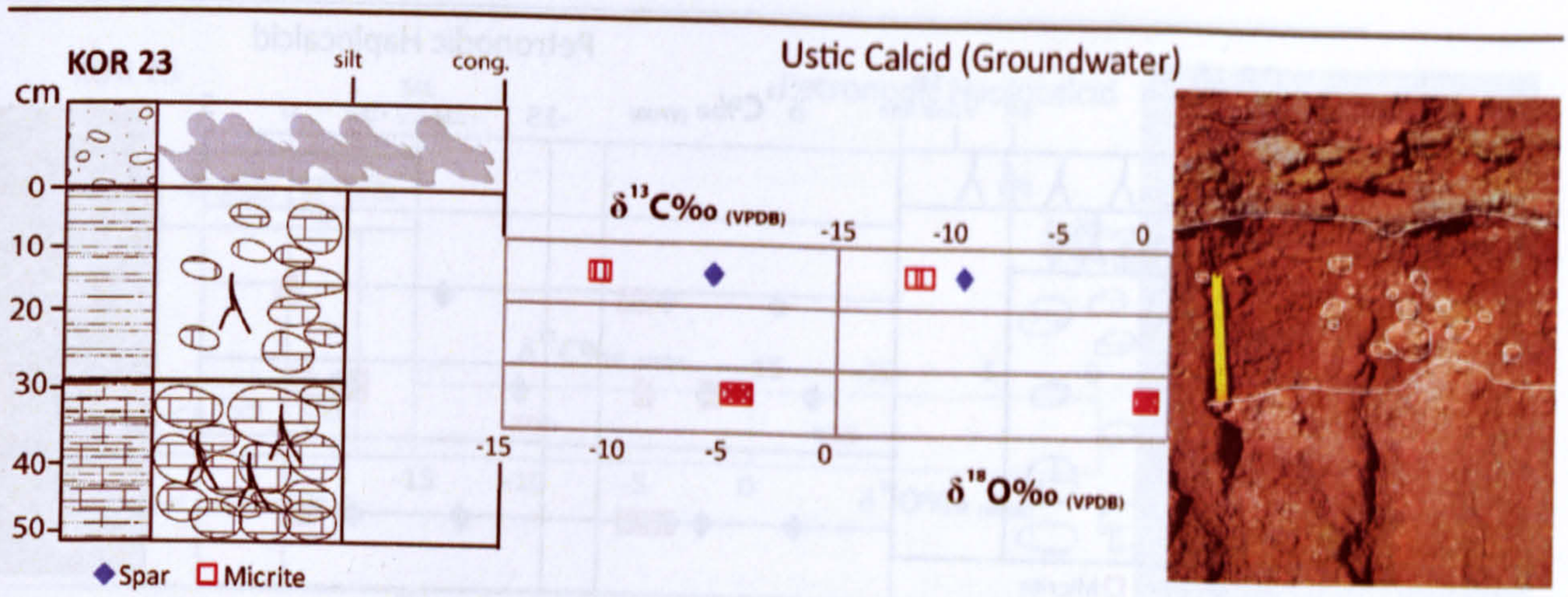
KOR 23
silt
cong.
cm
0
10
20
30
40
50
Spar
Micrite
Ustic Calcid (Groundwater)
δ13C‰ (VPDB)
-15
-10
-5
0
δ18O‰ (VPDB)

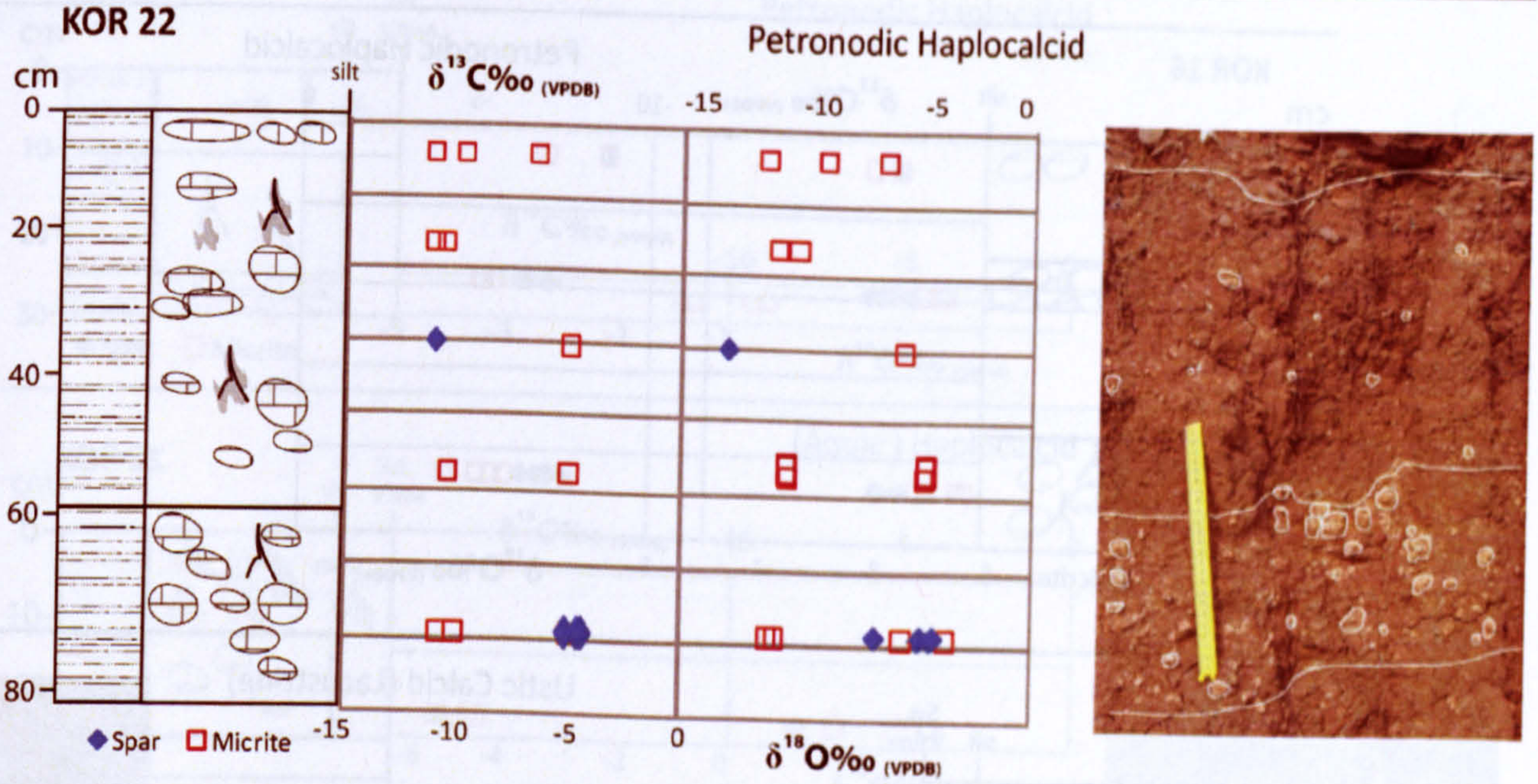
KOR 22
cm
silt
0
20
40
60
80
Spar
Micrite
Petronodic Haplocalcid
δ13C‰ (VPDB)
-15
-10
-5
0
δ18O‰ (VPDB)

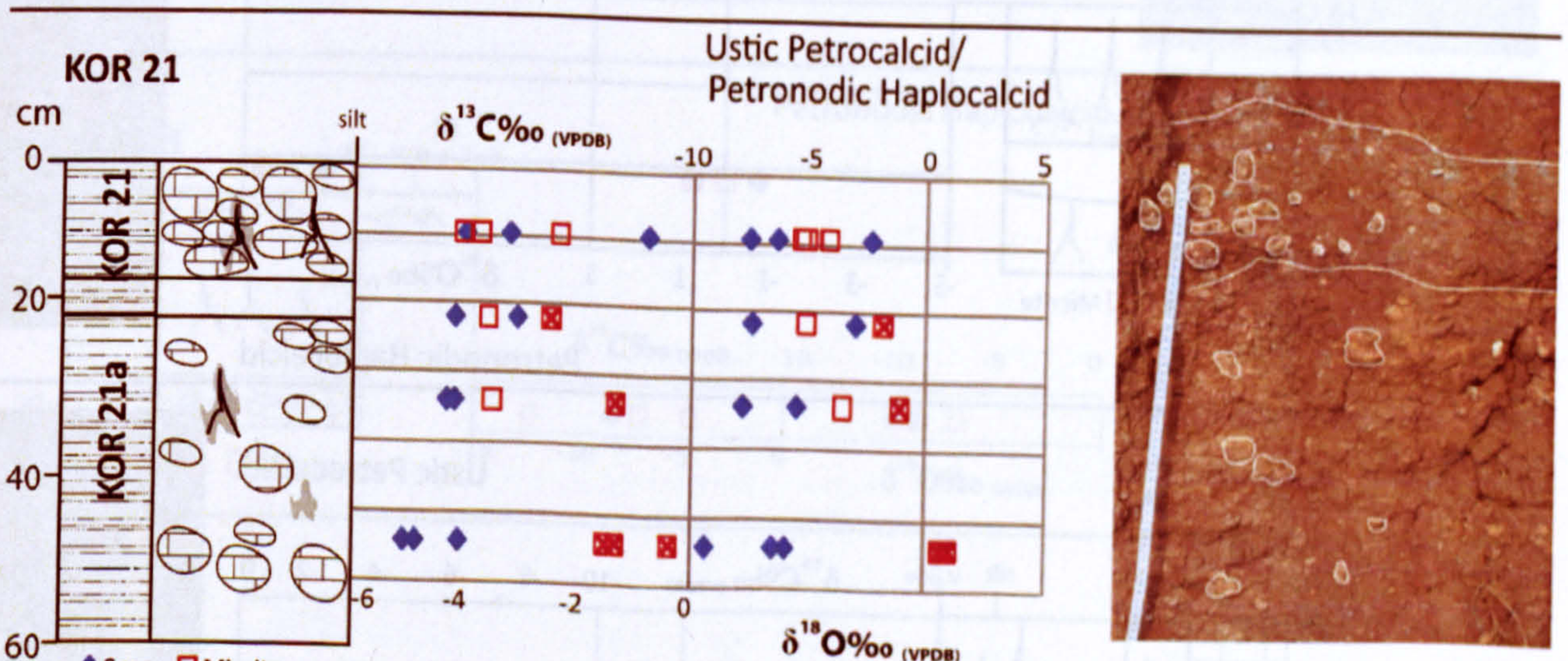
KOR 21
cm
silt
0
20
40
60
KOR 21
KOR 21a
Spar
Micrite
Ustic Petrocalcid/
Petronodic Haplocalcid
δ13C‰ (VPDB)
-10
-5
0
5
-6
-4
-2
0
δ18O‰ (VPDB)

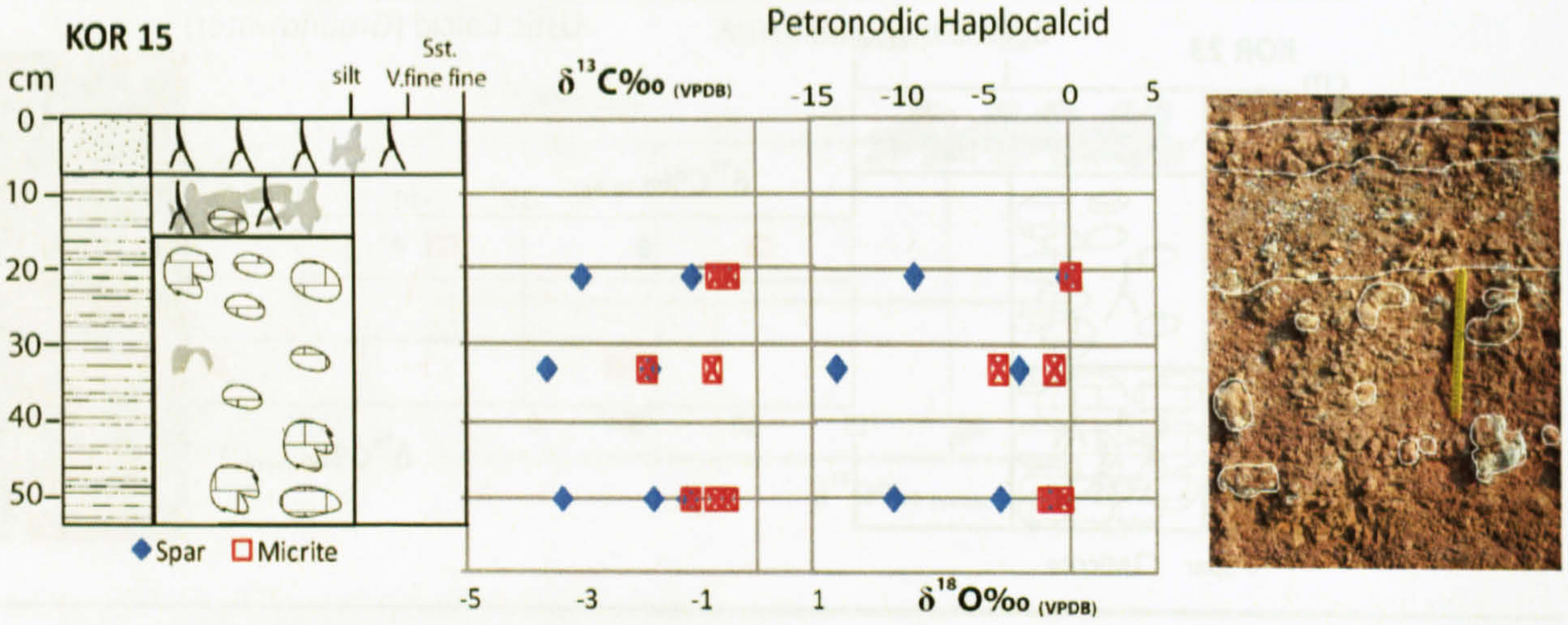

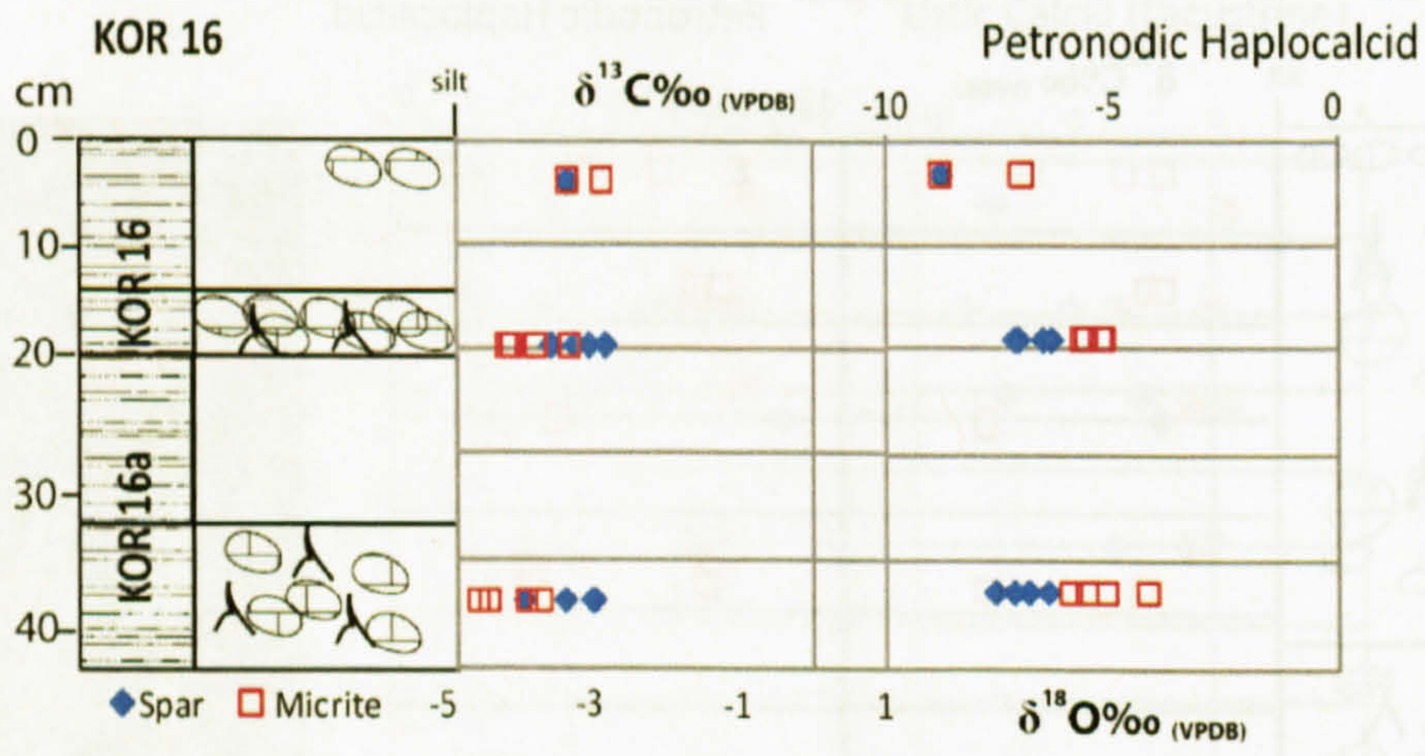

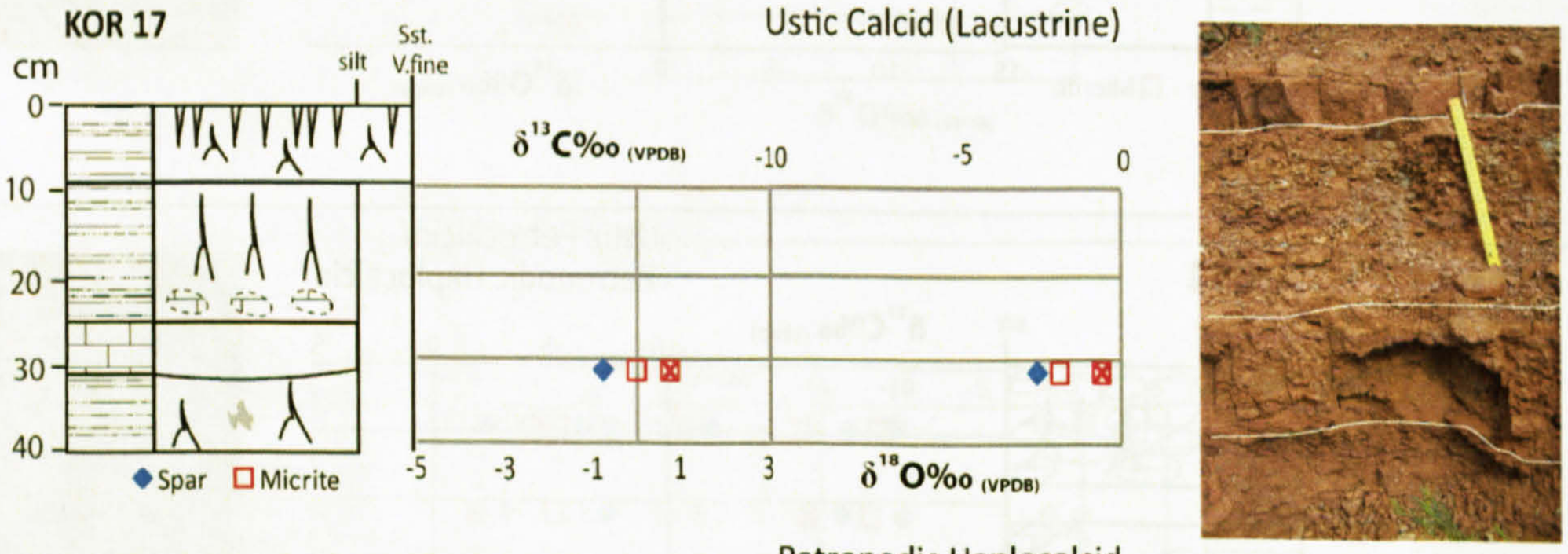

Petronodic Haplocalcid

Ustic Petrocalcid

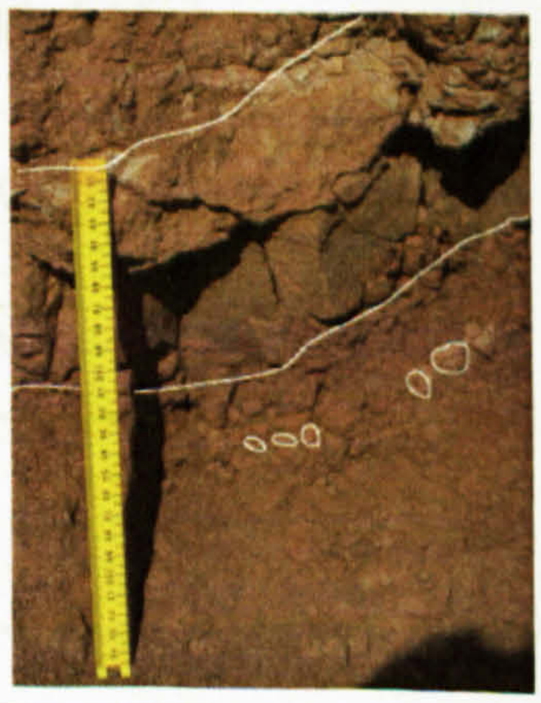

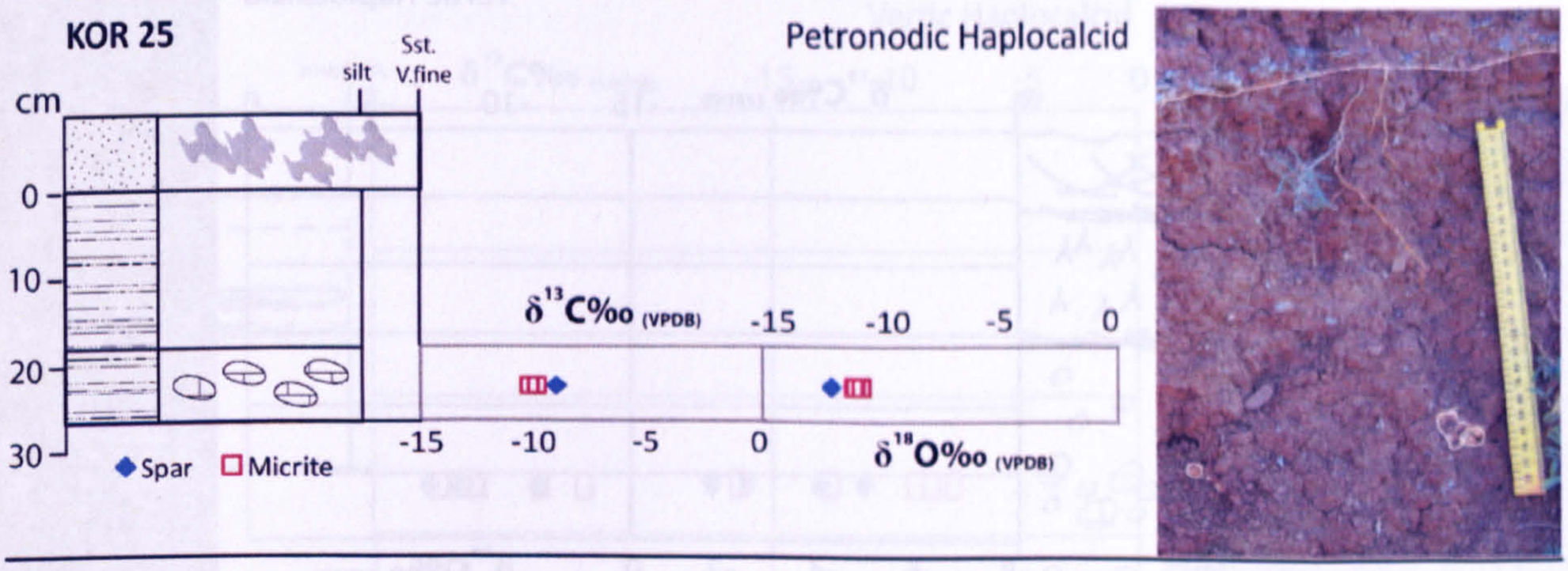
KOR 25
Petronodic Haplocalcid
silt
Sst.
V.fine
cm
0
10
20
30
δ13C‰ (VPDB)
-15
-10
-5
0
-15
-10
-5
0
δ18O‰ (VPDB)
Spar
Micrite
KOR 27
Petronodic Haplocalcid
silt
Sst.
V.fine
cm
0
10
20
30
δ13C‰ (VPDB)
-10
-5
0
-5
-3
-1
1
δ18O‰ (VPDB)
Spar
Micrite
KOR 31
(Aquic) Haplocalcid
silt
Sst.
V.fine
cm
0
10
20
30
δ13C‰ (VPDB)
-10
-5
0
-6
-4
-2
0
δ18O‰ (VPDB)
Spar
Micrite
KOR 35
Petronodic Haplocalcid
silt
V.fine
fine
Sst.
cm
0
10
20
δ13C‰ (VPDB)
-15
-10
-5
0
-15
-10
-5
0
δ18O‰ (VPDB)
Spar
Micrite

Vertic Haplocalcid

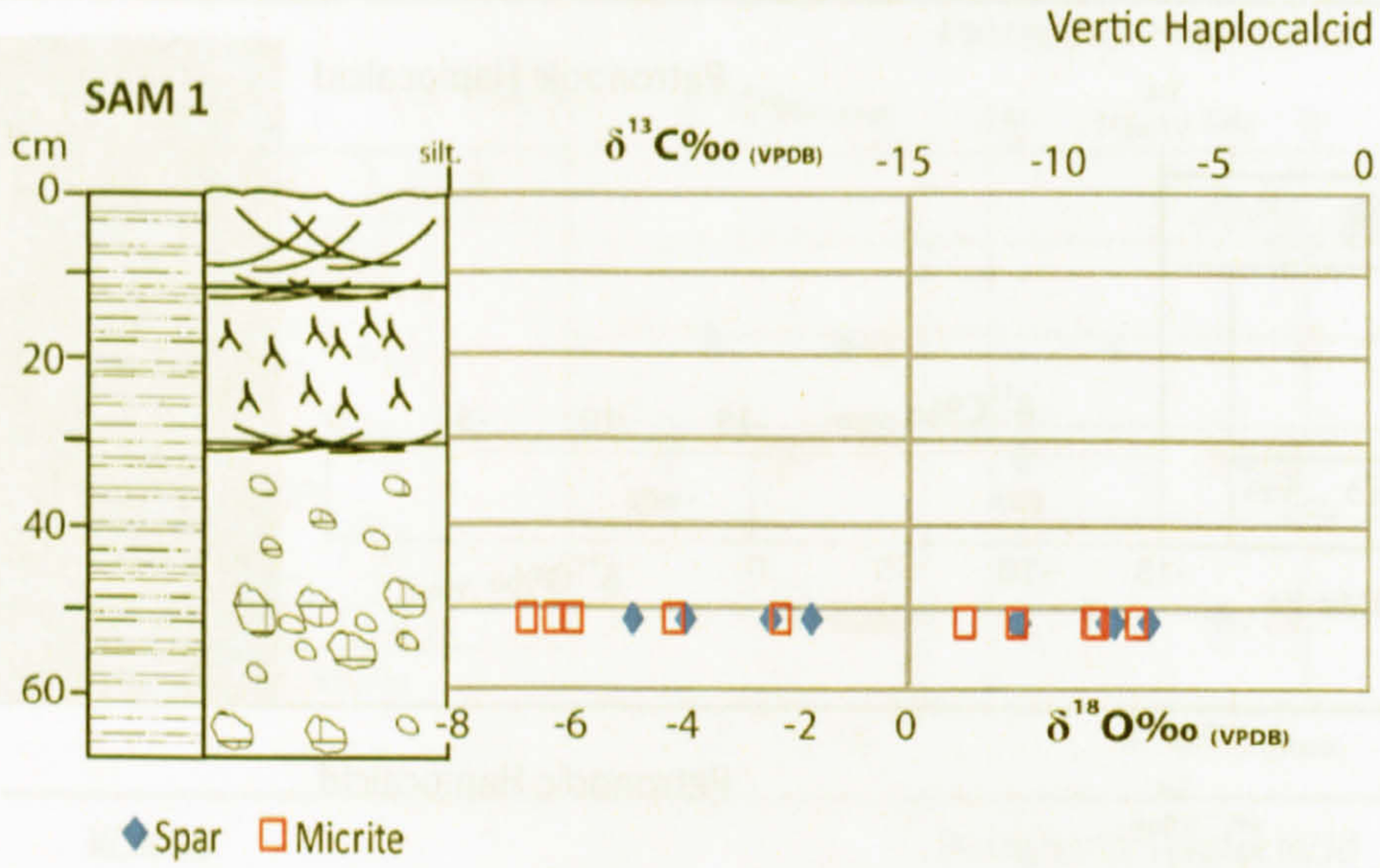

Petronodic Haplocalcid

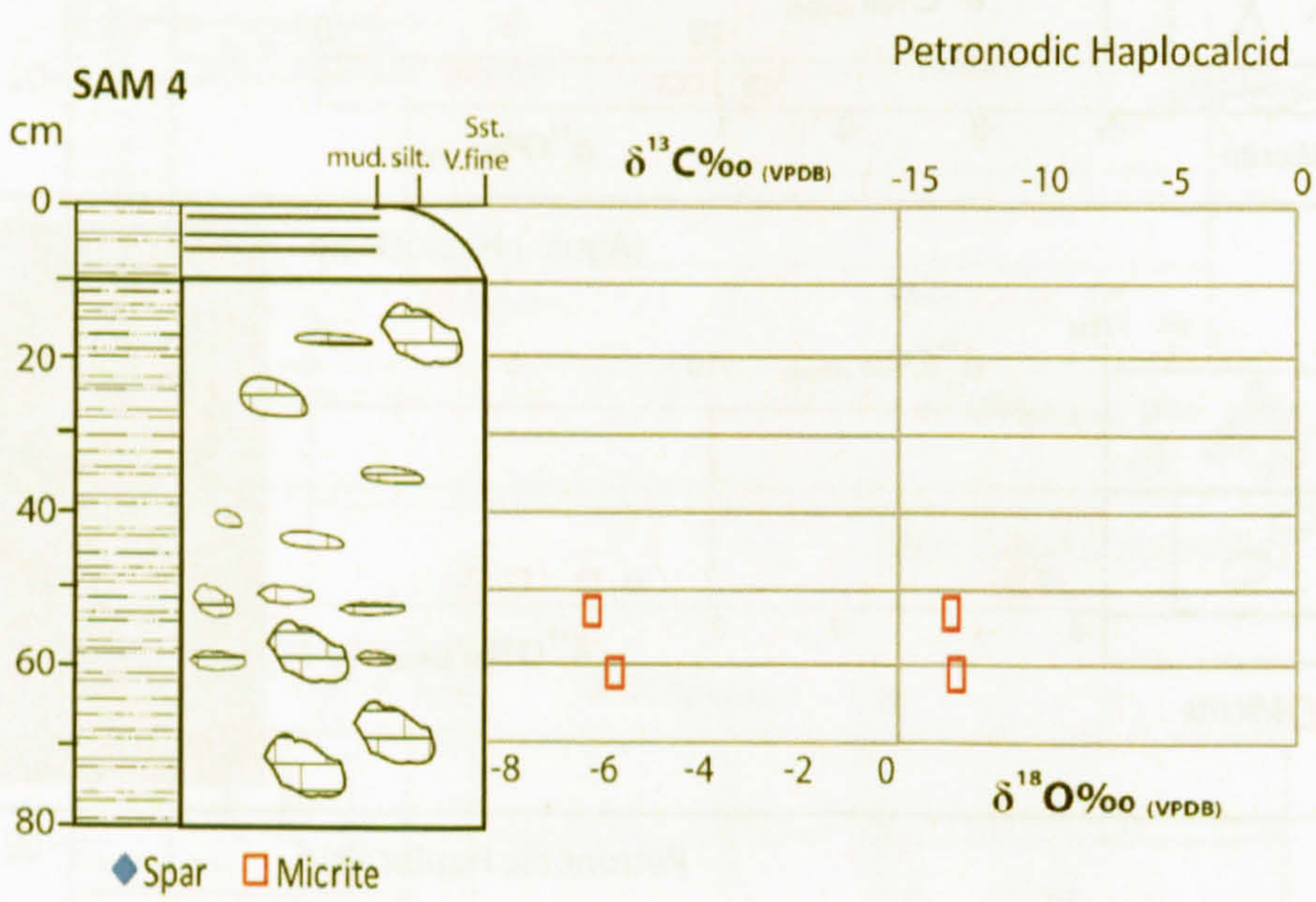

Ustic Calcid (Lacustrine)

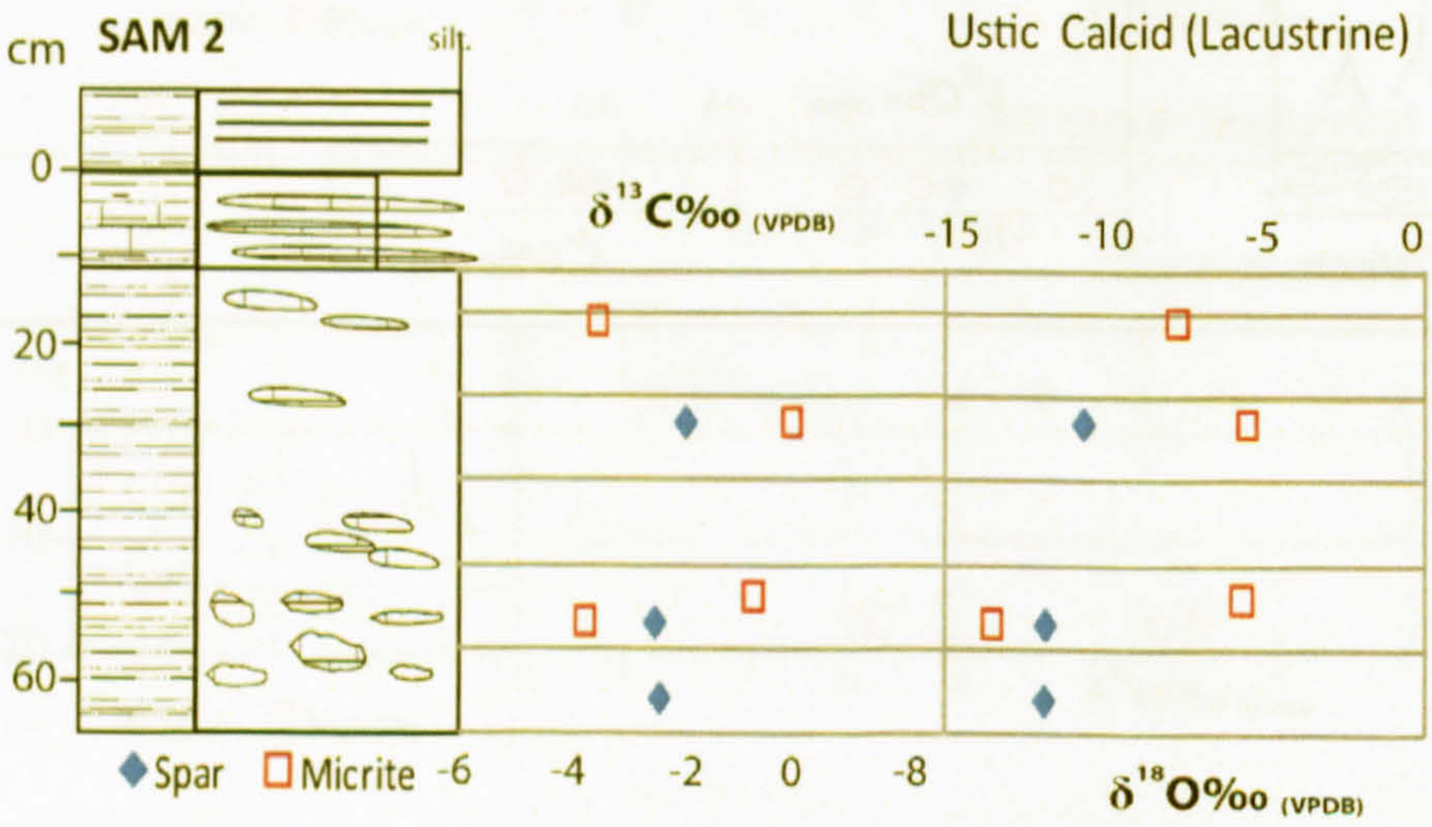

Vertic Haplocalcid

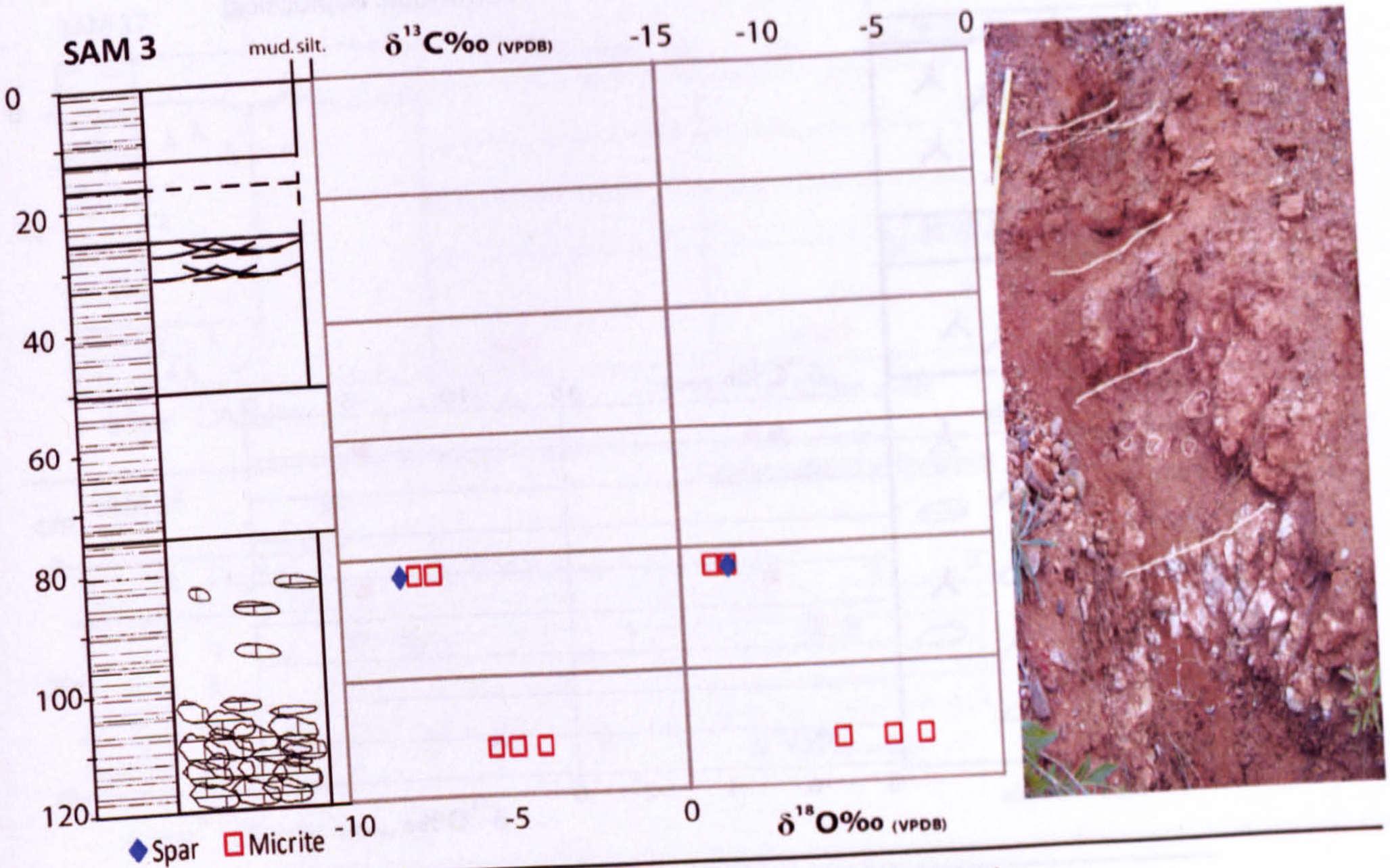

Petronodic Haplocalcid

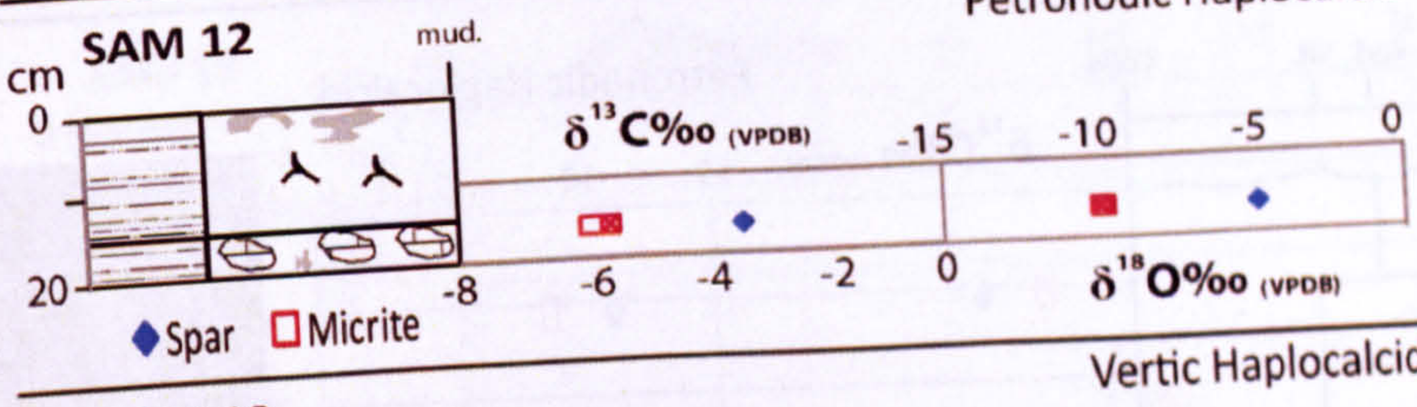

Vertic Haplocalcid

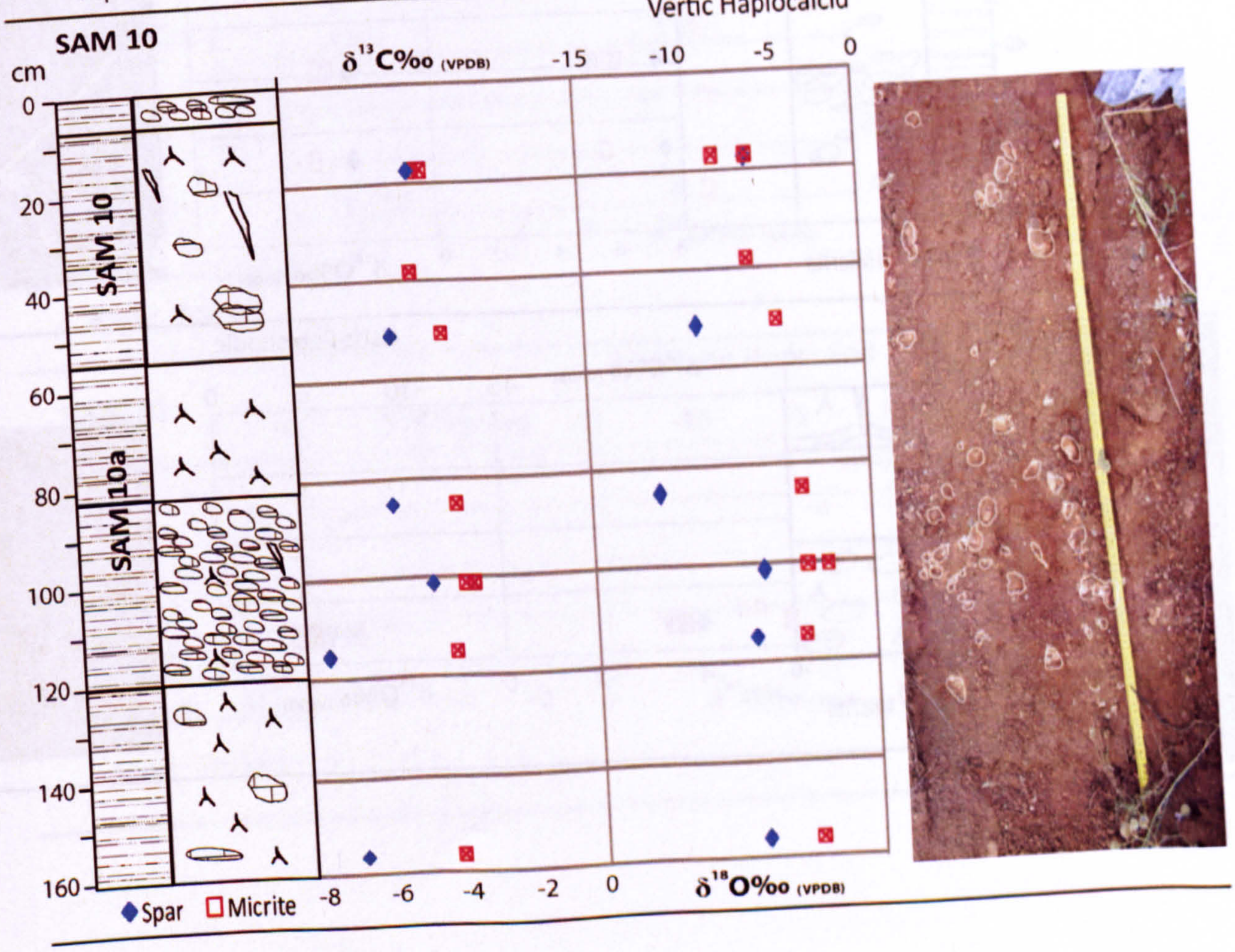

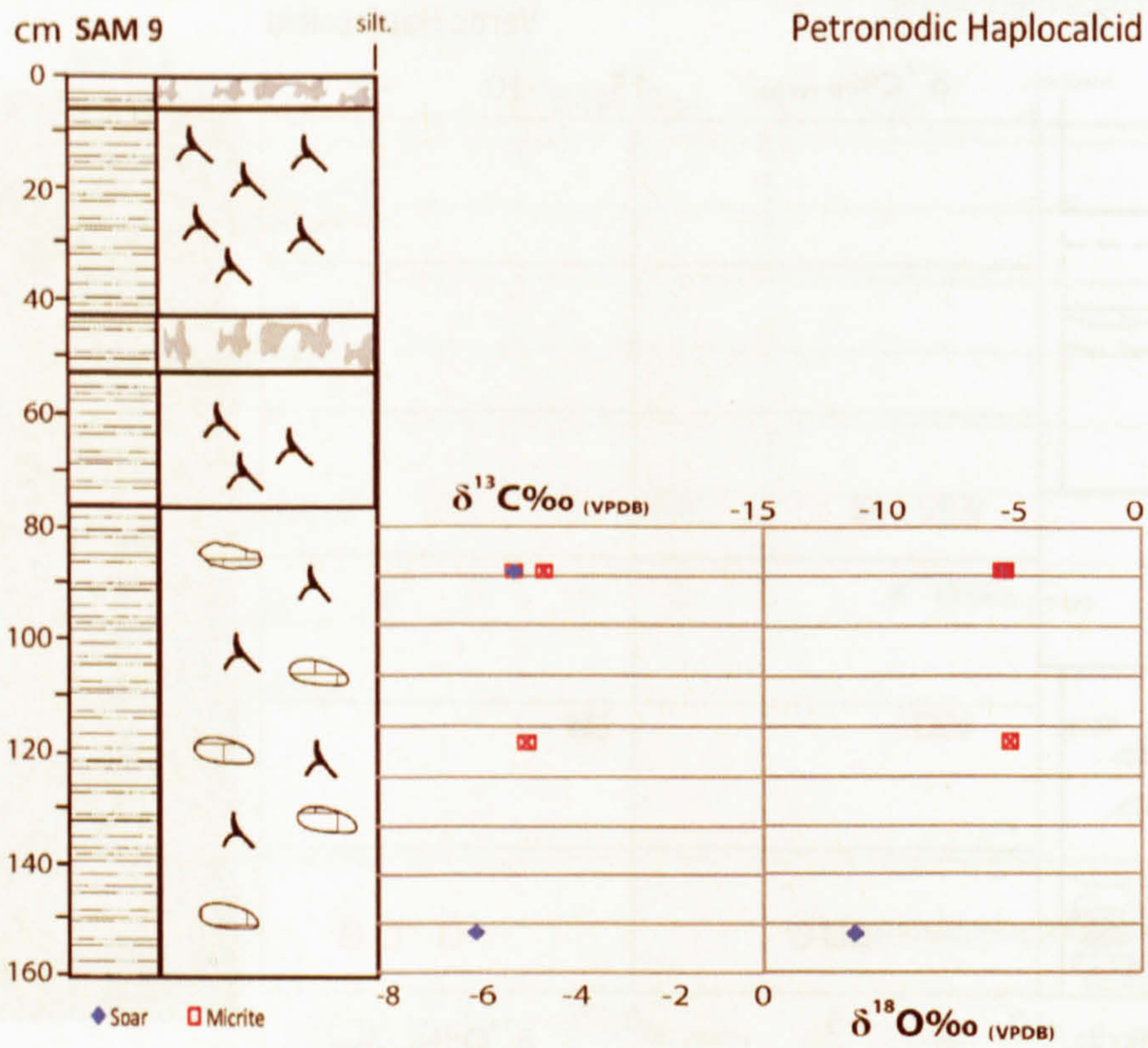
cm SAM 9
silt.
Petronodic Haplocalcid
0
20
40
60
80
100
120
140
160
δ13C‰ (VPDB)
-15
-10
-5
0
-8
-6
-4
-2
0
δ18O‰ (VPDB)
Soar
Micrite

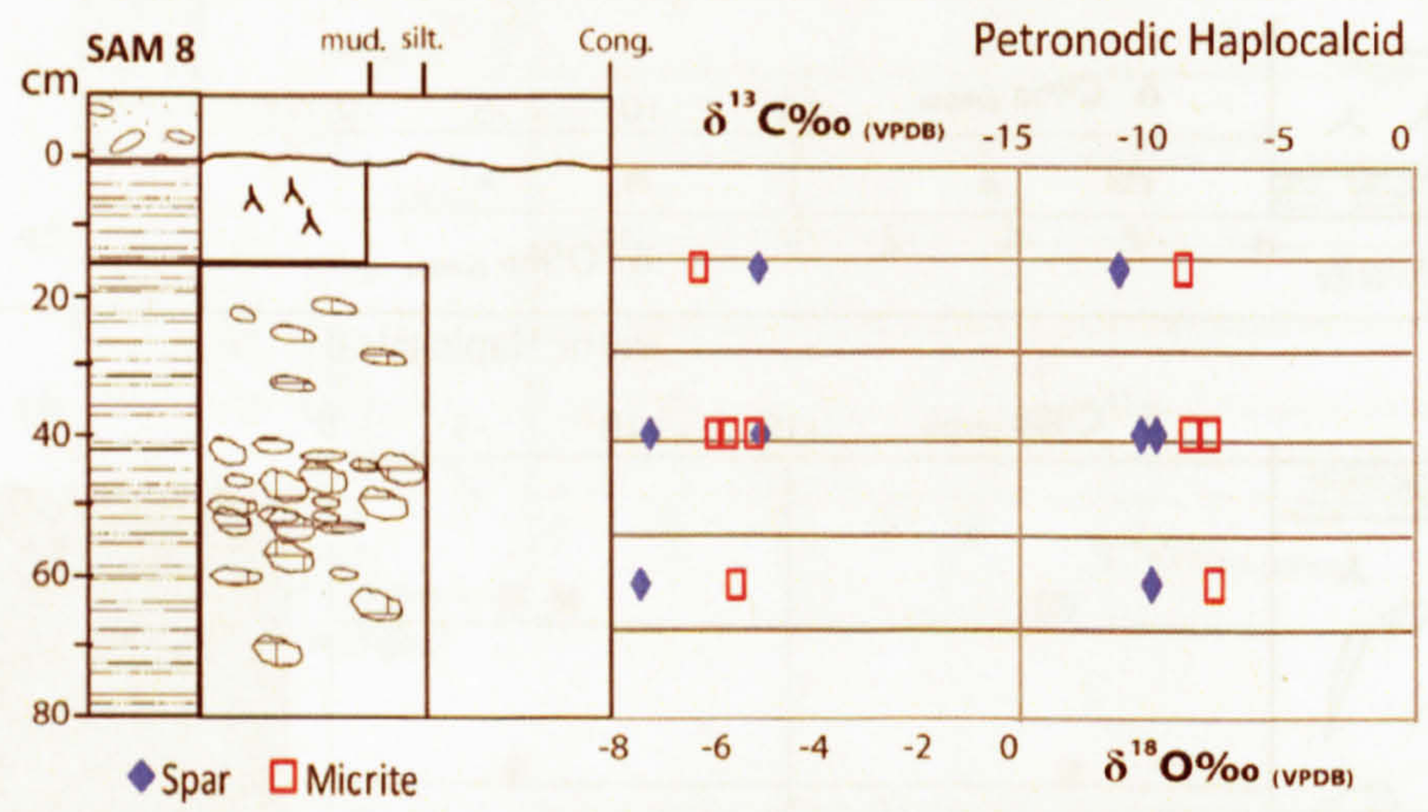
SAM 8
mud. silt.
Cong.
Petronodic Haplocalcid
cm
0
20
40
60
80
δ13C‰ (VPDB)
-15
-10
-5
0
-8
-6
-4
-2
0
δ18O‰ (VPDB)
Spar
Micrite

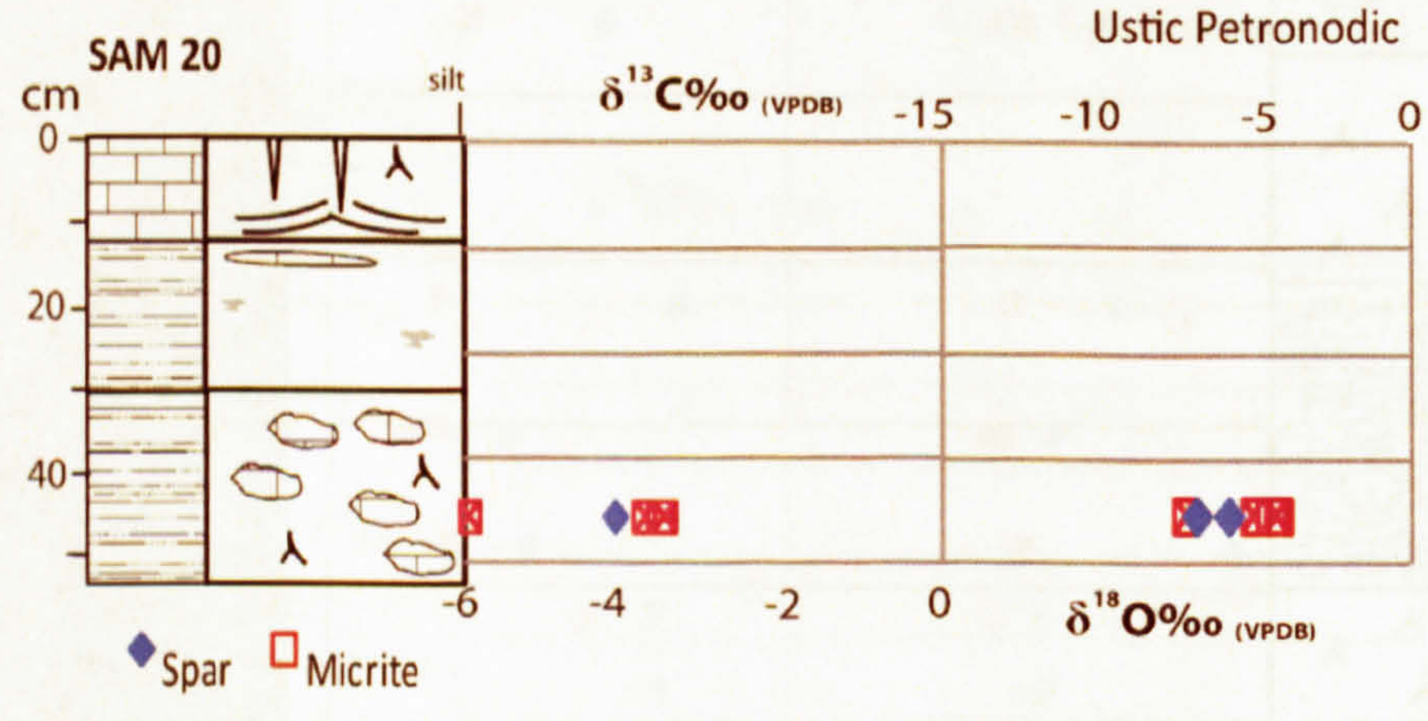
SAM 20
cm
silt
Ustic Petronodic
0
20
40
δ13C‰ (VPDB)
-15
-10
-5
0
-6
-4
-2
0
δ18O‰ (VPDB)
Spar
Micrite

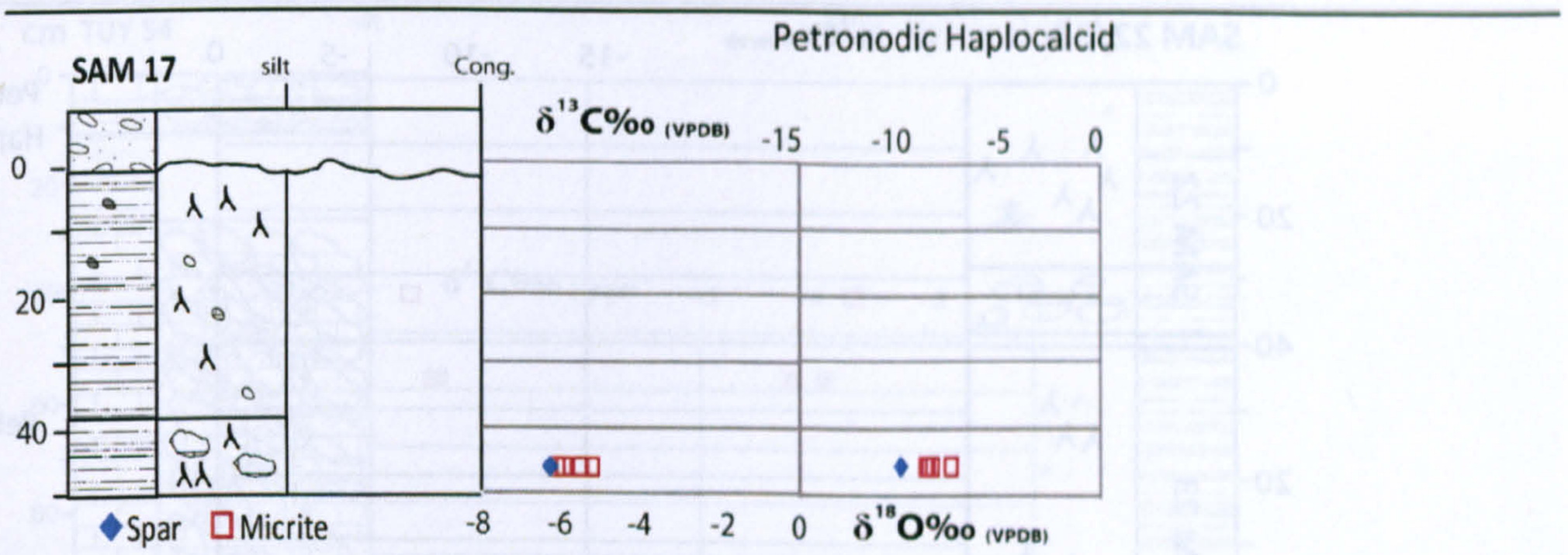
SAM 17
silt
Cong.
Petronodic Haplocalcid
δ13C‰ (VPDB)
-15
-10
-5
0
0
20
40
Spar
Micrite
-8
-6
-4
-2
0
δ18O‰ (VPDB)

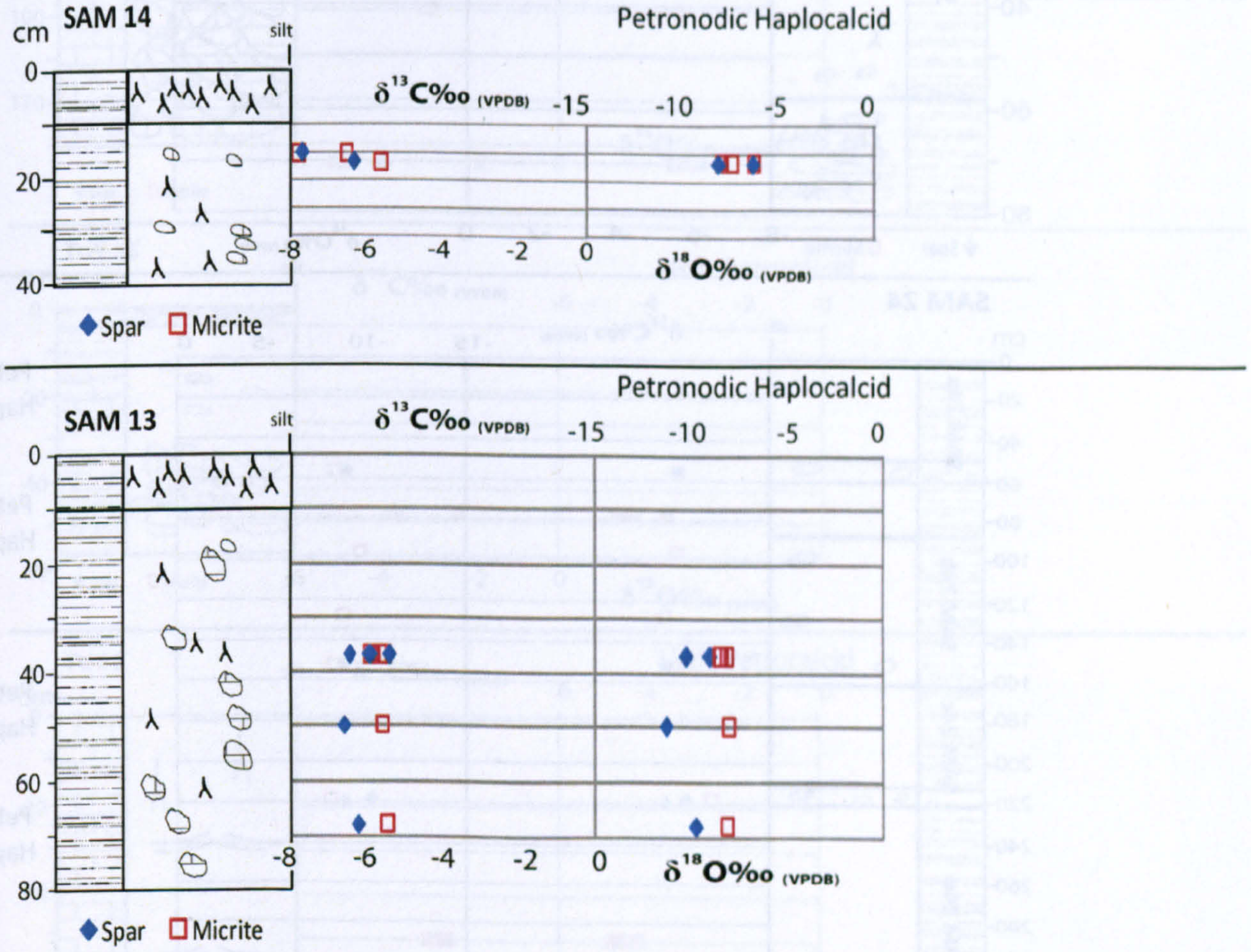
cm
SAM 14
silt
Petronodic Haplocalcid
δ13C‰ (VPDB)
-15
-10
-5
0
0
20
40
-8
-6
-4
-2
0
δ18O‰ (VPDB)
Spar
Micrite

SAM 13
silt
Petronodic Haplocalcid
δ13C‰ (VPDB)
-15
-10
-5
0
0
20
40
60
80
-8
-6
-4
-2
0
δ18O‰ (VPDB)
Spar
Micrite

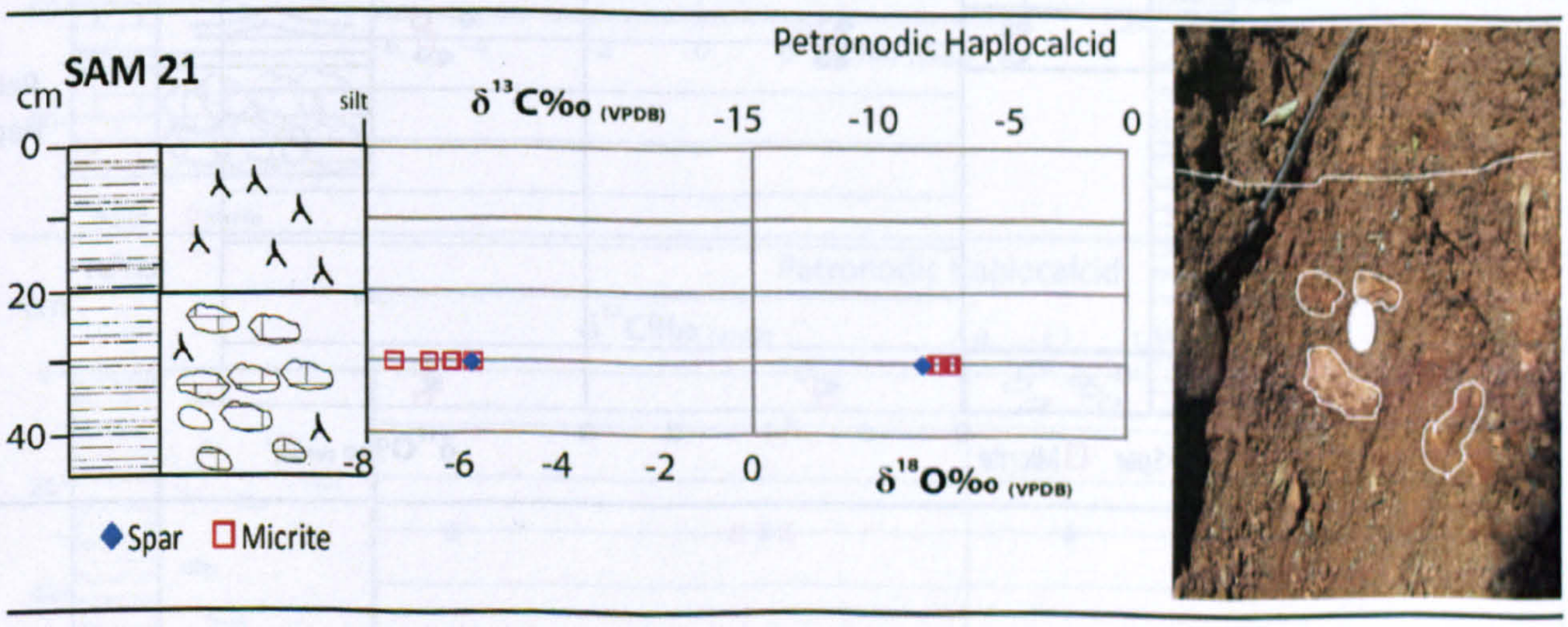
SAM 21
cm
silt
Petronodic Haplocalcid
δ13C‰ (VPDB)
-15
-10
-5
0
0
20
40
-8
-6
-4
-2
0
δ18O‰ (VPDB)
Spar
Micrite

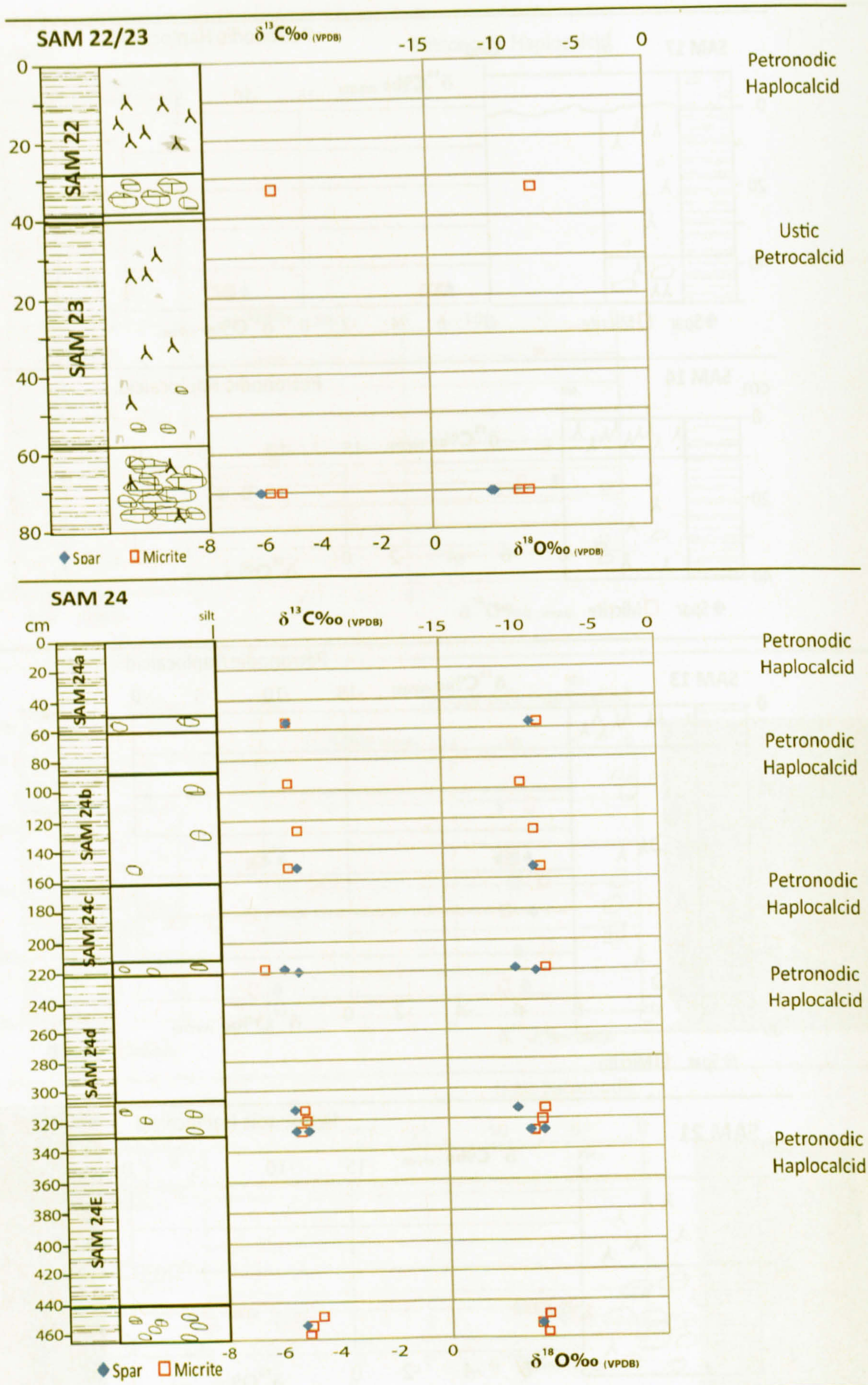
SAM 22/23
δ13C‰ (VPDB)
-15
-10
-5
0
SAM 22
SAM 23
0
20
40
60
80
Petronodic Haplocalcid
Ustic Petrocalcid
Spar
Micrite
-8
-6
-4
-2
0
δ18O‰ (VPDB)
SAM 24
cm
silt
δ13C‰ (VPDB)
-15
-10
-5
0
SAM 24a
SAM 24b
SAM 24c
SAM 24d
SAM 24E
0
20
40
60
80
100
120
140
160
180
200
220
240
260
280
300
320
340
360
380
400
420
440
460
Petronodic Haplocalcid
Petronodic Haplocalcid
Petronodic Haplocalcid
Petronodic Haplocalcid
Spar
Micrite
-8
-6
-4
-2
0
δ18O‰ (VPDB)

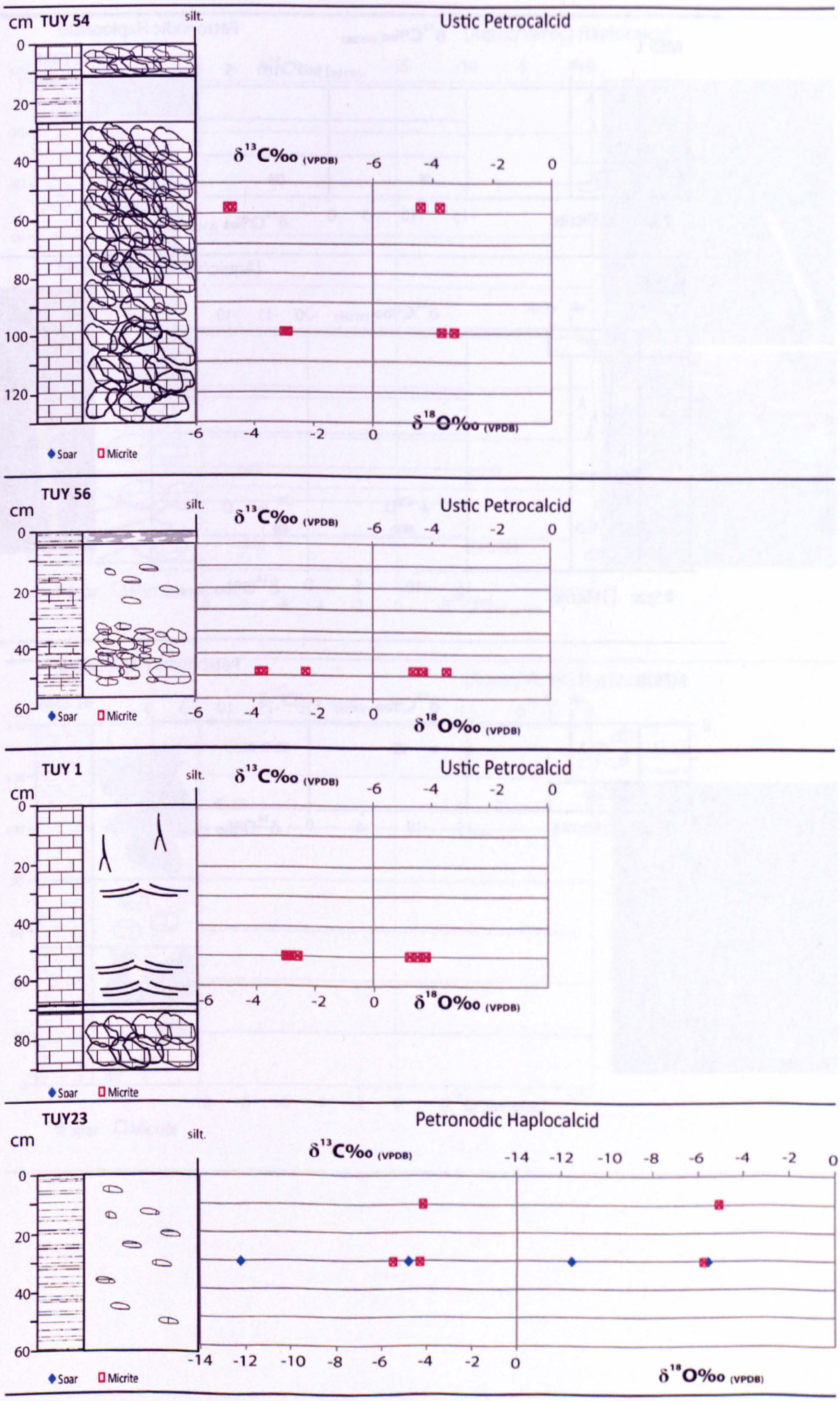
cm TUY 54
silt.
Ustic Petrocalcid
δ13C‰ (VPDB)
-6
-4
-2
0
0
20
40
60
80
100
120
δ18O‰ (VPDB)
Spar
Micrite
TUY 56
cm
silt.
Ustic Petrocalcid
δ13C‰ (VPDB)
δ18O‰ (VPDB)
Spar
Micrite
TUY 1
cm
silt.
Ustic Petrocalcid
δ13C‰ (VPDB)
δ18O‰ (VPDB)
Spar
Micrite
TUY23
cm
silt.
Petronodic Haplocalcid
δ13C‰ (VPDB)
-14
-12
-10
-8
δ18O‰ (VPDB)
Spar
Micrite

MES 1

Petronodic Haplocalcid

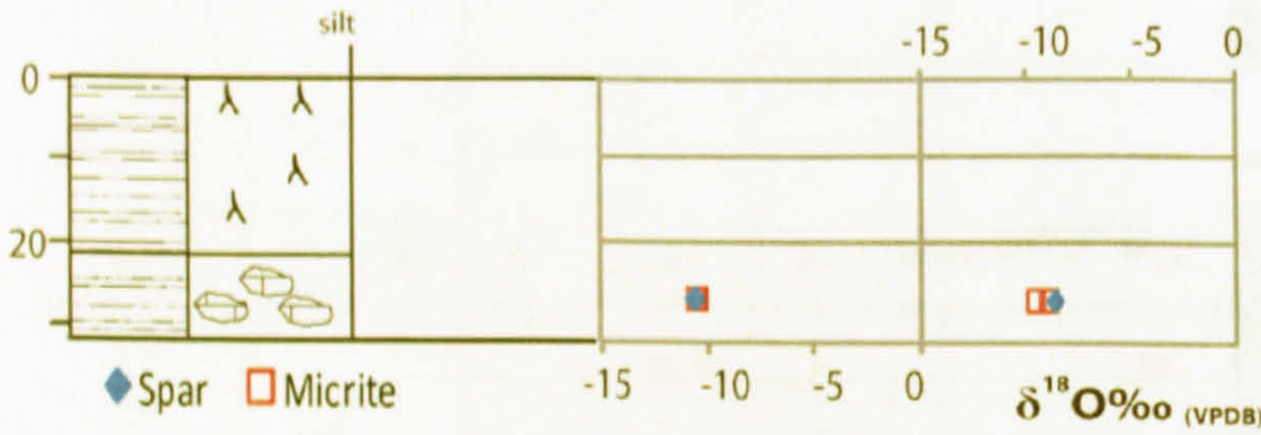

MES8

(Aquic/Vertic) Haplocalcid

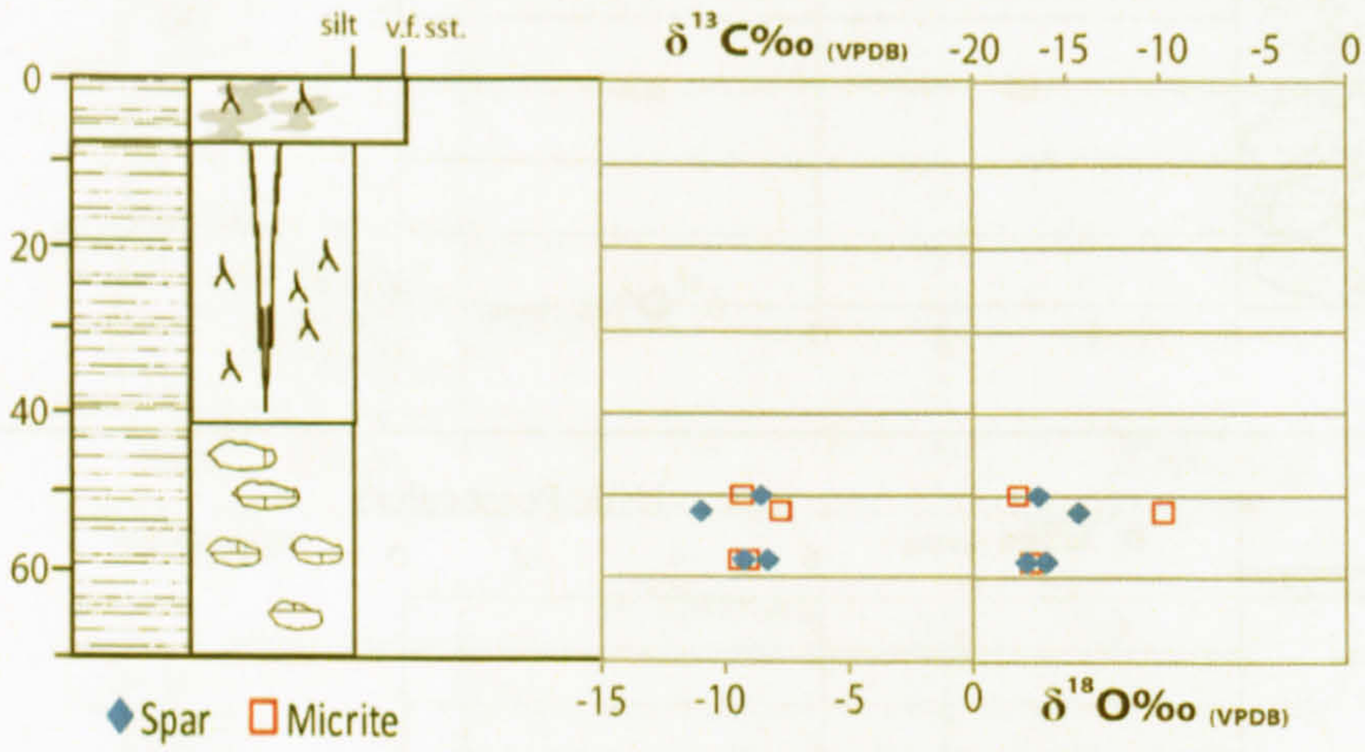

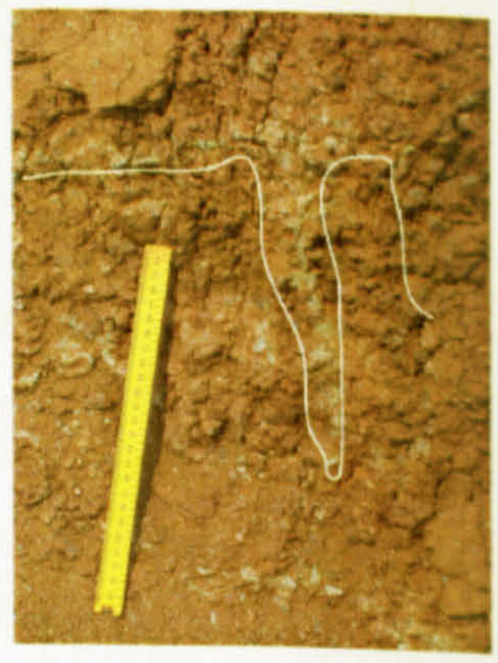

MES10

Petronodic Haplocalcid

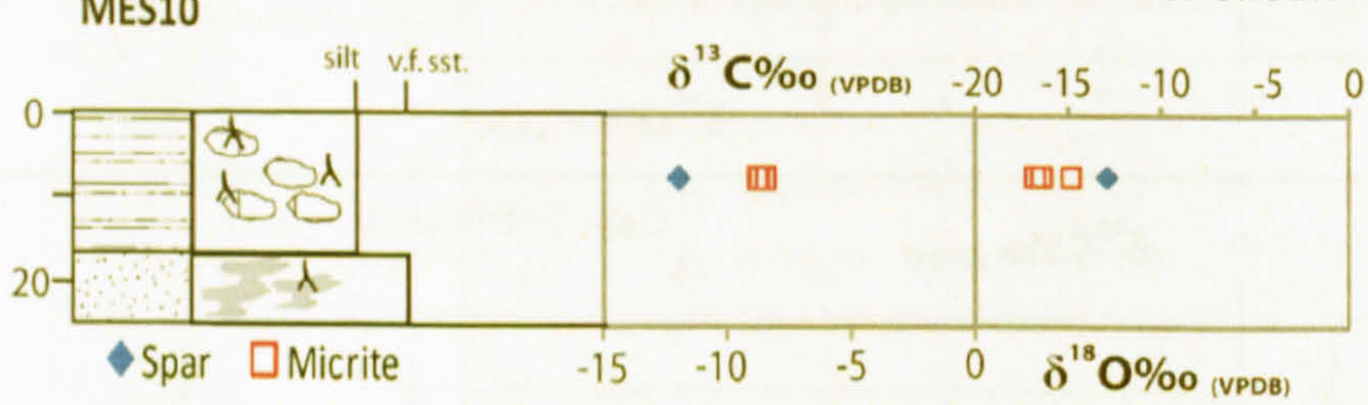

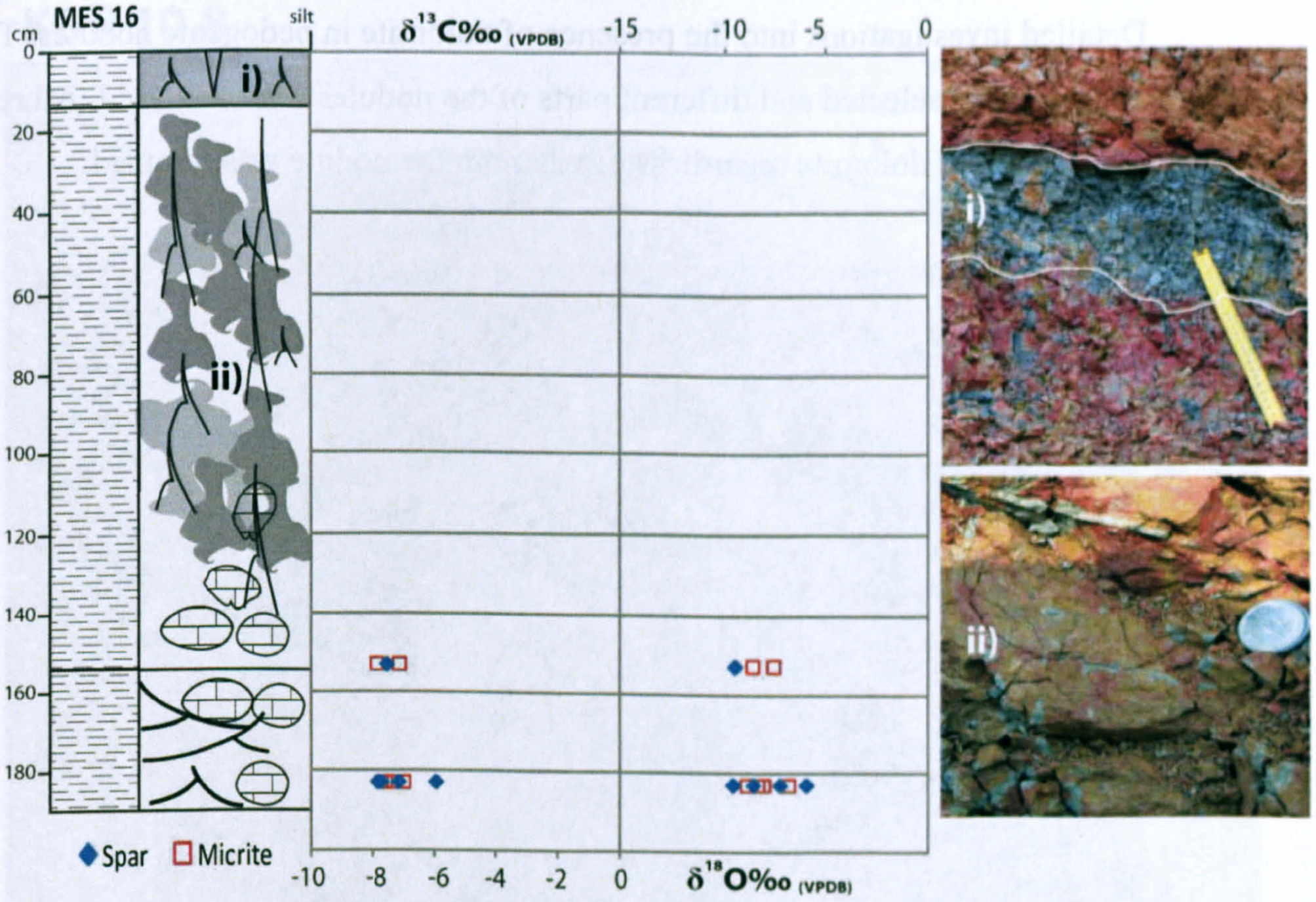
(Aquic/Vertic) Haplocalcid
MES 16
silt
cm
0
20
40
60
80
100
120
140
160
180
i)
ii)
δ13C‰ (VPDB)
-15
-10
-5
0
Spar
Micrite
-10
-8
-6
-4
-2
0
δ18O‰ (VPDB)

i)

ii)

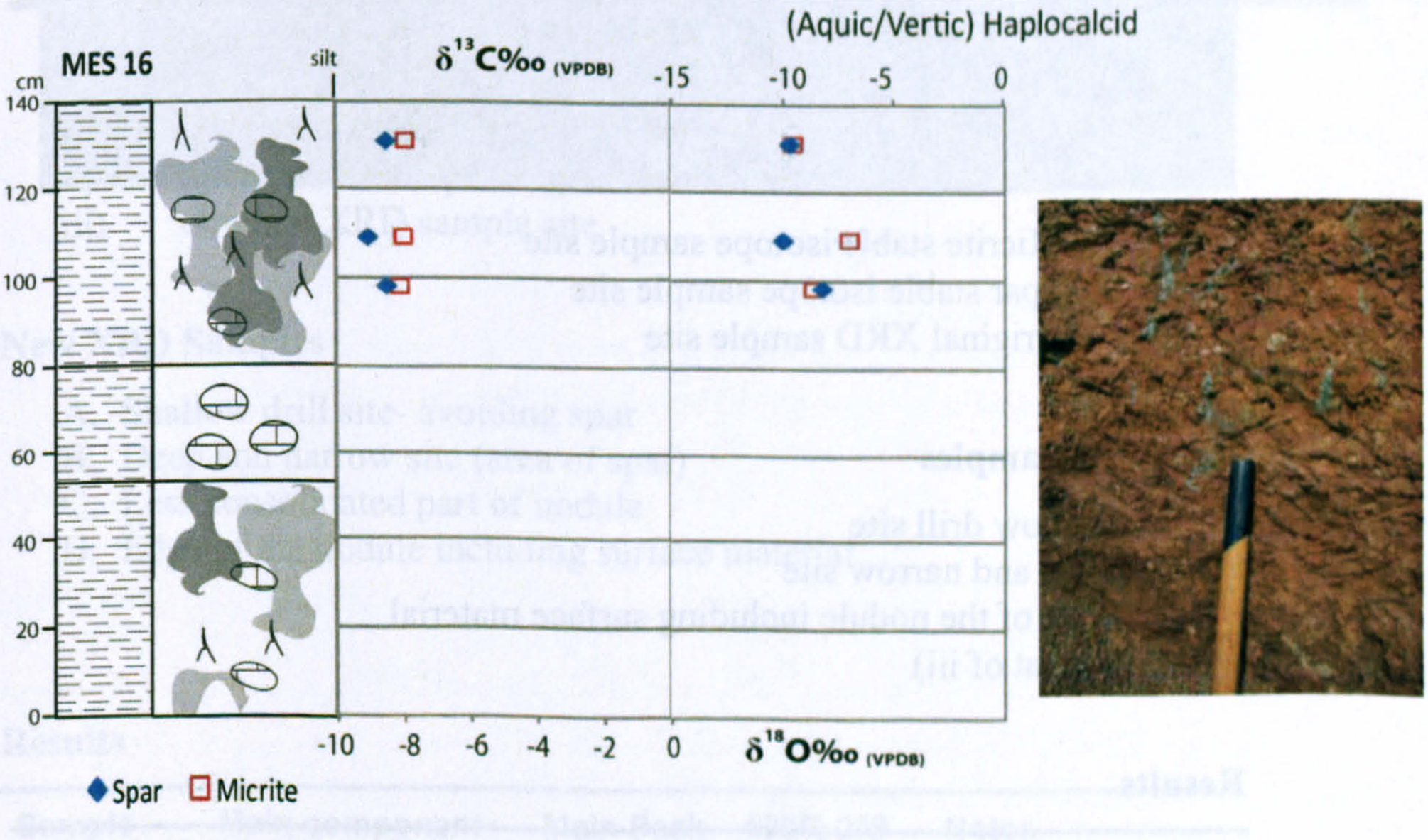
(Aquic/Vertic) Haplocalcid
MES 16
silt
cm
140
120
100
80
60
40
20
0
δ13C‰ (VPDB)
-15
-10
-5
0
Spar
Micrite
-10
-8
-6
-4
-2
0
δ18O‰ (VPDB)

A2.3

Detailed investigations into the presence of dolomite in pedogenic nodules. Three nodules were selected and different parts of the nodules were analysed. All returned a XRD result of dolomite regardless of where in the nodule was sampled

KOR 2.4

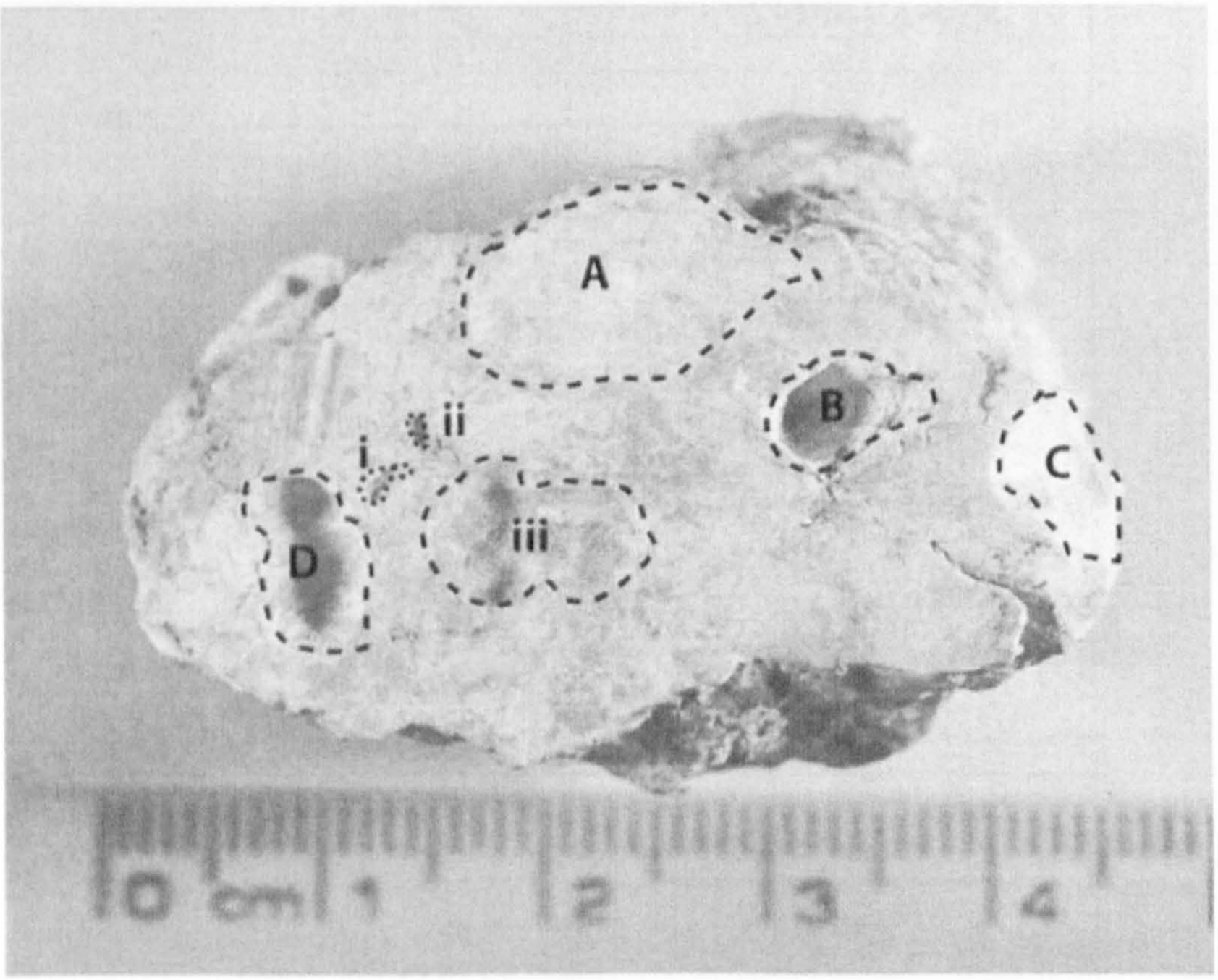

i) Micrite stable isotope sample site
ii) Spar stable isotope sample site
iii) Original XRD sample site

New XRD Samples

A. Shallow drill site
B. Deep and narrow site
C. Edge of the nodule including surface material
D. Repeat of iii)

Results

Sample	Main component	Main Peak	100% 2°θ	Notes
iii	Dolomite	580	30.7749	Calcite III (29.4016)
A	Dolomite	796	30.7089	
B	Dolomite	298	30.8873	Calcite III (29.5649)
C	Dolomite	891	30.7478	Calcite III (29.3763)
D	Dolomite	933	30.8295	

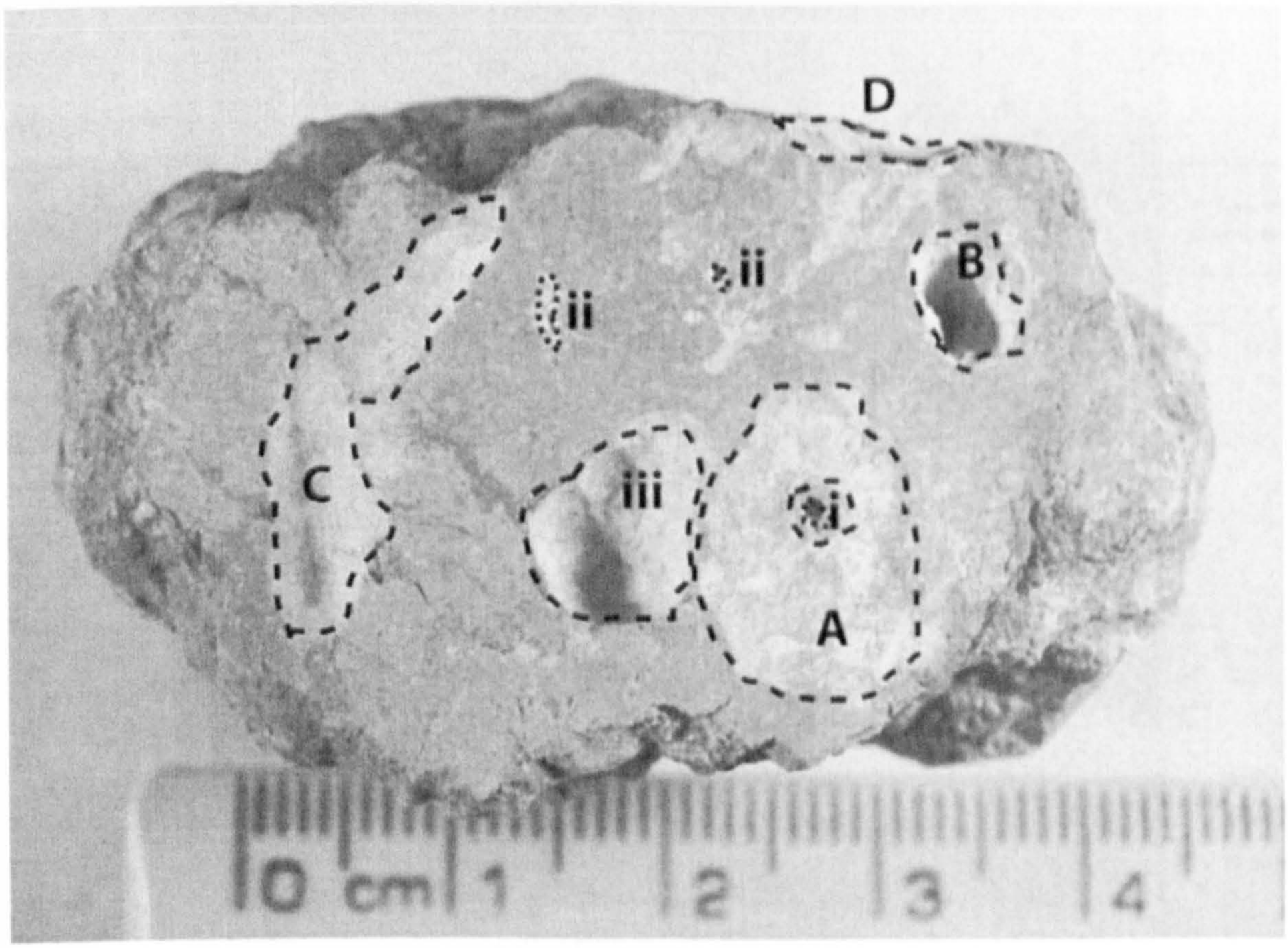

i) Micrite stable isotope sample site
ii) Spar stable isotope sample site
iii) Original XRD sample site

New XRD Samples

A. Shallow drill site- avoiding spar
B. Deep and narrow site (area of spar)
C. Less consolidated part of nodule
D. Edge of the nodule including surface material

Results

Sample	Main component	Main Peak	100% 2°θ	Notes
iii	Dolomite *	874.84	30.6249	Quartz High
A	Dolomite *	1027.87	30.6143	Quartz
B	Dolomite	506	30.7588	Quartz low
C	Dolomite	626.26	30.5844	Quartz
D	Dolomite	579.23	30.5719	

KOR 21.10

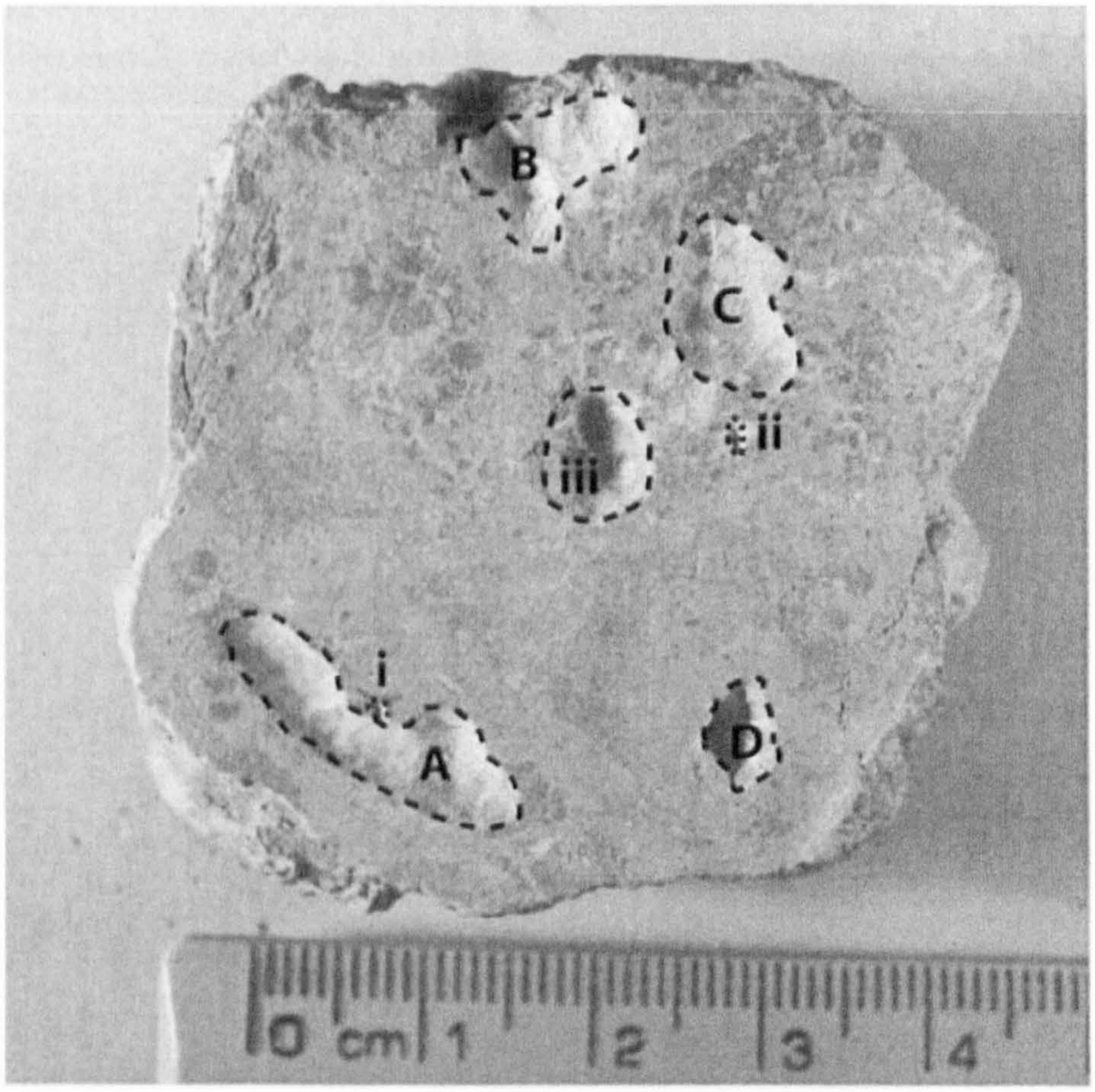

i) Micrite stable isotope sample site
ii) Spar stable isotope sample site
iii) Original XRD sample site

New XRD Samples

A. Shallow drill site
B. Redden less consolidated area of nodule (altered?)
C. In area of high amount of small spar cracks
D. Deep and narrow site

Results

Sample	Main component	Main Peak	100% 2°θ	Notes
iii	Dolomite	896	30.7348	
A	Dolomite	636.92	30.6562	
B*	Dolomite	616.59	30.6596	Quartz (50)
C	Dolomite	510.2	30.7603	Calcite (100% 2°θ= 29.3826)*
D	Dolomite	777.8	30.6271	Quartz (31)

* only one with 'calcite' peak

A2.4

X-ray diffraction results. Main component refers to the largest peak recorded in a sample. The 100% 2°θ is the 2°θ of the maximum peak in the sample. The second component is the second match after the main component had been removed.

Sample	Section	Main Component	Max Number of counts	100% 2°θ	100% d-spacing (Å)	Second Component
KOR 1.7	Boyevaya Gora	Dolomite	1254	31.5633	2.83462	-
KOR 1.8	Boyevaya Gora	Dolomite	1217	31.4403	2.84543	-
KOR 1.9	Boyevaya Gora	Dolomite	512	31.8326	2.81125	-
KOR 1.10	Boyevaya Gora	Dolomite	872	31.5266	2.83703	-
KOR 1.8	Boyevaya Gora	Dolomite	1217	31.4403	2.84543	-
KOR 2.1	Boyevaya Gora	Dolomite	779	31.8540	2.80941	-
KOR 2.2	Boyevaya Gora	Dolomite	1709	31.5273	2.83777	-
KOR 2.3	Boyevaya Gora	Dolomite	1233	31.6074	2.83076	-
KOR 2.4	Boyevaya Gora	Dolomite	580	31.7748	2.81623	Calcite
KOR 2.5	Boyevaya Gora	Dolomite	757	31.7169	2.82124	-
KOR 2.6	Boyevaya Gora	Dolomite	1140	31.6193	2.82972	-
KOR 2.7	Boyevaya Gora	Dolomite	1088	31.2852	2.85918	Quartz
KOR 2.8	Boyevaya Gora	Dolomite	938	31.5512	2.83568	Quartz
KOR 2.9	Boyevaya Gora	Dolomite	1304	31.5682	2.83490	-
KOR 3.1	Boyevaya Gora	Dolomite	531	31.5412	2.83658	Calcite, magnesian
KOR 4.1	Boyevaya Gora	Dolomite	1079	31.6145	2.83015	-
KOR 5.1	Boyevaya Gora	Quartz	561	27.3632	3.25941	Dolomite
KOR 5.2	Boyevaya Gora	Dolomite	955	31.5646	2.83450	Quartz
KOR 5.3	Boyevaya Gora	Dolomite	798	31.7591	2.81759	-
KOR 5.4	Boyevaya Gora	Dolomite	853	31.5276	2.83775	Quartz
KOR 5.5	Boyevaya Gora	Dolomite	942	31.5960	2.83176	Quartz
KOR 6.1	Boyevaya Gora	Dolomite	893	31.5059	2.83965	-
KOR 6.2	Boyevaya Gora	Dolomite	439	31.6571	2.82643	-
KOR 6.3	Boyevaya Gora	Dolomite	753	31.6416	2.82778	Calcite III
KOR 6.4	Boyevaya Gora	Dolomite	938	31.6681	2.82541	-
KOR 6.5	Boyevaya Gora	Dolomite	362	31.7096	2.82187	Calcite III
KOR 6.6	Boyevaya Gora	Dolomite	750	31.6856	2.82396	-
KOR 6.7	Boyevaya Gora	Dolomite	399	31.7531	2.81810	Quartz
KOR 6.8	Boyevaya Gora	Dolomite	450	31.5936	2.83197	-
KOR 7.1	Boyevaya Gora	Dolomite	807	31.5337	2.83686	Quartz
KOR 9.1	Boyevaya Gora	Dolomite	701	31.5439	2.83631	-
KOR 9.2	Boyevaya Gora	Dolomite	781	31.6584	2.82632	-
KOR 9.3	Boyevaya Gora	Dolomite	645	31.5298	2.83755	Quartz
KOR 9.4	Boyevaya Gora	Dolomite	612	31.6678	2.82550	Quartz
KOR 10.2	Boyevaya Gora	Dolomite	689	31.6786	2.82457	Quartz
KOR 10.3	Boyevaya Gora	Dolomite	1356	31.5795	2.83320	-
KOR 10.4	Boyevaya Gora	Dolomite	974	31.4688	2.84292	Quartz
KOR 10.5	Boyevaya Gora	Dolomite	471	31.8014	2.81394	-
KOR 10.6	Boyevaya Gora	Quartz	484	27.3632	3.25941	Dolomite

Sample	Section	Main Component	Max Number of counts	100% 2°θ	100% d-spacing (Å)	Second Component
KOR 10.7	Boyevaya Gora	Dolomite	509	31.7508	2.81831	–
KOR 10.8	Boyevaya Gora	Dolomite	875	31.6249	2.82924	best match Kutnohorite
KOR 10.10	Boyevaya Gora	Dolomite	518	31.5156	2.83880	Quartz
KOR 10.11	Boyevaya Gora	Dolomite	283	31.7619	2.81735	–
KOR 10.12	Boyevaya Gora	Dolomite	434	31.6732	2.82504	Quartz
KOR 10.B1	Boyevaya Gora	Quartz	764	31.6830	2.82418	Dolomite
KOR 11.1	Boyevaya Gora	Dolomite	910	31.6244	2.82928	–
KOR 12.1	Boyevaya Gora	Dolomite	525	31.6181	2.82983	Quartz
KOR 12.2	Boyevaya Gora	Dolomite	785	31.5407	2.83660	Quartz
KOR 12.3	Boyevaya Gora	Dolomite	769	31.6671	2.82557	Quartz
KOR 13.1	Boyevaya Gora	Dolomite	963	31.5759	2.33510	Quartz
KOR 14.1	Boyevaya Gora	Dolomite	1098	31.5750	2.83359	–
KOR 14.2	Boyevaya Gora	Dolomite	810	31.5392	2.83673	–
KOR 14.3	Boyevaya Gora	Dolomite	688	31.5683	2.83418	–
KOR 14.7	Boyevaya Gora	Dolomite	860	31.6006	2.83133	Quartz
KOR 14.6	Boyevaya Gora	Dolomite	773	31.5045	2.83977	–
KOR 14.8	Boyevaya Gora	Dolomite	895	31.4686	2.84930	Quartz
KOR 14.10	Boyevaya Gora	Dolomite	889	31.5506	2.83570	Quartz
KOR 14.11	Boyevaya Gora	Dolomite	740	31.6716	2.82517	–
KOR 14.14	Boyevaya Gora	Dolomite	768	31.5542	2.83542	Quartz
KOR 14.15	Boyevaya Gora	Dolomite	1103	31.6730	2.82505	–
KOR 15.2	Boyevaya Gora	Dolomite	519	31.8074	2.81345	Quartz
KOR 15.3	Boyevaya Gora	Dolomite	527	31.4837	2.84161	–
KOR 15.4	Boyevaya Gora	Dolomite	632	31.7288	2.82021	–
KOR 15.5	Boyevaya Gora	Dolomite	718	31.6647	2.82577	–
KOR 15.6	Boyevaya Gora	Dolomite	713	31.7108	2.82177	Quartz
KOR 15.6	Boyevaya Gora	Dolomite	711	31.5483	2.83593	–
KOR 15.7	Boyevaya Gora	Dolomite	642	31.6811	2.82435	–
KOR 15.8	Boyevaya Gora	Dolomite	1964	31.7314	2.81999	–
KOR 15.9	Boyevaya Gora	Dolomite	1173	31.5511	2.83569	Quartz
KOR 15.B2	Boyevaya Gora	Quartz	834	27.4080	3.25419	–
KOR 16.1	Boyevaya Gora	Calcite, magnesian	774	30.3301	2.94700	–
KOR 16.2	Boyevaya Gora	Calcite, magnesian	456	30.4822	2.93264	–
KOR 16.3	Boyevaya Gora	Calcite	1159	30.3550	2.94938	–
KOR 16.4	Boyevaya Gora	Calcite, magnesian	990	30.4075	2.93968	–
KOR 16.5	Boyevaya Gora	Calcite, magnesian	1178	30.2699	2.95273	–
KOR 16.6	Boyevaya Gora	Calcite, magnesian	816	30.2943	2.95040	–
KOR 16.7	Boyevaya Gora	Calcite	920	30.3167	2.94828	–
KOR 16.8	Boyevaya Gora	Calcite, magnesian	871	30.3376	2.94629	–
KOR 16.9	Boyevaya Gora	Calcite, magnesian	724	30.3077	2.94912	–
KOR 17.2	Boyevaya Gora	Calcite	673	30.3557	2.94457	–
KOR 17.3	Boyevaya Gora	Dolomite	397	31.6304	2.82875	Quartz
KOR 17.4	Boyevaya Gora	Dolomite	557	31.7635	2.81721	Quartz/ Calcite, magnesian
KOR 18.2	Boyevaya Gora	Calcite	491	30.5462	2.92665	–
KOR 18.4	Boyevaya Gora	Calcite	404	30.4684	2.99339	–
04.8.1.I	Boyevaya Gora	Dolomite	854	31.6494	2.82710	–

Sample	Section	Main Component	Max Number of counts	100% 2°θ	100% d-spacing (Å)	Second Component
04.8.1.l.i	Boyevaya Gora	Dolomite	641	31.7873	2.81516	Quartz
04.8.1.l.ii	Boyevaya Gora	Dolomite	1110	31.5155	2.83881	-
04.8.1.l.iii	Boyevaya Gora	Dolomite	964	31.4570	2.84396	Quartz
KOR 21.1	Boyevaya Gora	Calcite (Mg)	620	30.2867	2.95112	-
KOR 21.2	Boyevaya Gora	Calcite, magnesian	699	30.2624	2.95344	-
KOR 21.3	Boyevaya Gora	Calcite (CaCO3)	621	30.3548	2.94466	-
KOR 21.4	Boyevaya Gora	Calcium Carbonate	598	30.3825	2.94204	-
KOR 21.5	Boyevaya Gora	Dolomite	309	31.8131	2.81293	-
KOR 21.6	Boyevaya Gora	Quartz	498	30.3145	2.94848	Calcite, magnesian
KOR 21.7	Boyevaya Gora	Dolomite	760	31.6952	2.82312	-
KOR 21.8	Boyevaya Gora	Dolomite	482	31.8487	2.80987	Quartz
KOR 21.9	Boyevaya Gora	Dolomite	625	31.6169	2.82994	-
KOR 21.10	Boyevaya Gora	Dolomite	806	31.7348	2.81969	-
04.8.1.p	Boyevaya Gora	Dolomite	1191	31.6651	2.82574	-
KOR 22.1	Boyevaya Gora	Calcite (CaCO3)	401	30.3207	2.94786	-
KOR 22.2a	Boyevaya Gora	Calcite (Mg, CaCO3)	376	30.2494	2.95468	-
KOR 22.2b	Boyevaya Gora	Calcite (Mg, CaCO3)	961	30.2654	2.95316	-
KOR 22.3	Boyevaya Gora	Calcium Carbonate	869	30.1836	2.96097	-
KOR 22.4	Boyevaya Gora	Calcite, magnesian	901	30.3640	2.94379	Quartz
KOR 22.5	Boyevaya Gora	Quartz	463	26.7236	3.33596	-
KOR 22.6	Boyevaya Gora	Calcite	946	30.3095	2.94896	-
KOR 22.7	Boyevaya Gora	Calcite	498	30.3949	2.94087	-
KOR 22.8	Boyevaya Gora	Calcite	985	30.2524	2.95439	-
KOR 22.9	Boyevaya Gora	Calcite	1045	30.2094	2.95853	-
KOR 22.10	Boyevaya Gora	Calcite	1505	30.2863	2.95116	-
KOR 22.11	Boyevaya Gora	Calcite, magnesian	948	30.2881	2.95099	Calcite
KOR 22.12	Boyevaya Gora	Calcite	1102	30.1514	2.96406	-
KOR 22.13	Boyevaya Gora	Calcite	683	30.2223	2.95727	-
KOR 22.14	Boyevaya Gora	Calcite, magnesian	1277	30.2451	2.95509	Calcite syn
KOR 23.1	Boyevaya Gora	Calcite, magnesian	525	30.4233	2.93815	-
KOR 23.2	Boyevaya Gora	Calcite, magnesian	1090	30.2855	2.95124	-
KOR 23.3	Boyevaya Gora	Dolomite	533	31.7121	2.82165	-
KOR 23.4	Boyevaya Gora	Dolomite	468	31.6946	2.82318	Calcite
04.8.1.r	Boyevaya Gora	Dolomite	404	31.4222	2.84614	Calcite
04.8.1.r.i	Boyevaya Gora	Dolomite	499	31.4609	2.84361	Calcite
04.8.1.r.ii	Boyevaya Gora	Dolomite	786	31.4327	2.83280	Calcite
04.8.1.r.iii	Boyevaya Gora	Dolomite	810	31.5046	2.83977	Calcite
KOR 24.6	Boyevaya Gora	Calcite, magnesian	1291	30.2714	2.95259	-
KOR 24.5	Boyevaya Gora	Calcite	983	30.1801	2.92131	-
KOR 25.1	Boyevaya Gora	Calcite	998	30.3554	2.94461	-
KOR 25.5	Boyevaya Gora	Calcite, magnesian	1133	30.2963	2.95021	-
KOR 25.3	Boyevaya Gora	Calcite	958	30.3564	2.94614	-
04.8.1.g	Boyevaya Gora	Calcite	112	30.1714	2.96214	-
KOR 27.2	Boyevaya Gora	Quartz	378	27.6516	3.22607	Dolomite
KOR 27.3	Boyevaya Gora	Quartz	845	27.3539	3.29051	Calcite
KOR 27.4	Boyevaya Gora	Quartz	386	27.4625	3.24786	-

Sample	Section	Main Component	Max Number of counts	100% 2°θ	100% d-spacing (Å)	Second Component
04.8.1.f	Boyevaya Gora	Calcite	312	30.1134	2.96772	-
04.8.1.e	Boyevaya Gora	Dolomite	432	31.4767	2.84222	Calcite
04.8.1.c	Boyevaya Gora	Dolomite	495	31.5352	2.83708	-
04.8.1.c.i	Boyevaya Gora	Dolomite	582	31.6029	2.83116	-
04.8.1.c.ii	Boyevaya Gora	Dolomite	519	31.5053	2.89700	-
04.8.1.c.iii	Boyevaya Gora	Dolomite	418	31.4062	2.84844	Calcite
KOR 31.1	Boyevaya Gora	Calcite, magnesian	810	30.3260	2.94740	-
KOR 31.2	Boyevaya Gora	Calcite	526	30.4800	2.93285	-
KOR 31.5	Boyevaya Gora	Calcite	590	30.2711	2.95261	-
04.8.1.b.ii	Boyevaya Gora	Calcite	805	30.1484	2.96434	-
04.8.1.b.iii	Boyevaya Gora	Calcite	423	30.1242	2.96667	Quartz
KOR 32.2	Boyevaya Gora	Calcite	1200	30.1522	2.96398	-
KOR 32.8	Boyevaya Gora	Calcite	621	30.3779	2.94247	-
KOR 32.7	Boyevaya Gora	Calcite	829	30.1803	2.96129	-
KOR 33.3	Boyevaya Gora	Calcite	1048	30.1523	2.96398	Quartz
KOR 33.1	Boyevaya Gora	Calcite, magnesian	864	30.3867	2.41640	-
KOR 33.2	Boyevaya Gora	Calcite, magnesian	1055	30.1724	2.96204	Quartz
KOR 34.1	Boyevaya Gora	Calcite	1302	30.1462	2.96456	-
KOR 34.2	Boyevaya Gora	Calcite	739	30.4058	2.93984	-
KOR 34.3	Boyevaya Gora	Calcite	699	30.3990	2.94048	-
KOR 34.4	Boyevaya Gora	Calcite	644	30.3535	2.94478	-
KOR 34.5	Boyevaya Gora	Calcite, magnesian	876	30.3327	2.94676	Quartz
KOR 34.6	Boyevaya Gora	Calcite	837	30.2202	2.95747	-
KOR 34.7	Boyevaya Gora	Calcite	586	30.0209	2.97664	-
KOR 35.1	Boyevaya Gora	Calcite, magnesian	821	30.2370	2.95507	-
KOR 35.3	Boyevaya Gora	Quartz	391	27.6186	3.22986	Calcite
KOR 35.4	Boyevaya Gora	Quartz	503	27.5255	3.24056	Dolomite, High background
KOR 35.5	Boyevaya Gora	Calcite, syn	460	30.5144	2.92962	-
KOR 36.1	Boyevaya Gora	Calcium Carbonate	1043	30.2186	2.95762	Quartz
KOR 36.2	Boyevaya Gora	Calcite	1564	30.1481	2.96438	Quartz
KOR 36.3	Boyevaya Gora	Calcite	428	30.5073	2.93081	-
KOR 36.5	Boyevaya Gora	Calcite	939	30.0905	2.96992	Quartz
KOR 36.6	Boyevaya Gora	Quartz	494	27.5600	3.24351	-
KOR 36.4	Boyevaya Gora	Quartz	882	27.3167	3.26485	-
KOR 37.2	Boyevaya Gora	Quartz	1032	27.3489	3.26109	Calcite
KOR 37.3	Boyevaya Gora	Calcite	788	30.1765	2.96165	Quartz
KOR 37.4	Boyevaya Gora	Calcite	679	30.1796	2.96135	Quartz
KOR 37.5	Boyevaya Gora	Calcite	1523	30.2219	2.95730	Allophane
KOR 37.1	Boyevaya Gora	Quartz	750	27.3036	3.26639	-
KOR 39	Boyevaya Gora	Quartz, low	1027	26.6990	3.33897	-
04.8.2.a	Boyevaya Gora	Calcite	389	30.4881	2.93209	-
04.8.2.e	Boyevaya Gora	Quartz	594	27.5049	3.24940	-
04.8.2.f	Boyevaya Gora	Calcite, magnesian	350	30.3946	2.94089	-
04.8.1.l	Boyevaya Gora	Calcite	171	30.3734	2.94252	-
SAM 1.1	Sambullak	Calcite, magnesian	506	30.5414	2.92709	-
SAM 1.2	Sambullak	Calcite	767	30.4235	2.93817	Quartz

Sample	Section	Main Component	Max Number of counts	100% 2°θ	100% d-spacing (Å)	Second Component
SAM 1.3	Sambullak	Calcite	1142	30.3775	2.94252	Quartz
SAM 1.4	Sambullak	Calcite	562	30.3061	2.94928	-
SAM 1.5	Sambullak	Calcite, magnesian	1196	30.3067	2.94923	Quartz
SAM 2.1	Sambullak	Calcite, magnesian	1374	30.2569	2.95396	Quartz
SAM 2.2	Sambullak	Dolomite	1080	31.6675	2.82553	Quartz
SAM 2.3	Sambullak	Calcite, magnesian	680	30.3760	2.94265	-
SAM 2.4	Sambullak	Calcite, magnesian	984	30.4156	2.93891	-
SAM 2.5	Sambullak	Calcite, magnesian	895	30.2868	2.95112	Quartz
SAM 3.1	Sambullak	Calcite, magnesian	1385	30.3346	2.94657	Calcite
SAM 3.2	Sambullak	Calcite	1114	30.1511	2.96409	-
SAM 3.3	Sambullak	Dolomite	1647	31.7487	2.81849	Calcite
SAM 3.4	Sambullak	Dolomite	608	31.6725	2.82509	Calcite
SAM 3.5	Sambullak	Dolomite	550	31.9118	2.80446	Quartz
SAM 4.2	Sambullak	Calcite	750	30.3658	2.94362	Quartz
SAM 4.3	Sambullak	Calcite, magnesian	1204	30.2550	2.95415	Calcite
SAM 4.4	Sambullak	Calcite	726	30.1257	2.96653	Quartz
SAM 8.1	Sambullak	Calcite, magnesian	662	30.3793	2.94234	-
SAM 8.2	Sambullak	Calcite	285	30.4847	2.93240	-
SAM 8.3	Sambullak	Calcite	556	30.4441	2.93622	-
SAM 8.4	Sambullak	Calcite, magnesian	494	30.3622	2.94396	-
SAM 8.5	Sambullak	Calcite	860	30.1896	2.96040	-
SAM 9.1	Sambullak	Calcite, magnesian	856	30.3107	2.94884	-
SAM 9.2	Sambullak	Dolomite	833	31.7992	2.81413	-
SAM 9.3	Sambullak	Dolomite	892	31.8439	2.81028	-
SAM 9.4	Sambullak	Dolomite	911	31.6793	2.82450	Quartz
SAM 10.1	Sambullak	Dolomite	1251	31.7161	2.82131	-
SAM 10.2	Sambullak	Dolomite	443	31.8640	2.80855	-
SAM 10.3	Sambullak	Dolomite	788	31.7021	2.82252	Quartz
SAM 10.4	Sambullak	Dolomite	401	31.9494	2.79868	Quartz
SAM 10.5	Sambullak	Dolomite	605	31.8401	2.81060	Quartz
SAM 10.6	Sambullak	Dolomite	183	32.0066	2.79636	Quartz
SAM 10.7	Sambullak	Dolomite	128	31.6293	2.82886	-
SAM 10.8	Sambullak	Dolomite	337	31.7830	2.81552	Quartz
SAM 10.9	Sambullak	Calcite, magnesian	239	30.3818	2.94210	Quartz
SAM 12.1	Sambullak	Calcite	566	30.2255	2.95696	-
SAM 12.2	Sambullak	Dolomite	645	31.7125	2.82162	Quartz
SAM 13.1	Sambullak	Calcite	522	30.0544	2.97340	Quartz
SAM 13.2	Sambullak	Calcite, magnesian	901	30.3296	2.94705	Calcite
SAM 13.3	Sambullak	Calcite, magnesian	507	30.2293	2.95659	-
SAM 13.4	Sambullak	Calcite, magnesian	654	30.2192	2.95757	-
SAM 13.5	Sambullak	Calcite, magnesian	424	30.3089	2.94901	-
SAM 14.1	Sambullak	Calcite, magnesian	452	30.3387	2.94619	-
SAM 14.2	Sambullak	Calcite, magnesian	805	30.3818	2.94210	-
SAM 17.1	Sambullak	Calcite	548	30.4738	2.93343	Quartz
SAM 17.3	Sambullak	Calcite	688	30.0765	2.97127	-
SAM 17.4	Sambullak	Calcium Carbonate	426	30.2520	2.95444	-

Sample	Section	Main Component	Max Number of counts	100% 2°θ	100% d-spacing (Å)	Second Component
SAM 19.5	Sambullak	Dolomite	1085	31.6440	2.82757	–
SAM 20.2	Sambullak	Dolomite	549	31.7059	2.82220	Quartz
SAM 20.3	Sambullak	Dolomite	856	31.6440	2.82758	Quartz
SAM 20.4	Sambullak	Dolomite	487	31.7537	2.88050	–
SAM 20.5	Sambullak	Dolomite	579	31.7278	2.82030	–
SAM 21. 1	Sambullak	Calcite	330	30.4106	2.93987	–
SAM 21. 2	Sambullak	Calcite, magnesian	541	30.1148	2.96758	–
SAM 21.3	Sambullak	Calcite, magnesian	375	30.4091	2.93953	–
SAM 21.4	Sambullak	Calcite	417	30.3825	2.94204	–
SAM 21.4	Sambullak	Calcium Carbonate	819	30.1894	2.96042	Ankerite (25)
SAM 22. 1	Sambullak	Calcite, magnesian	279	30.3487	2.94523	–
SAM 23.3	Sambullak	Calcite	540	30.2155	2.95792	–
SAM 23. 2	Sambullak	Dolomite	202	30.2578	2.95388	–
SAM 24.1	Sambullak	Calcite	500	30.1662	2.96264	–
SAM 24.10	Sambullak	Calcite	403	30.2323	2.95631	Quartz
SAM 24.11	Sambullak	Calcite, magnesian	203	30.2341	2.95614	–
SAM 24.12	Sambullak	Calcite	257	30.3315	2.94687	–
SAM 24.13	Sambullak	Calcite	481	30.1737	2.96192	–
SAM 24.14	Sambullak	Calcite	424	30.1941	2.95996	–
SAM 24.3	Sambullak	calcite	314	30.3813	2.94215	–
SAM 24.5	Sambullak	Calcite, magnesian	448	30.2659	2.95311	–
SAM 24.6	Sambullak	Calcite	333	30.1427	2.96490	–
SAM 24.7	Sambullak	Calcite	673	30.3330	2.94672	–
SAM 24.8	Sambullak	Calcite, magnesian	703	30.2977	2.95008	–
SAM 24.9	Sambullak	Calcite	424	30.1213	2.96660	–
04.7.23.i II	Sambullak	Dolomite	650	31.3528	2.85316	Quartz
04.7.23.k I	Sambullak	Dolomite	378	31.3802	2.85074	Quartz
04.7.24.a	Sambullak	Dolomite	553	31.4085	2.84824	Quartz
04.7.24.c	Sambullak	Dolomite	416	31.6863	2.82390	–
04.7.24.d	Sambullak	Calcite, magnesian	468	30.1377	2.96537	–
04.7.24.i	Sambullak	Dolomite	782	31.8124	2.81299	–
04.7.24.j	Sambullak	Dolomite	890	31.6129	2.83029	–
04.7.24.p	Sambullak	Calcite	668	30.1627	2.96298	–
04.7.24s	Sambullak	Calcite	605	30.1208	2.96700	–
04.7.23.f	Sambullak	Dolomite	647	31.6873	2.82380	–
04.7.23.h	Sambullak	Dolomite	702	31.6503	2.82700	Quartz
04.7.23.n	Sambullak	Dolomite	300	31.5383	2.83681	–
04.7.23.o	Sambullak	Quartz	626	27.5465	3.23814	Dolomite
04.7.23.J 2	Sambullak	Dolomite	1048	31.5622	2.83472	–
04.7.23.o	Sambullak	Dolomite	380	31.6562	2.82265	Calcite
04.7.23.o2	Sambullak	Quartz	896	27.4778	3.24608	–
04.7.24.e	Sambullak	Calcite	487	30.3680	2.94341	–
04.7.23.J	Sambullak	Dolomite	796	31.5708	2.83397	–
04.7.24.h	Sambullak	Dolomite	429	31.3834	2.85046	–
04.7.24.k	Sambullak	Dolomite	374	31.4229	2.84696	–
04.7.24.a I	Sambullak	Dolomite	316	31.3727	2.85140	–

Sample	Section	Main Component	Max Number of counts	100% 2°θ	100% d-spacing (Å)	Second Component
04.7.24.a II	Sambullak	Dolomite	489	31.4796	2.84197	Quartz
04.7.24.k.II	Sambullak	Dolomite	326	31.3886	2.84999	-
04.7.24.j	Sambullak	Dolomite	890	31.6129	2.83029	-
04.7.24.b	Sambullak	Dolomite	646	31.3641	2.85217	-
04.7.23.e	Sambullak	Dolomite	632	31.3332	2.85491	-
04.7.23.g	Sambullak	Quartz	1425	27.1899	3.27979	Dolomite
04.7.23.i.II	Sambullak	Dolomite	588	31.5330	2.83728	-
04.7.23.a	Sambullak	Dolomite	390	31.3659	2.85201	-
04.7.23.l	Sambullak	Calcite	632	30.1510	2.96410	-
04.7.23.k	Sambullak	Dolomite	1084	31.5045	2.83977	-
04.7.24.f	Sambullak	Dolomite	301	31.3417	2.85416	-
04.7.24.l	Sambullak	Dolomite	360	31.4178	2.84741	-
04.7.24.m	Sambullak	Dolomite	294	31.2950	2.85830	Quartz
04.7.24.q	Sambullak	Calcite, magnesian	764	30.1841	2.96092	-
04.7.26.a	Tuyembetka	Calcite	461	30.4611	2.93403	Montmorillinite
04.7.26.b	Tuyembetka	Dolomite	797	31.7620	2.81753	-
04.7.26.c	Tuyembetka	Dolomite	497	31.5522	2.83559	-
04.7.26.c I	Tuyembetka	Dolomite	493	31.6619	2.82602	Quartz
04.7.26.d	Tuyembetka	Dolomite	478	31.5555	2.83530	-
04.7.26.e	Tuyembetka	Dolomite	860	31.6734	2.82501	-
04.7.26.f	Tuyembetka	Dolomite	528	31.6151	2.83009	Quartz
04.7.26.g	Tuyembetka	Dolomite	361	31.5103	2.83926	-
04.7.26.h	Tuyembetka	Dolomite	631	31.5564	2.83522	-
04.7.26.i	Tuyembetka	Dolomite	534	31.6875	2.82379	-
04.7.26.j	Tuyembetka	Dolomite	753	31.6573	2.82641	-
04.7.26.k	Tuyembetka	Dolomite	664	31.5175	2.83864	Quartz
04.7.26.l	Tuyembetka	Dolomite	647	31.5893	2.83234	-
04.7.26.m	Tuyembetka	Dolomite	591	31.6520	2.82688	Quartz
04.7.26.n	Tuyembetka	Dolomite	635	31.5491	2.83586	Quartz
04.7.26.o	Tuyembetka	Dolomite	568	31.5989	2.83150	Quartz
04.7.26.p	Tuyembetka	Dolomite	686	31.3230	2.83815	-
04.7.26.q	Tuyembetka	Dolomite	1036	31.5145	2.83889	-
04.7.26.q III	Tuyembetka	Dolomite	675	31.5029	2.83994	Quartz
04.7.26.r	Tuyembetka	Dolomite	771	31.6828	2.82420	Quartz
04.7.26.s	Tuyembetka	Dolomite	1016	31.6048	2.83094	Quartz
04.7.26.t	Tuyembetka	Dolomite	680	31.6400	2.82792	-
04.7.26.u	Tuyembetka	Halite?	283	31.1337	2.87274	-
TUY 23.4	Tuyembetka	Dolomite	368	31.4838	2.84159	-
TUY 23.3	Tuyembetka	Dolomite	778	31.5982	2.83156	-
TUY 27.7	Tuyembetka	Dolomite	513	31.5084	2.89430	-
TUY 31.3	Tuyembetka	Dolomite	580	31.5931	2.83202	-
TUY 23.2	Tuyembetka	Dolomite	446	31.4409	2.84538	-
TUY 27.3	Tuyembetka	Dolomite	782	31.5895	2.83233	-
TUY 31.4	Tuyembetka	Dolomite	351	31.5872	2.83253	Calcite
TUY 38.1	Tuyembetka	Calcium Carbonate	316	30.1841	2.96930	-
TUY 23.4	Tuyembetka	Dolomite	368	31.4838	2.84159	-

Sample	Section	Main Component	Max Number of counts	100% 2°θ	100% d-spacing (Å)	Second Component
KRA 2.2	Krasnogor	Quartz	321	27.5015	3.24329	calcite
KRA 1.1	Krasnogor	Calcite	673	30.1927	2.82769	Quartz
KRA 5.14	Krasnogor	Dolomite	633	31.6426	3.25639	Quartz
MES 7.2	Mescheryakovka	Calcite	568	30.1447	2.96470	-
MES 3.3	Mescheryakovka	Calcite	607	30.3145	2.94890	-
MES 1.2	Mescheryakovka	Calcite (mg)	642	30.3456	2.94556	-
MES 1.4	Mescheryakovka	Calcite	162	30.1230	2.96732	Quartz
MES 8.4	Mescheryakovka	Calcite	419	30.2348	2.95607	-
MES 8.5	Mescheryakovka	Calcite (mg)	691	30.1606	2.96318	-
MES 8.2	Mescheryakovka	Calcite	634	30.1933	2.95966	Quartz
MES 8.1	Mescheryakovka	Calcium Carbonate	1061	30.2335	2.95619	-
MES 10.3	Mescheryakovka	Calcite	773	30.2110	2.95834	-
MES 10.5	Mescheryakovka	Calcite	643	30.2414	2.95544	-
MES 16.5	Mescheryakovka	Calcite	344	30.4718	2.93362	Quartz
MES 16.6	Mescheryakovka	Calcite	200	30.2641	2.95703	-
MES 16.1	Mescheryakovka	Calcite (mg)	529	30.2972	2.95013	-

A2.5

Statistical treatment paleosols from Boyevaya Gora and Sambullak to ascertain whether the excursions identified represent true variation from the background values. The Mann-Whitney was used as this is a nonparametric test which does not assume a normal distribution within the data. The test assumes uses as a null hypothesis that the two datasets, in this case two paleosols, are from the same population (Conover 1971). Below a $p \leq 0.1$ it is statistically likely that the null hypothesis is invalid (to a 90% confidence interval) and the two datasets are from separate populations (Dr R. Moyced *pers. comm.*; Conover 1971).

Boyevaya Gora

All data - *Results*

Test	$\delta^{13}C$ (p values)	$\delta^{18}O$ (p values)
P1 v 'Background'	0.0022	0.0011
P2 v 'Background'	0.0007	0.0000
P3 v 'Background'	0.0000	0.0000
Triassic v 'Background Permian'	0.6073	0.0000

Input values

	$\delta^{13}C$	$\delta^{18}O$
P1		
Median (‰)	-5.85	-7.79
number of values	4	4
P2		
Median (‰)	-10.04	-8.03
number of values	4	4
P3		
Median (‰)	-6.59	-7.67
number of values	24	24
Background		
Median (‰)	-1.29	-0.40
number of values	119	119
Triassic		
Median (‰)	-1.23	-0.40
number of values	42	42

Pedogenic calcite only- *Results*

Test	$\delta^{13}C$ (p values)	$\delta^{18}O$ (p values)
P1 v 'Background'	0.0803	0.1064
P2 v 'Background'	0.0693	0.2528
P3 v 'Background'	0.0000	0.0005
Triassic v 'Background Permian'	0.4757	0.0003

Input values

	$\delta^{13}C$	$\delta^{18}O$
P1		
Median (‰)	-4.62	-6.79
number of values	3	3
P2		
Median (‰)	0.36	-8.85
number of values	3	3
P3		
Median (‰)	-10.43	-11.00
number of values	14	14
Background Permian		
Median (‰)	-2.47	-5.15
number of values	13	13
Triassic		
Median (‰)	-2.76	-9.88
number of values	10	10

Sambullak

All data - *Results*

Test	$\delta^{13}C$ (p values)	$\delta^{18}O$ (p values)
P3 v 'Background'	0.0000	0.0000
P4 v 'Background'	0.0004	0.0000

Input values

	$\delta^{13}C$	$\delta^{18}O$
P3		
Median (‰)	-5.6	-8.2
number of values	31	31
P4		
Median (‰)	-5.0	-9.4
number of values	34	34
Background		
Median (‰)	-3.7	-4.3
number of values	49	49

Pedogenic calcite only- *Results*

Test	$\delta^{13}C$ (p values)	$\delta^{18}O$ (p values)
P3 v 'Background'	1.0000	0.5160
P4 v 'Background'	0.2703	0.0200

Input values

	$\delta^{13}C$	$\delta^{18}O$
P3		
Median (‰)	-5.509	-8.08
number of values	7	7
P4		
Median (‰)	-6.054	-12.944
number of values	4	4
Background permian		
Median (‰)	-5.57	-7.446
number of values	5	5

A2.6

Calibrated values for NBS 19 for all stable isotope runs undertaken as part of this project with the deviation from the published values for that standard (National Bureau of Standards 19 published values; $\delta^{13}C = 1.95‰$ $\delta^{18}O = -2.20‰$).

Date	$\delta^{13}C$ (‰,VPDB)	*difference from given values*	$\delta^{18}O$ (‰,VPDB)	*difference from given values*	Field Area
15/07/2008	1.95	0.00	-2.83	-0.63	Russia
15/07/2008	1.95	0.00	-2.83	-0.63	Russia
15/07/2008	1.95	0.00	-2.83	-0.63	Russia
14/07/2008	2.12	0.17	-2.46	-0.26	Russia
14/07/2008	2.04	0.09	-2.42	-0.22	Russia
14/07/2008	2.00	0.05	-2.21	-0.01	Russia
14/07/2008	2.01	0.06	-2.01	0.19	Russia
14/07/2008	1.51	-0.44	-1.15	1.05	Russia
09/07/2008	2.04	0.09	-2.64	-0.44	Russia
09/07/2008	2.04	0.09	-2.64	-0.44	Russia
09/07/2008	2.13	0.18	-2.09	0.11	Russia
09/07/2008	2.13	0.18	-2.09	0.11	Russia
09/07/2008	2.07	0.12	-2.03	0.17	Russia
09/07/2008	2.07	0.12	-2.03	0.17	Russia
09/07/2008	2.09	0.14	-1.97	0.23	Russia
09/07/2008	2.09	0.14	-1.97	0.23	Russia
18/06/2008	2.16	0.21	-2.26	-0.06	Russia
18/06/2008	2.28	0.33	-2.21	-0.01	Russia
18/06/2008	2.29	0.34	-1.95	0.25	Russia
18/06/2008	2.05	0.10	-1.72	0.48	Russia
18/06/2008	2.33	0.38	-1.64	0.56	Russia
02/06/2008	1.99	0.04	-2.59	-0.39	Russia
02/06/2008	1.98	0.03	-2.11	0.09	Russia
02/06/2008	2.19	0.24	-1.96	0.24	Russia
02/06/2008	1.93	-0.02	-1.90	0.30	Russia
02/06/2008	2.01	0.06	-1.86	0.34	Russia
21/05/2008	2.24	0.29	-2.26	-0.06	Russia
21/05/2008	2.24	0.29	-2.26	-0.06	Russia
21/05/2008	2.24	0.29	-2.26	-0.06	Russia
21/05/2008	2.24	0.29	-2.26	-0.06	Russia
21/05/2008	2.03	0.08	-1.97	0.23	Russia
21/05/2008	2.03	0.08	-1.97	0.23	Russia
21/05/2008	2.03	0.08	-1.97	0.23	Russia
21/05/2008	2.03	0.08	-1.97	0.23	Russia
21/05/2008	2.09	0.14	-1.80	0.40	Russia
21/05/2008	2.09	0.14	-1.80	0.40	Russia
21/05/2008	2.09	0.14	-1.80	0.40	Russia
21/05/2008	2.09	0.14	-1.80	0.40	Russia

Date	$\delta^{13}C$ (‰,VPDB)	*difference from given values*	$\delta^{18}O$ (‰,VPDB)	*difference from given values*	Field Area
21/05/2008	2.20	0.25	-1.80	0.40	Russia
21/05/2008	2.20	0.25	-1.80	0.40	Russia
21/05/2008	2.20	0.25	-1.80	0.40	Russia
21/05/2008	2.20	0.25	-1.80	0.40	Russia
28/11/2007	2.05	0.10	-2.72	-0.52	Russia
28/11/2007	1.90	-0.05	-2.44	-0.24	Russia
28/11/2007	1.92	-0.03	-2.38	-0.18	Russia
28/11/2007	2.07	0.12	-2.23	-0.03	Russia
28/11/2007	2.02	0.07	-2.18	0.02	Russia
18/11/2007	2.02	0.07	-2.56	-0.36	Russia
17/11/2007	2.17	0.22	-2.16	0.04	Russia
16/11/2007	2.06	0.11	-2.16	0.04	Russia
15/11/2007	2.05	0.10	-2.37	-0.17	Russia
14/11/2007	2.20	0.25	-3.05	-0.85	Russia
14/11/2007	2.02	0.07	-2.35	-0.15	Russia
14/11/2007	2.04	0.09	-2.19	0.01	Russia
14/11/2007	2.20	0.25	-2.03	0.17	Russia
11/11/2007	1.99	0.04	-2.34	-0.14	Russia
11/11/2007	1.99	0.04	-2.34	-0.14	Russia
11/11/2007	2.15	0.20	-2.28	-0.08	Russia
11/11/2007	2.15	0.20	-2.28	-0.08	Russia
11/11/2007	2.02	0.07	-2.21	-0.01	Russia
11/11/2007	2.02	0.07	-2.21	-0.01	Russia
10/11/2007	1.73	-0.22	-2.57	-0.37	Russia
10/11/2007	1.73	-0.22	-2.57	-0.37	Russia
10/11/2007	1.95	0.00	-2.53	-0.33	Russia
10/11/2007	1.95	0.00	-2.53	-0.33	Russia
10/11/2007	2.03	0.08	-2.34	-0.14	Russia
10/11/2007	2.03	0.08	-2.34	-0.14	Russia
10/11/2007	2.02	0.07	-2.26	-0.06	Russia
10/11/2007	2.02	0.07	-2.26	-0.06	Russia
19/09/2007	2.41	0.46	-2.46	-0.26	Russia
19/09/2007	2.41	0.46	-2.46	-0.26	Russia
19/09/2007	2.41	0.46	-2.46	-0.26	Russia
19/09/2007	2.41	0.46	-2.46	-0.26	Russia
10/09/2007	2.08	0.13	-3.01	-0.81	Russia
10/09/2007	2.14	0.19	-2.88	-0.68	Russia
10/09/2007	2.29	0.34	-2.24	-0.04	Russia
10/09/2007	2.26	0.31	-2.20	0.00	Russia
10/09/2007	2.28	0.33	-2.11	0.09	Russia
10/09/2007	1.78	-0.17	-2.08	0.12	Russia
05/09/2007	2.11	0.16	-3.21	-1.01	Russia
05/09/2007	2.00	0.05	-2.58	-0.38	Russia
05/09/2007	2.12	0.17	-2.54	-0.34	Russia
05/09/2007	2.07	0.12	-2.17	0.03	Russia
05/09/2007	2.15	0.20	-1.95	0.25	Russia

Date	$\delta^{13}C$ (‰,VPDB)	*difference from given values*	$\delta^{18}O$ (‰,VPDB)	*difference from given values*	Field Area
25/08/2007	1.71	-0.24	-2.84	-0.64	Russia
25/08/2007	1.71	-0.24	-2.84	-0.64	Russia
25/08/2007	1.85	-0.10	-2.79	-0.59	Russia
25/08/2007	1.85	-0.10	-2.79	-0.59	Russia
25/08/2007	1.99	0.04	-2.45	-0.25	Russia
25/08/2007	1.99	0.04	-2.45	-0.25	Russia
12/11/2006	1.93	-0.02	-2.63	-0.43	Russia
12/11/2006	1.96	0.01	-2.35	-0.15	Russia
12/11/2006	1.99	0.04	-2.04	0.16	Russia
12/11/2006	1.99	0.04	-2.00	0.20	Russia
10/05/2006	2.11	0.16	-2.50	-0.30	Russia
10/05/2006	2.11	0.16	-2.50	-0.30	Russia
10/05/2006	1.96	0.01	-2.34	-0.14	Russia
10/05/2006	1.96	0.01	-2.34	-0.14	Russia
10/05/2006	2.12	0.17	-2.34	-0.14	Russia
10/05/2006	2.12	0.17	-2.34	-0.14	Russia
10/05/2006	2.28	0.33	-2.27	-0.07	Russia
10/05/2006	2.28	0.33	-2.27	-0.07	Russia
10/05/2006	2.02	0.07	-2.27	-0.07	Russia
10/05/2006	2.02	0.07	-2.27	-0.07	Russia
10/05/2006	2.11	0.16	-2.18	0.02	Russia
10/05/2006	2.11	0.16	-2.18	0.02	Russia
10/05/2006	1.96	0.01	-2.07	0.13	Russia
10/05/2006	1.96	0.01	-2.07	0.13	Russia
10/05/2006	2.02	0.07	-2.02	0.18	Russia
10/05/2006	2.02	0.07	-2.02	0.18	Russia
10/05/2006	2.01	0.06	-2.00	0.20	Russia
10/05/2006	2.01	0.06	-2.00	0.20	Russia
10/05/2006	1.95	0.00	-1.98	0.22	Russia
10/05/2006	1.95	0.00	-1.98	0.22	Russia
10/05/2006	2.11	0.16	-1.95	0.25	Russia
10/05/2006	2.11	0.16	-1.95	0.25	Russia
10/05/2006	1.99	0.04	-1.94	0.26	Russia
10/05/2006	1.99	0.04	-1.94	0.26	Russia
10/05/2006	2.05	0.10	-1.84	0.36	Russia
10/05/2006	2.05	0.10	-1.84	0.36	Russia
08/05/2006	2.11	0.16	-2.40	-0.20	Russia
08/05/2006	2.19	0.24	-2.35	-0.15	Russia
08/05/2006	2.02	0.07	-2.34	-0.14	Russia
08/05/2006	2.03	0.08	-2.25	-0.05	Russia
08/05/2006	2.05	0.10	-2.21	-0.01	Russia
08/05/2006	2.00	0.05	-2.18	0.02	Russia
08/05/2006	2.05	0.10	-2.17	0.03	Russia
08/05/2006	2.06	0.11	-2.11	0.09	Russia
08/05/2006	2.08	0.13	-2.10	0.10	Russia
08/05/2006	2.02	0.07	-2.04	0.16	Russia

Date	$\delta^{13}C$ (‰,VPDB)	*difference from given values*	$\delta^{18}O$ (‰,VPDB)	*difference from given values*	Field Area
08/05/2006	2.22	0.27	-2.04	0.16	Russia
08/05/2006	2.15	0.20	-2.03	0.17	Russia
08/05/2006	1.96	0.01	-1.87	0.33	Russia
05/04/2006	1.05	-0.90	-2.91	-0.71	Russia
05/04/2006	1.05	-0.90	-2.91	-0.71	Russia
05/04/2006	1.06	-0.89	-2.73	-0.53	Russia
05/04/2006	1.06	-0.89	-2.73	-0.53	Russia
05/04/2006	1.23	-0.72	-2.56	-0.36	Russia
05/04/2006	1.23	-0.72	-2.56	-0.36	Russia
29/03/2006	0.81	-1.14	-3.27	-1.07	Russia
29/03/2006	0.81	-1.14	-3.27	-1.07	Russia
29/03/2006	0.81	-1.14	-3.27	-1.07	Russia
29/03/2006	1.08	-0.87	-3.26	-1.06	Russia
29/03/2006	1.08	-0.87	-3.26	-1.06	Russia
29/03/2006	1.08	-0.87	-3.26	-1.06	Russia
29/03/2006	1.19	-0.76	-3.16	-0.96	Russia
29/03/2006	1.19	-0.76	-3.16	-0.96	Russia
29/03/2006	1.19	-0.76	-3.16	-0.96	Russia
29/03/2006	1.05	-0.90	-3.11	-0.91	Russia
29/03/2006	1.05	-0.90	-3.11	-0.91	Russia
29/03/2006	1.05	-0.90	-3.11	-0.91	Russia
29/03/2006	1.12	-0.83	-3.04	-0.84	Russia
29/03/2006	1.12	-0.83	-3.04	-0.84	Russia
29/03/2006	1.12	-0.83	-3.04	-0.84	Russia
29/03/2006	0.95	-1.00	-2.70	-0.50	Russia
29/03/2006	0.95	-1.00	-2.70	-0.50	Russia
29/03/2006	0.95	-1.00	-2.70	-0.50	Russia
29/03/2006	1.11	-0.84	-2.51	-0.31	Russia
29/03/2006	1.11	-0.84	-2.51	-0.31	Russia
29/03/2006	1.11	-0.84	-2.51	-0.31	Russia
29/03/2006	1.27	-0.68	-2.23	-0.03	Russia
29/03/2006	1.27	-0.68	-2.23	-0.03	Russia
29/03/2006	1.27	-0.68	-2.23	-0.03	Russia
24/03/2006	1.44	-0.51	-3.39	-1.19	Russia
24/03/2006	1.52	-0.43	-3.13	-0.93	Russia
24/03/2006	1.17	-0.78	-3.04	-0.84	Russia
24/03/2006	1.22	-0.73	-2.89	-0.69	Russia
24/03/2006	1.22	-0.73	-2.81	-0.61	Russia
24/03/2006	1.15	-0.80	-2.74	-0.54	Russia
21/03/2006	1.12	-0.83	-3.36	-1.16	Russia
21/03/2006	1.12	-0.83	-3.36	-1.16	Russia
21/03/2006	0.99	-0.96	-3.29	-1.09	Russia
21/03/2006	0.99	-0.96	-3.29	-1.09	Russia
21/03/2006	0.91	-1.04	-3.20	-1.00	Russia
21/03/2006	0.91	-1.04	-3.20	-1.00	Russia
21/03/2006	1.05	-0.90	-3.08	-0.88	Russia

Date	$\delta^{13}C$ (‰,VPDB)	*difference from given values*	$\delta^{18}O$ (‰,VPDB)	*difference from given values*	Field Area
21/03/2006	1.05	-0.90	-3.08	-0.88	Russia
21/03/2006	1.19	-0.76	-3.07	-0.87	Russia
21/03/2006	1.19	-0.76	-3.07	-0.87	Russia
21/03/2006	1.19	-0.76	-2.99	-0.79	Russia
21/03/2006	1.19	-0.76	-2.99	-0.79	Russia
21/03/2006	1.20	-0.75	-2.94	-0.74	Russia
21/03/2006	1.20	-0.75	-2.94	-0.74	Russia
21/03/2006	1.18	-0.77	-2.89	-0.69	Russia
21/03/2006	1.18	-0.77	-2.89	-0.69	Russia
21/03/2006	0.95	-1.00	-2.89	-0.69	Russia
21/03/2006	0.95	-1.00	-2.89	-0.69	Russia
21/03/2006	0.95	-1.00	-2.88	-0.68	Russia
21/03/2006	0.95	-1.00	-2.88	-0.68	Russia
12/07/2007	1.66	-0.29	-3.44	-1.24	Italy
12/07/2007	2.04	0.09	-3.82	-1.62	Italy
12/07/2007	2.03	0.08	-2.50	-0.30	Italy
02/03/2007	2.20	0.25	-2.98	-0.78	Italy
02/03/2007	2.17	0.22	-2.56	-0.36	Italy
02/03/2007	2.02	0.07	-3.48	-1.28	Italy
02/03/2007	2.16	0.21	-2.23	-0.03	Italy
02/03/2007	2.22	0.27	-2.47	-0.27	Italy
21/01/2007	2.01	0.06	-2.98	-0.78	Italy
21/01/2007	1.98	0.03	-3.65	-1.45	Italy
21/01/2007	1.99	0.04	-3.36	-1.16	Italy
21/01/2007	1.99	0.04	-3.76	-1.56	Italy
18/01/2007	1.86	-0.09	-2.56	-0.36	Italy
18/01/2007	2.08	0.13	-3.88	-1.68	Italy
18/01/2007	2.17	0.22	-3.62	-1.42	Italy
18/01/2007	2.05	0.10	-2.33	-0.13	Italy

Appendix 3

Palaeoprecipitation, Palaeotemperature, and pCO_2calculations

(Chapter 5 and 7)

A3.1

Palaeoprecipitation estimates from Chapter 5 from Boyevaya Gora, Sambullak, Tuyembetka, and Mescheryakovka.

Paleosol Horizon	Location	Strat Height (m)	Height from palaeo surface (cm)	De-compressed height (cm)	MAP Calculation			
					Equation 5.2 (mm)	Equation 5.3 (mm)	Equation 5.3a (mm)	Equation 5.4 (mm)
KOR 33	Boyevaya Gora	199	3	3.3	159	418	1043	177
KOR 32	Boyevaya Gora	198	8	8.7	195	395	1035	181
KOR 37	Boyevaya Gora	196	9	9.8	202	390	1034	183
KOR 01	Boyevaya Gora	171	49	53.5	521	204	965	284
KOR 06	Boyevaya Gora	169	34	37.1	395	274	992	233
KOR 10	Boyevaya Gora	163	27	29.5	339	307	1004	215
KOR 11	Boyevaya Gora	160	18	19.6	269	349	1019	196
KOR 12	Boyevaya Gora	158	36	39.3	411	265	989	239
KOR 02	Boyevaya Gora	157	25	27.3	323	316	1008	210
KOR 14	Boyevaya Gora	155	26	28.4	331	311	1006	212
KOR 14	Boyevaya Gora	154	18	19.6	269	349	1019	196
KOR 23	Boyevaya Gora	145	28	30.6	347	302	1003	217
KOR 22	Boyevaya Gora	142	64.5	70.4	658	132	936	354
KOR 21	Boyevaya Gora	142	23	25.1	308	325	1011	206
KOR 15	Boyevaya Gora	140	17	18.6	262	353	1021	194
KOR 16	Boyevaya Gora	136	13	14.2	231	372	1027	188
KOR 17	Boyevaya Gora	136	24	26.2	315	321	1010	208
KOR 16	Boyevaya Gora	136	14	15.3	239	367	1026	189
KOR 25	Boyevaya Gora	105	21	22.9	292	335	1014	201
KOR 26	Boyevaya Gora	99	41	44.8	453	242	980	255
KOR 27	Boyevaya Gora	99	26	28.4	331	311	1006	212
KOR 30	Boyevaya Gora	79	18	19.6	269	349	1019	196
SAM 01	Sambullak	131.13	31	33.84	371	288	998	225
SAM 10	Sambullak	123.28	42	45.85	461	237	978	259
SAM 03	Sambullak	122.62	49	53.49	521	204	965	284
SAM 10	Sambullak	122.6	24	26.20	315	321	1010	208
SAM 12	Sambullak	114.38	14	15.28	239	367	1026	189
SAM 11	Sambullak	113.45	28	30.56	347	302	1003	217
SAM 09	Sambullak	102.48	80	87.33	803	60	904	439
SAM 08	Sambullak	98.61	18	19.65	269	349	1019	196
SAM 05	Sambullak	91.48	37	40.39	420	260	987	242
SAM 20	Sambullak	87.76	27	29.47	339	307	1004	215
SAM 17	Sambullak	80.435	39	42.57	436	251	984	249

Paleosol Horizon	Location	Strat Height (m)	Height from palaeo surface (cm)	De-compressed height (cm)	MAP Calculation			
					Equation 5.2 (mm)	Equation 5.3 (mm)	Equation 5.3a (mm)	Equation 5.4 (mm)
SAM 19	Sambullak	80.14	33	36.02	387	279	994	230
SAM 18	Sambullak	79.116	17	18.56	262	353	1021	194
SAM 15	Sambullak	73.965	27	29.47	339	307	1004	215
SAM 16	Sambullak	69.2225	37	40.39	420	260	987	242
SAM 14	Sambullak	68.205	15	16.37	246	363	1024	191
SAM 13	Sambullak	66.8	14	15.28	239	367	1026	189
SAM 21	Sambullak	62.44	19	20.74	277	344	1018	198
SAM 22	Sambullak	60.97	27	29.47	339	307	1004	215
SAM 23	Sambullak	60.15	47	51.31	503	214	969	277
SAM 24	Sambullak	57.44	51	55.67	538	195	962	292
SAM 24	Sambullak	57.02	31	33.84	371	288	998	225
SAM 24	Sambullak	56.29	54	58.95	564	181	956	305
SAM 24	Sambullak	56.28	88	96.06	880	22	887	490
MES 1	Mescheryakovka	10	24	26.36	317	320	1009	208
MES 8	Mescheryakovka	140	44	48.33	480	226	974	267
MES 4	Mescheryakovka	8	43	47.23	472	231	976	263
MES 6	Mescheryakovka	8	38	41.74	430	255	985	246
MES 16	Mescheryakovka	183	100	109.83	1007		859	579
TUY 56	Tuyembetka	107	3	3	159	418	1043	177
TUY 58	Tuyembetka	104	54	59	567	180	955	306
TUY 2	Tuyembetka	95	62	68	639	142	940	343
TUY 46	Tuyembetka	95	10	11	210	386	1032	184
TUY 4	Tuyembetka	93	26	29	332	311	1006	213
TUY 5	Tuyembetka	93	18	20	270	348	1019	196
TUY 6	Tuyembetka	91	62	68	639	142	940	343
TUY 7	Tuyembetka	90	26	29	332	311	1006	213
TUY 8	Tuyembetka	89	21	23	293	334	1014	202
TUY 13	Tuyembetka	74	33	36	389	278	994	231
TUY 15	Tuyembetka	71	18	20	270	348	1019	196
TUY 16	Tuyembetka	66	32	35	380	283	996	228
TUY 18	Tuyembetka	61	40	44	446	245	981	253
TUY 23	Tuyembetka	56	58	64	603	161	948	324
TUY 24	Tuyembetka	55	48	53	515	208	967	282
TUY 25	Tuyembetka	49	100	110	1007	-37	859	579
TUY 28	Tuyembetka	43	34	37	397	273	992	234
TUY 31	Tuyembetka	34	20	22	285	339	1016	200
TUY 39	Tuyembetka	21	25	27	324	315	1008	210
TUY 40	Tuyembetka	18	22	24	301	329	1013	204
TUY 41	Tuyembetka	16	23	25	309	325	1011	206

Paleosol Horizon	Location	Strat. Height (m)	Height from palaeo surface (cm)	De-compressed height (cm)	MAP Calculation			
					Equation 5.2 (mm)	Equation 5.3 (mm)	Equation 5.3a (mm)	Equation 5.4 (mm)
TUY 42	Tuyembetka	16	34	37	397	273	992	234
TUY 45	Tuyembetka	0	28	31	348	301	1002	218

A3.2

Mean annual range precipitation estimates from Chapter 5 from Boyevaya Gora, Sambullak, Tuyembetka, and Mescheryakovka.

Paleosol Horizon	Location	Strat. Height (m)	Thickness of nodule horizon (cm)	Decompressed Thickness (cm)	Equation 5.5 (mm)
KOR 36	Boyevaya Gora	211	37	40.39	45.62
KOR 33	Boyevaya Gora	199	29	31.66	38.72
KOR 37	Boyevaya Gora	196	71	77.50	74.94
KOR 34	Boyevaya Gora	199	22	24.02	32.68
KOR 32	Boyevaya Gora	198	43	46.94	50.79
KOR 1	Boyevaya Gora	173	10	10.92	22.33
KOR 1a	Boyevaya Gora	171	45	49.12	52.52
KOR 2	Boyevaya Gora	170	58	63.31	63.73
KOR 9	Boyevaya Gora	165	20	21.83	30.96
KOR 6	Boyevaya Gora	163	44	48.03	51.65
KOR 10	Boyevaya Gora	159	69	75.32	73.21
KOR 11	Boyevaya Gora	158	40	43.66	48.20
KOR 12	Boyevaya Gora	157	6	6.55	18.88
KOR 14	Boyevaya Gora	155	24	26.20	34.41
KOR 14a	Boyevaya Gora	154	40	43.66	48.20
KOR 14b	Boyevaya Gora	154	9	9.82	21.47
KOR 22	Boyevaya Gora	144	76	82.96	79.25
KOR 21a	Boyevaya Gora	142	19	20.74	30.09
KOR 21	Boyevaya Gora	142	38	41.48	46.48
KOR 15	Boyevaya Gora	140	38	41.48	46.48
KOR 16	Boyevaya Gora	136	6	6.55	18.88

Paleosol Horizon	Location	Strat. Height (m)	Thickness of nodule horizon (cm)	Decompressed Thickness (cm)	Equation 5.5 (mm)
KOR 16a	Boyevaya Gora	136	13	14.19	24.92
KOR 18	Boyevaya Gora	128	7	7.64	19.75
KOR 25	Boyevaya Gora	105	8	8.73	20.61
KOR 26	Boyevaya Gora	99	5	5.46	18.02
KOR 27	Boyevaya Gora	99	4	4.37	17.16
KOR 28	Boyevaya Gora	96	15	16.37	26.65
KOR 31	Boyevaya Gora	80	11	12.01	23.20
KOR 35	Boyevaya Gora	79	5	5.46	18.02
SAM 1	Sambullak	131	35	38.21	43.89
SAM 4	Sambullak	131	82	89.51	84.42
SAM 10	Sambullak	123	43	46.94	50.79
SAM 10a	Sambullak	122	38	41.48	46.48
SAM 12	Sambullak	114	6	6.55	18.88
SAM 11	Sambullak	113	6	6.55	18.88
SAM 9	Sambullak	102	85	92.79	87.01
SAM 8	Sambullak	98	65	70.95	69.76
SAM 20	Sambullak	88	20	21.83	30.96
SAM 17	Sambullak	80	13	14.19	24.92
SAM 16	Sambullak	76	18	19.65	29.23
SAM 15	Sambullak	73	42	45.85	49.93
SAM 14	Sambullak	68	25	27.29	35.27
SAM 13	Sambullak	67	69	75.32	73.21
SAM 21	Sambullak	62	23	25.11	33.54
SAM 22	Sambullak	61	11	12.01	23.20
SAM 24a	Sambullak	57	10	10.92	22.33
SAM 24b	Sambullak	57	71	77.50	74.94
SAM 24c	Sambullak	57	6	6.55	18.88
SAM 24d	Sambullak	56	18	19.65	29.23
SAM 24e	Sambullak	53	14	15.28	29.23
04.7.24.d	Sambullak	51	25	27.29	35.27
04.7.23.o	Sambullak	33	20	21.83	30.96
04.7.23.j	Sambullak	11	15	16.37	26.65
04.7.23.h	Sambullak	10	35	38.21	43.89
TUY 56	Tuyembetka	107	52	56.76	58.55
TUY 58	Tuyembetka	104	88	96.06	89.60
TUY 46	Tuyembetka	95	70	76.41	74.08
TUY 4	Tuyembetka	93	8	8.73	20.61
TUY 5	Tuyembetka	93	45	49.12	52.52
TUY 7	Tuyembetka	90	98	106.98	98.22
TUY 13	Tuyembetka	74	58	63.31	63.73
TUY 15	Tuyembetka	71	11	12.01	23.20
TUY 16	Tuyembetka	66	20	21.83	30.96

Paleosol Horizon	Location	Strat. Height (m)	Thickness of nodule horizon (cm)	Decompressed Thickness (cm)	Equation 5.5 (mm)
TUY 18	Tuyembetka	61	50	54.58	56.83
TUY 23	Tuyembetka	56	5	5.46	18.02
TUY 24	Tuyembetka	55	49	53.49	55.97
TUY 31	Tuyembetka	34	67	73.14	71.49
TUY 39	Tuyembetka	21	10	10.92	22.33
TUY 41	Tuyembetka	16	23	25.11	33.54
TUY 42	Tuyembetka	16	7	7.64	19.75
TUY 45	Tuyembetka	0	9	9.82	21.47
MES 5	Mescheryakovka	7	70	76.41	74.08
MES 7	Mescheryakovka	7	5	5.46	18.02
MES 6	Mescheryakovka	8	76	82.96	79.25
MES 4	Mescheryakovka	8	13	14.19	24.92
MES 3	Mescheryakovka	9	43	46.94	50.79
MES 2	Mescheryakovka	9	6	6.55	18.88
MES 1	Mescheryakovka	10	10	10.92	22.33
MES 10	Mescheryakovka	137	23	25.11	33.54
MES 9	Mescheryakovka	140	37	40.39	45.62
MES 8	Mescheryakovka	140	39	42.57	47.34
MES 12	Mescheryakovka	142	23	25.11	33.54
MES 11	Mescheryakovka	142	10	10.92	22.33
MES 13	Mescheryakovka	178	20	21.83	30.96
MES 14	Mescheryakovka	180	46	50.21	53.38
MES 15	Mescheryakovka	183	15	16.37	26.65
MES 16	Mescheryakovka	183	37	40.39	45.62
MES 17	Mescheryakovka	186	140	152.82	134.44

A3.3

Palaeotemperature estimates from Chapter 5 from Boyevaya Gora, Sambullak, and Mescheryakovka. For method by which these equations are generated is by using the methods described in Chapter 2.

				Equations (°C)					
Sample	Section height (m)	Section	$\delta^{18}O$ (‰, VPDB)	6	8a	8b	8c	9	10
SU06 KOR 36.1	79	Boyevaya Gora	-6.79	21	11	142	32	10	38
SU06 KOR 36.4	79	Boyevaya Gora	-8.79	31	3	79	-409	3	44
SU06 KOR 36.5	79	Boyevaya Gora	-6.00	18	14	-436	-410	2	45
SU06 KOR 36.6	80	Boyevaya Gora	-2.64	4	27	83	-409	3	44
04.8.2.f	80	Boyevaya Gora	-5.85	17	15	132	22	9	37
04.8.2.f	99	Boyevaya Gora	-4.10	10	21	146	36	11	42
04.8.2.f	99	Boyevaya Gora	-8.84	31	2	145	35	11	42
SU06 KOR 33.1	99	Boyevaya Gora	-9.26	34	0	108	-409	6	39
SU06 KOR 37.4	105	Boyevaya Gora	-11.31	45	-10	109	-409	6	42
SU06 KOR 37.5	105	Boyevaya Gora	-11.24	45	-9	149	39	12	41
SU06 KOR 34.7	105	Boyevaya Gora	-11.29	45	-9	115	-409	6	37
04.8.2.e.i	105	Boyevaya Gora	-11.01	43	-8	119	-408	7	41
04.8.2.e.iii	136	Boyevaya Gora	-5.51	16	16	118	-408	7	41
04.8.2.e.iv	136	Boyevaya Gora	-5.08	14	18	147	37	11	41
SU06 KOR 32.2	136	Boyevaya Gora	-6.16	18	14	107	-409	5	37
SU06 KOR 32.7	136	Boyevaya Gora	-5.64	16	16	114	-409	6	37
SU06 KOR 23.1	136	Boyevaya Gora	-5.15	14	17	66	-409	2	45
SU06 KOR 23.2	141	Boyevaya Gora	0.73	-9	38	84	-409	3	44
04.8.1.q.I	141	Boyevaya Gora	1.03	-10	39	71	-409	2	46
04.8.1.q.II	141	Boyevaya Gora	0.64	-8	38	123	7	8	44
SU06 KOR 22.10	142	Boyevaya Gora	-1.09	-2	32	86	-409	3	44
SU06 KOR 22.11	142	Boyevaya Gora	-1.81	0	30	105	-409	5	42
SU06 KOR 22.12	142	Boyevaya Gora	-5.27	14	17	165	52	14	44
SU06 KOR 22.14	142	Boyevaya Gora	-4.10	9	21	-437	-410	1	40
SU06 KOR 22.2	143	Boyevaya Gora	-11.30	45	-10	77	-409	3	44
SU06 KOR 22.4	143	Boyevaya Gora	-11.00	43	-8	175	60	16	44
SU06 KOR 22.5	143	Boyevaya Gora	-5.60	16	16	97	-409	4	34
SU06 KOR 22.6	143	Boyevaya Gora	-4.66	12	19	77	-409	3	33
SU06 KOR 22.7	143	Boyevaya Gora	-10.49	40	-5	86	-409	3	43
SU06 KOR 22.8	144	Boyevaya Gora	-12.14	50	-14	165	52	14	34
SU06 KOR 21.10	144	Boyevaya Gora	-11.30	45	-10	169	55	15	24
SU06 KOR 21.5	144	Boyevaya Gora	-5.57	16	16	181	64	17	28
SU06 KOR 21.7	144	Boyevaya Gora	-10.99	43	-8	203	81	22	27

Sample	Section height (m)	Section	$\delta^{18}O$ (‰, VPDB)	Equations (°C)					
				6	8a	8b	8c	9	10
SU06 KOR 21.8	144	Boyevaya Gora	-10.12	38	-4	210	85	24	23
SU06 KOR 21.9	144	Boyevaya Gora	-11.45	46	-10	227	97	27	24
SU06 KOR 21.1	144	Boyevaya Gora	-8.96	32	2	229	98	28	34
SU06 KOR 21.2	145	Boyevaya Gora	-11.55	47	-11	226	96	27	32
04.8.1.n*	145	Boyevaya Gora	-11.05	44	-8	165	52	14	35
SU06 KOR 16.5	196	Boyevaya Gora	-10.01	38	-3	170	56	15	34
SU06 KOR 16.6	196	Boyevaya Gora	-9.54	35	-1	159	47	13	34
SU06 KOR 16.3	198	Boyevaya Gora	-7.15	23	10	166	53	15	34
SU06 KOR 16.4	198	Boyevaya Gora	-9.48	35	-1	171	57	15	34
SU06 KOR 25.1	198	Boyevaya Gora	-9.21	33	1	76	-409	3	44
SU06 KOR 25.3	198	Boyevaya Gora	-9.31	34	0	79	-409	3	44
SU06 KOR 25.4	198	Boyevaya Gora	-7.01	22	10	77	-409	3	44
SU06 KOR 25.5	199	Boyevaya Gora	-7.36	24	9	85	-409	3	44
04.8.1.f*	199	Boyevaya Gora	-9.92	37	-3	181	64	17	32
SU06 KOR 27.2	199	Boyevaya Gora	-9.84	37	-2	125	11	8	40
SU06 KOR 27.4	199	Boyevaya Gora	-7.21	23	9	119	-408	7	41
04.8.1.b*	199	Boyevaya Gora	-8.32	29	5	195	75	20	29
04.8.1.b.I	211	Boyevaya Gora	-11.25	45	-9	162	50	14	35
04.8.1.a	211	Boyevaya Gora	-11.77	48	-12	161	48	14	35
SU06 KOR 35.1	211	Boyevaya Gora	-11.09	44	-8	151	41	12	36
SU06 KOR 35.5	211	Boyevaya Gora	-7.60	25	8	126	12	8	40
04.7.24.u.I	131	Sambullak	-14.15	67	-28	-438	-411	-3	49
04.7.24.u.II	131	Sambullak	-12.82	57	-18	-437	-410	0	47
SU06 SAM 1.3	131	Sambullak	-13.07	59	-20	-437	-410	-1	47
SU06 SAM 1.5	131	Sambullak	-11.38	48	-10	74	-409	3	44
04.7.24.t	131	Sambullak	-9.50	37	-1	115	-409	6	41
04.7.24.t.I	131	Sambullak	-7.95	29	6	137	27	10	38
04.7.24.t.II	131	Sambullak	-7.99	29	6	137	27	9	38
04.7.24.t.III	131	Sambullak	-7.57	27	8	142	32	10	38
SU06 SAM 4.3	130	Sambullak	-12.98	59	-19	-437	-410	-1	47
SU06 SAM 4.4	130	Sambullak	-12.77	57	-18	-437	-410	0	47
SU06 SAM 12.1	114	Sambullak	-9.78	39	-2	110	-409	6	42
SU06 SAM 8.3	98	Sambullak	-8.32	31	5	132	22	9	39
SU06 SAM 8.1	98	Sambullak	-7.45	27	8	143	34	11	38
SU06 SAM 17.2	80	Sambullak	-7.46	27	8	143	34	11	38
SU06 SAM 13.2	67	Sambullak	-8.08	30	6	135	25	9	39
SU06 SAM 13.1	66	Sambullak	-8.18	30	5	134	24	9	39
SU06 SAM 21.5	62	Sambullak	-7.00	25	10	149	39	12	37
SU06 SAM 22.1	61	Sambullak	-7.79	28	7	139	29	10	38
SU06 SAM 24.3	57	Sambullak	-9.49	37	-1	115	-409	6	41
SU06 SAM 24.4	57	Sambullak	-8.62	33	3	128	16	8	40

Sample	Section height (m)	Section	$\delta^{18}O$ (‰, VPDB)	Equations (°C)					
				6	8a	8b	8c	9	10
04.7.24.d	51	Sambullak	-4.98	15	18	172	57	16	33
04.7.24.d	51	Sambullak	-6.27	21	13	157	46	13	36
MES 8.2	80	Mescheryakovka	-9.85	39	-2	-275	-409	6	42
MES 16.6	183	Mescheryakovka	-8.12	30	5	-268	25	9	39
MES 16.1	184	Mescheryakovka	-7.64	28	8	-265	31	9	38
MES 17.9	186	Mescheryakovka	-7.00	25	10	-263	39	10	37

A3.4

Atmospheric carbon dioxide (pCO_2 ppmV) estimates for those pedogenic carbonate isotope results which passed all screening tests laid out in Chapter 4 and thus most likely to represent pedogenic calcite and represent a fractionation from meteoric water. All other variables were generated as described in Chapter 7.

Sample	Section height	Mineral composition	Age	$\delta^{13}C$ (‰,VPDB)	Temp (°C)[a]	Method 1		Method 2		Method 3	
						Sz= 3000 ppmV	Sz= 4000 ppmV	Sz= 3000 ppmV	Sz= 4000 ppmV	Sz= 3000 ppmV	Sz= 4000 ppmV
MES 7.2	5	Calcite	Olenekian	-10	44	715	953	716	954	–	–
MES 8.4	80	Calcite	Olenekian	-9	54	1292	1722	1233	1643	–	–
MES 8.2	80	Calcite	Olenekian	-8	42	1375	1834	1316	1755	–	–
MES 8.1	80	Calcite	Olenekian	-9	55	1412	1883	1339	1786	–	–
MES 10.3	137	Calcite	Olenekian	-8	53	1767	2356	1654	2205	–	–
MES 10.4	137	Calcite	Olenekian	-9	54	1670	2226	1568	2091	–	–
MES 10.5	137	Calcite	Olenekian	-9	50	1429	1905	1357	1810	–	–
MES 16.6	183	Calcite	Olenekian	-7	39	1438	1918	1375	1833	–	–
MES 16.1	184	Calcite	Olenekian	-8	38	1149	1531	1115	1487	–	–
MES 17.9	186	Calcite	Olenekian	-8	37	1058	1411	1034	1379	–	–
SU06 KOR 36.1	211	Calcite	Induan	-2	38	10755	14340	8437	11250	–	–
SU06 KOR 36.4	211	Calcite	Induan	-5	44	5847	7795	5042	6722	–	–
SU06 KOR 36.5	211	Calcite	Induan	-6	45	3932	5243	3543	4724	–	–
SU06 KOR 36.6	211	Calcite	Induan	-6	44	3592	4789	3266	4355	–	–
04.8.2.f	199	Calcite	Induan	-2	37	10476	13969	8263	11017	–	–

Sample	Section height	Mineral composition	Age	$\delta^{13}C$ (‰,VPDB)	Temp (°C)[a]	Method 1		Method 2		Method 3	
						Sz= 3000 ppmV	Sz= 4000 ppmV	Sz= 3000 ppmV	Sz= 4000 ppmV	Sz= 3000 ppmV	Sz= 4000 ppmV
04.8.2.f	199	Calcite	Induan	-3	42	10537	14050	8287	11049	–	–
04.8.2.f	199	Calcite	Induan	-3	42	9843	13123	7842	10456	–	–
SU06 KOR 33.1	199	Calcite	Induan	-3	39	8582	11443	7011	9349	–	–
SU06 KOR 37.1	197	Calcite	Induan	-1	41	3297	4396	3079	4105	–	–
SU06 KOR 37.2	197	Calcite	Induan	-1	43	2927	3903	2764	3686	–	–
SU06 KOR 37.3	197	Calcite	Induan	-2	41	2812	3749	2665	3554	–	–
SU06 KOR 37.4	196	Calcite	Induan	-1	42	46269	61692	22135	29513	–	–
SU06 KOR 37.5	196	Calcite	Induan	0	41	56152	74869	24262	32350	–	–
SU06 KOR 23.1	145	Calcite	Changhsingian	-11	45	351	468	374	498	277	369
SU06 KOR 23.2	145	Calcite	Changhsingian	-11	44	392	522	412	549	309	411
04.8.1.q.I	144	Calcite	Changhsingian	-11	46	415	553	432	576	326	434
04.8.1.q.II	144	Calcite	Changhsingian	-10	44	563	751	571	761	440	587
SU06 KOR 22.10	144	Calcite	Changhsingian	-11	44	262	349	291	388	207	277
SU06 KOR 22.11	144	Calcite	Changhsingian	-11	42	347	463	371	495	275	367
SU06 KOR 22.12	144	Calcite	Changhsingian	-11	44	279	373	307	409	221	294
SU06 KOR 22.14	144	Calcite	Changhsingian	-10	40	516	688	529	706	406	541
SU06 KOR 22.2	143	Calcite	Changhsingian	-10	44	583	777	589	785	455	607
SU06 KOR 22.4	143	Calcite	Changhsingian	-11	44	334	445	358	478	264	352
SU06 KOR 22.5	143	Calcite	Changhsingian	-5	34	2426	3235	2235	2980	1720	2293
SU06 KOR 22.6	143	Calcite	Changhsingian	-5	33	2250	3000	2085	2780	1611	2149
SU06 KOR 22.7	143	Calcite	Changhsingian	-10	43	422	563	441	588	333	443
SU06 KOR 22.8	144	Calcite	Changhsingian	-5	34	2423	3231	2232	2976	1718	2291
SU06 KOR 21.10	141	Calcite	Changhsingian	-1	24	4801	6402	4185	5580	3026	4035
SU06 KOR 21.5	142	Calcite	Changhsingian	-2	28	3960	5280	3514	4685	2598	3464
SU06 KOR 21.7	142	Calcite	Changhsingian	-1	27	5391	7188	4635	6180	3302	4403

Sample	Section height	Mineral composition	Age	$\delta^{13}C$ (‰,VPDB)	Temp (°C)[a]	Method 1		Method 2		Method 3	
						Sz= 3000 ppmV	Sz= 4000 ppmV	Sz= 3000 ppmV	Sz= 4000 ppmV	Sz= 3000 ppmV	Sz= 4000 ppmV
SU06 KOR 21.8	141	Calcite	Changhsingian	0	23	6379	8505	5378	7171	3739	4985
SU06 KOR 21.9	141	Calcite	Changhsingian	-2	24	4577	6103	4010	5347	2916	3889
SU06 KOR 21.1	142	Calcite	Changhsingian	-4	34	3058	4078	2769	3692	2097	2796
SU06 KOR 21.2	142	Calcite	Changhsingian	-2	32	4758	6344	4140	5520	2998	3998
04.8.1.n*	136	Calcite	Changhsingian	-2	35	5637	7515	4807	6409	3405	4540
SU06 KOR 16.5	136	Calcite	Changhsingian	-4	34	2912	3883	2646	3528	2012	2682
SU06 KOR 16.6	136	Calcite	Changhsingian	-4	34	3177	4237	2868	3824	2165	2887
SU06 KOR 16.3	136	Calcite	Changhsingian	-5	34	2678	3571	2449	3266	1873	2498
SU06 KOR 16.4	136	Calcite	Changhsingian	-5	34	2506	3342	2304	3072	1770	2360
SU06 KOR 25.1	105	Calcite	Changhsingian	-10	44	518	691	529	705	406	541
SU06 KOR 25.3	105	Calcite	Changhsingian	-10	44	513	685	525	700	402	536
SU06 KOR 25.4	105	Calcite	Changhsingian	-10	44	604	806	609	812	471	628
SU06 KOR 25.5	105	Calcite	Changhsingian	-10	44	592	790	598	797	462	617
04.8.1.f*	99	Calcite	Changhsingian	-1	32	7201	9602	5954	7939	4063	5417
SU06 KOR 27.2	99	Calcite	Changhsingian	0	40	23429	31239	14696	19594	7783	10378
SU06 KOR 27.4	99	Calcite	Changhsingian	0	41	23186	30914	14591	19455	7749	10332
04.8.1.b*	80	Calcite	Changhsingian	-3	29	3953	5271	3507	4676	2593	3458
04.8.1.b.I	80	Calcite	Changhsingian	-4	35	3102	4136	2804	3739	2121	2829
04.8.1.a	79	Calcite	Changhsingian	-3	35	4255	5673	3741	4987	2745	3660
SU06 KOR 35.1	79	Calcite	Changhsingian	-5	36	2828	3771	2573	3431	1961	2614
SU06 KOR 35.5	79	Calcite	Changhsingian	-7	40	1519	2025	1439	1919	1129	1505
04.7.24.u.I	131	Calcite	Changhsingian	-6	49	3055	4074	2750	3667	2084	2779
04.7.24.u.II	131	Calcite	Changhsingian	-5	47	3640	4854	3233	4310	2412	3216
SU06 SAM 1.3	131	Calcite	Changhsingian	-6	47	2580	3440	2354	3138	1805	2407
SU06 SAM 1.5	131	Calcite	Changhsingian	-7	44	2029	2706	1884	2512	1464	1952

Sample	Section height	Mineral composition	Age	$\delta^{13}C$ (‰,VPDB)	Temp (°C)[a]	Method 1		Method 2		Method 3	
						Sz= 3000 ppmV	Sz= 4000 ppmV	Sz= 3000 ppmV	Sz= 4000 ppmV	Sz= 3000 ppmV	Sz= 4000 ppmV
04.7.24.t	131	Calcite	Changhsingian	-3	41	4928	6571	4259	5679	3072	4096
04.7.24.t.I	131	Calcite	Changhsingian	-5	38	2926	3901	2653	3538	2017	2689
04.7.24.t.II	131	Calcite	Changhsingian	-3	38	5396	7194	4620	6160	3293	4391
SU06 SAM 4.3	130	Calcite	Changhsingian	-6	47	2747	3663	2495	3326	1905	2540
SU06 SAM 4.4	130	Calcite	Changhsingian	-6	47	3089	4118	2780	3707	2105	2807
SU06 SAM 12.1	114	Calcite	Changhsingian	-6	42	2374	3165	2183	2911	1683	2244
SU06 SAM 8.3	98	Calcite	Changhsingian	-6	39	2063	2751	1917	2557	1489	1985
SU06 SAM 8.1	98	Calcite	Changhsingian	-6	38	2222	2963	2056	2742	1591	2121
SU06 SAM 17.2	80	Calcite	Changhsingian	-5	38	2430	3240	2235	2980	1720	2294
SU06 SAM 13.2	67	Calcite	Changhsingian	-6	39	2325	3100	2144	2859	1655	2206
SU06 SAM 13.1	66	Calcite	Changhsingian	-5	39	2422	3229	2227	2969	1714	2286
SU06 SAM 21.5	62	Calcite	Changhsingian	-7	37	1201	1601	1157	1543	911	1214
SU06 SAM 22.1	61	Calcite	Changhsingian	-6	38	2311	3081	2132	2843	1646	2195
SU06 SAM 24.3	57	Calcite	Changhsingian	-6	41	2515	3353	2304	3072	1770	2360
SU06 SAM 24.4	57	Calcite	Changhsingian	-5	40	2615	3487	2391	3187	1832	2442
04.7.24.d	51	Calcite	Changhsingian	-3	33	3649	4865	3256	4341	2427	3237
04.7.24.d	51	Calcite	Changhsingian	-5	36	2280	3040	2108	2810	1628	2171
04.8.1.ac*	171	Dolomite	Changhsingian	0	49	38417	51222	19694	26258	9238	12317
04.8.1.ac.I	171	Dolomite	Changhsingian	0	49	33490	44653	18246	24328	8852	11803
04.8.1.ac.II	171	Dolomite	Changhsingian	0	49	49013	65351	22294	29725	9869	13159
SU06 KOR 1.10	170	Dolomite	Changhsingian	0	49	45421	60561	21480	28640	9679	12906
SU06 KOR 1.8	170	Dolomite	Changhsingian	0	49	37269	49693	19372	25829	9154	12206
SU06 KOR 1.9	170	Dolomite	Changhsingian	0	49	31396	41862	17575	23433	8664	11552
SU06 KOR 2.1	170	Dolomite	Changhsingian	0	49	34657	46209	18605	24807	8950	11933
SU06 KOR 9.1	165	Dolomite	Changhsingian	0	49	27068	36091	16063	21418	8217	10957

Sample	Section height	Mineral composition	Age	$\delta^{13}C$ (‰,VPDB)	Temp (°C)[a]	Method 1		Method 2		Method 3	
						Sz= 3000 ppmV	Sz= 4000 ppmV	Sz= 3000 ppmV	Sz= 4000 ppmV	Sz= 3000 ppmV	Sz= 4000 ppmV
SU06 KOR 9.2	165	Dolomite	Changhsingian	-1	49	23304	31072	14593	19458	7749	10333
SU06 KOR 9.3	165	Dolomite	Changhsingian	0	49	29566	39422	16957	22609	8485	11314
04.8.1.z	163	Dolomite	Changhsingian	-1	49	20934	27911	13582	18109	7406	9875
SU06 KOR 5.1	163	Dolomite	Changhsingian	0	49	27676	36901	16286	21715	8285	11047
SU06 KOR 5.3	163	Dolomite	Changhsingian	-1	49	19036	25381	12718	16958	7098	9464
SU06 KOR 5.4	163	Dolomite	Changhsingian	-2	49	13066	17422	9635	12846	5867	7822
SU06 KOR 5.5	163	Dolomite	Changhsingian	-1	49	18189	24252	12316	16422	6949	9266
SU06 KOR 6.2	163	Dolomite	Changhsingian	-1	49	15388	20518	10906	14542	6401	8535
SU06 KOR 6.3	163	Dolomite	Changhsingian	-1	49	17051	22734	11759	15678	6738	8983
SU06 KOR 6.4	163	Dolomite	Changhsingian	-2	49	13600	18134	9936	13248	5997	7996
SU06 KOR 6.5	163	Dolomite	Changhsingian	-1	49	14959	19946	10679	14238	6308	8411
SU06 KOR 6.6	163	Dolomite	Changhsingian	-1	49	15537	20716	10984	14646	6432	8577
SU06 KOR 6.7	163	Dolomite	Changhsingian	-1	49	16235	21647	11346	15128	6577	8769
SU06 KOR 6.8	163	Dolomite	Changhsingian	-1	49	17548	23398	12005	16006	6832	9109
SU06 KOR 14.8	154	Dolomite	Changhsingian	-1	49	15645	20860	11041	14721	6455	8607
SU06 KOR 14.9	154	Dolomite	Changhsingian	-1	49	14555	19407	10462	13949	6219	8291
04.8.1.s	154	Dolomite	Changhsingian	-2	49	12886	17182	9532	12709	5822	7762
04.8.1.o	140	Dolomite	Changhsingian	-1	49	19371	25827	12874	17166	7155	9539
SU06 KOR 15.3	140	Dolomite	Changhsingian	-1	49	22558	30077	14283	19044	7646	10195
SU06 KOR 15.4	140	Dolomite	Changhsingian	-1	49	25336	33782	15407	20542	8013	10684
SU06 KOR 15.5	140	Dolomite	Changhsingian	-1	49	21371	28494	13774	18365	7473	9964
SU06 KOR 15.7	140	Dolomite	Changhsingian	-1	49	22086	29448	14082	18777	7578	10104
SU06 KOR 15.9	140	Dolomite	Changhsingian	0	49	26155	34874	15721	20962	8112	10816
SU06 SAM 12.2	114	Dolomite	Changhsingian	-5	49	3404	4539	3038	4050	2281	3041
SU06 SAM 10.6	123	Dolomite	Changhsingian	-4	49	5455	7274	4649	6199	3310	4414

Sample	Section height	Mineral composition	Age	$\delta^{13}C$ (‰,VPDB)	Temp (°C)[a]	Method 1		Method 2		Method 3	
						Sz= 3000 ppmV	Sz= 4000 ppmV	Sz= 3000 ppmV	Sz= 4000 ppmV	Sz= 3000 ppmV	Sz= 4000 ppmV
SU06 SAM 10.5	123	Dolomite	Changhsingian	-4	49	5774	7699	4888	6517	3453	4604
SU06 SAM 10.4	122	Dolomite	Changhsingian	-3	49	6524	8698	5437	7250	3773	5030
SU06 SAM 10.2	122	Dolomite	Changhsingian	-4	49	5458	7277	4651	6201	3311	4415
SU06 SAM 10.1	122	Dolomite	Changhsingian	-4	49	5329	7106	4554	6071	3253	4337
04.7.24.m	102	Dolomite	Changhsingian	-2	49	12352	16470	9223	12297	5685	7580
SU06 SAM 9.3	102	Dolomite	Changhsingian	-5	49	4505	6006	3919	5225	2859	3812
04.7.24.l	98	Dolomite	Changhsingian	-2	49	10060	13413	7829	10439	5034	6712
04.7.24.j	88	Dolomite	Changhsingian	-2	49	9099	12132	7210	9614	4726	6302
SU06 SAM 20.2	88	Dolomite	Changhsingian	-4	49	5744	7659	4865	6487	3440	4587
SU06 SAM 20.5	88	Dolomite	Changhsingian	-4	49	5866	7822	4956	6608	3494	4658
04.7.23.o	33	Dolomite	Changhsingian	-2	49	11826	15768	8913	11884	5545	7393
04.7.23.j	11	Dolomite	Changhsingian	-2	49	13592	18122	9931	13242	5995	7993
04.7.23.h	10	Dolomite	Changhsingian	-3	49	8442	11256	6774	9032	4502	6003
04.7.23.i	10	Dolomite	Changhsingian	-2	49	12381	16508	9240	12320	5692	7590

Appendix 4

Italian dolomite brachiopods and bulk rock isotope results and palaeotemperature estimates

(Chapter 6)

A4.1

Isotope results and palaeotemperature estimates for brachiopods recovered from Val Brutta and Tesero in the Italian Dolomites. Material refers to the part of the specimen sampled: p= prismatic layer of the shell; f = fibrous layer of the shell; m = micrite associated with the shell. Cl luminescence: NL= Non-Luminescent; NL+SL= Non-Luminescent with Slightly Luminescent; L+SNL= Luminescent and Slightly Non- Luminescent shells; L= those areas that were completely luminescent (see Chapter 2 for fuller description) Palaeotemperature A was calculated using equation 6.1 and Palaeotemperature B was calculated using equation 6.2 (see Chapter 6). All collations were performed at a $\delta^{18}O$ seawater of 0.0‰ (VSMOW). Fossil identifications based on Posenato (2001) for Val Brutta and Chen *et al.* (2006) for Tesero. Note that the CL analysis for TS1 was undertaken by Nikita Jacobsen (unpublished data).

Fossil	Taxon	Drill site	From outer to inner part of the shell (mm)	Material	CL luminescence	Discounted because	Date run	$\delta^{13}C$ (‰,VPDB)	$\delta^{18}O$ (‰,VPDB)	Temp A (°C)	Temp B (°C)
VB1	*Comelicania? Sp.*	Bulk		m	L	CL	02/03/07	2.18	-5.68		
VB1		ii	4	p	NL+SNL	CL	02/03/07	4.22	-2.33		
VB1		iii	3	p	NL+SNL	CL	02/03/07	3.19	-2.82		
VB1		iv	1.9	p	NL+SNL	CL	02/03/07	4.09	-2.31		
VB1		v	0.6	f	L+SNL	CL	02/03/07	3.19	-4.30		
VB1		vi	2.1	p	NL		02/03/07	3.96	-2.83	30	29
VB1		vii	1.4	p	NL		02/03/07	4.38	-1.87	25	24
VB1		viii	0.6	f	NL		02/03/07	3.25	-2.73	29	28
VB1		ix	1.4	p	NL		02/03/07	3.82	-2.80	30	29
VB1		x	0.9	p	NL		02/03/07	4.35	-1.95	25	25
VB2	*Janiceps aff.paracuta.*	Bulk		m	L	CL	12/07/07	2.02	-6.16		
VB2		i	0.4	f	NL		12/07/07	0.96	-2.64	29	28
VB2		ii	1.5	p	NL+SNL	CL	12/07/07	4.27	-2.20		
VB2		iii	2	p	NL+SNL	CL	12/07/07	4.09	-1.81		
VB2		iv	1.8	p	NL		12/07/07	1.94	-2.48	28	27
VB2		v	1.1	p	NL		12/07/07	3.45	-1.81	25	24
VB2		vi	0.4	f	NL		12/07/07	3.63	-2.33	27	26
VB2		vii	0.4	f	NL		12/07/07	1.48	-3.29	32	31
VB2		viii	1	f	NL		12/07/07	2.82	-3.63	34	33
VB3	*Comelicania? Sp.*	Bulk		m	L	CL + TRACE	02/03/07	2.49	-5.62		

Fossil	Taxon	Drill site	From outer to inner part of the shell (mm)	Material	CL luminescence	Discounted because	Date run	$\delta^{13}C$ (‰,VPDB)	$\delta^{18}O$ (‰,VPDB)	Temp A (°C)	Temp B (°C)
VB3		i	7.8	p	L+SNL	CL + TRACE	02/03/07	3.79	-1.86		
VB3		ii	6.8	p	L+SNL	CL + TRACE	02/03/07	4.18	-1.47		
VB3		iii	5.4	p	L+SNL	CL + TRACE	02/03/07	3.60	-1.96		
VB3		iv	3.7	p	L+SNL	CL + TRACE	02/03/07	2.15	-2.30		
VB3		v	2.2	p	L+SNL	CL + TRACE	02/03/07	4.32	-2.29		
VB3		vi	0.9	p	L+SNL	CL + TRACE	02/03/07	4.07	-1.91		
VB3		viii	7.1	p	NL+SNL	CL + TRACE	02/03/07	3.29	-1.74		
VB3		x	3.7	p	NL+SNL	CL + TRACE	02/03/07	2.79	-2.02		
VB3		xi	2.5	p	NL+SNL	CL + TRACE	02/03/07	3.43	-3.76		
VB3		xii	1.4	p	NL+SNL	CL + TRACE	02/03/07	3.74	-2.03		
VB4	*Comelicania? Sp.*	Bulk		m	L	CL	12/07/07	2.00	-4.35		
VB4		i	0.5	p	L+SNL	CL	12/07/07	4.01	-1.68		
VB4		ii	1.6	f	NL+SNL	CL	12/07/07	3.36	-2.09		
VB4		iii	1.1	p	NL+SNL	CL	12/07/07	4.04	-2.13		
VB4		iv	0.6	p	NL+SNL	CL	12/07/07	3.67	-2.03		
VB4		v	0.7	p	NL+SNL	CL	12/07/07	3.82	-2.14		
VB4		vi	0.4	p	NL+SNL	CL	12/07/07	3.38	-2.20		
VB5	*Janiceps sp.*	Bulk		m	L	CL	12/07/07	2.50	-6.74		
VB5		i	4.8	p	NL+SNL	CL	12/07/07	5.05	-2.12		
VB5		ii	1.1	p	L+SNL	CL	12/07/07	4.40	-3.42		
VB5		iii	2.5	p	NL+SNL	CL	12/07/07	5.12	-1.73		
VB5		iv	0.8	f	NL		12/07/07	4.26	-2.17	27	26
VB5		v	4.1	p	NL		12/07/07	5.13	-1.91	25	24
VB5		vii	7.1	p	NL		12/07/07	4.78	-2.31	27	26
VB5		viii	10.2	p	NL		12/07/07	4.17	-2.67	29	28
VB5		ix	12.9	p	NL		12/07/07	4.28	-2.64	29	28
VB6	*Comelicania? Sp*	Bulk			L	CL + TRACE	02/03/07	2.58	-4.67		
VB6		i	0.6	p	NL		02/03/07	2.63	-3.17	31	30
VB6		ii	2	p	NL		02/03/07	2.97	-1.93	25	24
VB6		iii	1	p	NL		02/03/07	3.63	-1.97	26	25
VB6		iv	2	p	NL		02/03/07	3.27	-1.77	25	24
VB6		v	3.5	p	NL+SNL	CL	02/03/07	2.63	-3.17		

Fossil	Taxon	Drill site	From outer to inner part of the shell (mm)	Material	CL luminescence	Discounted because	Date run	$\delta^{13}C$ (‰,VPDB)	$\delta^{18}O$ (‰,VPDB)	Temp A (°C)	Temp B (°C)
VB6		vii	1.8	p	NL+SNL	CL	02/03/07	3.84	-1.74		
VB6		viii	0.6	p	NL+SNL	CL	02/03/07	3.02	-2.11		
VB6		ix	0.4	f	NL+SNL	CL	02/03/07	2.96	-2.15		
TS1	*Orbicoelia dolomitensis.*	Bulk			L		12/07/07	1.09	-6.86		
TS1		i	2.8	p	NL		12/07/07	1.29	-3.82	35	34
TS1		ii	4.1	p	NL		12/07/07	1.31	-4.59	39	38
TS1		iii	5.5	p	NL+SNL		12/07/07	1.13	-5.25		
TS1		v	8.3	p	NL		12/07/07	1.74	-3.74	34	33
TS1		vii	11.0	p	NL+SNL		12/07/07	1.25	-5.93		

A4.2

Bulk rock isotope results from Val Brutta results from across the P/Tr boundary.

Sample number	Strat. height with respect to the PTB (m)	Lithology	Date run	$\delta^{13}C$ (‰, VPDB)	$\delta^{18}O$ (‰, VPDB)
TKD_VB_2_35	-6.86	Grey blocky micrite	18/01/07	3.51	-0.68
TKD_VB_2_36	-6.76	Grey blocky micrite	18/01/07	3.09	-0.77
TKD_VB_2_37	-6.66	Grey blocky micrite	18/01/07	2.87	-1.35
TKD_VB_2_38	-6.56	Blocky white micrite	18/01/07	2.97	-0.68
TKD_VB_2_39	-6.46	Blocky white micrite	18/01/07	3.23	-1.01
TKD_VB_2_40	-6.36	Blocky white micrite	18/01/07	3.31	-0.76
TKD_VB_2_41	-6.26	Burrowed mottled wackestone	18/01/07	3.54	-0.88
TKD_VB_2_42	-6.16	Burrowed mottled wackestone	18/01/07	3.35	-1.00
TKD_VB_2_43	-6.06	Burrowed mottled wackestone	18/01/07	3.35	-0.77
TKD_VB_2_44	-5.96	Burrowed mottled wackestone	18/01/07	3.39	-0.94
TKD_VB_2_45	-5.86	Burrowed mottled wackestone	18/01/07	3.45	-0.90
TKD_VB_2_46	-5.14	Grey clay	18/01/07	3.30	-1.35
TKD_VB_2_47	-5.04	Recrystallised micrite	18/01/07	3.44	-1.85
TKD_VB_2_48	-3.98	Grey burrowed recrystallised micrite	18/01/07	3.12	-1.53
TKD_VB_2_49	-3.88	Grey burrowed recrystallised micrite	18/01/07	2.94	-1.17
TKD_VB_2_50	-3.8	Grey burrowed recrystallised micrite	18/01/07	2.91	-1.25
TKD_VB_2_51	-3.7	Grey burrowed recrystallised micrite	18/01/07	2.70	-1.26
TKD_VB_2_52	-3.6	Grey burrowed recrystallised micrite	18/01/07	2.09	-1.87
TKD_VB_2_53	-3.5	Grey burrowed recrystallised micrite	18/01/07	2.04	-1.69
TKD_VB_2_54	-3.4	Grey burrowed recrystallised micrite	18/01/07	2.52	-1.36
TKD_VB_2_55	-3.3	Cream recrystallised micrite	18/01/07	2.81	-1.64
TKD_VB_2_56	-3.2	White blocky burrowed micrite	18/01/07	2.91	-1.63
TKD_VB_2_57	-3.1	Grey with plant fragments	18/01/07	2.88	-1.31
TKD_VB_2_58	-3	White recrystallised micrite	18/01/07	3.09	-1.29
TKD_VB_2_59	-2.9	White recrystallised micrite	18/01/07	2.91	-1.53
TKD_VB_2_60	-2.83	White recrystallised micrite	18/01/07	2.35	-1.11
TKD_VB_2_61	-2.71	White recrystallised micrite	18/01/07	2.36	-0.93
TKD_VB_2_63	-2.62	Thinly bedded clay rich micrite	18/01/07	2.45	-0.91
TKD_VB_2_62	-2.61	White recrystallised micrite	18/01/07	1.99	-1.69
TKD_VB_2_64	-2.43	Thinly bedded clay rich micrite	18/01/07	2.32	-0.91
TKD_VB_2_87	-1.33	Bioturbated, recrystallised wackestone	18/01/07	2.11	-2.49
TKD_VB_2_65	-1.19	Bioturbated, recrystallised wackestone	18/01/07	2.13	-1.25
TKD_VB_2_66	-0.99	Clay micrite	18/01/07	2.61	-1.93
TKD_VB_2_67	-0.91	Dark grey clay	18/01/07	2.82	-1.18
TKD_VB_2_68	-0.81	Grey recrystallised wackestone	18/01/07	2.87	-0.74
TKD_VB_2_69	-0.68	Nodular grey recrystallised wackestone	18/01/07	1.55	-1.29
TKD_VB_2_89	-0.68	Nodular grey recrystallised wackestone	18/01/07	1.64	-1.53
TKD_VB_2_90	-0.61	Recrystallised wackestone/packstone	18/01/07	0.83	-3.62
TKD_VB_2_70	-0.59	Recrystallised wackestone/packstone	18/01/07	1.69	-1.95
TKD_VB_2_71	-0.5	Recrystallised wackestone/packstone	18/01/07	0.49	-4.02
TKD_VB_2_91	-0.43	Recrystallised wackestone/packstone	18/01/07	2.17	-3.87
TKD_VB_2_72	-0.4	Recrystallised wackestone/packstone	18/01/07	-2.14	-4.39
TKD_VB_2_73	-0.31	Bioclastic 'wavy' packstone	18/01/07	1.78	-3.97
TKD_VB_2_74	-0.2	Bioclastic 'wavy' packstone	18/01/07	2.96	-4.45
TKD_VB_2_78	-0.1	Bioclastic 'wavy' packstone	18/01/07	1.89	-3.60
TKD_VB_2_76	-0.01	Bioclastic 'wavy' packstone	18/01/07	2.10	-3.86
TKD_VB_2_92	-0.01	Oolitic stylolitic packstone	18/01/07	1.45	-4.27

Sample number	Strat. height with respect to the PTB (m)	Lithology	Date run	$\delta^{13}C$ (‰, VPDB)	$\delta^{18}O$ (‰, VPDB)
TKD_VB_2_82	0.05	Oolitic stylolitic packstone	18/01/07	1.16	-3.91
TKD_VB_2_84	0.14	Oolitic stylolitic packstone	18/01/07	1.14	-4.08
TKD_VB_2_94	0.16	Oolitic stylolitic packstone	18/01/07	0.97	-5.41
TKD_VB_2_85	0.23	Oolitic packstone	18/01/07	0.66	-2.95
TKD_VB_2_86	0.34	Oolitic stylolitic packstone	18/01/07	1.78	-3.29
TKD_VB_2_95	0.36	Oolitic packstone	18/01/07	1.53	-3.89
TKD_VB_2_96	0.41	Oolitic stylolitic packstone	18/01/07	1.01	-4.21
TKD_VB_2_97	0.51	Oolitic stylolitic packstone	18/01/07	0.69	-5.70
TKD_VB_2_98	0.61	Oolitic stylolitic packstone	18/01/07	0.17	-4.75
TKD_VB_2_99	0.71	Oolitic stylolitic packstone	21/01/07	0.29	-4.43
TKD_VB_2_100	0.79	Oolitic stylolitic packstone	21/01/07	0.71	-4.67
TKD_VB_2_101	0.91	Oolitic stylolitic packstone	21/01/07	1.07	-4.27
TKD_VB_2_102	1.01	Oolitic stylolitic packstone	21/01/07	0.78	-3.93
TKD_VB_2_103	1.11	Oolitic stylolitic packstone	21/01/07	0.67	-4.41
TKD_VB_2_104	1.21	Oolitic stylolitic packstone	21/01/07	0.72	-4.49
TKD_VB_2_105	1.29	Oolitic stylolitic packstone	21/01/07	0.96	-4.41
TKD_VB_2_106	1.37	Oolitic stylolitic packstone	21/01/07	0.96	-4.68
TKD_VB_2_107	1.47	Oolitic stylolitic packstone	21/01/07	0.85	-4.97
TKD_VB_2_108	1.61	Oolitic stylolitic packstone	21/01/07	0.84	-4.50
TKD_VB_2_109	1.71	Oolitic stylolitic packstone	21/01/07	0.97	-4.83
TKD_VB_2_110	1.81	Oolitic stylolitic packstone	21/01/07	1.11	-4.56
TKD_VB_2_111	1.91	Oolitic stylolitic packstone	21/01/07	0.98	-4.96
TKD_VB_2_112	1.94	Oolitic stylolitic packstone	21/01/07	0.77	-4.74
TKD_VB_2_113	2.05	Oolitic stylolitic packstone	21/01/07	1.02	-5.22
TKD_VB_2_114	2.21	Oolitic stylolitic packstone	21/01/07	0.54	-5.11
TKD_VB_2_115	2.29	Oolitic stylolitic packstone	21/01/07	0.91	-5.78
TKD_VB_2_116	2.45	Oolitic stylolitic packstone	21/01/07	0.62	-5.35
TKD_VB_2_117	2.52	Oolitic stylolitic packstone	21/01/07	0.74	-5.77
TKD_VB_2_118	2.73	Oolitic stylolitic packstone	21/01/07	0.26	-5.92
TKD_VB_2_119	2.8	Oolitic stylolitic packstone	21/01/07	0.30	-4.92
TKD_VB_2_120	2.9	Oolitic stylolitic packstone	21/01/07	0.81	-4.76
TKD_VB_2_121	3.01	Oolitic stylolitic packstone	21/01/07	-0.41	-5.15
TKD_VB_2_122	3.11	Oolitic stylolitic packstone	21/01/07	-0.14	-5.48
TKD_VB_2_123	3.18	Oolitic stylolitic packstone	21/01/07	0.07	-4.86
TKD_VB_2_124	3.3	Oolitic stylolitic packstone	21/01/07	0.62	-5.33
TKD_VB_2_125	3.4	Oolitic stylolitic packstone	21/01/07	0.20	-5.67
TKD_VB_2_126	3.5	Oolitic stylolitic packstone	21/01/07	0.38	-5.39
TKD_VB_2_127	3.6	Oolitic stylolitic packstone	21/01/07	0.21	-5.80
TKD_VB_2_128	3.7	Oolitic stylolitic packstone	21/01/07	0.58	-5.64
TKD_VB_2_129	3.79	Oolitic stylolitic packstone	21/01/07	0.16	-5.53
TKD_VB_2_130	3.89	Oolitic stylolitic packstone	21/01/07	0.20	-5.42
TKD_VB_2_131	3.99	Oolitic stylolitic packstone	21/01/07	0.35	-4.93
TKD_VB_2_132	4.07	Oolitic stylolitic packstone	21/01/07	0.51	-5.33
TKD_VB_2_133	4.17	Oolitic stylolitic packstone	21/01/07	0.65	-5.58
TKD_VB_2_134	4.27	Oolitic stylolitic packstone	21/01/07	0.38	-5.60

A4.3

Cross plots and isotopic variation across the shell for all the brachiopods analyzed in this study

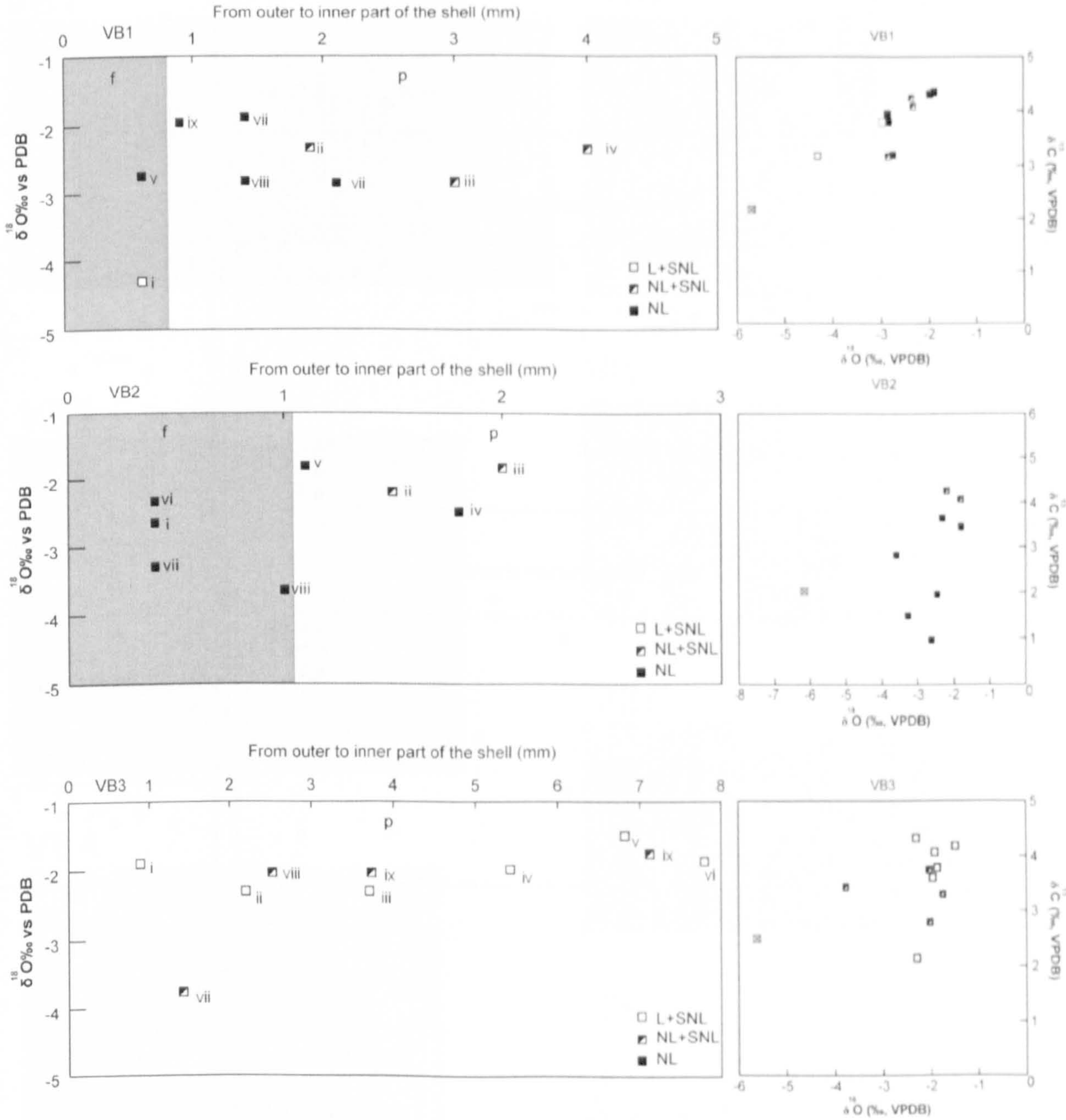

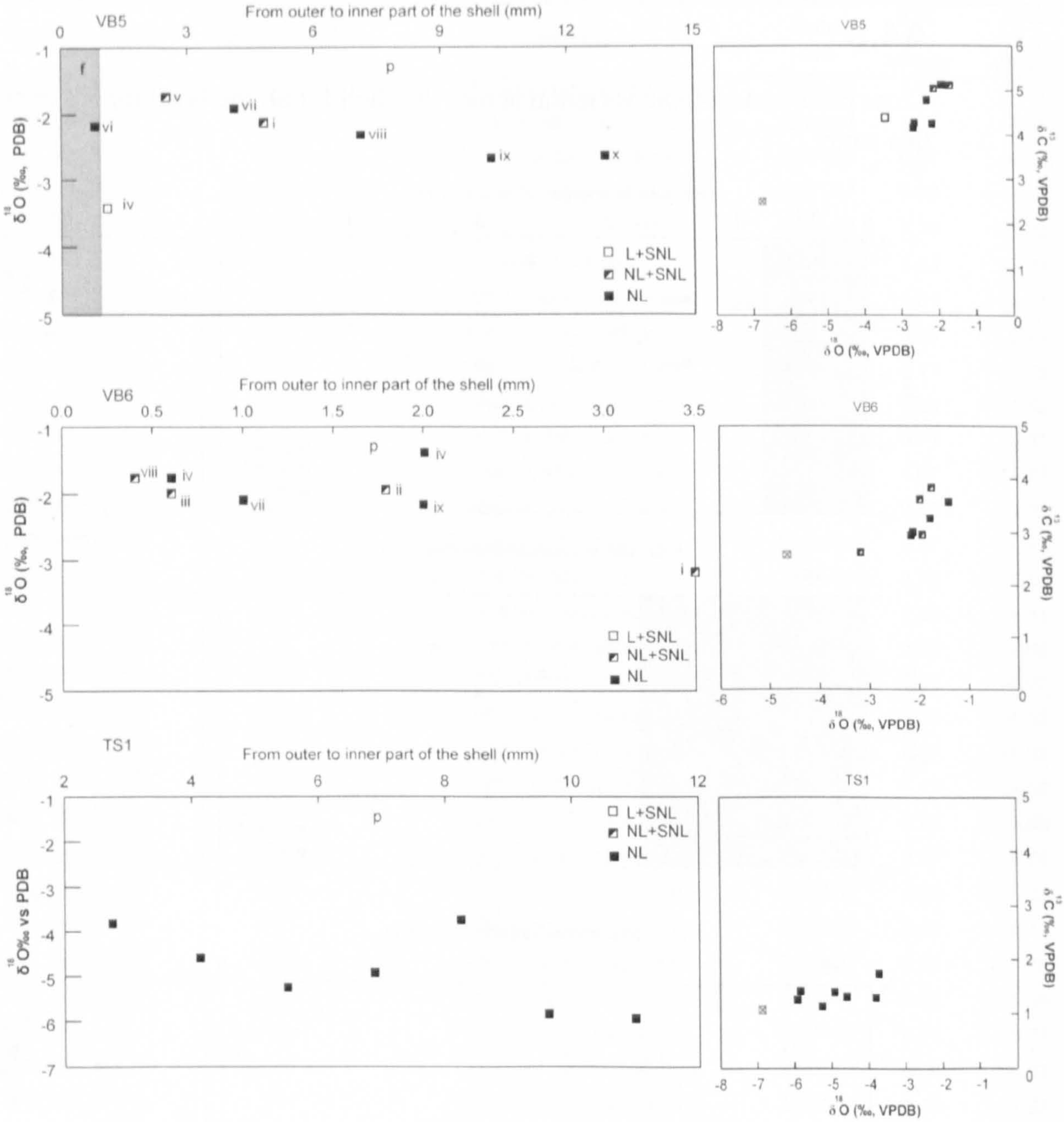
VB5
From outer to inner part of the shell (mm)
f
p
vi
v
vii
i
viii
ix
x
iv
L+SNL
NL+SNL
NL
δ18O (‰, PDB)
δ13C (‰, VPDB)
δ18O (‰, VPDB)
VB6
From outer to inner part of the shell (mm)
p
viii
iv
iii
vii
ii
iv
ix
i
L+SNL
NL+SNL
NL
δ18O (‰, PDB)
δ13C (‰, VPDB)
δ18O (‰, VPDB)
TS1
From outer to inner part of the shell (mm)
p
L+SNL
NL+SNL
NL
δ18O‰ vs PDB
δ13C (‰, VPDB)
δ18O (‰, VPDB)

A4.4

Isotope drill sites, with ornament showing the CL results from each drill site.

VB1

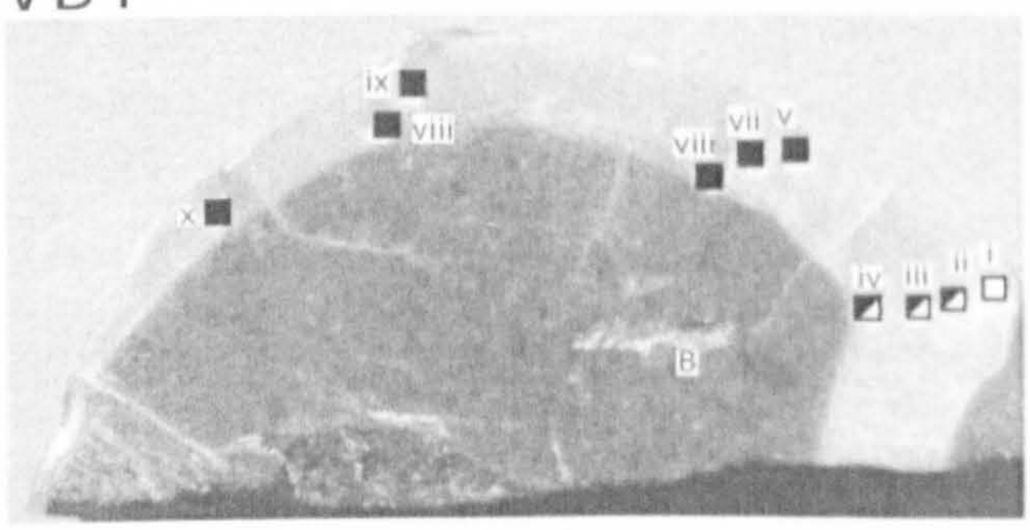

10mm

VB2

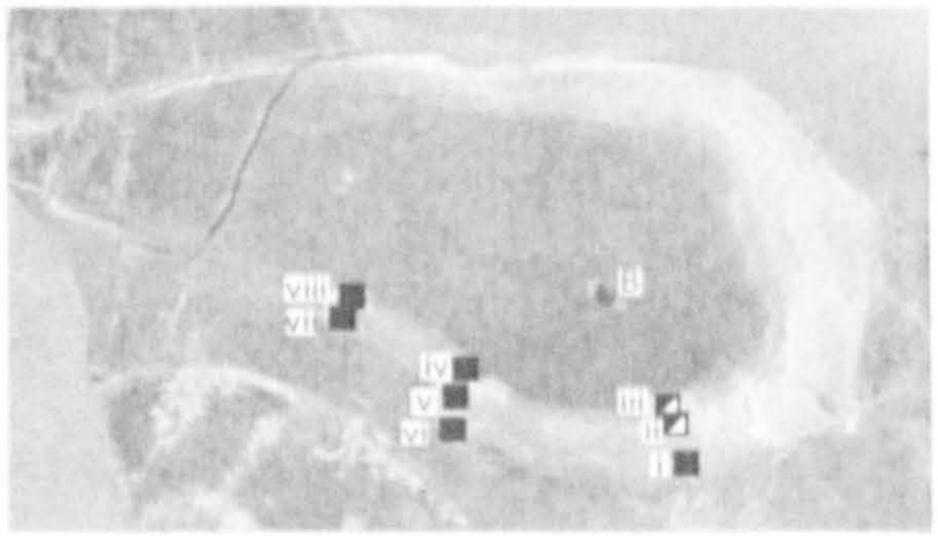

10mm

VB3

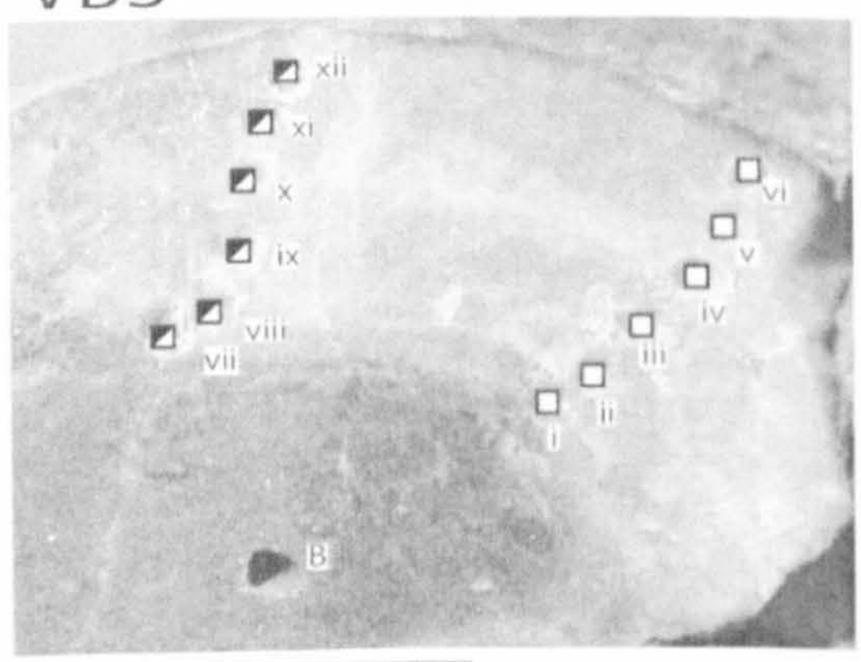

10mm

VB4

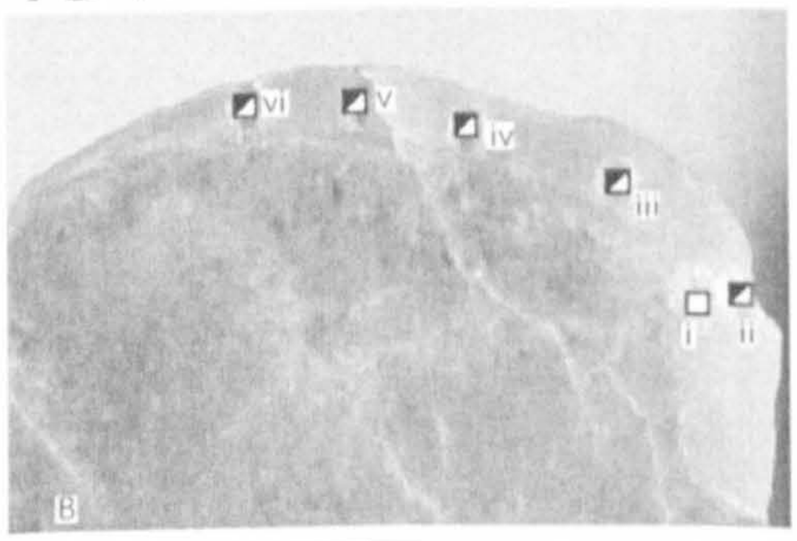

10mm

VB5

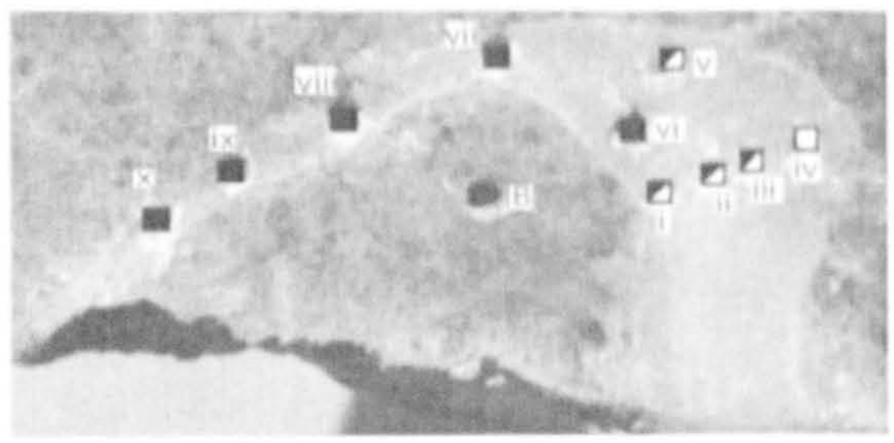

10mm

VB6

10mm

TS1

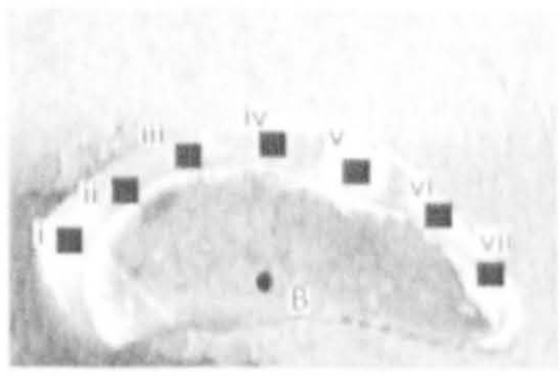

10mm

Appendix 5

A study of the effects of diagenetic dolomitisation on the isotopic composition of paleosols from the Italian Dolomites (Chapter 4)

1.1 Introduction

To investigate the effect diagenetic dolomitisation on pedogenic carbonates and their isotopic composition diagenetically altered paleosols from the Italian Dolomites were studied. This locality is close to Sass di Putia at Rü D'Antermeia (N 46°40.320', E011°49.366'). The section investigated is a Permian section of paleosols from the Val Grade formation and sits unconformably on the Hercynian metamorphic basement (Broglio Loriga *et al.* 1986). The Italian Dolomites region has been affected by a low-pressure-high-temperature metamorphic regime (Schuster and Stüwe 2008) and thus an excellent case study for as studying the effects of alteration on the isotopic signal of a paleosol. This provides also a direct comparison to the pedogenic and lacustrine dolomites from the South Urals of Russia.

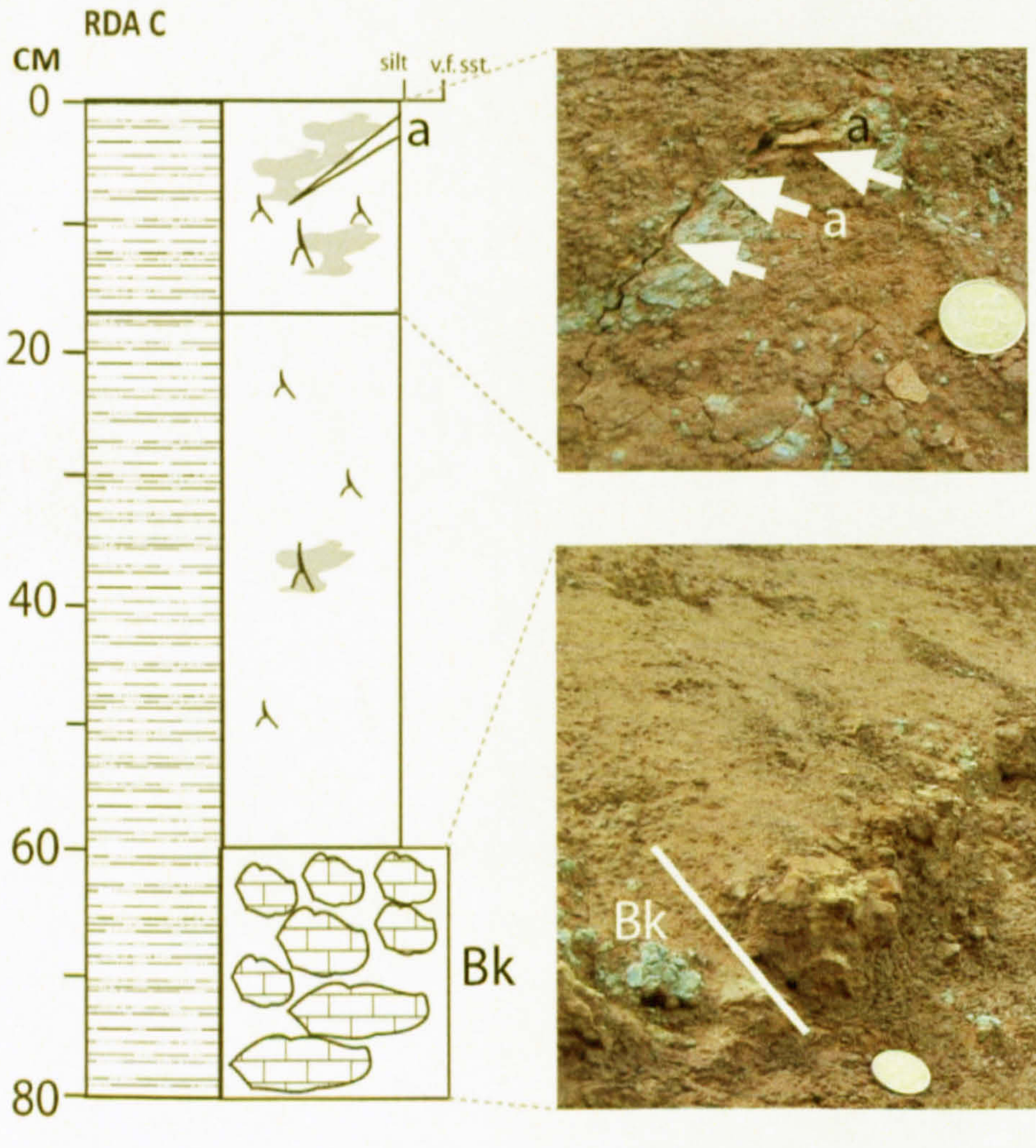

Figure 1 Typical paleosol from Rü D'Antermeia. (a) is a thin 2mm thick calcite vain cutting though the top of the soil.

1.2 Paleosols

In total 10 paleosols were identified at this locality. All contained pedogenic carbonate at stage II nodule development. The paleosols were all pale reddish brown (10R 5/4) in colour although many of the soils had pale blue green (5BG 7/2) mottled A horizons. These gleys are concentrated in the very top of the paleosols although some are drab root halos (Figure 1). The only field evidence of later alteration or recrystallisation are occasional fine carbonate veins 2mm in width. Which are filled with a fibrous calcite spar and are only present in the very top of the paleosols (Figure 1). Bases on the depth to the Bk horizon and the presence of nodular carbonate they classified as Aridisols or Petronodic Haplocalcids (see Chapter 3 for classification scheme).

1.3 Petrographic evidence of recrystallisation

Although the paleosols in the field do not appear to be intensely altered by later diagenesis, when the nodules are petrographically thin sectioned it is evident that the majority of the carbonate has been recrystallised.

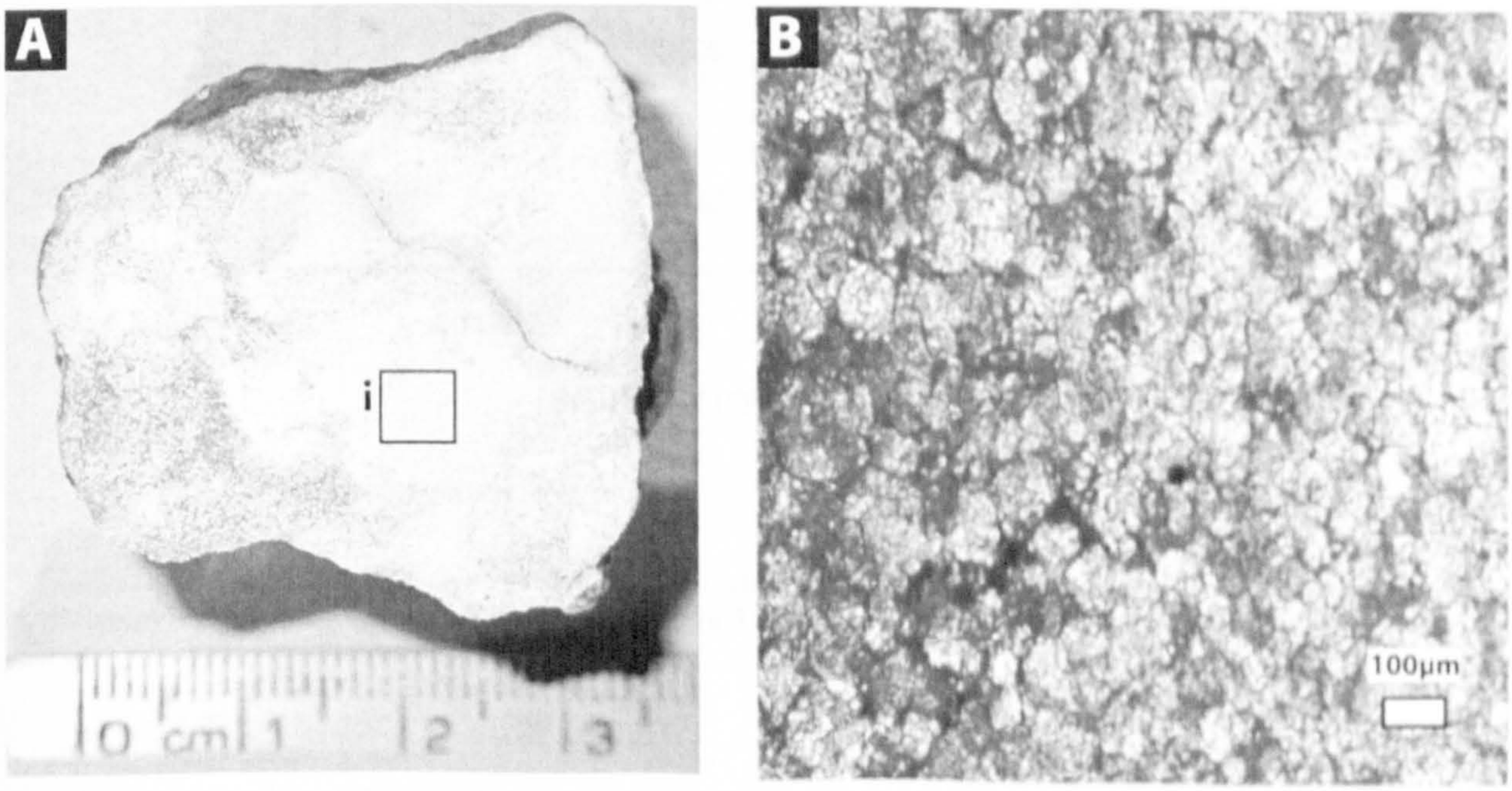

Figure 2 (A) shows the saccharoidal texture of the carbonate material within a nodule. (B) shows a petrographic thin section of area (i) showing the equigranular nature of the crystals (B has been stained with Dixons stain and shows no reaction suggesting it is dolomite).

Figure 2 shows the extent of the recrystallisation in the nodules. The dolomite crystals all are equigranular and show interlocking structures. This is similar to the Micro- to coarsely

crystalline, rhombohedral dolomites described by Quast *et al.* (2006) which they ascribe to burial and recrystallisation textures.

1.4 Isotopic results

Stable isotope analysis was carried out on 30 carbonate nodules. The carbonate material was divided into microcrystalline (crystal size ≤100μm) and spar (crystal size >100 μm). Figure 3 shows the results from the analysis (values see Table 1). Unlike the pedogenic carbonates from Russia there is no positive correlation between $\delta^{13}C_{carb}$ and $\delta^{18}O_{carb}$ (compare with Chapter 4, Figure 4.16) also while there is a wide range of $\delta^{18}O_{carb}$ values the $\delta^{13}C_{carb}$ values are restricted to a 2‰ range.

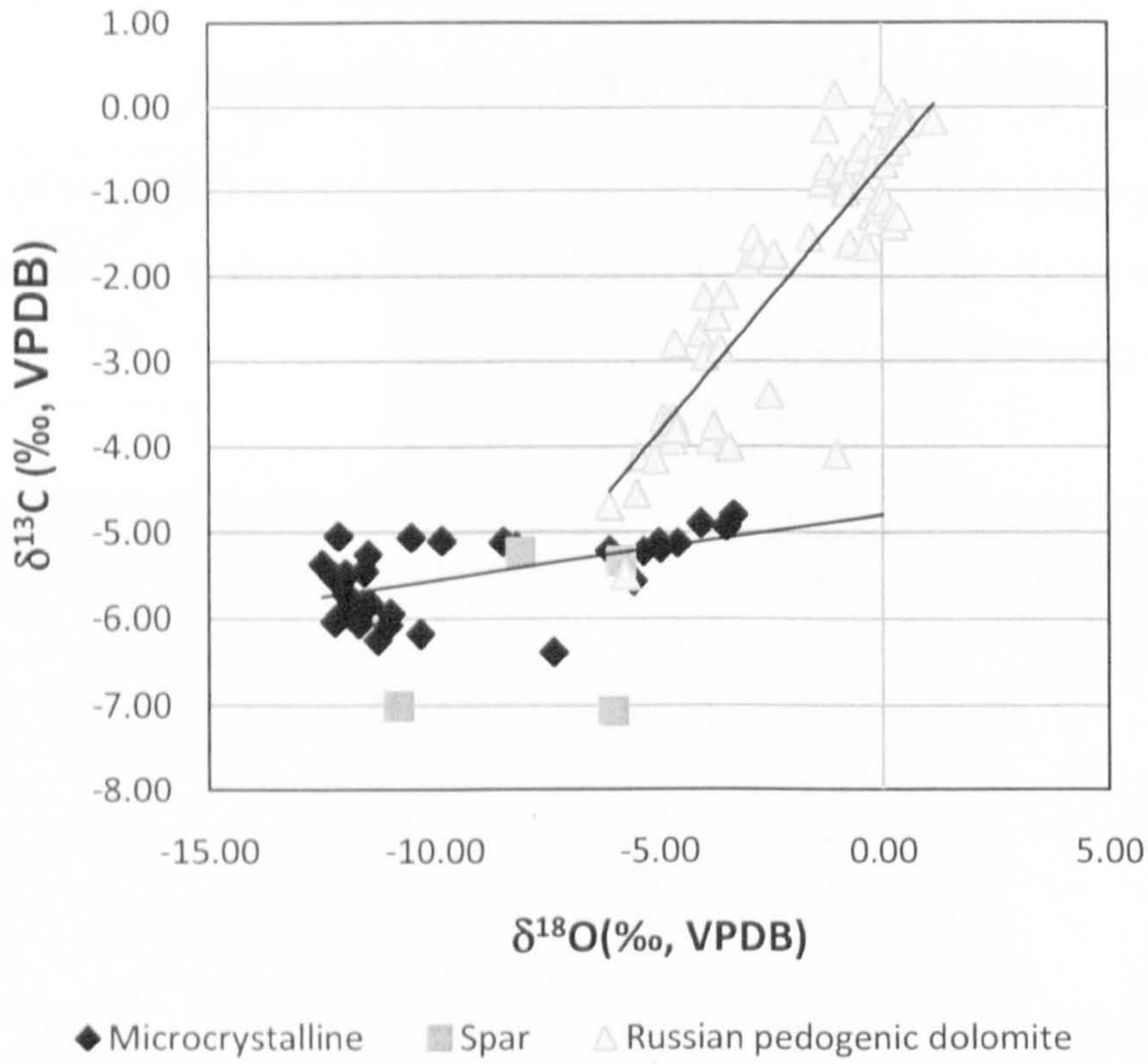

Figure 3 Cross plot of the isotopic results from Rü D'Antermeia. Microcrystalline (crystal size ≤100μm, blue diamonds) and spar (crystal size >100 μm, red squares). Compared against the pedogenic dolomite values from the Russian sections (in grey triangles).

There is no distinct difference between the fine (microcrystalline) dolomite and the large spar crystals suggesting the recrystallisation event effected different grain sizes in the similar ways. Other studies into recrystallisation in paleosols (e.g. Quast *et al.* 2006) have observed that diagenetically altered paleosol carbonates show little isotopic difference between the microcrystalline and spar component of a paleosol. Equally it appears that recrystallisation destroys the positive correlation between oxygen and carbon, restricting the carbon range, and

although the oxygen range is still similar to that from modern soils (Cerling and Quade 1993) there is no way of determining if these too have altered from their original composition.

Table 1 Isotopic and classification of paleosols from Rü D'Antermeia

Classification	Calcrete stage	Depth to Bk horizon (cm)	Sample	Section height (m)	Paleosol depth (m)	Texture	microcrystalline areas ≤100µm		Spar	
							$\delta^{13}C‰$ VPDB	$\delta^{18}O‰$ VPDB	$\delta^{13}C‰$ VPDB	$\delta^{18}O‰$ VPDB
Aridisol	II / III	eroded	07RDA A.2	16.36	8	MCR	-5.18	-8.17	–	–
			07RDA A.3	16.22	22	MCR	-6.38	-7.34	–	–
			07RDA A.4	16.04	40	MCR	-5.19	-4.96	–	–
Vertisol?	II	70	07RDA C.1	22.07	258	MCR	–	–	-5.24	-8.07
			07RDA C.2	22.83	182	MCR	-6.17	-10.30	–	–
			07RDA C.3	22.83	182	MCR	-6.07	-11.02	–	–
			07RDA C.4	23.18	147	MCR	-5.13	-4.58	–	–
Aridisol	II	59	07RDA D.1	23.98	67	MCR	-5.12	-4.98	-5.34	-5.84
			07RDA D.2	23.98	67	MCR	-5.23	-5.33	–	–
			07RDA D.3	23.9	75	MCR	-5.22	-6.09	–	–
			07RDA D.4	23.9	75	MCR	-4.80	-3.33	–	–
Aridisol	II	119	07RDA E.1	24.86	277	MCR	-4.93	-3.49	–	–
			07RDA E.2	26.41	122	MCR	-5.46	-11.56	–	–
			07RDA E.3	26.41	122	MCR	-5.94	-10.96	–	–
			07RDA E.4	26.09	154	MCR	–	–	–	–
			07RDA E.5	27.03	60	MCR	-5.12	-8.46	–	–
			07RDA E.5a	27.02	61	MCR	-5.49	-11.96	–	–
Aridisol	II	56	07RDA F.3	28.1	222	MCR	-5.10	-9.82	–	–
			07RDA F.4	28.1	222	Spa	-5.72	-11.94	-7.07	-6.02
Aridisol	II	70	07RDA G.1	29.58	74	MCR	-6.05	-11.68	–	–
			07RDA G.2	28.87	145	MCR	-5.38	-12.48	–	–
			07RDA G.3	28.87	145	MCR	-5.05	-12.12	–	–

Classification	Calcrete stage	Depth to Bk horizon (cm)	Sample	Section height (m)	Paleosol depth (m)	Texture	microcrystalline areas ≤100µm		Spar	
							$\delta^{13}C$‰ VPDB	$\delta^{18}O$‰ VPDB	$\delta^{13}C$‰ VPDB	$\delta^{18}O$‰ VPDB
Aridisol	II	32	07RDA H.1	32.8	91	MCR	-5.82	-11.44	–	–
			07RDA H.2	32.63	108	MCR	-6.03	-12.20	–	–
			07RDA H.3	32.63	108	MCR	-6.24	-11.25	–	–
			07RDA H.4	32.61	110	MCR	-5.95	-12.07	–	–
Aridisol	II		07RDA I.3	32.93	78	Spa	-5.83	-11.59	-7.01	-10.79
			07RDA I.4	32.93	78	MCR	-5.53	-12.19	–	–
			07RDA I.5	32.87	84	MCR	-5.26	-11.47	–	–
			07RDA I.6	32.87	84	MCR	-5.49	-11.97	–	–